Measurements of differential cross sections for $t\bar{t}$ production in proton-proton collisions at $\sqrt{s} = 13$ TeV using events containing two leptons with the CMS experiment

Dissertation

zur Erlangung des Doktorgrades
an der Fakultät für Mathematik, Informatik und Naturwissenschaften
Fachbereich Physik
der Universität Hamburg

vorgelegt von

Mykola Savitskyi
aus Slavuta, Ukraine

Hamburg
2018

Gutachterinnen der Dissertation:	Dr. Maria Aldaya Martin Prof. Dr. Elisabetta Gallo
Zusammensetzung der Prüfungskommission:	Dr. Maria Aldaya Martin Prof. Dr. Elisabetta Gallo Prof. Dr. Dieter Horns Prof. Dr. Gudrid Moortgat-Pick Dr. Christian Sander
Vorsitzender der Prüfungskommission:	Prof. Dr. Dieter Horns
Datum der Disputation:	18.06.2018
Vorsitzender Fach-Promotionsausschusses PHYSIK:	Prof. Dr. Wolfgang Hansen
Leiter des Fachbereichs PHYSIK:	Prof. Dr. Michael Potthoff
Dekan der Fakultät MIN:	Prof. Dr. Heinrich Graener

I dedicate this thesis to my loving family . . .

Abstract

This work presents measurements of the normalized and absolute differential top-quark pair ($t\bar{t}$) production cross sections in proton-proton collisions at a centre-of-mass energy of 13 TeV. The data were collected by the CMS experiment at the CERN LHC in 2016 and correspond to an integrated luminosity of 35.9 fb^{-1}. The measurements are performed using events with two oppositely charged leptons (e^+e^-, $\text{e}^\pm\mu^\mp$, $\mu^+\mu^-$). The differential cross sections are measured as a function of kinematic observables of the top quarks, the $t\bar{t}$-system, and the top quark decay products, as well as of the jet multiplicity in the event. Differential measurements are based on an event counting method and involve a regularized unfolding technique to correct the reconstructed distributions for acceptance and detector effects. Depending on the observable, differential cross sections are presented in the full phase space at parton level and/or in a fiducial phase space at particle level. The results are compared to standard model predictions from Monte Carlo generators at next-to-leading-order accuracy in QCD, based on matrix element level interfaced to parton shower simulations. None of the predictions provide a uniformly good description of data for all measured distributions. In particular, a substantial disagreement is observed between data and predictions for the transverse momentum distributions of top quarks and their decay products. Measured differential cross sections are used to extract the $t\bar{t}$ and leptonic charge asymmetries, and, for the first time at 13 TeV, to constrain the top quark chromomagnetic dipole moment in an effective field theory.

Zusammenfassung

In dieser Arbeit werden Messungen normalisierter und absoluter differenzieller Wirkungsquerschnitte der Top-Quark-Paarproduktion ($t\bar{t}$) bei Proton-Proton-Kollisionen mit einer Schwerpunktsenergie von 13 TeV vorgestellt. Die Daten wurden im Jahr 2016 vom CMS-Experiment am LHC (CERN) aufgezeichnet und entsprechen einer integrierten Luminosität von 35.9 fb^{-1}. Grundlage der Messungen sind Kollisionsereignisse mit zwei unterschiedlich geladenen Leptonen (e^+e^-, $\text{e}^\pm\mu^\mp$, $\mu^+\mu^-$). Differenzielle Wirkungsquerschnitte werden als Funktionen kinematischer Observablen der Top-Quarks, des $t\bar{t}$-Systems und der Top-Quark-Zerfallsprodukte sowie der jet-Multiplizität im Ereignis gemessen. Differenzielle Messungen basieren auf der Zählung von Ereignissen und bedienen sich regularisierter Entfaltungstechniken zur Korrektur der rekonstruierten Verteilungen der Akzeptanz und anderer Eigenschaften der Detektoren. Abhängig von der betrachteten Observable werden differenzielle Wirkungsquerschnitte im gesamten Phasenraum auf Partonebene und/oder im Selektionsphasenraum auf Teilchenebene dargestellt. Die Ergebnisse werden mit Vorhersagen des Standardmodells verglichen basierend auf Monte Carlo-Generatoren mit NLO-Genauigkeit in QCD auf Matrixelementebene und anschliessender Simulation der Partonschauer. Keine der Vorhersagen beschreibt alle experimentell gemessenen Verteilungen mit einheitlicher Güte. Insbesondere ist eine deutliche Unstimmigkeit zwischen Daten und Vorhersagen hinsichtlich der Verteilung des Transversalimpulses der Top-Quarks und ihrer Zerfallsprodukte beobachtbar. Aus den gemessenen differenziellen Wirkungsquerschnitten werden $t\bar{t}$ und leptonische Ladungsasymmetrien abgeleitet und – erstmals für Schwerpunktsenergien von 13 TeV – zur Eingrenzung des chromomagnetischen Dipolmoments des Top-Quarks im Rahmen Effektiver Feldtheorien genutzt.

Contents

Introduction

The top quark is the heaviest elementary particle that has been observed to date and it is described by the standard model (SM) of particle physics. The top quark has a mass of about 173.1 GeV [1, 2], which implies it has a large Yukawa coupling to the Higgs boson and, thus, hints to a special role in the electroweak symmetry breaking of the SM. The top quark is the only quark that decays before hadronizing, which provides a unique opportunity to measure the properties of a bare quark. Precision measurements of the differential top-quark pair ($t\bar{t}$) production cross sections provide a stringent test of the SM predictions, and they may reveal evidence of new-physics phenomena as deviations from these predictions. The $t\bar{t}$ production processes are a dominant source of background for Higgs boson processes, various rare processes, and many beyond-SM (BSM) searches.

Differential $t\bar{t}$ production cross sections have been measured by the ATLAS and CMS Collaborations at the CERN LHC in proton-proton (pp) collisions at a centre-of-mass energies of 7, 8, and 13 TeV [3–11].

In this work, three separate measurements of differential $t\bar{t}$ production cross sections in the dilepton channel (e^+e^-, $e^\pm\mu^\mp$, $\mu^+\mu^-$) in pp collisions at 13 TeV were performed. The studied event topology after the decay of a top-quark pair includes two oppositely charged leptons, two b quarks and two neutrinos. The data were collected by the CMS experiment in 2015 and 2016. Overall, absolute and normalized differential cross sections were measured as a function of kinematic observables of the top quarks, the $t\bar{t}$-system and the top quark decay products, as well as of the jet multiplicity in the event. Absolute differential cross sections are sensitive to a rate and shape of the measured distribution. Normalized differential cross sections are not sensitive to the rate component and, thus, uncertainties in the data are reduced. Measurements are based on an event counting method and involve a regularized unfolding technique to correct the reconstructed distributions for acceptance and detector effects. Depending on the observable, the results are presented in the full phase space at parton level and/or in a fiducial phase space, close to the experimental acceptance, at particle level. Three separate measurements are detailed in the following.

The data collection at the new energy frontier of $\sqrt{s}$ = 13 TeV provided an exciting opportunity to discover new-physics phenomena beyond the SM and, alternatively, to confirm the SM predictions. As first step of this work, measurements of the normalized differential $t\bar{t}$ production cross sections were performed using the first data sample collected in 2015 corresponding to an integrated luminosity (L) of 42 pb^{-1}. Measurements were performed at the parton level as a function of only few kinematic observables of the top quarks and the $t\bar{t}$-system, and at the particle level as a function of the jet multiplicity in the event. These differential cross sections are the first results of their kind at 13 TeV [12].

In a second step of this work, measurements of the normalized differential $t\bar{t}$ production cross sections, as done in the analysis of the first 2015 data, were repeated with the use of the complete 2015 data sample corresponding to L = 2.2 fb^{-1} [13]. The larger data sample allowed the improvement in the precision of results. These measurements confirmed a slope between data and SM predictions for the distribution of the top quark transverse momentum already observed in similar measurements performed at 7 and 8 TeV [3, 4, 7, 8]. After the measurements based on 2015 data, the analysis strategy was reconsidered, leading to the measurements described below.

As main results and third step of this work, the normalized and absolute differential $t\bar{t}$ production cross sections are measured using the complete 2016 data sample corresponding to L = 35.9 fb^{-1}. Here, the differential cross sections are presented as a function of kinematic observables of the top quarks, the $t\bar{t}$-system, and the top quark decay products (leptons and lepton pair, b-jets and b-jet pair), as well as of the jet multiplicity in the event. Providing a comprehensive study of $t\bar{t}$ production, 34 observables were probed according to 98 unique differential measurements, given an availability of the normalized/absolute results defined at parton/particle level, where possible. All results are compared to several SM predictions from Monte Carlo (MC) generators at next-to-leading-order (NLO) accuracy in quantum chromodynamics (QCD), based on matrix element level interfaced to parton shower simulations.

The presented measurements of the differential $t\bar{t}$ production cross sections provide an important input for the improvement of the SM predictions. Their results may be used to extract the top quark mass, strong coupling, and parton distribution functions. Results defined at parton level may be compared to state-of-the-art perturbative calculations of a higher accuracy, which also facilitates an extraction of the aforementioned parameters. Results defined at particle level are usually more precise with respect to those from parton level as they have reduced dependence on extrapolation effects introduced during the data unfolding. Particle level results are particularly important for tuning of parton shower, hadronization, underlying event and colour reconnection models, involved in MC simulations.

At beyond-leading-order accuracy, the SM predicts a nonzero, but rather small, charge asymmetry in the $t\bar{t}$ production via $q\bar{q}$ interaction [14]. This asymmetry is also diluted through the top quark decay products. The normalized differential $t\bar{t}$ production cross sections based on 2016 data are used to extract the $t\bar{t}$ and leptonic charge asymmetries in pp collisions for the first time at 13 TeV. These asymmetries may be used to test different BSM physics scenarios, e.g. those predicting axigluons [15] or Z′ bosons [16].

New physics could manifest itself as the production of new particles, that decay or strongly couple to top quarks, or as a modification of the production rates and event kinematics of known processes. However, the absence of signals of new physics in the LHC data available to date hints that new physics could be directly manifested at an energy scale larger than energy scales within the direct reach of the LHC. Thus, the new particles could be produced only virtually at the LHC. In this case, the search of new-physics phenomena is particularly attractive in the context of an effective field theory (EFT). In this work, for the first time at 13 TeV, the chromomagnetic dipole moment (CMDM) of the top quark is constrained in an EFT at NLO accuracy in QCD using the absolute differential $t\bar{t}$ production cross sections from 2016 data. A nonzero CMDM of the top quark could hint a presence of a new physics scenario such as the two-Higgs-doublet model [17], the little Higgs model [18], the minimal supersymmetric standard model [19], and the top quark compositeness model [20].

The thesis is organized as follows. In Chapter 1, a concise overview of the standard model of particle physics is given, describing elementary particles and fundamental interactions. The same chapter includes an introduction to top quark physics, outlining the production and decay mechanisms of top quarks, as described by the SM. The importance of top quarks and related measurements in the SM and in BSM theories is also discussed. The experimental setup is described in Chapter 2, where the Large Hadron Collider and the Compact Muon Solenoid experiment are detailed. The simulation of pp collisions is explained in Chapter 3, emphasizing aspects relevant for $t\bar{t}$ processes and simulation programs used in this work. In Chapter 4, the signal and background processes are defined, followed by descriptions of the analyzed data and simulations of signal and background processes. Afterwards, a detailed description of the event reconstruction and selection is provided, where a particular attention is devoted to the kinematic reconstruction of the top-quark pair. In Chapter 5, the precise definitions of the inclusive and differential $t\bar{t}$ production cross sections are described. In particular, an emphasis is given to the relevance of normalized/absolute differential cross sections defined either at parton or particle level. A discussion of the regularized unfolding technique used to determine differential cross sections is also provided. The same chapter includes definitions of phase spaces used for a presentation of differential results. The uncertainties of the $t\bar{t}$ production cross section measurements are discussed in Chapter 6. The

method used to compute total covariance and correlation matrices in the context of differential measurements is summarized in the same chapter. In Chapters 4 to 6, all descriptions and materials are given in the context of differential measurements based on 2016 data, as they are the main results of this work. In Chapter 7, all results that were previously described in the introduction are presented, providing a detailed discussion of measurements and their relevance. After Chapter 7, the thesis is concluded and an outlook is presented.

Chapter 1

Theoretical Overview

The foundation of modern particle physics is formulated in a theory called the standard model (SM) of particle physics (referred to as standard model). In Section 1.1, an overview of the SM is given. As this thesis is aimed at the study of top quarks, a brief description of top quark physics is given in Section 1.2.

1.1 Standard model of particle physics

The SM describes elementary particles that compose the fundamental structure of nature surrounding us. Elementary particles are understood as point-like and indivisible objects, whose substructure has not been observed up to now at present experiments. Each elementary particle is characterized by a unique set of properties determining the particle's behaviour, namely mass, spin and quantum numbers. Depending on these properties, elementary particles are governed by fundamental interactions. The SM describes three of the four known fundamental interactions, which are the electromagnetic, weak and strong interaction.

The SM classifies elementary particles into fermions (particles with half-integer spin) and bosons (particles with integer spin). Undergoing a particular type of the interaction, fermions can combine into more complex objects, eventually forming the matter that we observe in everyday life. The interaction itself is mediated by bosons, referred to as gauge bosons.

The SM is a gauge quantum field theory based on a symmetry group SU(3)×SU(2)×U(1). The mathematical formulation of the SM can be found, for example, in [21, 22]. In the following, a concise overview of the standard model is given emphasizing aspects important for this work. The classification of elementary fermions is described in Section 1.1.1. The fundamental interactions and gauge bosons are described in Section 1.1.2. A mechanism allowing massive elementary particles to acquire their masses is discussed in Section 1.1.3. An overview of the limitations of the SM is provided in Section 1.1.4.

1.1.1 Fermions

The SM includes 12 elementary particles of spin 1/2. As shown in Figure 1.1, these fermions are classified into 6 quarks (q), 3 electrically charged leptons (ℓ) and 3 electrically neutral leptons (ν_ℓ or simply ν).

The quarks with negative electric charge[†] of $-1/3$ are referred to as down-type quarks, named as d, s and b quarks. The up-type quarks, corresponding to u, c and t quarks, are carrying the positive electric charge of $2/3$. In addition, the characteristic property of quarks is that they hold the colour charge, given by one of three conventional states: red, green and blue. The electrically charged leptons are denoted as e, μ and τ, and will be simply referred hereafter as leptons. The electrically neutral leptons are called neutrinos, and are denoted as ν_e, ν_μ and ν_τ.

In this way, each fermion is distinguished according to its so-called flavour, e.g. top or charm quark, electron or muon, muonic or tauonic neutrino. Moreover, each fermion has its own antiparticle, which holds the same mass and spin as the original fermion, but is characterized by an opposite sign of the relevant quantum numbers. In particular, the colour charge is inverted to the corresponding anticolour: antired, antigreen and antiblue. For an arbitrary particle x, the antiparticle[‡] is indicated by the bar-sign as $\bar{x}$.

The fermions are grouped into three so-called generations. Each generation contains one up-type and down-type quark, as well as one charged and neutral lepton. Generations primarily differ in the masses of particles belonging to them. For instance, the tau lepton is much heavier than the muon, which is much heavier than the electron (see Figure 1.1). In particular, the top quark is the heaviest elementary particle that is observed to date, with a mass[††] of about 173.1 GeV [1, 2]. As discussed in the following, the main goal of this work is to study top-quark pair ($t\bar{t}$) production in proton-proton (pp) collisions.

1.1.2 Gauge bosons and fundamental interactions

In the SM, an interaction of two particles is understood as an exchange of a gauge boson between them. The gauge bosons (see Figure 1.1) have spin equal to 1 and act as force carriers for the corresponding type of the fundamental interaction. Each type of interaction

[†]here and elsewhere in the text, the electric charge of elementary particles is given in units of the elementary charge (e_{charge}) of about $1.602 \cdot 10^{-19}$ coulomb, corresponding to the electric charge carried by a proton.

[‡]in further, a notion of particle also implies the corresponding antiparticle, unless stated otherwise; i.e. top quark can refer to the t and $\bar{t}$.

[††]in this work, the system of natural units is used, where $\hbar$ (the reduced Planck constant), c (the speed of light in vacuum) and ε_0 (the electric constant) are set to 1; masses, energies and momenta of particles are given in electronvolts (eV).

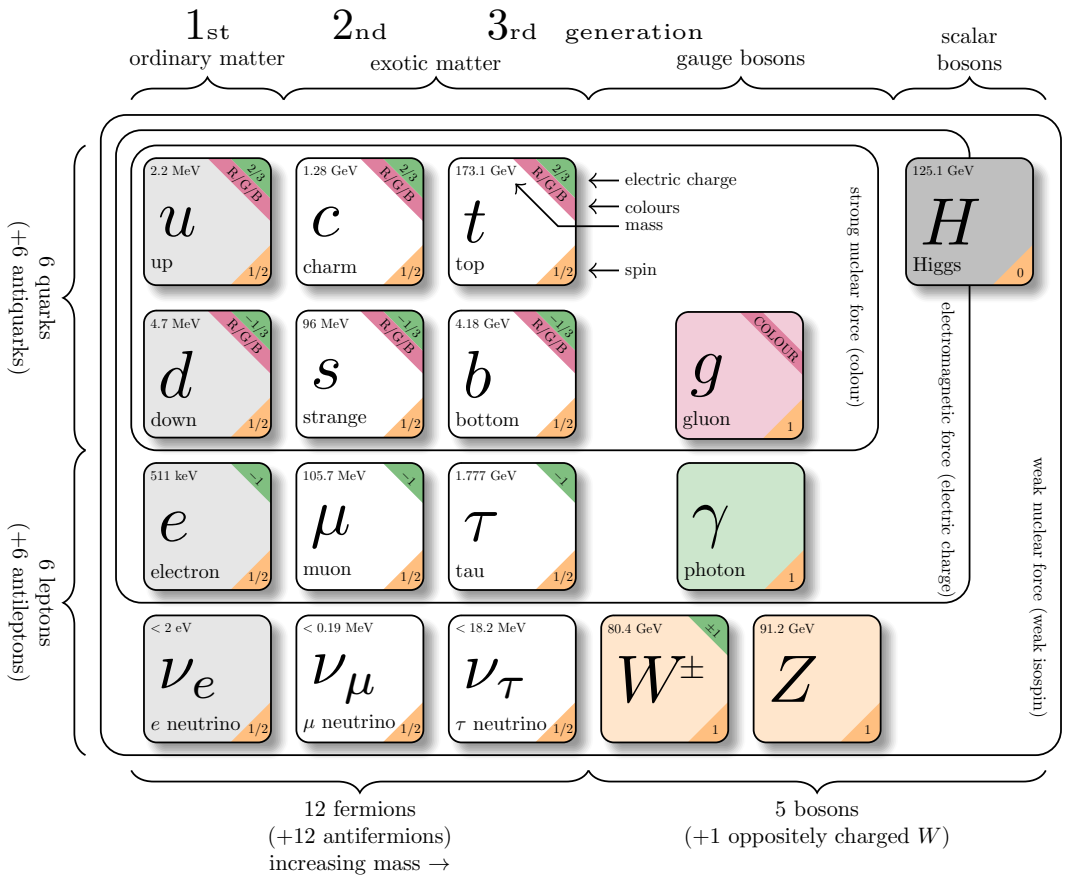

Figure 1.1 A summary of the standard model of elementary particles. The three generations of fermions, as well as the gauge and Higgs bosons are shown. The three fundamental interactions described in the standard model are also indicated. Figure from [23], modified. The masses of particles are taken from [1].

is governed by the relevant quantum number, which is required to be conserved within the interaction. The SM describes the electromagnetic, weak and strong interactions.

The electromagnetic interaction

The electromagnetic interaction occurs only between electrically charged particles, i.e. holding nonzero electrical charge, and is mediated by the photon (γ), a massless and electrically neutral gauge boson. This interaction is described by quantum electrodynamics (QED) with the symmetry group U(1).

The strength of the electromagnetic interaction is given by the coupling constant known as fine-structure constant

$$\alpha_{EM} = \frac{e_{charge}}{4\pi} \approx \frac{1}{137}, \tag{1.1}$$

where e_{charge} denotes the elementary charge. However, despite the fact that α_{EM} is regarded as constant, its value is known to vary with respect to the energy scale of the interaction. The variation of α_{EM} is usually parametrized as a function of Q^2, the square of the momentum transferred in the interaction. The corresponding Q^2-dependence, i.e. $\alpha_{EM}(Q^2)$, is referred to as running of α_{EM}. In this manner, the value of α_{EM} given in Equation 1.1 corresponds to the value at zero momentum transfer [24]. The α_{EM} increases with energy, e.g. $\alpha_{EM}(Q^2 = m_Z^2 = (91.2\ \text{GeV})^2) \approx 1/129$ [24], which implies that the interaction becomes stronger. As $\alpha_{EM} \ll 1$, QED accommodates perturbation theory to describe the interaction phenomena in power series of α_{EM}.

The weak interaction

The weak interaction is responsible for weak decays of fermions. In the SM, it is described by the symmetry group SU(2). In the weak interaction, particles can exchange one of the following gauge bosons: W^+, $W^-$and Z, where W^+ and W^- (also referred to as $W^\pm$ or simply as W bosons) are electrically charged and the Z boson is electrically neutral. The W and Z bosons themselves can also undergo the weak interaction. Owing to the significant masses (see Figure 1.1), the W and Z bosons have a short lifetime of about 10^{-25} s [1, 25], which limits the range of the weak interaction. The strength of weak interaction is largely suppressed at energy scales that are below the masses of the W and Z bosons. However, at energy scales of few hundreds GeV, the electromagnetic and weak interactions have strengths of comparable order as described within the SM in the unified electroweak interaction.

While the electromagnetic interaction is governed by the electric charge, the weak interaction is governed by the so-called weak isospin (T_3). The up-type quarks and neutrinos

have $T_3 = +1/2$; the down-type quarks and charged leptons have $T_3 = -1/2$. The W^+, W^- and Z bosons have $T_3 = +1, -1, 0$, respectively. At the interaction vertex, Z bosons couple to fermion-antifermion pair. For instance, a Z boson can decay to a quark pair, where quark and antiquark are of the same flavour ($Z \to q\bar{q}$). W bosons couple either to a charged lepton and a corresponding neutrino (e.g. $W^- \to \ell^- \bar{\nu}_\ell$) or to an up-type quark and a down-type quark ($W \to q\bar{q}'$, where q and q' indicate that quarks are of different flavours). Accordingly, as example, the muon can decay to W^- and ν_μ ($\mu \to W^- \nu_\mu$). An up-type quark can be converted into a down-type quark via a W emission, and vice versa, e.g. $t \to W^+ b$ or $d \to W^- u$. This phenomenon is known as flavour mixing for weak decays of quarks. The conversion probability between the up-type and down-type quarks is described by the Cabibbo–Kobayashi–Maskawa (CKM) matrix [26].

The strong interaction

The strong interaction is possible only between particles that carry the colour charge and is mediated by the gluon (g), a massless boson with zero electric charge. As mentioned previously, quarks and antiquarks carry a colour charge. However, the gluon itself carries colour and anticolour charges simultaneously. For example, a quark holding red colour charge can emit a gluon with red-antiblue colour charge. As a result, the colour charge of the quark will be converted to blue. Moreover, as gluons carry colour charge, they can interact with each other (gluon self-coupling).

The strong interaction is described by quantum chromodynamics (QCD) with the symmetry group SU(3). QCD defines eight linearly-independent colour states of gluons. The strong coupling constant (α_S) determines the strength of the strong interaction. As for the electromagnetic interaction, the value of α_S runs with respect to the momentum transfer. The dependence of α_S as a function of momentum transfer (Q) is shown in Figure 1.2, from several GeV up to TeV-scale. When the momentum transfer approaches zero, α_S is close to 1 ($\alpha_S \approx 1$). With an increase in the momentum transfer, α_S diminishes. In the limit of the infinite momentum transfer, the value of α_S asymptotically approaches zero. In particular, $\alpha_S(Q = m_Z = 91.2\ \text{GeV}) \approx 0.119$ [27].

The strength of the strong interaction at different energies changes according to the running of α_S. At high energies (equivalent to short-distance interactions), quarks and gluons interact weakly or behave like free particles, i.e. the effect known as asymptotic freedom. At low energies (equivalent to long-distance interactions) colour confinement occurs, i.e. the phenomenon according to which particles carrying colour charge cannot be directly observed as bare states. Instead, the colour confinement leads to the formation of hadrons, i.e. colourless bound states composed of quarks. The formation of hadrons is known as

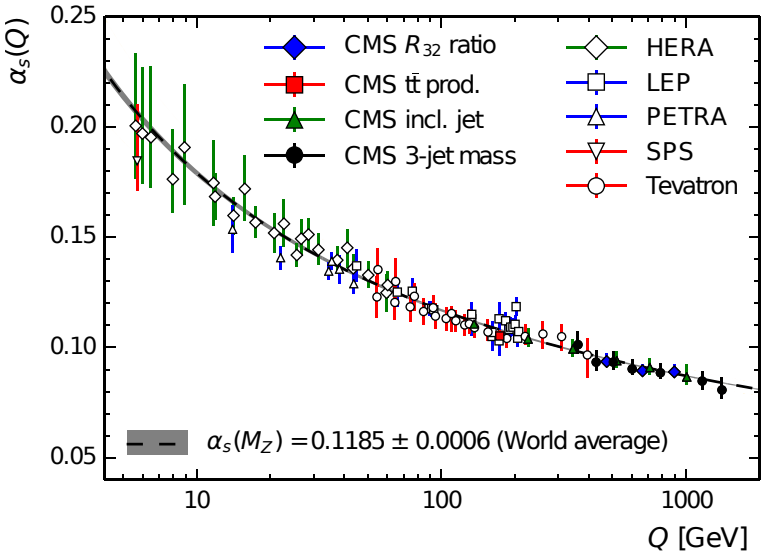

Figure 1.2 Experimental results on the running of the strong coupling constant (α_S) with respect to the momentum transfer (Q). The world average parametrization of $\alpha_S(Q)$ is shown as dashed black line with grey uncertainty band. The world average value at m_Z is also indicated. All uncertainties that are given correspond to total uncertainties. Figure from [27], modified.

hadronization process[†], and will be described in Chapter 3. The hadrons are classified into mesons, i.e. objects composed of a quark and an antiquark that carry opposite colour charges, and baryons, i.e. three quarks/antiquarks carrying the combination of all three colours/anticolours, and other exotic states[‡]. This classification is performed according to the quarks that determine the quantum numbers of the corresponding mesons or baryons, the so-called valence quarks. For instance, protons are baryons that are formed of "u, u, d" valence quarks. The valence quarks govern the structure of hadrons at low energies. However, at high energies, their structure is more complex, as discussed in the following.

As valence quarks interact via gluons, a gluon field is present inside hadrons. Moreover, gluons can interact among themselves and may split into a virtual quark pair ($g \rightarrow q\bar{q}$). Thus, in addition to valence quarks, hadrons may contain many virtual quarks that are referred to as sea quarks. Sea quarks themselves can radiate inside hadrons producing new gluons. The gluons and sea quarks do not contribute to the quantum numbers of hadrons and are understood as a virtual component of their structure. The contribution of the virtual component becomes larger as long as the energy of a hadron increases. In this manner, the hadron can be represented by a collection of point-like constituents called partons. Each

[†]a quark or a gluon that undergoes the hadronization process leads to the formation of a jet, i.e. a cone-shaped group of hadrons that move in similar directions.

[‡]experimentally observed pentaquark states are composed of four quarks and an antiquark.

parton[††], either a valence/sea quark or a gluon, carries a certain fraction of the energy of a hadron. According to the parton model, the hadron structure is described by the parton distribution functions (PDF), which will be discussed in greater detail in Section 1.2.1.

1.1.3 Electroweak symmetry breaking

The electromagnetic and weak interactions act as two distinct forces at low energies. However, at energies of about few hundreds GeV, these two interactions would merge and act as a single interaction, the electroweak interaction. In the SM, the electroweak interaction is described by the unified electroweak theory [28, 29] with the symmetry group $SU(2)_L \times U(1)_Y$ of weak left–handed isospin and hypercharge.

A generic representation of SU(2)×U(1) predicts massless W and Z bosons. However, experimental results show with a very good precision that their masses are significantly larger than zero [30]. The W and Z bosons acquire their masses through the so-called Higgs mechanism [31]. To introduce the Higgs mechanism, the SM is expanded with an additional self-interacting quantum field that pervades the whole space of our universe. This field is known as the Higgs field. Mathematically, the Higgs field is postulated as a complex doublet of the SU(2) symmetry with two electrically neutral and two electrically charged scalar components. The potential of the Higgs field has a symmetric shape resembling a mexican hat (known as Mexican-hat potential). This potential exhibits a set of equivalent minimum vacuum states located around its center, which are characterized by a nonzero vacuum expectation value $v \approx 246$ GeV [1]. In contrast, the center of the potential corresponds to an energy state with a nonzero potential energy. Thus, a presence of the Higgs field leads to the spontaneous breaking of the electroweak symmetry.

As a result of the EWSB, the electrically charged components of the Higgs field are absorbed to generate the masses of the $W^{\pm}$ bosons, while one neutral component is absorbed to generate the Z boson mass. A remaining neutral component of the Higgs field splits into the aforementioned vacuum expectation value and a dynamic field, which physically manifests itself as Higgs boson, a massive boson of spin 0. The existence of the Higgs boson with its mass of about 125 GeV was confirmed by the LHC experiments in 2012 [32, 33].

Charged leptons and quarks (and possibly neutrinos, see Section 1.1.4) also interact with the Higgs field via the exchange of virtual Higgs bosons. The coupling between the Higgs field and elementary fermions is described by the Yukawa interactions, where the corresponding coupling strength for a given fermion is governed by the so-called Yukawa coupling. After the EWSB and owing to their interaction with the Higgs field, elementary

[††]elsewhere in the text, the notion of partons is also used as reference to quarks and gluons.

fermions acquire their masses proportional to the corresponding Yukawa coupling and the vacuum expectation value of the Higgs field.

A detailed decription of the SM electroweak theory and the Higgs mechanism can be found, for example, in [29].

1.1.4 Limitations and challenges

The SM has been verified in numerous experiments conducted throughout the 20th and 21st centuries. In particular, the discovery of the Higgs boson, predicted in 1964 [31], at the LHC experiments in 2012 [32, 33] confirmed the credibility of the SM. Despite the success of the SM predictions, the SM is not able to explain all known fundamental phenomena and is inconsistent with several experimental observations. Few examples of SM limitations are briefly discussed in the following.

The SM does not include the description of gravity, the weakest interaction among the four known fundamental interactions. Gravity is about 10^{39} times weaker than the strong interaction. In analogy to other fundamental interactions, gravity is assumed to be mediated by the hypothetical particle called graviton, a massless boson of spin 2. Even if the existence of the graviton would be confirmed, the SM lacks a formulation of a valid quantum field theory that would be consistent with the general theory of relativity at distances of the order of the Planck length ($1.62 \cdot 10^{-35}$ m).

The SM does not explain from first principles why three generations of fermions exist, why coupling constants and particle masses and charges appear to be as they are, or why our universe exhibits an asymmetry between matter and antimatter. In particular, it is not clear why there is such a big gap between the strengths of gravity and the weak interaction (order of about 10^{30}), i.e. a problem known as hierarchy problem. The experimental observation of neutrino oscillations indicates that neutrinos have nonzero masses. In principle, massive neutrinos can be accommodated in the SM modifying an interaction of leptons with the Higgs field, but at the cost of extending the SM with several new constants [34]. However, the underlying reason behind the shape of the Higgs potential is not explained. The phenomenon of colour confinement is also not theoretically explained in the SM, as well as the reason of its existence. Finally, the SM does not predict any particle candidates and interactions that could underlie the nature of dark matter and dark energy. An overview of unsolved problems in the SM can be found in [35].

Several solutions for these problems have been proposed. Some of the (known) extensions of the SM are supersymmetry [36] (new fermion-boson symmetry) or extra dimensions [37] (dimensions of invisible size up to now), both motivated by the superstring theories, *little-Higgs* models [38] (new boson-boson and fermion-fermion symmetry), or the existence of

new fundamental interactions at energy scales not yet explored. The most intriguing feature of all these theoretical models is that they predict the existence of new physics phenomena not considered by the SM at the TeV energy scale. However, no signals of such new particles and new interactions have been found so far.

1.2 Top quark physics

The top quark is the heaviest elementary particle that is observed to date. The top quark has a mass (m_t) of about 173.1 GeV [1, 2] (for other properties see Figure 1.1), which implies a large Yukawa coupling to the Higgs boson and, thus, hints its special role in the stabilization of the Higgs field. Moreover, the top quark is the only quark that decays before hadronizing (see Section 1.2.2 for more details), which provides a unique opportunity to measure the properties of an isolated (bare) quark.

The main goal of this thesis is the study of top-quark pair production. Since the top quark is very heavy, an experimental observation of its production requires collisions of high-energetic particles at particle accelerators. So far, the observation of top quarks has been possible at only two circular collider facilities, the Tevatron and the Large Hadron Collider (LHC).

At the Tevatron, the proton-antiproton beams collided at a centre-of-mass energy ($\sqrt{s}$) of 1.96 TeV. Its operation for data taking started in 1987 and with a few breaks it lasted until 2011, when the collider was shut down completely. Owing to the data from Tevatron, the top quark was discovered in 1995, more than twenty years after its prediction [39].

Starting from 2010, the study of top quarks continued at the Large Hadron Collider (LHC) through proton-proton collisions. The LHC is designed to collide *pp* beams at centre-of-mass energies of up to 14 TeV. The results presented in this work are based on the data collected during the LHC operation at $\sqrt{s}$ = 13 TeV in 2015 and 2016. The experimental setup will be described in greater detail in Chapter 2.

The production and decay mechanisms of top quarks are described in Sections 1.2.1 and 1.2.2, respectively. The relevance of top quark measurements in the context of the standard model and beyond the standard model is explained in Section 1.2.3. A list of observables related to top quarks that are relevant for this work is given in Section 1.2.4. An extensive review of top quark physics can be found in [40].

1.2.1 Top quark production

In particle collisions, top quarks are produced predominantly in pairs, i.e. top quark and top antiquark (referred to as top-quark pair or simply as $t\bar{t}$). Top quarks can also be produced individually (single top processes). Other modes of top quark production are not discussed in the following as they are extremely rare.

Production cross section

The occurrence rate of a particular physics process as result of the interaction between two hadrons is given by the inclusive cross section. In pp collisions, this cross section can be calculated according to the factorization theorem [41], which separates the evolution of the collision event into relevant subprocesses occuring at different energy/length scales. Thus, the inclusive cross section is given by the convolution of the partonic cross section, describing the short-distance interaction of two partons that originate from one or another hadron, and the parton distribution functions, accounting for the long-distance effects among partons inside the hadrons. These subprocesses are separated by the so-called factorization scale μ_F, which value is arbitrarily chosen and is usually set to the momentum transfer Q.

In case of the process $AB \to X$, where A and B are two colliding hadrons giving rise to an arbitrary final state X, the inclusive cross section is written as

$$\sigma_{AB\to X} = \sum_{a,b} \int_{x_a} \int_{x_b} \hat{\sigma}_{AB\to X} \cdot f_{a/A}(x_a, \mu_F) \cdot f_{b/B}(x_b, \mu_F) \cdot dx_a dx_b, \tag{1.2}$$

where $\hat{\sigma}_{AB\to X} \equiv \hat{\sigma}_{AB\to X}(\hat{s}, m_X, \alpha_S(\mu_R), \mu_R, \mu_F)$ is the aforementioned partonic cross section of two partons participating in the hard scattering process. Here, $\hat{s} = x_a x_b s$ is the effective centre-of-mass energy, m_X implies the dependence on the mass of outgoing partons in the final state X, and the parameter μ_R is discussed later in the text. The parton constituents of the hadron A are denoted by a, i.e. valence/sea quarks and gluons, and its corresponding PDF is indicated by $f_{a/A}(x_a, \mu_F)$, where x_a refers to the fraction of the hadron's momentum carried by a parton. The same system of notation is used regarding the hadron B. The integration is performed over the momentum fractions of two partons participating in the hard scattering process and the sum runs over all possible types of partons a and b.

As the hard scattering between two partons occurs at energy scales where $\alpha_S \ll 1$, $\hat{\sigma}_{AB\to X}$ can be calculated in perturbation theory in power series of α_S. This calculation involves the computation of the scattering matrix, which relates the incoming (initial state) and outgoing (final state) partons of the hard scattering process. Thus, the calculation of $\hat{\sigma}_{AB\to X}$ is also referred to as matrix element calculation. The accuracy of these calculations at $O(\alpha_S^2)$ is

referred to as leading order (LO), at $O(\alpha_S^3)$ as next-to-leading order (NLO), at $O(\alpha_S^4)$ as next-to-next-to-leading order (NNLO), etc. The renormalization scale μ_R is the parameter of the renormalization procedure [42], which is applied in perturbation theory to remove divergences appearing in higher-order calculations due to loop corrections (see Section 3.1). The choice of μ_R is arbitrary and its value is usually set to μ_F.

At leading order, the parton distribution functions $f_{a/A}(x_a, \mu_F)$ describe the probability density of finding a parton in hadron A carrying a momentum fraction x_a at the energy scale μ_F. The PDFs cannot be calculated in perturbation theory, but they can be extracted from the experimental data. An example of proton PDF parametrization is shown in Figure 1.3, provided by the NNPDF Collaboration [43].

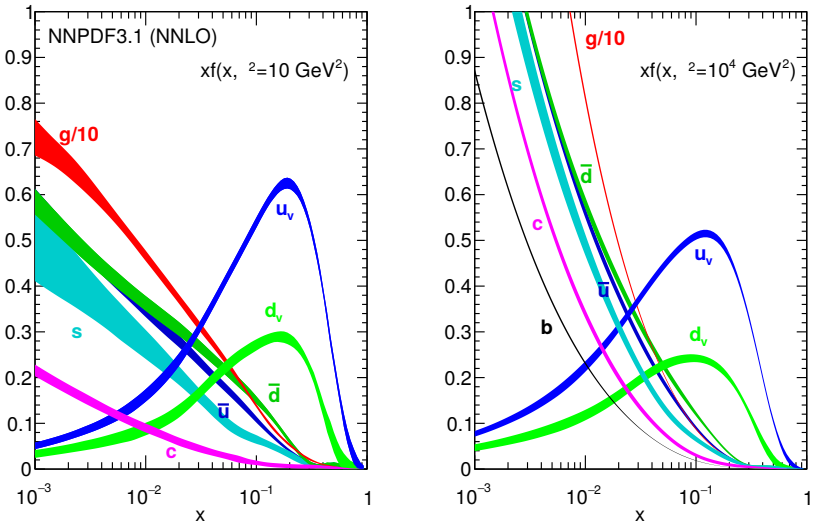

Figure 1.3 The NNPDF3.1 NNLO [43] parton distribution functions of the proton are shown at $\mu_F^2 = 10$ GeV^2 (left) and $\mu_F^2 = 10^4$ GeV^2 (right) separately for valence quarks u_v and d_v, for sea (anti)quarks $\bar{u}$, $\bar{d}$, $c = \bar{c}$, $s = \bar{s}$, $b = \bar{b}$, and gluons. For high x, the parton distribution inside the proton is dominated by valence quarks. At low x, the parton distribution is dominated by gluons and sea quarks. Figure from [43].

Top-quark pair production

The top-quark pair production occurs predominantly by means of the strong interaction. In pp collisions, top-quark pairs are produced mainly via the gg-fusion ($gg \to t\bar{t}$) and $q\bar{q}$-annihilation ($q\bar{q} \to t\bar{t}$). The corresponding LO Feynman diagrams are shown in Figure 1.4. In pp collisions at 13 TeV, $t\bar{t}$ production via gg-fusion occurs in about 90% of cases. The $q\bar{q}$-mode is suppressed, since an antiquark can arise only as sea quark. The $t\bar{t}$ production can

occur also by means of qg- or $\bar{q}g$-scattering (e.g. $qg \rightarrow t\bar{t}$), but only at NLO. At $\sqrt{s} = 13$ TeV, $\sigma_{t\bar{t}}^{incl}$ is predicted to be $831.76\ ^{+19.77}_{-29.20}$ (scale) $\pm$ 35.06(PDF + α_S) pb. This value is obtained at NNLO accuracy with next-to-next-to-leading-logarithmic (NNLL) precision [44–49], using the Top++2.0 program [50] and assuming a top quark mass of 172.5 GeV. The predictions of differential $t\bar{t}$ production cross sections are available at full NNLO [51, 52] and approximate next-to-NNLO (N^{3}LO) [53].

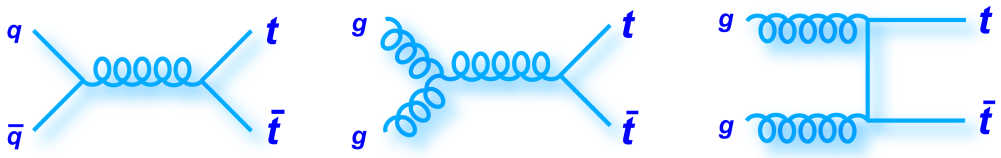

Figure 1.4 Examples of Feynman diagrams representing the $t\bar{t}$ production via the $q\bar{q}$-annihilation (left) and the gg-fusion (middle, right) at leading order. From [54].

Single top quark production

The production of single top quarks occurs via the weak interaction. At LO, single top quark production is possible in three channels, namely in s-channel and t-channel via the exchange of the virtual W boson, and in the so-called tW-channel, where the top quark is produced in association with a W boson. The LO Feynman diagrams corresponding to these processes are shown in Figure 1.5. Among these processes, the most abundant process is the single top quark production in the t-channel. The corresponding inclusive cross section accounting for the top quark and antiquark components at $\sqrt{s} = 13$ TeV is predicted to be $216.99\ ^{+6.62}_{-4.64}$ (scale) $\pm$ 6.16(PDF + α_S) pb [55] at NLO accuracy, using the HATHOR (v2.1) program [56, 57] and setting $m_t = 172.5$ GeV. More information on physics of single top quark processes can be found in [58].

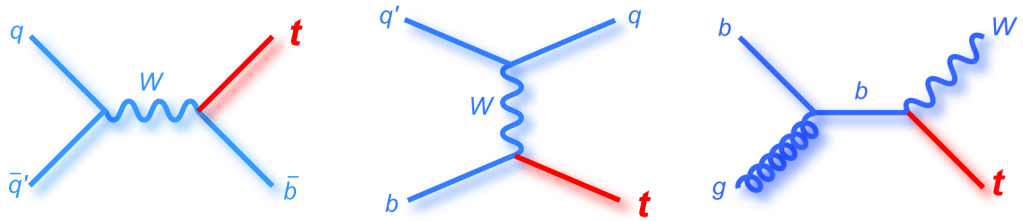

Figure 1.5 Examples of Feynman diagrams representing the single top quark production at leading order in the s-channel (left), t-channel (middle) and tW-channel (right). From [54].

1.2.2 Top quark decay

Top quarks decay via the weak interaction to a W boson and to a down-type quark (d, s or b), i.e. via the processes $t \to W^+q$ and $\bar{t} \to W^-\bar{q}$. Due to corresponding elements of the CKM matrix ($|V_{tb}| \approx 0.999$, $|V_{ts}| \approx 40.3 \cdot 10^{-3}$, and $|V_{td}| \approx 8.75 \cdot 10^{-3}$ [1]), top quarks decay with a branching ratio (BR) of about 0.957 to a b quark and a W boson [1, 2].

The total decay width of the top quark Γ_t is proportional to m_{top}^3 and at leading order is about 1.5 GeV [40]. Thus, top quarks are short-lived particles with a mean lifetime τ_t of about $4.4 \cdot 10^{-25}$ s, which is given by $\tau_t = 1/\Gamma_t$. Unlike other quarks, top quarks decay before they can form any bound states, since τ_t is smaller than the timescale of the hadronization process ($1/\Lambda_{QCD} \approx 3 \cdot 10^{-24}$ s). This characteristic provides a unique opportunity to study bare quarks. Moreover, τ_t is also smaller than the spin decorrelation timescale ($m_{top}/\Lambda_{QCD}^2 \approx 3 \cdot 10^{-21}$ s) [59], which implies that the top quark polarization and the $t\bar{t}$ spin correlations are propagated to the decay products of top quarks.

The decay channels of the top-quark pair are classified according to decays of W bosons originating from top quarks. As mentioned in Section 1.1.2, W bosons can decay either to a charged lepton and a corresponding neutrino (e.g. $W^- \to \ell^-\bar{\nu}_\ell$; referred to as leptonic mode) or to an up-type quark and a down-type quark ($W \to q\bar{q}'$, where q and q' indicate that quarks are of different flavours; referred to as hadronic mode). As shown in Figure 1.6, three $t\bar{t}$ decay channels are distinguished: all-hadronic, lepton+jets and dilepton. The probability that $t\bar{t}$ decay will occur in one of these channels is quantified by the corresponding BR. All values of BR that are indicated below are taken from [1, 25].

The all-hadronic channel corresponds to cases where both W bosons decay in the hadronic mode: $t\bar{t} \to q\bar{q}'bq''\bar{q}'''\bar{b}$. The all-hadronic channel has the largest BR of about 0.454, but is characterized by the largest contamination from background processes, e.g. multijet and combinatorial backgrounds.

The lepton+jets (ℓ+jets) channel corresponds to cases where one W boson decays in the hadronic mode, while the other does it in the leptonic mode: $t\bar{t} \to \bar{\ell}\nu_\ell bq\bar{q}'\bar{b}$ or $t\bar{t} \to q\bar{q}'b\ell\bar{\nu}_\ell\bar{b}$. Sometimes, the lepton+jets channel is referred to as golden channel, since its contamination by background processes is moderate, while BR ≈ 0.441 is rather large.

The dilepton channel corresponds to cases where both W bosons decay in the leptonic mode: $t\bar{t} \to \bar{\ell}\nu_\ell b\ell'\bar{\nu}_{\ell'}\bar{b}$. In contrast to other channels, the dilepton channel has the lowest BR ≈ 0.107, but is also affected by lowest backgrounds.

The BR values for the lepton+jets and dilepton channels are given above for the case where leptons can be e, μ or τ. The τ leptons decay via the weak interaction to a W boson and a τ neutrino, where the W boson subsequently decays either leptonically or hadronically (i.e. $\tau \to W\nu_\tau \to \ell\nu_\ell\nu_\tau$ and $\tau \to W\nu_\tau \to q\bar{q}'\nu_\tau$). The $t\bar{t}$ events with decays via τ leptons are

usually excluded from the experimental analysis aiming at lepton+jets and dilepton final states. This is done to simplify the reconstruction of event kinematics and the event selection, and to reduce combinatorial backgrounds. Excluding decays via τ leptons, the corresponding BR for $t\bar{t}$ decays in the lepton+jets channel is ≈ 0.288 and in the dilepton channel is ≈ 0.0455. In this case, owing to the presence of one (two) well-isolated high-energetic lepton (leptons of opposite electrical charges) in the lepton+jets (dilepton) event final state, $t\bar{t}$ signal events can be better separated from background events.

This thesis is dedicated to a study of $t\bar{t}$ production with the subsequent decay into dilepton final state, where decays via τ leptons are not included in the signal definition and are, instead, regarded as background. The signal definition and relevant background processes will be discussed in Chapter 4.

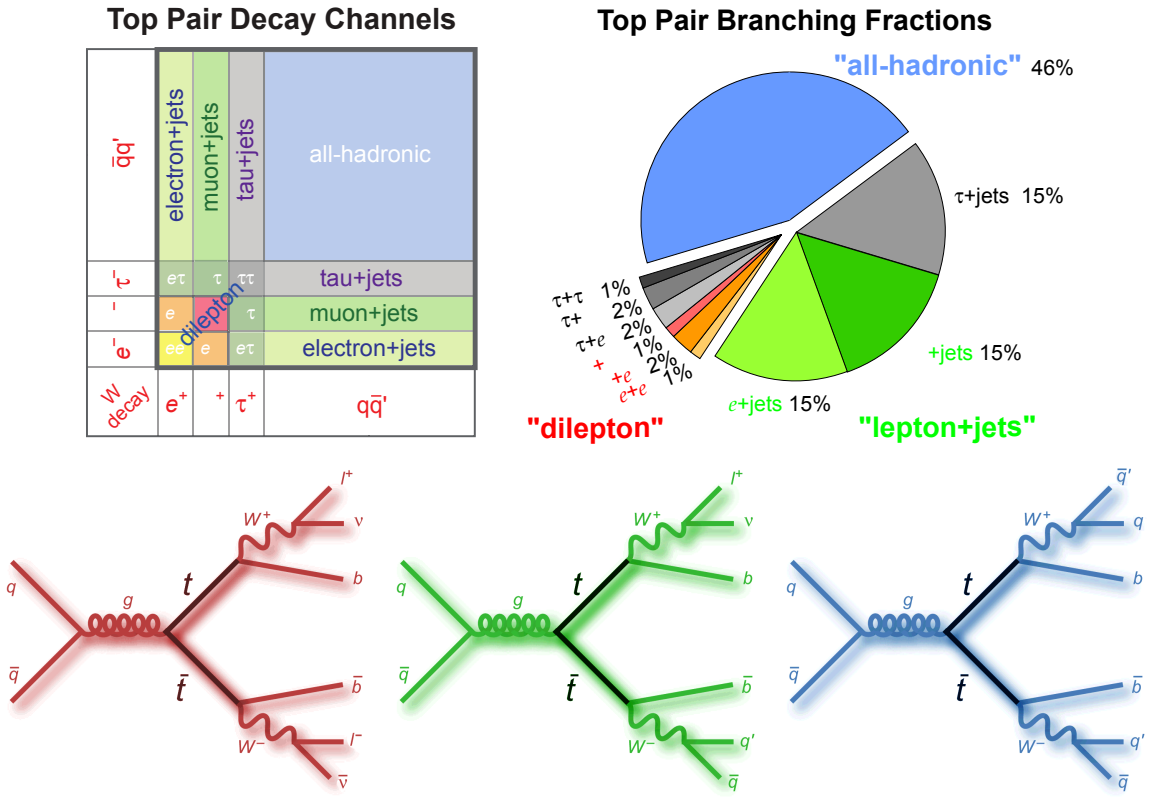

Figure 1.6 A schematic classification of the top-quark pair decay channels (upper left) is shown together with the distribution of corresponding branching ratios (upper right; numbers are approximate). In the lower row, examples of LO Feynman diagrams are shown for the $t\bar{t}$ production with the subsequent decays in the dilepton (left), lepton+jets (middle) and all-hadronic (right) channels. From [54], modified.

1.2.3 Relevance of top quark physics in the standard model and beyond

As mentioned earlier, the top quark is the heaviest known elementary particle. Because of its large mass, the top quark is an extremely interesting object to study. Unlike other quarks, top quarks decay before hadronizing and, thus, can be studied as bare quarks. The spin properties of top quarks are directly transferred to their decay products and, thus, are more easily accessible in comparison to other quarks. As this thesis is aimed at the study of the $t\bar{t}$ production, the following explanations emphasize relevant aspects for this process.

As can be seen from Equation 1.2, the $t\bar{t}$ production cross section is sensitive to the top quark mass (m_t), strong coupling constant (α_S) and parton distribution functions. The large mass of the top quark, i.e. about 173.1 GeV [1, 2], implies a large value of the top quark Yukawa coupling to the Higgs boson, which demonstrates a direct connection between the top and Higgs sectors. For instance, the shape information contained in the differential $t\bar{t}$ production cross sections is sensitive to electroweak loop corrections, which are dependent on the top quark Yukawa coupling and provide indirect constraints on the mass of the Higgs boson. Moreover, differential $t\bar{t}$ production cross sections measured as a function of the top quark decay products are sensitive to the top quark decay width, top quark spin properties and $t\bar{t}$ spin correlations, and even to the polarization of the W boson. In particular, differential measurements can also be used to extract the charge asymmetry in $t\bar{t}$ production, as described in Section 7.4. The measurements related to the single top quark production directly probe the Wtb vertex and the $|V_{tb}|$ element of the CKM matrix.

The $t\bar{t}$ production processes are a dominant source of background for Higgs processes, various rare processes (e.g. four top quark production ($t\bar{t}t\bar{t}$), the associated production of top quark-antiquark pairs with a Higgs, Z, or W boson, or a photon ($t\bar{t}H$, $t\bar{t}Z$, $t\bar{t}W$, $t\bar{t}\gamma$, respectively) and many beyond-SM (BSM) searches. Moreover, top quark measurements provide an important input for the improvement of the fixed-order and Monte Carlo SM predictions.

New physics could manifest itself as the production of new particles, that decay or strongly couple to top quarks, or as a modification of the production rates and event kinematics of known processes. In this respect, new physics could become evident as a peak in the invariant mass spectrum of the $t\bar{t}$ system, e.g. models involving Z' bosons [16] and extra dimensions [37]. Alternatively, different BSM scenarios predict anomalous couplings that lead to a modification of various top quark properties. For example, $t\bar{t}$ charge asymmetry can be enhanced by BSM scenarios that predict axigluons [15] and Z' bosons [16]. Dark matter could be produced in association with the top-quark pair [60], exhibiting the presence of a significant missing transverse energy in the event and a modification of the $t\bar{t}$ spin correlations.

In particular, an effect of BSM physics on the top quark properties can be studied in the framework of an effective field theory as described in Section 7.5. Therefore, precision SM measurements involving top quarks provide not only a stringent test of the SM predictions, but can also reveal evidence of new-physics phenomena as deviations from these predictions.

1.2.4 List of studied observables in the context of differential $t\bar{t}$ production cross sections

This thesis presents differential $t\bar{t}$ production cross sections measured in the dilepton channel as a function of observables listed below. This list is given to familiarize the reader with the naming conventions used throughout the text of this work.

Observables related to the top quarks and the top-quark pair:

- transverse momentum of the top quark p_T^t,
- transverse momentum of the top antiquark $p_T^{\bar{t}}$,
- transverse momentum of the leading top quark p_T^t *(leading)*,
- transverse momentum of the trailing top quark p_T^t *(trailing)*,
- transverse momentum of the top quark in the rest frame of the $t\bar{t}$-system p_T^t *($t\bar{t}$ rest frame)*,
- transverse momentum of the top antiquark in the rest frame of the $t\bar{t}$-system $p_T^{\bar{t}}$ *($t\bar{t}$ rest frame)*,
- rapidity of the top quark y_t,
- rapidity of the top antiquark $y_{\bar{t}}$,
- rapidity of the leading top quark y_t *(leading)*,
- rapidity of the trailing top quark y_t *(trailing)*,
- difference in absolute rapidity between the top quark and antiquark $\Delta|y|(t,\bar{t})$,
- difference in azimuthal angle between the top quark and antiquark $\Delta\phi(t,\bar{t})$,
- transverse momentum of the top-quark pair $p_T^{t\bar{t}}$,
- invariant mass of the top-quark pair $m_{t\bar{t}}$,
- rapidity of the top-quark pair $y_{t\bar{t}}$.

Observables related to the top quark decay products:

- transverse momentum of the lepton p_T^{ℓ},
- transverse momentum of the antilepton $p_T^{\bar{\ell}}$,
- transverse momentum of the leading lepton p_T^{ℓ} *(leading)*,
- transverse momentum of the trailing lepton p_T^{ℓ} *(trailing)*,
- pseudorapidity of the lepton η_{ℓ},
- pseudorapidity of the antilepton $\eta_{\bar{\ell}}$,

- pseudorapidity of the leading lepton η_ℓ *(leading)*,
- pseudorapidity of the trailing lepton η_ℓ *(trailing)*,
- difference in absolute pseudorapidity between the lepton and antilepton $\Delta|\eta|(\ell, \bar{\ell})$,
- difference in azimuthal angle between the lepton and antilepton $\Delta\phi(\ell, \bar{\ell})$,
- transverse momentum of the lepton pair $p_T^{\ell\bar{\ell}}$,
- invariant mass of the lepton pair $m_{\ell\bar{\ell}}$,
- transverse momentum of the leading b-jet p_T^b *(leading)*,
- transverse momentum of the trailing b-jet p_T^b *(trailing)*,
- pseudorapidity of the leading b-jet η_b *(leading)*,
- pseudorapidity of the trailing b-jet η_b *(trailing)*,
- transverse momentum of the b-jet pair $p_T^{b\bar{b}}$,
- invariant mass of the b-jet pair $m_{b\bar{b}}$,
- jet multiplicity N_{jets}.

In the list given above, the adjective "leading" ("trailing") refers to particles that have the largest (next-to-largest) transverse momentum p_T among particles of the same type within an event. The other designations relevant for definitions of these observables will be described in Section 2.2.1 together with the coordinate system used in this work. The motivation for the study of each individual observable given in the list will be explained in Section 7.3, where the main results of this work are presented.

Chapter 2

Experimental Setup

The Large Hadron Collider (LHC) is designed to collide the proton-proton (pp) beams at the unprecedented centre-of-mass energy ($\sqrt{s}$) of 14 TeV, making it the most powerful collider in the world. In particular, this huge energy allows a relatively high rate of top quark production. At the LHC, the beams are collided at several interaction points, at one of those the Compact Muon Solenoid (CMS) experiment is located, providing the data used to derive the results in this work.

The key points in the designs of the LHC collider and the CMS detector are described in this chapter.

2.1 The Large Hadron Collider

The LHC is a two-ring-superconducting-hadron accelerator and collider [61], belonging to the accelerator complex at CERN (the European Organization for Nuclear Research, located near Geneva), shown in Figure 2.1. The LHC has a circumference of about 27 km and it is installed 100 m underground in the tunnel that was formerly used for the operation of the Large Electron–Positron collider. As previously mentioned, the LHC is designed to accelerate and collide two beams of protons (heavy ions) at collision energies up to $\sqrt{s}$ = 14 TeV (2.8 TeV per nucleon for Pb-Pb collisions). In the following, only pp collisions at the LHC are explained.

Before the injection to the LHC ring, the proton beams are accelerated in the sequential system of smaller particle accelerators. Each accelerator boosts the proton energy to a higher value. The protons are produced applying an electric field to a tank filled with hydrogen gas, splitting the gas into the proton and electron components. Then, protons are transferred to the Linear Accelerator 2 (LINAC 2), where they are accelerated to 50 MeV. These protons are injected into a chain of the Proton Synchrotron Booster (PSB), the Proton Synchrotron

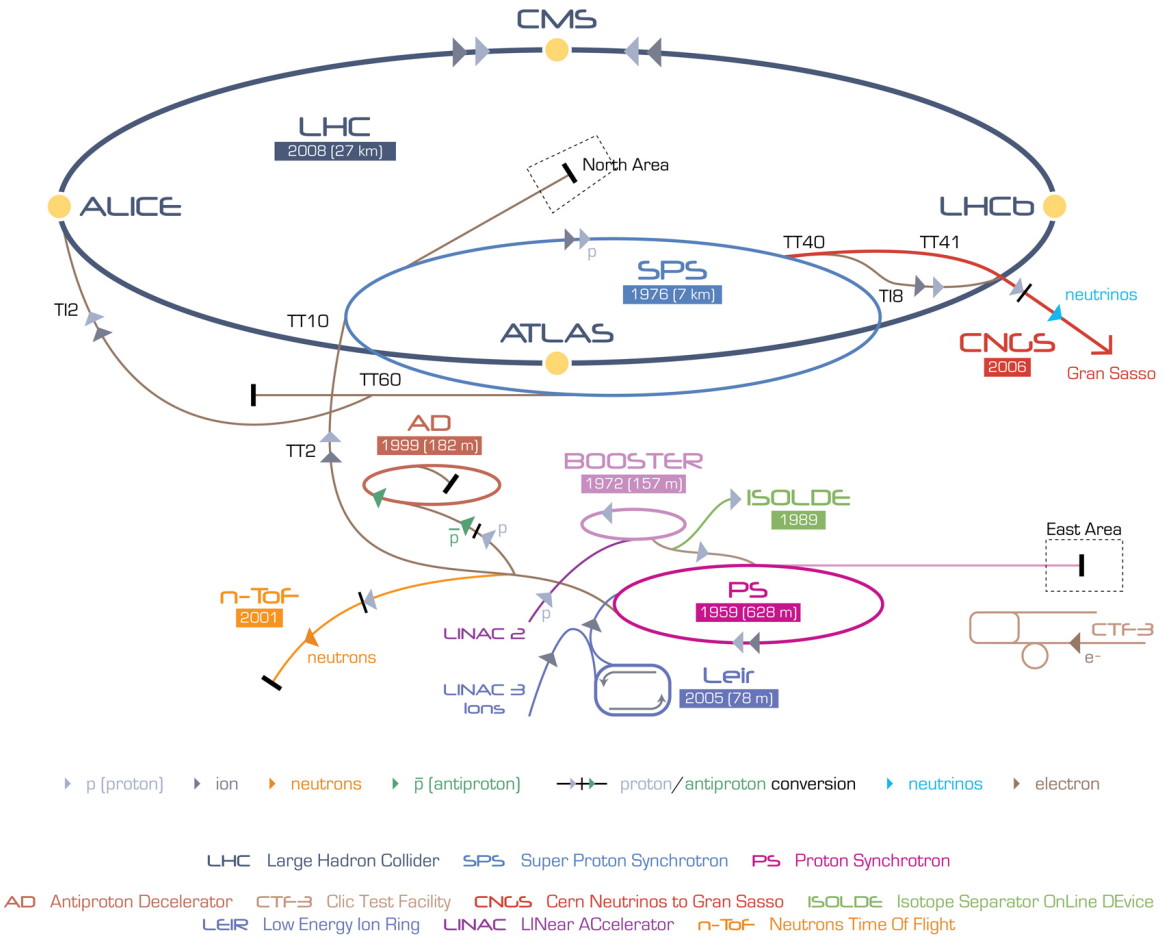

Figure 2.1 The CERN accelerator complex with the LHC ring. From [62].

(PS; this acronym is applicable only to Figure 2.1) and the Super Proton Synchrotron (SPS). Respectively, protons are accelerated to the energies of 1.4 GeV, 25 GeV and 450 GeV. In the Proton Synchrotron, protons are divided into bunches.

The pre-accelerated proton beams are injected into the two beampipes of the LHC. The beams are counter-rotated and accelerated with the superconducting radiofrequency cavity system, providing an electromagnetic field. The beam is controlled, i.e. bended and collimated, with the superconducting magnet system, where the magnets are cooled to a temperature below 2 K with superfluid helium and are operated at fields of above 8 T. The dipole magnets keep the beam at its circular trajectory, while the quadrupole magnets are responsible for its focusing. In addition, the magnets of few other configurations are used to correct the beam further. The proton energy is increased by 0.5 MeV per turn. The design energy of 7 TeV per beam can be achieved in about 25 minutes after the injection. The two beams are collided at four interaction points, dedicated to the ALICE [63], ATLAS [64], CMS [65] and LHCb [66] experiments.

Beam structure and luminosity

The proton beam at the LHC has a structure of repeating proton bunches (about 30 cm long) separated with 25 ns spacing (about 7.5 m long gaps). The LHC is designed to collide proton beams at a rate of 40 MHz.

During the collisions, the expected number of events per second N for a physics process is given by $N = L_{inst} \cdot \sigma$, where L_{inst} is the instantaneous luminosity and σ is the total cross section for a given process. The high L_{inst} plays an essential role in the study of ultra-rare physics processes.

The instantaneous luminosity L_{inst} for the pp collisions at the LHC is given by the machine parameters of the collider and beam properties [67]

$$L_{inst} = \frac{\gamma f_r k_b N_p^2}{4\pi\varepsilon_n\beta^*} F_X, \tag{2.1}$$

where γ is the Lorentz factor, f_r is the revolution frequency, k_b is the number of bunches per beam, N_p is the number of protons per bunch, ε_n is the normalized transverse emittance, β^* is the beta function at the interaction point and F_X is the reduction factor dependent on the crossing angle of two beams.

The integrated luminosity L of the dataset recorded during the collisions is obtained via the integration of the instantaneous luminosity over the corresponding period of time as $L = \int \mathrm{L}_{inst}\,\mathrm{d}t$. The expected number of events in this dataset for a given physics process is $N = L \cdot \sigma$.

LHC operation

During 2009-2013, the first operational run (Run-I) of LHC occurred, bestowing the pp collisions at the energies up to $\sqrt{s} = 8$ TeV. After the long shut down, the LHC was restarted in 2015 for the Run-II operation and it will continue until the end of 2018, colliding protons at $\sqrt{s} = 13$ TeV. The main results in this work are based on the dataset of $L = 35.9$ fb^{-1} recorded by the CMS detector in 2016 [68] (those results are complemented by the early measurements at $\sqrt{s} = 13$ TeV performed using the data collected in 2015). During that year, the LHC achieved a peak $L_{inst} = 1.1 \cdot 10^{34}$ cm^{-2}s^{-1}, at maximum colliding $k_b = 2076$ bunches with $N_p = 1.18 \cdot 10^{11}$ protons each. Other parameters that are relevant for the definition of L_{inst} can be found in [69].

2.2 The Compact Muon Solenoid

The CMS detector [67] is a general-purpose experiment targeting many topics of modern particle physics [70]. One of its primary goals was the search for Higgs boson, which was discovered in 2012. Other topics include searches for physics phenomena beyond the SM, e.g. supersymmetric particles, new massive vector bosons, extra dimensions etc. The CMS physics program also includes the SM precision measurements and heavy-ion physics.

The CMS detector is installed in the underground cavern (about 100 m deep) at the LHC interaction point 5, nearby the village Cessy (France). The detector is built in a 4π-geometry around the LHC beampipe. It is symmetrical with respect to the nominal interaction point of the two colliding beams (IP). The detector dimensions are 21.6 m in length and 14.6 m in diameter, while the total weight is about 12 500 tons. The detector subsystems are organized in barrel-like layers and endcap disks that are built on top of each other (see Figure 2.2). The innermost layer is the silicon pixel tracker, followed by the silicon strip tracker. The electromagnetic calorimeter, including preshower detectors as the first layer, and hadronic calorimeter are sequentially installed after the tracking system. These subsystems are contained inside the superconducting solenoid. The muon system is embedded in the return yoke installed outside the solenoid. The outer endcaps correspond to the very-forward calorimeter, an external subdetector of the hadronic calorimeter system.

2.2.1 The coordinate system

The CMS experiment uses a right-handed Cartesian coordinate system for the indication of relevant positions. Its origin is located inside the detector at the IP, while the x-axis is pointing

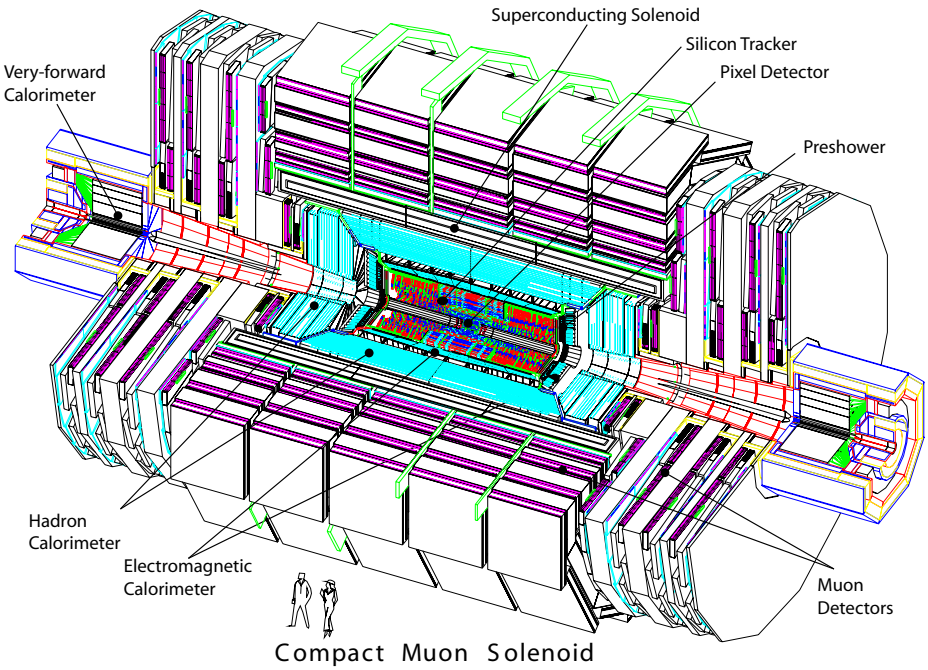

Figure 2.2 An overview of the CMS detector with the indication of its subsystems. From [71].

towards the centre of the LHC ring; y-axis points vertically upwards and is perpendicular to the plane of LHC; z-axis points along the direction of the anticlockwise rotating beam.

The positions are also presented in the alternative coordinate system, which is defined as follows. The radial distance r is defined as the distance from the z-axis, while the polar angle θ is measured from the positive z-axis and the azimuthal angle is measured from the positive x-axis in the xy-plane.

Remarks on the measured observables

The measured physics object is characterized by its respective 4-momentum of the form (E, p_x, p_y, p_z). Here, E is the energy of the physics object, while (p_x, p_y, p_z) is its momentum 3-vector $\vec{p}$ and, for example, p_x is the scalar projection of $\vec{p}$ on the x-axis.

The 3-vector $\vec{p}$ itself can be factorized into the transverse p_T and longitudinal p_L components. The transverse momentum is measured in the transverse plane to the beam direction (xy-plane) according to $p_T = \sqrt{p_x^2 + p_y^2}$, while the longitudinal momentum is measured along the beam axis and, thus, $p_L = p_z$.

It is convenient to present the equivalent 4-vector in the another set of components (E, p_T, η, ϕ), representing different aspects of the dynamics of the physics objects. The

pseudorapidity η is the spatial coordinate that is closely related to the polar angle

$$\eta = -\ln\left(\tan\frac{\theta}{2}\right) = \frac{1}{2}\ln\left(\frac{|\vec{p}| + p_z}{|\vec{p}| - p_z}\right). \tag{2.2}$$

The pseudorapidity is usually used to describe the particles with negligible masses ($E \approx |\vec{p}|$). For the considerably heavy particles, the rapidity y is used (historically, denoted with the same symbol as the y-coordinate)

$$y = \frac{1}{2}\ln\left(\frac{E + p_z}{E - p_z}\right). \tag{2.3}$$

The benefit in use of the η as the coordinate is that the difference in the pseudorapidities of two particles $\Delta\eta = \eta_1 - \eta_2$ is invariant with respect to the Lorentz boost along the beam axis. The same quality is true for the difference in rapidities.

The summarized above notations are applicable not only to the individual physics objects, e.g. leptons, photons, hadrons, etc., but also to the composite objects such as jets, top-quark pair and similar.

2.2.2 The magnet

A key component in the design of the CMS detector is its superconducting (niobium-titanium) solenoid, providing a magnetic field of 3.8 T. The solenoid is 12.9 m long with the inner diameter of 5.9 m, which grants enough space to house the calorimeters and tracking detectors inside its volume. The magnetic flux is returned by the iron yoke surrounding the solenoid. The strength of magnetic field inside the yoke is 2 T. The yoke itself is divided in five barrel wheels and three endcap disks at both sides. It also serves as the detector shielding, which, however, can be penetrated by the muons or neutrinos. The muon detectors are set between the yoke layers.

The movement trajectories (tracks) of charged particles are bended in the magnetic field depending on their momenta and the signs of their charges. This feature is used in the reconstruction of the particles arising from the pp collisions.

2.2.3 Tracking detectors

The tracker is the innermost partition of the CMS detector and it is fully assembled from silicon modules. As can be seen in Figure 2.3, it consists of two subsystems, the pixel and strip detectors. The pixel detector is installed around the LHC beampipe centered at the IP. The pixel detector is surrounded by the strip detector. The coverage of the strip detector

extends up to the calorimeter systems. Both pixel and strip detectors are structured with multiple barrel layers and endcap disks, allowing their effective operation at high track multiplicities. The number of layers is chosen in a way that the tracker is capable to provide highly precise measurement of the particle tracks, while minimally disturbing the flow of particles.

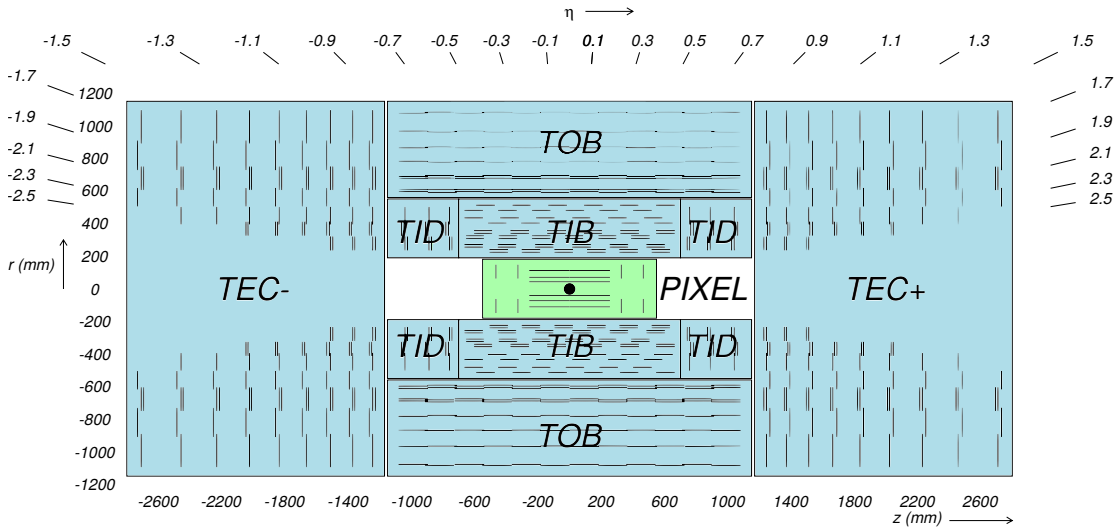

Figure 2.3 The CMS tracking system comprised of the pixel (green) and strip (blue) detectors (black lines inside the coloured areas). The black dot in the center corresponds to the nominal interaction point. From [65], modified.

The purpose of the CMS tracker is to collect the early stage information about the charged particles as they emerge from the *pp* collision. This includes the precise measurement of the particle momenta, charges and impact parameters (see Section 4.4.6) of their tracks. For this purpose, the particle track is reconstructed out of a few hits, the points where the particle interacts with the detector material. The momentum and charge is determined from the curvature of the corresponding track. In addition, the inner pixel tracker is the crucial tool in the identification of the so-called primary and secondary vertices. The primary vertex is a point where two colliding protons interact with each other. The secondary vertex is a point associated with the decay of a particle stemming from the primary vertex.

The pixel tracker

The silicon pixel tracker is located in the extremely harsh environment, close to the region where the *pp* collisions occur. At the design luminosity of the LHC, the expected particle flux near the pixel tracker ($r \approx 10$ cm) is nearly 10^7 per second. The pixel occupancy of

about 10^{-4} per LHC crossing is achieved owing to the high granularity of the sensors. The size of the pixels is 100 μm $\times$ 150 μm.

The pixel tracker is comprised of 1440 modules with $66 \cdot 10^6$ pixels, which are divided into the 3 barrel layers and 2 endcap disks on each side of the tracker. The barrel layers are 53 cm long and are correspondingly localized at the radii of 4.4 cm, 7.3 cm and 10.2 cm. The 2 endcap disks with radii of 6 cm (15 cm) are installed at the z-position of ±34.5 cm (±46.5 cm). The pixel tracker provides coverage up to $|\eta| = 2.5$ with spatial resolution of 10 μm (20 μm) for the measurements in the $r\phi$ (z) coordinates.

The strip tracker

The silicon strip tracker surrounding the pixel tracker is 5.8 m long and has an outer radius of 1.1 m. It consists of 15148 modules with $9.6 \cdot 10^6$ microstrip channels in total. The strip tracker is divided into the barrel and endcap regions covering up to $|\eta| = 2.5$.

The barrel region is structured into the inner and outer parts (TIB and TOB, respectively). The TIB is composed of 4 layers, which extend up to $|z| = 65$ cm and are placed within 20 cm $< r <$ 55 cm. The TOB is built from 6 layers covering the area up to $|z| = 110$ cm and between 55 cm $< r <$ 110 cm. The endcap region consists of 3 inner disks and 9 outer disks (TID and TEC, respectively) on both sides of the tracker. The TEC is located in the area within 120 cm $< |z| <$ 280 cm, while the TID is situated in the gap between the TIB and TEC.

The sensors in the silicon strip tracker are of 15 different geometries [72], that are designed according to the aforementioned regions. Depending on the geometry type, the strip length (∼cm) and pitch (∼μm) are varied in order to ensure the strip occupancy to be less than 3% per LHC crossing. The strips in the barrel (endcap) sensors are parallel (pointing) to the beam axis.

2.2.4 Calorimeters

The calorimeter detector is intended to measure the energy of the particles penetrating through it. Typically, those particles lead to a particle shower, i.e. electromagnetic or hadronic, inside the calorimeter, which is required to be fully captured. For this reason, the calorimeter design is based on a balance between the density of a building material and the effective volume. In order to gain sensitivity to the particle position and its flight direction, the calorimeters are segmented in the longitudinal and transversal directions with respect to the particle tracks. The segmented geometry allows not only to distinguish particle showers in space, but also to study their shapes.

The calorimeter system of CMS surrounds the tracker. It is separated into the electromagnetic and hadronic calorimeters (ECAL and HCAL, respectively), which, as a whole, are designed to measure the energy deposits from the photons, electrons and strongly-interacting particles.

The electromagnetic calorimeter

The ECAL measures the energy of the particles that mainly interact by means of the electromagnetic force. It is capable to provide an excellent energy resolution for the photons and electrons [73]. The ECAL is installed next to the tracker and it is built from 75848 lead tungstate ($PbWO_4$) scintillating crystals, which are grouped into the barrel part (EB) and two endcaps (EE).

The EB covers the range up to $|\eta| < 1.479$ and has an inner radius of 129 cm. Its crystals are 23 cm long and have a frontal cross section of 22 mm $\times$ 22 mm. The EE corresponds to $1.479 < |\eta| < 3.0$ and is placed at $|z| = 314$ cm. The crystals in EE have a length of 22 cm with a 28.6 mm $\times$ 28.6 mm frontal cross section.

The lead tungstate is an extremely heavy, but fully transparent material. It serves as absorber, with a radiation length of $X_0 = 0.89$ cm, that stops the traversing photons and electrons. According to their energy deposits, the scintillation light is produced in the crystal volume. About 80% of the light is radiated in the interval of 25 ns, which suits well for the LHC crossing time. In the EB (EE) region, the light is detected using silicon avalanche photodiodes (vacuum phototriodes), which are glued to the back side of crystals.

The preshower detectors (the silicon strip sensors shielded by the absorbing lead plates) are placed in front of the EE calorimeter. They are designed to distinguish between the prompt high-energetic photons emerging from *pp* collisions and the low-energetic photons from π^0 decays.

The hadronic calorimeter

The HCAL calorimeter is designed to measure the energy deposits left by strongly-interacting particles, which cause the hadronic showers inside the calorimeter volume. In particular, it is an essential tool for the detection of jets and the evaluation of the missing transverse energy (E_T^{miss}), due to particles escaping detection (see Section 4.4.5). The jet energy resolution is similar across the HCAL, being about 12% for 100 GeV jets in the transverse component. The resolution for E_T^{miss} is discussed in [67]. The HCAL is divided into the barrel (HB), outer (HO), endcap (HE) and very-forward (HF) calorimeter subsystems.

The HB [74] and HE [75] are composed of brass layers, serving as the absorber (X_0 = 1.49 cm), interleaving with the plastic scintillator tiles. The thickness of brass (scintillator) plates is 5 cm (first plate is 0.9 cm, other are 0.37 cm). The emitted scintillation light due to hadronic showers is collected by wavelength-shifting fibres inserted in the scintillator. Afterwards, the light is transmitted through clear optical fibres to the read-out system based on hybrid photodiodes. The HB and HE are mounted inside the solenoid and next to the ECAL, providing the coverage in the intervals $0 < |\eta| < 1.4$ and $1.3 < |\eta| < 3.0$, respectively.

In the pseudorapidity region of $0 < |\eta| < 1.26$, the HB is complemented by additional scintillator tiles (plastic, 1 cm thick) placed outside the magnet coil. This part of HCAL is referred to as the HO calorimeter. In the central area, two layers of scintillators are separated by the iron absorber (18 cm thick). In the region close to the coil sides, only one scintillator layer is used. In particular, the coil itself serves as the absorber, preceding to the HO. The HO design increases the effective thickness of the HCAL. This allows an improvement in the E_T^{miss} resolution, as well as capturing the tails of high-energetic hadronic showers.

The HCAL is extended by the HF calorimeter [76]. It is installed on both sides of CMS outside the yoke and provides a coverage in $3.0 < |\eta| < 5.0$, region with unprecedented particle fluxes. The front side of HF is 11.2 m away from the IP. The HF has steel absorber (1.65 m deep) with the embedded quartz fibres, serving as an active material. The quartz fibers of 0.6 mm in diameter are inserted with 5 mm steps using a square grid. They are parallel to the beam. The particle showers lead to Cherenkov radiation in the quartz. The light is channeled through the air-core light guides to the photomultipliers for the read-out. The HF allows the detection of forward jets and the hermeticity of the E_T^{miss} measurement.

2.2.5 The muon system

The muon detectors are situated outside the solenoid, since the muons, typically, are the only detectable particles that traverse the detector up to this point. The muon system is organized in the 4 barrel stations (MB) and 4 endcap disks (ME) on each side of the CMS detector, providing a coverage in $0 < |\eta| < 2.4$. The stations and disks are interleaved with the yoke layers. The muon system is composed out of three types of gaseous detectors, which are the drift tube (DT) chambers, cathode strip chambers (CSC) and resistive plate chambers (RPC) [77]. The chambers are installed according to the geometry shown in Figure 2.4.

The MB consists of 250 DT chambers. One layer of DT chambers is installed per station (MB1, MB2, MB3 and MB4 in Figure 2.4). Each DT chamber is accompanied by one or two RPC chambers, depending on the station. The ME is built in similar way, but using the combination of 468 CSC chambers with the RPC chambers (ME1, ME2, ME3 and ME4 in

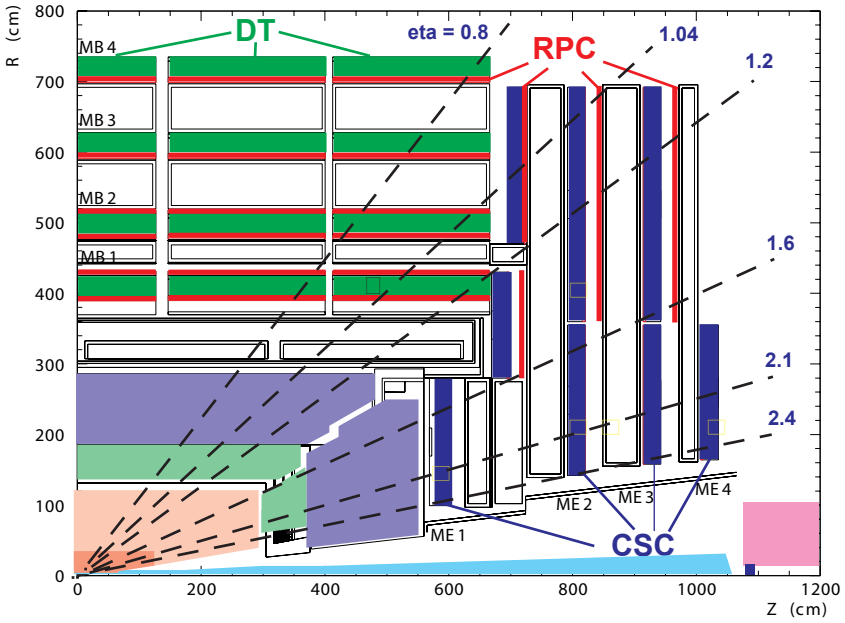

Figure 2.4 A quadrant of the CMS muon system, showing the installation geometry of the muon subdetectors (DT, CSC and RPC chambers). They are interleaved with the return yoke plates. The *y*-axis R points in the upward direction from the IP (the coordinate origin), while the *x*-axis Z is parallel to the beam. From [71].

Figure 2.4). The CSC chambers are used in the endcap region, where high muon signal and neutron background rate are present. The MB and ME house 912 RPC chambers in total.

The DT and CSC chambers are used to measure the position of the muon, and therefore its momentum. Each DT station (CSC chamber) has a resolution of 100 μm (100-200 μm, depending on the layer) in the position and about 1 mrad (10 mrad) in the direction. The RPC chambers are designed for a fast response to the muon signal, allowing the precise identification of the correct bunch crossing. Due to this, the spatial resolution for RPC chambers is lower, than for DT or CSC, and is about 1 cm. In total, the time resolution for the muon system is only 3 ns, which makes it an essential tool for the event triggering. More detailed information about the muon system performance is available in [78].

Overall, the muon system includes about 1 million electronic channels spanned over the 25000 m^2 of the effective detection surface. The information from the muon system can be combined with the other CMS subsystems for tracing the muons, which also plays an important role in the CMS detector calibration. The momentum resolution for 100 GeV (1 TeV) muons is about 1% (5%) across the detector, when combining the information from the tracker and muon systems.

2.2.6 Event triggering and data acquisition systems

At the design luminosity of LHC, approximately 10^9 *pp* interactions per second occur inside the CMS detector, owing to the bunch crossing rate of 40 MHz and assuming 25 *pp* interactions per collision of the beams. Only a tiny fraction of these interactions are the high-energetic direct collisions, which are more likely to originate the events with the physics processes of a particular interest. In addition, the information from only up to 10^3 bunch crossings per second can be written to the archival storage, mostly because of the technical limitations in its maximum capacity and data rate. Due to these reasons, the CMS trigger system serves for the selection of potentially interesting events during the collisions, while reducing the event rate before a storage by the factor of 10^6. The event triggering is performed involving the two tiers, namely the Level-1 (L1) trigger and High Level Trigger (HLT).

The L1 trigger is based on custom hardware processors, determining the decision whether to keep the data from a particular bunch crossing [67]. For a rapid achievement of the decision, the L1 trigger involves the reduced-granularity and reduced-resolution data from the calorimeter and muon systems. Forming the decision, the L1 trigger checks for a presence of the trigger objects, such as electrons, muons, jets and photons above the preset thresholds regarding their transverse energy and momentum. The total E_T and E_T^{miss} observed in the detector are also considered. The decision is reached within 3.2 μs after the collision. During this time, the data is stored in the memory buffers. The decision itself is computed in less than 1 μs, while the rest of the time is allocated for the data transfer. The L1 trigger is designed for the reduction of the event rate from 40 MHz to 16-100 kHz.

For an event passing the L1 trigger, the full-granularity and full-resolution data from all CMS detector subsystems is transferred to the data acquisition system, emptying the memory buffers. Afterwards, the combined detector information is sent to the HLT trigger for further tests.

The HLT trigger decides whether to keep the data for the offline analysis. The HLT is based on the software algorithms that are run on a powerful computing farm. It relies on the event reconstruction methods, which are similar to the ones used in the offline reconstruction, while searching for the interesting event signatures. Owing to the inclusion of the tracker information in this process and more stringent selection requirements, the event rate is reduced to 100-1000 Hz. Typically, the HLT decision for a single event is processed in 40 ms.

After the HLT triggering, the obtained event collections are stored in the data storage system at CERN.

2.2.7 Detector upgrades

The CMS Collaboration prepared an extensive roadmap for the detector upgrade through 2025 [79, 80] according to milestones of the LHC operation. The previously explained design of the CMS detector in this chapter is the primary design that was used throughout the LHC Run-I operation. During the first long shut down of the LHC, the CMS detector was upgraded in view of the Run-II data taking. The upgrades of the CMS detector for the Run-II data taking are briefly summarized in the following, as they are relevant for the data studied in this work.

In the muon system, a fourth layer of CSC chambers was added in the interval $1.6 < |\eta| < 1.8$, improving the trigger efficiency in this region. The CSC electronics were upgraded to allow the effective performance of the muon triggers at high instantaneous luminosity. In addition, a fourth layer of RPC chambers was installed in the region $1.2 < |\eta| < 1.6$, enhancing the timing and redundancy to the accompanying CSC chambers and, thus, the muon reconstruction and triggering. The trigger logic itself was updated according to the new chambers. Some of the DT electronics were moved out from the detector periphery to prevent their further exposure to radiation and high magnetic field.

The read-out system in the HO part of the HCAL was upgraded replacing the hybrid photodiodes with silicon photomultipliers, which possess a better quantum efficiency, higher gain, and superior immunity to magnetic fields. This upgrade improves the reconstruction of high-energetic jets and response to minimum ionizing particles.

Chapter 3

Event Simulation

A physics analysis of the collision data requires perfect understanding of the detector response in the context of a studied physics model. This information can be obtained by means of an event simulation, which implies separate simulations of a physics model and the detector response.

An event simulation makes use of various generator programs implementing the Monte-Carlo (MC) method [81], which relies on the random sampling to perform relevant numerical calculations. A *pp*-collision can be predicted by perturbation theory only at a certain level of accuracy due to limitations in the computing power. Different non-perturbative effects are required to be considered. The approximate description of these effects is provided by corresponding phenomenological models implemented in dedicated MC generators. Generating the 4-momenta of particles on an event-by-event basis, the MC simulation provides predictions of the rate and event kinematics for the signal process, as well as for the background processes. The MC simulation is also used to perform the study of detector calibrations, efficiencies and corrections for the detector response, as well as to study the event selection involved in the physics analysis. The comparison of MC predictions to experimental data may provide insights about the goodness of the models used by generators and an input for their improvement.

In perturbation theory, the factorization theorem [41] separates the evolution of a collision event into relevant subprocesses occuring at different energy scales, as was mentioned in Section 1.2.1. Therefore, the total cross section of the interesting process can be calculated accounting separately for the hard scattering process and other contributing subprocesses. Owing to this property, the MC simulation of the *pp*-collision is separated in the sequential steps shown in Figure 3.1 and it develops as follows. The proton structure is described by the parton distribution functions (see Chapter 1), which provide the modelling of partons that interact in the hard scattering process. The matrix element calculations are used to predict

the partonic cross section for the hard scattering (see Section 3.1). The partons present in the initial and final states of the event can emit additional radiation (referred to as initial or final state radiation, denoted as ISR and FSR, respectively), producing the so-called parton shower (see Section 3.2). Once the evolution of the parton shower reaches an energy regime where the perturbation theory is not applicable ($\approx$ 1 GeV), the partons undergo the hadronization process (see Section 3.3). The matrix element calculations require a proper matching to the parton shower simulation, as discussed in Section 3.4. The modelling of the underlying event and colour connections in the collision affect the outcome of the parton shower and hadronization processes, as described in Sections 3.5 and 3.6, respectively. Afterwards, the generated particles are propagated through the dedicated simulation accounting for the detector response (see Section 3.7).

All aforementioned simulation steps are described in greater detail in the following, where particular attention is devoted to the generator programs used in this work.

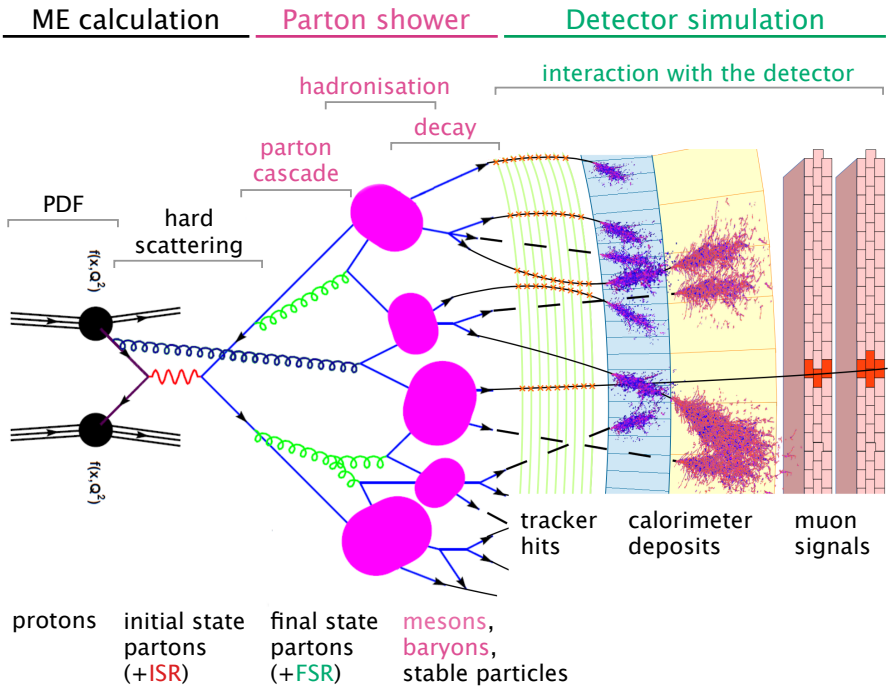

Figure 3.1 The schematic demonstration of the MC simulation is shown with respect to the sequence of involved subprocesses. From [82].

3.1 Matrix element calculation

The matrix element (ME) of the hard scattering process is calculated in perturbation theory at a fixed order of α_S (see Chapter 1), where the accuracy of these calculations at $O(\alpha_S^2)$ is referred to as leading order (LO), at $O(\alpha_S^3)$ as next-to-leading order (NLO), at $O(\alpha_S^4)$ as next-to-next-to-leading order (NNLO≡N^{2}LO), etc. At LO, the initial state configuration of the interacting partons in the hard scattering is determined by the PDF. These initial state partons produce after their interaction the outgoing partons, e.g. $gg \to t\bar{t}$ (depending on the process of interest), corresponding to the final state of the hard scattering. At NLO, the ME calculation includes either the first real emission correction or the first virtual (one-loop) correction. At N^{n}LO, the ME calculation includes the combination of the corresponding number of real (n_{real}) and virtual ($n_{virtual}$) corrections according to $n_{real} + n_{virtual} \leq n$. The additionally radiated partons as result of the real emission corrections contribute to the ISR and FSR, depending on their origin. Examples of Feynman diagrams corresponding to LO and NLO matrix elements for the $t\bar{t}$ production are shown in Figure 3.2.

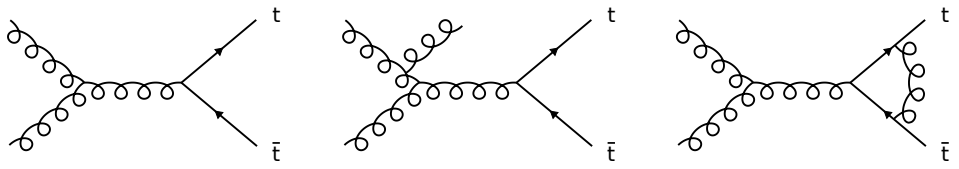

Figure 3.2 Feynman diagrams representing the $t\bar{t}$ production via the gg-fusion at the leading order (left) and at the next-to-leading order for the first real emission correction (middle) or for the first virtual correction (right). The middle diagram also represents the initial state radiation, where an additional gluon is radiated by one of the gluons participating in the hard scattering.

As described in Section 4.2.1, the matrix element calculations for the $t\bar{t}$ process are performed using two distinct ME generators, which are introduced in the following.

The Powheg v2 (POsitive Weight Hard Event Generator v2) [83–86] event generator is capable to perform the ME calculations at NLO accuracy for different processes of heavy flavour production in hadronic collisions. The Powheg method allows the ME interface to other MC programs for the parton shower simulation. The generated top quarks are decayed at leading order accuracy, defining a final state, e.g. $t\bar{t} \to \bar{\ell}\nu b\ell\bar{\nu}\bar{b}$. In particular, for processes of top quark production, calculations in Powheg v2 directly account for spin correlations in the decay products of top quarks.

An alternative ME calculation is provided by the MadGraph5_aMC@NLO (v.2.2.2) [87] event generator, which offers an automated computation of tree-level LO and NLO matrix elements together with their matching (see Section 3.4) to the parton shower simulation. Here, a

notion of tree-level matrix element implies that calculations may include the additional higher order corrections only due to real emissions. In particular, the MadGraph5_aMC@NLO is capable to compute LO and NLO matrix elements with up to several additional partons (e.g. for $t\bar{t}$ production, such processes are referred to as "$t\bar{t}$+1jet", "$t\bar{t}$+2jet", etc., for processes with one additional parton, two additional partons, etc., respectively). Within the MadGraph5_aMC@NLO, the MadSpin [88] package is used to model the decays of narrow resonances while preserving spin correlation effects.

The ME calculations for most background processes rely on the use of Powheg v2 and MadGraph5_aMC@NLO. Only for diboson processes (see Section 4.3), the multipurpose event generator Pythia (v.8.2) [89] (referred to as Pythia8) is used to calculate the relevant matrix elements at LO. Pythia8 also provides the complete functionality to perform the simulation of parton shower and hadronization processes.

3.2 Parton shower simulation

High-energetic partons present in the initial and final states of the event can produce QCD and QED radiation emissions, i.e. gluons and photons, respectively. The following branching processes can occur: $q \to qg$, $q \to q\gamma$, $g \to gg$, $g \to q\bar{q}$ and $\gamma \to q\bar{q}$. Leptons can also contribute to the aforementioned branchings by the processes: $\ell \to \ell\gamma$ and $\gamma \to \ell\bar{\ell}$. All these processes will iteratively continue as long as they are energetically allowed. The resulting cascades of partons are called parton shower (PS) and the corresponding process of their evolution is called parton showering.

The parton shower emissions serve as higher-order corrections to the ME calculation (beyond the order of α_S). Even though parton showers are predicted in the perturbation theory, their precise computation is technically impossible due to substantial increase in the number of allowed processes, when increasing the accuracy of the calculations. Instead, different generator programs for the PS simulation provide an approximate solution, relying on a probabilistic approach to determine the occurrence of additional emissions. In this work, the PS is modelled using either the Pythia8 or the Herwig++ (v.2.7.1) [90] generator.

The additional emissions in the PS are ordered by the energy-dependent scale μ, the so-called evolution scale. The definition of the evolution scale is different depending on the PS model. Pythia8 implements the transverse-momentum-ordered parton shower defining the scale as $\mu = p_T^2$, where p_T is the transverse momentum of the radiating parton. Herwig++ provides the angular-ordered parton shower using $\mu \approx E^2\theta^2$ (in approximation of small angles; exact expression in [90]), where E is the energy of the radiating parton and θ is the angle between two radiated partons.

The PS evolution proceeds as follows. The probability that a parton does not split between the two scales μ_1 and μ_2, where $\mu_1 > \mu_2$, is given by the Sudakov form factor [91]. The PS evolution starts at the user-defined scale μ_{max}, which is usually chosen according to the scale of the hard process. Solving the Sudakov form factor with the input scale $\mu_1 = \mu_{max}$, the scale μ_2 of the new emission can be found and the corresponding emission is generated. The PS is iteratively evolved until the so-called cut-off scale μ_{min} is reached. The μ_{min} is usually chosen of the order of 1 GeV or as equal to Λ_{QCD} [92], below which perturbation theory is not applicable.

3.3 Hadronization process

When the parton shower evolution approaches the cut-off scale μ_{min}, the event starts to enter the non-perturbative regime ($\alpha_S \approx 1$). Below the cut-off scale, the direct consequence of the colour confinement is the so-called hadronization, the process of the formation of hadrons out of the available partons in the event. The hadronization process cannot be explained within the perturbative theory and, therefore, is modelled phenomenologically.

Pythia8 uses the Lund string hadronization model [93, 94], which assumes a linear colour potential between/among interacting partons (for two/several-body processes). This colour potential is represented by a colour string connecting the corresponding parton pair with a tension of about 1 GeV/fm [91]. For instance, the string hadronization for the case of two quarks produced in pair ($q\bar{q}$) by the PS evolves as shown in Figure 3.3. During the evolution of a quark pair, the distance between quarks increases, resulting in an increasing energy of the colour field. If energetically allowed, the string breaks to produce a new quark pair out of the QCD vacuum, where each new quark connects through a colour string to one of the initial quarks. The hadron production continues as long as some string has enough energy to produce a hadron of the required mass.

The cluster hadronization model [91], used in Herwig++, is based on the preconfinement property of parton showers [95], where the colour structure of showers is assigned already during their evolution. The hadronization process starts by decaying all gluons (produced by the PS and evolved down to the cut-off scale) to $q\bar{q}$ pairs. Afterwards, the initial clusters are combined out of the quark pairs connected by the colour. In the sequence of two-body decays of initial clusters to clusters of lighter invariant masses, all clusters are decayed to hadrons.

Given the use of many non-perturbative assumptions, hadronization models require their tuning to the experimental data, as well as input information about possible hadron states and corresponding decay modes.

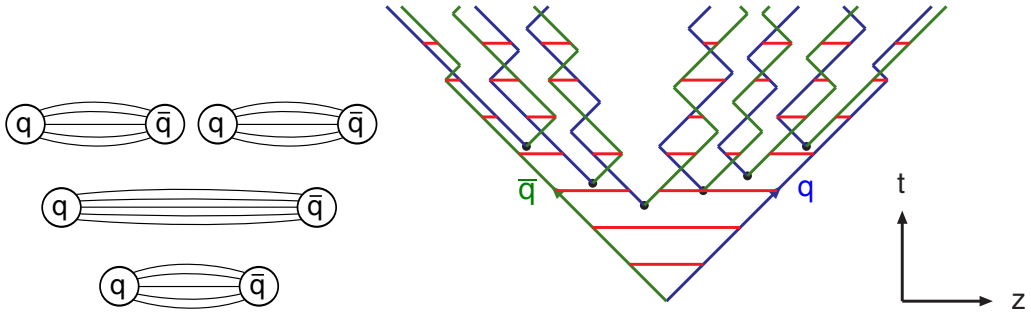

Figure 3.3 Left: The schematic evolution of the colour string connecting the quark pair in the Lund string model. String breaks to produce a new quark pair out of the QCD vacuum. **Right:** The evolution of the string system connecting quark pair in time (axis pointing upwards). The hadrons are produced with an increase in distance (axis pointing right) between initial quarks. From [91].

3.4 Matching matrix element to parton shower

The ME calculation needs to be interfaced to a PS simulation in order to give a reliable prediction of exclusive final states. This procedure requires particular attention because some processes can be similarly produced by the ME calculation and by the PS. For instance, the process of a kind $gg \to t\bar{t}$ + 1jet can be generated as a result of the ME calculation at NLO accuracy, where the first real emission correction is included, or by applying the PS simulation to the LO matrix element. In cases where the ME calculation and PS simulation generate additional jet emissions in the same energy range, a double-counting of the same events may occur while calculating the corresponding contributions to the cross section. For the case where ME and PS simulations are performed together using the same event generator (e.g. Pythia8), the aforementioned double-counting is prevented directly via the functionality within the generator. In contrast, for the simulation relying on the interface between standalone ME and PS generators (e.g. Powheg v2+Pythia8), the double-counting is avoided through a dedicated technique known as matching procedure (between the matrix element and the parton shower). The matching procedure depends on the implementation of involved generators.

The Powheg v2 generator implements the requirement that the first generated emission, i.e. the one from the ME, must be the hardest in scale, while all subsequent emissions must be generated below the transverse momentum of the hardest emission. Thus, when Powheg v2 is interfaced to the PS simulation (e.g. Pythia8), the latter can produce only softer jet emissions with respect to the first generated emission. In this case, the matching procedure is performed by vetoing those jet emissions from the PS that are above or equal to the scale of the first generated emission. In Powheg v2, the hardness of the first generated emission is

regulated by the so-called damping parameter denoted as h_{damp}. Lower values of h_{damp} lead to generally softer p_T-spectrum of additional jet emissions.

In simulation setups involving MadGraph5_aMC@NLO, the matching is performed by subtracting the relevant contribution to the cross section predicted by the PS from the total cross section predicted by the ME calculation.

3.5 Underlying event model

The underlying event (UE) denotes those processes within the *pp*-collision event that are not associated with the hard scattering of interest. These processes comprise multi-parton interactions (MPI) and beam-beam remnants (BBR). In MPI, several pairs of partons from colliding protons lead to multiple hard scatterings. In BBR, colliding protons leave behind beam remnants, which are required to form corresponding bound states and to be colour-connected with the other particles produced in the event. The UE enhances the jet activity in the event. Therefore, the modelling of jet activity by the PS simulation may be affected by the involved UE model. Since the UE simulation is governed by free phenomenological parameters, the UE models require tuning to the experimental data [96].

3.6 Colour reconnection model

In QCD, the colour confinement implies that all partons in the event are required to be connected in terms of the colour flow, leading to the neutralization of colours among them. However, it was found that a rearrangement of the perturbative colour-flow configuration leads to a better description of the experimental data [91]. Many phenomenological models explain this observation by the so-called colour reconnection (CR) [97], which implements non-perturbative rearrangements in the colour flow among the partons by changing which partons are connected among each other by colour. The CR plays an important role in the PS tuning, since it can significantly alter the hardness and multiplicity of the jet activity in the event. In particular, the CR also affects top quarks, which before decaying can interact with the colour-charged partons present in proximity of the respective *pp*-collision. A schematic demonstration of the colour reconnection process is shown in Figure 3.4.

Pythia8 implements several models of colour reconnection [97, 99, 100]. The default model in Pythia8 is the MPI-based scheme, which allows the reconnection of colour flows between two different MPI-systems. For colour reconnection, the MPI-systems are merged according to a probability governed by the p_T-scales of both systems [100]. It is more probable that a low-p_T MPI-system would be merged with a high-p_T MPI-system, while

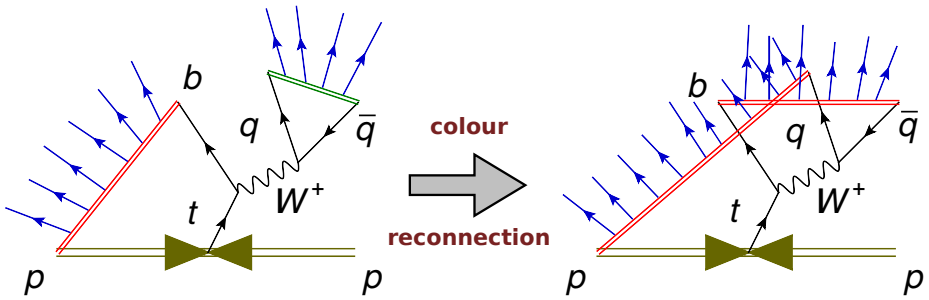

Figure 3.4 A schematic example of the colour reconnection process for the Lund string hadronization model. The left figure shows the decay of the top quark in the hadronic mode, where the initial colour structure of the system is represented by the red-coloured and green-coloured strings. The right figure shows the colour structure of the system after the colour reconnection. The hadrons are produced in the directions indicated by blue arrows. From [98, 97], modified.

merging of two high-p_T MPI-systems is rare. The merging is performed in such a way that it minimizes the total length of strings inside the resulting MPI-system. This procedure operates iteratively over all MPI-systems available in the event. The MPI-based scheme serves as a reference for the PYTHIA8-based simulations used in this work.

A basic idea behind the CR models implemented in HERWIG++ is the minimization of the invariant masses of the resulting clusters with respect to those available when the CR is not performed [101].

3.7 Simulation of the detector response

In order to perform a proper comparison between the reconstructed data and the MC simulation, the latter is propagated through the simulation of the detector response. The interaction of stable particles, generated after the complete ME+PS and hadronization simulation, with the CMS detector is simulated using the GEANT4 (v.9.4) [102] toolkit. GEANT4 performs the simulation of the passage of particles through detector materials relying on MC methods, geometrical modelling of the detector and a wide range of experimental data parametrizing the interaction of different particles with particular materials. In particular, test-beam data are used to parametrize the response of each subsystem of the CMS detector [67]. To reproduce the conditions of the real detector operation, the specific information about calibrations of the CMS detector, performance of electronic readout systems and non-operating channels is considered in the simulation. The simulation of the detector response is also complemented by the emulation of the CMS triggering system.

Chapter 4

Event Reconstruction and Selection

In this work the top-quark pair ($t\bar{t}$) production is studied. The signal process is $t\bar{t}$ production with the following decay modes $t \rightarrow W^{+}b$ and $\bar{t} \rightarrow W^{-}\bar{b}$, where each W boson decays subsequently into an electron or muon and the associated neutrino. In the following, these processes are referred to as $t\bar{t}$ production with prompt decays into dileptonic final states, or are simply mentioned as $t\bar{t}$ decays in dilepton channel. Their event signature in the detector is characterized by two isolated and oppositely charged leptons, at least two high energetic jets and the presence of significant missing transverse energy from neutrinos escaping the direct detection.

The signature of signal events can be mimicked by other physics processes. It can happen because of the physics process nature itself or due to instrumental detector effects, e.g. a jet can be misreconstructed as an electron. These physics processes are referred to as background processes. The background processes that are considered in this analysis are summarized in Section 4.3. The determination of their contributions is discussed in Section 4.5.

In order to perform an accurate and precise $t\bar{t}$ production cross section measurement, it is essential to use a set of events of high signal purity. The event selection, described in Section 4.4, serves this purpose. Prior to the selection, a thourough reconstruction of particle candidates is performed for each event, as explained in the same section.

The top quarks decay before they can form hadronic bound states. Due to this reason, a kinematic reconstruction of the top-quark pair is required in each event passing the selection to access the kinematics of the individual top quarks. The reconstruction algorithm is explained in Section 4.6.

Finally, this chapter is concluded in Section 4.7 with a summary of the total event reconstruction and selection procedures.

4.1 Data sample

The data sample used in this measurement was recorded with the CMS detector during the Run-II period of LHC operation at $\sqrt{s}$ = 13 TeV in 2016. The total integrated luminosity of this sample is 35.9 fb^{-1} [68]. Considering the total $t\bar{t}$ production cross section, roughly 30 millions $t\bar{t}$ events were produced in these collisions. A subset data sample is classified as "good" for physics analysis by the CMS Collaboration, after conducting data quality monitoring [103] and offline certification procedures. Only the "good" *pp* collision runs at LHC are taken. The list of used datasets is summarized in Table A.2.

4.2 Signal definition

In this analysis, the measured signal process is the $t\bar{t}$ production with following decays $t \to W^+b$ and $\bar{t} \to W^-\bar{b}$, where W bosons decay afterwards in the leptonic modes $W^+ \to \bar{\ell}\nu_\ell$ and $W^- \to \ell'\bar{\nu}_{\ell'}$ ($\bar{\ell}$, ℓ' refers to an electron or a muon). The final state of this decay topology, $t\bar{t} \to \bar{\ell}\ell' b\bar{b}\nu_\ell\bar{\nu}_{\ell'}$, includes two oppositely charged leptons, two b-quark jets and two neutrinos. Only the processes with direct decays of both W bosons into an electron or a muon and the corresponding neutrino are considered as signal. Further in the text, these processes are referred to as *$t\bar{t}$ signal*. From now on, all the groups of particular physics processes, indicating the signal or background contributions, will be referred to with the *cursive* font.

The processes including a decay $W \to \tau\nu_\tau$, disregarding whether the final state includes an electron or muon originating from the decay of the τ lepton, are not regarded as signal. This is done to simplify the reconstruction of event kinematics and the event selection, and to reduce combinatorial backgrounds. The $t\bar{t}$ decays via τ lepton and all other $t\bar{t}$ event topologies are treated as background and are referred to as *$t\bar{t}$ other* (see Section 4.3).

The $t\bar{t}$ signal definition is closely related to the experimental definition of the top quark as an object. In this analysis, two distinct definitions of the top quark are used, which are known as parton and particle level definitions. The parton level definition refers to the top quark just before its decay. In the particle definition, the top quark is explored after its decay, studying the corresponding object which is reconstructed out of associated decay products. The control distributions and event yields that will be presented in this chapter (see Section 4.7) correspond to the parton level definition. A complete discussion on both top quark definitions and their effect will be provided in Chapter 5.

4.2.1 Signal simulation

Monte Carlo (MC) simulation samples are used to model the expected signal and background events. The set of simulated samples that is used in this analysis to obtain the central measurement results will be referred to as "reference simulation".

The hard scattering process in the reference $t\bar{t}$ sample is simulated with the next-to-leading order event generator Powheg v2. The obtained sample is interfaced to Pythia8 for the simulation of parton shower and hadronization, where the underlying event is modelled with the tune CUETP8M2T4 [104, 105] (sample referred to as Powheg v2+Pythia8).

Alternative $t\bar{t}$ simulated samples are also used in this analysis to evaluate several systematic uncertainties (see Chapter 6). Additionally, $t\bar{t}$ samples produced with other event generators are used for comparisons with data (see Chapter 7). Details of these samples are given in the following.

In order to test the impact of alternative assumptions behind the modelling of the hard scattering process, the MadGraph5_aMC@NLO generator, relying on tree-level matrix elements modelled at NLO, is used in the interface with Pythia8. Here, from two up to five outgoing partons are generated in the hard scattering process, i.e. $t\bar{t}$+0,1,2 partons at NLO and 3^{rd} parton at LO, which are subsequently combined with the PS simulation following the FxFx matching procedure [106]. This alternative simulation is referred to as MG5_aMC@NLO+Pythia8 [FxFx].

Another $t\bar{t}$ sample is generated with Powheg v2, but interfaced to Herwig++, which serves as alternative model for PS and hadronization, incorporating the tune EE5C [107]. The corresponding event sample is mentioned as Powheg v2+Herwig++.

For all described $t\bar{t}$ simulations, the value of top quark mass is set to $m_t = 172.5$ GeV, while the proton structure is taken from the NNPDF3.0 [108] parton distribution functions. The renormalization (μ_R) and factorization (μ_F) scales are regarded as equal ($\mu_R = \mu_F$). In the definition of both scales, the transverse mass is used as given by $m_T = \sqrt{m^2 + p_T^2}$. For setups with Powheg v2, the nominal values are set to the transverse mass of the top quark as $\mu_R = \mu_F = \sqrt{m_t^2 + (p_T^t)^2}$. For setups with MadGraph5_aMC@NLO, both scales are set to $\sum_{t,\bar{t},jets} m_T/2$ [105]. The response of the CMS detector is simulated using Geant4.

The $t\bar{t}$ simulated samples are normalized[†] to the data (35.9 fb^{-1}integrated luminosity) using the inclusive $t\bar{t}$ production cross section of 831.76 pb. This value is calculated at NNLO accuracy with next-to-next-to-leading-logarithmic (NNLL) precision [44–49], which is performed using the Top++2.0 program [50] and assuming $m_t = 172.5$ GeV.

[†]for a given simulated sample, relevant event yields are scaled by a factor $\sigma \cdot L/\sum w$, where σ is the inclusive production cross section for the corresponding process, L is the integrated luminosity, and w denotes a weight assigned to each event by the relevant ME generator; the sum runs over all generated events.

The set of considered $t\bar{t}$ samples is summarized in Table 4.1 (reference MC) and Table A.3 (alternative MC). The samples are indicated in accordance with corresponding physics processes considered in this work.

Table 4.1 Reference simulated samples for the $t\bar{t}$ signal and relevant backgrounds that are considered in this measurement. Samples are indicated alongside corresponding generators used for the ME and PS+hadronization modelling. Inclusive production cross sections used for the normalization of samples are also listed (references for the quoted values are given in the text). All samples were generated by the CMS Collaboration.

Sample	ME generator	PS+hadronization	σ [pb]	Accuracy	
				ME	σ
$t\bar{t}$ *signal* / $t\bar{t}$ *other*	POWHEG v2	PYTHIA8	831.76	NLO	NNLO+NNLL
Single top : tW^-	POWHEG v1	PYTHIA8	35.85	NLO	approx. NNLO
Single top : $\bar{t}W^+$	POWHEG v1	PYTHIA8	35.85	NLO	approx. NNLO
Z+jets : $m_{\ell^+\ell^-} \geq 50$ GeV	MG5_aMC@NLO [FxFx]	PYTHIA8	5765.4	NLO	NNLO
Z+jets : 10 GeV $< m_{\ell^+\ell^-} <$ 50 GeV	MG5_aMC@NLO [FxFx]	PYTHIA8	22635.1	NLO	NNLO
W+jets : $W \to \ell\nu$	MG5_aMC@NLO [MLM]	PYTHIA8	61526.7	LO	NNLO
Diboson : WW	PYTHIA8	PYTHIA8	118.7	LO	NLO
Diboson : WZ	PYTHIA8	PYTHIA8	47.13	LO	NLO
Diboson : ZZ	PYTHIA8	PYTHIA8	16.523	LO	NLO
$t\bar{t}$+W : $W \to \ell\nu$	MG5_aMC@NLO [FxFx]	PYTHIA8	0.2043	NLO	NLO
$t\bar{t}$+W : $W \to q\bar{q}'$	MG5_aMC@NLO [FxFx]	PYTHIA8	0.4062	NLO	NLO
$t\bar{t}$+Z : $Z \to \ell\bar{\ell}, Z \to \nu\bar{\nu}$	MG5_aMC@NLO	PYTHIA8	0.2529	NLO	NLO
$t\bar{t}$+Z : $Z \to q\bar{q}$	MG5_aMC@NLO	PYTHIA8	0.5297	NLO	NLO

4.3 Background processes

The dilepton channel is expected to have the least background contamination for $t\bar{t}$ production with respect to other channels (as was previously discussed in Section 1.2.2). Still, the $t\bar{t}$ *signal* event signature is imitated by a large number of other physics processes. Those background contributions whose production rates are negligible compared to the signal contribution are not taken into account in this work. The background sources which are considered as relevant are described in the following.

- $t\bar{t}$ ***other*** are all other $t\bar{t}$ event topologies that are not regarded as signal. In its majority, this $t\bar{t}$-related background includes dileptonic decays that occur through a τ lepton. It also contains events which actually belong to ℓ+jets or all-hadronic decay modes, but are misreconstructed as dileptonic events. The $t\bar{t}$ *other* contribution is estimated from the same simulated samples as the $t\bar{t}$ *signal* (see Section 4.2.1), and normalized in the same way.

- $t\bar{t}$**+Z (**$t\bar{t}$**+W)** is a process where the top-quark pair is produced in association with a Z (W) boson. The $t\bar{t}$+Z and $t\bar{t}$+W processes are generated with MadGraph5_aMC@NLO at NLO accuracy. For the $t\bar{t}$+W process, matrix elements include up-to one extra parton (i.e. from two up to five outgoing partons are generated in the hard scattering process), combined with the PS simulation via the FxFx matching procedure. Both processes are normalized with cross sections that are predicted by their MC simulation, as the rate of these processes is very small and the accuracy of modelling in the simulation is good enough.

  For the $t\bar{t}$+Z events where the Z boson decays into a lepton (quark) pair the cross section of 0.2529 pb (0.5297 pb), predicted by the corresponding MC simulations.

  The events where the associated W boson decays leptonically (hadronically) are normalized with the cross section of 0.2043 pb (0.4062 pb), predicted by the corresponding MC simulations.

  The combined contribution of $t\bar{t}$+Z and $t\bar{t}$+W processes is referred to as $t\bar{t}$+Z/W, hereafter.

- ***Single top*** background are the processes where only one top quark is produced by means of the electroweak interaction. The processes with single top quark production were previously introduced in Section 1.2.1. Only one of them can lead to a final state with two leptons. This is the single top production in association with a W boson, e.g. $gb \rightarrow t\mathrm{W}^-$ and $g\bar{b} \rightarrow \bar{t}\mathrm{W}^+$, which is commonly known as tW process. Only this process is considered in this work, as s-channel and t-channel production have negligible contribution.

  The tW simulation sample is generated at NLO accuracy with the Powheg v1 [83–85, 109] generator, and is normalized according to the theoretical cross section of 35.85 pb from approximate-NNLO calculations [110, 111] for both top quark and antiquark.

  In the following, the contribution form tW process is mentioned as *single t*.

- ***Diboson*** background consists of processes in which Z and W bosons are produced in pairs (WW, WZ and ZZ) [112]. The corresponding matrix elements are generated with Pythia8 at LO.

  The WW simulated samples are normalized with a cross section of 118.7 pb, which is obtained with the NNLO QCD calculations in [113]. The WZ and ZZ events are normalized with the cross sections of 47.13 pb and 16.523 pb, respectively, obtained from MCFM [114] NLO predictions.

- ***Z+jets*** background refers to Drell-Yan (DY) production with several jets. At LO at the LHC, the DY process starts with the annihilation of a quark originating from one proton and an antiquark of the same flavour from another proton, where the Z boson or virtual photon (γ^*) is produced. The produced Z boson or γ^* subsequently decays into a pair of oppositely charged leptons. At higher orders, the jets in *Z+jets* arise from initial state radiation (ISR).

  The rate of *Z+jets* production is much larger than the rate of $t\bar{t}$ production. Thus, the *Z+jets* background is one of the most important and requires a careful estimation (see Section 4.5). However, the corresponding contribution can be strongly suppressed with the selection requirements described in Section 4.4.

  In this analysis, the *Z+jets* simulation includes *Z+jets*$\rightarrow \ell^+\ell^-$ processes, where $\ell^+\ell^-$is either e^+e^-, $\mu^+\mu^-$or $\tau^+\tau^-$. The corresponding NLO-matrix elements are generated with MadGraph5_aMC@NLO in two regions of the invariant mass of the lepton pair $m_{\ell^+\ell^-}$. The simulation in the first (second) mass region of 10 GeV $< m_{\ell^+\ell^-} <$ 50 GeV ($m_{\ell^+\ell^-} \geq$ 50 GeV) is normalized with the cross section of 22635.09 pb (5765.4 pb) that is computed at NNLO accuracy with FEWZ v.3.1 (v.3.1.b2) [115–117]. The matrix element calculations include up-to two extra partons, which are matched with the PS using the FxFx method.

- ***W+jets*** background corresponds to a process that, in essence, is very similar to the *Z+jets* process, but where a W boson is produced instead of a Z boson. However, the W boson is produced from an up-type quark from one proton and a down-type quark from another proton. Afterwards, the event is classified according to the W boson decay modes.

  Only one charged lepton can be present after the decay of a W boson and only if it decays in the leptonic mode. However, a misreconstructed jet might appear as a second charged lepton in the detector, which would give rise to a signal-like event. Due to a rare occurence of the jet misreconstruction of this kind, only *W+jets* processes where the W boson decays into a charged lepton (either e, μ or τ) and the associated neutrino are considered for the background determination. For these processes, additional jets originate purely from the ISR.

  The simulation of *W+jets* events is performed with the LO matrix elements from MadGraph5_aMC@NLO, generating up-to four extra partons and matching them to PS simulation via the MLM [118, 87] approach. The corresponding sample is normalized with a cross section of 61526.7 pb, which is evaluated with FEWZ v.3.1 at NNLO accuracy.

The generated samples for all background processes are interfaced with PYTHIA8 for the modelling of PS and hadronization. The UE is described with the tune CUETP8M1 [104, 119], except of single top quark samples where the tune CUETP8M2T4 is used. As in the case of the *$t\bar{t}$ signal*, the simulation is completed using the GEANT4 to model the CMS detector response. The summary of background samples is provided in Table 4.1.

4.4 Reconstruction of physics objects and event selection

In this measurement, the selection of signal $t\bar{t}$ events follows the event selection used for a similar measurement performed at 8 TeV [8], but with the necessary optimization of selection requirements for 13 TeV. First of all, as mentioned in Section 4.1, only the data events which are classified, by the CMS Collaboration, as good for a physics analysis are considered. Afterwards, the selection requirements, targeting dilepton final states, are imposed on the data and simulation. The selection requirements are based on multiplicities and properties of physics objects reconstructed in the event. The reconstruction of physics objects is performed with the Particle Flow (PF) algorithm [120], combining the information from all subdetectors to identify individual particle candidates. In the following, the event selection requirements are described, as well as the reconstruction of the relevant physics objects in a greater detail.

4.4.1 Tracks and primary vertices

The track reconstruction implies a procedure that uses hits, measured in detector systems, to estimate the momenta and positions of the charged particles causing the hits and, thus, tracks [121]. During this procedure, a mapping between coordinates of the hits, measured in a coordinate system associated with a plane of each subdetector, and the global coordinate system of CMS is performed. The reconstruction of a track begins with a generation of the seed, defining the initial parameters of a particle trajectory associated with the track. Afterwards, the reconstruction builds-up on a sequential search of best-matching hits measured in the detector layers. In order to complete the reconstruction, the track candidate is obtained as a result of a fit, accompanied by a smoothing procedure over the relevant hits.

As mentioned in Section 2.2.3, the primary vertex is a point where two colliding protons interact with each other. During the crossing of beams, several proton-proton collisions might occur and, therefore, leading to several primary vertices. These vertices are measured at the same time by the detector, using a pile-up of signals from different vertices, and can be attributed to the same event. In the following, a presence of several primary vertices within the same event is referred to as pile-up.

The primary vertex candidates are identified and reconstructed using tracks measured in the tracker. For each candidate, a collection of relevant tracks is selected using criteria based on track properties, whether tracks arise directly from a region where beams are crossed, and the distance between tracks and the vertex. Only the vertex candidates reconstructed in a region close to the nominal interaction point are considered (a cylindrical volume of 48 cm in height and 2 cm in radius with a center placed at the nominal interaction point and an axis pointing along the beam axis). In addition, these candidates are required to satisfy a good-quality criterion dependent on a number of tracks associated with the vertex and a likelihood for a track to originate truly from this vertex. Finally, only events which have at least one primary vertex reconstructed and selected according to the previous description are considered in the further analysis. In case of multiple vertex candidates in the event, the vertex candidate with the highest sum of associated track momenta is classified as selected vertex, representing an interesting hard interaction of two protons. All other vertex candidates in the same event are called pile-up vertices.

Even though the primary vertex reconstruction is an excellent-performing algorithm [121], the reconstructed distribution of the number of primary vertices per event $N_{vertices}$ can be marginally different between the data and simulation. In addition, the simulation is produced using a predefined underlying event model, which can be potentially different from the data. In order to consider these effects, the true-level $N_{vertices}$ distribution in the simulation is reweighted to match the corresponding profile in data (reference profile). The reference profile is measured using the instantaneous luminosity per bunch crossing, the integrated luminosity of the data taking period and the total pp inelastic cross section. A comparison of the reconstructed $N_{vertices}$ distributions in the data and simulation is shown in Figure 4.1, before and after the reweighting.

4.4.2 Dilepton event triggering

The event triggering system used at the CMS experiment is previously explained in Section 2.2.6.

In this analysis, events are selected by a trigger requiring leptons. In particular, the trigger paths which are used require one or two leptons (e or μ) with transverse momenta above the predefined thresholds. The dielectron (dimuon) trigger checks for a presence of two electrons (muons), where one electron (muon) is required to have $p_T > 23$ GeV (17 GeV) and the other to have $p_T > 12$ GeV (8 GeV). The $e\mu$-trigger requires either an electron with $p_T > 23$ GeV and a muon with $p_T > 8$ GeV or, alternatively, a muon with $p_T > 23$ GeV and an electron with $p_T > 12$ GeV. The single-electron (single-muon) trigger requires an electron (muon) with $p_T > 27$ GeV (24 GeV). The dilepton trigger is not 100% efficient.

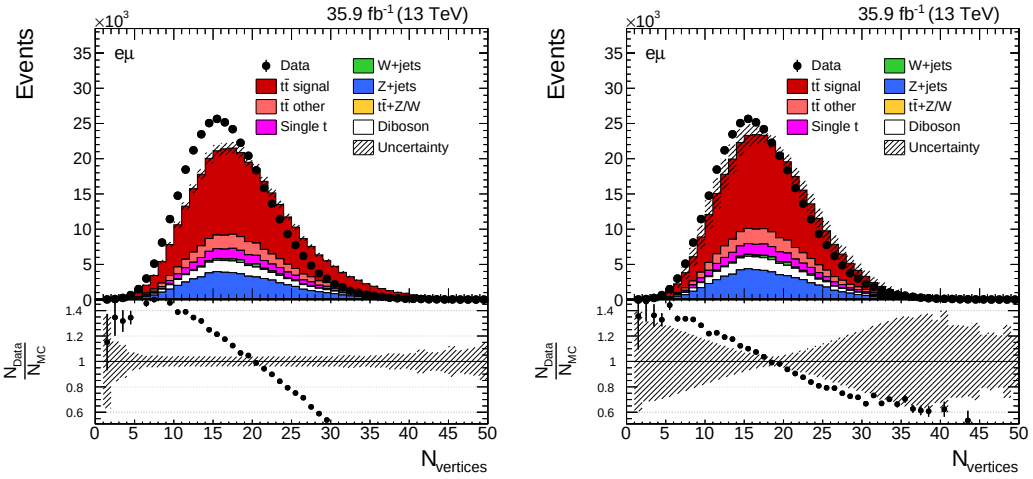

Figure 4.1 The reconstructed distribution of the number of proton-proton interaction vertices per event before (left) and after (right) the reweighting of the simulation according to the true-level pile-up profile in data. The distributions are obtained after the lepton-pair requirement of the event selection (see Section 4.4.3). The hatched area indicates the shape systematic uncertainties on the $t\bar{t}$ signal and backgrounds (see Chapter 6).

Therefore, to increase the efficiency, events are selected involving the logical OR between the dilepton and single lepton triggers (the operation of logical OR implies that the event is accepted if one or more trigger paths are fired). The inclusion of single lepton triggers allows the recovery of approximately 10% of dilepton events. The same triggers are configured for use in the data and simulation; a complete list is given in Table A.1.

The trigger efficiencies are measured in the data and simulation as a function of $|\eta|$ of the two leading leptons in the event. The measurement method follows [122, 123] and is based on a use of monitoring triggers that are uncorrelated to the lepton triggers, namely the E_T^{miss}-based triggers. The efficiency is defined as ratio of the number of events passing the lepton and monitoring triggers, as well as $t\bar{t}$ dilepton event selection, over the number of events passing only the monitoring triggers and same selection. The efficiencies are determined differentially with the binning shown in Figure A.1. The multiplicative scale factors $SF_{trigger}$, presented in Figure A.1, are used to correct the MC simulation to the observed efficiency in data. The scale factors are typically close to unity, which demonstrates a good agreement in the trigger performance between the data and MC.

4.4.3 Lepton reconstruction and selection

The reconstruction and selection of electrons and muons, as well as lepton pairs, are described in the following.

Muons

The muon candidates are reconstructed as so-called *global muons* [124], involving the PF algorithm. A reconstruction of a muon track begins with the hits measured in the muon chambers. Afterwards, an interesting track candidate is combined with the best-matching track from the tracker system.

The muon candidates are identified according to tight selection criteria, imposing quality requirements on muon tracks and exploiting the information about track properties [124]. Additionally, the muon candidates are required to be isolated involving a relative criterion, where an estimate of the energy flow of particles that are close to a muon trajectory is divided by the muon transverse momentum. A muon candidate is considered as isolated, if its momentum is significantly larger than the energy flow in its proximity. The isolation criterion includes a correction for energy contributions from pile-up. Both selection requirements serve in a removal of fake muons, i.e. not stemming from the hard scattering (non-prompt muons). These fakes are either muons originating from hadronic decays or hadron shower tails that are measured in muon chambers and are misreconstructed as a muon candidate.

Reconstruction and selection efficiencies for the muon candidates are calculated using the so-called *tag-and-probe* data-driven method [123, 125], relying on a use of muon pairs stemming from a decay of Z-boson resonances. The event is selected by requiring a muon candidate, referred to as "tag", passing a single muon trigger and tight selection requirements, while the other muon candidate, referred to as "probe", is used to measure the corresponding efficiency. The combined efficiency of the muon reconstruction and selection is about 94%.

The muon efficiencies measured in the simulation are slightly higher than those in data. Therefore, the simulation is corrected by dedicated scale factors, defined as a data-to-MC ratio of efficiencies and centrally provided by the CMS Collaboration. The combined scale factors are differential in bins of the p_T and $|\eta|$ of the muon candidate, as shown in Figure A.2. The scale factors are slightly less than 1 in all bins.

Electrons

The electron candidates are reconstructed with the PF algorithm, relying on the combined information from the ECAL and tracker detectors. An electron is determined as a combination of a track from the tracker with a corresponding supercluster from the ECAL, i.e. a group of several energy clusters associated with the passing electron through the ECAL and possible bremsstrahlung photons.

Prompt electrons are selected with a dedicated tight identification and isolation criteria [126]. The electron identification uses properties of the track and supercluster associated

to an electron candidate, as well as applying quality requirements to them. In particular, electrons associated with the superclusters reconstructed in $1.4442 < |\eta| < 1.5660$, i.e. a gap between the barrel and endcap regions of the ECAL, are excluded. The electron isolation is based on a relative criterion, defined in a similar way as done for muons. Those requirements allow to reduce the rate of background electrons, which mostly arise from the semileptonic decays of b and c quarks, photon conversions and jets misreconstructed as electrons.

As in case of muons, the electron reconstruction and selection efficiencies are calculated with the *tag-and-probe* method using electron pairs to reconstruct the Z-boson resonances. The combined electron efficiency is roughly 65%. The simulation is corrected for differences in efficiencies with the data. The differential scale factors are determined as a function of the electron candidate p_T and the η of an associated supercluster. The corresponding values are presented together with the total uncertainties in Figure A.2, showing that the simulation is required to be typically scaled down in order to match the data.

Lepton pair

Lepton candidates (muons and electrons) are required to have $p_T > 20$ GeV and to be localized within $|\eta| < 2.4$. For the leading lepton in the event, the minimum p_T is required to be 25 GeV. Only events with exactly two isolated leptons of an opposite electric charge, fulfilling all previously described criteria, are selected for further consideration. Depending on lepton flavours of the lepton pair, events are assorted into dilepton decay channels, namely e^+e^-, $e^\pm\mu^\mp$ and $\mu^+\mu^-$.

Events containing a lepton pair with an invariant mass $m_{\ell\bar{\ell}} < 20$ GeV are discarded in order to reduce the contamination from low-mass DY processes and events associated with decays of heavy flavour resonances. Moreover, only in the e^+e^- and $\mu^+\mu^-$ channels, the events in a region 76 GeV $< m_{\ell\bar{\ell}} <$ 106 GeV (a region of ±15 GeV with respect to assumed m_Z) are vetoed to further suppress Drell-Yan processes.

4.4.4 Jet reconstruction and selection

A jet is a collimated group of hadrons and other particles, arising from the hadronization of a quark or gluon, that are moving roughly in the same direction. Reconstruction of jets relies on a clustering of the colourless stable particles, which performs a mapping of the particle momenta to relevant jet candidates.

In this analysis, the jets and their kinematics are reconstructed via the anti-k_t jet clustering algorithm [127, 128], using the radius parameter $R = 0.4$, i.e. a parameter controlling a size of the jet. The clustering is performed over the particle candidates identified by the PF

algorithm [129], namely charged and neutral hadrons, photons, electrons and muons. The isolated electron and muon candidates as well as charged hadrons from pile-up interactions are removed prior to the clustering. The momentum of a jet is quantified as the vectorial sum of all particle momenta clustered in the jet.

The clustered jets require a calibration of their energies and momenta to account for inefficiencies in the detector response and reconstruction. The jet energy scale (JES) correction [130] is used to translate the jet energy deposits in the detector into a true energy of the jet. The jet 4-momenta are scaled with the scale factors dependent on jet properties, e.g. p_T, η and flavour. The scale factors [131], applied sequentially, account for the energy contributions incoming from pile-up interactions, detector response to jets and for residual differences in the jet response between the data and simulation.

The jet energy resolution (JER) in the data is worse than in the simulation [130]. Therefore, the jet 4-momenta in the simulation are smeared in order to describe the data. The JER correction [131], determined in bins of jet $|\eta|$ as shown in Table A.4, is applied after the JES correction.

The physical jet candidates are identified requiring loose criteria [129]. These criteria serve to reject jets originating from calorimetric noise. The criteria are based on the jet energy fractions contributed by the different types of the PF candidates clustered into a jet, as well as on their multiplicity. The jet identification algorithm shows a very good performance in a wide kinematic range of jet p_T and η [129].

Fully reconstructed and identified jets are selected if they have $p_T > 30$ GeV and $|\eta| < 2.4$. Also, jets which overlap with any of the two selected leptons are rejected. This is performed requiring a jet to be separated from each selected lepton with an angular distance $\Delta R(\ell, j) > 0.4$, where $\Delta R(\ell, j) \equiv \sqrt{(\Delta\phi(\ell, j))^2 + (\Delta\eta(\ell, j))^2} = \sqrt{(\phi_\ell - \phi_j)^2 + (\eta_\ell - \eta_j)^2}$.

Finally, events are selected if they contain at least two fully selected jets. Selection requirements imposed on jets allow a further improvement in a signal purity of the event sample.

4.4.5 Missing transverse energy

In pp collisions, the initial longitudinal momenta of the interacting partons are not known, since the momentum of each proton is shared by its parton constituents. However, the initial momentum in the plane perpendicular to the beam axis (transverse momentum) is known to be equal to 0. Owing to momentum conservation, an imbalance in the transverse momentum of all particles directly measured in the detector is usually an evidence that some particles escaped the detection. This imbalance is referred to as missing transverse energy in the event. For example, neutrinos escape the direct detection, because they are very weakly interacting

particles, being electrically neutral with an extremely low invariant mass. Thus, the missing transverse energy can be used for an estimation of their momenta. A schematic diagram demonstrating the principle of missing transverse energy is shown in Figure 4.2.

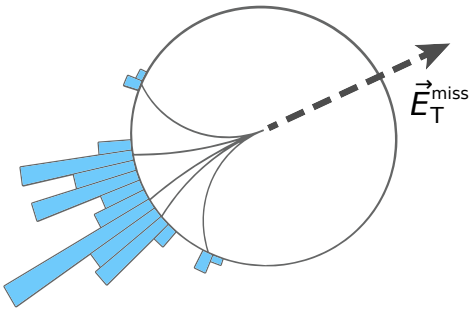

Figure 4.2 A schematic diagram showing the vector of missing transverse energy ($\vec{E}_T^{miss}$) in the event. The circle corresponds to a slice of the tracker in the plane perpendicular to the beam axis, where the trajectories of visible particles are shown as bended lines. The blue columns show the associated energy deposits by those particles in the calorimeter. From [132], modified.

The vector of missing transverse energy $\vec{E}_T^{miss}$ is defined as the negative vector sum of the transverse momenta of all reconstructed particles i in the event

$$\vec{E}_T^{miss} = -\sum_i \vec{p}_T(i). \tag{4.1}$$

The scalar missing transverse energy E_T^{miss} is given by the magnitude of $\vec{E}_T^{miss}$.

For an accurate estimation, the jet energy correction is propagated to the missing transverse energy vector.

The true distribution of the $\vec{E}_T^{miss}$ is uniform in terms of the ϕ-direction, since the collisions have a rotational symmetry with respect to the beam axis. However, the reconstructed ϕ-distribution possesses a sinusoidal-like modulation [133, 134]. This behaviour is caused by different features in the detector operation, such as anisotropic response, non-active channels, imperfect detector alignment and the shift between the beam axis and the detector center. In particular, an amplitude of the modulation depends on the multiplicity of pile-up vertices. In order to mitigate all aforementioned effects and, therefore, reduce the modulation, the $\vec{E}_T^{miss}$ is corrected via a shift of its components in the x and y directions. This correction is applied on an event-by-event basis and separately in the data and simulation.

Large E_T^{miss} can have not only a genuine origin, i.e. particles escaping the detection, but also can be caused by different instrumental effects, e.g. such as detector noise and beam-halo particles which interact with a beampipe. Events which are severely affected by these instrumental effects are excluded in order to avoid a misreconstruction of the E_T^{miss}.

The DY events do not have neutrinos in a final state and, thus, are not expected to possess a large missing transverse energy. Therefore, only in the e^+e^- and $\mu^+\mu^-$ channels, events are selected if they pass the requirement of $E_T^{miss} > 40$ GeV, which leads to a further reduction of the DY background.

4.4.6 Identification of b-jets

Due to a presence of at least two b quarks in the final state of signal events, an efficient identification of b-jets, i.e. originating from b quarks, is very relevant for this measurement. In the following, the Combined Secondary Vertex v2 (CSVv2) algorithm [135] that is used to identify b-jets, referred to as *b-tagging*, is described.

The b-tagging is based on the properties of the heavy flavour hadrons associated with the jets. For example, hadrons containing b quarks have an average lifetime of about $1.5 \cdot 10^{-12}$ s. Owing to this, these hadrons can traverse several millimeters from the primary vertex before their decay (see Figure 4.3). Depending on the momentum of a hadron, the flight distance can be up to 1 cm. The hadron decay results a secondary vertex producing displaced tracks with respect to the primary vertex. In about 20% of the cases, an electron or a muon is produced in the decay chain of a B-hadron [135]. The position of a displaced track with respect to the primary vertex is evaluated in terms of its impact parameter (Figure 4.3), which is defined as the distance of closest approach between the primary vertex and a track.

The CSVv2 b-tagging algorithm exploits the combined information about the relevant secondary vertex and displaced tracks relying on a multivariate analysis. The algorithm is applied to all reconstructed jets in the event, where for each jet a discriminator value is calculated. A higher discriminator value means that a jet is more likely to be originated from a b quark. The distribution of the b-tagging discriminator comparing the data and simulation is shown in Figure 4.3. This distribution is obtained after the selection requirement on E_T^{miss}.

In the case when a jet is characterized by a discriminator higher than a certain threshold value, the jet is considered as originating from a b quark and is referred to as b-tagged jet. However, it can occur that a c-jet or a light flavour jet (l-jet), i.e. originating from u, d or s quarks or a gluon, is misidentified as a b-jet. Further in the text, the misidentification probability is referred to as mistag rate. In contrast, a tagging efficiency of b-jets is given by the probability to correctly identify a b-jet.

The b-tagging discriminator threshold used in this work is 0.5426. For jets with $p_T > 30$ GeV, this value corresponds to an approximately 80% b-tagging efficiency, 35% mistag rate for c-jets and 10% mistag rate for l-jets.

The tagging efficiency of b-jets, as well as the mistag rates of c-jets and l-jets, is different between the data and simulation. The CMS Collaboration provides the data-to-MC correc-

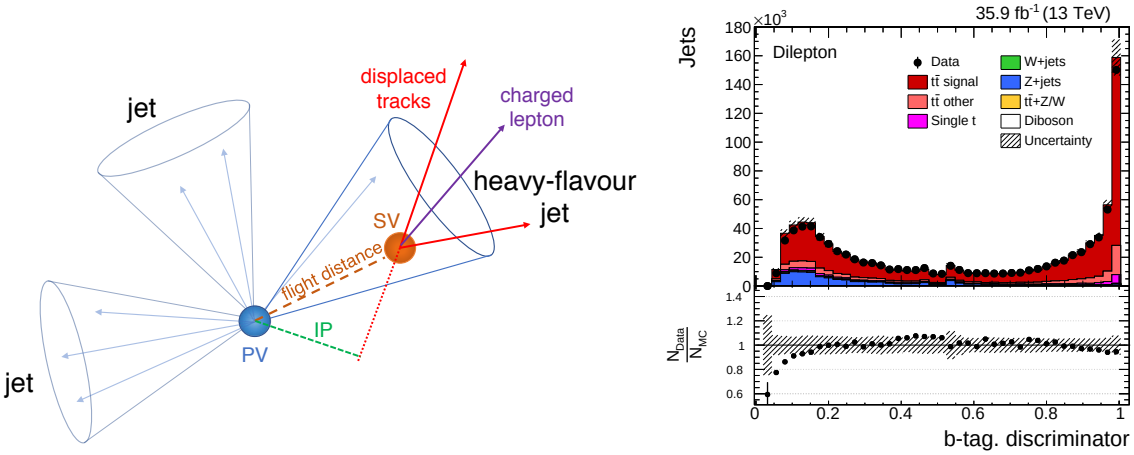

Figure 4.3 Left: Diagram representing a heavy flavour jet including the secondary vertex (SV) from the decay of a heavy flavour hadron. The hadron gives a rise to displaced tracks, one of which can be a potential charged lepton. The position of displaced track with respect to primary vertex (PV) is given by the impact parameter (IP). From [135]. **Right:** The distribution of b-tagging discriminator in the combined event sample is shown after the selection requirement on missing transverse energy. At this selection step, the simulation is not yet corrected for the differences in tagging efficiencies between the data and simulation. The hatched area indicates the shape systematic uncertainties on the $t\bar{t}$ signal and backgrounds (see Chapter 6).

tions [135] accounting for those differences. The correction factors (SF_{b-tag}) are determined using multijet event samples, i.e. events are composed solely out of jets arising from the strong interaction. The SF_{b-tag} are dependent on jet p_T, $|\eta|$ and flavour.

The correction mentioned above also accounts for the potential differences, due to event kinematics, in the tagging efficiencies between the multijet and the $t\bar{t}$ simulated samples. The b-tagging efficiency (mistag rate) of b-jets (c-jets and l-jets) in the $t\bar{t}$ simulation is calculated as a function of jet p_T and $|\eta|$ using $t\bar{t}$ *signal* events. An example of these quantities for the reference $t\bar{t}$ simulation is shown in Figure A.3.

Finally, events are accepted if at least one jet among fully selected jets in the event is identified as a b-jet. After this requirement, events in the simulation are reweighted using relevant b-tagging efficiencies and SF_{b-tag} values discussed previously.

4.4.7 Requirement of the top-quark pair

As the last selection criterion, an event is required to have a valid candidate of the top-quark pair reconstructed according to an algorithm described in Section 4.6. Otherwise, the event is excluded from further consideration.

4.5 Background estimation

The main background processes considered in this analysis are: $t\bar{t}$ *other*, *Z+jets*, *single t* (tW), $t\bar{t}$*+Z/W*, *diboson* (WW, WZ, ZZ) and *W+jets*. The event selection, described in Section 4.4, allows reducing the contamination of the signal by these background processes. Despite this, a noticeable amount of background events survive the event selection and therefore their total contributions must be carefully estimated.

In this measurement, the background estimation is performed using simulation-based and data-driven techniques. The background contribution from processes that are expected to be relatively small and/or well described by the simulation ($t\bar{t}$ *other*, *single t*, $t\bar{t}$*+Z/W*, *diboson* and *W+jets*) is estimated directly from the MC samples.

The *Z+jets* processes feature large E_T^{miss} due to substantial influence of instrumental effects, which are hard to reproduce in the simulation. The rates of these *Z+jets* contributions are extracted from data, while their shapes are estimated from the simulated samples. *Z+jets* is the largest background in the e^+e^- and $\mu^+\mu^-$ channels.

As is explained above, the estimation of *Z+jets* background normalization is based on data, using a method known as $R_{out/in}$-method [136]. The corresponding number of *Z+jets* events in data originating from outside the Z-peak region is extracted using a control region

associated with the inside Z-peak region. The events in the Z-peak region contain the dilepton system with an invariant mass between 76 GeV and 106 GeV and are rejected by the Z-veto requirement during the event selection (see Section 4.4). The good modelling of the Z-peak region in the simulation facilitates the estimation of *Z+jets* background normalization using $R_{out/in}$-method.

In this analysis, the determination of normalization scale factors for the *Z+jets* simulation is performed using an event sample that is obtained after the application of "2 jets" selection requirement (precedes the selection requirement on the missing transverse energy). This selection step is chosen to reduce the effect from the modelling of missing transverse energy on the Z-peak region. The determination of normalization scale factors is described in the following.

The expected number of *Z+jets* events that are observed in data outside the Z-peak region for decay channels $\ell^+\ell^- = \mathrm{e}^+\mathrm{e}^-$ or $\mu^+\mu^-$ after applying a given set of selection requirements (here, after applying "2 jets" selection requirement, as mentioned above) can be estimated as

$$N^{\ell^+\ell^-}_{out,data} = R^{\ell^+\ell^-}_{out/in}(N^{\ell^+\ell^-}_{in,data} - 0.5 \cdot k^{\ell^+\ell^-} N^{\mathrm{e}^\pm\mu^\mp}_{in,data}), \tag{4.2}$$

where the index *out* (*in*) indicates the number of events outside (inside) the Z-peak region for a corresponding dilepton channel. $R^{\ell^+\ell^-}_{out/in}$ denotes the ratio between number of *Z+jets* events outside and inside the Z-peak region, which are estimated from the *Z+jets* MC simulation, using the expression

$$R^{\ell^+\ell^-}_{out/in} = \frac{N^{\ell^+\ell^-}_{out,MC}}{N^{\ell^+\ell^-}_{in,MC}}. \tag{4.3}$$

The term $N^{\ell^+\ell^-}_{in,data}$ in Equation 4.2 includes all events in data within the Z-peak control region. Therefore, this number has to be corrected for the contributions that are originating from non-*Z+jets* processes, which is performed by subtracting the term $0.5 \cdot k^{\ell^+\ell^-} N^{\mathrm{e}^\pm\mu^\mp}_{in,data}$. The background contribution is estimated using the number of data events in the $\mathrm{e}^\pm\mu^\mp$channel belonging to the Z-peak region, $N^{\mathrm{e}^\pm\mu^\mp}_{in,data}$, and scaling it with the corresponding $k^{\ell^+\ell^-}$ correction factors, which are explained in the following. The additional multiplication by 0.5 is done to account for the higher combinatorics in $\mathrm{e}^\pm\mu^\mp$ events (i.e. $e^-\mu^+$ and $e^+\mu^-$).

In Equation 4.2, the $k^{\ell^+\ell^-}$ is a correction factor that accounts for the differences between the electron and muon selection efficiencies. The values of these factors are computed from the observed numbers of data events within the Z-peak region in $\mathrm{e}^+\mathrm{e}^-$ and $\mu^+\mu^-$ channels,

using the expressions

$$k^{e^+e^-} = \sqrt{\frac{N^{e^+e^-,*}_{in,data}}{N^{\mu^+\mu^-,*}_{in,data}}}, \qquad k^{\mu^+\mu^-} = \sqrt{\frac{N^{\mu^+\mu^-,*}_{in,data}}{N^{e^+e^-,*}_{in,data}}}. \tag{4.4}$$

The $N^{e^+e^-,*}_{in,data}$ and $N^{\mu^+\mu^-,*}_{in,data}$ are proportional to the square of the underlying selection efficiency for single lepton candidates and, thus, for example, leading to $k^2 = N_1/N_2$.

The scale factor used to correct the *Z+jets* normalization is defined as the ratio

$$SF^{\ell^+\ell^-}_{Z+jets} = \frac{N^{\ell^+\ell^-}_{out,data}}{N^{\ell^+\ell^-}_{out,MC}}. \tag{4.5}$$

The scale factor in $e^{\pm}\mu^{\mp}$channel is determined according to $SF^{e^{\pm}\mu^{\mp}}_{Z+jets} = \sqrt{SF^{e^+e^-}_{Z+jets} \cdot SF^{\mu^+\mu^-}_{Z+jets}}$, assuming that the efficiency to select both leptons in the $e^{\pm}\mu^{\mp}$ channel factorizes into the corresponding selection efficiencies for single lepton candidates.

The results of the data-driven *Z+jets* background estimation described previously are summarized in Table A.5. The obtained normalization scale factors $SF^{\ell^+\ell^-}_{Z+jets}$ are: 1.0547 in e^+e^-, 0.9911 in $\mu^+\mu^-$, and 1.0224 in $e^{\pm}\mu^{\mp}$ channels. The uncertainties of the extracted values are covered by the systematic uncertainty due to DY background normalization (see Section 6.3). In Figure 4.4, the $m_{\ell\bar{\ell}}$ distributions for the e^+e^- and $\mu^+\mu^-$ channels are shown after the application of aforementioned normalization scale factors to the *Z+jets* simulation.

4.6 Kinematic reconstruction of the top-quark pair

Top quarks decay before they can form hadronic bound states, unlike other quarks. Due to this reason, top quarks cannot be measured directly in the detector. However, their properties can be investigated by reconstructing the top quarks from their decay products, that are experimentally detected. The reconstruction of the top-quark pair requires different approaches depending on the decay channel. For example, in the case of all-hadronic channel, the full event information is available in the detector, while in the dilepton channel not all decay products are measured due to undetected neutrinos.

The precise solution of the $t\bar{t}$ kinematics in the dilepton channel can be obtained using the algebraic method suggested in [137, 138]. This method was implemented and used by the CMS Collaboration for differential $t\bar{t}$ cross section measurements in the dilepton channel at 8 TeV, e.g. [8, 139]. The method was adapted to the measurement at 13 TeV for this analysis. In the following, a comprehensive description of this method is given.

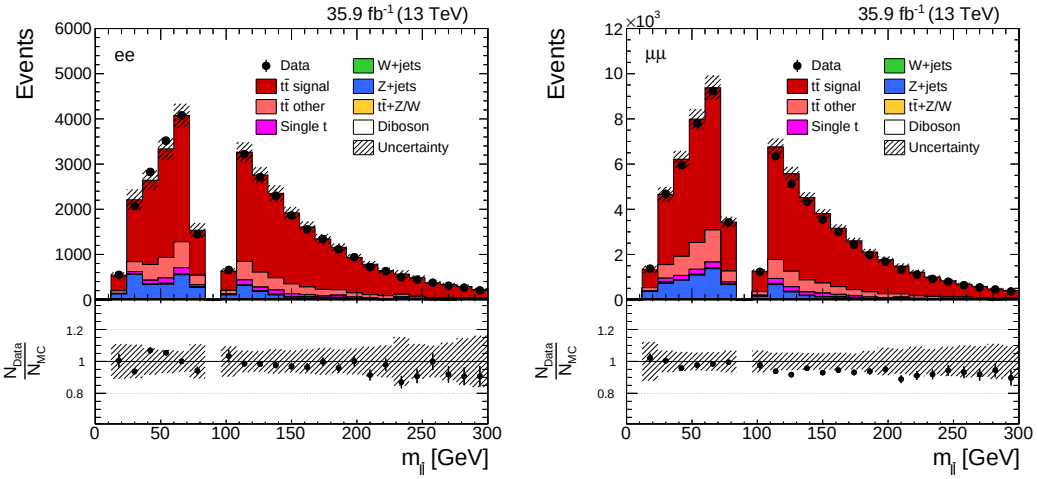

Figure 4.4 The $m_{\ell\bar{\ell}}$ distribution is shown separately for the e^+e^- and $\mu^+\mu^-$ channels after the application of full event selection, including the Z-veto requirement ($76\ GeV < m_{\ell\bar{\ell}} < 106\ GeV$). The *Z+jets* simulation (blue) is scaled by 1.0547 in $e^+e^-$and 0.9911 in $\mu^+\mu^-$, following the results of data-driven background estimation. The hatched area indicates the shape systematic uncertainties on the $t\bar{t}$ signal and backgrounds (see Chapter 6).

4.6.1 Description of the method

As previously mentioned, the kinematics of the top quark and top antiquark are reconstructed out of their decay products. The dileptonic $t\bar{t}$ decays are characterized by the presence of two oppositely charged leptons, two b-jets and two neutrinos in the final state, i.e. $t \to W^+b \to \ell^+\nu_\ell b$ and $\bar{t} \to W^-\bar{b} \to \ell^-\bar{\nu}_\ell\bar{b}$. In practice, information about leptons and their electric charges can be obtained studying their trajectories in the magnetic field. The b-jets are usually reliably identified with the b-tagging algorithm. On the other hand, both neutrinos, escaping the detection, contribute to the same E_T^{miss}-vector in the event. Thus, the genuine information about the components of the 4-momenta of both neutrinos, $\nu \equiv (E_\nu, p_{\nu_x}, p_{\nu_y}, p_{\nu_z})$ and $\bar{\nu} \equiv (E_{\bar{\nu}}, p_{\bar{\nu}_x}, p_{\bar{\nu}_y}, p_{\bar{\nu}_z})$, is unknown. Basically, the main objective of the $t\bar{t}$ kinematic reconstruction is to find out these unknown values prior to the construction of the top quark objects.

Assuming that the presence of E_T^{miss} is solely caused by two neutrinos, the kinematics of $t\bar{t}$ dilepton events can be described by a system of two linear and six non-linear equations:

$$E_x^{miss} = p_{\nu_x} + p_{\bar{\nu}_x}, \tag{4.6}$$

$$E_y^{miss} = p_{\nu_y} + p_{\bar{\nu}_y}, \tag{4.7}$$

$$E_\nu^2 = m_\nu^2 + p_{\nu_x}^2 + p_{\nu_y}^2 + p_{\nu_z}^2, \tag{4.8}$$

$$E_{\bar{\nu}}^2 = m_{\bar{\nu}}^2 + p_{\bar{\nu}_x}^2 + p_{\bar{\nu}_y}^2 + p_{\bar{\nu}_z}^2, \tag{4.9}$$

$$m_{W^+}^2 = (E_{\ell^+} + E_\nu)^2 - (p_{\ell_x^+} + p_{\nu_x})^2 - (p_{\ell_y^+} + p_{\nu_y})^2 - (p_{\ell_z^+} + p_{\nu_z})^2, \tag{4.10}$$

$$m_{W^-}^2 = (E_{\ell^-} + E_{\bar{\nu}})^2 - (p_{\ell_x^-} + p_{\bar{\nu}_x})^2 - (p_{\ell_y^-} + p_{\bar{\nu}_y})^2 - (p_{\ell_z^-} + p_{\bar{\nu}_z})^2, \tag{4.11}$$

$$\begin{aligned} m_t^2 = {} & (E_{\ell^+} + E_\nu + E_b)^2 - (p_{\ell_x^+} + p_{\nu_x} + p_{b_x})^2 \\ & - (p_{\ell_y^+} + p_{\nu_y} + p_{b_y})^2 - (p_{\ell_z^+} + p_{\nu_z} + p_{b_z})^2, \end{aligned} \tag{4.12}$$

$$\begin{aligned} m_{\bar{t}}^2 = {} & (E_{\ell^-} + E_{\bar{\nu}} + E_{\bar{b}})^2 - (p_{\ell_x^-} + p_{\bar{\nu}_x} + p_{\bar{b}_x})^2 \\ & - (p_{\ell_y^-} + p_{\bar{\nu}_y} + p_{\bar{b}_y})^2 - (p_{\ell_z^-} + p_{\bar{\nu}_z} + p_{\bar{b}_z})^2. \end{aligned} \tag{4.13}$$

Assuming that the neutrino and antineutrino have zero masses (e.g. $m_\nu \equiv 0$), the E_ν and $E_{\bar{\nu}}$ components can be obtained using Equations 4.8 and 4.9. The remaining six equations appear as a fully constrained system with six unknown parameters p_{ν_x}, p_{ν_y}, p_{ν_z} and $p_{\bar{\nu}_x}$, $p_{\bar{\nu}_y}$, $p_{\bar{\nu}_z}$, which are the momentum components of both neutrinos, once imposing the following constraints

- **Missing transverse energy** solely originates from the neutrinos that stem from the corresponding top quark decays. In this way, two unknown parameters are constrained with the balance Equations 4.6 and 4.7 between the x, y-components of the missing energy vector and the corresponding sum of the neutrino and antineutrino momenta.
- **Masses of W^+ and W^- bosons** are the same and equal to 80.4 GeV [1, 25], which further constrains two more unknowns with Equations 4.10 and 4.11.
- **Masses of top quark and top antiquark** are required to be equal to 172.5 GeV. This condition alongside Equations 4.12 and 4.13 constrains the last two unknowns.

Considering those constraints and assumptions, the system of equations given by Equations 4.6-4.13 can be expressed as a function of a polynomial $\mathcal{P}$ that includes the only remaining uknown p_{ν_x}

$$\mathcal{P} = h_0 p_{\nu_x}^4 + h_1 p_{\nu_x}^3 + h_2 p_{\nu_x}^2 + h_3 p_{\nu_x} + h_4, \tag{4.14}$$

where the coefficients h_i depend on the 4-momenta of the two leptons, two b-jets and x, y-components of the missing energy vector, which are measured by the detector:

$$f(m_{t,\bar{t}}, m_{W^\pm}, m_{b,\bar{b}}, m_{\ell^\pm}, \vec{p}_{b,\bar{b}}, \vec{p}_{\ell^\pm}, E_{b,\bar{b}}, E_{\ell^\pm}, E_x^{miss}, E_y^{miss}).$$

The masses of b-jets $m_{b,\bar{b}}$ are set to 4.8 GeV, the value corresponding to the b quark mass used in the reference $t\bar{t}$ simulation. The lepton masses $m_{\ell^\pm}$ are neglected for simplification. Hence, the coefficients h_i can be fully evaluated using the values of $m_{t,\bar{t}}$ and $m_{W^\pm}$ that are required by the constraining assumptions.

In Equation 4.14, the polynomial $\mathcal{P}$ is of the 4^{th} order. Thus, the quartic equation

$$\mathcal{P} = 0, \tag{4.15}$$

can be analitically solved in terms of p_{ν_x} with an ambiguity of up to four solutions at most. In this analysis, the solution providing the smallest value of reconstructed $m_{t\bar{t}}$ is selected. This is done based on the conclusions from [140], where it was demonstrated that this mass-dependent criterion gives the best results in a wide kinematic range.

There are additional experimental implications that prevent a straightforward evaluation of p_{ν_x}. In a considerable number of events, it might happen that Equation 4.15 cannot be solved for the input values of particle momenta and E_T^{miss}. This mostly happens due to imperfections in the detector response. However, the solution can be recovered by smearing the relevant input observables according to their detector resolutions. For each corresponding smearing, the solution is recalculated and an outcome is stored for further use. As was shown in [140], 100 smearing attempts in each event are enough to recover the solution. A determination of the solution is discussed in the following.

Once Equation 4.15 is solved, all other unknown components in the 4-momenta of the neutrinos can be computed using the value of p_{ν_x}.

Event smearing

In order to account for resolution effects, the energies and flight directions of the considered leptons and b-jets are varied. The energy variation is implemented as a multiplicative correction factor for the reconstructed energy. These correction factors are randomly evaluated from the corresponding probability density distributions, that are shown in Figure 4.5 for leptons and b-jets. Each distribution is based on the ratio between the true energy of the particle and its reconstructed energy in the detector. The values of true energies are taken from the reference $t\bar{t}$ simulation after matching the reconstructed leptons (b-jets) to the true leptons (b quarks) from the corresponding top quark decays. The matching for

leptons (b-jets) is performed using an angle-dependent (energy- and position-dependent) criterion. The relative differences between the true and reconstructed energies are found to be very similar in the whole kinematic range for leptons and b-jets. Thus, the probability density distributions in Figure 4.5 can be used for the smearing of leptons or b-jets of various energies. The directional smearing is performed in a similar manner, but by means of two consecutive angular rotations. At first, the flight direction of an input particle is randomly chosen according to the probability density distribution, displayed in Figure 4.6, depending on the angles between the reconstructed and true directions of leptons (b-jets). And for the second, the previously chosen direction is radially rotated with the randomly selected angle that is uniformly distributed in the interval $[0, 2\pi]$. The changes in lepton and b-jet 4-momenta owing to the energy and directional smearings are propagated to the E_T^{miss}.

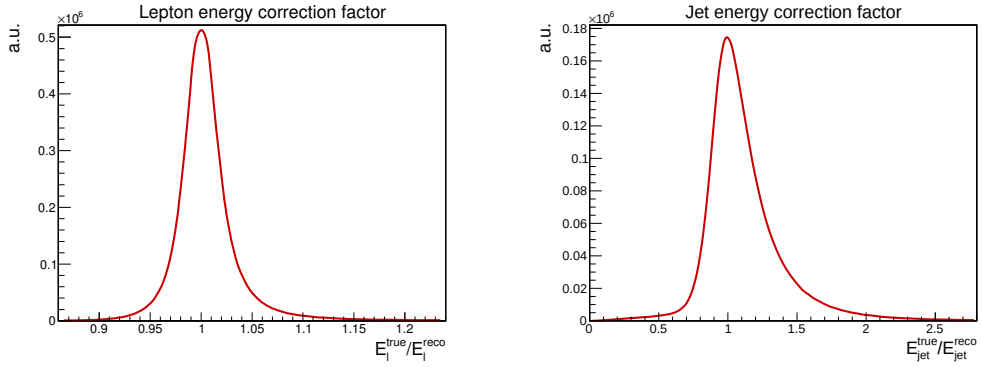

Figure 4.5 Distributions of the ratio between the true energy characterizing the particle and its reconstructed energy in the detector for the leptons (left) and b-jets (right). These distributions are determined from the reference $t\bar{t}$ simulation using an event sample obtained after the b-jet selection requirement, i.e. an event sample prior to the top-quark pair kinematic reconstruction.

Besides energy and direction variations, an additional smearing is introduced for the W boson mass, which is used as a constraining parameter for Equations 4.6-4.13. The value of W mass is randomly chosen accordingly to the relativistic Breit-Wigner distribution, shown in Figure 4.7, that is determined from the generator level quantities of the reference $t\bar{t}$ simulation.

Assignment of lepton-b-jet pairs

As discussed in Section 4.6, owing to two leptons and at least two jets, there are several permutations of the lepton-jet pairs to reconstruct the top quarks. Only two permutations are possible for events with exactly two jets. With an increase in jet multiplicity N_{jets}, the number of potential permutations in an event grows as $\frac{N_{jets}!}{(N_{jets}-N_{leptons})!}$. In the measurement

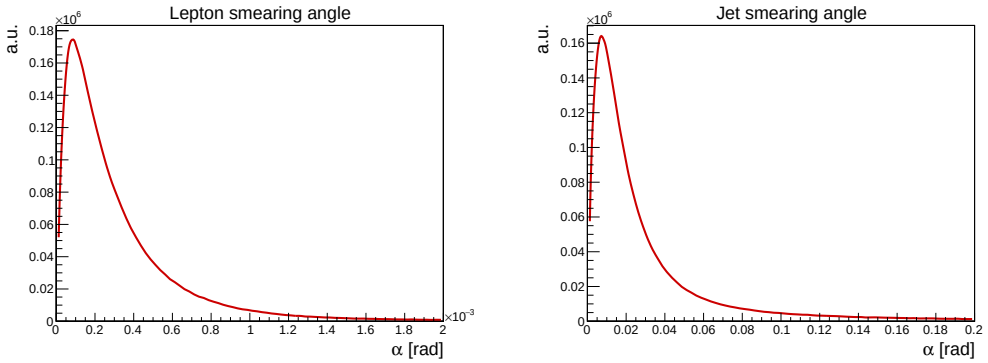

Figure 4.6 Distributions of the angle between the reconstructed and true directions of the lepton (left) or b-jet (right), obtained after the matching. These distributions are determined from the reference $t\bar{t}$ simulation using an event sample obtained after the b-jet selection requirement, i.e. an event sample prior to the top-quark pair kinematic reconstruction.

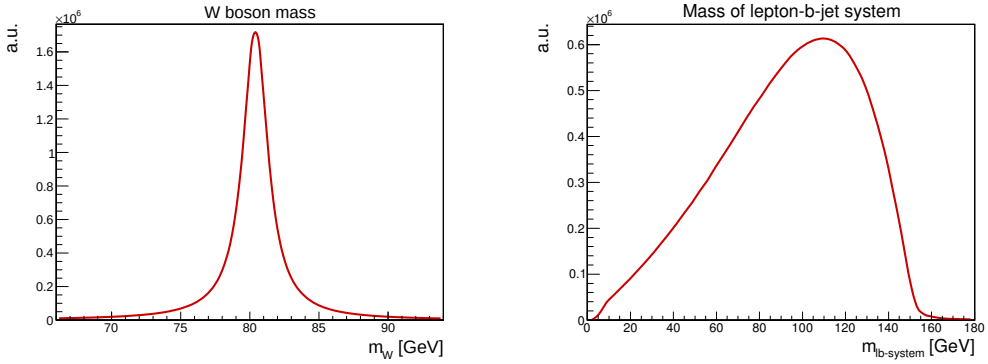

Figure 4.7 Generator level distributions of the W boson mass (left) and invariant mass of the lepton-b-jet system (right), taken from the reference $t\bar{t}$ simulation using the full set of dileptonic events.

presented here, the preference is always given to the lepton-jet permutation including the highest number of b-tagged jets, if a physical solution exists for that permutation. This implies that combinations with 2 b-tagged jets are prioritized over combinations with 1 b-tagged jet, while the latter is prefered over combinations with no b-tagged jets. In the cases where multiple combinations of the same rank in terms of b-tagged jets are available, the following additional criterion is used to distinguish them.

In every smearing attempt, all possible lepton-jet permutations are tested for the solution of Equation 4.15. In cases where a physical solution is found, a weight $w = w_{m_{\ell^+ b}} \cdot w_{m_{\ell^- \bar{b}}}$ is assigned to the examined lepton-jet permutation after its smearing, where $m_{\ell^+ b}$ and $m_{\ell^- \bar{b}}$ denote the invariant masses of the reconstructed lepton-jet pairs which are associated with the top quark and top antiquark decays, respectively. The weights $w_{m_{\ell^+ b}}$ and $w_{m_{\ell^- \bar{b}}}$ are evaluated using the generator level lepton-b-jet mass spectrum as is predicted by the reference $t\bar{t}$ simulation, which is shown in Figure 4.7. For those smeared permutations that do not provide a meaningful solution, the weight is set to $w = 0$. Finally, only the lepton-jet permutation with the largest $w_\Sigma = \sum_i w_i$, where the sum runs over all i smearings, is accepted for further consideration. Each jet involved in the accepted permutation is considered in the further analysis as b-(anti)quark jet from the corresponding top (anti)quark decay, depending on the charge of the lepton assigned to the jet.

Averaging the smeared solutions

The 3-momentum of the top quark is calculated as a weighted average according to

$$\vec{p}_t = \frac{1}{w_\Sigma} \sum_{i=1}^{100} w_i \cdot \vec{p}_{t_i}, \tag{4.16}$$

where i indicates the smearing attempt of an event and $w_\Sigma = \sum_{i=1}^{100} w_i$. In each smearing attempt, the reconstructed top quark momentum $\vec{p}_{t_i}$ is obtained with the 4-vectors of the corresponding decay products as explained in Section 4.6.1, after the solution of Equation 4.14 substituting the chosen assignment of lepton-b-jet pairs with the weight w_i (if no solution is found, the $\vec{p}_{t_i}$ and w_i are set to 0). As the final result, the top quark 4-momentum is constructed evaluating the energy component from the $\vec{p}_t$ and m_t =172.5 GeV. The final solution for the top antiquark is determined following the same approach. Afterwards, all observables related to the $t\bar{t}$-system can be determined from the resultant top quark and top antiquark 4-momenta.

4.6.2 Performance of the kinematic reconstruction

Only events for which solutions of the kinematic reconstruction are found are accepted in this analysis.

The efficiency of the kinematic reconstruction is given by

$$\epsilon_{kin.reco.} = \frac{N_{solved}}{N_{preselected}}, \tag{4.17}$$

where $N_{preselected}$ indicates the number of events in the preselected sample before the kinematic reconstruction, N_{solved} denotes the number of remaining events with a physical solution. This efficiency is calculated separately for data and simulation samples, and is designated as $\epsilon^{data}_{kin.reco.}$ and $\epsilon^{MC}_{kin.reco.}$, respectively. The efficiencies in data and MC are found to be about 87%, 88% and 92% in e^+e^-, $\mu^+\mu^-$ and $e^\pm\mu^\mp$ channels, respectively; events without a valid solution are excluded from further analysis. This step completes the full event selection described in Section 4.4. These efficiencies are studied as a function of the input observables to the kinematic reconstruction, such as p_T and η of both leptons and the two leading jets, in addition to N_{jets} and E_T^{miss}. The data and MC efficiencies, as well as their ratio $\epsilon^{data}_{kin.reco.}/\epsilon^{MC}_{kin.reco.}$, are shown in Figure 4.8 for the $e^\pm\mu^\mp$ channel. Here, only comparisons for the negatively charged leptons and leading jets are shown, since the distributions related to antileptons and subleading jets are similar. A similar behaviour is observed in the e^+e^- and $\mu^+\mu^-$ channels.

Figure 4.8 demonstrates that $\epsilon^{data}_{kin.reco.}$ and $\epsilon^{MC}_{kin.reco.}$ are very similar across all bins in each distribution, leading to an almost flat ratio between them. This illustrates a good agreement between simulation and data. In order to correct for the remaining small differences, a uniform scale factor $SF_{kin.reco.} = \epsilon^{data}_{kin.reco.}/\epsilon^{MC}_{kin.reco.}$ (see Equation 4.17) is calculated per channel using the total event numbers from the data sample and from the simulation sample (total of signal and background processes). These scale factors are applied to the simulation to further improve the description of the data and are found to be 1.0010 ± 0.0011 in the $e^\pm\mu^\mp$ channel, 1.0070 ± 0.0027 in the e^+e^- channel and 0.9993 ± 0.0019 in the $\mu^+\mu^-$ channel, where the statistical uncertainties are indicated.

4.7 Summary of event reconstruction and selection

In summary, the event selection consists of the following criteria:

- **triggering:** Events passing the summarized trigger requirements in Section 4.4.2. The same trigger menu is applied on the data and simulated event samples. The full separation of event samples into e^+e^-, $e^\pm\mu^\mp$and $\mu^+\mu^-$decay channels is achieved at the

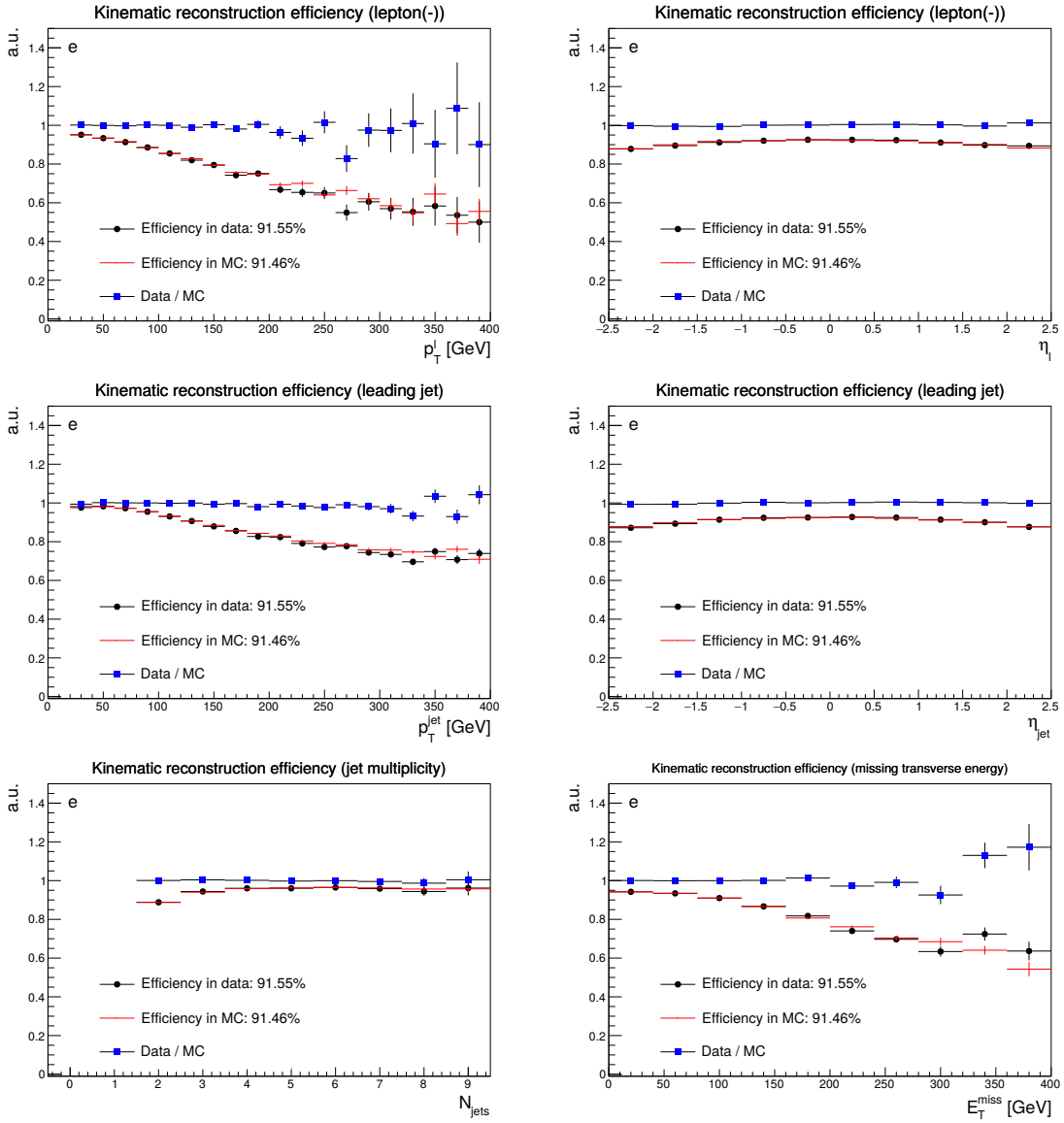

Figure 4.8 Data (black) and simulation (red) efficiencies of the $t\bar{t}$ kinematic reconstruction in the $e^{\pm}\mu^{\mp}$ channel. The efficiencies, as well as the ratio between data and simulation (blue), are shown in bins of negatively charged lepton p_T (upper left) and η (upper right), leading jet p_T (middle left) and η (middle right), jet multiplicity (lower left) and missing transverse energy (lower right). The data sample is collected by the CMS experiment in 2016 (35.9 fb^{-1}). The simulation consists of $t\bar{t}$ signal and all background processes. The given uncertainties correspond to the statistical uncertainty (for efficiencies, the binomial errors are calculated). The data and simulation efficiencies show very similar behaviour across all bins in every distribution, leading to an almost flat ratio between them.

next selection criterion, due to the combination of single-lepton and double-lepton data streams (see Table A.2) avoiding the potential event double-counting.

- **= 2 leptons:** Events with exactly 2 oppositely-charged isolated leptons with an invariant mass $m_{\ell\bar{\ell}} > 20$ GeV. The leading (trailing) lepton is required to have $p_T > 25$ (20) GeV and $|\eta| < 2.4$. Moreover, in the e^+e^- and $\mu^+\mu^-$ channels, a Z-veto requirement is applied, rejecting events close to the Z boson mass region with 76 GeV $< m_{\ell\bar{\ell}} <$ 106 GeV.

- **≥ 2 jets:** Events contain at least 2 jets with $p_T > 30$ GeV and $|\eta| < 2.4$. Jets are excluded if the angular distance between the jet and cone around the selected lepton $\Delta R(\ell, j)$ is below 0.4.

- **missing transverse energy:** In the e^+e^- and $\mu^+\mu^-$ channels, only events with $E_T^{miss} >$ 40 GeV are selected.

- **b-tagging:** At least one jet among the fully selected jets is required to be identified as a b-jet (b-tagged). The description of the b-jet identification method is provided in Section 4.4.6.

- **kinematic reconstruction:** Events after the kinematic reconstruction must have a physical solution for a top-quark pair.

4.7.1 Event yields

In Table 4.2, the number of observed events in data is given for each consecutive selection requirement and for all individual dilepton channels, i.e. e^+e^-, $\mu^+\mu^-$, and $e^\pm\mu^\mp$ channels, as well as for the combined dilepton channel (the sum of e^+e^-, $\mu^+\mu^-$, and $e^\pm\mu^\mp$ channels). These numbers are compared to the expected number of signal and background events (see Sections 4.2 and 4.3). The expected number of events in simulation is normalized to the luminosity in data and corrected for reconstruction and selection efficiencies (see Section 4.4). As already stated, the $t\bar{t}$ *signal* implies only the prompt $t\bar{t}$ decays into dileptonic final states that are characterized by the presence of e^+e^-, $e^\pm\mu^\mp$ or $\mu^+\mu^-$ systems. All other $t\bar{t}$ event topologies, i.e. $t\bar{t}$ *other*, are treated as background.

4.7.2 Control distributions

In the following, several kinematic distributions in data and MC are presented at different stages of the event selection. Each selection step contains all previous ones. In these

Table 4.2 Event yields corresponding to an integrated luminosity of 35.9 fb^{-1} of the collected data at 13 TeV are compared with the numbers of expected signal and background events as estimated from the simulation. The values are given for the e^+e^-, $\mu^+\mu^-$, $e^\pm\mu^\mp$ and combined channels after each consecutive selection step.

e^+e^- channel	2 leptons	2 jets	E_T^{miss}	b-tag.	kin. reco.
$t\bar{t}$ signal	55218.3	40277.5	31733.0	29212.5	26764.7
$t\bar{t}$ other	8232.3	6028.5	4844.5	4426.5	4147.1
$t\bar{t}$+Z/W	181.7	169.8	138.5	126.1	99.6
single t	6318.8	2463.9	1971.4	1740.2	1142.4
diboson	8267.2	1061.2	575.2	191.9	102.0
W+jets	1449.2	160.6	76.7	51.9	25.6
Z+jets	719056.0	52289.4	12847.2	4840.2	3135.8
Expected events	798724.0	102451.0	52186.5	40589.3	35417.2
Data	867766	100137	51336	39984	34890
$\mu^+\mu^-$ channel	2 leptons	2 jets	E_T^{miss}	b-tag.	kin. reco.
$t\bar{t}$ signal	113220.0	82209.7	64914.8	59839.5	54873.5
$t\bar{t}$ other	18487.6	13471.2	10813.1	9832.7	9137.7
$t\bar{t}$+Z/W	343.6	321.0	262.6	237.0	189.9
single t	12815.5	4928.1	3880.2	3331.1	2257.1
diboson	17960.5	2042.9	1103.8	358.8	194.7
W+jets	1508.5	211.8	185.7	162.7	77.3
Z+jets	1826020.0	113921.0	27896.7	10328.5	6881.8
Expected events	1990350.0	217106.0	109057.0	84090.2	73612.0
Data	2032080	208732	104491	80359	70346
$e^\pm\mu^\mp$ channel	2 leptons	2 jets	E_T^{miss}	b-tag.	kin. reco.
$t\bar{t}$ signal	199001.0	145498.0	145498.0	134325.0	124539.0
$t\bar{t}$ other	32478.1	23730.4	23730.4	21662.6	20356.6
$t\bar{t}$+Z/W	555.3	515.2	515.2	466.5	394.7
single t	22815.8	8900.5	8900.5	7667.7	5490.3
diboson	26721.7	2085.2	2085.2	688.9	406.5
W+jets	3943.1	433.8	433.8	120.8	74.0
Z+jets	62613.8	4891.3	4891.3	1729.0	1305.8
Expected events	348129.0	186054.0	186054.0	166660.0	152567.0
Data	353773	184529	184529	164297	150410
combined channel	2 leptons	2 jets	E_T^{miss}	b-tag.	kin. reco.
$t\bar{t}$ signal	367440.0	267985.0	242145.0	223377.0	206177.0
$t\bar{t}$ other	59198.0	43230.1	39388.1	35921.8	33641.3
$t\bar{t}$+Z/W	1080.5	1006.0	916.3	829.7	684.2
single t	41950.1	16292.4	14752.1	12739.0	8889.9
diboson	52949.4	5189.3	3764.2	1239.6	703.2
W+jets	6900.7	806.1	696.2	335.5	176.9
Z+jets	2607690.0	171090.0	45587.5	16877.5	11311.8
Expected events	3137210.0	505599.0	347250.0	291320.0	261585.0
Data	3253620	493398	340356	284640	255646

distributions, the hatched area denotes the shape-dependent systematic uncertainties on the $t\bar{t}$ signal and backgrounds, which are described in Chapter 6. In particular, starting from Figure 4.11 and onwards, the rates in *Z+jets* simulations are scaled by the normalization scale factors obtained from data-driven background estimation (see Section 4.5) and leads to an improved description of data by the simulation.

Figure 4.9 shows the invariant mass of the dilepton system in the e^+e^-, $\mu^+\mu^-$ and $e^\pm\mu^\mp$ decay channels after the trigger and lepton pair selection criteria, as well as the combination determined by adding all channels. Due to the requirement of the presence of a lepton pair, the *W+jets* background is largely suppressed.

In Figure 4.10, the jet multiplicity distributions are presented after applying the Z-veto on the same flavour dilepton channels. This requirement reduces the *Z+jets* background by about 92% in e^+e^- and $\mu^+\mu^-$ channels. It can be seen that the region with at least 2 jets is mostly populated by the *$t\bar{t}$ signal*.

Starting from Figure 4.11, all events contain at least two jets satisfying the previously described jet selection requirements. The distributions of these events as a function of E_T^{miss} are shown in Figure 4.11 for the e^+e^- and $\mu^+\mu^-$ channels. It can be seen that the region with $E_T^{miss} < 40$ GeV is dominated by the *Z+jets* background.

Solely in the same flavour dilepton channels, the events that are characterized by the missing transverse energy of a value above 40 GeV pass the selection. The multiplicity distributions for the jets which are identified as b-jets are displayed in Figure 4.12. A region with at least one b-jet is dominated by the *$t\bar{t}$ signal*. The distributions for the pseudorapidity of the selected jet and lepton candidates are shown in Figures 4.13 and 4.14, respectively. As can be seen in these distributions, the *Z+jets* background contamination is largely reduced.

Starting from Figure 4.15, along the mentioned above selection requirements, a presence of at least one b-tagged jet is demanded in each event. The remaining event sample serves as the input to a next essential element of the analysis - the kinematic reconstruction of the $t\bar{t}$ system, which is discussed in Section 4.6. As an example, the related distributions to the corresponding input quantities, such as the p_T of the selected b-jet and lepton candidates, as well as E_T^{miss} in the event, are respectively given in Figures 4.15, 4.16, 4.17. After the b-tagging requirement, the S/B in the combined channel is 3.29.

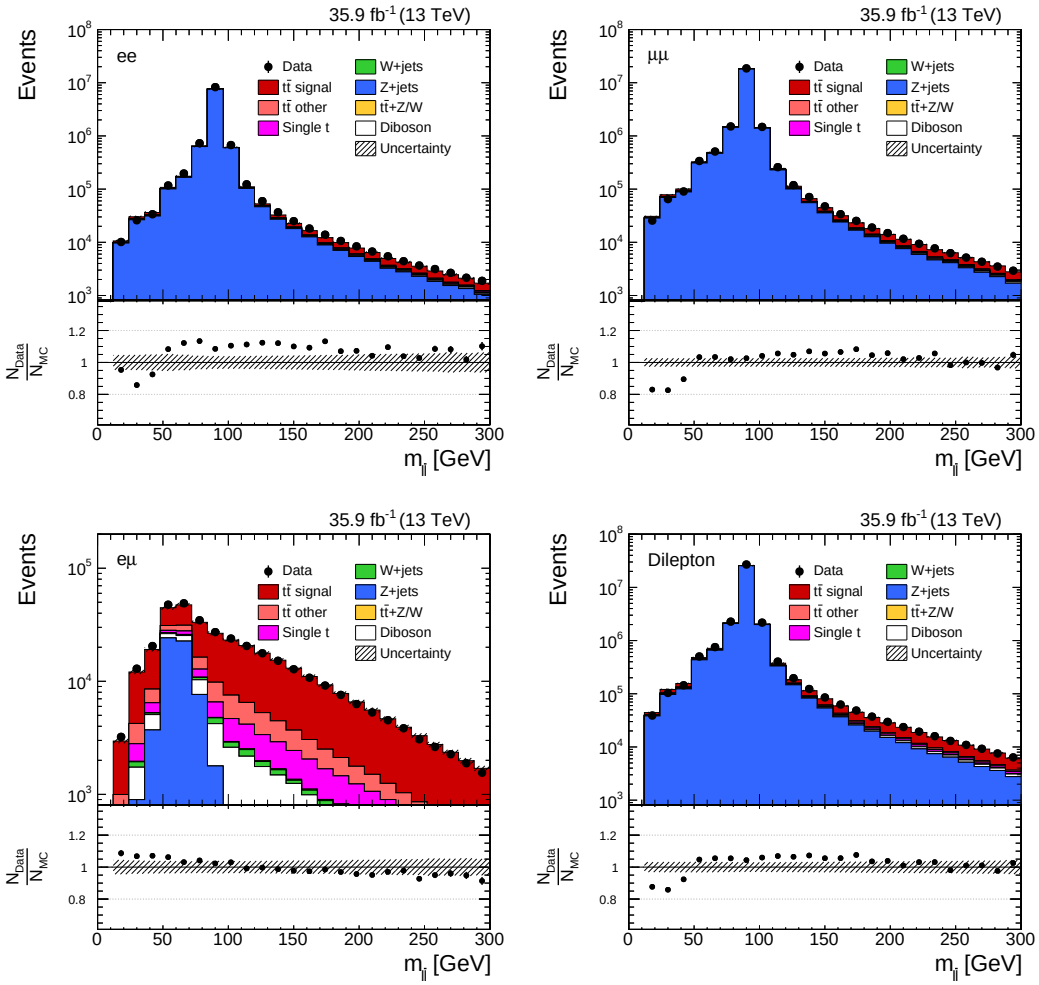

Figure 4.9 Invariant mass of the dilepton system. Events satisfy the trigger and $m_{\ell\bar{\ell}} > 20$ GeV requirements. The scale factors accounting for the trigger and lepton selection efficiencies, described in Sections 4.4.2 and 4.4.3, are used to correct the simulation. The distributions are separately shown for the e^+e^- (upper left), $\mu^+\mu^-$ (upper right), $e^\pm\mu^\mp$ (lower left) channels and for their combination "Dilepton" (lower right). The hatched area indicates the shape systematic uncertainties on the $t\bar{t}$ signal and backgrounds (see Chapter 6).

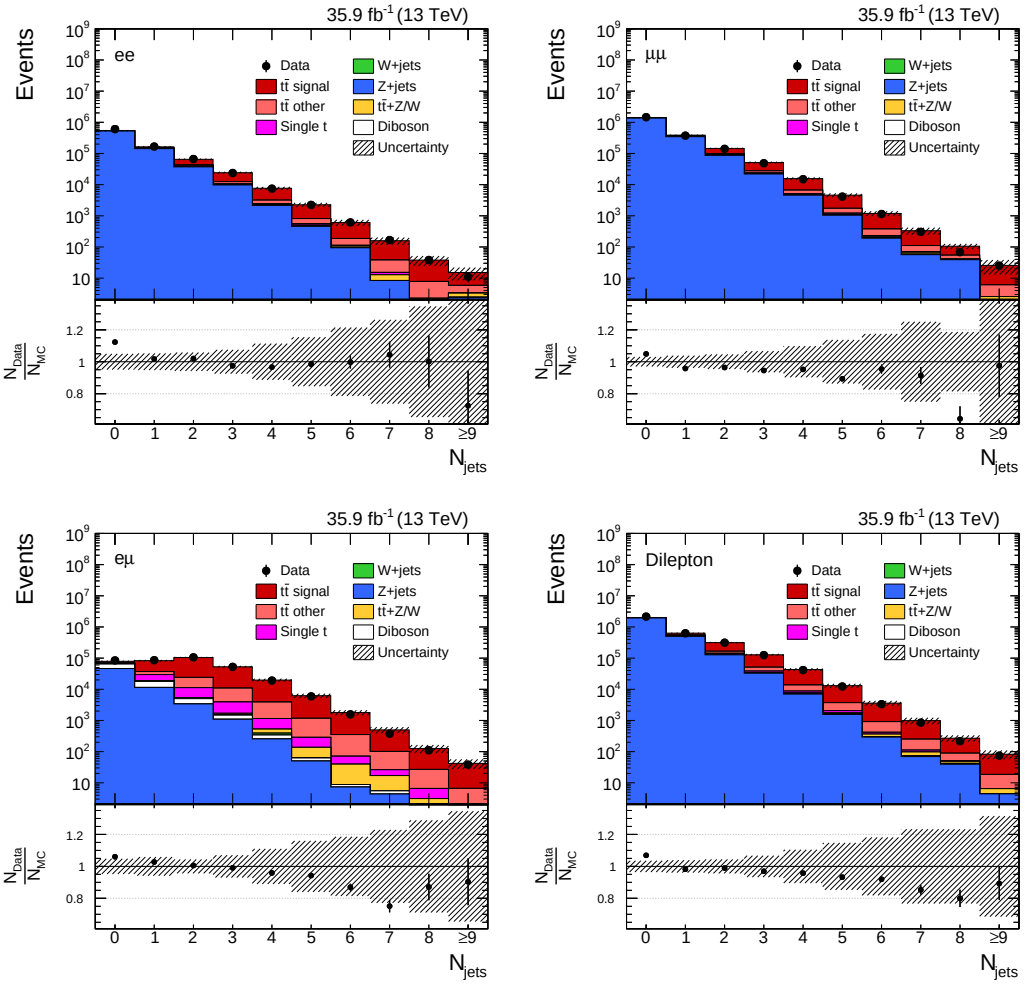

Figure 4.10 Number of jets per event after the Z-veto requirement, which is applied only in the same-flavour dilepton channels. Events contain the accordingly preselected lepton pair. The distributions are separately shown for the e^+e^- (upper left), $\mu^+\mu^-$ (upper right), $e^\pm\mu^\mp$ (lower left) channels and for their combination "Dilepton" (lower right). The hatched area indicates the shape systematic uncertainties on the $t\bar{t}$ signal and backgrounds (see Chapter 6).

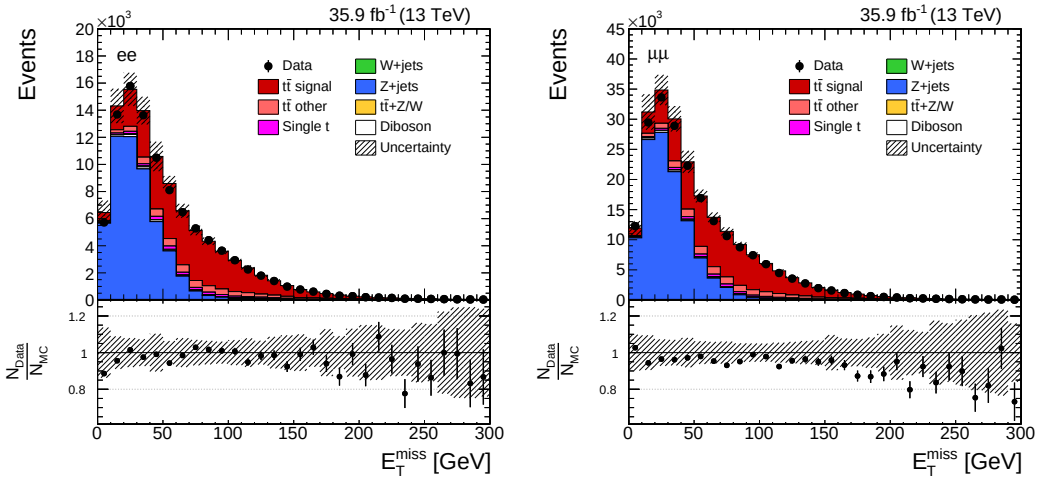

Figure 4.11 Missing transverse energy in the e^+e^- (left) and $\mu^+\mu^-$ (right) channels after the jet-related selection requirements. Events have the dilepton invariant mass of the values $m_{\ell\bar{\ell}} < 76$ GeV or $m_{\ell\bar{\ell}} > 106$ GeV and remain after the application of lepton pair requirement. The *Z+jets* simulation is scaled according to results of the data-driven background estimation. The hatched area indicates the shape systematic uncertainties on the $t\bar{t}$ signal and backgrounds (see Chapter 6).

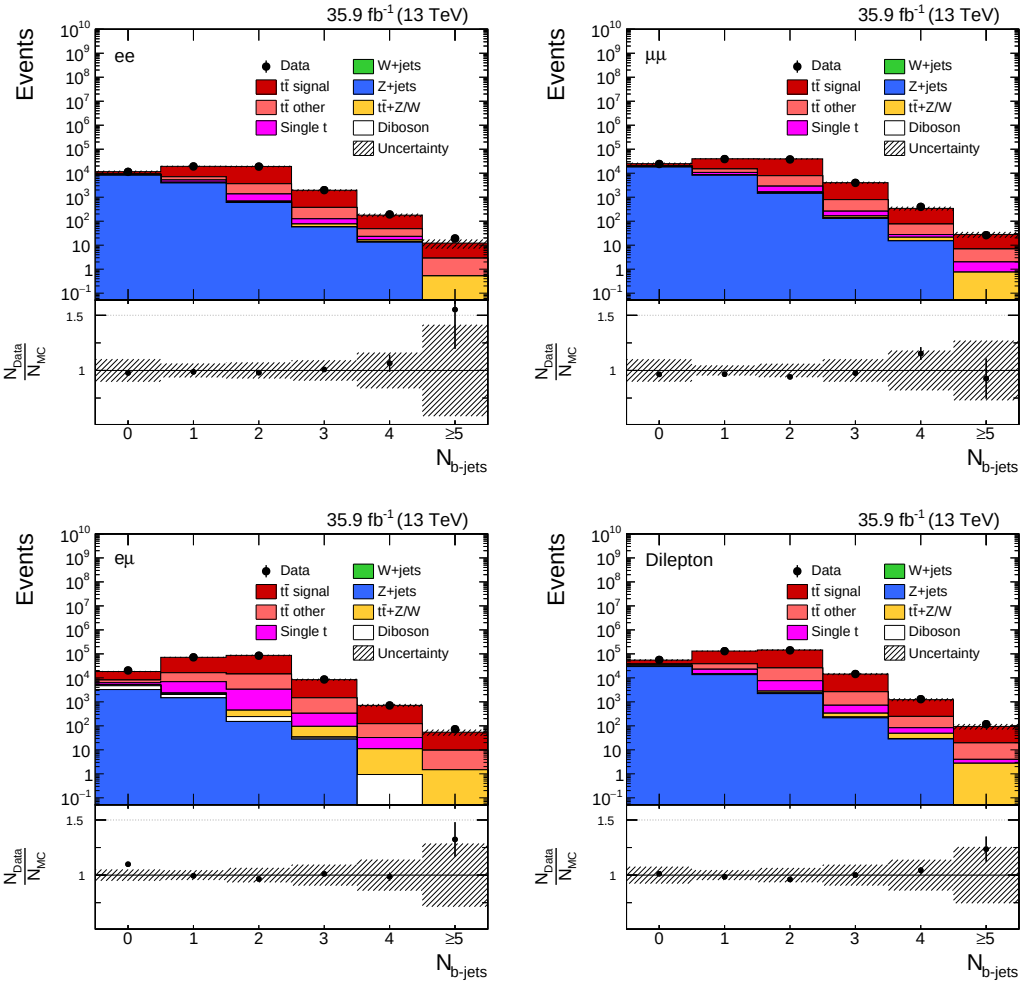

Figure 4.12 Multiplicity of b-jets after the lepton pair and jet-related selection requirements. In the e^+e^- and $\mu^+\mu^-$ channels, events satisfying 76 GeV $< m_{\ell\bar{\ell}} <$ 106 GeV and $E_T^{miss} <$ 40 GeV conditions are excluded. The distributions are separately shown for the e^+e^- (upper left), $\mu^+\mu^-$ (upper right), $e^{\pm}\mu^{\mp}$ (lower left) channels and for their combination "Dilepton" (lower right). The *Z+jets* simulation is scaled according to results of the data-driven background estimation. The hatched area indicates the shape systematic uncertainties on the $t\bar{t}$ signal and backgrounds (see Chapter 6).

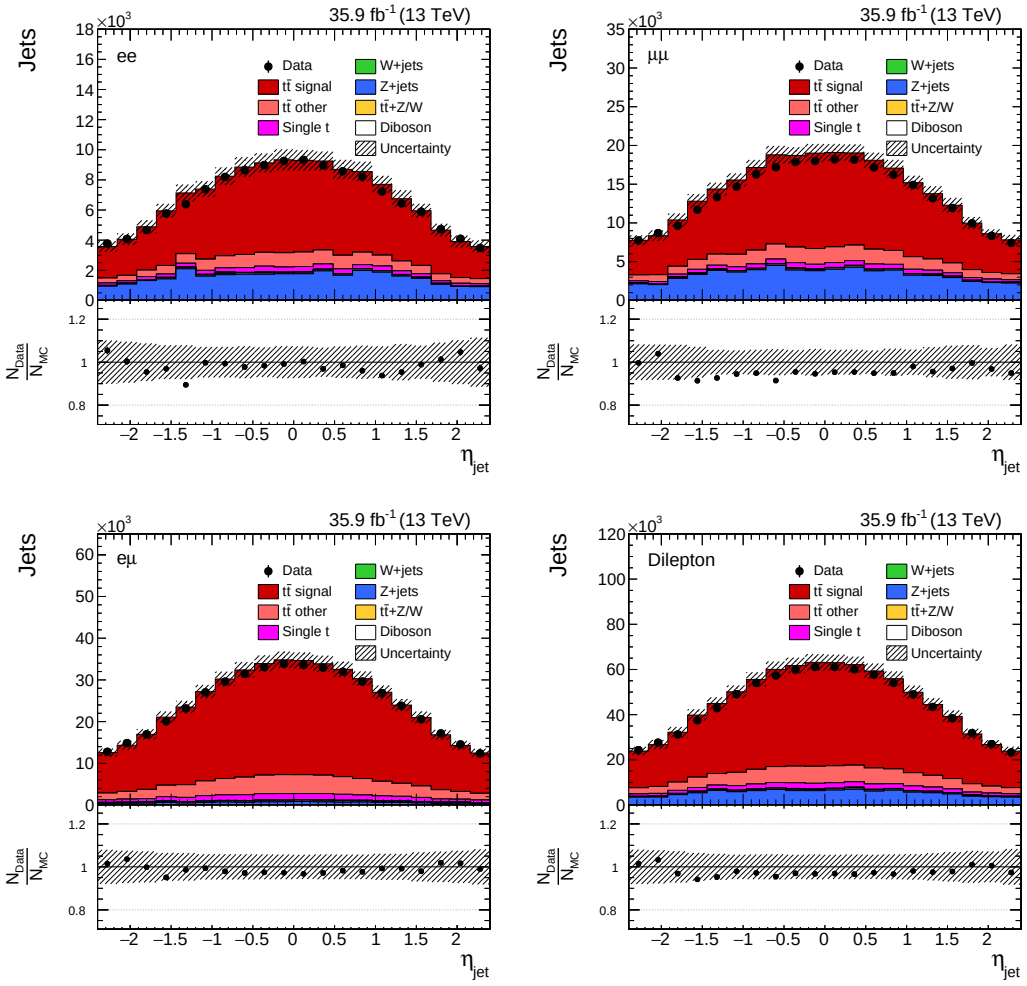

Figure 4.13 Pseudorapidity of jets after the lepton pair and jet-related selection requirements. In the e^+e^- and $\mu^+\mu^-$ channels, events satisfying 76 GeV $< m_{\ell\bar{\ell}} <$ 106 GeV and $E_T^{miss} <$ 40 GeV conditions are excluded. The distributions are separately shown for the e^+e^- (upper left), $\mu^+\mu^-$ (upper right), $e^{\pm}\mu^{\mp}$ (lower left) channels and for their combination "Dilepton" (lower right). The *Z+jets* simulation is scaled according to results of the data-driven background estimation. The hatched area indicates the shape systematic uncertainties on the $t\bar{t}$ signal and backgrounds (see Chapter 6).

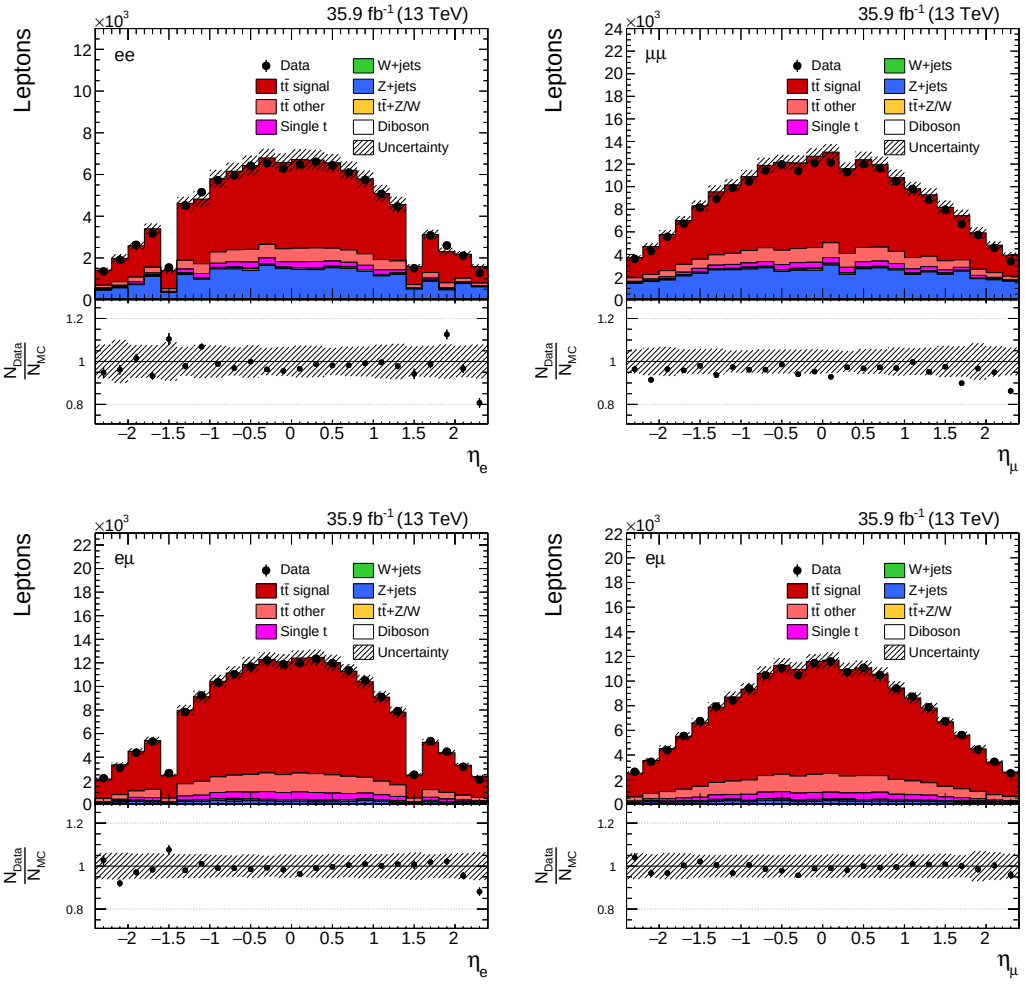

Figure 4.14 Pseudorapidity of electrons (left) and muons (right) in the e^+e^- (top left), $\mu^+\mu^-$(top right), and $e^\pm\mu^\mp$ (bottom) channels after the lepton pair and jet-related selection requirements. In the e^+e^- and $\mu^+\mu^-$ channels, events satisfying 76 GeV $< m_{\ell\bar{\ell}} <$ 106 GeV and $E_T^{miss} <$ 40 GeV conditions are excluded. The *Z+jets* simulation is scaled according to results of the data-driven background estimation. The hatched area indicates the shape systematic uncertainties on the $t\bar{t}$ signal and backgrounds (see Chapter 6).

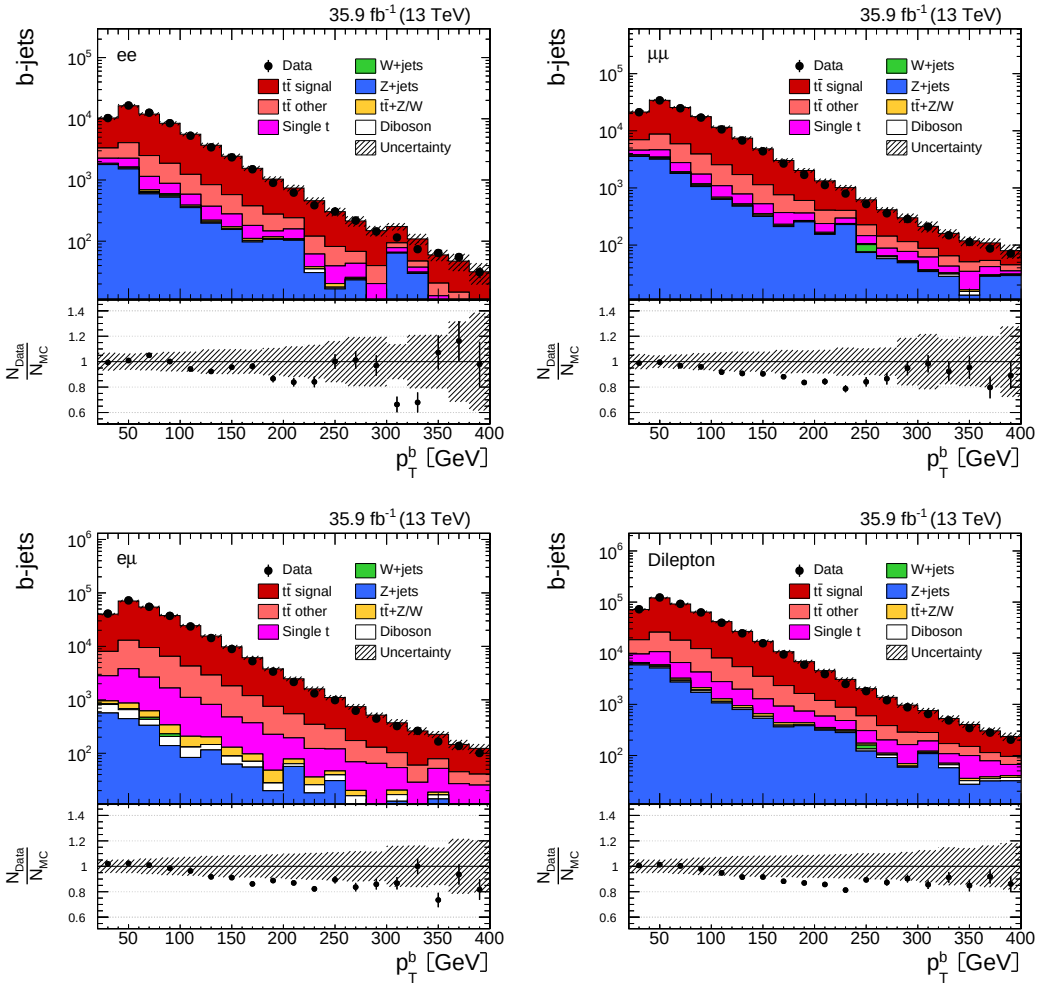

Figure 4.15 Transverse momentum of b-jets. Events fulfill the lepton pair and jet-related selection requirements, as well as the criterion demanding the presence of at least one b-tagged jet in the event. In the e^+e^- and $\mu^+\mu^-$ channels, events satisfying 76 GeV $< m_{\ell\bar{\ell}} <$ 106 GeV and $E_T^{miss} < 40$ GeV conditions are excluded. The distributions are separately shown for the e^+e^- (upper left), $\mu^+\mu^-$ (upper right), $e^{\pm}\mu^{\mp}$ (lower left) channels and for their combination "Dilepton" (lower right). The *Z+jets* simulation is scaled according to results of the data-driven background estimation. The hatched area indicates the shape systematic uncertainties on the $t\bar{t}$ signal and backgrounds (see Chapter 6). The displayed quantities are used as an input to the top-quark pair kinematic reconstruction in each event.

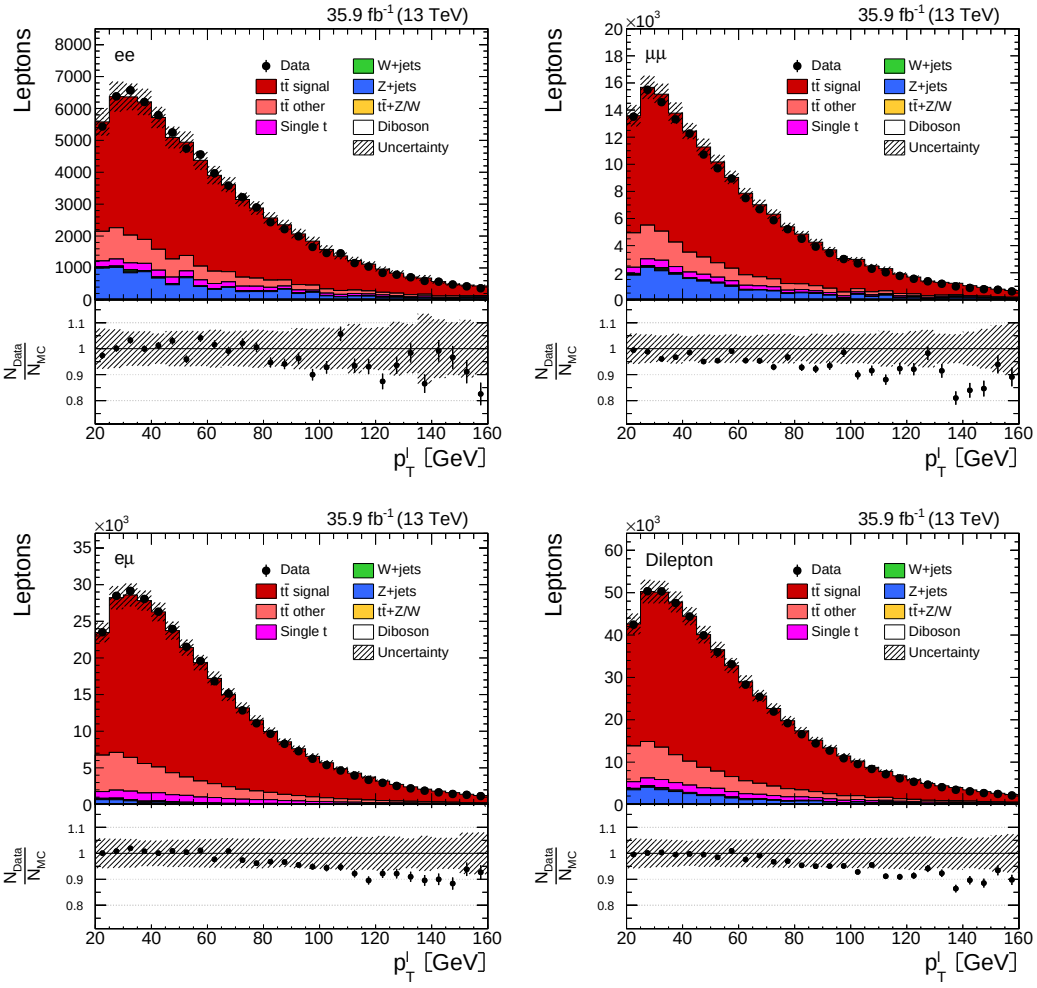

Figure 4.16 Transverse momentum of leptons. Events fulfill the lepton pair and jet-related selection requirements, as well as the criterion demanding the presence of at least one b-tagged jet in the event. In the e^+e^- and $\mu^+\mu^-$ channels, events satisfying 76 GeV $< m_{\ell\bar{\ell}} <$ 106 GeV and $E_T^{miss} < 40$ GeV conditions are excluded. The distributions are separately shown for the e^+e^- (upper left), $\mu^+\mu^-$ (upper right), $e^\pm\mu^\mp$ (lower left) channels and for their combination "Dilepton" (lower right). The *Z+jets* simulation is scaled according to results of the data-driven background estimation. The hatched area indicates the shape systematic uncertainties on the $t\bar{t}$ signal and backgrounds (see Chapter 6). The displayed quantities are used as an input to the top-quark pair kinematic reconstruction in each event.

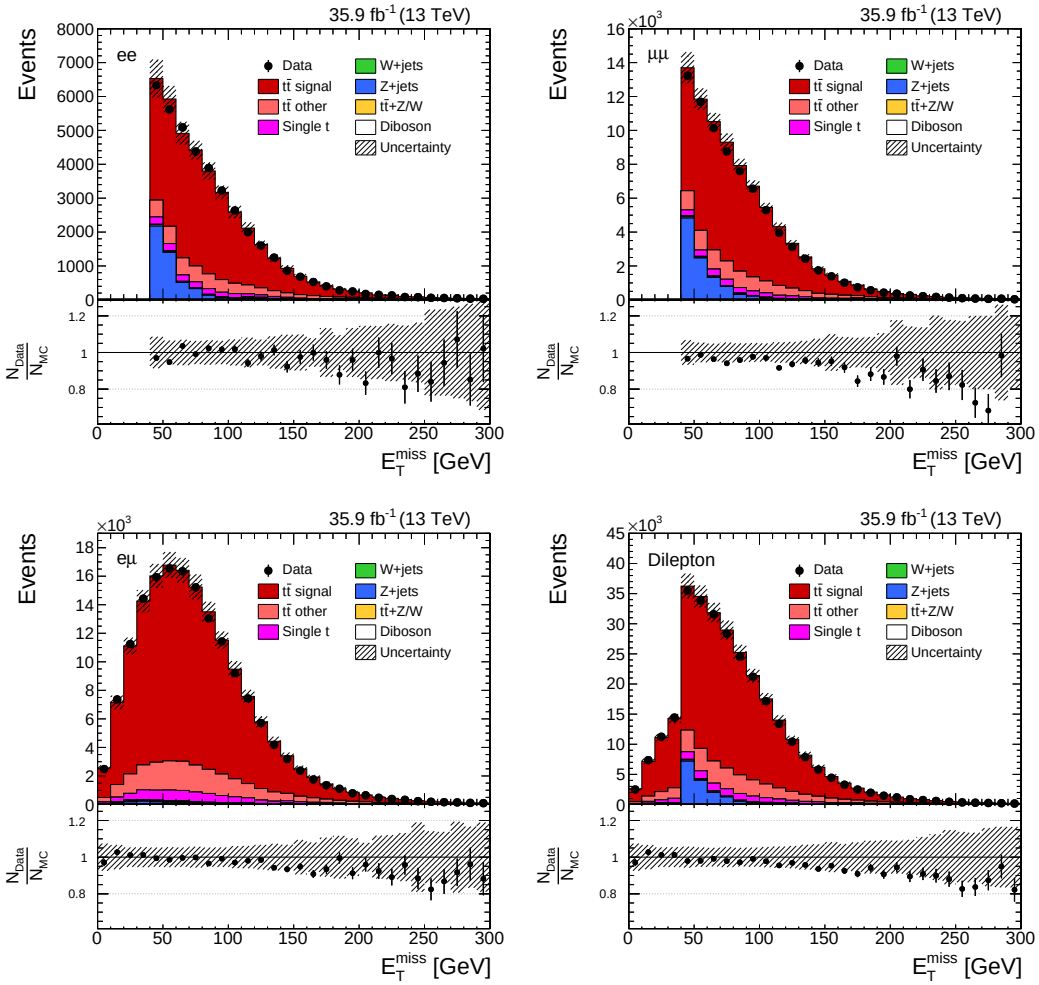

Figure 4.17 Missing transverse energy in the event. Events fulfill the lepton pair and jet-related selection requirements, as well as the criterion demanding the presence of at least one b-tagged jet in the event. In the e^+e^- and $\mu^+\mu^-$ channels, events satisfying 76 GeV $< m_{\ell\bar{\ell}} <$ 106 GeV and $E_T^{miss} < 40$ GeV conditions are excluded. The distributions are separately shown for the e^+e^- (upper left), $\mu^+\mu^-$ (upper right), $e^{\pm}\mu^{\mp}$ (lower left) channels and for their combination "Dilepton" (lower right). The *Z+jets* simulation is scaled according to results of the data-driven background estimation. The hatched area indicates the shape systematic uncertainties on the $t\bar{t}$ signal and backgrounds (see Chapter 6). The displayed quantities are used as an input to the top-quark pair kinematic reconstruction in each event.

4.7.3 Top quark and top-quark pair kinematics

The kinematics of top quarks and $t\bar{t}$-system are determined using the event kinematic reconstruction method that is described in Section 4.6.

The distributions of jet multiplicity and invariant mass of the lepton-b-jet system after the full event selection are shown in Figure 4.18 for the combined decay channel. The expected fraction of signal events is 78.8%.

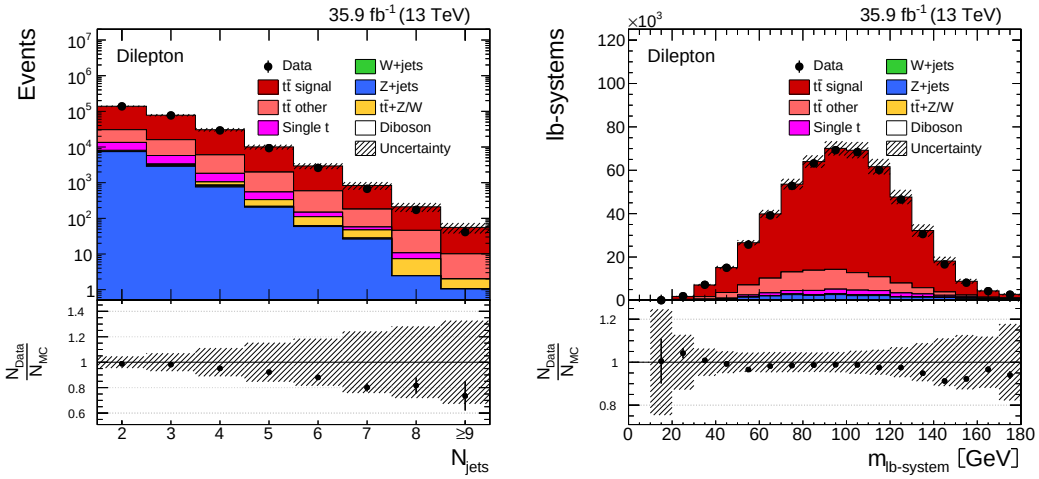

Figure 4.18 Jet multiplicity (left) and invariant mass of the lepton-b-jet system (right) after the full event selection (see Section 4.4). The distributions are shown for the combined decay channel (the sum of e^+e^-, $\mu^+\mu^-$, and $e^\pm\mu^\mp$ channels). The hatched area indicates the shape systematic uncertainties on the $t\bar{t}$ signal and backgrounds (see Chapter 6).

The distributions for the reconstructed top quark and antiquark candidates and $t\bar{t}$-system are presented in Figures 4.19 and 4.20, respectively. These *canonic* distributions represent different aspects of the top quark and $t\bar{t}$-system dynamics and are usually among most prioritized observables for the differential $t\bar{t}$ production cross section measurements. These figures show a reasonable data-to-MC agreement, considering the observation of a slope in the p_T spectrum of top quarks. This behaviour was firstly encountered in similar $t\bar{t}$ production cross section measurements that were performed at 7 TeV [7] and 8 TeV [8], and confirmed at 13 TeV in [9–11], as well as in the context of this work (see Section 7.1).

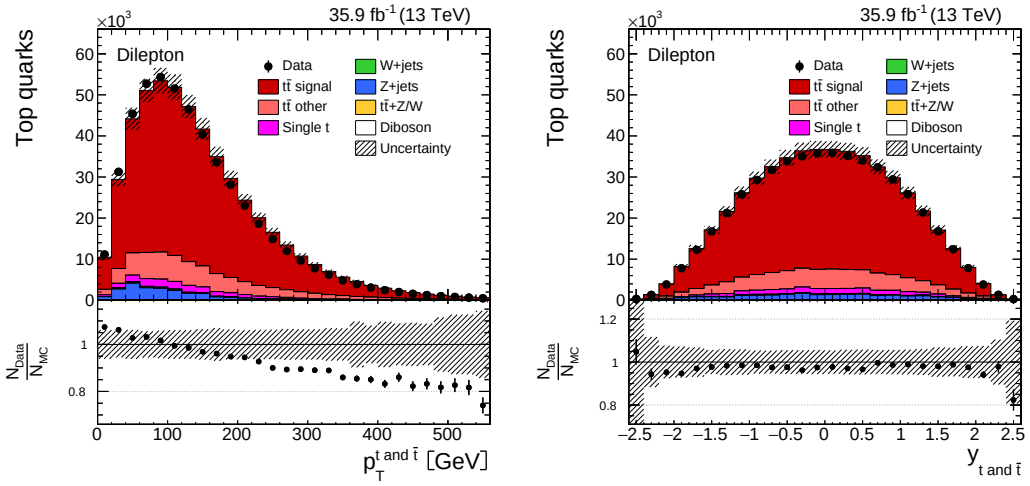

Figure 4.19 Transverse momentum (left) and rapidity (right) of the reconstructed top quark and antiquark candidates. Events fulfill all selection requirements described in Section 4.4. The distributions are shown for the combined decay channel (the sum of e^+e^-, $\mu^+\mu^-$, and $e^\pm\mu^\mp$ channels). The hatched area indicates the shape systematic uncertainties on the $t\bar{t}$ signal and backgrounds (see Chapter 6).

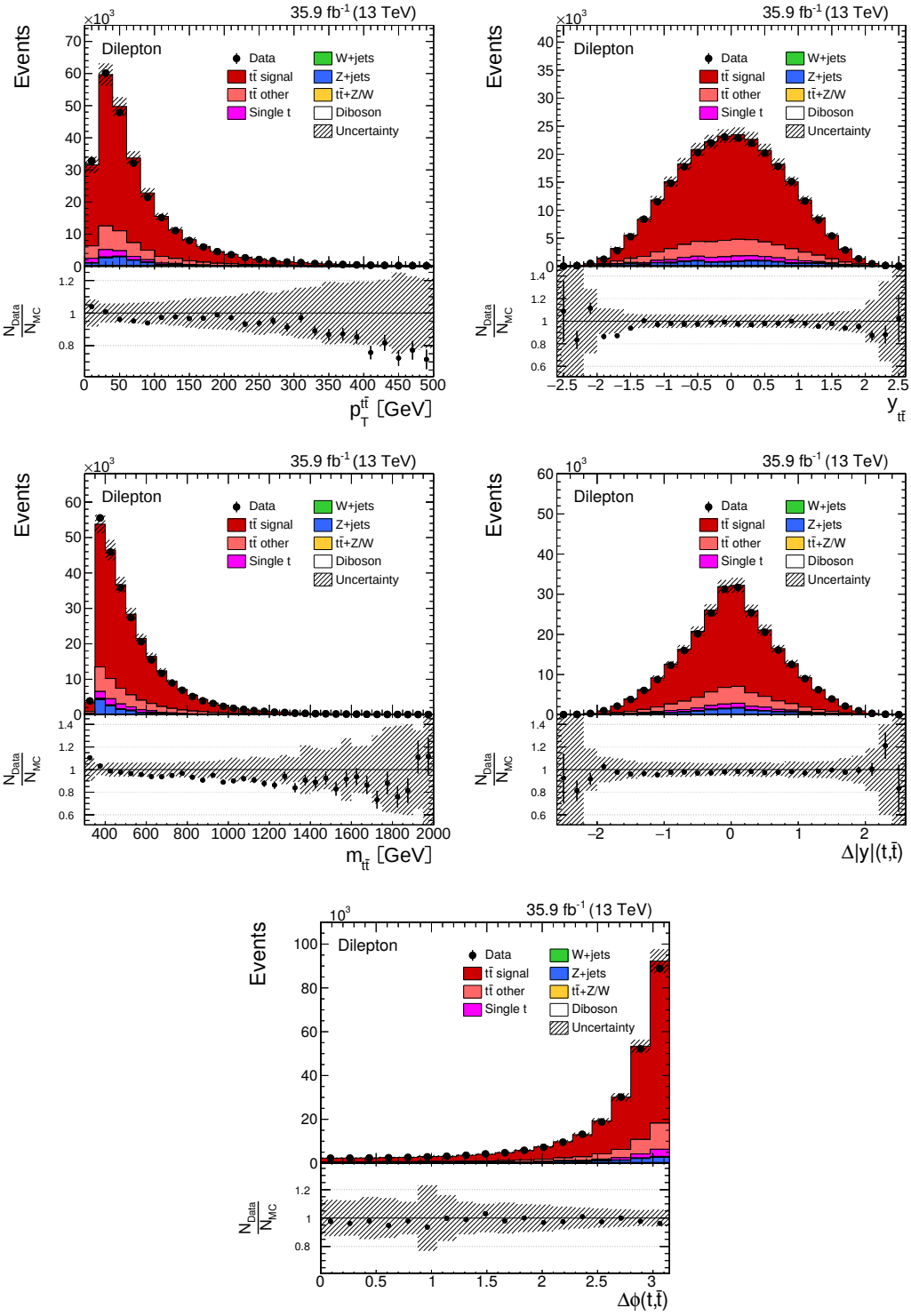

Figure 4.20 Transverse momentum (upper left), rapidity (upper right), invariant mass (middle left), $|y_t| - |y_{\bar{t}}|$ (middle right) and $\Delta\phi_{t\bar{t}}$ (bottom) of the reconstructed $t\bar{t}$-system. Events fulfill all selection requirements described in Section 4.4. The distributions are shown for the combined decay channel (the sum of e^+e^-, $\mu^+\mu^-$, and $e^\pm\mu^\mp$ channels). The hatched area indicates the shape systematic uncertainties on the $t\bar{t}$ signal and backgrounds (see Chapter 6).

Chapter 5

Top-Quark Pair Production Cross Sections

The main goal of this work is to perform the measurement of differential $t\bar{t}$ production cross sections. The studied signal process is top-quark pair production with the subsequent decays into dilepton final states.

The first important step towards the measurement of differential cross sections is the precise understanding of the total production rate. This can be achieved via a dedicated measurement of the inclusive $t\bar{t}$ production cross section.

The differential measurements are mainly targeting at the production rate in a certain kinematic range. For example, the events can be measured in terms of their content, e.g. how many jets are present in the event final state. The jet multiplicity can be of a value $1, 2, 3, \ldots n$ jets per event. The events can be separated into n corresponding groups, which will be used for a measurement of the production cross section in the associated differential bin. In this case, the differential cross sections are measured in bins of the jet multiplicity. The differential cross sections can be also measured with respect to kinematics of the decay products, i.e. the lepton, antilepton, related dilepton system, leading or subleading jet, etc.

This analysis pursues the measurements of absolute and normalized differential cross sections. The absolute differential cross sections are sensitive to the $t\bar{t}$ *signal* production rate and the associated shape as a function of the measured observable, while normalized cross sections are only probing the shape dependence in this function. However, the latter has the advantage of a better precision.

The information about physics objects measured in the detector is distorted due to the detector response. Thus, all reconstructed observables must be corrected for the underlying detector effects. In the context of differential measurements, this correction is performed applying the procedure of data unfolding (see Section 5.3).

The top quark kinematic observables are corrected to such a degree that they correspond to the top quarks just before the decay (at the parton level) and to the particle level, where top quarks are reconstructed using the decay products as they are before the detector simulation. Similarly, the observables related to the decay products of top quarks are corrected back to the particle level only.

Both parton and particle top quark definitions, thoroughly explained in Section 5.5, affect the definition of $t\bar{t}$ *signal*. In this analysis, the $t\bar{t}$ *signal* is measured either in the full or fiducial phase spaces (see Section 5.4).

In this chapter the different steps towards the measurement of the $t\bar{t}$ production cross sections are presented.

5.1 Inclusive cross section

In this work, the inclusive cross section is calculated with an event counting approach, which is based on a simple counting of events after the application of certain selection requirements. For doing so, the same event sample is used as for the differential measurements. This event sample is obtained after the application of the full event selection described in Section 4.4, including the kinematic reconstruction of the $t\bar{t}$-system.

In each channel (e^+e^-, $e^\pm\mu^\mp$, $\mu^+\mu^-$ and their combination), the inclusive cross section is calculated from the observed number of selected events in data after subtracting background contributions and accounting for the detector efficiencies and phase space, which can be expressed as

$$\sigma_{t\bar{t}}^{incl} = \frac{(N_{data} - N_{bg}) \cdot f_{sig}}{\epsilon \cdot A \cdot L \cdot BR}. \tag{5.1}$$

In this formula, N_{data} and N_{bg} denote the number of data and non-$t\bar{t}$ background events after the full event selection. Their difference corresponds to the observed $t\bar{t}$ events in data, including signal and background events. In order to obtain the number of $t\bar{t}$ *signal* events, this difference is then multiplied by the fraction (f_{sig}) of $t\bar{t}$ *signal* events ($N_{t\bar{t}\ signal}$) over the total $t\bar{t}$ events ($N_{t\bar{t}\ signal} + N_{t\bar{t}\ other}$) predicted by the reference $t\bar{t}$ simulation

$$f_{sig} = \frac{N_{t\bar{t}\ signal}}{N_{t\bar{t}\ signal} + N_{t\bar{t}\ other}}. \tag{5.2}$$

The use of f_{sig} allows to avoid the dependence of the result from the normalization in the input $t\bar{t}$ simulation (in particular, from the total production cross section assumed for the normalization). Finally, the measured inclusive cross section is obtained by dividing

the number of $t\bar{t}$ *signal* events in data by the product of the detector efficiency ϵ, detector acceptance A, integrated luminosity L, branching ratio BR for prompt $t\bar{t}$ decays into dileptonic final states. The detector efficiency ϵ accounts for the event reconstruction and selection efficiencies, while the acceptance A gives the extrapolation of the result to the full phase space (both notions are explained in greater detail in Section 5.4).

5.2 Absolute and normalized differential cross sections

The differential $t\bar{t}$ production cross sections are measured as a function of the kinematic properties of the top quarks and their corresponding $t\bar{t}$-system, and in bins of observables that are related to top quark decay products. Additionally, differential cross sections are measured in bins of jet multiplicity in the event (N_{jets}). The kinematics of the top quarks, $t\bar{t}$-system, and the associated final state objects are obtained with the kinematic reconstruction of the $t\bar{t}$ events decaying into dilepton final states. In this thesis, both absolute and normalized differential cross sections are measured. In the following, X denotes an observable that is measured.

In this work, the top quark and $t\bar{t}$-system differential cross section measurements are performed at parton and particle levels, which depend on the model assumptions behind the top quarks used in the signal definition. These results are complemented by the particle level measurements that are performed in bins of the top quark decay product observables and N_{jets} distribution. The parton level cross sections are extrapolated to the full phase space, while the cross sections at particle level are presented in the fiducial phase space. The phase space definitions are discussed in Section 5.4 and definitions of top quarks either at parton or particle level are discussed in Section 5.5.

In order to perform the differential measurements, the input distribution corresponding to each measured observable X is rebinned to a number of bins i.

The absolute differential $t\bar{t}$ production cross section in bin i for a variable X is given by

$$\frac{d\sigma}{dX}^{i} = \frac{x_i}{\Delta_i^X \cdot L \cdot BR}, \tag{5.3}$$

where x_i is the observed number of signal events in a bin i that is calculated from the measured event counts in data after the background subtraction. The value of x_i is also corrected for the detector efficiency and acceptance, and also for the migrations between the bins using a method of data unfolding described in Section 5.3. Afterwards, the corrected number of signal events is divided by the bin width Δ_i^X, the integrated luminosity L and the dilepton branching ratio BR.

The product $\frac{x_i}{L \cdot BR}$ in Equation 5.3 is the total cross section in the bin i for an observable X. Hence, the total $t\bar{t}$ production cross section corresponding to the visible range of an observable X can be calculated via a sum over all bins using the formula

$$\sigma_X^{\Sigma} = \frac{1}{L \cdot BR} \sum\nolimits_i x_i. \tag{5.4}$$

The BR in Equations 5.3 and 5.4 is only used for results presented at the parton level.

The normalized differential cross sections are defined dividing Equation 5.3 by Equation 5.4, which leads to the following expression

$$\frac{1}{\sigma}\frac{d\sigma}{dX}^{i} = \frac{1}{\Delta_i^X}\frac{x_i}{\sum_i x_i}. \tag{5.5}$$

In Equation 5.5, any flat components affecting only the rate in a distribution of any observable X cancel out, since they enter each value of x_i as a multiplicative factor and scale the numerator and denominator in the same way. Thus, the normalized differential cross sections are independent from the rate of input distribution, and, by construction and per observable, they sum up to unity ($\sum_i \frac{1}{\sigma}\frac{d\sigma}{dX}^{i}\Delta_i^X = 1$). The related normalization components of the systematic uncertainties are cancelled out, e.g. like in the case of uncertainty on integrated luminosity. Therefore, measurements of normalized differential cross sections feature better precision than the absolute ones. However, they can only be used for the shape comparisons between the measured and theoretically predicted differential distributions.

The differential measurements are done individually for each considered observable and using the combined dileptonic event sample (quoted to as *Dilepton* or *combined*) as an input.

5.2.1 Detector response and migrations

An ideal detector can be introduced as satisfying the condition that the true information about an observable, serving as an input of a certain form that is registered by the detector, can be fully correctly retrieved out of the output data incoming from the detector. This can be formulated as equality $\mathcal{A}_{meas}^{out} = \mathcal{A}_{true}^{in}$, where $\mathcal{A}_{meas}^{out}$ ($\mathcal{A}_{true}^{in}$) symbolizes a full set of information about the observable that is measured (governed) by the detector (nature). This means that the incoming true information is not distorted by the ideal detector in any possible way.

In reality, each complex detector has its own response function, here denoted as $\mathcal{F}_{resp}$, which parametrizes the level of true signal distortion that is introduced by the detector and is dependent from the detector design, configuration and an arbitrary set of parameters affecting the response. This quality can be expressed as $\mathcal{A}_{meas}^{out} = \mathcal{F}_{resp} \cdot \mathcal{A}_{true}^{in}$, and the true information

about the measured observable can be retrieved as

$$\mathcal{A}^{in}_{true} = \mathcal{F}^{-1}_{resp} \cdot \mathcal{A}^{out}_{meas}. \tag{5.6}$$

The response of the detector is usually studied by means of the MC and detector response simulations using the assumption that the detector reacts to the data and MC events in the same way. However, some differences (e.g. real and assumed jet shapes) in the event reconstruction between the real data, obtained with the detector, and the MC simulation might be present. These effects are taken into account by applying dedicated calibrations and scale factors to the MC simulation, accounting for the detector resolutions, reconstruction and selection efficiencies (see Chapter 4).

The event misreconstruction due to the detector response can lead to two distortion effects:

1. the interesting (fake) event can be lost (accepted);

2. an interesting event can remain after the full selection, but some of the true event parameters (e.g. particle multiplicities, kinematics of particles) influencing the outcome of the measurement might be altered (e.g. the true transverse momentum of an electron is 100 GeV, while for the corresponding reconstructed electron candidate is 90 GeV).

In case of the inclusive cross section measurement, the event counting is impacted only by the first distortion effect, which is accounted for with the multiplicative application of the detector efficiency and acceptance corrections in Equation 5.1. For the differential cross sections, the detector response additionally leads to event migrations through the bin boundaries (the so-called *bin-to-bin* migrations). This means that an event can be generated in a particular bin of the measured spectrum, but might be reconstructed in another bin. The first effect can be accounted for with the acceptance and efficiency driven corrections as done for the inclusive measurement, while the second one needs a dedicated treatment regarding all bins. For the differential measurements presented in this work, both distortion effects are simultaneously considered using the full unfolding procedure (see Section 5.3).

5.2.2 Choice of the binning: purity, stability and resolutions

For each differentially measured observable, the bin-to-bin migrations are studied in terms of the purity and stability. These two criteria are determined from the reference $t\bar{t}$ simulation

and are defined as

$$p_i = \frac{N_i^{rec\&gen}}{N_i^{rec}}, \qquad s_i = \frac{N_i^{rec\&gen}}{N_i^{gen}}. \tag{5.7}$$

Purity p_i in bin i corresponds to the ratio between the number of reconstructed events that are also generated in bin i and the total number of reconstructed events in the same bin. Stability s_i in bin i is the ratio of the same numerator to the number of generated events in bin i. Here, the generated events (as well the "gen" label in Equation 5.7) imply a set of generated events that satisfy the definition of a chosen reference phase space, i.e. full or fiducial (see Section 5.4). The purity and stability are respectively sensitive to the migrations into and out of the bin, and, ideally, would be equal to unity with the absence of bin-to-bin migrations.

The binning, i.e. the number of bins and their boundaries (centers and widths), of the differential cross section measurement must be carefully chosen in order to limit the migration effects. This condition helps to avoid the bias towards the $t\bar{t}$ simulation during the unfolding procedure. The amount of bin-to-bin migrations can be decreased by the expansion of bin widths. In opposite, the desirable strategy is to maximize the number of bins, reducing their widths, to scrutinize the measured spectrum in detail. Thus, a choice of the appropriate binning is closely related to a balance between the two objectives.

The binning of the differential measurements that are presented in this work is optimized according to the following criteria and guidelines:

Approximately flat purities and stabilities across all bins help to diagonalize response matrices (see Section 5.3), reducing the strength of correlations between bins, and to smooth the regularization function involved in the unfolding method. However, while it is straightforward to maintain this condition for a flat distribution or the one with an almost uniform resolution (e.g. the pseudorapidity of leptons), it is very hard to keep the flat purity for a steeply falling spectrum (e.g. transverse momentum of the top quark) with the desirably narrow bin widths. This happens due to the fact that the low-populated regions of the distribution are affected by migrations from the highly-populated bins, which are comparably large with respect to the number of signal events that are generated and reconstructed in the low-populated bins. Therefore, this requirement is loosened with regard to purities in the steeply falling spectra.

Purity and stability are above a certain threshold. This condition allows to ensure that the majority of events are reconstructed in the correct bins. Usually, purities and stabilities are required to be above a threshold close to 50%, while for the steeply falling spectra this requirement is loosened towards 30% in some bins (see previous

item in this list). However, for the observables which are characterized by high resolutions (usually these are the observables related to the top quark decay products) the values of purities and stabilities can be very high (for instance, see Figures C.16-C.21). In this case, the choice of the binning starts to be mainly driven by other requirements.

Bin width must be larger than at least 1σ of the related resolution in a given range of the measured observable. In particular, this criterion simplifies the control over the required level of purities and stabilities, and thus constrains the migration effects.

Sufficient number of events per bin helps to avoid large statistical uncertainties in the results. In this measurement, each bin is required to have at least 1000 data events.

The side-bin boundaries match the kinematic range of the fiducial phase space, if corresponding differential cross sections are measured in the fiducial phase space (see Section 5.4).

In this analysis, the binning choice is complemented by few more less-strong requirements. For the measured observables which are involved in the application of a particular set of scale factors (e.g. the scale factors accounting for the lepton identification are applied in bins of the pseudorapidity and transverse momentum of leptons), the bin centers and widths are chosen to be of the comparable order with the binning in which the scale factors are derived. Also, the decision on the binning structure attempts to account for the shape of the measured distribution, which allows to study certain interesting regions in greater detail, e.g. tails of the top quark rapidity provide crucial information for the PDF-related studies. Finally, the binning is not expanded to the non-physical regions, such as regions below the physical zero, or above the value of π when the azimuthal distance $\Delta\phi$ is measured.

As an example, Figure 5.1 shows the purity and stability per bin, as well as the product of the detector efficiency and acceptance, for the differential measurements performed as a function of the top quark p_T.

5.3 Unfolding of signal spectrum

The differential cross section measurements, presented in this work, are defined either at the parton or particle level. Thus, the observed number of $t\bar{t}$ *signal* events in data per bin i of the studied spectrum, given by (see Equations 5.1 and 5.3)

$$N^{data}_{t\bar{t}\ signal}(i) = f^i_{sig}(N^i_{data} - N^i_{bg}), \tag{5.8}$$

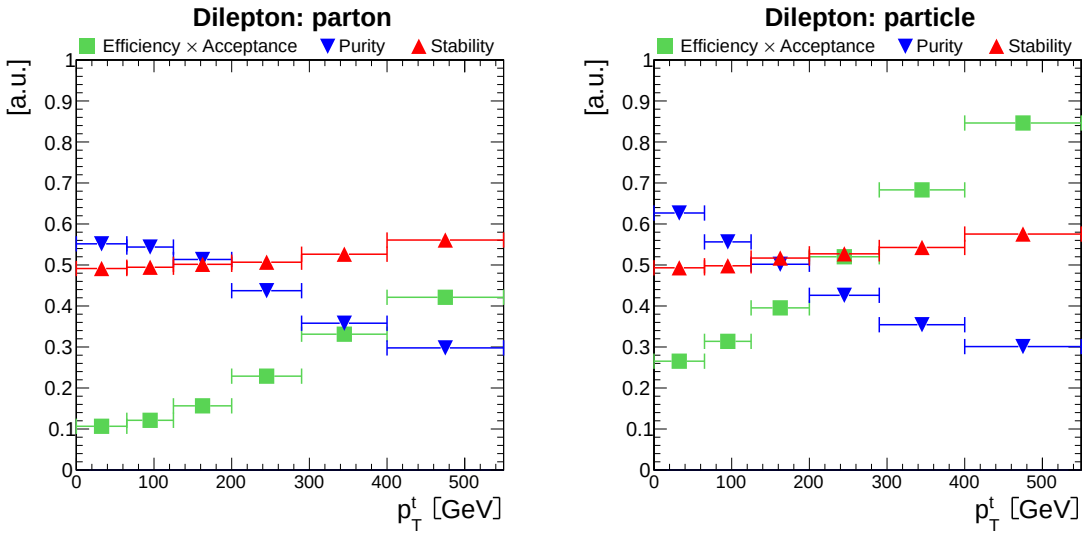

Figure 5.1 The purity and stability, as well as the product of the detector efficiency and acceptance, as a function of the transverse momentum of top quarks. The corresponding quantities, determined from the reference $t\bar{t}$ simulation, are shown in the context of differential measurements defined at parton (left) and particle (right) levels.

must be corrected for the detector acceptance and response, i.e. detector efficiency and migrations among bins. In this work, the combined correction for these effects is performed using the so-called unfolding, which is described in the following.

The sufficient information about migrations among bins as well as the detector efficiency and acceptance is contained in a response matrix $\mathcal{A}^{\mathbf{resp}}$. The response matrix is determined from a relevant $t\bar{t}$ simulation for each measured observable and separately for both definitions of the reference phase space (full or fiducial, see Section 5.4). Elements of the response matrix for a studied spectrum with n bins are calculated as

$$\mathcal{A}_{ij}^{resp} = \frac{N_{i\to j}^{gen\to rec}}{N_i^{gen}}, \; 1 \leq i \leq n, \; 1 \leq j \leq n, \tag{5.9}$$

where N_i^{gen} is the number of $t\bar{t}$ dileptonic events generated in bin i and belonging to a reference phase space and $N_{i\to j}^{gen\to rec}$ is the number of those events which are reconstructed in bin j while being generated in bin i. In this manner, each element $\mathcal{A}_{ij}^{resp}$ denotes a probability of the event generated in bin i to be reconstructed in bin j after the full event selection, the so-called transition probability. The diagonal elements of $\mathcal{A}^{\mathbf{resp}}$ correspond to those events which are correctly reconstructed in a bin of their origin. As an example, Figure 5.2 shows response matrices determined in bins of the p_T of top quarks for the full and fiducial phase spaces.

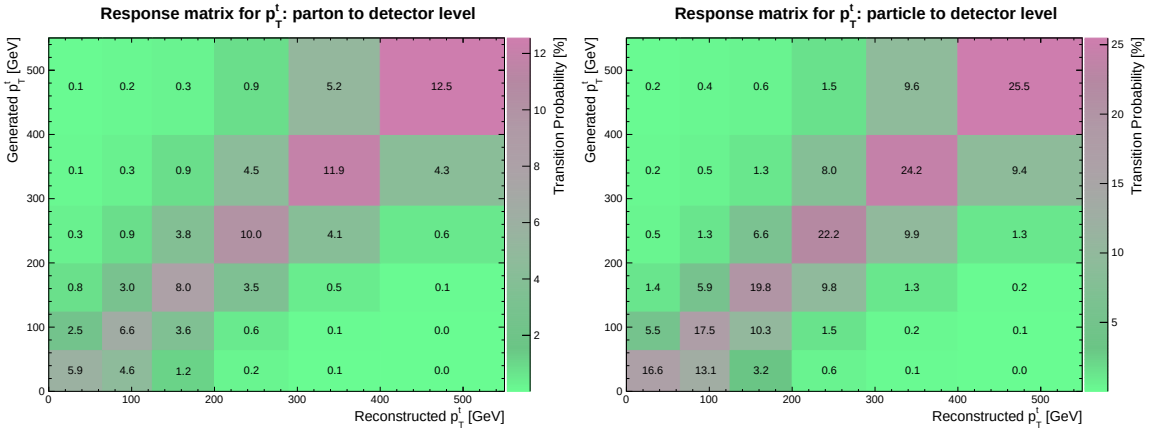

Figure 5.2 The response matrices determined as a function of the transverse momentum of top quarks. The corresponding matrix is used to unfold the reconstructed signal spectrum either to parton (left) or particle (right) level, presenting the results either in a full or fiducial phase spaces, respectively.

Denoting bins of the studied spectrum as a vector, the response matrix $\mathcal{A}^{\mathbf{resp}}$ connects the true signal spectrum $\vec{x} \equiv (x_1, ..., x_i, ...x_n)$ with the observed signal spectrum from data $\vec{N}^{data}_{t\bar{t}\ signal}$ as

$$\mathcal{A}^{\mathbf{resp}}\vec{x} = \vec{N}^{data}_{t\bar{t}\ signal}. \tag{5.10}$$

The unfolding problem is formulated as a retrieval of the $\vec{x}$ vector from the $\vec{N}^{data}_{t\bar{t}\ signal}$ knowing the $\mathcal{A}^{\mathbf{resp}}$. However, the unfolding problem is known as an ill-posed problem [141] leading to an instability against small variations in the input assumptions. The statistical uncertainties of the observed vector $\vec{N}^{data}_{t\bar{t}\ signal}$ and response matrix serve as sources of those variations. A simple way to perform the unfolding is based on an inversion of the response matrix in Equation 5.10, i.e. $\vec{x} = (\mathcal{A}^{\mathbf{resp}})^{-1}\vec{N}^{data}_{t\bar{t}\ signal}$. Even in case when the inverted Equation 5.10 is unambiguously solved, the solution usually features rapidly oscillating components, i.e. due to an amplification of the aforementioned small variations by the matrix inversion, leading to a large bin-to-bin anticorrelations between neighbouring bins [142]. This tendency is not physical and, thus, a solution of this kind cannot be used further. However, this problem can be overcome using the unfolding method described below.

The solution of Equation 5.10 in terms of $\vec{x}$ can be obtained performing a χ^2-minimization [142], i.e. the solution of the least square problem, according to

$$\chi^2_A(\vec{x}) = \left(\mathcal{A}^{\mathbf{resp}}\vec{x} - \vec{N}^{data}_{t\bar{t}\ signal}\right)^T \mathbf{Cov}^{-1}_{\vec{N}^{data}_{t\bar{t}\ signal}} \left(\mathcal{A}^{\mathbf{resp}}\vec{x} - \vec{N}^{data}_{t\bar{t}\ signal}\right), \tag{5.11}$$

where $\mathbf{Cov}_{\vec{N}^{data}_{t\bar{t}\ signal}}$ is the statistical covariance matrix of the observed vector $\vec{N}^{data}_{t\bar{t}\ signal}$. Elements of the $\mathbf{Cov}_{\vec{N}^{data}_{t\bar{t}\ signal}}$ include information about statistical per-bin variations of $\vec{N}^{data}_{t\bar{t}\ signal}$ and are defined as a covariance coefficient

$$(\mathbf{Cov}_{\vec{N}^{data}_{t\bar{t}\ signal}})_{ij} = \Delta^{stat}_i \Delta^{stat}_j \delta_{ij},\ 1 \leq i \leq n,\ 1 \leq j \leq n, \tag{5.12}$$

where Δ^{stat}_i is the absolute statistical uncertainty in bin i of the $\vec{N}^{data}_{t\bar{t}\ signal}$ (see Chapter 6) and δ_{ij} is the Kronecker delta. The covariance coefficient is different from 0 only in the case when two variables, here Δ^{stat}_i and Δ^{stat}_j, are correlated. Hence, $\mathbf{Cov}_{\vec{N}^{data}_{t\bar{t}\ signal}}$ is the diagonal matrix, since bins of the observed vector $\vec{N}^{data}_{t\bar{t}\ signal}$ are statistically uncorrelated.

Large bin-to-bin fluctuations in the solution can be reduced via a smoothing of the solved spectrum, i.e. by means of the regularization method [143], relying on certain a priori information about the solution (basis model). For doing so, the following regularization term is added to the minimized χ^2-function [141]

$$\chi^2_C(\vec{x}) = \left(C^{\mathbf{reg}}\vec{\omega}\right)^T C^{\mathbf{reg}}\vec{\omega}, \tag{5.13}$$

where $\vec{\omega}$ is a vector, which components $\omega_i = x_i / x^{gen}_i$ quantify the per-bin deviation of the unknown vector $\vec{x}$ from the signal spectrum predicted by the simulation $\vec{x}^{gen}$, serving as basis model. The $C^{\mathbf{reg}}$ is the regularization condition given by the matrix

$$C^{\mathbf{reg}} = \begin{pmatrix} -1 & 1 & 0 & 0 & & \cdots & \\ 1 & -2 & 1 & 0 & & \cdots & \\ 0 & 1 & -2 & 1 & & \cdots & \\ & & \ddots & \ddots & \ddots & \ddots & \\ & \cdots & & 0 & 1 & -2 & 1 \\ & \cdots & & 0 & 0 & 1 & -1 \end{pmatrix}. \tag{5.14}$$

The $C^{\mathbf{reg}}$ is chosen in a way that it suppresses those solutions $\vec{x}$ that are associated with large curvatures in $\vec{\omega}$.

Accordingly, the regularized unfolding problem corresponds to

$$\chi^2_{unf}(\vec{x}) = \chi^2_A(\vec{x}) + \tau\chi^2_C(\vec{x}) \tag{5.15}$$

where the regularization strength is governed by a parameter τ.

In this work, differential cross section measurements are performed using the regularized unfolding based on the Singular Value Decomposition (SVD) of the response matrix [141],

as implemented in the TSVD unfolding code [144]. Once the unfolded solution $\vec{x}$ is obtained, the statistical covariance matrix of the true spectrum $\vec{x}$, denoted as $\mathbf{Cov}_{\vec{x}}$, is derived by an error propagation from the $\mathbf{Cov}_{\vec{N}^{data}_{t\bar{t}\ signal}}$, exploiting the pseudo-experiment technique. In each pseudo-experiment, the input data is varied according to its statistical uncertainty and the unfolding is performed as usual. The statistical uncertainty on $\vec{x}$ is taken as the variation in a spread of obtained results. In this way, all bin-to-bin correlations are naturally propagated to the $\mathbf{Cov}_{\vec{x}}$. For this purpose, 1000 pseudo-experiments are deployed using the TSVD unfolding code.

A choice of the regularization strength

The choice of a proper regularization strength adds another layer of complication to the unfolding problem. A very high τ-value, i.e. $\tau \to \infty \equiv$ strong regularization, can lead to an over-smoothing of obtained results. In addition, any variations of true spectrum from a basis model are strongly constrained, which basically introduces a bias towards the simulation. Due to this, the features of a true spectrum, i.e. the genuine shape and correlations among bins, might be lost. In contrast, a low τ-value, i.e. $\tau \to 0 \equiv$ weak regularization or its omission, leads to an under-smoothing, which means that rapidly oscillating components of the solution remain weakly-suppressed. In total, the choice of a proper regularization strength is equivalent to the search of a balance between the acceptable magnitude of the variance in results and the bias, introduced by the regularization, such that the bias is covered by those variances.

In this analysis, the optimal regularization strength τ_{opt} for the unfolding is selected at the minimum of the averaged global correlation coefficient $\bar{\rho}$. This condition corresponds to a requirement which minimizes possible correlations among bins. The averaged global correlation coefficient is defined as [142]

$$\bar{\rho} = \frac{1}{n} \sum_{i=1}^{n} \sqrt{1 - \frac{1}{(\mathbf{Cov}_{\vec{x}})_{ii} (\mathbf{Cov}^{-1}_{\vec{x}})_{ii}}}. \tag{5.16}$$

The $\bar{\rho}$-minimization is performed via the repetition of the unfolding using various τ-values, spanning a large range. The $\bar{\rho}$ is recomputed in each unfolding attempt and mapped to the considered τ. Examples of $\bar{\rho}$-minimization are shown in Figure 5.3. The aforementioned optimization of a τ-value is performed individually for each measured spectrum and separately for the parton and particle level measurements, the results of which are presented in Table A.6.

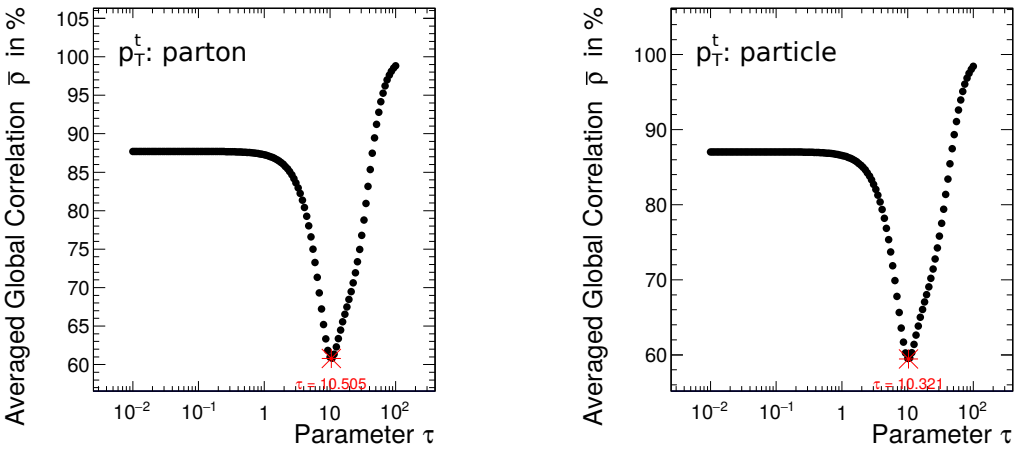

Figure 5.3 The results of the $\bar{\rho}$-minimization for the differential measurements performed as a function of the transverse momentum of top quarks at parton (right) and (particle) levels. The optimal regularization strength τ_{opt}, used for the unfolding, is selected at the minimum of the $\bar{\rho}$ and is indicated with the red asterisk.

5.3.1 Quality tests of the unfolding method

Several quality tests of the unfolding method are conducted in order to validate its performance. Main goal of these tests is to check whether the unfolding introduces a distortion to measured $t\bar{t}$ differential cross sections. Being sensitive to the rate and shape, absolute differential measurements serve as a sufficient basis for this purpose. The same quality tests are repeated for the parton level and particle level measurements, since the unfolding operates slightly different inputs with respect to both cases.

In the following, the results of quality tests are presented in terms of the top quark p_T distribution. The top quark p_T distribution features a large slope in the data-to-MC description (see Figure 4.19). In this case, the unfolding relies on a largely different basis model (from the simulation) with respect to data. Thus, the top quark p_T distribution serves as a good tool for tests of the unfolding.

Consistency check

The first, and simplest, quality test is performed via the replacement of the data by a so-called pseudo-data sample, which is constructed as a sum of all reference simulated samples, i.e $t\bar{t}$ *signal* and backgrounds, without any additional variations in the rate and shape. The whole analysis is repeated using the pseudo-data in completely the same way as done with a real data.

Accordingly, the observed signal spectrum, based on the pseudo-data, is unfolded relying on the reference $t\bar{t}$ simulation (POWHEG v2+PYTHIA8). As shown in Figure 5.4, the unfolded pseudo-data spectrum (black dots) is expected to be fully consistent with the prediction from the reference $t\bar{t}$ simulation (red solid line). The meaning of the pink dashed line will be explained in the later text. It can be concluded that the corrections for detector efficiency, aceptance and migrations effects, applied during the unfolding, fulfill their purpose according to expectations.

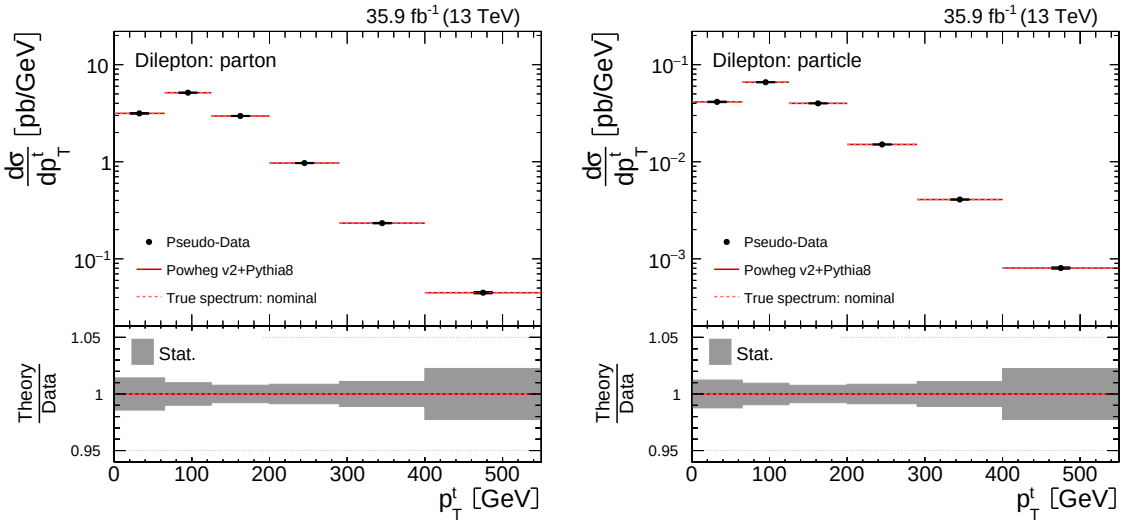

Figure 5.4 Absolute $t\bar{t}$ differential cross sections, together with their statistical uncertainty, measured as a function of the top quark transverse momentum using the pseudo-data sample, constructed as a sum of all reference simulated samples without any additional variations. The pseudo-data is unfolded either to parton (left) or particle (right) level using the reference $t\bar{t}$ simulation, i.e. POWHEG v2+PYTHIA8. The statistical uncertainty corresponds to the uncertainty of the unfolding method.

Check for a bias towards the simulation

The second quality test is intended to check the unfolded results for the presence of a bias towards the simulation. For doing so, the pseudo-data is varied with the dedicated weighting procedure. Each $t\bar{t}$ event in pseudo-data, i.e. $t\bar{t}$ *signal* and $t\bar{t}$ *other*, is assigned with a weight w based on the true level information. The weights are determined as a function of the generated top quark and antiquark transverse momenta (p_T^t and $p_T^{\bar{t}}$, respectively)

$$w = max\Big\{(1 + s \cdot (p_T^t/GeV - 100)) \cdot (1 + s \cdot (p_T^{\bar{t}}/GeV - 100)) \; ; \; 0.1\Big\}, \tag{5.17}$$

where the parameter s controls the strength of the applied variation. An operation $max\{A; B\}$ implies that a higher value between A and B is taken. This operation is imposed to prevent weights spanning the negative values, as well as values close to 0. The corresponding distortion of the pseudo-data spectrum, after applying event weights, behaves as a linear function with respect to p_T of each quark with the rotation point at $p_T = 100$ GeV (at this point, the weight contribution due to corresponding top quark turns to 1).

After the reweighting, the varied pseudo-data is treated as a real data, which implies that any true level information serving as a base for the pseudo-data is ignored. The default analysis is repeated and the varied pseudo-data is unfolded using the reference (non-reweighted) $t\bar{t}$ simulation. As an evidence of unbiased results, the unfolded pseudo-data is expected to agree with the input true spectrum obtained after the reweighting.

The previously described quality test is performed varying the pseudo-data according to two opposite variations, given by $s = 0.001$ and $s = -0.001$, respectively. The variation strengths are chosen as such to cover, with a certain margin, the observed slope in the reconstructed p_T^t between the data and simulation (see Figure 4.19).The results of the test with these two variations are shown in Figure 5.5. The unfolded pseudo-data spectrum is in a good agreement with the reweighted input spectrum (pink dashed line) across all bins, even though the basis model used to perform the unfolding is largely inconsistent with the input shape. This demonstrates that the unfolding method is capable to restore the true features of the data spectrum without introducing a substantial bias towards the simulation.

Testing a choice of the optimal regularization strength

A choice of the optimal regularization strength, given by the parameter τ_{opt}, used for the regularized unfolding (see Equation 5.15) is tested. For doing so, the absolute $t\bar{t}$ differential cross sections are measured using the default analysis setup, i.e. using the real data and reference simulated samples without any additional variations. However, measurements are repeated with different choices of the regularization strength in the data unfolding. The following choices of the τ-parameter are considered: $\tau = \tau_{opt}$ (optimal choice), $\tau = 0 \cdot \tau_{opt}$ (no regularization), $\tau = 0.01 \cdot \tau_{opt}$ (very weak regularization), $\tau = 0.1 \cdot \tau_{opt}$, $\tau = 10 \cdot \tau_{opt}$, $\tau = 100 \cdot \tau_{opt}$ (very strong regularization).

The obtained results are shown in Figure 5.6, where the data points of compared measurements are slightly shifted within relevant bins for demonstration purposes. Several interesting conclusions can be derived from the presented comparison. As can be seen, the choice $\tau = \tau_{opt}$ is in agreement within the statistical uncertainties with the case when the regularization is omitted. This means that the selected τ_{opt} introduces a rather small regularization. When comparing to the $\tau = \tau_{opt}$ spectrum, one could notice a presence of anticorrelations

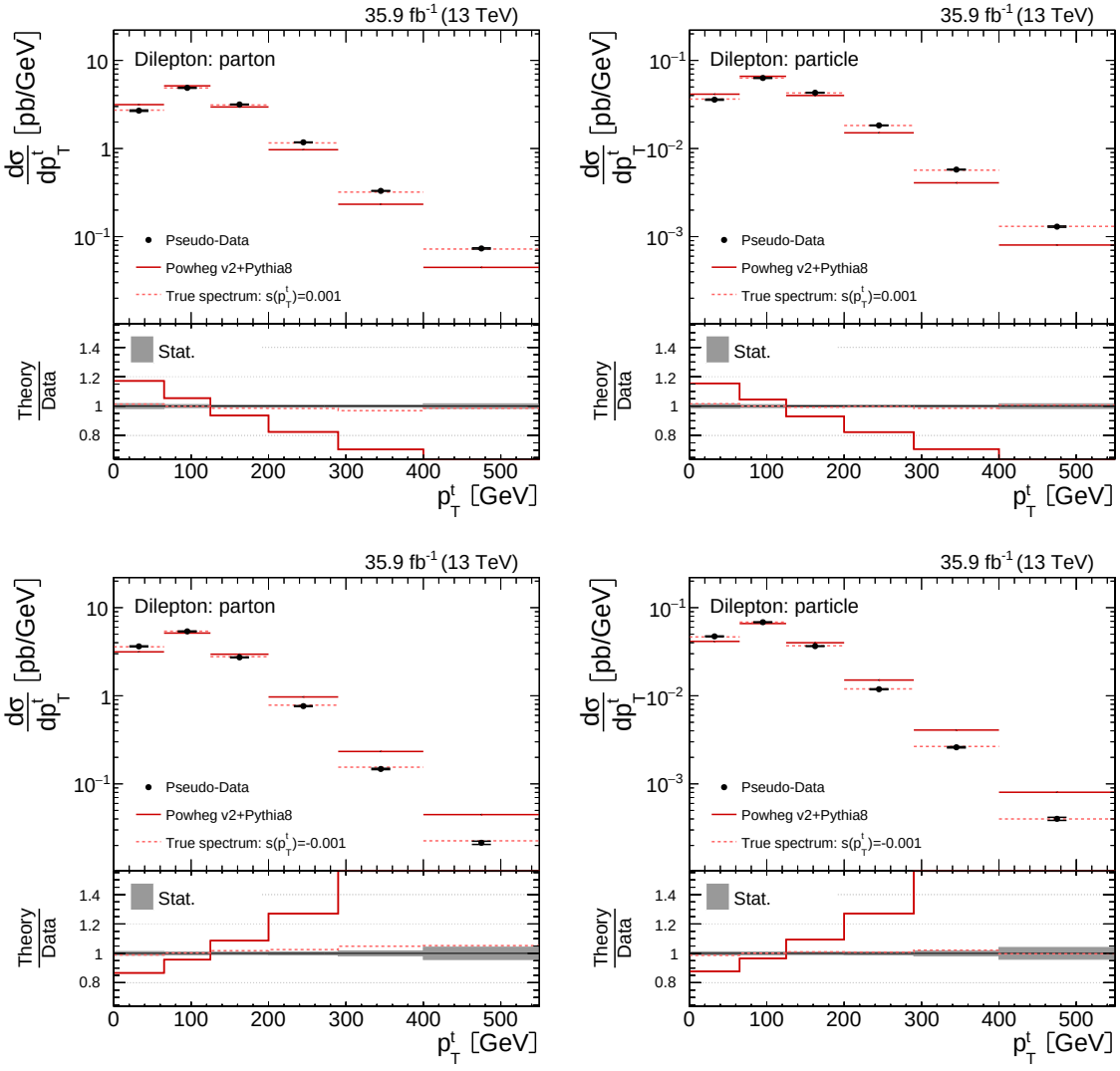

Figure 5.5 Absolute $t\bar{t}$ differential cross sections, together with their statistical uncertainty, measured as a function of the top quark transverse momentum using the pseudo-data sample, which includes the dedicated variation of $t\bar{t}$ events using the variation strength $s = 0.001$ (up) and $s = -0.001$ (down). The pseudo-data is unfolded either to parton (left) or particle (right) level using the reference $t\bar{t}$ simulation, i.e. POWHEG v2+PYTHIA8. The statistical uncertainty corresponds to the uncertainty of the unfolding method.

between neighbouring bins in spectra featuring weaker regularization, which emphasizes a benefit of the regularized unfolding. As expected, the variance of results reduces with an increase in the regularization strength. Moreover, the results remain mostly unbiased towards the reference $t\bar{t}$ simulation (Powheg v2+Pythia8), even in the case when the optimal choice is strengthen by the factor of 10. Only the results obtained with the very strong regularization ($\tau = 100 \cdot \tau_{opt}$) feature a significant bias of this kind, which happens due to a dominance of the regularization term in Equation 5.15.

In total, this quality test demonstrates that the bias introduced by the regularization, with its strength selected at the minimum of the averaged global correlation coefficient $\bar{\rho}$, is weak enough and it appears to be within the variance of unfolded results.

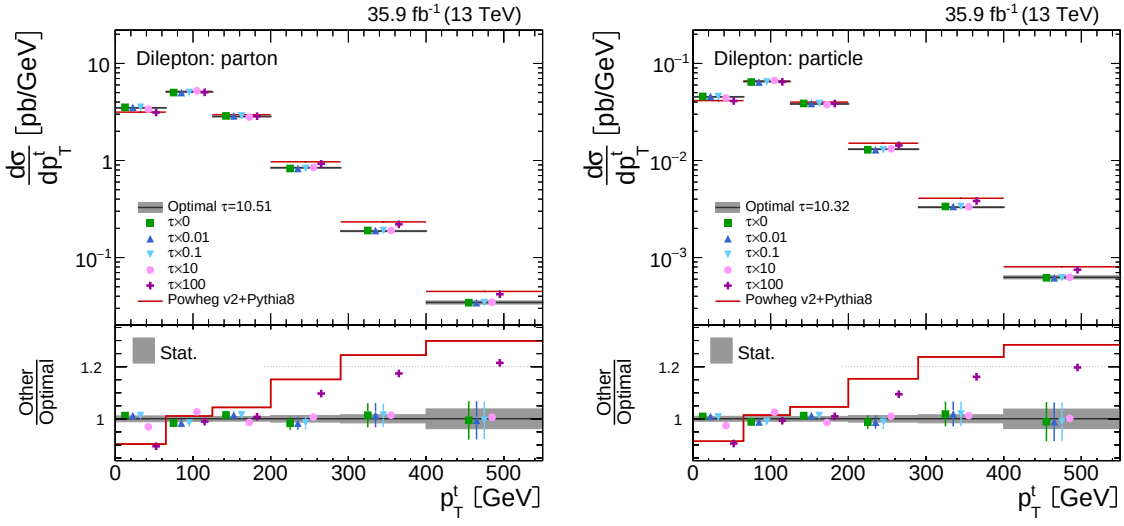

Figure 5.6 Absolute $t\bar{t}$ differential cross sections, together with their statistical uncertainty, measured as a function of the top quark transverse momentum using the default analysis setup, i.e. using the real data and reference simulated samples without any additional variations. Data is unfolded either to parton (left) or particle (right) level using different choices of the regularization strength and relying on the reference $t\bar{t}$ simulation, i.e. Powheg v2+Pythia8. The statistical uncertainty corresponds to the uncertainty of the unfolding method.

5.4 Phase space and correction of results

The measurements are performed in a certain phase space, which is defined in terms of the kinematics (e.g. p_T and η) of the physics objects, arising from the hard interaction, and their decay products. This implies that the phase space definition is also dependent on the definition of the physics objects and decay products themselves.

Three different definitions of a phase space are relevant for this work: the detector, full and fiducial phase spaces. The definition of each of them is as follows:

- The *detector phase space* (V_{det}), also referred to as *detector level*, is defined by the requirements of the event selection (see Section 4.4).
- The *full phase space* (V_{full}) refers to a phase space which is not limited by any kinematic requirements.
- The *fiducial phase space* (V_{fid}) denotes a phase space region which is constrained by a specific criterion. Any V_{fid} is always a part of V_{full}. The definition of the fiducial phase space in this measurement is thoroughly described in Section 5.5.2.

A schematic representation of the three phase spaces is shown in Figure 5.7.

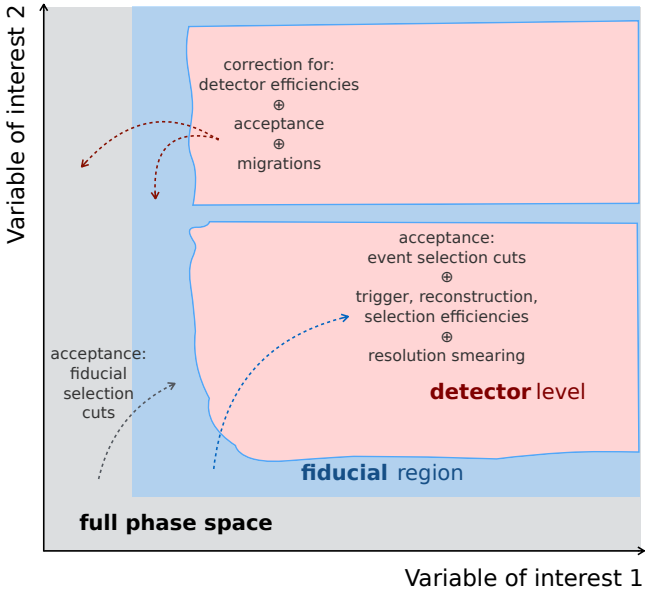

Figure 5.7 Schematic representation of the full, fiducial and detector phase spaces. In this example, the phase spaces are defined according to two arbitrary variables associated with the detector coverage. From [145], modified.

5.4.1 Detector efficiency

Not all $t\bar{t}$ events produced in the V_{det} are reconstructed due to misreconstruction effects affecting the detector response (see Section 5.2.1). In order to quantify those effects, the relevant $t\bar{t}$ simulation is used to evaluate the event reconstruction efficiency $\epsilon_{det}^{rec} = \frac{N^{rec}}{N_{det}^{gen}}$, where

N^{rec} is the number of events reconstructed in the detector and N_{det}^{gen} is the number of events generated in the V_{det}.

The combined efficiency after the event reconstruction and selection (see Chapter 4) is given by $\epsilon_{det}^{rec\&sel} = \epsilon_{det}^{rec} \cdot \epsilon_{det}^{sel} = \frac{N^{rec}}{N_{det}^{gen}} \cdot \frac{N^{rec\&sel}}{N^{rec}} = \frac{N^{rec\&sel}}{N_{det}^{gen}}$, where the $N^{rec\&sel}$ is the total number of reconstructed and selected events. The $\epsilon_{det}^{rec\&sel}$ indicates a fraction of N_{det}^{gen} events which are reconstructed in the detector and are selected afterwards, while the fraction $(1 - \epsilon_{det}^{rec\&sel})$ of events are lost.

In order to estimate a number of data events in the V_{det}, the $N^{rec\&sel}$ data events are corrected for the combined detector efficiency, which is expressed as $N_{det}^{data} = \frac{1}{\epsilon_{det}^{rec\&sel}} \cdot N_{data}^{rec\&sel}$.

5.4.2 Acceptance

An acceptance denotes a fraction of events produced in the full phase space which pass the requirements defining the detector phase space. In the same way, the acceptance can be defined in terms of events produced in the fiducial phase space. The values for both definitions of acceptance are derived using the relevant $t\bar{t}$ simulation as

$$A_{full}^{det} = \frac{N_{det}^{gen}}{N_{full}^{all\ gen}}, \qquad A_{fid}^{det} = \frac{N_{det}^{gen}}{N_{fid}^{gen}}, \tag{5.18}$$

where $N_{full}^{all\ gen}$ is the number of all generated $t\bar{t}$ events, i.e. associated with the V_{full}, and N_{fid}^{gen} is the number of events generated in the V_{fid}. Elsewhere in the text, the acceptance is referred to as A, which can imply either of the A_{full}^{det} and A_{fid}^{det}, depending on a context.

In order to compare the results with other experiments or theoretical predictions, they have to be determined in the same phase space, after correcting for the differences in acceptance between the V_{det} and a chosen reference phase space. The results in full (fiducial) phase space are extrapolated to the chosen reference phase space as $N_{full}^{data} = \frac{1}{A_{full}^{det}} \cdot N_{det}^{data}$ ($N_{fid}^{data} = \frac{1}{A_{fid}^{det}} \cdot N_{det}^{data}$).

5.4.3 Applications of full and fiducial phase spaces

While $\epsilon_{det}^{rec\&sel}$ can be measured directly from the data, the estimation of A relies on the simulation, depending on the theoretical assumptions involved in the implementation of the event generator. Various event generators might predict different kinematics of the physics objects used to define the V_{full} and, consequently, V_{fid}. Thus, the resulting acceptance correction is driven by a choice of the generator.

The measurement results extrapolated to the full phase space can be used to test different theoretical calculations of the fixed-order, which predictions are usually available in the full

phase space. Additionally, the extrapolation allows to probe various corners of the phase space which are experimentally inaccessible by any other means.

From experimental point of view, it is convenient to define the fiducial region in a similarity to the event selection requirements, as much as possible, which leads to V_{fid} being very similar to V_{det}. In this case, the potential extrapolation is minimized. Thus, the use of the fiducial phase space as the reference reduces an impact of extrapolation on measured results, as well as dependency on the theoretical assumptions used in the simulation. Moreover, this quality is expected to result into a reduction of the measurement uncertainties due to theory related sources (see Chapter 6).

5.5 Top quark definitions

The top quark and $t\bar{t}$ differential cross sections are defined according to the use of two distinct definitions of top quarks and top antiquarks. The first one is the *parton level* definition, which corresponds to the top quark objects before their decay and after QCD radiation as are available in the generator chain of the simulation. The so-called *particle level* definition, the top quark proxy is constructed out of the stable particles before their propagation through the detector simulation. This means that both top quark definitions largely rely on the different kinds of generator (true level) information that is used later for the calculation of the differential cross sections, and in particular for the correction of the reconstructed data back to the certain level when using the unfolding procedure. However, the complementary measurements with both definitions lead to more coherent picture of results unveiling the nature of $t\bar{t}$ production mechanisms in greater detail.

In the following, more detailed description of the parton and particle level top quark definitions is provided, as well as the discussion of their main features.

5.5.1 Parton level definition

As was already mentioned, the parton level top quark is the generator-type object which represents the natural top quark in the considered MC simulation and is in a state before its decay and after the QCD radiation. This implies that all types of the potential corrections interesting for the measurement, e.g. due to the initial or final state radiation, are already applied, if allowed or required during the simulation. The measurements aiming at parton level are performed only in bins of top quark and $t\bar{t}$-system observables.

The described above MC-based definition attempts to imitate the model assumptions of the bare top quark that are universally used in different theoretical calculations of fixed order.

In most cases, the differential cross sections defined at parton level are used for the validation of theory models behind the MC or fixed order predictions, and specifically for fitting or extraction of PDF sets and various parameters, e.g. such as α_S, m_{top}.

All parton level differential cross sections are extrapolated to the full phase space, which is done in order to enable the comparisons with modern QCD theory predictions within the SM, as well as models beyond the SM. For the central results of the measurements, the extrapolation is performed using the reference Powheg v2+Pythia8 $t\bar{t}$ simulation, where parton level top quarks are accessed with the Pythia8 status code of the value "62" [146]. Also, this definition is consistent with the recommendations provided by the LHCTopWG working group [147], which are commonly used in the ATLAS [3, 4] and CMS [8] Collaborations.

The parton level measurements usually have larger systematic uncertainties due to the extrapolation relying on certain theoretical assumptions.

5.5.2 Particle level definition

The main idea behind measurements of the top quark kinematics at particle level is a minimized dependence on the theoretical assumptions used in the simulation, i.e. the generator implementation and its tuning. The top quark decay products, in a state of stable particles, fulfill the previously mentioned requirement and can be used for the reconstruction of a particle level proxy corresponding to their parental top quark. The measured results defined at particle level are presented in the fiducial phase space, which provides the potential to reduce the theory dependent uncertainties. In the following, a summary of conventions that are used for the construction of the particle level top quarks and the fiducial phase space is provided.

The particle level top quarks are defined at generator level with a reconstruction procedure aiming at the dilepton decay channel. The final state particles, roughly with a lifetime $> 0.3 \cdot 10^{-10}$ s, are used for the reconstruction. The final state particles are determined from $t\bar{t}$-event records just before their propagation through the detector simulation. The definition of physics objects at particle level is:

Leptons are constructed following the so-called *dressed* definition, which allows to correct the lepton momentum according to their final state photon radiation. Prompt electrons, muons and photons are propagated to the anti-k_t clustering algorithm [127] using the radius parameter $R = 0.1$. Afterwards, the 4-momentum of the electron (muon) particle candidate is determined from the clustered object associated with the respective prompt electron (muon). During the clustering, leptons and photons stemming from the hadron decays are not considered. Otherwise, those non-prompt leptons may lead

Table 5.1 Kinematic selection requirements applied on the particle objects.

Particle object	Selection criteria
Dressed lepton	$p_T > 20$ GeV, $\|\eta\| < 2.4$
Neutrino	no criterion
Jet or b-quark jet	$p_T > 30$ GeV, $\|\eta\| < 2.4$

to the reconstruction of a particle W boson out of the wrong leptonic permutation, i.e. using a lepton which is not arising from the top quark decay, which can introduce the dependency on the occurring underlying event.

Neutrinos are assumed to be detectable, and therefore all required information about the W-boson decay products is known. Only prompt neutrinos originating from the non-hadronic decays are used.

Jets are reconstructed exploiting the anti-k_t jet clustering algorithm with the radius parameter R configured to 0.4. All final state particles in the event are considered during the jet clustering procedure, except for the neutrinos and all particle entries that were already included for a construction of the dressed leptons. In order to identify the b-quark jets, the *ghost* B-hadrons, explained in the following, are injected to the collection of final state particles and then the jet clustering is performed. A ghost B-hadron is assigned for each unstable B-hadron present in the event. This is done by copying all of the original B-hadron properties, but scaling down the momentum component to a negligible value (to the order of $\sim 10^{-20}$). The ghost B-hadron itself is treated as a stable non-decaying B-hadron. In this way, the ghost B-hadron carries the information about the flight direction of the original B-hadron, while not distorting the jets emerging after their clustering. Finally, the ghost B-hadrons are used for the matching of jets to their parental B-hadrons. More detailed explanation of the ghost B-hadron tecnhique can be found in [148].

b-quark jets are identified using the ghost B-hadron tecnhique. A jet is labelled as b-quark jet, if a ghost B-hadron is found among its constituents.

The fiducial phase space is limited by the kinematic requirements on particle leptons and jets, following the event selection requirements imposed at the reconstruction level. This condition allows to minimize the differences between the fiducial and detector level phase spaces, and, thus, reduce the extrapolation in the relevant measurements.

The applied kinematic requirements to particle leptons, neutrinos, jets and b-quark jets are summarized in Table 5.1. Each event is required to have exactly two selected lepton

candidates with the opposite charge, used to define the lepton pair. Jets, and hence the b-jets, are removed from the particle collection, if the spatial separation of a jet against the selected leptons, $\Delta R(\ell, j)$, is less than 0.4. Events are also required to contain at least two neutrino and b-quark jets, as well as the invariant mass of the lepton pair $m_{\ell\bar{\ell}} > 20$ GeV.

At this point, all necessary elements for the reconstruction of the particle W bosons, and subsequently top quarks, are available in any selected event. Each of the two W bosons is defined as the combination of a dressed lepton and the leading or trailing prompt neutrino. The lepton-neutrino permutations that minimize the value of Δm, defined as

$$\Delta m = |m(\ell_1, \nu_1) - m_W| + |m(\ell_2, \nu_2) - m_W|\,, \tag{5.19}$$

are assigned respectively to the particle W^+ or W^-, depending on the sign of the lepton's charge. Here, $m_W = 80.4$ GeV and denotes the mass of the W boson [1, 25], and $m(\ell_i, \nu_i)$ corresponds to the invariant mass of possible combinations of leptons and neutrinos.

In a similar manner, a pair of particle level top quarks is reconstructed out of the possible combinations of a W boson and a b-jet using a similar mass-dependent criterion, which can be expressed as

$$\Delta m = |m(W_1, b_1) - m_t| + |m(W_2, b_2) - m_t|\,, \tag{5.20}$$

where $m(W, b)$ is the invariant mass of the considered combinations and $m_t = 172.5$ GeV is the value of the top quark mass used as the default in the MC simulation as well as in the kinematic reconstruction procedure of the $t\bar{t}$-system. The charge of the reconstructed top quark at particle level is then assigned with respect to a charge of W boson entering the permutation.

It can be concluded, that the fiducial phase space is defined in a way that each event, belonging to it, contains the top-quark pair that is defined at the particle level according to all described above requirements.

The particle level definition used in this analysis follows the convention developed by the CMS Collaboration in a context of the similar measurement [9], based on the full 2015 dataset ($L = 2.1$ fb^{-1}) collected at 13 TeV.

5.5.3 Remarks on the signal definition

Some aspects of the *$t\bar{t}$ signal* definition were already discussed in Section 4.2.

Here, the *$t\bar{t}$ signal* definition is revisited in terms of the notions of the parton or particle level top quarks and fiducial phase space, which were previously explained in this chapter.

The common features behind the $t\bar{t}$ signal definition at the parton and particle levels:

- The *$t\bar{t}$ signal* is the top-quark pair production with the following decays $t \to W^+b$ and $\bar{t} \to W^-\bar{b}$, where each W boson promptly decays into an electron or a muon and the corresponding neutrino.
- The *$t\bar{t}$ other* background consists of all other $t\bar{t}$ event topologies that are not regarded as the signal. It includes the dileptonic decays that occur through a τ lepton, as well as the ℓ+jets and all-hadronic event topologies, which are misreconstructed as the dileptonic ones.
- The total $t\bar{t}$ event sample leads to the same distributions with respect to their normalization and shape (the sum of *$t\bar{t}$ signal* and *$t\bar{t}$ other* remains intact). It implies that only the fraction of *$t\bar{t}$ signal* and *$t\bar{t}$ other* contributions vary, once using either parton or particle level definition, as shown in Figure 5.8.

Only for the particle level definition, the *$t\bar{t}$ other* also includes all dileptonic $t\bar{t}$ events that originate from the region outside of the fiducial phase space, while being registered inside the visible acceptance at detector level due to misreconstruction effects. In this case, those events appear as fakes for the $t\bar{t}$ signal and, thus, are treated as background. Hence, the particle level *$t\bar{t}$ signal* includes solely the events which originally belong to the fiducial phase space and are fully reconstructed in the detector acceptance.

For clarification, the mentioned above fakes are in fact considered as part of the parton level *$t\bar{t}$ signal* (this quality is the consequence of the measurement in the full phase space and cannot be avoided). Exactly this component determines the variation in fractions of *$t\bar{t}$ signal* and *$t\bar{t}$ other* contributions, when performing the differential measurements according to one or another definition.

5.6 Combination of the results

The inclusive cross section measurements are separately performed in each of the three dilepton channels (e^+e^-, $e^\pm\mu^\mp$, $\mu^+\mu^-$) and, thus, are statistically independent. Therefore, the result of the combined inclusive measurement σ_{comb} can be achieved with the calculation of the weighted average out of the central results per individual channel σ_i and their statistical uncertainties $\Delta\sigma_i$ as follows [149]

$$\sigma_{comb} = \sum\nolimits_i \left(\frac{\sigma_i}{\Delta\sigma_i^2}\right) \Big/ \sum\nolimits_i \left(\frac{1}{\Delta\sigma_i^2}\right). \tag{5.21}$$

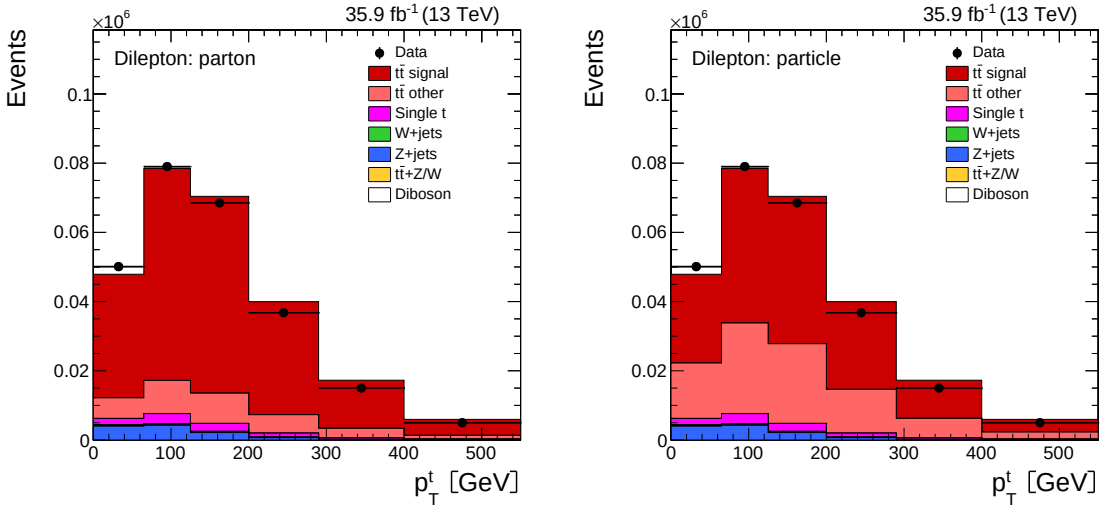

Figure 5.8 The transverse momentum of the reconstructed top quark candidates. The *$t\bar{t}$ signal* and *$t\bar{t}$ other* background contributions correspond to a case when differential measurements are targeting at the parton (left) or particle (right) level. Events fulfill all requirements of the event selection. The distributions are shown for the combined decay channel (the sum of e^+e^-, $\mu^+\mu^-$, and $e^\pm\mu^\mp$ channels) and are rebinned prior to the unfolding.

The statistical uncertainty of σ_{comb} is evaluated as

$$\Delta\sigma_{comb} = 1/\sqrt{\sum_i \frac{1}{\Delta\sigma_i^2}}. \tag{5.22}$$

The combined measurement of the inclusive cross section is repeated for each systematic source, involving the full analysis sequence with all individual channels. The systematic uncertainty per source is estimated out of the difference between the nominal value of σ_{comb} and the corresponding result obtained with a use of varied inputs. The correlations between the arising systematic uncertainties in different dilepton channels are considered via the computation of the weighted average itself.

As mentioned in Section 5.2, all needed inputs for the normalized and absolute differential cross section measurements are combined out of the event samples obtained in individual decay channels (e^+e^-, $e^\pm\mu^\mp$and $\mu^+\mu^-$), after the $t\bar{t}$ event selection and kinematic reconstruction. Afterwards, the differential measurement is conducted in the same way as it would be done in the case of an individual decay channel. The combined measurement is repeated for every systematic variation. The difference between the result per systematic source and the central measured value in each bin is taken as the systematic uncertainty of the measurement. Using this approach, all possible correlations between the individual channels are naturally

accounted during the unfolding procedure. The corresponding combination of response matrices from individual channels helps to reduce the influence of statistical fluctuations, which are dependent on a finite number of generated events in the MC simulation and are expected to mostly affect the low-populated bins. Thus, the aforementioned combination of response matrices leads to a more robust estimation of measurement uncertainties.

Chapter 6

Statistical and Systematic Uncertainties

The individual quantities that enter the calculation of the inclusive and differential $t\bar{t}$ cross sections (see Equations 5.1 and 5.3) are not known perfectly, but are affected by uncertainties that limit the precision of the measurements. Therefore, it is important to estimate these uncertainties in order to know the precision of the measurements and to facilitate comparisons to other experimental results or theoretical models.

Uncertainties can either be of statistical or systematic nature. Statistical uncertainties arise from stochastic fluctuations in the finite-statistics measurements, while systematic uncertainties originate from imperfect modelling of the detector response or from limited knowledge of the underlying theory.

This chapter introduces the different sources of uncertainties that are relevant for the presented measurements in this work. The sources of systematic uncertainties can be categorized into two groups. Experimental uncertainties originate from detector effects and reflect the experimental precision of the measured analysis input (luminosity, measured energies of the jets, etc.). In contrast, theoretical uncertainties originate from assumptions made on the modelling of the $t\bar{t}$ signal and background processes and reflect the precision of the theoretical prediction of the simulation. The total uncertainty on a given measurement is obtained by summing all individual sources of statistical and systematic (both experimental and theoretical modelling) uncertainties.

Section 6.1 introduces the method used to estimate the total uncertainties on the measurements. The statistical and systematic sources of uncertainty are explained in Sections 6.2 and 6.3, respectively, while Section 6.5 describes their propagation to the measured quantities.

A method used to derive the total covariance matrices of uncertainties for all presented differential cross sections is introduced in Section 6.4.

6.1 Uncertainty estimation method

The method used to calculate the total uncertainties affecting the measurements is presented in this section. It follows, to a large extent, the standard methods and recommendations widely used for related top quark measurements within the Top Quark Physics Analysis Group (TOP PAG) of the CMS Collaboration [150]. The uncertainties are generally determined by up and down variations of the corresponding quantity by one standard deviation (assuming Gaussian behaviour [149]).

Evaluation of uncertainties

For an arbitrary observable $\mathcal{X}$, its associated central value X and its total uncertainty Δ_X^{tot}, estimated in the measurement, are written as

$$\mathcal{X} \equiv X \pm \Delta_X^{tot}. \tag{6.1}$$

This formulation implies that the true value characterizing $\mathcal{X}$ belongs to the interval $[X - \Delta_X^{tot}, X + \Delta_X^{tot}]$ with the confidence level of 68%.

The total uncertainty consists of the statistical Δ_X^{stat} and systematic Δ_X^{syst} components, independent from each other. Thus, the total uncertainty is given by the square root of their sum in quadrature $\Delta_X^{tot} = \sqrt{(\Delta_X^{stat})^2 + (\Delta_X^{syst})^2}$.

The measurement of an observable $\mathcal{X}$ can depend on an arbitrary parameter $\mathcal{Y}$, characterized by the value Y. In this case, the central value X depends on Y: $X = f(Y)$. The value Y itself can also be affected by an uncertainty $Y \pm \Delta_Y^{tot}$. The corresponding variations in the value of Y can lead to a change of the central result X

$$X_{up}^Y = f(Y + \Delta_Y^{tot}), \qquad X_{down}^Y = f(Y - \Delta_Y^{tot}). \tag{6.2}$$

For the observable $\mathcal{X}$, the difference between X and varied result X_{up}^Y (X_{down}^Y) denote the up(down)-component of the uncertainty due to source $\mathcal{Y}$

$$\Delta_X^Y(up) = X - X_{up}^Y, \qquad \Delta_X^Y(down) = X - X_{down}^Y. \tag{6.3}$$

In order to reduce an impact of statistical fluctuations, the total uncertainty associated with the source $\mathcal{Y}$ is calculated as a symmetrical average

$$\Delta_X^Y = \frac{1}{2}(\left|\Delta_X^Y(up)\right| + \left|\Delta_X^Y(down)\right|). \tag{6.4}$$

Application in cross section measurements

The central values of the inclusive and differential $t\bar{t}$ production cross section measurements are calculated according to Equation 5.1 and Equations 5.3, 5.5, respectively. For the inclusive measurement the central value is given by $\sigma_{t\bar{t}}^{incl}$, while for the differential measurements it is given by a cross section per bin. In essence, the same ideology is followed for the uncertainty estimation in both kinds of measurements, implying an individual treatment either for one observable $\sigma_{t\bar{t}}^{incl}$ (which can be regarded as a special case of differential measurement with only one bin) or for each differential bin. This involves a determination of statistical and systematic uncertainty components, which is explained in the following.

For each central value, the statistical uncertainty Δ_X^{stat} arises from the data event number. See Section 6.2 for more details.

The systematic uncertainty Δ_X^{syst} is calculated from the variation of every uncertainty source (see Section 6.3). The different uncertainty sources are taken as fully uncorrelated, so their overall contribution to the uncertainty is computed as

$$\Delta_X^{syst} = \sqrt{\sum\nolimits_k \Delta_k^2}, \tag{6.5}$$

where $\Delta_k = \Delta_X^Y$ for a given systematic uncertainty source k.

Each source of systematic uncertainty (efficiency, energy scale etc.) is increased and decreased by its uncertainty corresponding to one standard deviation. However, in some cases of systematic uncertainties due to $t\bar{t}$ modelling, the nominal $t\bar{t}$ simulated sample is replaced by an alternative sample with varied input parameters (e.g. m_t, parton shower scales). The full analysis chain is repeated for each variation. The corresponding differences between the results obtained with varied input and the central value from the standard analysis are quoted as $\Delta_X^Y(up)$ and $\Delta_X^Y(down)$.

In some cases, the uncertainty associated to a specific systematic source is determined by testing different model assumptions (e.g. different colour reconnection schemes) that are expected to affect the corresponding uncertainty in a similar manner. Therefore, the determination of the uncertainty by adding in quadrature the contributions from the different model assumptions (see Equation 6.5) can lead to double-counting of effects. To avoid this, the uncertainty is evaluated by taking the envelope of the effect from the different contributions: the cross section is calculated for each contribution and the corresponding $\Delta_X^Y(up)$ and $\Delta_X^Y(down)$ values are derived; the highest value in the collections of $\Delta_X^Y(up)$ and $\Delta_X^Y(down)$ among all assumptions is assigned as the up-component of the uncertainty, and the lowest value is then assigned as the down-component.

As explained in Chapter 5, the inclusive and absolute differential $t\bar{t}$ production cross section measurements are sensitive to the $t\bar{t}$ production rate. Therefore, these measurements are influenced by both the normalization and shape uncertainty components that affect the data.

In contrast, the normalized differential cross section measurements probe only the shapes of the measured spectra. This leads to a cancellation of the normalization components in the considered systematic uncertainties. Due to this reason, only the uncertainty sources altering distribution shapes are considered as relevant for these measurements.

6.2 Statistical uncertainty

The statistical uncertainty of the event yield N_{data} (see Equations 5.1, 5.3 and 5.5) is given by the Poissonian standard deviation $\sqrt{N_{data}}$. For the inclusive cross section, it is propagated to the final result using simple Gaussian error propagation as approximation. For the normalized and absolute differential cross sections, the statistical uncertainty on N_{data} per bin is propagated with pseudo-experiments (series of 1000) in the TSVD unfolding code [141, 144] (see Section 5.3 for more details).

6.3 Systematic uncertainties

The systematic uncertainties on the presented $t\bar{t}$ production cross section measurements appear due to the two categories of sources. These are the experimental and theoretical sources. Any variations that are associated with them will lead to a change in the central results of the measurements.

6.3.1 Experimental sources

The sources of experimental uncertainty originate from the finite resolution and efficiency of the detectors. In order to account for these detector-related effects and improve the description of the data, the simulated samples are corrected by means of dedicated calibration techniques and efficiency-based corrections, which are usually done by applying correction factors or event weights. As these correction factors, also referred to as scale factors (SF), are measured with finite precision, any variation within their uncertainty can lead to a change in the shape and/or the normalization of the results. All of the variations that are relevant for the experimental uncertainty sources are applied to the simulations of all considered physics processes.

Trigger efficiency

As mentioned in Section 4.4.2, the trigger efficiencies are measured in the data and simulation as a function of $|\eta|$ of the two leading leptons in the event. The MC simulation is corrected to the observed efficiency in data with the dedicated scale factors $SF_{trigger}$.

For the assessment of related uncertainties on $t\bar{t}$ production cross section measurements, two types of the variation in trigger scale factors $SF_{trigger}$ are considered. These variations are independently propagated to the MC simulation.

In the first case, the $SF_{trigger}$ values are varied according to their total uncertainties (see Figure A.1) as they are estimated, which mostly leads to a change in the total event rate with respect to the reference simulation. Only this variation is used for the estimation of the related uncertainty in the inclusive cross section measurements.

The second variation is mainly introduced in order to evaluate the uncertainty on normalized differential cross sections, which are only sensitive to the shapes of measured spectra. This variation attempts to reproduce the potential shape dependence in a change of the trigger scale factors in different detector regions. The $SF_{trigger}$ are antagonistically varied by their uncertainties depending on the $|\eta|$ of both leptons. Two η-regions in the coverage of CMS detector are defined: $\eta_A \equiv 0.0 \leq |\eta| < 1.2$, $\eta_B \equiv 1.2 \leq |\eta| < 2.4$. The up-variation is performed in the following way:

- lepton-1 and lepton-2 in η_A: $SF_{trigger} + 1\Delta_{SF_{trigger}}$,
- lepton-1 in η_A, lepton-2 in η_B: $SF_{trigger} + \frac{1}{2}\Delta_{SF_{trigger}}$,
- lepton-1 in η_B, lepton-2 in η_A: $SF_{trigger} + \frac{1}{2}\Delta_{SF_{trigger}}$,
- lepton-1 and lepton-2 in η_B: $SF_{trigger} - 1\Delta_{SF_{trigger}}$.

Here, the $SF_{trigger}$ denotes the trigger scale factor for the associated bin and the $\Delta_{SF_{trigger}}$ is its total uncertainty. The down-variation is performed in the same manner, but using the coefficients preceding to $\Delta_{SF_{trigger}}$ with the opposite sign.

Both types of the variation in the trigger scale factors are applied to the normalized and absolute differential cross section measurements. Their combined effect is determined with the envelope approach.

Lepton efficiency

The identification and isolation efficiencies for the electron and muon candidate selection are derived as a function of p_T and η (see Section 4.4.3). The simulation is corrected to match the efficiency in data via the scale factors. These scale factors are varied within their total

uncertainties (see Figure A.2). The electron and muon components are treated as correlated in the estimation of the corresponding uncertainty.

Jet energy scale

The reconstructed jet energy scale is corrected in the data and simulation applying the relevant scale factors SF_{JES} (see Section 4.4.4). These scale factors are used to scale the reconstructed jet 4-momenta as a function of p_T, η and flavour.

The uncertainty of the JES correction itself is influenced by the 19 individual systematic sources which are relevant for this analysis [130]. Each of these sources is associated with one or another JES sub-correction.

For the determination of the total JES uncertainty in this analysis, the SF_{JES} are varied up and down within the uncertainties that are provided by the individual systematic sources of the JES correction. The obtained scale factors are used to rescale the reconstructed jet 4-momenta in the simulation. This change in the jet momenta is also propagated to the missing transverse energy vector. The measurement, involving the rescaled vectors, is repeated for all 19 individual systematic sources, and the difference with respect to the reference results is taken as the JES uncertainty due to a particular source. The cumulative uncertainty is calculated as the quadratic sum.

Jet energy resolution

The jets in simulation are smeared according to the jet energy resolution in data, which is performed with the designated scale factors SF_{JER} (see Section 4.4.4). These scale factors are varied up and down within their uncertainties for the different regions in $|\eta|$. The simulation with the respectively smeared jets is used to recompute the analysis results.

Unclustered missing transverse energy

The missing transverse energy is defined in Section 4.4.5. The uncertainty on the E_T^{miss} is factorized into the three components that are related to the jets, leptons and the so-called unclustered missing energy. The component due to jets is considered as a part of the jet energy scale uncertainty, while the uncertainty owing to the lepton energy scale is found to be negligible.

In order to account for the unclustered missing energy, the E_T^{miss} 4-vector is recomputed varying the energy deposits from the charged and neutral hadrons and photons according to their energy resolutions. The obtained 4-vector is propagated through the whole analysis chain for the estimation of the corresponding uncertainty.

Efficiency of b-tagging identification

The determination of the b-tagging efficiency of b-jets, as well as the mistag rates of c-jets or light flavour jets (l-jets; i.e. jets originating from u, d or s quarks or a gluon), in this analysis is discussed in Section 4.4.6. The efficiency and mistag rates (in the following, referred to as ϵ^{MC}_{b-tag}) are computed as a function of the jet p_T and $|\eta|$ using simulated $t\bar{t}$ *signal* events. Each simulated event is assigned a weight accounting for the differences between the b-tagging identification efficiencies in the data and simulation. This weight depends on the ϵ^{MC}_{b-tag} and the corresponding data-to-MC scale factors SF_{b-tag}. The SF_{b-tag} values are quantified as a function of the jet flavour, p_T and $|\eta|$.

The uncertainty due to the efficiency of b-tagging identification is estimated from the variations in the values of SF_{b-tag} per bin, which are subsequently propagated to the corresponding event weights. The variations in the ϵ^{MC}_{b-tag} values are negligible.

The normalization component is assessed varying the SF_{b-tag} values according to their total uncertainties (see Section 4.4.6) in the same direction ("up" or "down") in all p_T and η bins. Only this type of variation is relevant for the inclusive cross section measurements.

The shape uncertainty on the differential cross sections is determined with the antagonistic variations in the SF_{b-tag} values within their uncertainties $\Delta_{SF_{b-tag}}$. The variations are performed individually in terms of the jet p_T and $|\eta|$. For the up-component of the p_T-related uncertainty, the SF_{b-tag} is varied up (down), if it is associated with the jet p_T that is less (greater) than a threshold value $p_T^{threshold} = 65$ GeV. The down-component is evaluated from the opposite variations in the SF_{b-tag} values with respect to the $p_T^{threshold}$, i.e.

- up-component: $SF_{b-tag} - \Delta_{SF_{b-tag}}$ for jet $p_T < p_T^{threshold}$ and $SF_{b-tag} + \Delta_{SF_{b-tag}}$ for jet $p_T > p_T^{threshold}$,
- down-component: $SF_{b-tag} + \Delta_{SF_{b-tag}}$ for jet $p_T < p_T^{threshold}$ and $SF_{b-tag} - \Delta_{SF_{b-tag}}$ for jet $p_T > p_T^{threshold}$.

The variation in terms of jet $|\eta|$ is performed with a similar approach, but using $|\eta^{threshold}| = 0.75$.

The envelope out of the normalization and the resulting p_T and $|\eta|$ shape-dependent b-tagging uncertainties is quoted for the normalized and absolute differential cross section measurements.

The aforementioned scale factor variations depend on the jet flavour. The effect of heavy flavour jets (b-jets and c-jets) is asummed to be correlated, and is determined separately from the variation regarding the l-jets.

Kinematic reconstruction efficiency

The efficiency of the kinematic reconstruction method (see Section 4.6.2) in the simulation is scaled with the $SF_{kin.reco.}$ scale factors to account for the differences with data. The $SF_{kin.reco.}$ values are varied within their uncertainties.

Pile-up

The treatment of pile-up vertices in this analysis is described in Section 4.4.1. The simulation is reweighted to describe the pile-up profile in data. The reference data distribution is determined assuming the total pp inelastic cross section of $\sigma_{pp}^{MB} = 69.2$ mb. In order to estimate the impact from the pile-up modelling on the cross section measurements, the σ_{pp}^{MB} is varied within its uncertainty of ±4.6% [151].

The pile-up variation mostly leads to a change in the event selection efficiency with respect to the nominal simulation. The residual effects of the pile-up vertices on the lepton isolation and jet energy scale are respectively covered by the uncertainties due to the lepton efficiency and jet energy scale.

Luminosity

All simulated samples are normalized according to the total integrated luminosity of the data sample, which is 35.9 fb^{-1}. The uncertainty on the total integrated luminosity is 2.5% [68]. The corresponding uncertainty is assigned to the inclusive and absolute differential $t\bar{t}$ production cross sections. Since this uncertainty mostly affects the normalization of the differential measurement, its effect largely cancels out for the normalized differential cross section results.

Background normalization

The uncertainty due to the normalization of the expected background processes is estimated by the conservative variation of their corresponding contributions within ±30%, following what is done in [8]. The contribution from the $t\bar{t}$ *other* background is not included in this estimation. The uncertainty due to Drell-Yan processes is treated as uncorrelated from all other background sources, since the normalization of Drell-Yan contributions is determined with the data-driven technique (see Section 4.5).

6.3.2 Theoretical sources

Theoretical uncertainties arise from assumptions on the modelling of the underlying theory in the simulation. This affects, for example, the hard scattering process, the model chosen to describe the parton shower, or the particular choice of value of the top quark mass. Different assumptions on the modelling of the events in the simulation can result in differences in the kinematic properties of the final-state particles, resulting in changes in the event selection efficiencies, acceptance corrections or response matrices, which consequently affects the production cross section measurements. The uncertainties on the modelling of $t\bar{t}$ processes ($t\bar{t}$ *signal* and $t\bar{t}$ *other*) are determined by repeating the full analysis replacing the reference POWHEG v2+PYTHIA8 $t\bar{t}$ signal sample by either dedicated simulated samples or via the reweighting of the reference simulation with the relevant weights [152]. The prescription adopted in this analysis follows the most recent recommendations from the CMS TOP PAG [150].

Top quark mass

The reference $t\bar{t}$ sample is generated with a top quark mass value of $m_t = 172.5$ GeV. The top quark mass is known only with a certain precision. The two dedicated simulations with m_t values of 169.5 GeV and 175.5 GeV are used to evaluate the corresponding uncertainty. The obtained uncertainties are linearly scaled down by the factor of 3 to match the ±1 GeV variations in the m_t value. In comparison to the result of the single most precise CMS measurements of the top quark mass [153, 154], this is a rather conservative estimation.

Parton distribution functions

The proton structure is described by the NNPDF3.0 parton distribution functions set [108]. The uncertainty arising due to the PDF is assessed with two separate variations.

For the first one, the nominal value of the strong coupling constant $\alpha_S = 0.118$ is varied by ±0.001, as is provided by the NNPDF3.0 parametrization. This variation is propagated through the whole analysis chain as the event weight for the reference $t\bar{t}$ simulation.

In the second variation, the reference $t\bar{t}$ sample is reweighted according to the 100 error replica sets of NNPDF3.0. The analysis is repeated 100 times using the PDF replicas and the cumulative uncertainty is determined following the NNPDF3.0 prescription.

Matrix element μ_R and μ_F scales

The matrix element calculation of the hard process is governed by the renormalization and factorization scales (μ_R and μ_F, respectively). The uncertainty on the hard process modelling

is estimated by reweighting the POWHEG v2 matrix elements in the reference $t\bar{t}$ simulation. Three individual variations are computed changing the μ_R and μ_F with respect to their nominal values:

- μ_R is fixed, μ_F is varied by the relative factor of 2 ($\frac{1}{2}$) for the up (down) variation,
- μ_F is fixed, μ_R is varied by the relative factor of 2 ($\frac{1}{2}$) for the up (down) variation,
- μ_R and μ_F are simultaneously varied by the relative factor of 2 ($\frac{1}{2}$) for the up (down) variation.

The total uncertainty due to the variations in μ_R and μ_F scales is determined as an envelope out of the three above variations.

Parton shower and hadronization uncertainties

The top quark is a coloured particle that decays into another coloured particle, the b quark (in most cases), and most of the times accompanied by extra jets. The predictions are reliable only after the ME is interfaced to the parton shower (PS). In the simulation of top quark events, ambiguities arise from the PS scales, ME-PS matching, soft non-perturbative QCD effects, colour reconnection, fragmentation, flavour response and hadronization, and semi-leptonic B hadron branching ratio. For most measurements, experimental collaborations usually compare predictions from two different PS simulations, e.g. PYTHIA vs HERWIG. However, in experiments, the jet energy corrections and b-tagging scale factors are typically derived based on a single PS MC simulation. Therefore, comparing two PS simulations would require ad-hoc corrections. In some cases, even after corrections large discrepancies remain leading to overestimated or not-so-well understood PS uncertainties. To get a better insight in the PS uncertainties, the CMS TOP PAG has adopted a new method to calculate parton shower and hadronization uncertainties through variations in a single parton shower simulation (PYTHIA8). These variations cover uncertainties in the modelling of perturbative and non-perturbative QCD effects in a parton shower simulation.

The α_S in parton shower simulation. Dedicated samples are used in order to evaluate an impact of the choice of α_S values in the PYTHIA8 PS simulation. In PYTHIA8, the amount of ISR (FSR) is governed by a parameter α_S^{ISR} (α_S^{FSR}). The default values in the reference $t\bar{t}$ simulation are $\alpha_S^{ISR} = 0.1108$ [105] and $\alpha_S^{FSR} = 0.1365$ [119]. The scale of α_S^{ISR} is varied up and down by the relative factors of 2 and $\frac{1}{2}$, respectively. In a similar way, the scale of α_S^{FSR} is varied by the factors $\sqrt{2}$ and $\frac{1}{\sqrt{2}}$. The interval of these variations is chosen according to the PS tuning uncertainties from [105, 119].

The variations in α_S^{ISR} and α_S^{FSR} are treated as uncorrelated uncertainty sources.

ME-PS matching. The uncertainty on the matching of the matrix element to parton shower calculations is estimated with the dedicated POWHEG v2+PYTHIA8 simulations, where the h_{damp} parameter is varied according to $h_{damp} = 1.581^{+0.658}_{-0.585} m_t$ [105].

Underlying event tune. Several parameters that govern the underlying event modelling of the PS tune CUETP8M2T4 in PYTHIA8 are simultaneously varied up and down within their uncertainties. The three configuration handles "MultipartonInteractions:pT0Ref", "MultipartonInteractions:expPow" and "ColourReconnection:range" are varied according to the up/down intervals $2.20^{-0.07}_{+0.07}$, $1.61^{+0.10}_{-0.05}$ and $6.59^{-0.09}_{+2.12}$, respectively, as are determined in [105].

Colour reconnection. The default colour reconnection (CR) model in the PYTHIA8 simulation is the MPI-based scheme (see Section 3.6), which comes with two possibilities for the treatment of resonant systems [97].

The first approach assumes that the lifetime of the top quark is long enough to prevent the CR of its decay products with other partons in the event. This implies that the CR occurs before top quarks decay. Thus, only top quarks are considered in the CR, and the CR among the top quark decay products is not performed. The reference $t\bar{t}$ sample is simulated according to this assumption.

The second approach for the MPI-based scheme allows the early resonance decays (ERD) of the top quarks and corresponding W-bosons. These decays are assumed to happen before the CR starts. Thus, in contrast to the first approach, the top quark decay products also participate in the CR process.

Two more CR schemes are tested in this analysis, the so-called gluon-move and QCD-inspired schemes.

The gluon-move scheme [97] allows the reconnection of the top quark decay products with the rest of the event. The CR starts and proceeds as in the default MPI-based scheme, where the ERD are switched off, up to the point of top quark decays. Then, the top quarks are allowed to decay with the potentially radiating products. The resulting partons associated with the gluons are used for the further CR. In this scheme, the gluons are allowed to participate in the reconnection multiple times. They can be also moved to different locations, which eventually can lead to the reduction of the total length of colour strings.

The QCD-inspired scheme [99, 100] relies on the full QCD colour calculation in the colour reconnection process. It also performs the minimization of the potential colour

string length. In this measurement, the QCD-inspired scheme with enabled ERD is considered.

Dedicated $t\bar{t}$ simulations are used to assess the variations due to each alternative CR scheme. The envelope of the three variations is quoted as the uncertainty due to CR.

The b-fragmentation. The b-fragmentation is defined as the momentum transfer from the b quark to the B-hadron. In this analysis, the default b-fragmentation function that is used in the reference Powheg v2+Pythia8 $t\bar{t}$ simulation is of the Bowler-Lund type [155, 119, 156] with the Bowler-Lund parameter set to 0.855 [105]. The effect from the up(down)-variation in the Bowler-Lund parameter by +0.224 (−0.157) is assessed by the reweighting of the transfer function $x_b = p_T^B / p_T^{b-jet}$ at the generator level in the reference $t\bar{t}$ sample. This uncertainty interval follows the measurement [157, 11].

As an alternative to the Bowler-Lund fragmentation function, the function of Peterson [155, 158] is used and the reference $t\bar{t}$ simulation is accordingly reweighted.

The envelope out of the two aforementioned variations is constructed for the total uncertainty due to the b-fragmentation model.

B semi-leptonic decay branching ratio. The detector energy response to b-jets depends on a multiplicity of the undetectable neutrinos, which stem from the semi-leptonic B-hadron decays $B \to \ell\nu$. The rate of these decays is directly connected with the corresponding branching ratio (BR). The default value for the semi-leptonic BR in Pythia8 is varied up (down) by the uncertainty given in [1, 159]. The effect of these variations is determined using the accordingly reweighted reference $t\bar{t}$ sample.

Decay branching ratio of the signal process

The branching ratios of prompt $t\bar{t}$ decays into the e^+e^-, $e^\pm\mu^\mp$ and $\mu^+\mu^-$ final states are used to extrapolate the cross section results to full phase space. These BR respectively are 0.01147, 0.02277 and 0.01130, while their combination is 0.04554 [1, 25]. The BR uncertainty of 1.5% [1, 25] is propagated to the measured cross sections. This uncertainty cancels out for the normalized differential cross sections.

6.4 Covariance and correlation matrices

Relations among n bins of a particular differential measurement are studied in terms of the covariance and correlation matrices, which are symmetric matrices of a size $n \times n$, denoted as **Cov** and **Corr**, respectively. The ij-element of the **Cov** (**Corr**) matrix is given

by the covariance (correlation) coefficient between i^{th} and j^{th} bins of the same differential measurement. The covariance (correlation) coefficient between two bins is an estimate of how much (strongly) results in these bins vary together (are related).

The method which is used to determine matrices of each type in the context of differential measurements, presented in this work, is discussed in the following, as well as several alternative methods serving as a baseline.

Method I

The total covariance matrix is given by

$$\mathbf{Cov} = \mathbf{Cov}^{stat} + \mathbf{Cov}^{syst}, \tag{6.6}$$

where $\mathbf{Cov}^{stat}$ and $\mathbf{Cov}^{syst}$ are the covariance matrices that account for statistical and systematic uncertainties of the corresponding differential measurement, respectively. The statistical covariance matrix $\mathbf{Cov}^{stat}$, introduced in Section 5.3, is obtained directly from the unfolding procedure. Following the method from [139], which is well-suited for the symmetrized uncertainties, elements of the systematic covariance matrix $\mathbf{Cov}^{syst}$ can be calculated as

$$\mathbf{Cov}^{syst}_{ij} = \sum_{k} C_{i,k} C_{j,k} + \frac{1}{2}\left(\sum_{k'} C^{+}_{i,k'} C^{+}_{j,k'} + \sum_{k'} C^{-}_{i,k'} C^{-}_{j,k'} \right), \; 1 \leq i \leq n, \; 1 \leq j \leq n, \tag{6.7}$$

where $C_{i,k}$ ($C_{i,k'}$) denotes the absolute systematic uncertainty due to source k (k') in i^{th} bin. Here, sources k imply sources which are associated with a variation in a single direction. Sources k' correspond to sources which lead to the positive and negative variations, resulting into the up and down components of the uncertainty, denoted as $C^{+}_{i,k'}$ and $C^{-}_{j,k'}$, respectively (using notations from Section 6.1: $C_k \equiv \Delta^k_X$, $up \equiv +$ and $down \equiv -$). The indices i and j run over each of the n bins that are differentially measured.

The elements of covariance and correlation matrices are connected as

$$\mathbf{Corr}_{ij} = \frac{\mathbf{Cov}_{ij}}{\sqrt{\mathbf{Cov}_{ii}\mathbf{Cov}_{jj}}}. \tag{6.8}$$

Typically, the straightforward approach is a calculation of the covariance matrix at first.

By definition, the normalized differential cross sections sum up to unity, i.e. $\sum_i^n \sigma_i = 1$, where a measured cross section per bin σ_i is corrected for a bin width. This means that a result in one bin of normalized differential cross sections is a linear combination of results in other bins, owing to the normalization. In this case, the determinant of the covariance matrix is equal to 0. In order to preserve this quality for the normalized cross sections, the

uncertainty based on a single variation due to source k is required to satisfy $\sum_i^n(\sigma_i + C_i^k) = 1$ and, hence, $\sum_i^n C_i^k = 0$. In this measurement, uncertainties due to several systematic sources are calculated using the envelope-based approach (see Section 6.1). An uncertainty envelope, by construction, provides normalized differential cross sections which do not sum up to unity, i.e. $\sum_i^n C_i^k \neq 0$. In addition, during the construction of an envelope, the information about bin-to-bin correlations in terms of individual systematic subsources, used to determine the envelope, is lost. Therefore, a robust definition of the $\mathbf{Cov}^{syst}$ according to Equation 6.7 is not possible with a direct use of the envelope-based uncertainties, since they would be included into the sum running over k sources.

Method II

As an alternative approach, the systematic covariance matrix can be calculated using all individual systematic sources. This implies that systematic uncertainties due to subsources defining an envelope are treated individually as ordinary sources. In this way, elements of $\mathbf{Cov}^{syst}$ can be estimated directly following Equation 6.7, preserving the quality $|\mathbf{Cov}^{syst}| = 0$ for normalized measurements and considering all possible correlations among bins for each source. However, as in case of *Method I*, this approach is not well-suited for the measurements quoting envelope-based uncertainties. As commonly known, a covariance of a random variable with itself is a variance of this variable. Thus, the diagonal elements of $\mathbf{Cov}^{syst}$ are connected with the total systematic uncertainties in corresponding bins, i.e. $C_i^{syst} = \sqrt{\mathbf{Cov}_{ii}^{syst}}$. This equality is not fulfilled when comparing the diagonal elements, determined following the just-described method, with the total systematic uncertainties of measurements. The reason is that an additive treatment of all systematic sources does not result into the covariance matrix which normalization is compatible with a magnitude of envelope-based uncertainties.

Method III

The method, described in the following, was developed in the context of this work specifically for the use alongside envelope-based uncertainties.

Instead of computing the $\mathbf{Cov}^{syst}$ directly, the systematic correlation matrix $\mathbf{Corr}^{syst}$ is computed at first, deducing Equations 6.7 and 6.8. As done in *Method II*, the sums arising from Equation 6.7 are allowed to run over all individual systematic sources, including subsources defining the envelopes. In this way, the systematic correlation matrix keeps the information about all possible correlations among bins for each source and satisfies the criterion $|\mathbf{Corr}^{syst}| = 0$ in the case of normalized measurements. Afterwards, the elements of

$\mathbf{Cov}^{syst}$ are calculated from the $\mathbf{Corr}^{syst}$. For doing so, the $\mathbf{Corr}^{syst}$ is normalized to the total systematic uncertainties per bin of the measurement C_i^{syst}, those that are obtained exploiting the original envelope-based approach

$$\mathbf{Cov}_{ij}^{syst} = C_i^{syst} C_j^{syst} \mathbf{Corr}_{ij}^{syst},\ 1 \leq i \leq n,\ 1 \leq j \leq n. \tag{6.9}$$

Since Equation 6.9 operates with the absolute systematic errors of the measurement, the obtained $\mathbf{Cov}^{syst}$ is given in units that are compatible with a magnitude of measured differential cross sections, as well as $C_i^{syst} = \sqrt{\mathbf{Cov}_{ii}^{syst}}$ is fulfilled. Finally, the total covariance matrix of the measurement can be derived according to Equation 6.6, where the $\mathbf{Cov}^{stat}$ satisfies the necessary criteria by construction. The total correlation matrix is computed via the combination of the corresponding correlation matrices accounting for statistical and systematic components.

The method described above is used to compute all covariance and correlation matrices for the differential measurements that are presented. As example, Figure 6.1 shows the total covariance and correlation matrices for the normalized differential $t\bar{t}$ production cross sections measured at parton level as a function of the p_T^t. The matrix grid is given in the order of measurement bins, indicated in Table B.1. The matrices for all other measurements are summarized in Appendix B.

6.5 Summary of uncertainties

The breakdown of the relative uncertainties for the inclusive $t\bar{t}$ production cross section measurement is presented in Table 6.1. In the combined dilepton channel, the total uncertainty of the measurement is approximately 6.8%. The statistical uncertainty (0.2%) is negligible with respect to the systematic one (6.8%). The contribution from experimental sources (5.7%) is larger than from theoretical sources (3.7%). The dominant experimental sources are due to uncertainties on the lepton efficiency, jet energy scale and luminosity. The dominant theoretical sources are due to variations in the α_S^{FSR}, b-fragmentation and branching ratio of the signal process. The most precise result among individual channels is obtained in the $e^{\pm}\mu^{\mp}$ channel. A better precision in the $e^{\pm}\mu^{\mp}$ channel is mostly caused by a reduction of uncertainties due to unclustered E_T^{miss} and DY normalization. The $e^{\pm}\mu^{\mp}$ channel is less sensitive to these sources owing to a small rate of DY processes and omission of the selection requirement on E_T^{miss}.

Total uncertainties on the measured differential cross sections are between 1% - 24% (see Tables B.1-B.98), depending on the bin and measurement.

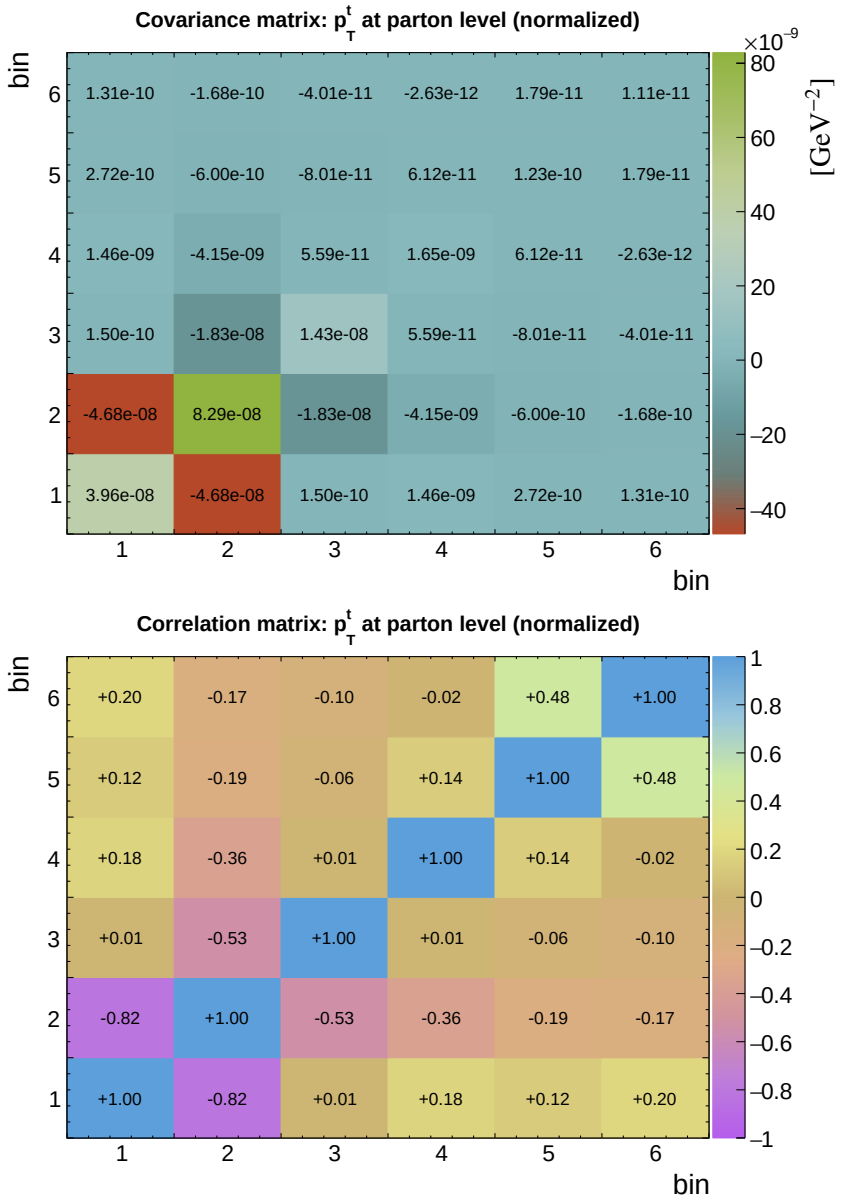

Figure 6.1 The total covariance and correlation matrices for the normalized differential $t\bar{t}$ production cross sections measured as a function of the p_T^t. The measurement is performed at parton level in the full phase space. The matrix grid is given in the order of measurement bins, indicated in Table B.1.

Table 6.1 The summary of uncertainties for the measurement of the inclusive $t\bar{t}$ production cross section. Uncertainties are given in percentages as the relative variations with respect to the central results. A breakdown of the systematic uncertainty into its components is also presented.

	Uncertainty (%)			
Channel	e^+e^-	$\mu^+\mu^-$	$e^\pm\mu^\mp$	*combined*
Experimental sources				
Trigger efficiency	0.9	0.8	0.7	0.7
Lepton efficiency	5.2	2.9	3.6	3.6
Jet energy scale sources	3.3	3.4	2.6	2.9
Jet energy resolution	0.1	< 0.1	0.1	0.1
Unclustered E_T^{miss}	1.3	1.3	0.1	0.4
b-tagging: heavy flavours	0.7	0.7	0.6	0.6
b-tagging: light flavours	0.7	0.8	0.2	0.4
Kinematic reconstruction	0.3	0.2	0.1	0.2
Pile-up	0.1	0.8	0.4	0.1
Luminosity	2.5	2.5	2.5	2.5
Background normalization	1.4	1.3	1.3	1.3
Drell-Yan normalization	3.1	3.4	0.3	1.4
Theoretical sources				
Top quark mass	1.1	1.0	0.9	0.9
PDF α_S	0.2	0.2	0.2	0.2
PDF replicas	0.5	0.5	0.5	0.5
ME μ_R and μ_F scales	0.2	0.1	0.3	0.2
PS α_S^{ISR}	0.1	0.3	0.3	0.3
PS α_S^{FSR}	2.9	2.9	2.8	2.9
ME-PS matching	0.5	0.5	0.4	0.4
Underlying event tune	0.8	0.6	0.3	0.3
Colour reconnection	0.8	0.4	0.4	0.4
b-fragmentation	1.3	1.2	1.2	1.2
B semi-leptonic BR	0.1	0.1	0.1	0.1
Signal process BR	1.5	1.5	1.5	1.5
Statistical uncertainty	0.6	0.4	0.3	0.2
Systematic uncertainty	8.6	7.6	6.5	6.8

As mentioned in Section 5.5, the differential cross sections measured at parton level are extrapolated to the full phase space. The extrapolated measurements are, therefore, also affected by differences in acceptances from the theoretical assumptions used to estimate the various modelling uncertainties, which can lead to larger uncertainties in the results. The differential cross sections measured at particle level are presented in the fiducial phase, which limits the extrapolation due to the similarity between the fiducial and detector phase spaces. Thus, the theory-related uncertainties of particle level cross sections are expected to be typically lower with respect to uncertainties of corresponding parton level cross sections. However, uncertainties in some bins of both measurement types are found to be very similar in magnitude. The same behaviour is also observed in other measurements of both cross section types at 13 TeV [9–11]. This behaviour can be explained by the shape of distributions in the fiducial region, as well as by remaining differences in the definition of the fiducial phase space with respect to the detector level phase space. In addition, the fiducial phase space is defined using a subset of the events that are associated with the full phase space, which reduces the statistical power of particle level measurements in low-populated bins in comparison to parton level ones, i.e. the response matrices used for measurements at particle level are more affected by statistical fluctuations. This might also affect the resulting uncertainties of particle level measurements.

As an example, Figure 6.2 shows the uncertainty per bin of the normalized differential $t\bar{t}$ production cross sections measured at parton level as a function of the transverse momentum of the top quark p_T^t. In the left figure, the relative uncertainties are given separately for statistical, experimental and theoretical sources, as well as for their total. The right figure demonstrates the squared sum of uncertainties due to all systematic sources which are considered (except of sources due to luminosity and branching ratio of the signal process, which are flat and therefore cancel out for the normalized results).

The per-bin uncertainties for all other differential cross sections measured in this work are presented in Figures C.1-C.25. Figures C.1-C.15 show uncertainties for normalized and absolute differential cross sections measured at parton and particle levels (4 types of measurements: normalized-parton, normalized-particle, absolute-parton and absolute-particle). As described in Appendix C, each figure corresponds to a measurement performed in bins of a certain observable which is related either to the top quarks or $t\bar{t}$-system. Figures C.16-C.25 show the same, but only for the particle level differential cross sections measured as a function of observables associated with the top quark decay products (2 types of measurements: normalized-particle and absolute-particle).

All measurements are typically dominated by the uncertainties due to experimental sources, with few exceptions that are described in the following. Largest uncertainties are

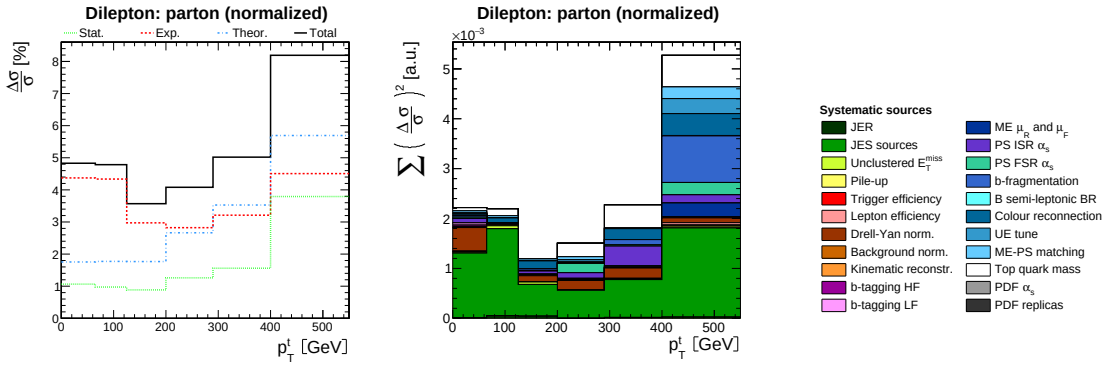

Figure 6.2 A summary of the uncertainties for the normalized differential $t\bar{t}$ production cross sections measured as a function of the p_T^t. The measurement is performed at parton level in the full phase space. **Left:** the relative uncertainties are given separately for statistical, experimental and theoretical sources, as well as for their total. **Right:** the breakdown of uncertainties due to different systematic sources (except of sources due to luminosity and branching ratio of the signal process) is given as the squared sum of uncertainties.

usually observed at the tails of the distributions, especially at higher values of transverse momenta (p_T) and invariant masses (m). The normalized differential cross sections have typically slightly larger experimental uncertainties than theoretical uncertainties. For the absolute measurements, the dominance of the experimental uncertainties over the theoretical ones is even more pronounced, especially for y and η observables. This kind of an increase happens since the rate components of uncertainties do not cancel out as a result of the omitted normalization of the cross sections. The notable exception are the uncertainties due to jet energy scale sources and unclustered E_T^{miss}. These sources involve variations in the 4-momenta of relevant physics objects, i.e. jets and $\vec{E}_T^{miss}$, respectively. Hence, the event content of a selected sample can be altered owing to selection requirements imposed on jets and E_T^{miss}.

However, the uncertainties due to experimental and theoretical sources are of the same order for the normalized cross sections measured as a function of the top quark p_T, as well as p_T and m of the $t\bar{t}$-system. The lower (higher) values of p_T and m are more sensitive to experimental (theoretical) sources for both absolute and normalized cross sections. These effects are expected, since the top quarks, as well as the $t\bar{t}$-system, are more dependent on theoretical assumptions in the simulation than their decay products.

The statistical uncertainties are lower than systematic uncertainties in all bins of measurements. Usually, statistical uncertainties do not exceed the uncertainties associated either with experimental or theoretical sources. An exception are all normalized measurements performed in bins of y and η, as well as measurements probing observables related to leptons. In these cases, the size of the statistical and systematic uncertainties per bin are similar, due

to a good resolution of these observables. Absolute differential cross sections are mostly not affected by the statistical component of uncertainties.

The most dominant systematic sources for differential cross sections are similar to those observed in the case of the inclusive measurement: the uncertainties on JES and parton shower. In addition, absolute differential cross sections are sensitive to the uncertainty on lepton efficiencies and luminosity.

Chapter 7

Results

The differential cross sections for the top-quark pair production have been measured at the LHC in pp collisions at $\sqrt{s} = 7$ and 8 TeV [3, 4, 7, 8].

This work presents the first measurements of the differential $t\bar{t}$ production cross sections performed at $\sqrt{s} = 13$ TeV in the dilepton final states, i.e. using events with two oppositely charged leptons (e^+e^-, $e^\pm\mu^\mp$, $\mu^+\mu^-$). In the context of this work, three separate measurements were performed using data collected by the CMS experiment in pp collisions at the LHC in 2015 and 2016. These three measurements are briefly introduced in the following.

The data collection at the new energy frontier of $\sqrt{s} = 13$ TeV provided an exciting opportunity to discover new-physics phenomena beyond the standard model and, alternatively, to confirm the accumulated knowledge about the SM. For this reason, as first step of this work (see Section 7.1.1), the measurements of the normalized differential $t\bar{t}$ production cross sections were performed using the early (rather small) dataset collected in 2015 corresponding to the integrated luminosity of 42 pb^{-1} [12]. Measurements were performed as a function of only few observables related to top quarks and the $t\bar{t}$-system, as well as a function of the jet multiplicity in the event. No significant deviations from the SM predictions were revealed.

As second step of this work (see Section 7.1.2), similar measurements of the normalized differential $t\bar{t}$ production cross sections were performed with the use of the complete 2015 dataset of 2.2 fb^{-1} [13]. The larger data sample allowed the improvement in the precision of results. Moreover, these measurements confirmed observations in the context of $t\bar{t}$ production that were obtained in similar measurements performed at 7 and 8 TeV. After the measurements based on 2015 data, the analysis strategy was reconsidered, leading to the measurements described below.

As main results and third step of this work (see Section 7.3), the differential cross sections for the $t\bar{t}$ production are measured using the data sample with the integrated luminosity of 35.9 fb^{-1} collected in 2016. Here, 34 observables related to top quarks, $t\bar{t}$-system and their

decay products are probed, providing unprecedented amount of detail. For the first time in the dilepton channel, four (two) different types of measurements are performed for each observable, where possible: normalized and absolute differential cross sections presented at the parton and particle levels, resulting in 98 unique measurements detailed in Section 7.3. The particle level results have typically better precision with respect to those from the parton level. The measurements of absolute differential cross sections allow the study of the rate and shape components of measured spectra.

The differential cross sections obtained using 2016 data are complemented with the measurement of the inclusive $t\bar{t}$ production cross section (see Section 7.2), using the same data sample. Moreover, these differential results are used to extract the $t\bar{t}$ and leptonic charge asymmetries, for the first time at 13 TeV (see Section 7.4). Additionally, they are used to constrain the top quark chromomagnetic dipole moment in an effective field theory (see Section 7.5).

7.1 Differential $t\bar{t}$ production cross sections with 2015 data

This section summarizes the measurements of the normalized differential $t\bar{t}$ production cross sections performed using the data sample collected by the CMS experiment at 13 TeV in 2015. These measurements follow to some extent the corresponding measurement performed at 8 TeV [8], while differing in several aspects such as simulation setups, relevant calibrations for the 13 TeV data, etc. Also, these measurements rely on the different event selection, fiducial phase space and particle level definitions with respect to the ones described in this work, aiming at the analysis of the 2016 data. All the analysis components for the 2015 measurements are described in [12, 13].

7.1.1 Results with the early data sample of L = 42 pb^{-1}

As presented in [12], the normalized differential $t\bar{t}$ production cross sections are measured using the dataset of $L = 42$ pb^{-1} (in the following, this measurement is referred to as early measurement). The presented results are the first measurements of the differential $t\bar{t}$ production cross sections at the centre-of-mass energy of 13 TeV.

The measurements are performed as a function of the transverse momentum (p_T^t) and the absolute rapidity ($|y_t|$) of the top quarks and antiquarks, as well as a function of the transverse momentum ($p_T^{t\bar{t}}$), the absolute rapidity ($|y_{t\bar{t}}|$) and the invariant mass ($m_{t\bar{t}}$) of the $t\bar{t}$-system (these notations are applicable only to the current section and Section 7.1.2). These results are extrapolated to the full phase space and are presented at the parton level. An additional

measurement is performed at the particle level as a function of the jet multiplicity in the event and presented in the fiducial phase space. The measured data are compared to the SM predictions from the POWHEG v2 generator (here, referred to as Powheg) interfaced either to PYTHIA8 or HERWIG++, and the MADGRAPH5_AMC@NLO generator with either NLO (referred to as aMC@NLO) or LO (referred to as MadGraph) matrix elements interfaced only to PYTHIA8. Here, only few most interesting results are highlighted.

As example, Figure 7.1 shows the results obtained as a function of p_T^t and $m_{t\bar{t}}$. A good agreement is observed between the data and MC predictions within large uncertainties, dominated by the statistical component. Given the relatively low integrated luminosity of the data sample, no statement can be made regarding the observation of any trends in the data-to-MC agreement in p_T^t, compared to what was found in [7, 8]. There is no evidence of the large excess/deficit in data across all bins of the $m_{t\bar{t}}$, which could hint the occurence of a beyond-SM scenario including heavy resonance states interfering with the $t\bar{t}$ production.

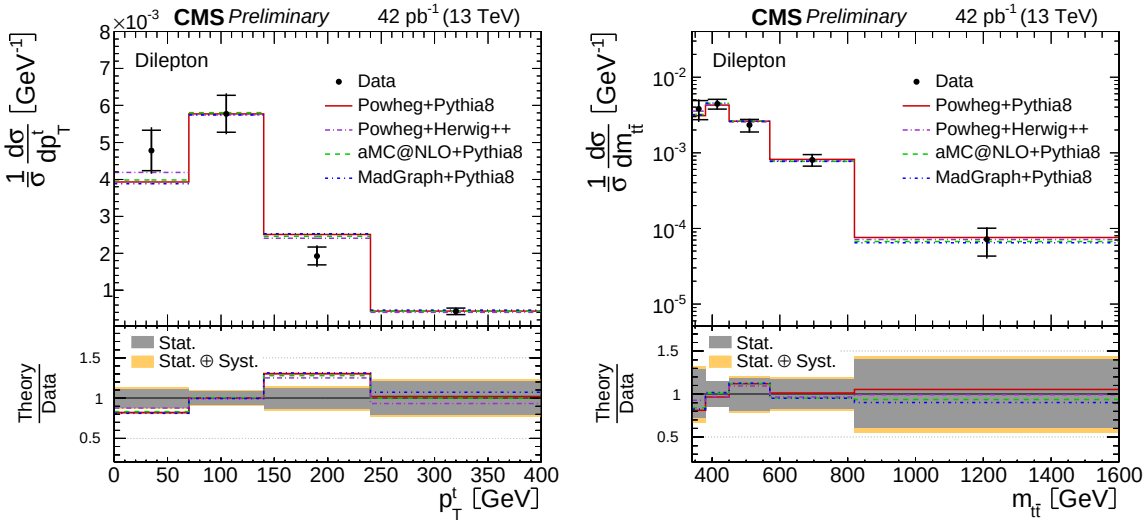

Figure 7.1 The normalized differential $t\bar{t}$ production cross sections measured (using the early 2015 dataset of $L = 42$ pb^{-1}) as a function of the transverse momentum of the top quarks and antiquarks (left) and the invariant mass of the $t\bar{t}$-system (right). The results are presented at the parton level in the full phase space. The measured data are confronted with the SM Monte Carlo predictions described in Section 7.1.1. The inner error bars show the particularly large statistical uncertainty, the outer error bars show a combination of the statistical and systematic uncertainties. Results published in [12].

One of the biggest challenges of the early measurement presented above is the small number of events per differential bins. In total, only 306 data events in the combined channel are observed. Thus, large statistical fluctuations per bin can potentially influence the unfolded result. Therefore, the unfolding method is tested to see whether it is sensitive to the true

shape of signal spectra and can provide a reasonable estimate of the statistical uncertainty due to the limited number of data events. This was successfully demonstrated using a dedicated closure test verifying the statistical properties of the unfolding method [142]. The results of this closure test are briefly summarized in Section D.1.

In view of the new measurements at 13 TeV, the Top Quark Physics Analysis Group (TOP PAG) [150] of the CMS Collaboration tested different MC setups as reference $t\bar{t}$ simulation for Run-II. The potential candidates were the possible combinations between Powheg v2 and MadGraph5_aMC@NLO (being the NLO ME generators) interfaced either to Pythia8 or Herwig++ (at that time, being the newest representatives of generators for the parton shower and hadronization). The MC setups planned to be used for analyses at 13 TeV were validated performing comparisons of their 8 TeV predictions to the 8 TeV data. The MC validation studies, conducted in the context of the early measurement, motivated the choice of the Powheg v2+Pythia8 by the TOP PAG as reference setup for Run-II, providing the best balance between the modelling of 8 TeV data and the required computation time.

7.1.2 Results with the complete data sample of L = 2.2 fb^{-1}

The measurement described in Section 7.1.1 was repeated using the complete data sample recorded in 2015 corresponding to $L = 2.2$ fb^{-1} [13], updating the relevant analysis components. The normalized differential $t\bar{t}$ production cross sections are measured as a function of the same observables (here, rapidities are measured in the negative and positive directions) as in the early measurement, using same definitions of the parton and particle levels. In addition to comparisons to MC predictions as done in the early measurement, the results are compared to several QCD calculations at beyond-NLO accuracy, depending on their availability. In the following, descriptions of tested calculations are given as summarized by the CMS Collaboration (2016) in [13] (p. 9-10):

- **"**An approximate next-to-next-to-leading-order (NNLO) calculation [160] (referred to as approx. NNLO) based on QCD threshold expansions beyond the leading logarithmic approximation using the CT14nnlo [161] PDF set. The top quark mass value is assumed to be $m_t = 172.5$ GeV, and the factorization and renormalization scales are fixed to the m_t value.

- An approximate next-to-next-to-next-to-leading-order calculation [53] (referred to as approx. N^{3}LO) based on the resummation of soft-gluon contributions in the double-differential cross section at next-to-next-to-leading-logarithm (NNLL) accuracy in the moment-space approach. The MSTW2008nnlo PDF set [162] is used and the top quark

mass value is $m_t = 172.5$ GeV. The renormalization and factorization scales are set to the m_t value.

- A full NNLO calculation [51] (referred to as NNLO) using the NNPDF3.0 PDF set, $m_t = 173.3$ GeV, and dynamic (i.e., kinematics-dependent) renormalization and factorization scales ($m_T/2$ for p_T^t, where $m_T = \sqrt{m_t^2 + (p_T^t)^2}$ [†], and $H_T/4$ [‡] for y_t, $p_T^{t\bar{t}}$, $y_{t\bar{t}}$, and $m_{t\bar{t}}$).

- An NLO+NNLL′ prediction [164] (referred to as NLO+NNLL′) that includes the simultaneous resummation of soft and small-mass logarithms to NNLL′ accuracy, matched with both the standard soft-gluon resummation at NNLL accuracy and the fixed-order calculation at NLO accuracy. These corrections are expected to affect the high-energy tails of the $t\bar{t}$ differential distributions. The calculation is performed using the MTSW2008nnlo PDF set[††], $m_t = 173.2$ GeV, and dynamic renormalization and factorization scales (m_T for p_T^t and $m_{t\bar{t}}/2$ for $m_{t\bar{t}}$).

All the calculations include an uncertainty on the change of the cross section due to variation of the renormalization and factorization scales. Moreover, the approx. NNLO calculation also includes uncertainties on the PDF, the choice of α_S, and the uncertainty on the variation of m_t by ± 1 GeV, which are all added in quadrature to the scale uncertainty.**"**

The measured results compared to fixed order calculations, as well as to Powheg v2+Pythia8 (here, using CUETP8M1), are shown in Figures 7.2 and 7.3. A good agreement is observed between the data and all predictions. As observed at 7 and 8 TeV [7, 8], the top quark p_T spectrum in data tends to be lower than all predictions at the higher values, confirming this effect at 13 TeV. For this spectrum, the best modelling of data (according to visual comparison) is provided by the NLO+NNLL′ fixed order calculation. The $p_T^{t\bar{t}}$ distribution is well-described by the full NNLO calculation. For measurements performed as a function of $m_{t\bar{t}}$, y_t and $y_{t\bar{t}}$, the relevent predictions demonstrate an agreement with the data within the uncertainties of results. The comparison of measured results to all other MC predictions considered can be found in [13].

The measurement presented above serves as cross-check analysis for the recently published CMS measurement in the dilepton channel at 13 TeV [9], based on the complete 2015 dataset.

[†] for the top antiquark, $m_T = \sqrt{m_t^2 + (p_T^{\bar{t}})^2}$, see [163].

[‡] $H_T = \sqrt{m_t^2 + (p_T^t)^2} + \sqrt{m_t^2 + (p_T^{\bar{t}})^2}$, see [163].

[††] typo: MSTW2008nnlo.

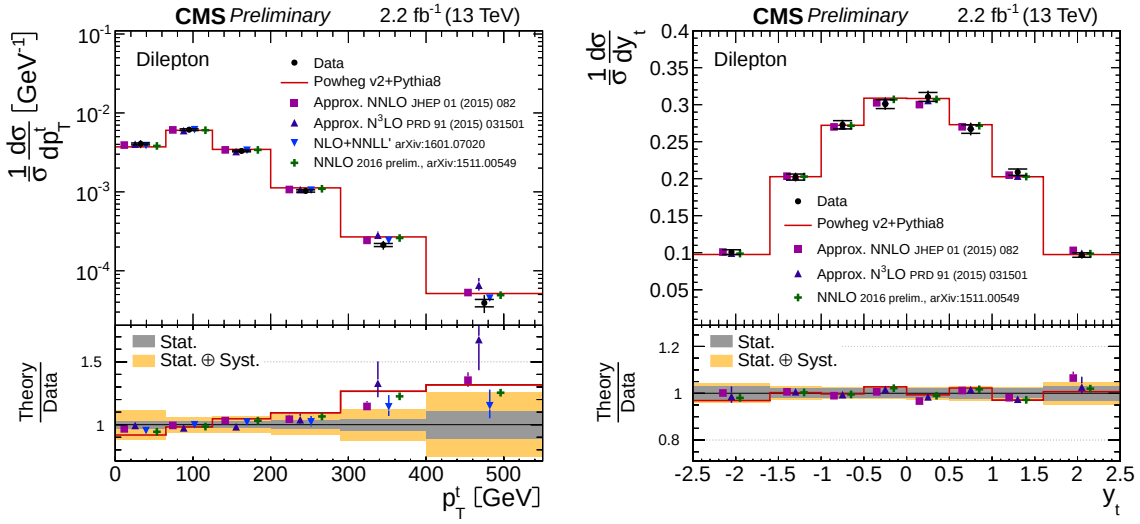

Figure 7.2 The normalized differential $t\bar{t}$ production cross sections measured (using the complete 2015 dataset of $L = 2.2$ fb^{-1}) as a function of the transverse momentum (left) and the rapidity (right) of the top quarks and antiquarks. The results are presented at the parton level in the full phase space. The measured data are confronted with the Monte Carlo and fixed order SM predictions described in Section 7.1.2. The inner error bars show the statistical uncertainty, the outer error bars show a combination of the statistical and systematic uncertainties. Results published in [13].

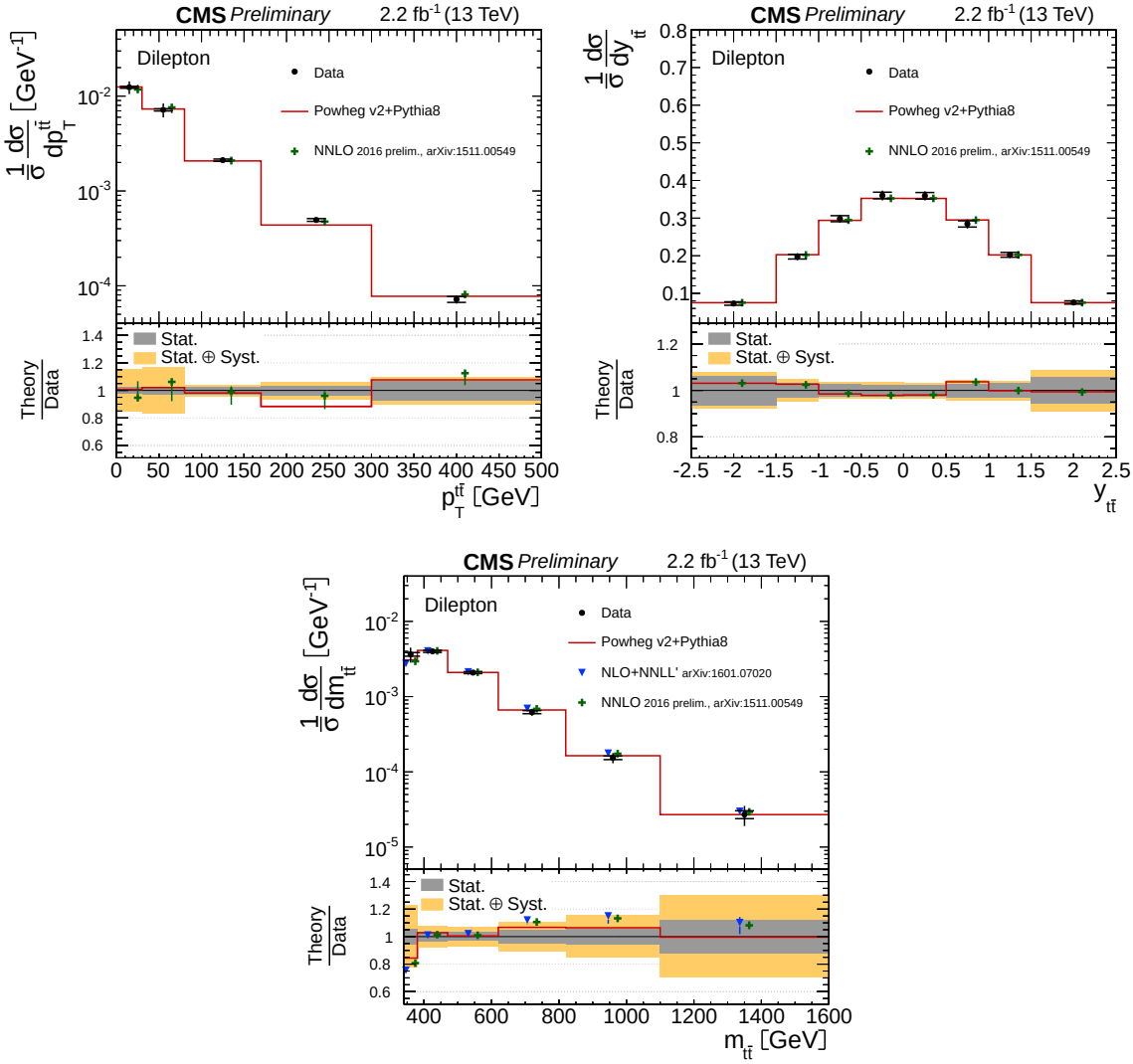

Figure 7.3 The normalized differential $t\bar{t}$ production cross sections measured (using the complete 2015 dataset of $L = 2.2$ fb^{-1}) as a function of the transverse momentum (upper left), the rapidity (upper right) and the invariant mass (bottom) of the $t\bar{t}$-system. The results are presented at the parton level in the full phase space. The measured data are confronted with the Monte Carlo and fixed order SM predictions described in Section 7.1.2. The inner error bars show the statistical uncertainty, the outer error bars show a combination of the statistical and systematic uncertainties. Results published in [13].

7.2 Inclusive $t\bar{t}$ production cross section with 2016 data

The measurement of the inclusive $t\bar{t}$ production cross section is performed using the dataset of 35.9 fb^{-1} collected by the CMS experiment at $\sqrt{s}$ = 13 TeV in 2016. The cross section is calculated using the data sample obtained after the full event selection according to Equation 5.1. The calculation is repeated for each individual dilepton channel and the result for their combination is determined as described in Section 5.6. The results are extrapolated to the full phase space.

The obtained results and their uncertainties are shown in Table 7.1, listing the product of the detector efficiency and acceptance, as well as the branching ratio, used for the computation of the respective cross section. The efficiency and acceptance correction is derived from the reference $t\bar{t}$ simulation (POWHEG v2+PYTHIA8). The inclusive $t\bar{t}$ production cross section measured in the combined channel is $\sigma_{t\bar{t}}^{incl} = 836.8 \pm 1.8(stat.) \pm 57.1(syst.)$ pb, which has a precision of about 6.8%. The measurement uncertainties were discussed in Section 6.5.

The results from all channels are summarized in Figure 7.4, where they are compared to the recent official CMS measurement performed in the $e^{\pm}\mu^{\mp}$ channel [123] and to the QCD prediction of NNLO+NNLL accuracy [49], showing a good agreement. As can be seen from the figure, the difference in central values between the official CMS measurement and the measurement presented in this work is about 29 pb. These measurements are based on two distinct data samples recorded under different experimental conditions. The difference in results is covered by experimental uncertainties (their total contribution is 5.7%, see Section 6.5) quoted in this work. In addition, the official CMS result is slightly more precise than the result presented here, even though the latter is based on the much larger data sample. However, the CMS measurement is different in several aspects with respect to the measurement implemented in this work. The CMS measurement involves $t\bar{t}$ decays via τ leptons as part of the signal definition and, thus, they are not regarded as background. The normalization of *Z+jets* background, as well as the contribution from other backgrounds except for single top quarks, are determined differently. As the official CMS measurement quotes the inclusive $t\bar{t}$ production cross section at the mass of m_t = 172.5 GeV, the uncertainty on the top quark mass is not included to the total uncertainty of the official result, while it has been considered in the context of this work. Moreover, in this work the new method to calculate parton shower and hadronization uncertainties adopted by the TOP PAG of the CMS Collaboration (see Section 6.3.2) is used, which was not the case for the aforementioned CMS result as it was performed before this method was defined.

Table 7.1 The results of the inclusive $t\bar{t}$ production cross section measurement performed using the dataset of 35.9 fb^{-1} collected by the CMS experiment at $\sqrt{s}$ = 13 TeV in 2016. The results are presented for each individual dilepton channel and for their combination.

Channel	e^+e^-	$\mu^+\mu^-$	$e^\pm\mu^\mp$	*combined*
Events in data	34890	70346	150410	255646
$t\bar{t}$ signal	26764.7	54873.5	124539.0	206177.0
$t\bar{t}$ other background	4147.1	9137.7	20356.6	33641.3
Non-*$t\bar{t}$* background	4505.4	9600.8	7671.3	21766.0
Total efficiency and acceptance [%]	7.632	15.650	17.775	14.706
Branching ratio [%]	1.147	1.130	2.277	4.554
Cross section [pb]	836.7	819.7	843.8	836.8
Statistical error [pb]	5.1	3.6	2.3	1.8
Systematic error [pb]	72.0	62.1	55.2	57.1
Total error [pb]	72.2	62.2	55.3	57.1

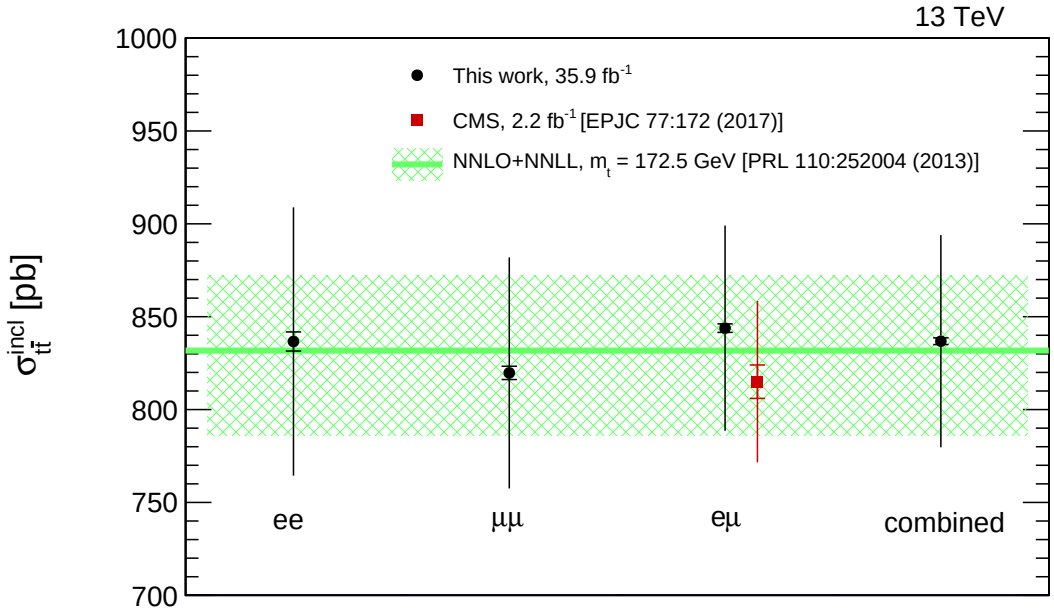

Figure 7.4 The summary of the inclusive $t\bar{t}$ production cross section measurement performed in this work. The results obtained in different dilepton channels are compared, where possible, to the recent CMS measurement and to the QCD prediction of NNLO+NNLL accuracy.

7.3 Differential $t\bar{t}$ production cross sections with 2016 data

In this section, the results of the normalized and absolute differential $t\bar{t}$ production cross section measurements, performed as described in Chapter 5 using the dataset of 35.9 fb^{-1} collected by the CMS experiment at $\sqrt{s}$ = 13 TeV in 2016, are presented. The results are presented at parton and/or particle levels, depending on the observable. Parton level results are extrapolated to the full phase space. Particle level results are presented in the fiducial phase space.

Observables measured at both parton and particle levels (60 measurements = 15 observables × 2 levels × 2 types of measurements, i.e. absolute and normalized):

- transverse momentum of the top quark p_T^t (Figure 7.5),
- transverse momentum of the top antiquark $p_T^{\bar{t}}$ (Figure 7.6),
- transverse momentum of the leading top quark p_T^t *(leading)* (Figure 7.7),
- transverse momentum of the trailing top quark p_T^t *(trailing)* (Figure 7.8),
- transverse momentum of the top quark in the rest frame of the $t\bar{t}$-system p_T^t *($t\bar{t}$ rest frame)* (Figure 7.9),
- transverse momentum of the top antiquark in the rest frame of the $t\bar{t}$-system $p_T^{\bar{t}}$ *($t\bar{t}$ rest frame)* (Figure 7.10),
- rapidity of the top quark y_t (Figure 7.11),
- rapidity of the top antiquark $y_{\bar{t}}$ (Figure 7.12),
- rapidity of the leading top quark y_t *(leading)* (Figure 7.13),
- rapidity of the trailing top quark y_t *(trailing)* (Figure 7.14),
- difference in absolute rapidity between the top quark and antiquark $\Delta|y|(t,\bar{t})$ (Figure 7.15),
- difference in azimuthal angle between the top quark and antiquark $\Delta\phi(t,\bar{t})$ (Figure 7.16),
- transverse momentum of the top-quark pair $p_T^{t\bar{t}}$ (Figure 7.17),
- invariant mass of the top-quark pair $m_{t\bar{t}}$ (Figure 7.18),
- rapidity of the top-quark pair $y_{t\bar{t}}$ (Figure 7.19).

Observables measured only at particle level (38 measurements = 19 observables × 2 types of measurements, i.e. absolute and normalized):

- transverse momentum of the lepton p_T^ℓ (Figure 7.20),
- transverse momentum of the antilepton $p_T^{\bar{\ell}}$ (Figure 7.20),
- transverse momentum of the leading lepton p_T^ℓ *(leading)* (Figure 7.21),
- transverse momentum of the trailing lepton p_T^ℓ *(trailing)* (Figure 7.21),
- pseudorapidity of the lepton η_ℓ (Figure 7.22),

- pseudorapidity of the antilepton $\eta_{\bar{\ell}}$ (Figure 7.22),
- pseudorapidity of the leading lepton η_{ℓ} *(leading)* (Figure 7.23),
- pseudorapidity of the trailing lepton η_{ℓ} *(trailing)* (Figure 7.23),
- difference in absolute pseudorapidity between the lepton and antilepton $\Delta|\eta|(\ell, \bar{\ell})$ (Figure 7.24),
- difference in azimuthal angle between the lepton and antilepton $\Delta\phi(\ell, \bar{\ell})$ (Figure 7.24),
- transverse momentum of the lepton pair $p_T^{\ell\bar{\ell}}$ (Figure 7.25),
- invariant mass of the lepton pair $m_{\ell\bar{\ell}}$ (Figure 7.25),
- transverse momentum of the leading b-jet p_T^b *(leading)* (Figure 7.26),
- transverse momentum of the trailing b-jet p_T^b *(trailing)* (Figure 7.26),
- pseudorapidity of the leading b-jet η_b *(leading)* (Figure 7.27),
- pseudorapidity of the trailing b-jet η_b *(trailing)* (Figure 7.27),
- transverse momentum of the b-jet pair $p_T^{b\bar{b}}$ (Figure 7.28),
- invariant mass of the b-jet pair $m_{b\bar{b}}$ (Figure 7.28),
- jet multiplicity N_{jets} (Figure 7.29).

The p_T of the top quarks and $t\bar{t}$-system, as well as $\Delta\phi(t, \bar{t})$, are measured since they are highly sensitive to the QCD radiation. In particular, perturbative calculations for the $p_T^{t\bar{t}}$ ($\Delta\phi(t, \bar{t})$) are more challenging with respect to those for top quarks, since this observable is equal to 0 (π) at the leading order of α_S for the $t\bar{t}$ production. Thus, measurements performed as a function of $p_T^{t\bar{t}}$ and $\Delta\phi(t, \bar{t})$ can be particularly useful for tests of perturbative calculations at higher-order terms (beyond-NLO). In order to scrutinize the top p_T spectrum, the measurements are performed as a function of p_T separately for the top quarks, top antiquarks, leading top quarks and trailing top quarks. Additionally, the p_T spectra of top quarks and antiquarks are studied in the $t\bar{t}$ rest frame to exclude an impact introduced by the boost of the $t\bar{t}$-system. The measurements as a function of y of the top quarks and, especially, $t\bar{t}$-system can help to reduce the uncertainties on the gluon PDF at large values of x, where x is the fraction of the proton momentum carried by a parton [139]. As done for the top p_T, separate measurements are performed as a function of y for the top quarks, top antiquarks, leading and trailing top quarks. The $\Delta|y|(t, \bar{t})$ is measured to extract the $t\bar{t}$ charge asymmetry as discussed in Section 7.4. The invariant mass of the $t\bar{t}$-system is of particular interest in searches for new-physics phenomena beyond the SM. As well as $y_{t\bar{t}}$, it can be used for fitting of the gluon PDF. Moreover, the absolute differential cross sections measured as a function of the top (anti)quark p_T and as a function of $m_{t\bar{t}}$ can be used to extract the pole mass of the top quark as done in [165].

The differential measurements performed as a function of the kinematics of the leptons and b-jets, as well as lepton and b-jet pairs, allow the study of $t\bar{t}$ production in a greater detail, in addition to the top quark- and $t\bar{t}$-related observables. Those measurements also allow to

probe the top quark decay. In particular, the $\Delta|\eta|(\ell,\bar{\ell})$ is measured to extract the leptonic charge asymmetry, complementing the $t\bar{t}$ charge asymmetry. The $\Delta\phi(\ell,\bar{\ell})$ distribution is sensitive to the spin correlation between the top quark and antiquark. It can also be used to set limits on new-physics phenomena, which are expected to severely affect the spin correlations and polarization in $t\bar{t}$ events. In this work, the $\Delta\phi(\ell,\bar{\ell})$ distribution is used to constrain the top quark chromo-magnetic dipole moment in an effective field theory, as discussed in Section 7.5. The differential measurements in bins of $m_{\ell\bar{\ell}}$ are also sensitive to the $t\bar{t}$ spin correlations, and results presented in bins of $m_{b\bar{b}}$ may be used for a PS tuning. Finally, the distribution of the jet multiplicity is sensitive to the QCD and parton shower radiation. Thus, it serves as essential tool in the tuning of the ME and PS event generators, as well as the UE models.

In total, 34 observables are probed and 98 differential cross section measurements are presented. Each bin of those measurements corresponds to the differential cross section integrated within the associated bin boundaries. Only in case of measurements performed as a function of N_{jets}, the last bin includes the integration over events with $N_{jets} \geq 7$.

As summarized previously, those observables that are measured at both parton and particle levels are shown in Figures 7.5-7.19. For each observable, the absolute and normalized differential measurements, performed either at parton or particle level, are shown in the same figure. In each figure, the upper row corresponds to parton level measurements and the lower row corresponds to particle level measurements. Normalized measurements are shown in the left column and absolute measurements are shown in the right column. In case of normalized measurements, the vertical axis is fixed to the same visible range to facilitate the comparisons between parton and particle level results.

Those observables that are measured only at the particle level are shown in Figures 7.20-7.29. Two observables are presented per figure, except Figure 7.29, where a single remaining observable is presented. Within a figure, the upper row corresponds to one observable and the lower row corresponds to another observable, as indicated in the caption. Normalized and absolute measurements for a given observable are shown in the left and right columns, respectively.

The precision of the measured differential cross sections is between 1% - 24% (see Tables B.1-B.98), depending on the bin and measurement. In particular, measurements performed as a function of leptonic observables are especially precise due to the excellent resolution of lepton energies and directions. The discussion of measurement uncertainties is given in Section 6.5.

The measured data are compared to Monte Carlo predictions. These comparisons are discussed in the following, as well as other interesting observations.

7.3.1 Comparison to Monte Carlo predictions

For all differential measurements (Figures 7.5-7.29), data are compared to the MC predictions from Powheg v2+Pythia8, Powheg v2+Herwig++ and MG5_aMC@NLO+Pythia8 [FxFx].

For a given observable, the agreement between the measured data and a prediction is quantitatively tested by means of the χ^2 per degree of freedom ($\chi^2/ndof$) defined as:

$$\chi^2/ndof = \frac{1}{ndof}\sum_{i=1}^{n}\sum_{j=1}^{n}(data_i - pred_i)\cdot \mathbf{Cov}_{ij}^{-1}\cdot(data_j - pred_j), \tag{7.1}$$

where $data_i$ is the measured differential cross section in i^{th} bin, $pred_i$ is the tested prediction in i^{th} bin, $\mathbf{Cov}_{ij}^{-1}$ is the ij-element of the inverse total covariance matrix of the data. The total covariance matrix, determined using the method described in Section 6.4 and presented in Appendix B, accounts for the statistical and systematic uncertainties, as well as the correlations among bins. In this way, $\chi^2/ndof$ takes into account that information as well. The sums run with indices i and j over all n bins of the studied differential measurement. The number of degrees of freedom ($ndof$) is taken to be n for the absolute measurements and $n-1$ for the normalized measurements, where one degree is reduced due to the normalization of results (i.e. the result in one measured bin can be expressed as the linear combination of results in other bins). A value $\chi^2/ndof \simeq 1$ indicates that the prediction is well-consistent with data. Larger values of $\chi^2/ndof$ indicate stronger disagreement between the prediction and data. Smaller values of $\chi^2/ndof$ indicate that the measurement uncertainties are overestimated and/or the results are strongly correlated. The $\chi^2/ndof = 0$ can indicate that predictions do not deviate from data at all (while testing the reference $t\bar{t}$ simulation, this can also indicate that the result is strongly biased towards the simulation), which is not expected statistically.

For each observed $\chi^2/ndof$-value, the probability value (p-value) can be computed [149]. The p-value corresponds to the probability to find a result (event sample) with $\chi^2 \geq \chi^2$ (*observed*), assuming that the prediction is valid. Higher (lower) p-values indicate better (worse) modelling of data by the prediction.

In Tables 7.2-7.5, the observed $\chi^2/ndof$ and corresponding p-values are shown for different types of differential measurements, comparing those for all observables and considered MC predictions. Additionally, Figure 7.30 shows the summary of p-values for all normalized measurements.

In general, an agreement is observed between the data and considered MC predictions within uncertainties for most differential measurements, where an especially good agreement is found for the y- and η-related observables. In the following, cases where a substantial

disagreement is found are discussed, where POWHEG v2+PYTHIA8 is referred to as POPY, POWHEG v2+HERWIG++ as POHE and MG5_aMC@NLO+PYTHIA8 [FXFX] as aMCPY.

Top quark observables

Consistently for all types of differential measurements, the top quark p_T spectrum in data exhibits a disagreement with respect to the POPY prediction, where an excess in data at low p_T gradually turns into a large deficit at high p_T (starting from $p_T^t > 200$ GeV). A similar behaviour is observed for the aMCPY, but with a smaller deficit in data at high p_T. The POHE prediction demonstrates the best agreement with data, where only a moderate deficit in data is present at high p_T for measurements performed at parton level. The same observations are relevant for the measurements of top antiquark, leading and trailing top quarks. In particular, the largest disagreement at high p_T is found for the trailing top quarks. Moreover, the presence of the same behaviour for the top quarks measured in the $t\bar{t}$ rest frame indicates that this effect is not introduced by the boost of the $t\bar{t}$-system.

A softer top quark p_T spectrum in data with respect to MC and fixed order predictions was also observed at $\sqrt{s}$ = 7, 8 and 13 TeV by the ATLAS [3–6] and CMS [8, 7, 9–11] Collaborations.

Top-quark pair observables

The $\Delta\phi(t,\bar{t})$ spectrum in data is well-modelled by the POPY prediction. For normalized measurement at parton level, an excess in data with respect to POHE is observed at low $\Delta\phi(t,\bar{t})$. As indicated by the corresponding p-value for the normalized measurement of $\Delta\phi(t,\bar{t})$ at particle level (see Table 7.4), the modelling by aMCPY is not compatible with data in this case, even though the prediction is within uncertainties. This effect is caused by the correlation pattern among bins (see Figure B.42), where bins are correlated in different direction with respect to the pattern of the agreement between data and the prediction.

A deficit in data is observed at high $p_T^{t\bar{t}}$ with respect to POPY and aMCPY predictions. The worst description of data for the $p_T^{t\bar{t}}$ is provided by the POHE, where a large excess in data is present at moderate values.

At very low $m_{t\bar{t}}$, data exhibits an excess with respect to the POPY and aMCPY predictions for all types of differential measurements. For both normalized measurements, the aMCPY prediction is higher than data at the peak of $m_{t\bar{t}}$. For all measurements of $m_{t\bar{t}}$, data features a deficit at moderate values with respect to the POPY. At the parton level, POHE shows a good description of the $m_{t\bar{t}}$ in data. In contrast, the normalized measurement at particle level has a

deficit in data with respect to the PoHe at low $m_{t\bar{t}}$, while having an excess at slightly higher values.

Observables related to decay products of top quarks

The kinematics of the leptons, b-jets, lepton and b-jet pairs are correlated to the top quarks. Thus, the corresponding measurements of their transverse momentum, as well as $m_{\ell\bar{\ell}}$ and $m_{b\bar{b}}$, exhibit a similar pattern of disagreements as observed for the measurements of the p_T^t, $p_T^{t\bar{t}}$ and $m_{t\bar{t}}$ distributions.

In particular, PoHe provides a good description of data in most leptonic observables, with an exception of $p_T^{\ell\bar{\ell}}$ (p_T^{ℓ} *(trailing)*), where an excess (a deficit) in data is observed. The aMCPy prediction demonstrates a good agreement with data for $m_{\ell\bar{\ell}}$. The normalized spectrum of $\Delta\phi(\ell, \bar{\ell})$ in data appears to have a slight slope with respect to considered MC predictions.

As described above, the PoPy and aMCPy predictions describe the data for all measurements of b-jet p_T, as well as $p_T^{b\bar{b}}$ and $m_{b\bar{b}}$, in a similar way as observed for corresponding observables related to top quarks. However, the PoHe provides an inferior modelling of those observables, in contrast to its generally better performance for top quarks.

The jet multiplicity

For measurements performed in bins of the jet multiplicity, the data exhibits a smoothly increasing deficit with respect to PoPy and PoHe predictions starting from $N_{jets} = 4$ in the direction of higher multiplicities. In contrast, aMCPy provides a good modelling of the region $N_{jets} \geq 4$, while having a disagreement with data at $N_{jets} = 2$ and 3.

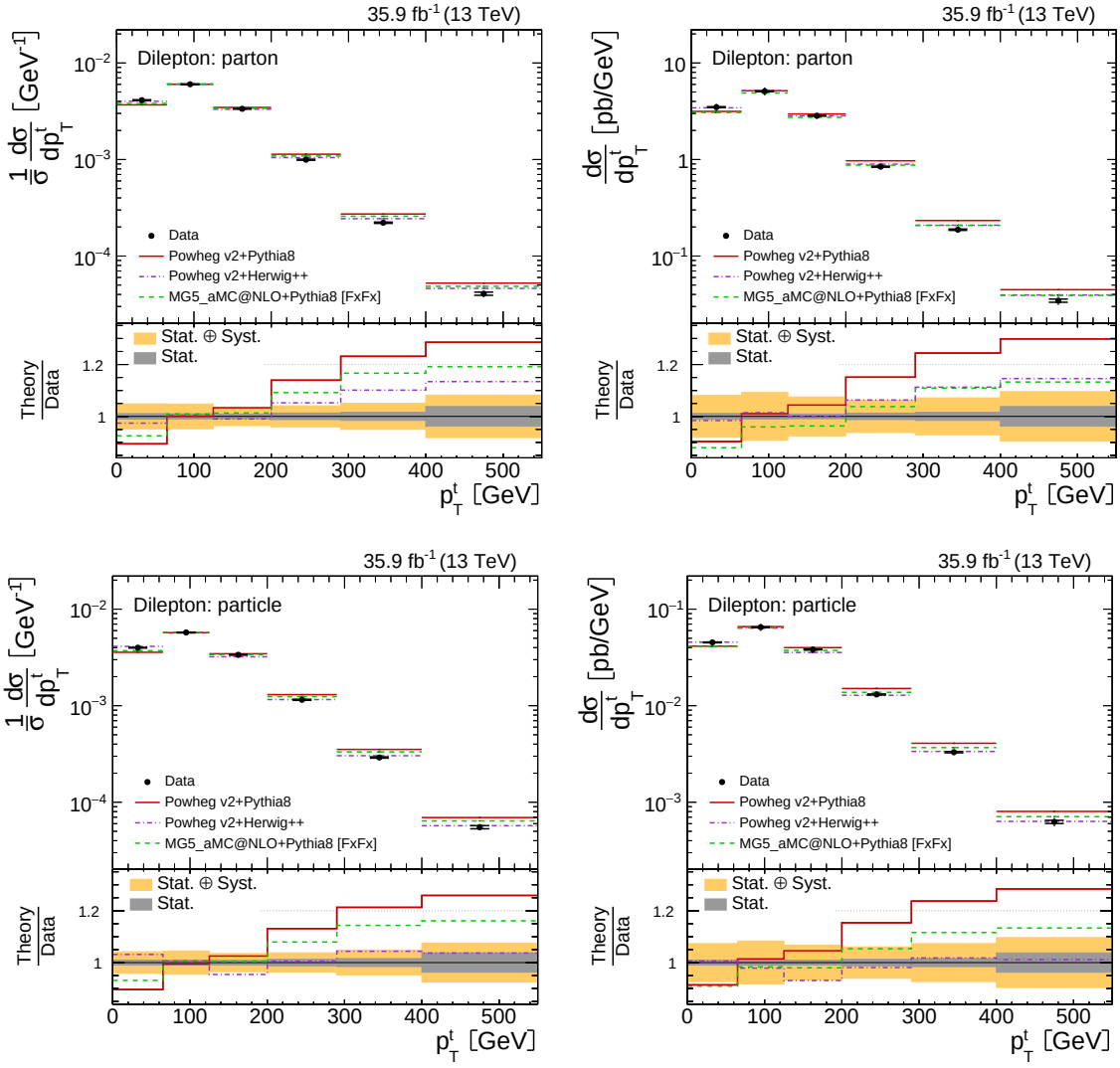

Figure 7.5 The normalized (left) and absolute (right) differential $t\bar{t}$ production cross sections as a function of the transverse momentum of the top quark p_T^t. Upper row corresponds to measurements at parton level in the full phase space. Lower row corresponds to measurements at particle level in a fiducial phase space. The data (black) are compared to the MC predictions from POWHEG v2+PYTHIA8 (red), POWHEG v2+HERWIG++ (violet) and MG5_aMC@NLO+PYTHIA8 [FxFx] (green). The inner error bars show the statistical uncertainty, the outer error bars show a combination of the statistical and systematic uncertainties.

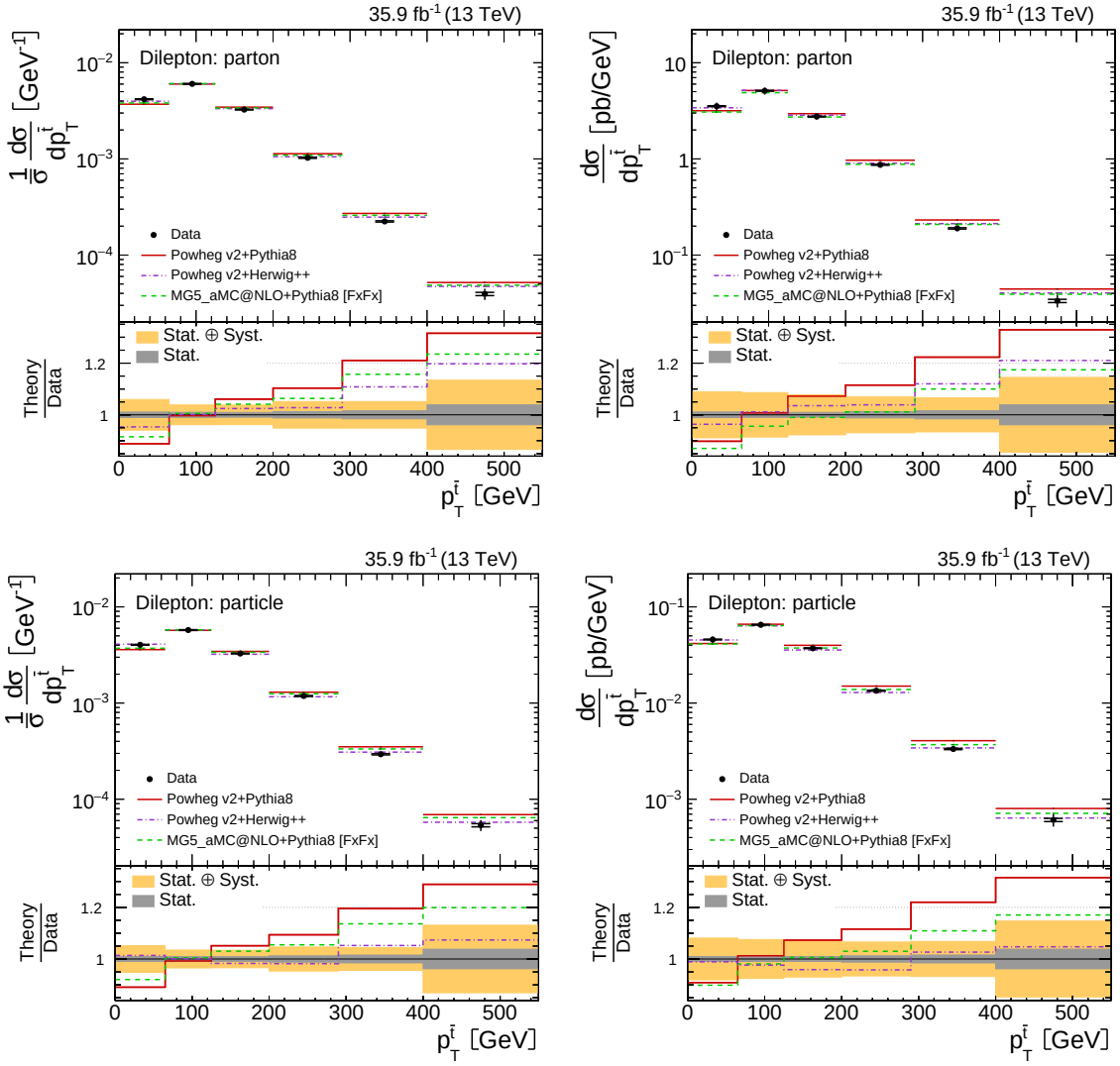

Figure 7.6 The normalized (left) and absolute (right) differential $t\bar{t}$ production cross sections as a function of the transverse momentum of the top antiquark $p_T^{\bar{t}}$. Upper row corresponds to measurements at parton level in the full phase space. Lower row corresponds to measurements at particle level in a fiducial phase space. The data (black) are compared to the MC predictions from POWHEG v2+PYTHIA8 (red), POWHEG v2+HERWIG++ (violet) and MG5_aMC@NLO+PYTHIA8 [FxFx] (green). The inner error bars show the statistical uncertainty, the outer error bars show a combination of the statistical and systematic uncertainties.

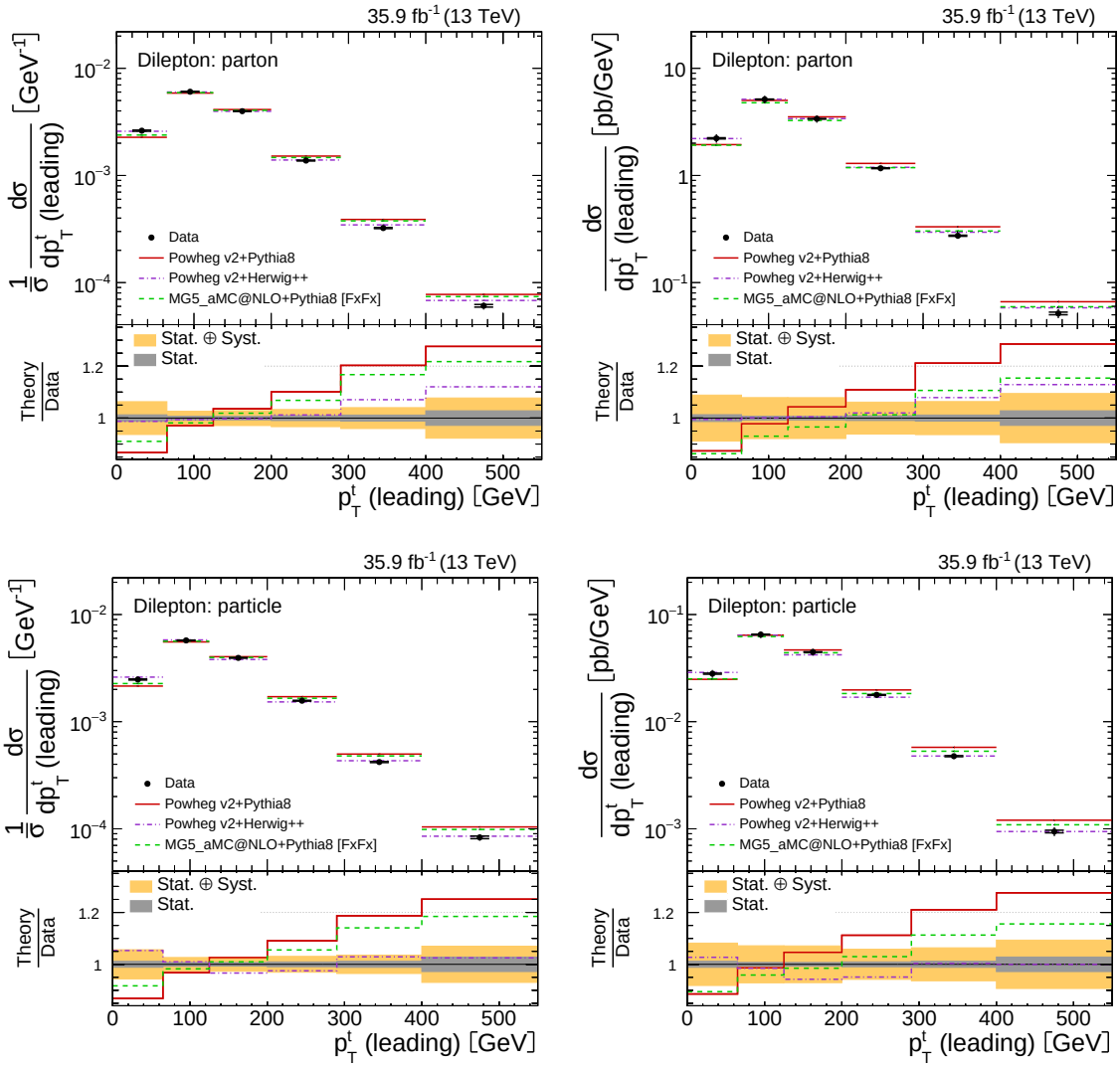

Figure 7.7 The normalized (left) and absolute (right) differential $t\bar{t}$ production cross sections as a function of the transverse momentum of the leading top quark p_T^t *(leading)*. Upper row corresponds to measurements at parton level in the full phase space. Lower row corresponds to measurements at particle level in a fiducial phase space. The data (black) are compared to the MC predictions from POWHEG v2+PYTHIA8 (red), POWHEG v2+HERWIG++ (violet) and MG5_aMC@NLO+PYTHIA8 [FxFx] (green). The inner error bars show the statistical uncertainty, the outer error bars show a combination of the statistical and systematic uncertainties.

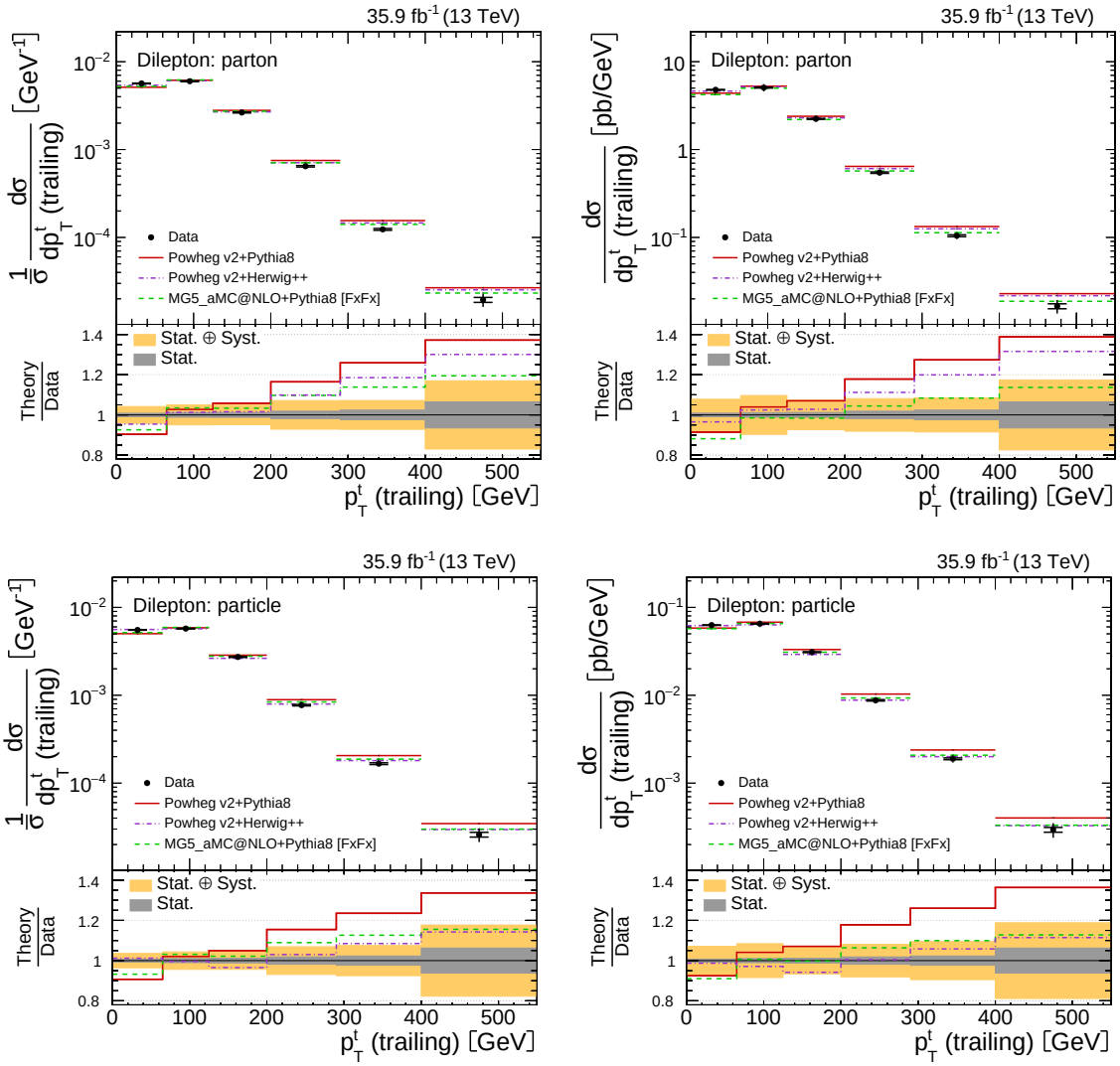

Figure 7.8 The normalized (left) and absolute (right) differential $t\bar{t}$ production cross sections as a function of the transverse momentum of the trailing top quark p_T^t *(trailing)*. Upper row corresponds to measurements at parton level in the full phase space. Lower row corresponds to measurements at particle level in a fiducial phase space. The data (black) are compared to the MC predictions from POWHEG v2+PYTHIA8 (red), POWHEG v2+HERWIG++ (violet) and MG5_aMC@NLO+PYTHIA8 [FxFx] (green). The inner error bars show the statistical uncertainty, the outer error bars show a combination of the statistical and systematic uncertainties.

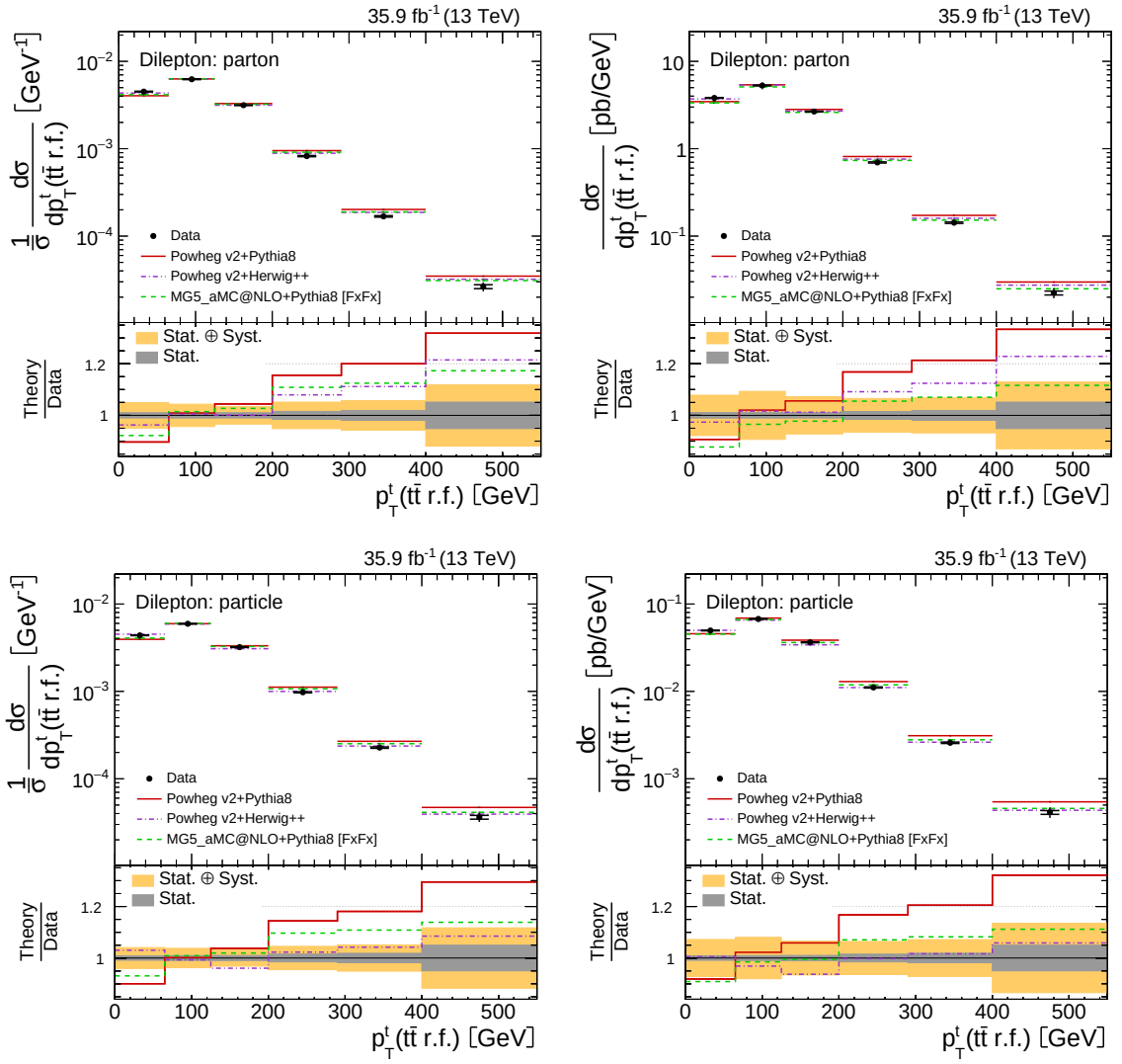

Figure 7.9 The normalized (left) and absolute (right) differential $t\bar{t}$ production cross sections as a function of the transverse momentum of the top quark in the rest frame of the $t\bar{t}$-system p_T^t *(*$t\bar{t}$ *rest frame)*. Upper row corresponds to measurements at parton level in the full phase space. Lower row corresponds to measurements at particle level in a fiducial phase space. The data (black) are compared to the MC predictions from POWHEG v2+PYTHIA8 (red), POWHEG v2+HERWIG++ (violet) and MG5_aMC@NLO+PYTHIA8 [FxFx] (green). The inner error bars show the statistical uncertainty, the outer error bars show a combination of the statistical and systematic uncertainties.

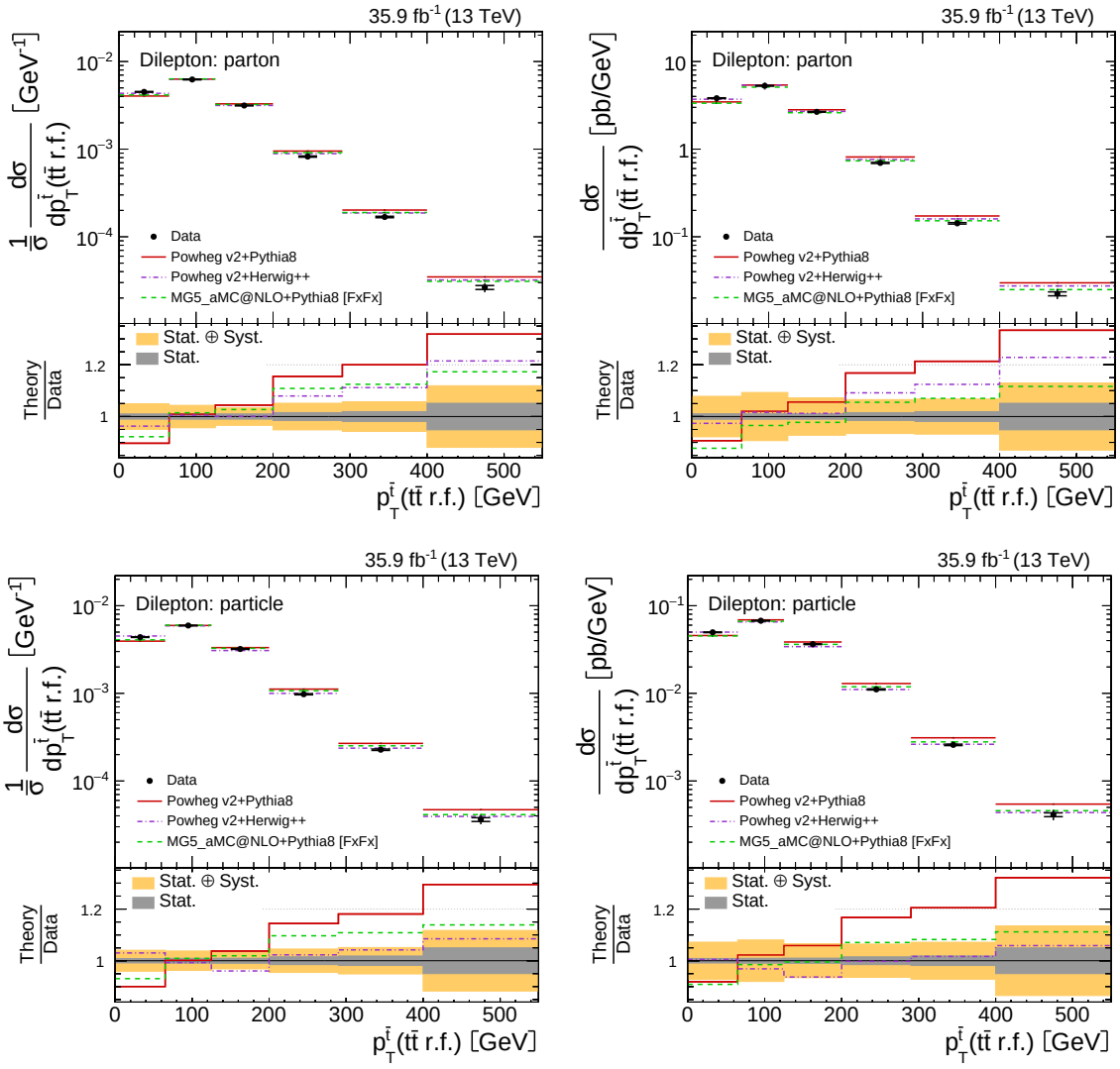

Figure 7.10 The normalized (left) and absolute (right) differential $t\bar{t}$ production cross sections as a function of the transverse momentum of the top antiquark in the rest frame of the $t\bar{t}$-system $p_T^{\bar{t}}$ *($t\bar{t}$ rest frame)*. Upper row corresponds to measurements at parton level in the full phase space. Lower row corresponds to measurements at particle level in a fiducial phase space. The data (black) are compared to the MC predictions from POWHEG v2+PYTHIA8 (red), POWHEG v2+HERWIG++ (violet) and MG5_aMC@NLO+PYTHIA8 [FxFx] (green). The inner error bars show the statistical uncertainty, the outer error bars show a combination of the statistical and systematic uncertainties.

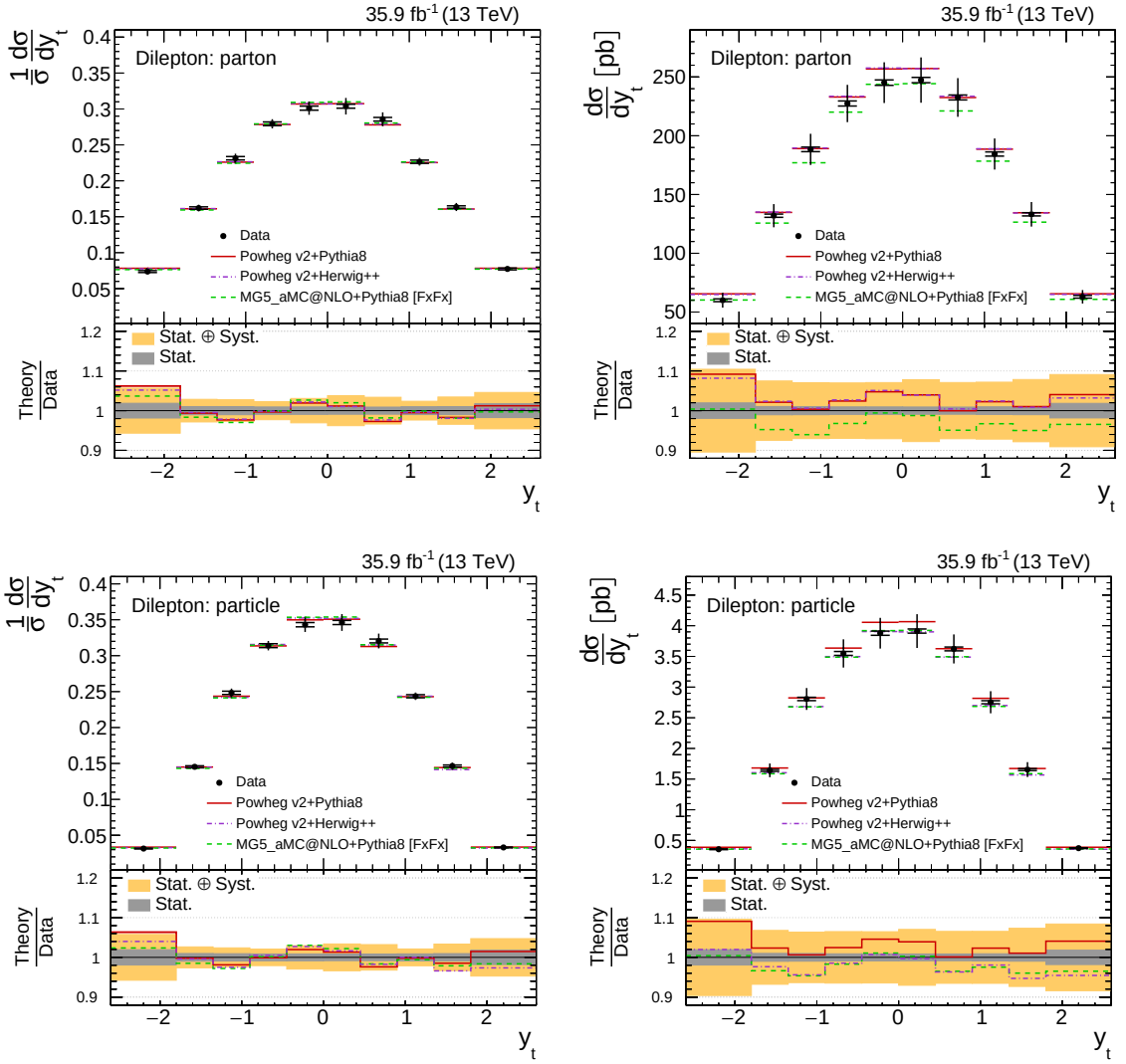

Figure 7.11 The normalized (left) and absolute (right) differential $t\bar{t}$ production cross sections as a function of the rapidity of the top quark y_t. Upper row corresponds to measurements at parton level in the full phase space. Lower row corresponds to measurements at particle level in a fiducial phase space. The data (black) are compared to the MC predictions from POWHEG v2+PYTHIA8 (red), POWHEG v2+HERWIG++ (violet) and MG5_aMC@NLO+PYTHIA8 [FXFX] (green). The inner error bars show the statistical uncertainty, the outer error bars show a combination of the statistical and systematic uncertainties.

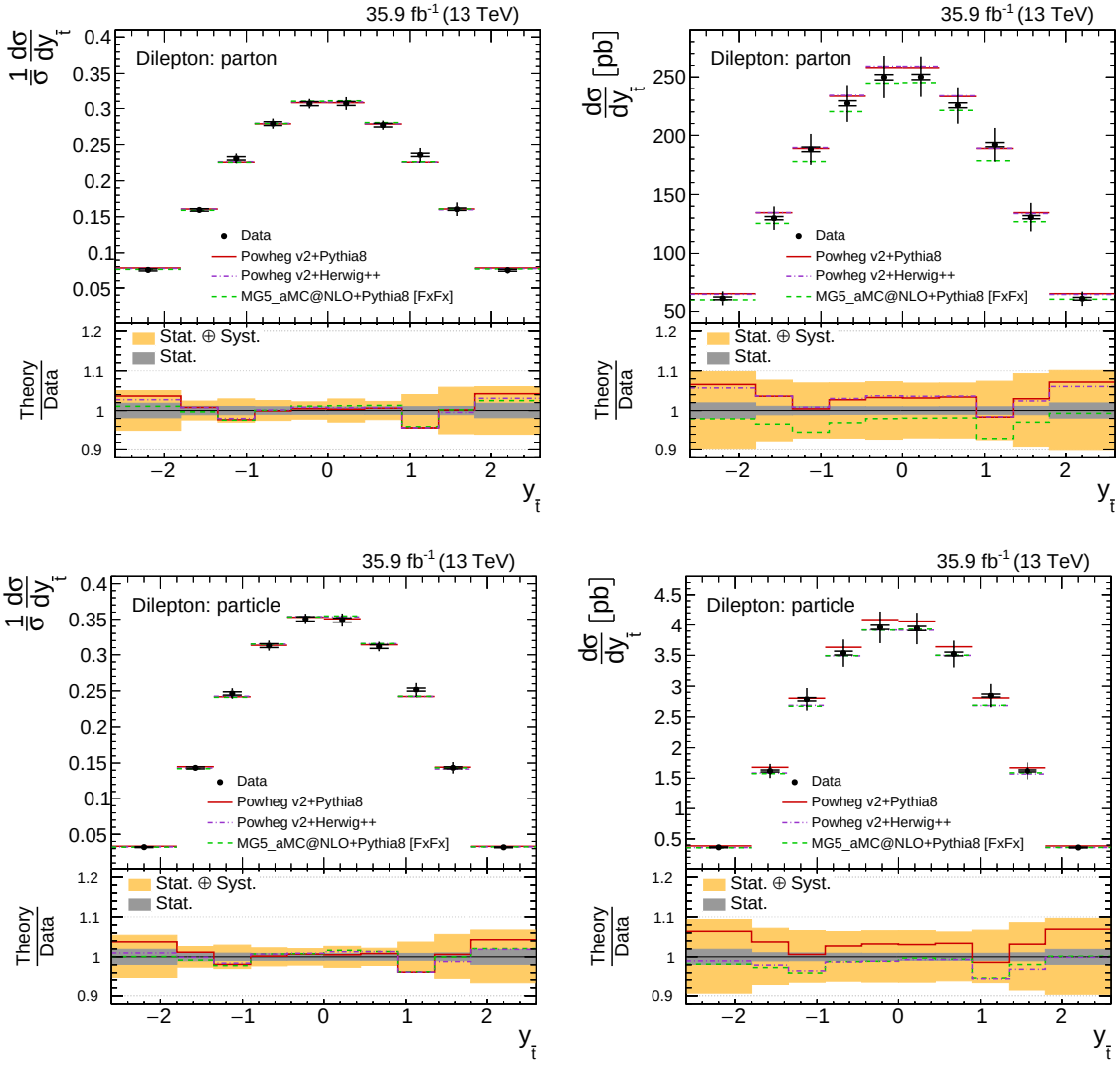

Figure 7.12 The normalized (left) and absolute (right) differential $t\bar{t}$ production cross sections as a function of the rapidity of the top antiquark $y_{\bar{t}}$. Upper row corresponds to measurements at parton level in the full phase space. Lower row corresponds to measurements at particle level in a fiducial phase space. The data (black) are compared to the MC predictions from POWHEG v2+PYTHIA8 (red), POWHEG v2+HERWIG++ (violet) and MG5_aMC@NLO+PYTHIA8 [FxFx] (green). The inner error bars show the statistical uncertainty, the outer error bars show a combination of the statistical and systematic uncertainties.

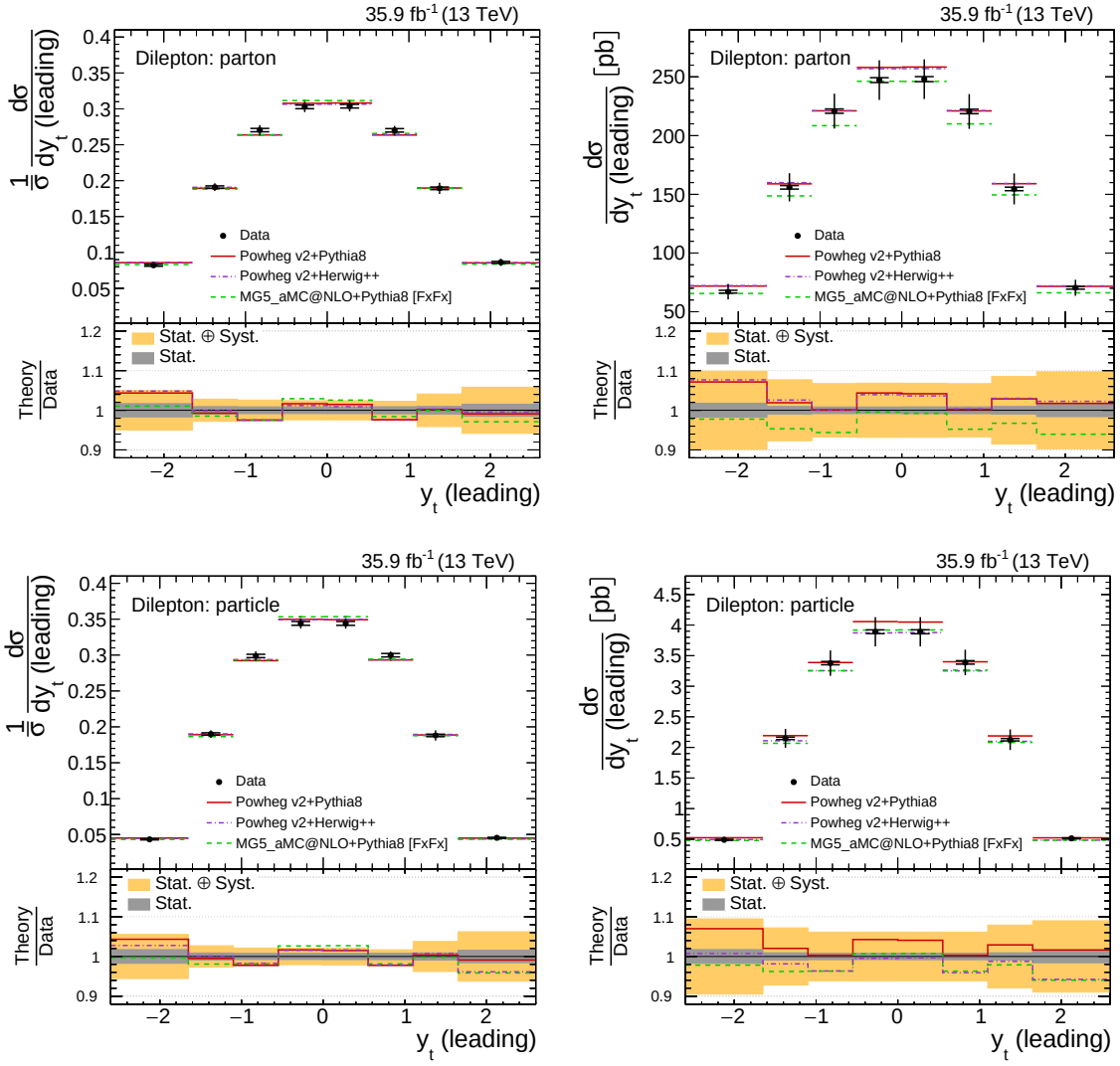

Figure 7.13 The normalized (left) and absolute (right) differential $t\bar{t}$ production cross sections as a function of the rapidity of the leading top quark y_t *(leading)*. Upper row corresponds to measurements at parton level in the full phase space. Lower row corresponds to measurements at particle level in a fiducial phase space. The data (black) are compared to the MC predictions from POWHEG v2+PYTHIA8 (red), POWHEG v2+HERWIG++ (violet) and MG5_aMC@NLO+PYTHIA8 [FxFx] (green). The inner error bars show the statistical uncertainty, the outer error bars show a combination of the statistical and systematic uncertainties.

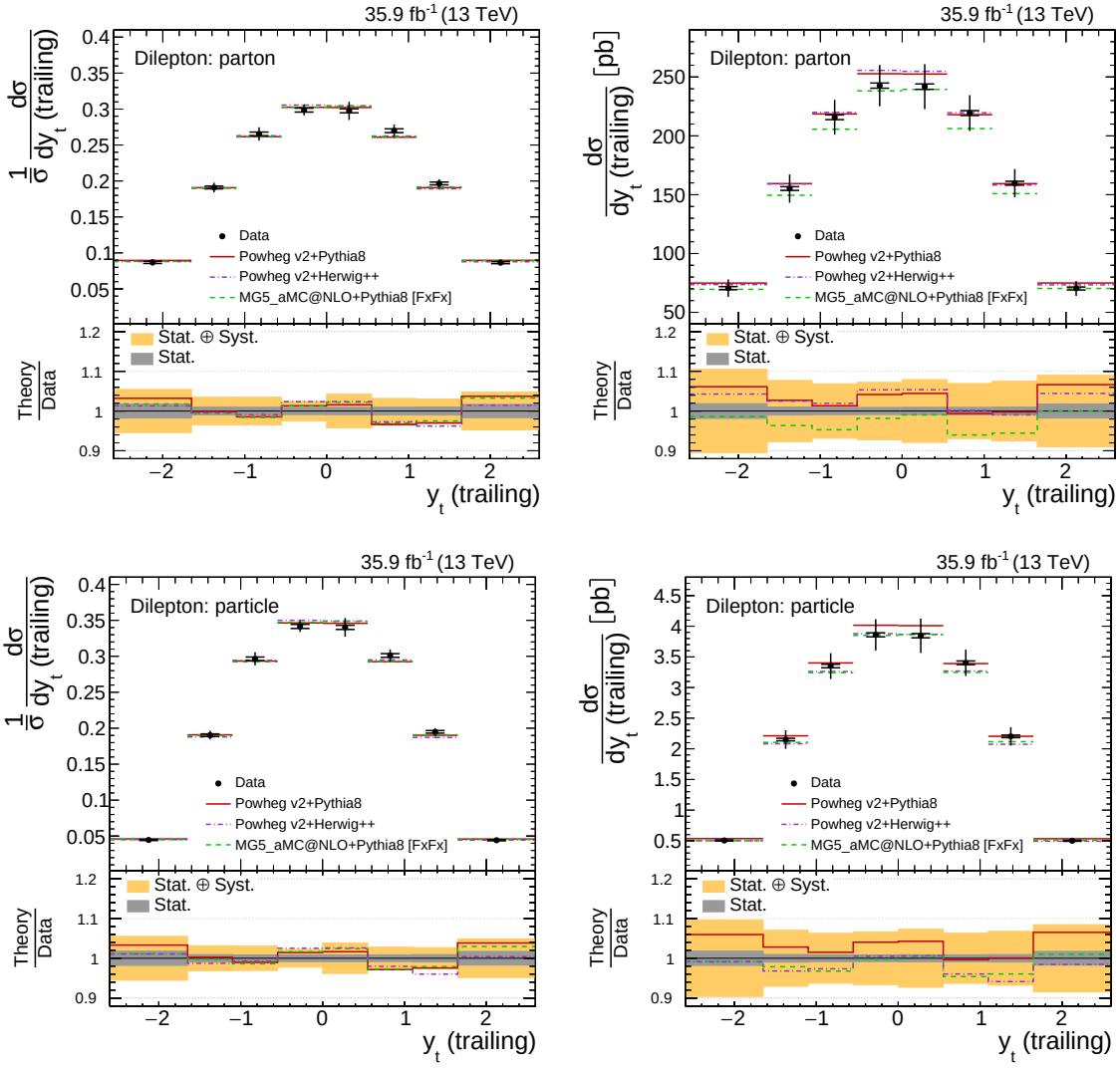

Figure 7.14 The normalized (left) and absolute (right) differential $t\bar{t}$ production cross sections as a function of the rapidity of the trailing top quark y_t *(trailing)*. Upper row corresponds to measurements at parton level in the full phase space. Lower row corresponds to measurements at particle level in a fiducial phase space. The data (black) are compared to the MC predictions from POWHEG v2+PYTHIA8 (red), POWHEG v2+HERWIG++ (violet) and MG5_aMC@NLO+PYTHIA8 [FxFx] (green). The inner error bars show the statistical uncertainty, the outer error bars show a combination of the statistical and systematic uncertainties.

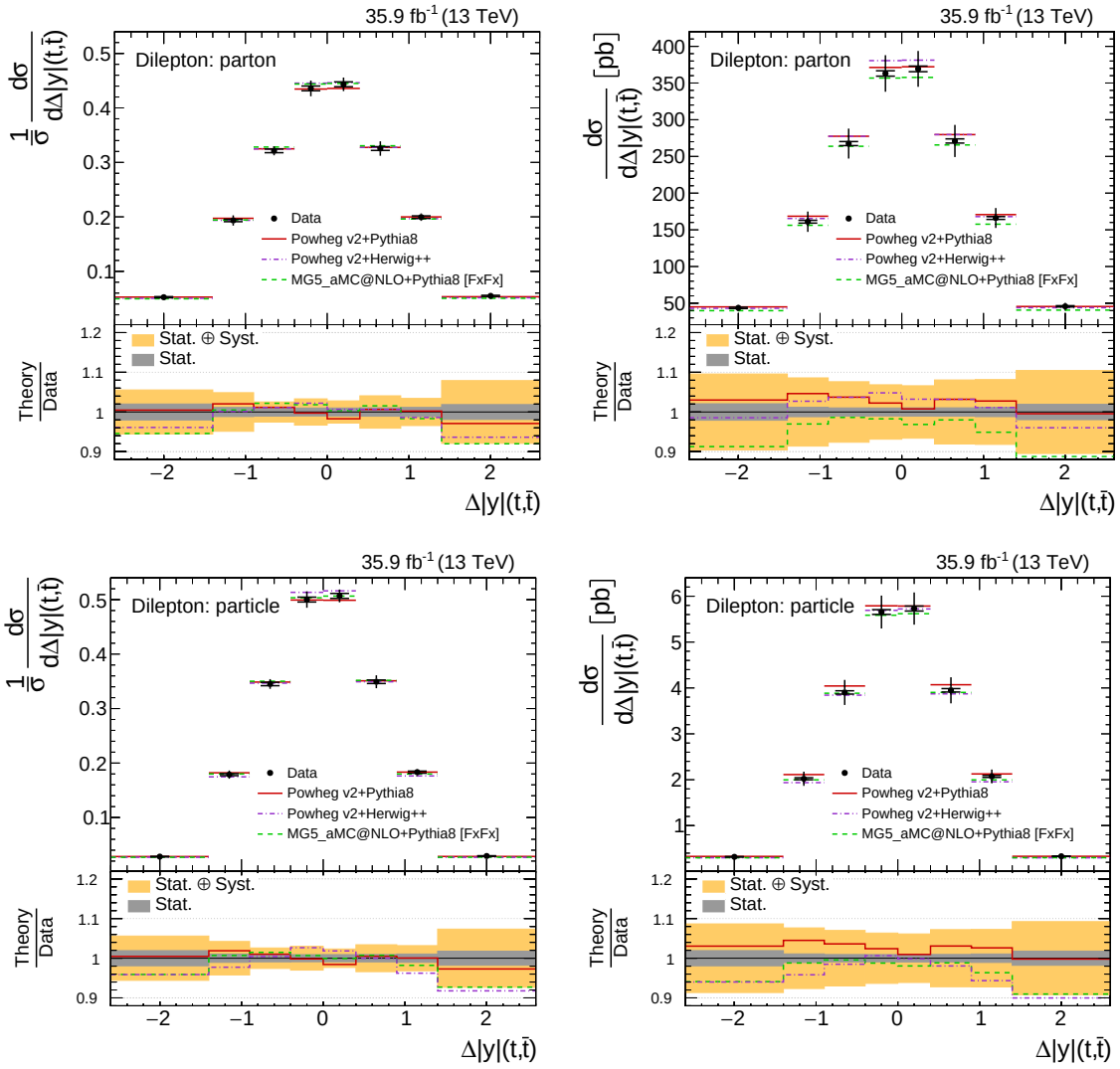

Figure 7.15 The normalized (left) and absolute (right) differential $t\bar{t}$ production cross sections as a function of the difference in absolute rapidity between the top quark and antiquark $\Delta|y|(t,\bar{t})$. Upper row corresponds to measurements at parton level in the full phase space. Lower row corresponds to measurements at particle level in a fiducial phase space. The data (black) are compared to the MC predictions from POWHEG v2+PYTHIA8 (red), POWHEG v2+HERWIG++ (violet) and MG5_aMC@NLO+PYTHIA8 [FxFx] (green). The inner error bars show the statistical uncertainty, the outer error bars show a combination of the statistical and systematic uncertainties.

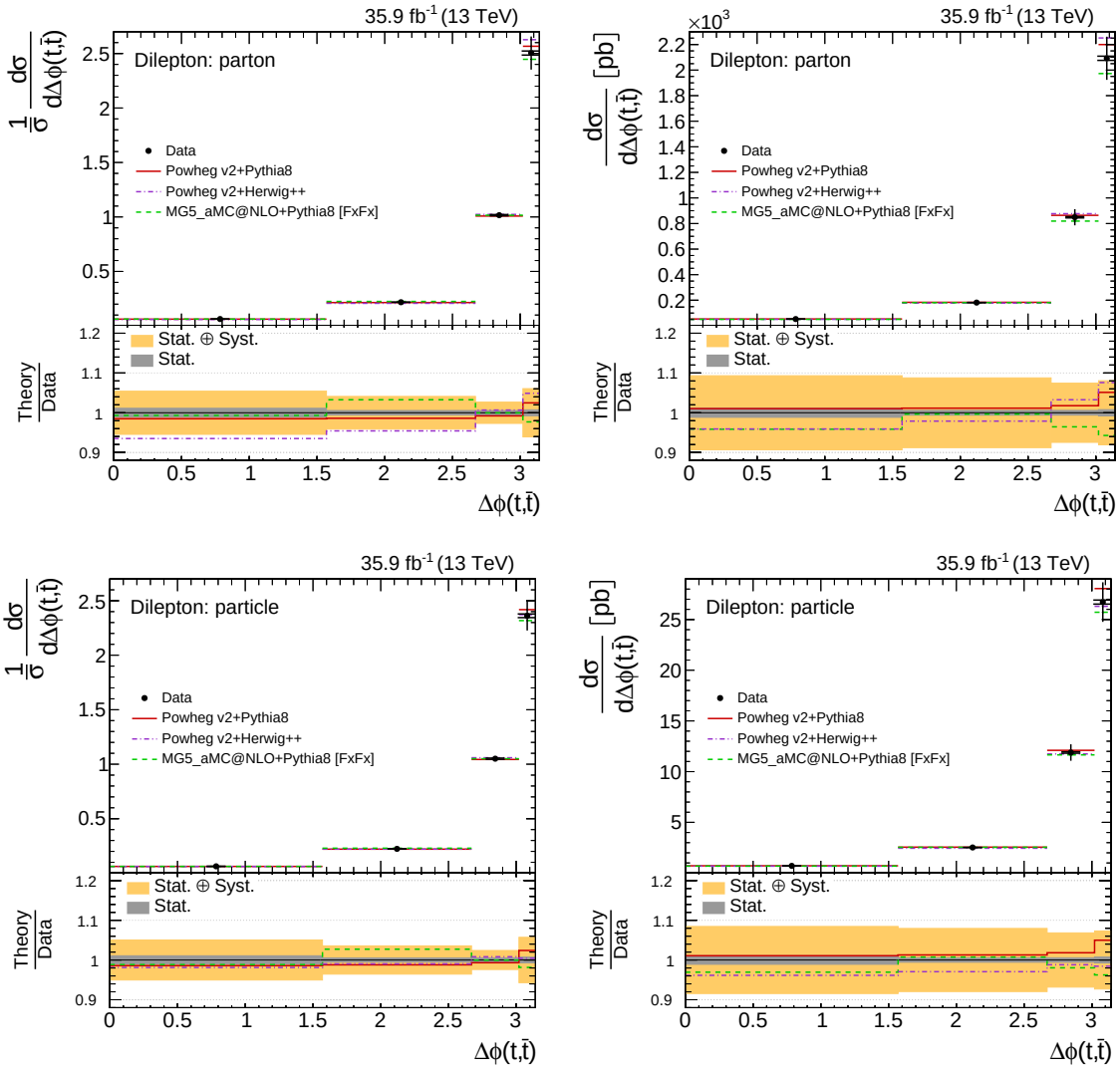

Figure 7.16 The normalized (left) and absolute (right) differential $t\bar{t}$ production cross sections as a function of the difference in azimuthal angle between the top quark and antiquark $\Delta\phi(t,\bar{t})$. Upper row corresponds to measurements at parton level in the full phase space. Lower row corresponds to measurements at particle level in a fiducial phase space. The data (black) are compared to the MC predictions from POWHEG v2+PYTHIA8 (red), POWHEG v2+HERWIG++ (violet) and MG5_aMC@NLO+PYTHIA8 [FxFx] (green). The inner error bars show the statistical uncertainty, the outer error bars show a combination of the statistical and systematic uncertainties.

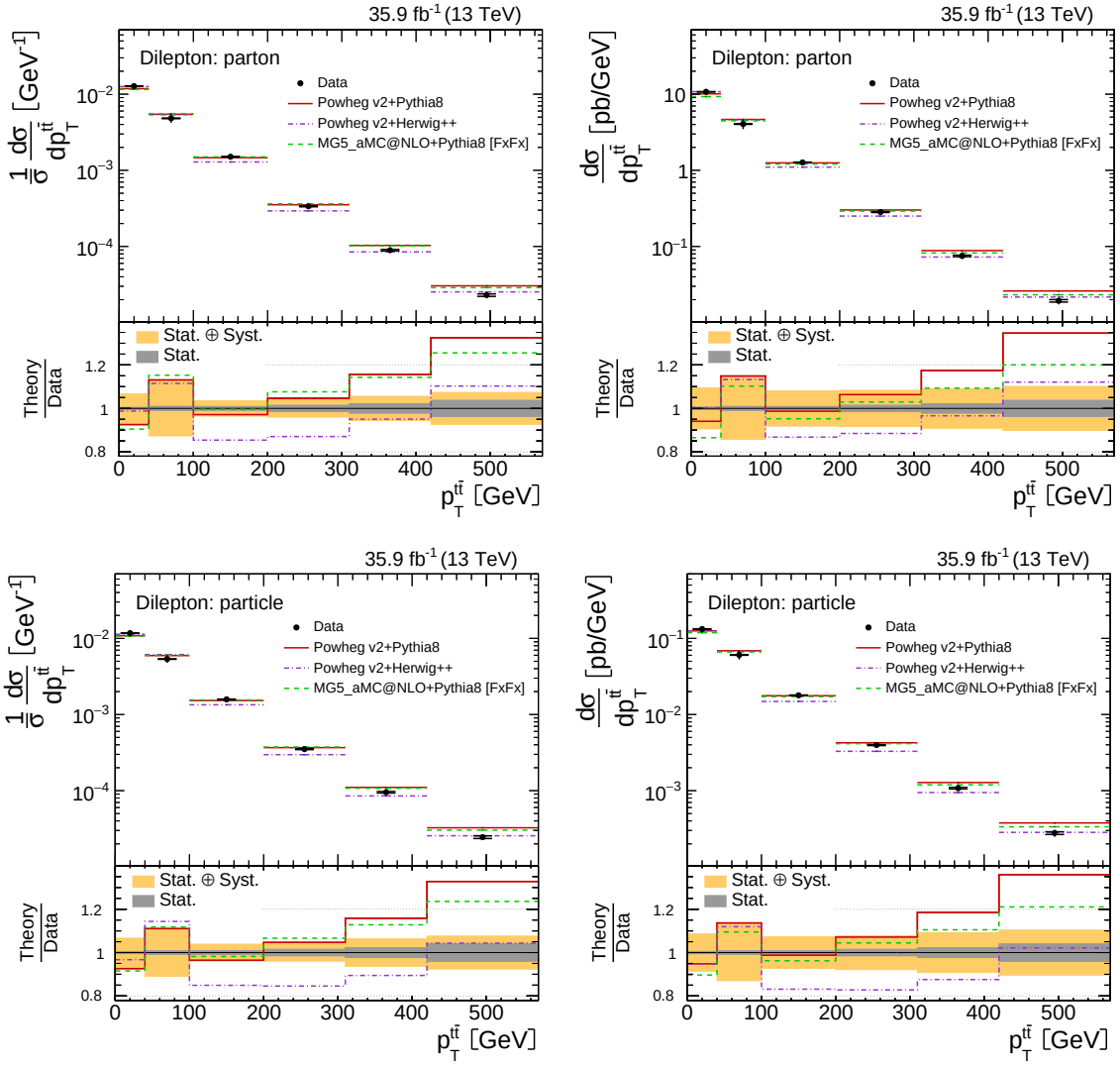

Figure 7.17 The normalized (left) and absolute (right) differential $t\bar{t}$ production cross sections as a function of the transverse momentum of the top-quark pair $p_T^{t\bar{t}}$. Upper row corresponds to measurements at parton level in the full phase space. Lower row corresponds to measurements at particle level in a fiducial phase space. The data (black) are compared to the MC predictions from POWHEG v2+PYTHIA8 (red), POWHEG v2+HERWIG++ (violet) and MG5_aMC@NLO+PYTHIA8 [FxFx] (green). The inner error bars show the statistical uncertainty, the outer error bars show a combination of the statistical and systematic uncertainties.

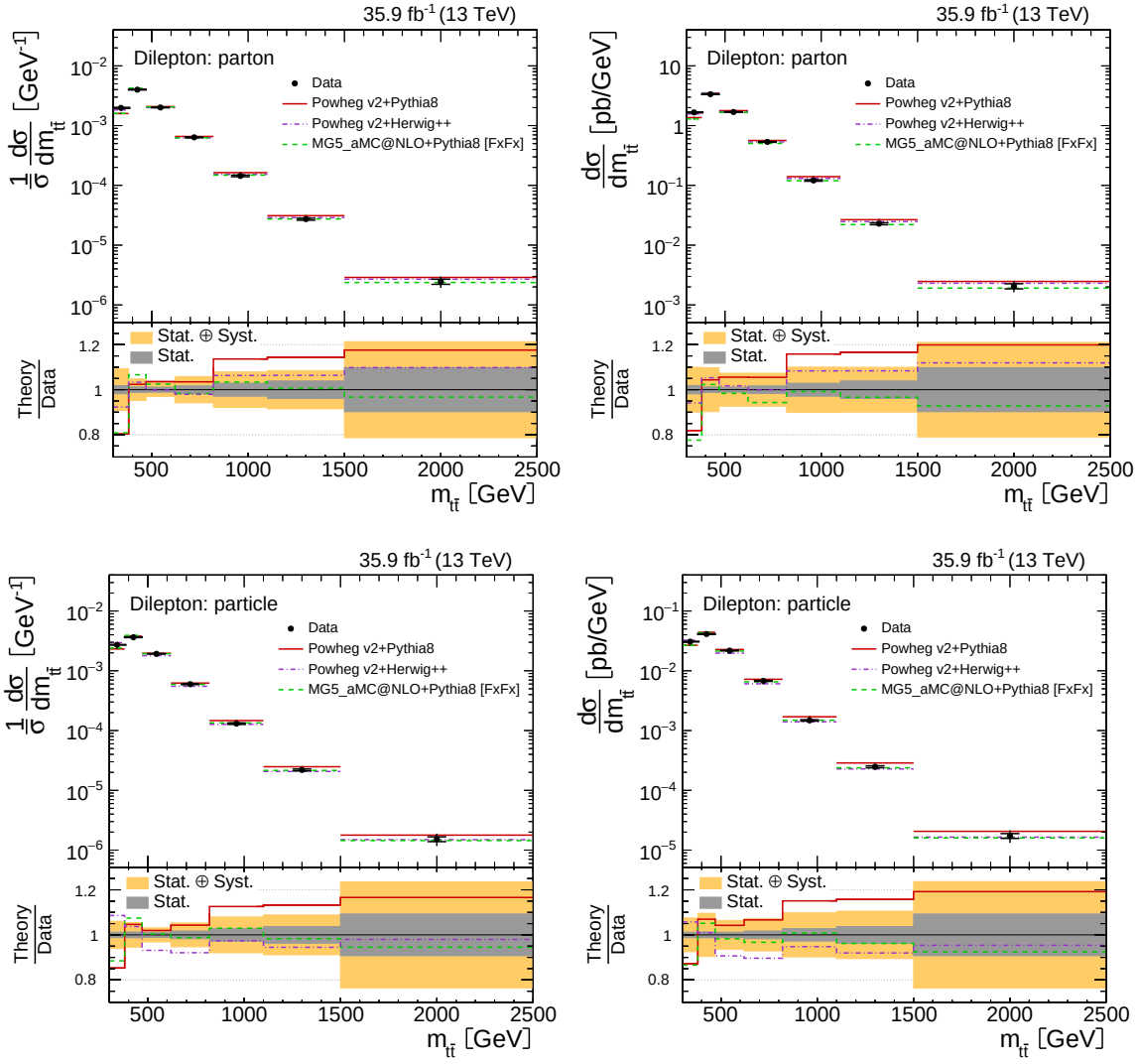

Figure 7.18 The normalized (left) and absolute (right) differential $t\bar{t}$ production cross sections as a function of the invariant mass of the top-quark pair $m_{t\bar{t}}$. Upper row corresponds to measurements at parton level in the full phase space. Lower row corresponds to measurements at particle level in a fiducial phase space. The data (black) are compared to the MC predictions from POWHEG v2+PYTHIA8 (red), POWHEG v2+HERWIG++ (violet) and MG5_aMC@NLO+PYTHIA8 [FxFx] (green). The inner error bars show the statistical uncertainty, the outer error bars show a combination of the statistical and systematic uncertainties.

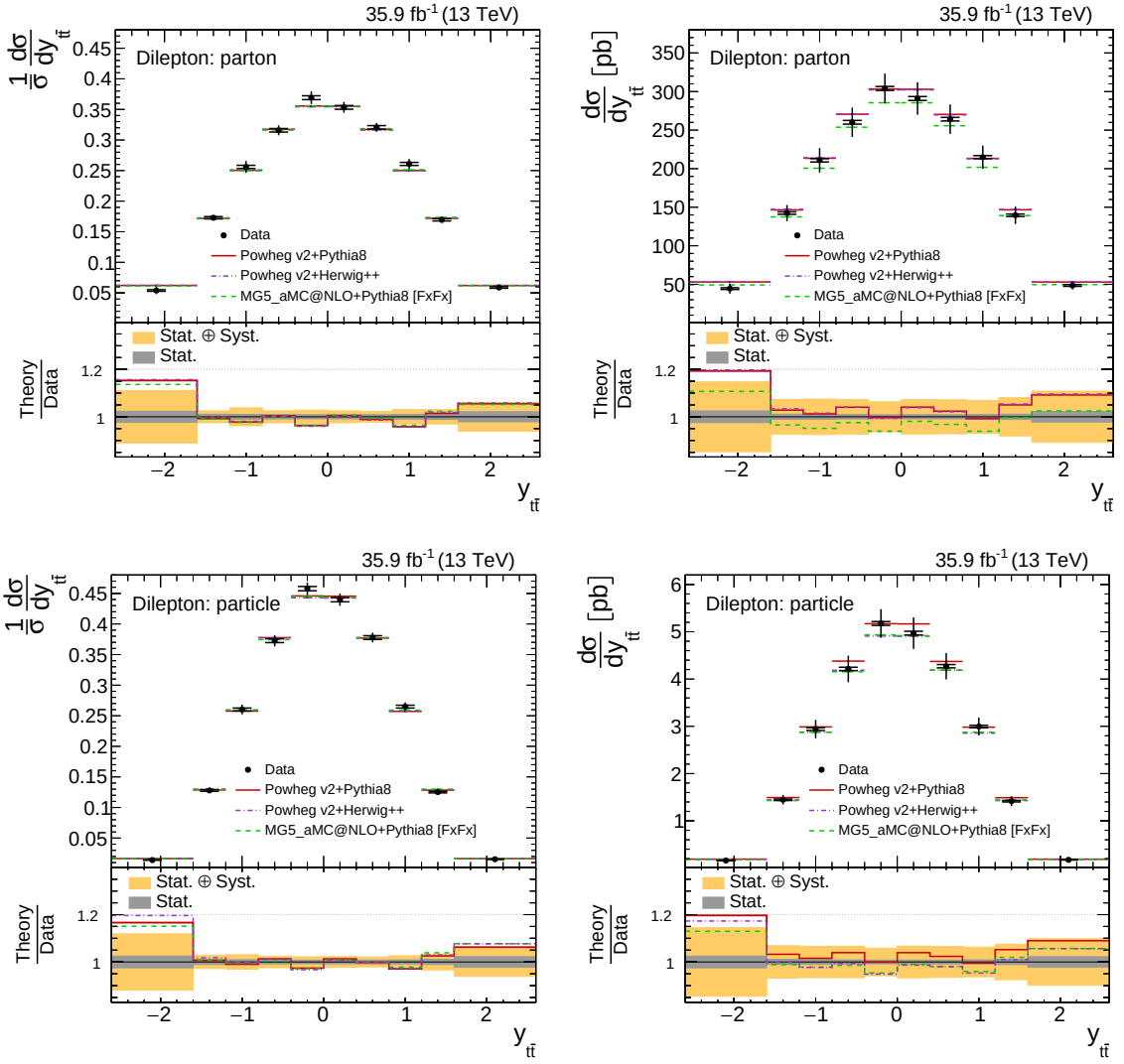

Figure 7.19 The normalized (left) and absolute (right) differential $t\bar{t}$ production cross sections as a function of the rapidity of the top-quark pair $y_{t\bar{t}}$. Upper row corresponds to measurements at parton level in the full phase space. Lower row corresponds to measurements at particle level in a fiducial phase space. The data (black) are compared to the MC predictions from POWHEG v2+PYTHIA8 (red), POWHEG v2+HERWIG++ (violet) and MG5_aMC@NLO+PYTHIA8 [FxFx] (green). The inner error bars show the statistical uncertainty, the outer error bars show a combination of the statistical and systematic uncertainties.

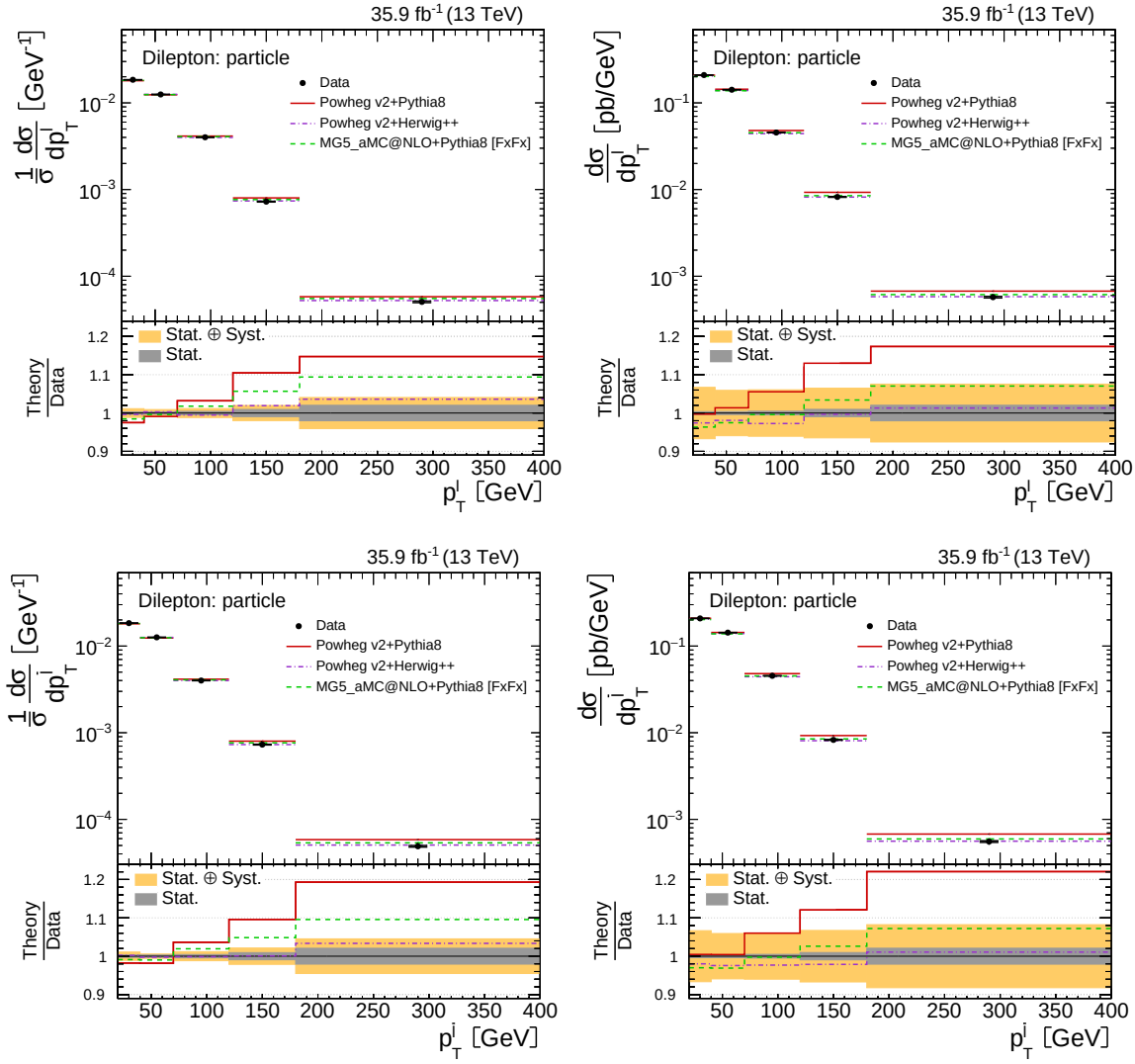

Figure 7.20 The normalized (left) and absolute (right) differential $t\bar{t}$ production cross sections as a function of the transverse momentum of the lepton p_T^{ℓ} (upper row) and as a function of the transverse momentum of the antilepton $p_T^{\bar{\ell}}$ (lower row). Measurements are performed at particle level in a fiducial phase space. The data (black) are compared to the MC predictions from POWHEG v2+PYTHIA8 (red), POWHEG v2+HERWIG++ (violet) and MG5_aMC@NLO+PYTHIA8 [FxFx] (green). The inner error bars show the statistical uncertainty, the outer error bars show a combination of the statistical and systematic uncertainties.

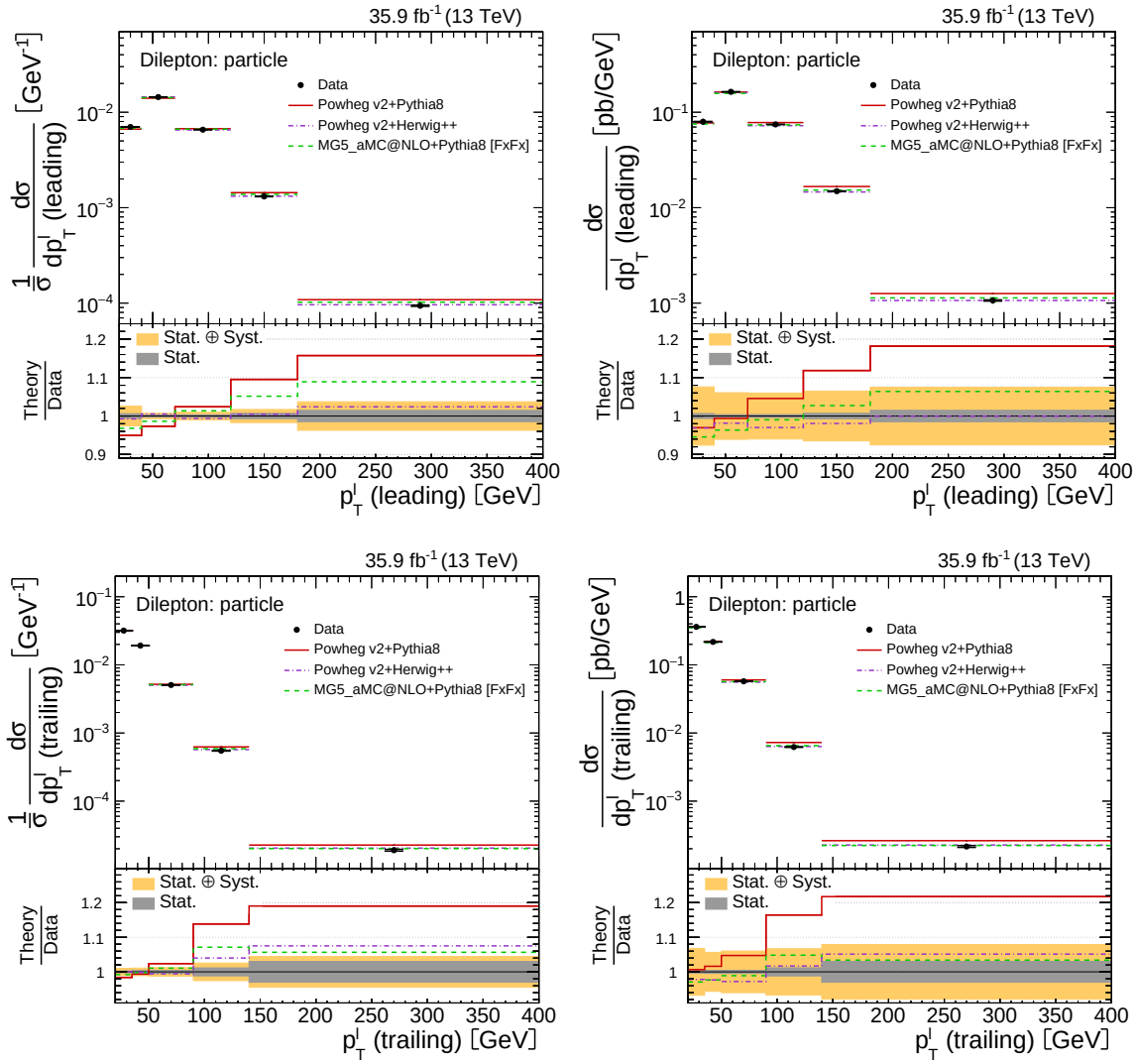

Figure 7.21 The normalized (left) and absolute (right) differential $t\bar{t}$ production cross sections as a function of the transverse momentum of the leading lepton p_T^{ℓ} *(leading)* (upper row) and as a function of the transverse momentum of the trailing lepton p_T^{ℓ} *(trailing)* (lower row). Measurements are performed at particle level in a fiducial phase space. The data (black) are compared to the MC predictions from Powheg v2+Pythia8 (red), Powheg v2+Herwig++ (violet) and MG5_aMC@NLO+Pythia8 [FxFx] (green). The inner error bars show the statistical uncertainty, the outer error bars show a combination of the statistical and systematic uncertainties.

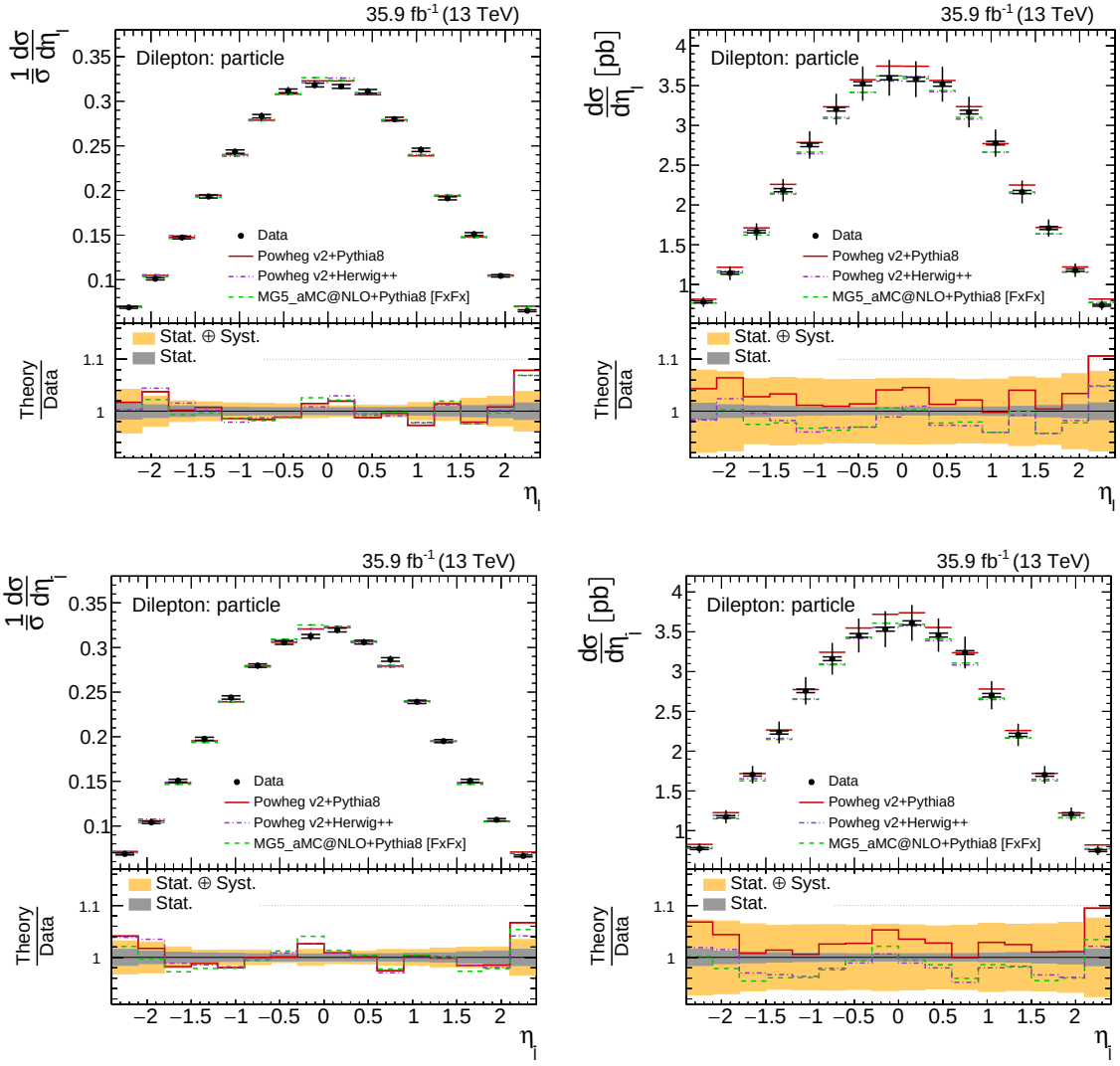

Figure 7.22 The normalized (left) and absolute (right) differential $t\bar{t}$ production cross sections as a function of the pseudorapidity of the lepton η_ℓ (upper row) and as a function of the pseudorapidity of the antilepton $\eta_{\bar{\ell}}$ (lower row). Measurements are performed at particle level in a fiducial phase space. The data (black) are compared to the MC predictions from POWHEG V2+PYTHIA8 (red), POWHEG V2+HERWIG++ (violet) and MG5_aMC@NLO+PYTHIA8 [FXFX] (green). The inner error bars show the statistical uncertainty, the outer error bars show a combination of the statistical and systematic uncertainties.

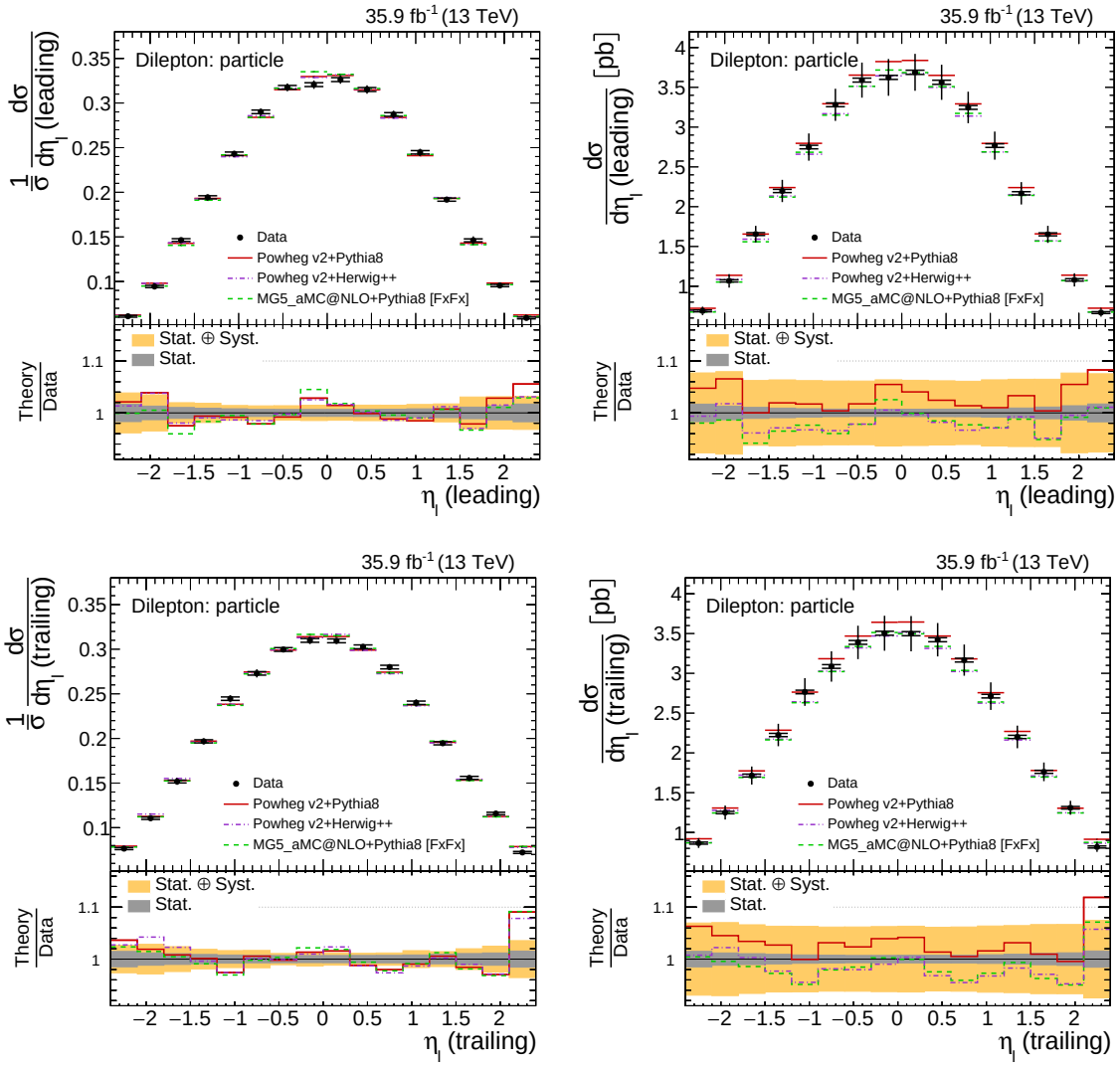

Figure 7.23 The normalized (left) and absolute (right) differential $t\bar{t}$ production cross sections as a function of the pseudorapidity of the leading lepton η_ℓ *(leading)* (upper row) and as a function of the pseudorapidity of the trailing lepton η_ℓ *(trailing)* (lower row). Measurements are performed at particle level in a fiducial phase space. The data (black) are compared to the MC predictions from POWHEG v2+PYTHIA8 (red), POWHEG v2+HERWIG++ (violet) and MG5_aMC@NLO+PYTHIA8 [FxFx] (green). The inner error bars show the statistical uncertainty, the outer error bars show a combination of the statistical and systematic uncertainties.

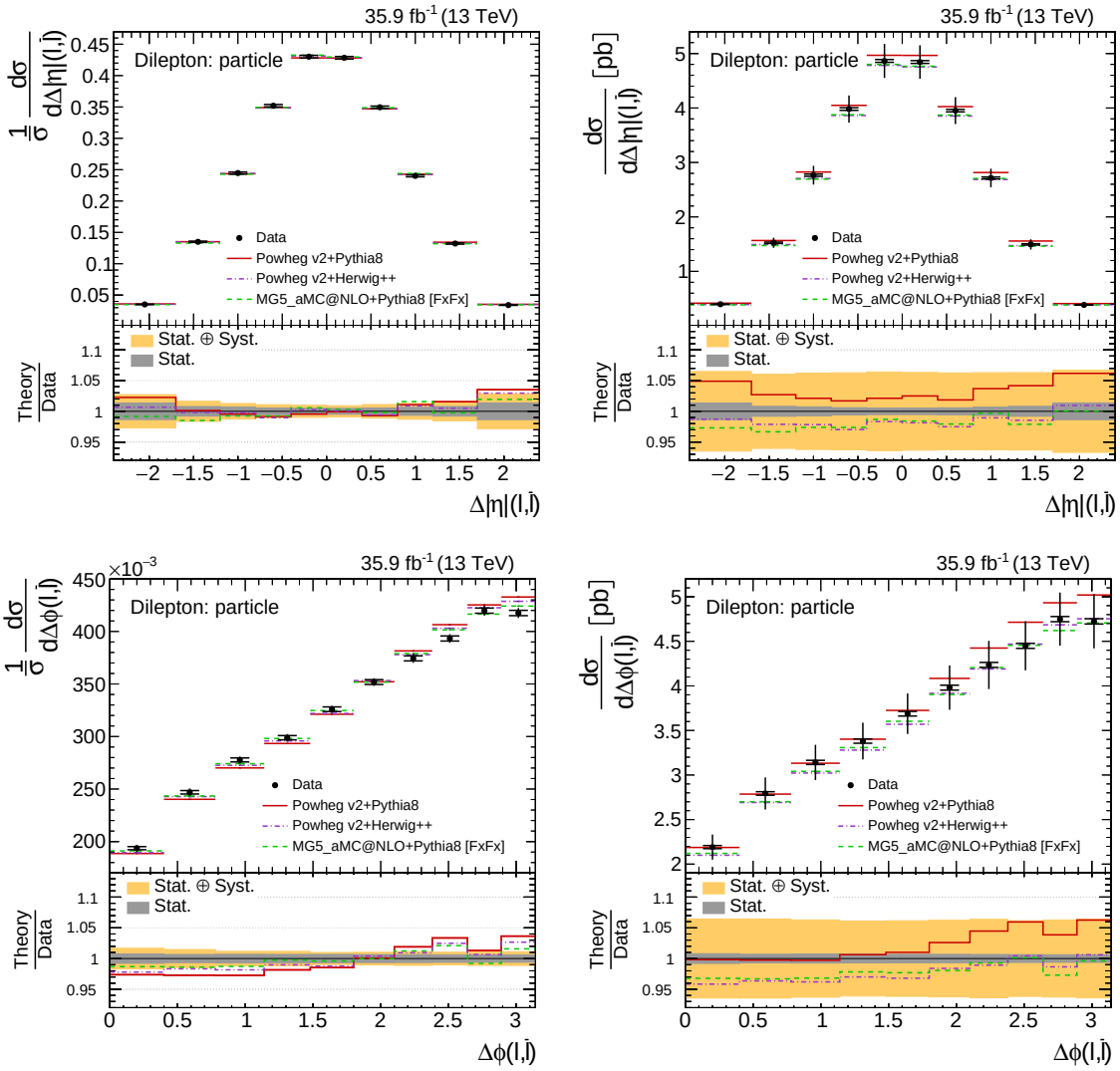

Figure 7.24 The normalized (left) and absolute (right) differential $t\bar{t}$ production cross sections as a function of the difference in absolute pseudorapidity between the lepton and antilepton $\Delta|\eta|(\ell,\bar{\ell})$ (upper row) and as a function of the difference in azimuthal angle between the lepton and antilepton $\Delta\phi(\ell,\bar{\ell})$ (lower row). Measurements are performed at particle level in a fiducial phase space. The data (black) are compared to the MC predictions from POWHEG v2+PYTHIA8 (red), POWHEG v2+HERWIG++ (violet) and MG5_aMC@NLO+PYTHIA8 [FxFx] (green). The inner error bars show the statistical uncertainty, the outer error bars show a combination of the statistical and systematic uncertainties.

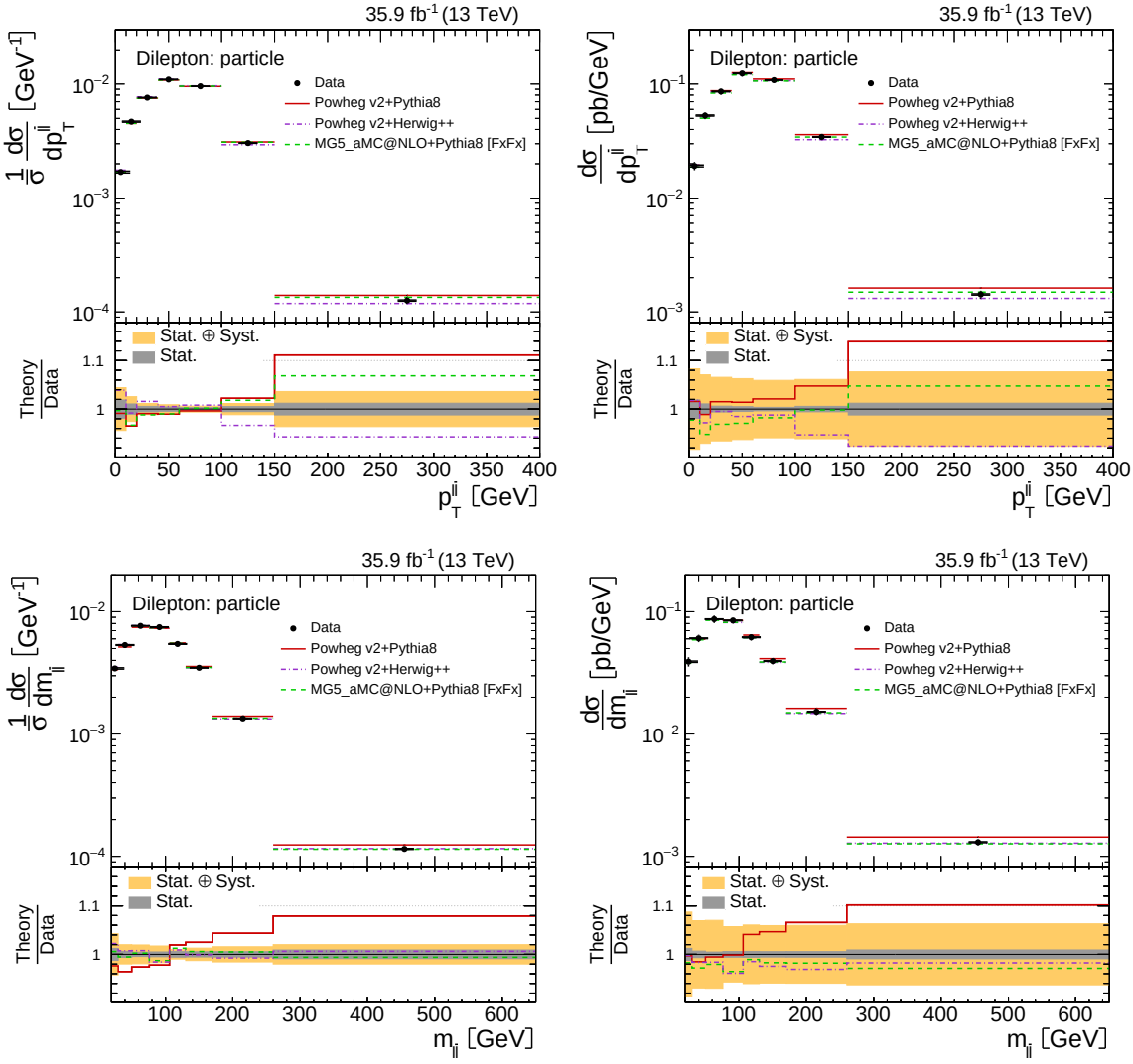

Figure 7.25 The normalized (left) and absolute (right) differential $t\bar{t}$ production cross sections as a function of the transverse momentum of the lepton pair $p_T^{\ell\bar{\ell}}$ (upper row) and as a function of the invariant mass of the lepton pair $m_{\ell\bar{\ell}}$ (lower row). Measurements are performed at particle level in a fiducial phase space. The data (black) are compared to the MC predictions from POWHEG v2+PYTHIA8 (red), POWHEG v2+HERWIG++ (violet) and MG5_aMC@NLO+PYTHIA8 [FxFx] (green). The inner error bars show the statistical uncertainty, the outer error bars show a combination of the statistical and systematic uncertainties.

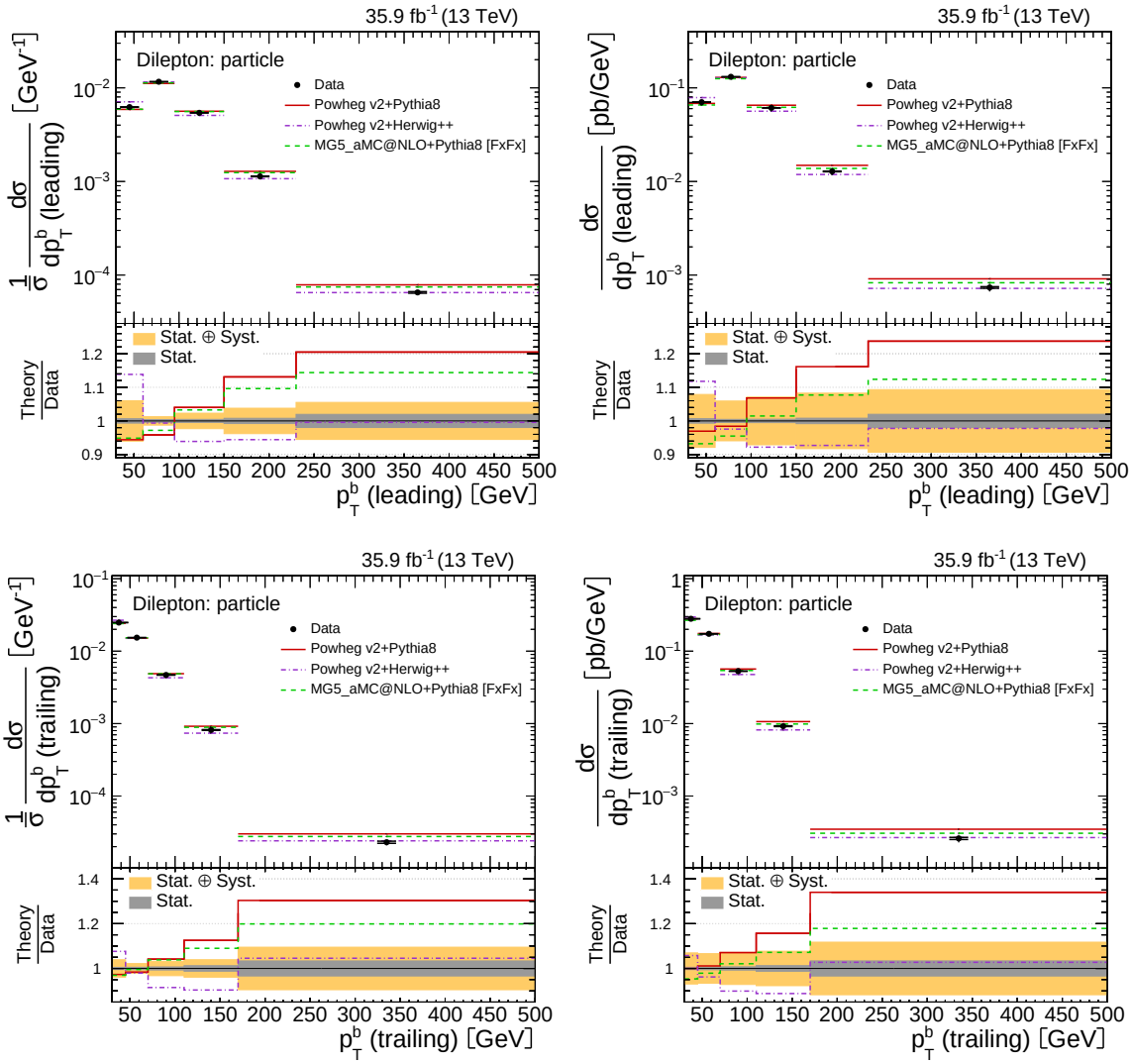

Figure 7.26 The normalized (left) and absolute (right) differential $t\bar{t}$ production cross sections as a function of the transverse momentum of the leading b-jet p_T^b *(leading)* (upper row) and as a function of the transverse momentum of the trailing b-jet p_T^b *(trailing)* (lower row). Measurements are performed at particle level in a fiducial phase space. The data (black) are compared to the MC predictions from POWHEG v2+PYTHIA8 (red), POWHEG v2+HERWIG++ (violet) and MG5_aMC@NLO+PYTHIA8 [FxFx] (green). The inner error bars show the statistical uncertainty, the outer error bars show a combination of the statistical and systematic uncertainties.

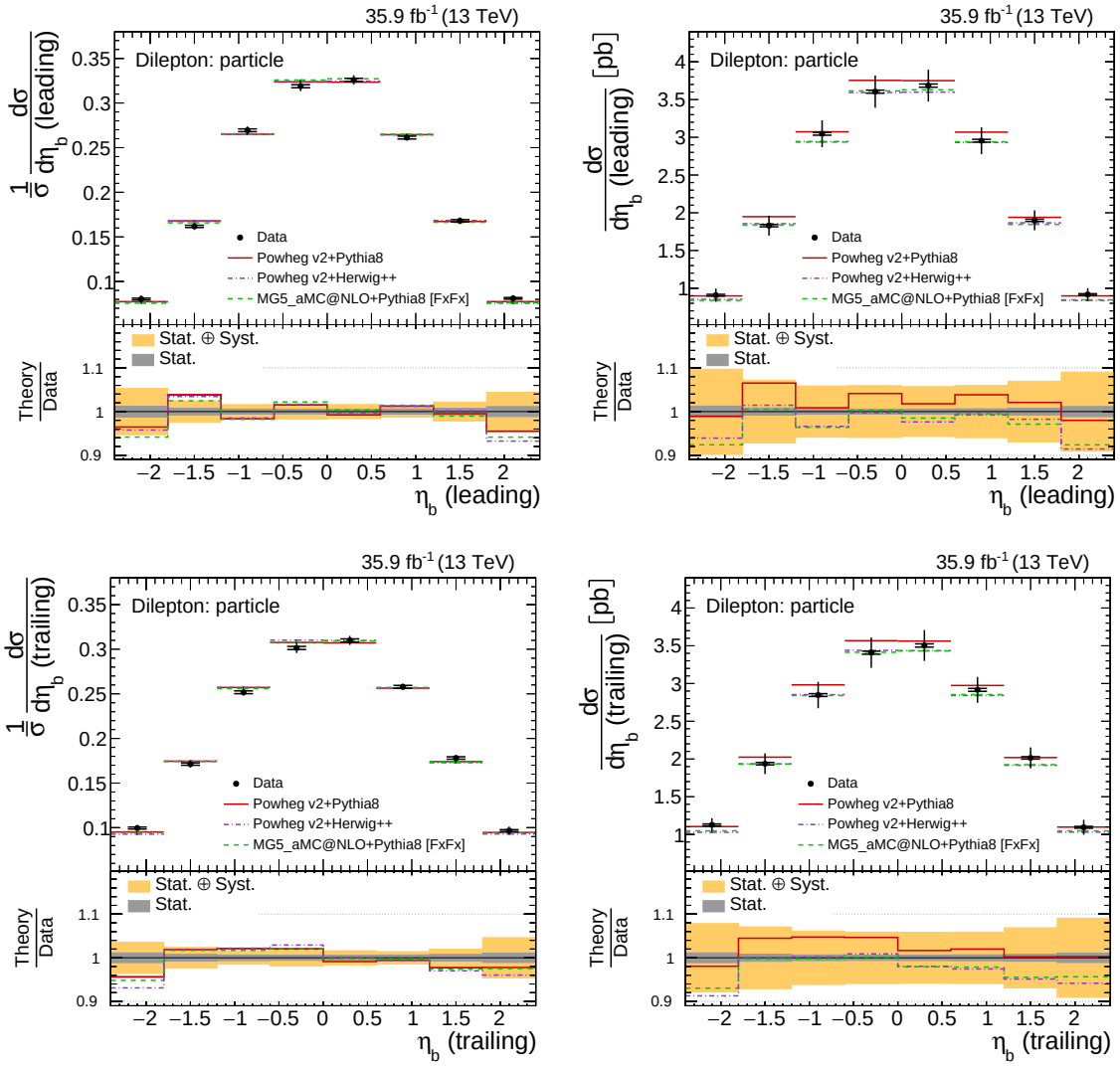

Figure 7.27 The normalized (left) and absolute (right) differential $t\bar{t}$ production cross sections as a function of the pseudorapidity of the leading b-jet η_b *(leading)* (upper row) and as a function of the pseudorapidity of the trailing b-jet η_b *(trailing)* (lower row). Measurements are performed at particle level in a fiducial phase space. The data (black) are compared to the MC predictions from Powheg v2+Pythia8 (red), Powheg v2+Herwig++ (violet) and MG5_aMC@NLO+Pythia8 [FxFx] (green). The inner error bars show the statistical uncertainty, the outer error bars show a combination of the statistical and systematic uncertainties.

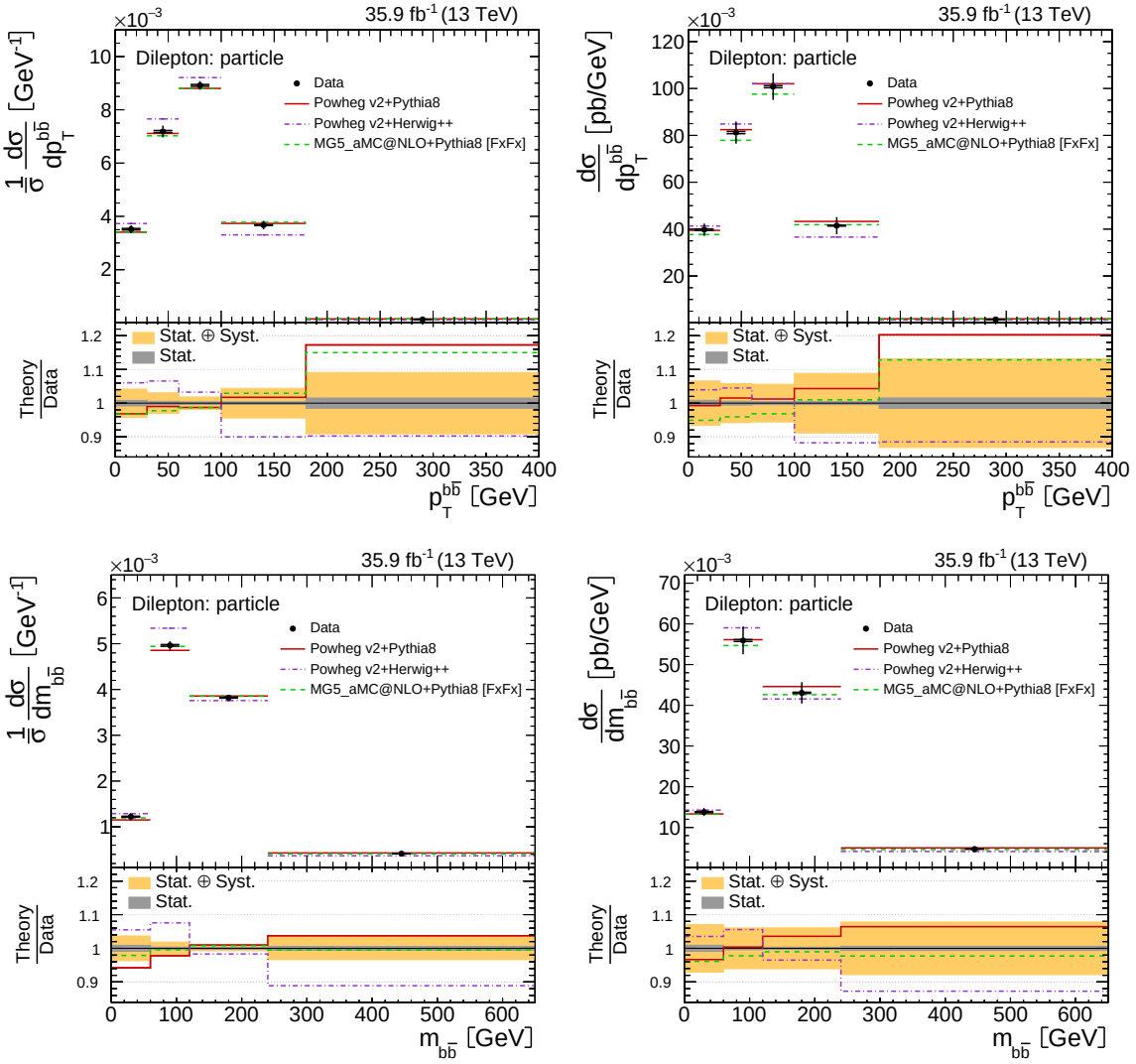

Figure 7.28 The normalized (left) and absolute (right) differential $t\bar{t}$ production cross sections as a function of the transverse momentum of the b-jet pair $p_T^{b\bar{b}}$ (upper row) and as a function of the invariant mass of the b-jet pair $m_{b\bar{b}}$ (lower row). Measurements are performed at particle level in a fiducial phase space. The data (black) are compared to the MC predictions from POWHEG v2+PYTHIA8 (red), POWHEG v2+HERWIG++ (violet) and MG5_aMC@NLO+PYTHIA8 [FxFx] (green). The inner error bars show the statistical uncertainty, the outer error bars show a combination of the statistical and systematic uncertainties.

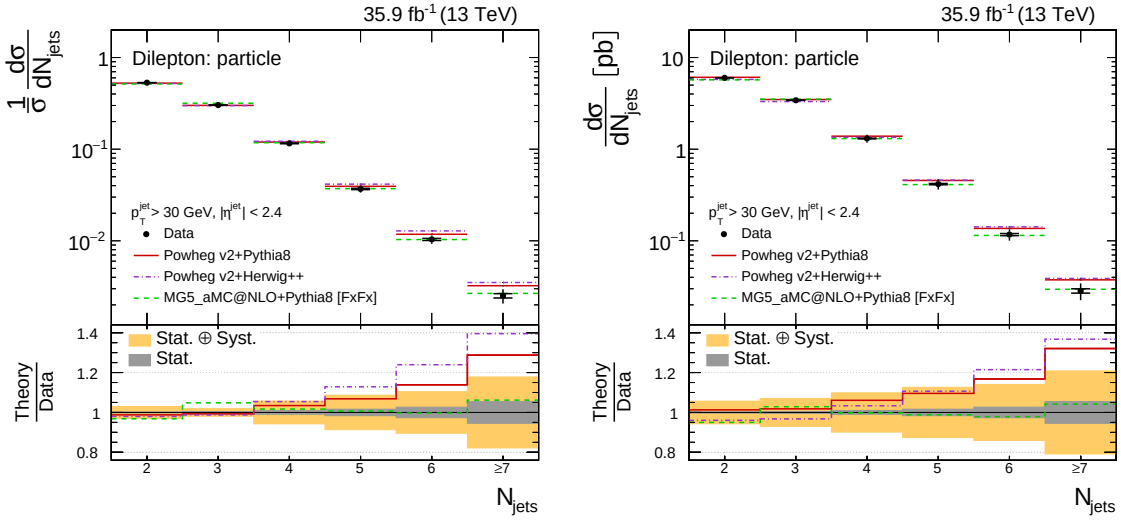

Figure 7.29 The normalized (left) and absolute (right) differential $t\bar{t}$ production cross sections as a function of the jet multiplicity N_{jets}. Measurements are performed at particle level in a fiducial phase space. The data (black) are compared to the MC predictions from POWHEG v2+PYTHIA8 (red), POWHEG v2+HERWIG++ (violet) and MG5_aMC@NLO+PYTHIA8 [FXFX] (green). The inner error bars show the statistical uncertainty, the outer error bars show a combination of the statistical and systematic uncertainties.

Table 7.2 The $\chi^2/ndof$ and p-values quantifying the agreement between the data and MC predictions are shown for normalized differential measurements performed at parton level.

Observable	Powheg v2+Pythia8		Powheg v2+Herwig++		MG5_aMC@NLO+Pythia8	
	$\chi^2/ndof$	p-value	$\chi^2/ndof$	p-value	$\chi^2/ndof$	p-value
p_T^t	63/5	< 0.01	9.6/5	0.09	28/5	< 0.01
$p_T^{\bar{t}}$	3.9e+02/5	< 0.01	83/5	< 0.01	2e+02/5	< 0.01
p_T^t *(leading)*	1.5e+02/5	< 0.01	18/5	< 0.01	90/5	< 0.01
p_T^t *(trailing)*	1.6e+02/5	< 0.01	41/5	< 0.01	68/5	< 0.01
p_T^t *($t\bar{t}$ r. f.)*	96/5	< 0.01	13/5	0.02	45/5	< 0.01
$p_T^{\bar{t}}$ *($t\bar{t}$ r. f.)*	96/5	< 0.01	13/5	0.02	45/5	< 0.01
y_t	12/9	0.22	9.3/9	0.41	6.7/9	0.67
$y_{\bar{t}}$	6.7/9	0.66	5/9	0.83	3.7/9	0.93
y_t *(leading)*	3.3/7	0.86	2.8/7	0.90	4.6/7	0.71
y_t *(trailing)*	6.6/7	0.47	5.4/7	0.61	4/7	0.78
$\Delta\|y\|(t,\bar{t})$	2.4/7	0.93	4.4/7	0.73	7.4/7	0.39
$\Delta\phi(t,\bar{t})$	0.24/3	0.97	19/3	< 0.01	2.7/3	0.43
$p_T^{t\bar{t}}$	25/5	< 0.01	1.8e+02/5	< 0.01	16/5	< 0.01
$m_{t\bar{t}}$	1.7e+02/6	< 0.01	5.1/6	0.53	30/6	< 0.01
$y_{t\bar{t}}$	4.1/9	0.91	4.3/9	0.89	4.4/9	0.89

Table 7.3 The $\chi^2/ndof$ and p-values quantifying the agreement between the data and MC predictions are shown for absolute differential measurements performed at parton level.

Observable	Powheg v2+Pythia8		Powheg v2+Herwig++		MG5_aMC@NLO+Pythia8	
	$\chi^2/ndof$	p-value	$\chi^2/ndof$	p-value	$\chi^2/ndof$	p-value
p_T^t	51/6	< 0.01	8/6	0.24	18/6	< 0.01
$p_T^{\bar{t}}$	41/6	< 0.01	9.3/6	0.16	14/6	0.03
p_T^t *(leading)*	47/6	< 0.01	4.4/6	0.63	20/6	< 0.01
p_T^t *(trailing)*	38/6	< 0.01	16/6	0.01	9.5/6	0.15
p_T^t *($t\bar{t}$ r. f.)*	40/6	< 0.01	11/6	0.08	13/6	0.05
$p_T^{\bar{t}}$ *($t\bar{t}$ r. f.)*	40/6	< 0.01	11/6	0.08	13/6	0.05
y_t	5.4/10	0.86	5.1/10	0.88	4.2/10	0.94
$y_{\bar{t}}$	2.5/10	0.99	2.4/10	0.99	3/10	0.98
y_t *(leading)*	2.8/8	0.95	2.4/8	0.97	3.2/8	0.92
y_t *(trailing)*	2.6/8	0.96	3.3/8	0.91	2.1/8	0.98
$\Delta\|y\|(t,\bar{t})$	1.4/8	0.99	3.5/8	0.90	4.1/8	0.85
$\Delta\phi(t,\bar{t})$	0.43/4	0.98	2.7/4	0.61	2/4	0.74
$p_T^{t\bar{t}}$	22/6	< 0.01	36/6	< 0.01	12/6	0.05
$m_{t\bar{t}}$	12/7	0.11	2.8/7	0.91	6.1/7	0.53
$y_{t\bar{t}}$	3.5/10	0.97	4.1/10	0.94	5/10	0.89

Table 7.4 The $\chi^2/ndof$ and p-values quantifying the agreement between the data and MC predictions are shown for normalized differential measurements performed at particle level.

Observable	Powheg v2+Pythia8		Powheg v2+Herwig++		MG5_aMC@NLO+Pythia8	
	$\chi^2/ndof$	p-value	$\chi^2/ndof$	p-value	$\chi^2/ndof$	p-value
p_T^t	1.3e+02/5	< 0.01	6/5	0.31	45/5	< 0.01
$p_T^{\bar{t}}$	5.2e+02/5	< 0.01	3.5/5	0.63	2.3e+02/5	< 0.01
p_T^t *(leading)*	2e+02/5	< 0.01	4.7/5	0.46	1.1e+02/5	< 0.01
p_T^t *(trailing)*	2e+02/5	< 0.01	9/5	0.11	68/5	< 0.01
p_T^t *($t\bar{t}$ r. f.)*	1.5e+02/5	< 0.01	20/5	< 0.01	58/5	< 0.01
$p_T^{\bar{t}}$ *($t\bar{t}$ r. f.)*	1.5e+02/5	< 0.01	20/5	< 0.01	58/5	< 0.01
y_t	6.7/9	0.67	11/9	0.31	11/9	0.28
$y_{\bar{t}}$	3.1/9	0.96	3.5/9	0.94	3.4/9	0.94
y_t *(leading)*	8.1/7	0.32	6.5/7	0.48	8.2/7	0.31
y_t *(trailing)*	4.7/7	0.70	5.5/7	0.60	4/7	0.78
$\Delta\|y\|(t,\bar{t})$	2/7	0.96	7.2/7	0.41	3.9/7	0.80
$\Delta\phi(t,\bar{t})$	1.9/3	0.60	4.5/3	0.21	12/3	< 0.01
$p_T^{t\bar{t}}$	34/5	< 0.01	2.2e+02/5	< 0.01	17/5	< 0.01
$m_{t\bar{t}}$	15/6	0.02	39/6	< 0.01	4.6/6	0.60
$y_{t\bar{t}}$	5.6/9	0.78	6/9	0.74	4.9/9	0.85
p_T^{ℓ}	1.3e+02/4	< 0.01	3.2/4	0.53	41/4	< 0.01
$p_T^{\bar{\ell}}$	42/4	< 0.01	1/4	0.91	11/4	0.03
p_T^{ℓ} *(leading)*	2.4e+02/4	< 0.01	4.6/4	0.33	75/4	< 0.01
p_T^{ℓ} *(trailing)*	1.6e+02/4	< 0.01	9.4/4	0.05	39/4	< 0.01
η_{ℓ}	24/15	0.07	27/15	0.03	26/15	0.04
$\eta_{\bar{\ell}}$	32/15	< 0.01	32/15	< 0.01	37/15	< 0.01
η_{ℓ} *(leading)*	13/15	0.58	14/15	0.56	23/15	0.08
η_{ℓ} *(trailing)*	25/15	0.05	37/15	< 0.01	35/15	< 0.01
$\Delta\|\eta\|(\ell,\bar{\ell})$	7/9	0.64	5.4/9	0.80	7.1/9	0.63
$\Delta\phi(\ell,\bar{\ell})$	35/9	< 0.01	17/9	0.04	13/9	0.15
$p_T^{\ell\bar{\ell}}$	14/6	0.03	17/6	< 0.01	7.7/6	0.26
$m_{\ell\bar{\ell}}$	1.4e+02/7	< 0.01	3.8/7	0.80	5.3/7	0.63
p_T^b *(leading)*	32/4	< 0.01	75/4	< 0.01	16/4	< 0.01
p_T^b *(trailing)*	28/4	< 0.01	1.3e+02/4	< 0.01	19/4	< 0.01
η_b *(leading)*	12/7	0.11	15/7	0.03	22/7	< 0.01
η_b *(trailing)*	16/7	0.02	16/7	0.02	12/7	0.11
$p_T^{b\bar{b}}$	25/4	< 0.01	3.3e+02/4	< 0.01	38/4	< 0.01
$m_{b\bar{b}}$	3.1/3	0.37	17/3	< 0.01	1.2/3	0.75
N_{jets}	13/5	0.02	38/5	< 0.01	90/5	< 0.01

Table 7.5 The $\chi^2/ndof$ and p-values quantifying the agreement between the data and MC predictions are shown for absolute differential measurements performed at particle level.

Observable	POWHEG v2+PYTHIA8		POWHEG v2+HERWIG++		MG5_aMC@NLO+PYTHIA8	
	$\chi^2/ndof$	p-value	$\chi^2/ndof$	p-value	$\chi^2/ndof$	p-value
p_T^t	52/6	< 0.01	2.8/6	0.83	17/6	< 0.01
p_T^t	44/6	< 0.01	3.2/6	0.79	16/6	0.01
p_T^t *(leading)*	50/6	< 0.01	3.4/6	0.76	21/6	< 0.01
p_T^t *(trailing)*	39/6	< 0.01	4.8/6	0.58	11/6	0.10
p_T^t *($t\bar{t}$ r. f.)*	38/6	< 0.01	3.8/6	0.71	12/6	0.05
$p_T^{\bar{t}}$ *($t\bar{t}$ r. f.)*	38/6	< 0.01	3.8/6	0.71	12/6	0.05
y_t	6.4/10	0.78	8/10	0.63	6.2/10	0.80
$y_{\bar{t}}$	2.6/10	0.99	3/10	0.98	2.9/10	0.98
y_t *(leading)*	3.1/8	0.93	3.6/8	0.89	4.2/8	0.84
y_t *(trailing)*	2.9/8	0.94	4.1/8	0.85	2.2/8	0.97
$\Delta\|y\|(t,\bar{t})$	1.4/8	0.99	6.5/8	0.60	3.4/8	0.91
$\Delta\phi(t,\bar{t})$	0.49/4	0.97	0.4/4	0.98	1.5/4	0.82
$p_T^{t\bar{t}}$	34/6	< 0.01	29/6	< 0.01	17/6	0.01
$m_{t\bar{t}}$	12/7	0.09	11/7	0.14	4.9/7	0.68
$y_{t\bar{t}}$	3.5/10	0.97	6.4/10	0.78	5.5/10	0.86
p_T^{ℓ}	36/5	< 0.01	2.5/5	0.77	11/5	0.06
$p_T^{\bar{\ell}}$	35/5	< 0.01	1.1/5	0.95	9.4/5	0.09
p_T^{ℓ} *(leading)*	41/5	< 0.01	2.8/5	0.73	12/5	0.04
p_T^{ℓ} *(trailing)*	33/5	< 0.01	5.1/5	0.40	5.9/5	0.32
η_{ℓ}	18/16	0.34	20/16	0.21	20/16	0.23
$\eta_{\bar{\ell}}$	29/16	0.02	28/16	0.03	33/16	< 0.01
η_{ℓ} *(leading)*	11/16	0.78	12/16	0.77	17/16	0.39
η_{ℓ} *(trailing)*	21/16	0.19	29/16	0.02	24/16	0.09
$\Delta\|\eta\|(\ell,\bar{\ell})$	5.6/10	0.85	4.3/10	0.93	5.7/10	0.84
$\Delta\phi(\ell,\bar{\ell})$	27/10	< 0.01	13/10	0.24	9.6/10	0.48
$p_T^{\ell\bar{\ell}}$	14/7	0.05	11/7	0.12	6.1/7	0.52
$m_{\ell\bar{\ell}}$	37/8	< 0.01	2.8/8	0.95	4.5/8	0.81
p_T^b *(leading)*	35/5	< 0.01	9.7/5	0.08	17/5	< 0.01
p_T^b *(trailing)*	27/5	< 0.01	10/5	0.06	11/5	0.05
η_b *(leading)*	10/8	0.25	11/8	0.19	7.8/8	0.45
η_b *(trailing)*	11/8	0.20	12/8	0.15	7.8/8	0.46
$p_T^{b\bar{b}}$	12/5	0.03	9.3/5	0.10	6.9/5	0.23
$m_{b\bar{b}}$	2.8/4	0.58	16/4	< 0.01	1.1/4	0.90
N_{jets}	14/6	0.04	37/6	< 0.01	18/6	< 0.01

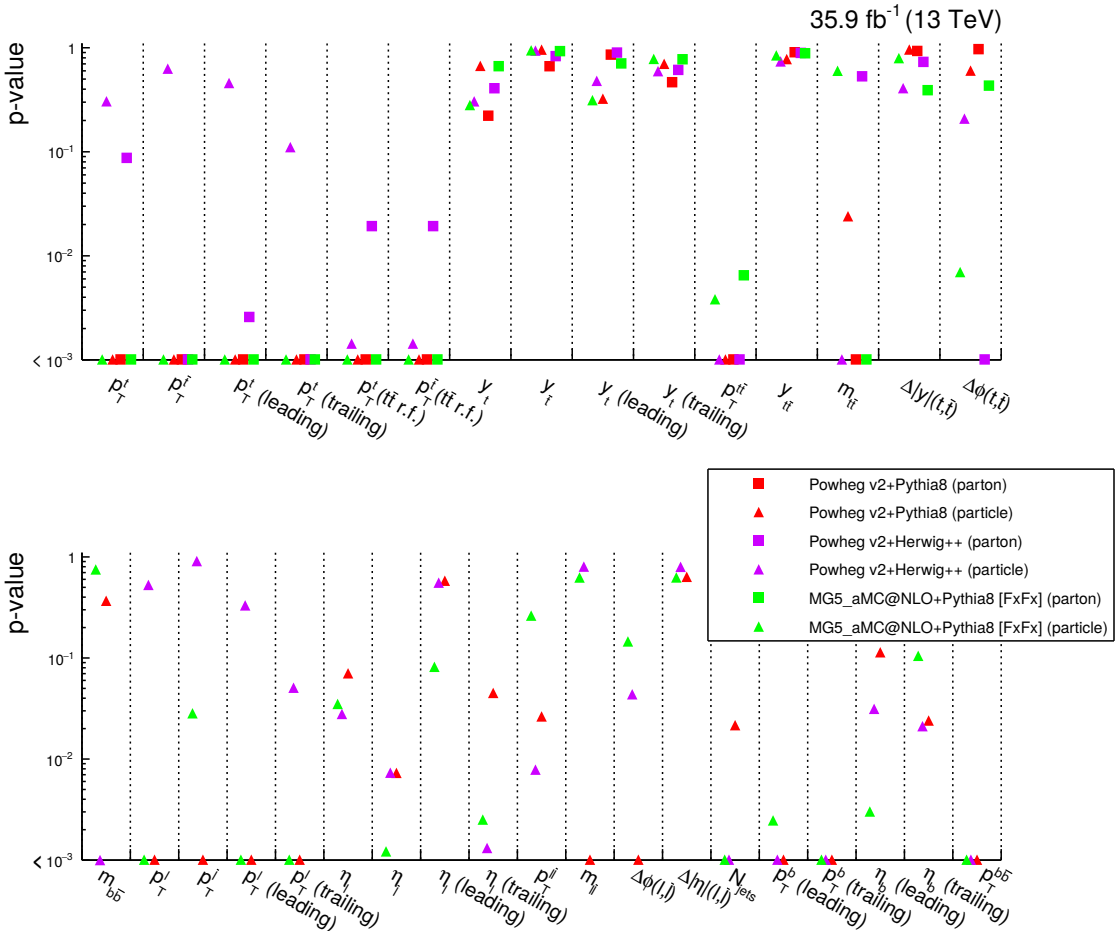

Figure 7.30 The p-values quantifying the agreement between the data and considered MC predictions for all normalized differential measurements. The p-values which are less than 0.001 are indicated by the markers on the horizontal axes.

7.4 Extraction of charge asymmetries

At beyond-LO accuracy, the SM predicts a nonzero charge asymmetry in the $t\bar{t}$ production occurring through $q\bar{q}$ annihilation [14]. This charge asymmetry, referred to as $A_C^{t\bar{t}}$, implies an excess of top quarks with respect to top antiquarks in certain regions of the phase space. As shown in Figure 7.31, it originates from the interference between the ISR and FSR diagrams and from the interference between the box and the LO diagram.

From the momentum conservation, after the $q\bar{q}$ annihilation, the top (anti)quark tends to be emitted in similar direction as the incoming q ($\bar{q}$). At the LHC, the $\bar{q}$ is always the sea quark (from a proton). The q can be a valence quark (from another proton) and, thus, having typically larger longitudinal momentum than $\bar{q}$. This leads to a higher production rate of top quarks in the forward region, which results into a broader rapidity distribution than for top antiquarks. Therefore, at the LHC, a different centrality in the rapidity of top quarks is observed with respect to top antiquarks; the principle is shown in Figure 7.31. Thus, the normalized differential cross sections measured as a function of the difference in absolute rapidity between the top quark and antiquark ($\Delta|y|(t,\bar{t})$) can be used to extract $A_C^{t\bar{t}}$. In this work, the extraction of $A_C^{t\bar{t}}$ is performed using results obtained at the parton and particle levels (see Figure 7.15). In addition, similarly, the extraction of the leptonic charge asymmetry in the $t\bar{t}$ dilepton events ($A_C^{\ell\bar{\ell}}$) is performed using the normalized results obtained as a function of difference in absolute pseudorapidity between the lepton and antilepton ($\Delta|\eta|(\ell,\bar{\ell})$), shown in Figure 7.24. The $A_C^{t\bar{t}}$ and $A_C^{\ell\bar{\ell}}$ are defined as

$$A_C^{t\bar{t}} = \frac{\sigma_{t\bar{t}}(\Delta|y|(t,\bar{t}) > 0) - \sigma_{t\bar{t}}(\Delta|y|(t,\bar{t}) < 0)}{\sigma_{t\bar{t}}(\Delta|y|(t,\bar{t}) > 0) + \sigma_{t\bar{t}}(\Delta|y|(t,\bar{t}) < 0)}, \quad A_C^{\ell\bar{\ell}} = \frac{\sigma_{t\bar{t}}(\Delta|\eta|(\ell,\bar{\ell}) > 0) - \sigma_{t\bar{t}}(\Delta|\eta|(\ell,\bar{\ell}) < 0)}{\sigma_{t\bar{t}}(\Delta|\eta|(\ell,\bar{\ell}) > 0) + \sigma_{t\bar{t}}(\Delta|\eta|(\ell,\bar{\ell}) < 0)},$$

where $\sigma_{t\bar{t}}$ denotes the measured differential $t\bar{t}$ production cross section integrated over the specified region.

The $A_C^{t\bar{t}}$ and $A_C^{\ell\bar{\ell}}$ can be enhanced by different beyond-SM scenarios with particle states coupling to top quarks, e.g. axigluons [15] and Z' bosons [16]. Since the measurement of the lepton pair does not require a kinematic reconstruction of the top-quark pair, the $A_C^{\ell\bar{\ell}}$ has better resolution with respect to $A_C^{t\bar{t}}$, which leads to more precise extraction of the former. However, the $A_C^{\ell\bar{\ell}}$ is only partially sensitive to the effects of the charge asymmetry in the $t\bar{t}$ production, since those are diluted through all decay products of top quarks.

Results of the extraction of both asymmetries from the data are shown in Figure 7.32, indicating the corresponding 68% and 95% confidence intervals. The confidence intervals are determined using the uncertainties on the measured data in each differential bin (of $\Delta|y|(t,\bar{t})$ or $\Delta|\eta|(\ell,\bar{\ell})$) and accounting for the correlations among bins [166]. The results are compared

to the SM predictions from POWHEG v2+PYTHIA8 and MG5_aMC@NLO+PYTHIA8 [FxFx], as well as to the NLO-accurate QCD calculations including electroweak corrections [167]. A good agreement is observed between the data and all considered predictions.

The presented $A_C^{t\bar{t}}$ and $A_C^{\ell\bar{\ell}}$ are the first measurements of these asymmetries in pp-collisions at 13 TeV.

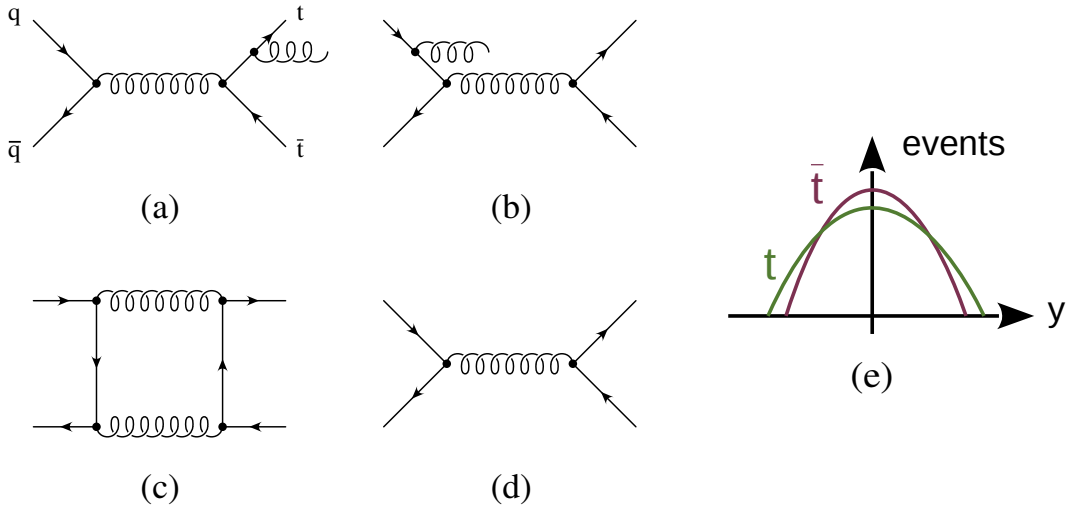

Figure 7.31 Feynman diagrams (a)-(d), from [14] (modified), represent the origin of the charge asymmetry in the $t\bar{t}$ production via $q\bar{q}$ annihilation from the two interferences between: the FSR (a) and the ISR (b) diagram, the box (c) and the LO (d) diagram. Subfigure (e) demonstrates the principle of observed differences in the centrality of rapidities between the top quarks and antiquarks at the LHC.

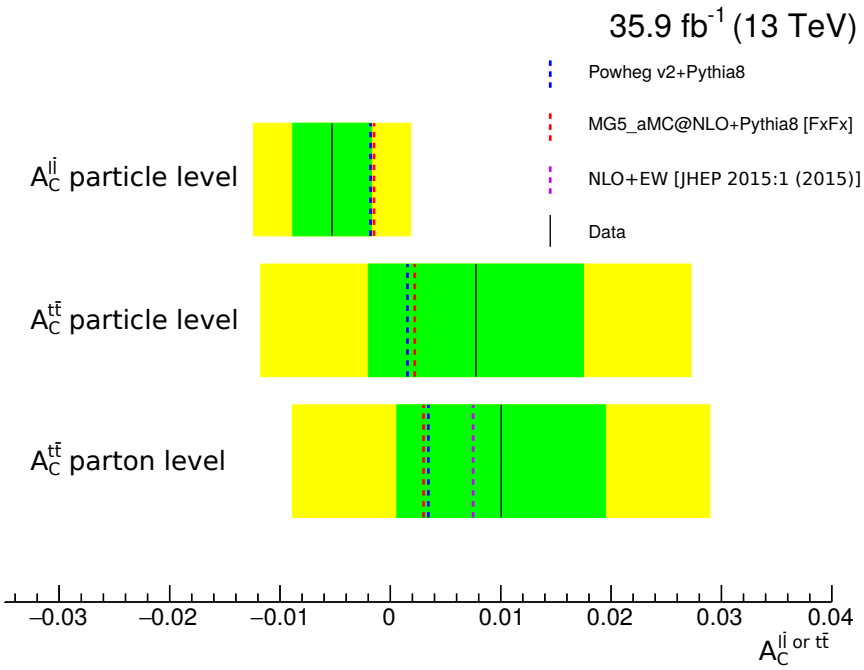

Figure 7.32 The extracted charge asymmetries $A_C^{t\bar{t}}$ and $A_C^{\ell\bar{\ell}}$ from the normalized differential cross section measurements performed at parton and particle levels. The data (black line), shown together with the 68% (green band) and 95 % (yellow band) confidence intervals, are compared to the SM predictions from: Powheg v2+Pythia8, MG5_aMC@NLO+Pythia8 [FxFx] and the NLO-accurate QCD calculations including the electroweak (EW) corrections. The presented results are the first measurements of corresponding asymmetries in *pp*-collisions at 13 TeV.

7.5 Constraining the chromomagnetic dipole moment of the top quark in an EFT

This section describes the result on constraining the chromomagnetic dipole moment of the top quark using the absolute differential $t\bar{t}$ production cross sections measured as a function of $\Delta\phi(\ell,\bar{\ell})$ at particle level, presented in Section 7.3.

7.5.1 Theoretical context

New physics could manifest itself as the production of new particles that decay or strongly couple to top quarks [168–170]. Many new physics scenarios predict corresponding particle states that are light enough to be directly produced at the LHC. However, no signals of such particle states have been observed at the LHC to date. Alternatively, one could consider that new physics is directly manifested at an energy scale (Λ_{NP}) that is larger than energy scales (Λ_{LHC}) within the direct reach of the LHC, which implies that new particles can be produced only virtually. In such scenarios, new physics manifests as a modification of the production rates and event kinematics of known processes that involve top quarks.

The effects of new physics Λ_{NP} on the LHC observables can be theoretically modelled in the framework of an effective field theory (EFT) [171], an approach that is based on the extension of the SM Lagrangian via the addition of a limited number of higher-dimensional operators. This approach allows a model-independent way to probe new-physics phenomena at the corresponding energy scales, i.e. the EFT approach is not tailored to a particular model of new physics.

Requiring the SM symmetries, the leading EFT operators that involve top quarks arise at dimension-6 and the extended Lagrangian can be written as [172]

$$\mathcal{L}_{EFT} = \mathcal{L}_{SM} + \sum_i \frac{C_i}{\Lambda_{NP}^2} O_i + h.c., \tag{7.2}$$

where O_i are the aforementioned dimension-6 operators and C_i are the dimensionless Wilson coefficients that parametrize the contribution of O_i to the Lagrangian, and $h.c.$ denotes a term that is the Hermitian conjugate of the preceding term. The size of the effects of new physics, induced by the particular operator O_i, is given by the ratio C_i/Λ_{NP}^2. In this way, new physics can be searched for by constraining the interesting values of C_i/Λ_{NP}^2 from the experimental data, which would require the use of relevant EFT predictions. For instance, to obtain the EFT predictions for top quark observables, one needs to identify the operators which affect

the processes involving top quarks, include these operators to the Lagrangian, and compute the sensitive observables as a function of C_i/Λ^2_{NP}.

The dimension-6 operator O_{tG} is known to provide the largest effect on the $t\bar{t}$ production [172]. The O_{tG} models the chromomagnetic and chromoelectric dipole moments (CMDM and CEDM, respectively) of the top quark. The Wilson coefficient associated with O_{tG} is referred to as C_{tG}, which real and imaginary parts correspond to the CMDM and CEDM, respectively. The addition of the O_{tG} to the SM Lagrangian modifies the $gt\bar{t}$ vertex and introduces a new $ggt\bar{t}$ vertex, causing a change in the rate and event dynamics of the $t\bar{t}$ production. In particular, the O_{tG} changes the chirality of top quarks, which alters the spin correlation between the top quark and antiquark. The tree-level Feynman diagrams for the $t\bar{t}$ production induced by O_{tG} are shown in Figure 7.33.

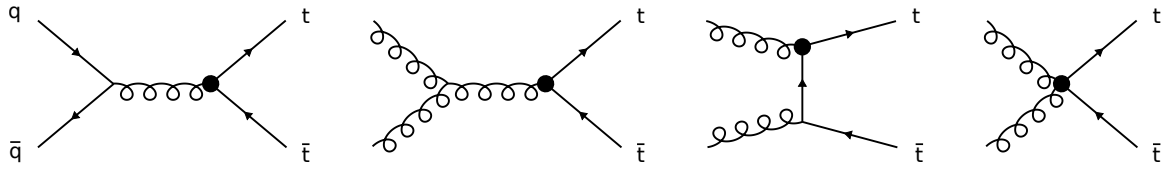

Figure 7.33 Examples of tree-level Feynman diagrams for the $t\bar{t}$ production induced by the dimension-6 EFT operator O_{tG}, which modifies the $gt\bar{t}$ vertex (effective vertices indicated by black dots) and introduces a new $ggt\bar{t}$ vertex (far-right). Only one effective vertex per diagram is assumed.

An NLO QCD calculation of the $t\bar{t}$ production at the 13 TeV LHC including the effects of O_{tG} has been performed in [172]. These calculations are performed up to order $O(\Lambda^{-2}_{NP})$ and, therefore, each Feynman diagram can include only up to one O_{tG}-induced vertex. In this case, the NLO cross section enhanced by O_{tG} is expressed as a quadratic function of C_{tG}/Λ^2_{NP}

$$\sigma_{SM+O_{tG}} = \sigma_{SM} + \frac{C_{tG}}{\Lambda^2_{NP}} \cdot \beta_1 + \left(\frac{C_{tG}}{\Lambda^2_{NP}}\right)^2 \cdot \beta_2, \tag{7.3}$$

where the term including β_1 (β_2) corresponds to the linear (quadratic) contributions in C_{tG}/Λ^2_{NP} at order $O(\Lambda^{-2}_{NP})$ ($O(\Lambda^{-4}_{NP})$). As the calculations are performed up to order $O(\Lambda^{-2}_{NP})$, the quadratic term does not have a physical meaning, e.g. diagrams with two O_{tG}-induced vertices, and consequently should be removed (see Section 7.5.2). Moreover, as concluded in [172], the contribution from the term including β_2 is negligible for the 13 TeV LHC, if the region is restricted to $C_{tG}/\Lambda^2_{NP} < 1$ TeV^{-2}. Thus, a linear dependence of $\sigma_{SM+O_{tG}}$ on C_{tG}/Λ^2_{NP} can be assumed in this region.

In this thesis, the C_{tG} is assumed to be real, which allows constraining the top quark CMDM only. Moreover, only the O_{tG} is assumed as non-vanishing operator for the $t\bar{t}$

production, i.e. any effects of new physics modelled in EFT are induced by O_{tG}. Both these assumptions follow the approach described in [172]. A nonzero CMDM of the top quark is predicted in many models of new physics such as the two-Higgs-doublet model [17], the little Higgs model [18], the minimal supersymmetric standard model [19], and the top quark compositeness model [20].

As given by Equation 7.3, the inclusive $t\bar{t}$ production cross section can be used to constrain the CMDM. However, as shown in [172], the shape of the distribution of the $\Delta\phi(\ell,\bar{\ell})$ is particularly sensitive to effects induced by O_{tG}. As previously mentioned, the distribution of $\Delta\phi(\ell,\bar{\ell})$ is sensitive to the spin correlations of the top-quark pair, which can be altered by O_{tG}. In order to account for the rate- and shape-dependent effects, the absolute differential distribution measured as a function of $\Delta\phi(\ell,\bar{\ell})$ at particle level, presented in Section 7.3, are used to constrain C_{tG}/Λ^2_{NP}. The use of the particle level measurement of this kind is beneficial owing to its reduced dependence on the extrapolation effects and the generator implementation, in comparison to the parton level results. Also, a generally-better precision of particle level measurements allows a more stringent constraint of C_{tG}/Λ^2_{NP}. The methodology used to constrain the C_{tG}/Λ^2_{NP} is described in the following.

7.5.2 Generation of differential predictions

As described previously, a prediction of the $t\bar{t}$ production induced by the top quark CMDM has been provided at NLO in QCD and the relevant calculations are implemented in MadGraph5_aMC@NLO [172]. This model can be used to obtain the predictions for the differential $t\bar{t}$ production cross sections as a function of $\Delta\phi(\ell,\bar{\ell})$ and C_{tG}/Λ^2_{NP}. In this thesis, such predictions are generated as follows. The aforementioned implementation in MadGraph5_aMC@NLO is used to generate the corresponding matrix elements for the $t\bar{t}$ production, at NLO accuracy and including contributions from the CMDM. The top quarks are decayed using MadSpin, preserving spin correlation and off-shell effects. Only final states that contain two prompt leptons (e or μ) are considered. The PS and hadronization is modelled in Pythia8. Finally, the generated predictions are propagated through the RIVET framework [173], which emulates the object and phase space definitions involved in the measurement of differential cross sections at particle level and produces the differential distributions of the interesting variables (here, $\Delta\phi(\ell,\bar{\ell})$).

The contribution to $\sigma_{SM+O_{tG}}$ from the quadratic term in C_{tG}/Λ^2_{NP} is removed according to the method suggested in [172]. The linear contribution to $\sigma_{SM+O_{tG}}$ induced by O_{tG} at

$C_{tG}/\Lambda^2_{NP} = 1$ TeV^{-2} can be isolated as given by

$$\sigma_{SM+O_{tG}}\left(\frac{C_{tG}}{\Lambda^2_{NP}} = 2\right) - \sigma_{SM+O_{tG}}\left(\frac{C_{tG}}{\Lambda^2_{NP}} = -2\right) = \\ \sigma_{SM} + 2\cdot\beta_1 + 2^2\cdot\beta_2 - \sigma_{SM} - (-2)\cdot\beta_1 - (-2)^2\cdot\beta_2 = 4\cdot\beta_1. \tag{7.4}$$

Here, coefficients $C_{tG}/\Lambda^2_{NP} = \pm 2$ are chosen according to [172]. The same idea is used to isolate the corresponding contribution for predictions of differential distributions. Firstly, three samples are generated with values $C_{tG}/\Lambda^2_{NP} = 0, \pm 2$ TeV^{-2}, where the sample with $C_{tG}/\Lambda^2_{NP} = 0$ TeV^{-2} corresponds to the SM scenario. Secondly, the $\Delta\phi(\ell,\bar{\ell})$ distribution generated with $C_{tG}/\Lambda^2_{NP} = -2$ TeV^{-2} is subtracted from the one generated with $C_{tG}/\Lambda^2_{NP} = 2$ TeV^{-2}. Thirdly, the obtained distribution is scaled by a factor 1/4, resulting into a distribution that contains only the linear contribution induced by O_{tG} at $C_{tG}/\Lambda^2_{NP} = 1$ TeV^{-2}, i.e. the distribution induced solely by β_1. Finally, to produce predictions for arbitrary values of C_{tG}/Λ^2_{NP}, the distribution derived previously is scaled by the desired value of C_{tG}/Λ^2_{NP} and is added to the SM prediction ($C_{tG}/\Lambda^2_{NP} = 0$ TeV^{-2}).

In order to improve the modelling of the aforementioned NLO predictions, the following corrections are applied. The rate component of the predictions is scaled with a dedicated factor that accounts for the NNLO+NNLL corrections to the total $t\bar{t}$ production cross section [49]. Still, the rate component after this correction is not fully NNLO+NNLL, since the acceptance of the fiducial phase space involved in the particle level definition is modelled only at NLO. As the event generators provide a poor modelling of the p_T^t distribution at NLO (see Section 7.3.1), the predictions are reweighted to be consistent with the fixed-order prediction of p_T^t from [52], which is calculated at NNLO accuracy in QCD and includes the electroweak corrections up to order $O(\alpha^3_{EW})$.

In Figure 7.34, the predictions produced with values $C_{tG}/\Lambda^2_{NP} = 0, \pm 1$ TeV^{-2} are compared to the absolute differential $t\bar{t}$ production cross sections measured as a function of $\Delta\phi(\ell,\bar{\ell})$ at particle level, presented in Figure 7.24. As can be seen, the measured data favours the prediction with $C_{tG}/\Lambda^2_{NP} = 0$ TeV^{-2}, while its rate and shape are noticeably different from predictions with $C_{tG}/\Lambda^2_{NP} = \pm 1$ TeV^{-2}.

7.5.3 Constraining C_{tG}/Λ^2_{NP}

The C_{tG}/Λ^2_{NP} is constrained performing the χ^2-minimization. The EFT predictions for the absolute differential $t\bar{t}$ production cross sections as a function of $\Delta\phi(\ell,\bar{\ell})$ are produced, as described in Section 7.5.2, for 1001 values of C_{tG}/Λ^2_{NP} that are evenly distributed in the range -1.0 TeV$^{-2} < C_{tG}/\Lambda^2_{NP} < 1.0$ TeV^{-2}, i.e. with a step of $2\cdot 10^{-3}$ TeV^{-2}. The χ^2 is calculated

between each prediction and the measured differential cross section presented in Figure 7.24. The χ^2-values are calculated according to Equation 7.1, but omitting the division by $\chi^2/ndof$.

The best-fit value provided by the χ^2-minimization is found to be $C_{tG}/\Lambda^2_{NP} = 0.18$ TeV^{-2}, yielding $\chi^2/ndof = 0.3$. The corresponding 68% and 95% confidence intervals are determined in terms of $\Delta\chi^2$, which distribution is defined by the subtraction of the χ^2 associated with the best-fit value from the obtained χ^2-distribution. The following variations are considered to estimate the uncertainty due to the modelling of EFT predictions. For the ME modelling provided by MadGraph5_aMC@NLO, the renormalization and factorization scales are simultaneously varied by factors of 2 and 1/2, which results in a change of the rate and shape components of the predictions. Additionally, the rate component of the predictions is varied by the factors 1.058 and 0.938 according to the uncertainties of the NNLO+NNLL calculations of the total $t\bar{t}$ production cross section [49]. The χ^2-minimization is repeated without the application of the p^t_T-dependent reweighting (see Section 7.5.2) and its impact is found to be negligible. Finally, repeating the χ^2-minimization for all aforementioned variations, the total theoretical uncertainty on the best-fit value of C_{tG}/Λ^2_{NP} is taken as the interval between the highest and the lowest best-fit value provided by the varied predictions.

Figure 7.34 shows the distribution of $\Delta\chi^2$ as a function of C_{tG}/Λ^2_{NP}, where the nominal fit to data and its best-fit value are indicated with the corresponding 68% and 95% confidence intervals. The C_{tG}/Λ^2_{NP} is constrained to an interval -0.06 TeV$^{-2} < C_{tG}/\Lambda^2_{NP} < 0.41$ TeV^{-2} at 95% confidence level. In Figure 7.34, uncertainties that affect only the theoretical predictions are shown separately to the nominal confidence intervals. These uncertainties are estimated by repeating the fit using predictions corresponding to the variations of the theoretical uncertainties. The two fits that produce the largest differences with respect to the best-fit value from the nominal fit amongst these variations are shown. These uncertainties are shown separately to facilitate future reinterpretations of the result using more precise calculations that should eventually become available. Furthermore, some of these uncertainties are not frequentist in their nature; for example, the uncertainties due to missing higher-orders in calculations are estimated with ad-hoc variations of the factorization and renormalization scales. Thus, their inclusion in the confidence intervals would preclude frequentist interpretation of the presented result.

As mentioned previously, the C_{tG} is assumed to be real in the context of this work. Thus, the presented constraint of C_{tG}/Λ^2_{NP} corresponds to the constraint of the top quark CMDM, the first result of this kind at 13 TeV. Moreover, for the first time for such kind of interpretations, the constraining technique involves the following aspects: use of differential cross sections measured at particle level, simultaneous use of rate and shape components of probed distributions, full NLO modelling of differential predictions in an EFT.

The CMDM was previously constrained using data from the 8 TeV LHC and the Tevatron. In [172], the 95% confidence interval $-0.42\ \text{TeV}^{-2} < C_{tG}/\Lambda^2_{NP} < 0.30\ \text{TeV}^{-2}$ ($-0.32\ \text{TeV}^{-2} < C_{tG}/\Lambda^2_{NP} < 0.73\ \text{TeV}^{-2}$) was determined using the predictions of NLO accuracy for the inclusive $t\bar{t}$ production cross section as a function of C_{tG}/Λ^2_{NP} and measurements based on the 8 TeV CMS data (the Tevatron data). In [174], the CMS Collaboration constrained the CMDM from the normalized differential $t\bar{t}$ production cross sections measured in the full phase space at parton level using 8 TeV data. Converting the results obtained in [174] into the parametrization of C_{tG}/Λ^2_{NP} via the relations from [175], the following 95% confidence interval can be derived $-0.89\ \text{TeV}^{-2} < C_{tG}/\Lambda^2_{NP} < 0.43\ \text{TeV}^{-2}$. Therefore, the results presented in this work are consistent and provide more stringent constraint of C_{tG}/Λ^2_{NP} with respect to previous results [172, 174].

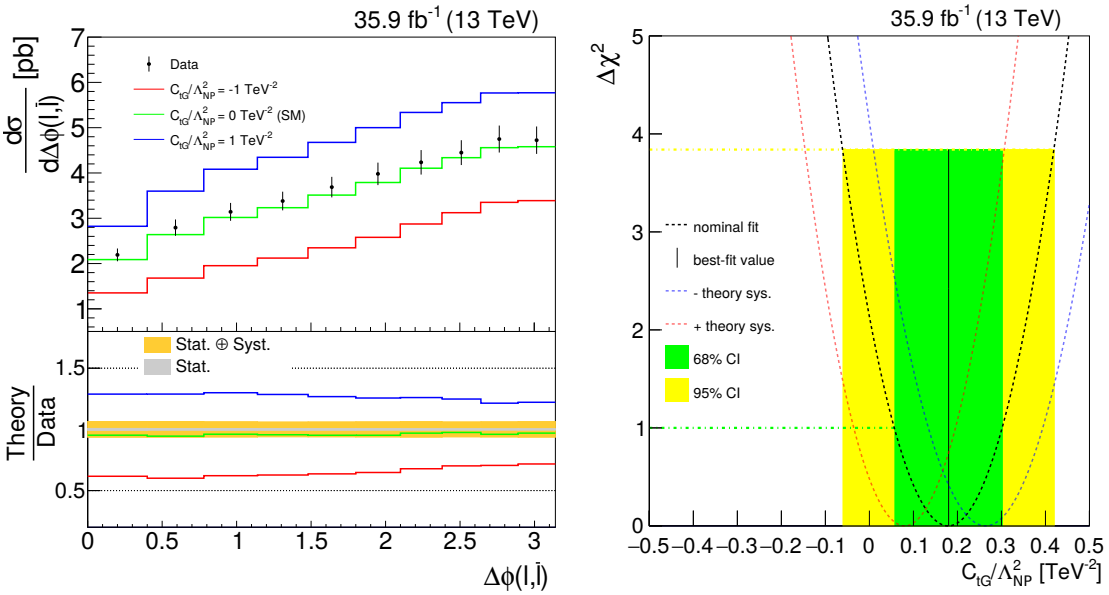

Figure 7.34 Left: The absolute differential $t\bar{t}$ production cross sections measured as a function of $\Delta\phi(\ell, \bar{\ell})$ at particle level in a fiducial phase space. The data (black) are compared to theoretical predictions (coloured lines) from MadGraph5_aMC@NLO+Pythia8 produced with C_{tG}/Λ^2_{NP} = -1.0, 0.0, 1.0 TeV^{-2}. The error bars show a combination of the statistical and systematic uncertainties. **Right:** The $\Delta\chi^2$ as a function of C_{tG}/Λ^2_{NP}. The nominal fit to data (dashed black line) is shown together with the 68% (green band) and 95 % (yellow band) confidence intervals. The best-fit value of C_{tG}/Λ^2_{NP} is shown with the black solid line. The red and blue dashed lines correspond to the fits which are obtained from those varied predictions, in terms of their rate and shape, that provide the largest differences with respect to the best-fit value.

Conclusions and Outlook

Conclusions

This work presented three separate measurements of differential cross sections for the $t\bar{t}$ production with subsequent decays into dilepton final states. The data were collected by the CMS experiment in pp collisions at $\sqrt{s} = 13$ TeV in 2015 and 2016 at the CERN LHC.

The measurements are based on an event counting method. All selected events are characterized by a presence of two prompt oppositely charged leptons (e^+e^-, $e^\pm\mu^\mp$, $\mu^+\mu^-$), at least two jets among which at least one jet is identified as originating from a b quark, and a significant missing transverse energy due to two neutrinos escaping the direct detection. In each event, kinematics of the top-quark pair were determined applying the reconstruction procedure based on an algebraic method. In order to measure differential cross sections, reconstructed distributions were corrected for acceptance and detector effects using a regularized unfolding technique. For each probed observable, the data unfolding was performed in a single dimension. It was demonstrated that the unfolded data are reliable.

Studying the first 42 pb^{-1} of data collected in 2015, the normalized differential $t\bar{t}$ production cross sections were measured at parton level in the full phase space as a function of a few kinematic observables of top quarks and the $t\bar{t}$-system. An additional measurement was performed at particle level in a fiducial phase space as a function of the jet multiplicity in the event. These results are the first differential $t\bar{t}$ production cross sections ever publicly released at 13 TeV [12]. The measured data exhibited an agreement with SM predictions within large uncertainties of the measurements, dominated by statistical uncertainties. Given the relatively low integrated luminosity of the data sample, no statement could be made regarding the observation of any trends in the agreement between data and simulation. The studies validating the simulation, conducted in a context of this measurement, motivated the choice of the Powheg v2+Pythia8 generator setup by the Top Quark Physics Analysis Group of the CMS Collaboration as reference $t\bar{t}$ simulation for analyses at 13 TeV. The same setup is used as reference up to the present time.

Measurements of the normalized differential $t\bar{t}$ production cross sections, as done in the analysis of the first 2015 data, were repeated with the use of the complete 2015 dataset corresponding to $L = 2.2$ fb^{-1} and were published in Ref. [13]. Owing to the larger data sample with respect to the previous analysis, the precision of the results improved and measurements started to be dominated by uncertainties due to theoretical sources. These results confirmed a slope between data and SM predictions for the distribution of the top quark transverse momentum (p_T) already observed in similar measurements performed at 7 and 8 TeV [3, 4, 7, 8]. A comparison of results to various SM predictions demonstrated that a better description of data, in particular for the top quark p_T, is provided by perturbative QCD calculations of beyond-next-to-leading-order accuracy. These results also motivated a new parton shower tuning in Pythia8 (CUETP8M2T4), published in Ref. [105] and eventually used for the analysis providing the main results of this work summarized in the next paragraph. Moreover, this measurement serves as cross-check analysis for another published CMS measurement which is also based on the complete 2015 dataset in the same final state [9].

As main results, this work presents the most comprehensive study of the differential $t\bar{t}$ production cross sections in the dilepton channel to date. Measurements are based on the complete 2016 data sample corresponding to $L = 35.9$ fb^{-1}. Here, normalized/absolute differential cross sections were measured as a function of 15 kinematic observables of the top quarks and the $t\bar{t}$-system, and the results were presented in the full phase space at parton level and in a fiducial phase space at particle level. In addition, normalized/absolute differential cross sections were measured at particle level in a fiducial phase space as a function of 18 kinematic observables of the top quark decay products (leptons and lepton pair, b-jets and b-jet pair), and as a function of the jet multiplicity in the event. In total, 34 observables were probed and 98 unique differential measurements were presented. The total uncertainties on the measured differential cross sections are between 1 – 24%, depending on the observable. As expected, normalized results are much more precise with respect to absolute ones. A special attention was devoted to the estimation of systematic uncertainties of the measurements. Overall, the most dominant systematic sources are due to the jet energy scale and the parton shower modelling. Absolute differential cross sections are also sensitive to the uncertainty in lepton efficiencies and luminosity. A particular effort was dedicated to the determination of covariance matrices of differential measurements. These matrices would serve as an essential tool for the improvement of modern SM predictions and for searches of new-physics phenomena beyond the SM, in which $t\bar{t}$ processes are important. These matrices also facilitate the extraction of the top quark mass, strong coupling, and parton distribution functions.

All differential results based on 2016 data were compared to SM predictions from Monte Carlo (MC) generators at NLO accuracy in QCD, based on matrix element level interfaced to parton shower simulations. Comparisons were performed to POWHEG v2+PYTHIA8, POWHEG v2+HERWIG++, and MG5_aMC@NLO+PYTHIA8 [FxFx]. None of the predictions provide a uniformly good description of data for all measured distributions. In particular, a substantial disagreement is observed between data and predictions for the transverse momentum distributions of top quarks and their decay products. The χ^2 normalized by the number of degrees of freedom and p-values quantifying the agreement between the data and MC predictions were presented for all differential measurements. Comparisons of measured results to state-of-the-art perturbative SM calculations of beyond-NLO accuracy in QCD were not feasible at the time of writing this document (the calculations were not available in the appropriate binning), but are anticipated to be performed in the near future.

The $t\bar{t}$ and leptonic charge asymmetries were extracted from normalized differential cross sections based on 2016 data, as they provide a better precision with respect to absolute results. The corresponding 68% and 95% confidence intervals were indicated. The results were compared to the SM predictions from POWHEG v2+PYTHIA8 and MG5_aMC@NLO+PYTHIA8 [FxFx], as well as to the calculations at NLO accuracy in QCD including electroweak corrections [167]. A good agreement is observed between the data and the SM expectations. The presented results are the first measurements of these asymmetries in pp collisions at 13 TeV.

Absolute differential cross sections based on 2016 data were used, for the first time at 13 TeV, to constrain the chromomagnetic dipole moment (CMDM) of the top quark in an effective field theory at NLO accuracy in QCD. The constraining power is mostly due to the sensitivity of absolute differential cross sections to the rate of $t\bar{t}$ production. The obtained results are consistent and provide more stringent constraints of the CMDM with respect to previous results [172, 174].

Finally, all presented results based on 2016 data that were summarized above are reviewed by the CMS Collaboration and being documented in a journal publication including comparisons to latest beyond-NLO QCD calculations [176]. Results of differential cross section measurements are planned for a submission to the HEPData repository [177].

Outlook

The measurements of the differential $t\bar{t}$ production cross sections presented in this work could be extended towards the measurement of other observables. For instance, angular kinematic observables of the $t\bar{t}$ decays in the dilepton channel allow the study of the top quark polarization and $t\bar{t}$ spin correlations. As done in Ref. [10], measurements could be performed

targeting processes where several additional jets that do not originate from the weak decay of the top-quark pair are present in the event. In this case, differential cross sections could be measured as a function of kinematic observables of additional jets. Such measurements are especially interesting in the dilepton channel, as it has the least combinatorial background with respect to other $t\bar{t}$ decay channels. These measurements provide a stringent test of perturbative QCD calculations at higher orders of accuracy.

The double-differential cross section measurements for $t\bar{t}$ production were already performed at 8 TeV [139]. Measurements of this kind are particularly sensitive to the gluon parton distribution functions. Considering a delivery of a large dataset during the Run-II operation of the LHC (about up to 120 fb^{-1}), measurements of multidifferential cross sections for $t\bar{t}$ production are expected.

The precision of differential cross section measurements with respect to those presented in this work could be improved by reducing the systematic uncertainties within the analysis. For example, a fitting technique based on nuisance parameters could be implemented in the framework of differential measurements to determine event yields of the signal and background processes. The improvement of the particle level definition, i.e. making it more similar to the reconstruction of data, could further reduce the dependence of measurements on extrapolation effects. For example, $t\bar{t}$ decays via τ leptons could be added as part of the signal, or a requirement on the missing transverse energy due to neutrinos could be introduced in the definition of the fiducial phase space. Obviously, a better precision of differential results would facilitate an improvement of SM predictions and a sensitivity to effects induced by new-physics phenomena that modify known $t\bar{t}$ processes.

The measurements of processes involving top quarks may play a key role in the discovery of new physics. The large mass of the top quark implies a large coupling to the Higgs boson, providing a direct connection between the top and Higgs sectors. Thus, the top quark plays a key role in measurements of Higgs boson properties, where deviations from SM expectations would indicate a presence of new physics. For instance, the four top quark production ($t\bar{t}t\bar{t}$) and the associated production of a Higgs boson with a top quark-antiquark pair ($t\bar{t}H$) can be used to constrain the Higgs boson width and the top quark Yukawa coupling [178]. In particular, the precise measurement of the top quark Yukawa coupling may shed light on the scale of new physics [179]. This knowledge is particularly important regarding physics planning in the context of next-generation collider facilities.

Exciting times of the High-Luminosity LHC project [180] are ahead. Excellent projects of future collider facilities, such as CLIC [181], FCC [182], and ILC [183], offer a new generation of experiments, extending our potential for discoveries. Thus, the future of particle physics is bright.

Appendix A

Additional experimental information

Here, additional experimental information for the measurements of differential $t\bar{t}$ production cross sections is given. The measurements are performed in the dilepton decay channel using the data of $L = 35.9$ fb^{-1} recorded by the CMS detector in 2016 during pp collisions at $\sqrt{s} = 13$ TeV.

Table A.1 Dilepton and single lepton triggers involved in the analysis of the data collected in 2016. These triggers are used to select events with two leptons in the three dilepton channels (e^+e^-, $e^\pm\mu^\mp$ and $\mu^+\mu^-$), which is done applying the logical OR between the dilepton and single lepton triggers. The same triggers are used in the data and simulation. The trigger names are given according to the nomenclature of CMS Collaboration.

Channel	Run	Trigger
e^+e^-	B-H	HLT_Ele23_Ele12_CaloIdL_TrackIdL_IsoVL_DZ_v*
	B-H	HLT_Ele27_WPTight_Gsf_v*
$e^\pm\mu^\mp$	B-G	HLT_Mu23_TrkIsoVVL_Ele12_CaloIdL_TrackIdL_IsoVL_v*
	B-G	HLT_Mu8_TrkIsoVVL_Ele23_CaloIdL_TrackIdL_IsoVL_v*
	H	HLT_Mu23_TrkIsoVVL_Ele12_CaloIdL_TrackIdL_IsoVL_DZ_v*
	H	HLT_Mu8_TrkIsoVVL_Ele23_CaloIdL_TrackIdL_IsoVL_DZ_v*
	B-H	HLT_Ele27_WPTight_Gsf_v*
	B-H	HLT_IsoMu24_v*
	B-H	HLT_IsoTkMu24_v*
$\mu^+\mu^-$	B-G	HLT_Mu17_TrkIsoVVL_Mu8_TrkIsoVVL_v*
	B-G	HLT_Mu17_TrkIsoVVL_TkMu8_TrkIsoVVL_v*
	H	HLT_Mu17_TrkIsoVVL_Mu8_TrkIsoVVL_DZ_v*
	H	HLT_Mu17_TrkIsoVVL_TkMu8_TrkIsoVVL_DZ_v*
	B-H	HLT_IsoMu24_v*
	B-H	HLT_IsoTkMu24_v*

Table A.2 The *pp* collision datasets that are used in this measurement. These datasets were recorded with the CMS detector during the Run-II period of LHC operation at $\sqrt{s} = 13$ TeV in 2016. The total integrated luminosity of the combined data sample is 35.9 fb^{-1}. The dataset names are given according to the nomenclature of CMS Collaboration, specifying the corresponding range of "good" collision runs at LHC in terms of their id-numbers.

Dataset	Run range
/MuonEG/Run2016B-03Feb2017_ver2-v2	272007–275376
/MuonEG/Run2016C-03Feb2017-v1	275657–276283
/MuonEG/Run2016D-03Feb2017-v1	276315–276811
/MuonEG/Run2016E-03Feb2017-v1	276831–277420
/MuonEG/Run2016F-03Feb2017-v1	277772–278808
/MuonEG/Run2016G-03Feb2017-v1	278820–280385
/MuonEG/Run2016H-03Feb2017_ver2-v1	281613–284035
/MuonEG/Run2016H-03Feb2017_ver3-v1	284036–284044
/DoubleEG/Run2016B-03Feb2017_ver2-v2	272007–275376
/DoubleEG/Run2016C-03Feb2017-v1	275657–276283
/DoubleEG/Run2016D-03Feb2017-v1	276315–276811
/DoubleEG/Run2016E-03Feb2017-v1	276831–277420
/DoubleEG/Run2016F-03Feb2017-v1	277772–278808
/DoubleEG/Run2016G-03Feb2017-v1	278820–280385
/DoubleEG/Run2016H-03Feb2017_ver2-v1	281613–284035
/DoubleEG/Run2016H-03Feb2017_ver3-v1	284036–284044
/DoubleMuon/Run2016B-03Feb2017_ver2-v2	272007–275376
/DoubleMuon/Run2016C-03Feb2017-v1	275657–276283
/DoubleMuon/Run2016D-03Feb2017-v1	276315–276811
/DoubleMuon/Run2016E-03Feb2017-v1	276831–277420
/DoubleMuon/Run2016F-03Feb2017-v1	277772–278808
/DoubleMuon/Run2016G-03Feb2017-v1	278820–280385
/DoubleMuon/Run2016H-03Feb2017_ver2-v1	281613–284035
/DoubleMuon/Run2016H-03Feb2017_ver3-v1	284036–284044
/SingleMuon/Run2016B-03Feb2017_ver2-v2	272007–275376
/SingleMuon/Run2016C-03Feb2017-v1	275657–276283
/SingleMuon/Run2016D-03Feb2017-v1	276315–276811
/SingleMuon/Run2016E-03Feb2017-v1	276831–277420
/SingleMuon/Run2016F-03Feb2017-v1	277772–278808
/SingleMuon/Run2016G-03Feb2017-v1	278820–280385
/SingleMuon/Run2016H-03Feb2017_ver2-v1	281613–284035
/SingleMuon/Run2016H-03Feb2017_ver3-v1	284036–284044
/SingleElectron/Run2016B-03Feb2017_ver2-v2	272007–275376
/SingleElectron/Run2016C-03Feb2017-v1	275657–276283
/SingleElectron/Run2016D-03Feb2017-v1	276315–276811
/SingleElectron/Run2016E-03Feb2017-v1	276831–277420
/SingleElectron/Run2016F-03Feb2017-v1	277772–278808
/SingleElectron/Run2016G-03Feb2017-v1	278820–280385
/SingleElectron/Run2016H-03Feb2017_ver2-v1	281613–284035
/SingleElectron/Run2016H-03Feb2017_ver3-v1	284036–284044

Table A.3 Alternative simulated samples for the $t\bar{t}$ process that are used in this measurement, either for the estimation of systematic uncertainties or for comparisons with the results. All samples are generated with NLO matrix elements and are normalized to the total cross section of 831.76 pb (NNLO+NNLL). The sample names are mentioned as given by the nomenclature of the CMS Collaboration.

Sample
TT_TuneCUETP8M2T4_13TeV-powheg-fsrdown-pythia8 TT_TuneCUETP8M2T4_13TeV-powheg-fsrup-pythia8
TT_TuneCUETP8M2T4_13TeV-powheg-isrdown-pythia8 TT_TuneCUETP8M2T4_13TeV-powheg-isrup-pythia8
TT_TuneCUETP8M2T4down_13TeV-powheg-pythia8 TT_TuneCUETP8M2T4up_13TeV-powheg-pythia8
TT_hdampDOWN_TuneCUETP8M2T4_13TeV-powheg-pythia8 TT_hdampUP_TuneCUETP8M2T4_13TeV-powheg-pythia8
TT_TuneCUETP8M2T4_mtop1695_13TeV-powheg-pythia8 TT_TuneCUETP8M2T4_mtop1755_13TeV-powheg-pythia8
TT_TuneCUETP8M2T4_erdON_13TeV-powheg-pythia8 TT_TuneCUETP8M2T4_GluonMoveCRTune_13TeV-powheg-pythia8 TT_TuneCUETP8M2T4_QCDbasedCRTune_erdON_13TeV-powheg-pythia8
TTJets_TuneCUETP8M2T4_13TeV-amcatnloFXFX-pythia8
TT_TuneEE5C_13TeV-powheg-herwigpp

Table A.4 The scale factors, accounting for differences in the jet energy resolution between the data and simulation, are used to smear jet 4-momenta in the simulation. The scale factors are determined in bins of the jet $|\eta|$ using the pp-collision data collected by the CMS experiment in 2016 (35.9 fb^{-1}). The given uncertainties correspond to total uncertainties of corresponding scale factors.

Interval in $\|\eta\|$	[0.0, 0.5)	[0.5, 0.8)	[0.8, 1.1)	[1.1, 1.3)	[1.3, 1.7)
Scale factor	1.109	1.138	1.114	1.123	1.084
Total uncertainty	±0.008	±0.013	±0.013	±0.024	±0.011

Interval in $\|\eta\|$	[1.7, 1.9)	[1.9, 2.1)	[2.1, 2.3)	[2.3, 2.5)
Scale factor	1.082	1.140	1.067	1.177
Total uncertainty	±0.035	±0.047	±0.053	±0.041

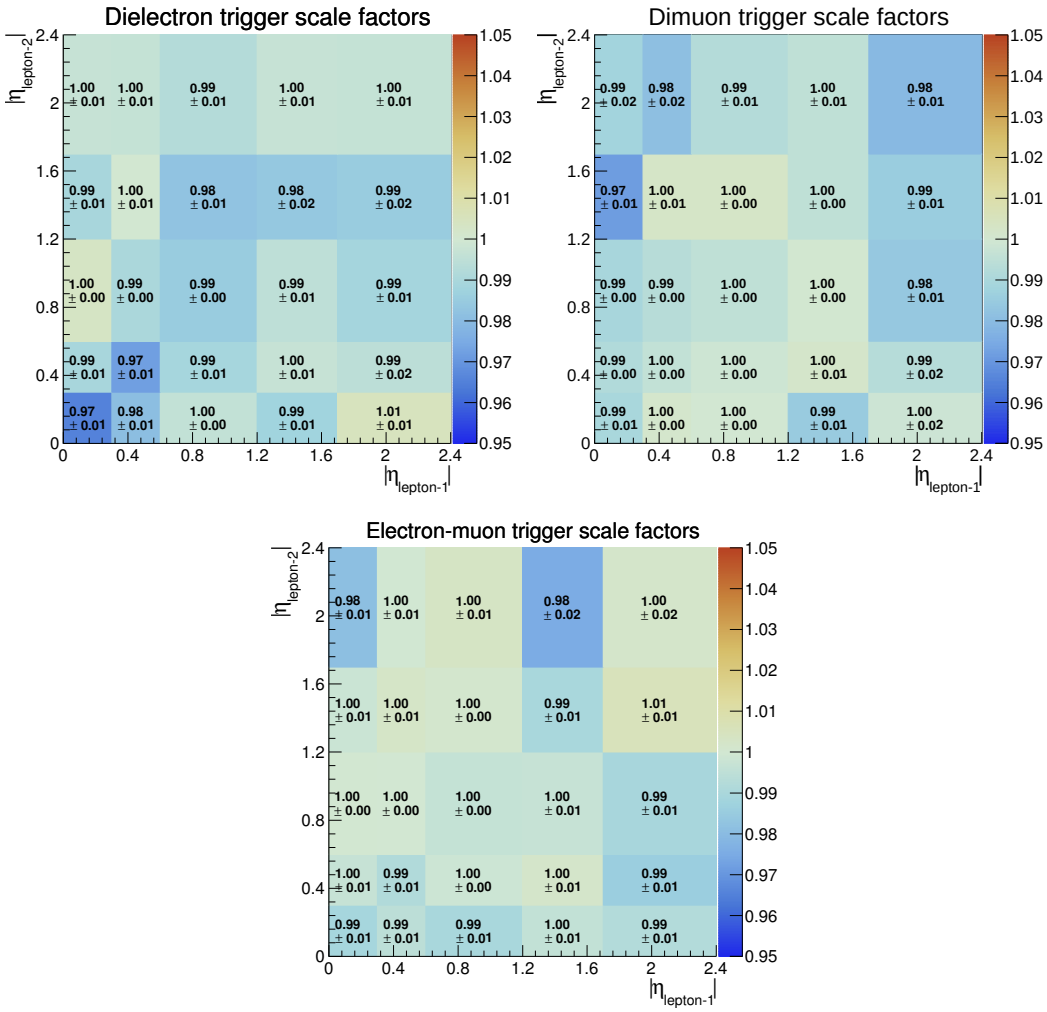

Figure A.1 The trigger data-to-MC scale factors are measured differentially as a function of $|\eta|$ of the two leading leptons in the event, as is shown for e^+e^- (top left), $\mu^+\mu^-$ (top right) and $e^\pm\mu^\mp$ (bottom) channels. The scale factors are determined using the *pp*-collision data collected by the CMS experiment in 2016 (35.9 fb^{-1}). The given uncertainties correspond to the statistical uncertainty added in quadratures to the additional systematic uncertainty of 0.3% on the measured value.

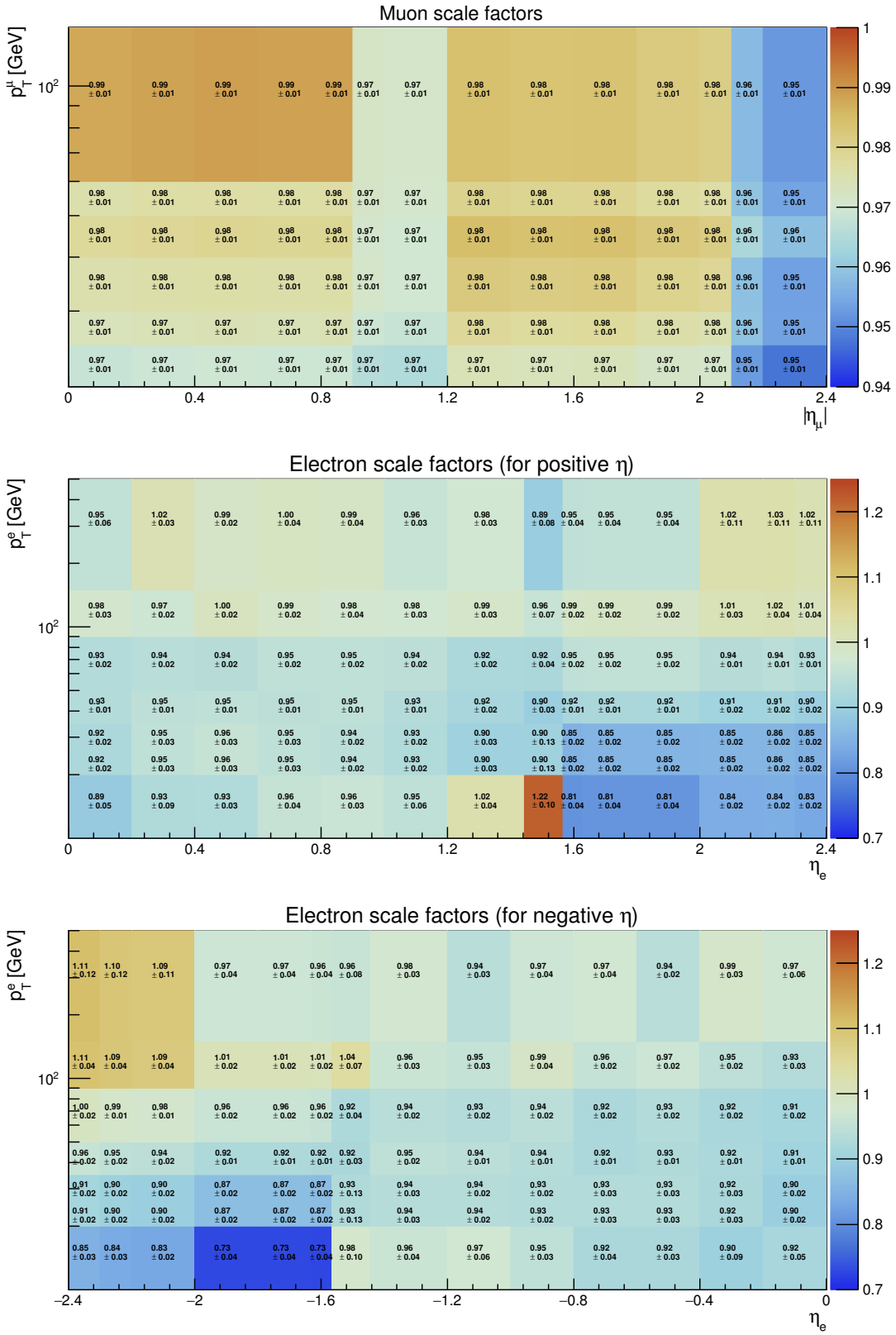

Figure A.2 The muon (top) and electron (middle and bottom for the positive and negative η, respectively) data-to-MC scale factors. The muon (electron) scale factors are differential in bins of the p_T and $|\eta|$ of muon candidates (the electron candidate p_T and the η of an associated supercluster). The scale factors are determined using the pp-collision data collected by the CMS experiment in 2016 (35.9 fb^{-1}). The given uncertainties correspond to the total uncertainty.

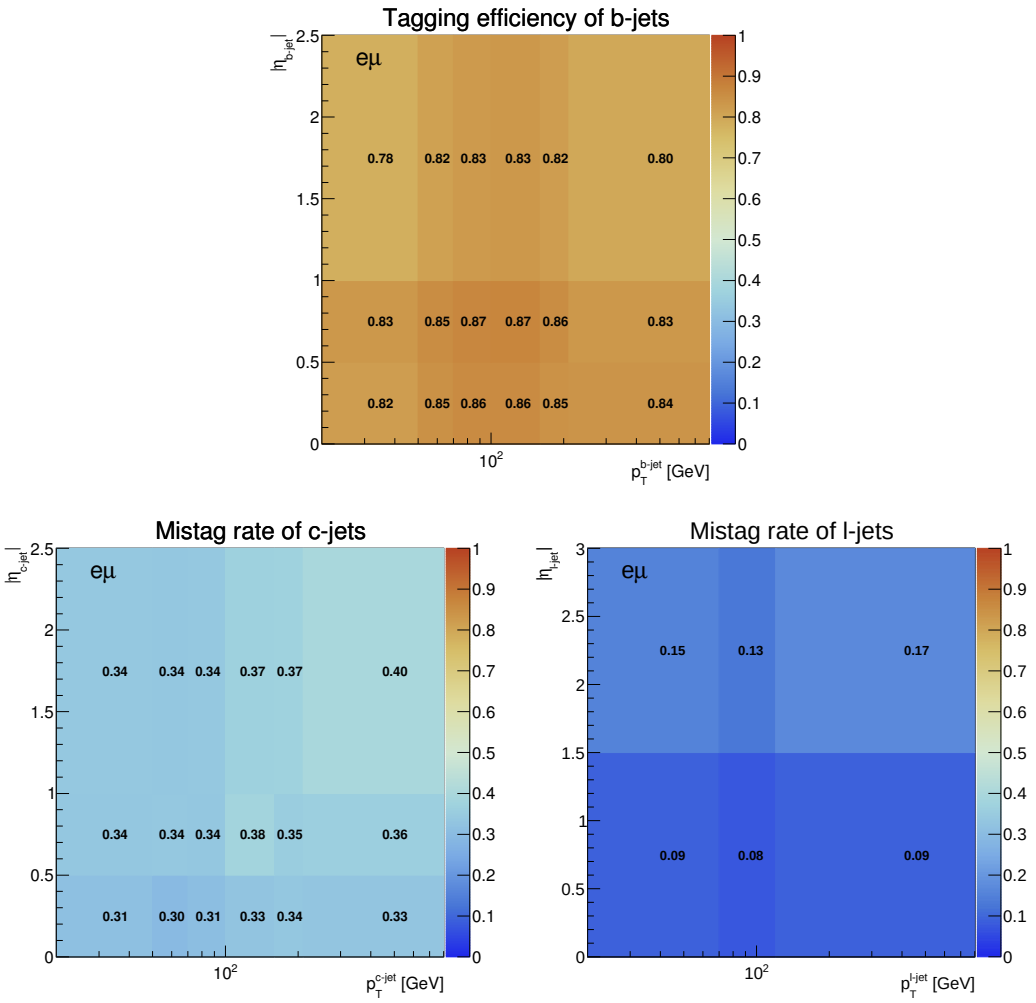

Figure A.3 The tagging efficiency of b-jets (top) and mistag rate of c-jets (bottom left) and l-jets (bottom right) determined as a function of jet p_T and $|\eta|$ from the reference *$t\bar{t}$ signal* simulation. The quantities are shown for the $e^{\pm}\mu^{\mp}$ decay channel.

Table A.5 The results of data-driven *Z+jets* background estimation in the e^+e^-, $\mu^+\mu^-$and $e^{\pm}\mu^{\mp}$ channels. The normalization scale factors are extracted using the event samples that are obtained after the application of "2 jets" selection requirement.

Variable	e^+e^-	$\mu^+\mu^-$	$e^{\pm}\mu^{\mp}$
$k^{\ell^+\ell^-}$	0.6967	1.4353	-
$R_{out/in}$	0.1210	0.1284	-
$N^{\ell^+\ell^-}_{out,data}$	51812.0	113317.0	-
$N^{\ell^+\ell^-}_{out,MC}$	49123.7	114339.0	-
$SF^{\ell^+\ell^-}_{Z+jets}$	1.0547	0.9911	1.0224

Table A.6 A list of optimal τ-values, i.e. τ_{opt} - a parameter controlling the regularization strength in the unfolding procedure, that are used to perform differential $t\bar{t}$ cross section measurements with the 2016 data (35.9 fb^{-1}). The τ-parameter is optimized separately for the parton level and particle level measurements, as well as for each measured observable.

Observable	τ_{opt}	
	parton level	particle level
p_T^t	10.51	10.32
$p_T^{\bar{t}}$	10.46	10.24
p_T^t *(leading)*	14.20	13.68
p_T^t *(trailing)*	6.67	6.66
p_T^t *($t\bar{t}$ rest frame)*	8.01	8.03
$p_T^{\bar{t}}$ *($t\bar{t}$ rest frame)*	8.01	8.03
y_t	14.71	15.47
$y_{\bar{t}}$	14.68	15.45
y_t *(leading)*	16.97	17.51
y_t *(trailing)*	15.63	16.53
$\Delta\|y\|(t,\bar{t})$	12.59	14.08
$\Delta\phi(t,\bar{t})$	25.39	26.89
$p_T^{t\bar{t}}$	8.64	8.28
$m_{t\bar{t}}$	3.99	4.06
$y_{t\bar{t}}$	13.90	14.29
p_T^{ℓ}		3.71
$p_T^{\bar{\ell}}$		3.92
p_T^{ℓ} *(leading)*		6.81
p_T^{ℓ} *(trailing)*		2.00
η_{ℓ}		2.16
$\eta_{\bar{\ell}}$		2.00
η_{ℓ} *(leading)*		2.55
η_{ℓ} *(trailing)*		2.63
$\Delta\|\eta\|(\ell,\bar{\ell})$		6.20
$\Delta\phi(\ell,\bar{\ell})$		5.38
$p_T^{\ell\bar{\ell}}$		11.36
$m_{\ell\bar{\ell}}$		12.36
p_T^b *(leading)*		17.34
p_T^b *(trailing)*		10.64
η_b *(leading)*		12.72
η_b *(trailing)*		14.23
$p_T^{b\bar{b}}$		26.20
$m_{b\bar{b}}$		31.82
N_{jets}		6.90

Appendix B

Result tables, covariance and correlation matrices

Here, a summary of results for the measurements of differential $t\bar{t}$ production cross sections is given. The measurements are performed in the dilepton decay channel using the data of $L = 35.9\ \text{fb}^{-1}$ recorded by the CMS detector in 2016 during pp collisions at $\sqrt{s} = 13$ TeV. Tables summarizing measured results and uncertainties per bins of differential measurements are presented together with the corresponding covariance and correlation matrices.

Normalized differential $t\bar{t}$ production cross sections measured in the full phase space at parton level are presented in Tables B.1-B.15.

Absolute differential $t\bar{t}$ production cross sections measured in the full phase space at parton level are presented in Tables B.16-B.30.

Normalized differential $t\bar{t}$ production cross sections measured in a fiducial phase space at particle level are presented in Tables B.31-B.64.

Absolute differential $t\bar{t}$ production cross sections measured in a fiducial phase space at particle level are presented in Tables B.65-B.98.

Table B.1 The result σ and its uncertainty per bin of the normalized differential $t\bar{t}$ production cross sections measured as a function of the transverse momentum of the top quark p_T^t. Measurement is performed at parton level in the full phase space. The corresponding covariance and correlation matrices are presented below the table.

bin	center (GeV)	left (GeV)	right (GeV)	σ (GeV^{-1})	Δ_σ^{stat} (%)	Δ_σ^{syst} (%)	Δ_σ^{tot} (%)
1	32.5	0.0	65.0	4.12e-03	1.1	4.7	4.8
2	95.0	65.0	125.0	6.02e-03	1.0	4.7	4.8
3	162.5	125.0	200.0	3.35e-03	0.9	3.5	3.6
4	245.0	200.0	290.0	9.95e-04	1.3	3.9	4.1
5	345.0	290.0	400.0	2.21e-04	1.6	4.8	5.0
6	475.0	400.0	550.0	4.07e-05	3.8	7.3	8.2

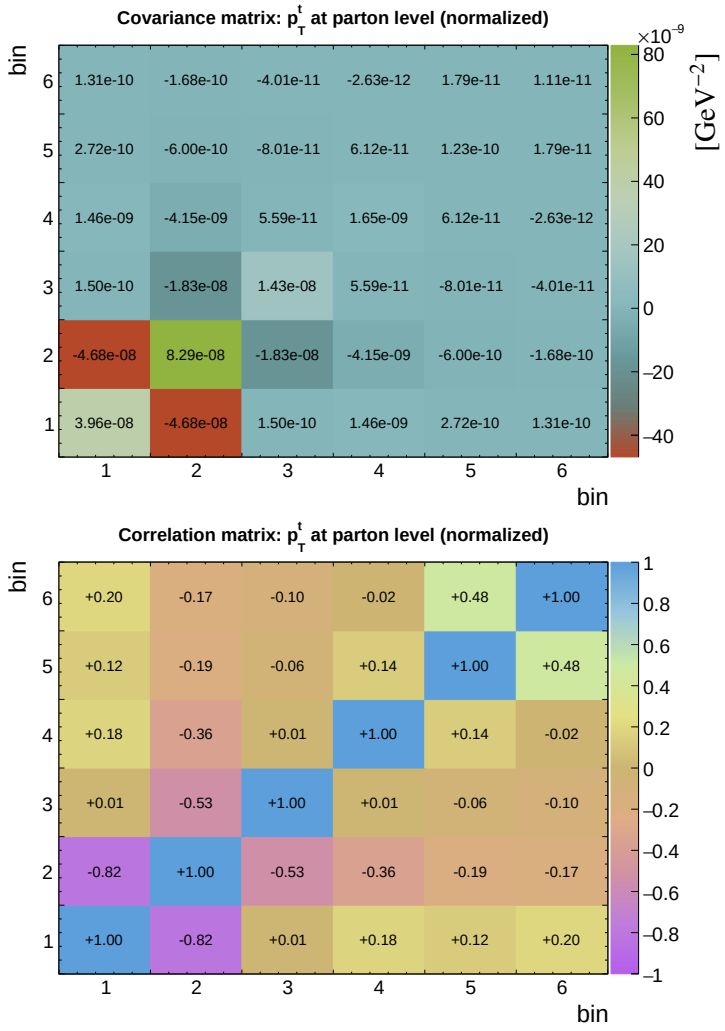

Table B.2 The result σ and its uncertainty per bin of the normalized differential $t\bar{t}$ production cross sections measured as a function of the transverse momentum of the top antiquark $p_T^{\bar{t}}$. Measurement is performed at parton level in the full phase space. The corresponding covariance and correlation matrices are presented below the table.

bin	center (GeV)	left (GeV)	right (GeV)	σ (GeV^{-1})	Δ_σ^{stat} (%)	Δ_σ^{syst} (%)	Δ_σ^{tot} (%)
1	32.5	0.0	65.0	4.17e-03	1.1	5.8	5.9
2	95.0	65.0	125.0	6.03e-03	1.0	3.7	3.8
3	162.5	125.0	200.0	3.25e-03	0.9	3.7	3.8
4	245.0	200.0	290.0	1.03e-03	1.2	5.0	5.2
5	345.0	290.0	400.0	2.24e-04	1.5	4.9	5.1
6	475.0	400.0	550.0	3.94e-05	3.9	12.8	13.4

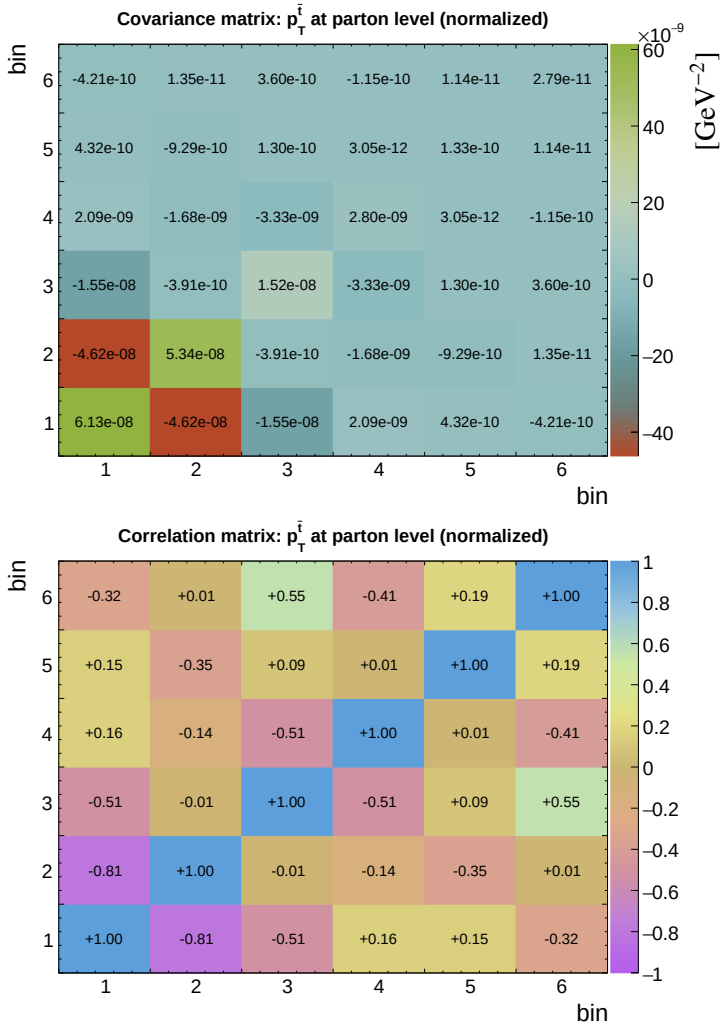

Table B.3 The result σ and its uncertainty per bin of the normalized differential $t\bar{t}$ production cross sections measured as a function of the transverse momentum of the leading top quark p_T^t *(leading)*. Measurement is performed at parton level in the full phase space. The corresponding covariance and correlation matrices are presented below the table.

bin	center (GeV)	left (GeV)	right (GeV)	σ (GeV^{-1})	Δ_σ^{stat} (%)	Δ_σ^{syst} (%)	Δ_σ^{tot} (%)
1	32.5	0.0	65.0	2.62e-03	1.3	6.2	6.3
2	95.0	65.0	125.0	6.05e-03	0.7	2.6	2.7
3	162.5	125.0	200.0	3.98e-03	0.7	2.8	2.9
4	245.0	200.0	290.0	1.38e-03	0.9	3.2	3.3
5	345.0	290.0	400.0	3.23e-04	1.2	3.9	4.0
6	475.0	400.0	550.0	6.08e-05	2.8	7.2	7.8

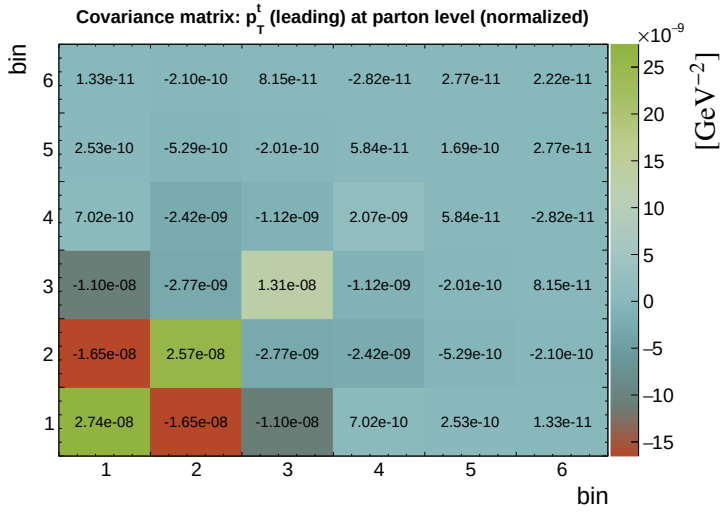

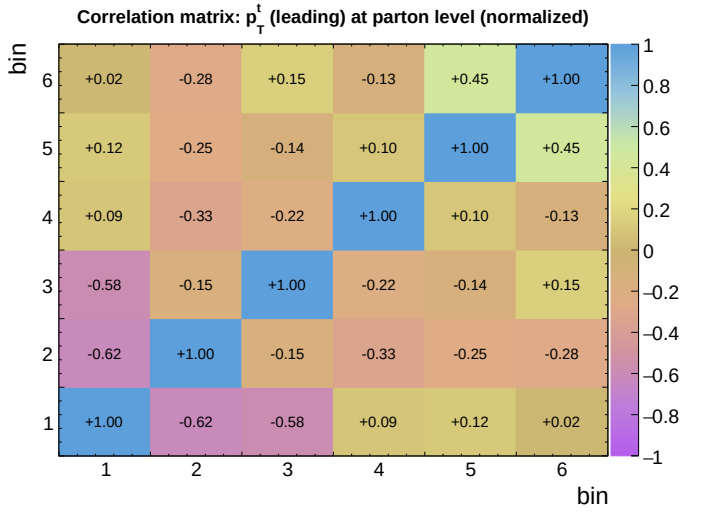

Table B.4 The result σ and its uncertainty per bin of the normalized differential $t\bar{t}$ production cross sections measured as a function of the transverse momentum of the trailing top quark p_T^t *(trailing)*. Measurement is performed at parton level in the full phase space. The corresponding covariance and correlation matrices are presented below the table.

bin	center (GeV)	left (GeV)	right (GeV)	σ (GeV^{-1})	Δ_σ^{stat} (%)	Δ_σ^{syst} (%)	Δ_σ^{tot} (%)
1	32.5	0.0	65.0	5.66e-03	0.8	4.1	4.2
2	95.0	65.0	125.0	5.99e-03	1.1	4.8	5.0
3	162.5	125.0	200.0	2.64e-03	1.2	4.7	4.9
4	245.0	200.0	290.0	6.45e-04	1.9	6.8	7.1
5	345.0	290.0	400.0	1.23e-04	2.4	6.7	7.2
6	475.0	400.0	550.0	1.95e-05	6.5	15.7	17.0

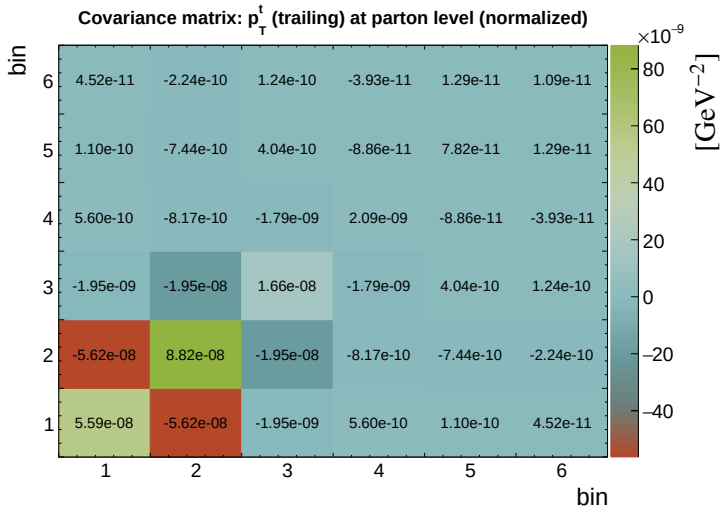

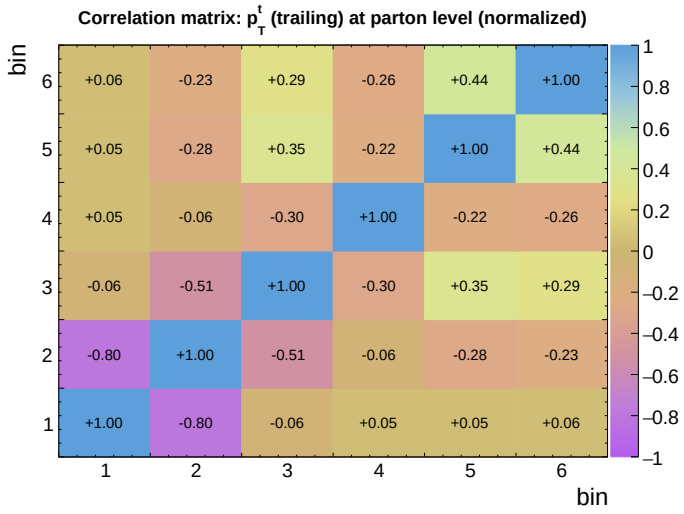

Table B.5 The result σ and its uncertainty per bin of the normalized differential $t\bar{t}$ production cross sections measured as a function of the transverse momentum of the top quark in the rest frame of the $t\bar{t}$-system p_T^t *($t\bar{t}$ rest frame)*. Measurement is performed at parton level in the full phase space. The corresponding covariance and correlation matrices are presented below the table.

bin	center (GeV)	left (GeV)	right (GeV)	σ (GeV^{-1})	Δ_σ^{stat} (%)	Δ_σ^{syst} (%)	Δ_σ^{tot} (%)
1	32.5	0.0	65.0	4.51e-03	1.0	4.8	5.0
2	95.0	65.0	125.0	6.24e-03	1.0	4.2	4.3
3	162.5	125.0	200.0	3.15e-03	1.0	3.2	3.4
4	245.0	200.0	290.0	8.23e-04	1.5	4.9	5.2
5	345.0	290.0	400.0	1.68e-04	1.9	5.4	5.7
6	475.0	400.0	550.0	2.64e-05	5.1	10.8	11.9

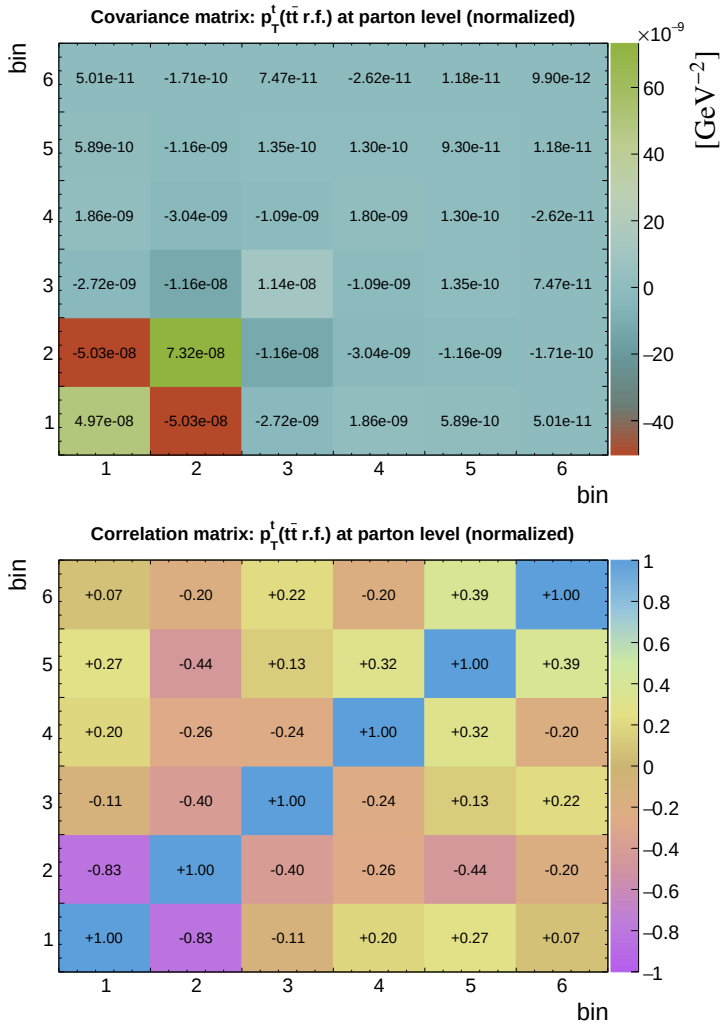

Table B.6 The result σ and its uncertainty per bin of the normalized differential $t\bar{t}$ production cross sections measured as a function of the transverse momentum of the top antiquark in the rest frame of the $t\bar{t}$-system $p_T^{\bar{t}}$ *($t\bar{t}$ rest frame)*. Measurement is performed at parton level in the full phase space. The corresponding covariance and correlation matrices are presented below the table.

bin	center (GeV)	left (GeV)	right (GeV)	σ (GeV^{-1})	Δ_σ^{stat} (%)	Δ_σ^{syst} (%)	Δ_σ^{tot} (%)
1	32.5	0.0	65.0	4.51e-03	1.0	4.8	5.0
2	95.0	65.0	125.0	6.24e-03	1.0	4.2	4.3
3	162.5	125.0	200.0	3.15e-03	1.0	3.2	3.4
4	245.0	200.0	290.0	8.23e-04	1.5	4.9	5.2
5	345.0	290.0	400.0	1.68e-04	1.9	5.4	5.7
6	475.0	400.0	550.0	2.64e-05	5.1	10.8	11.9

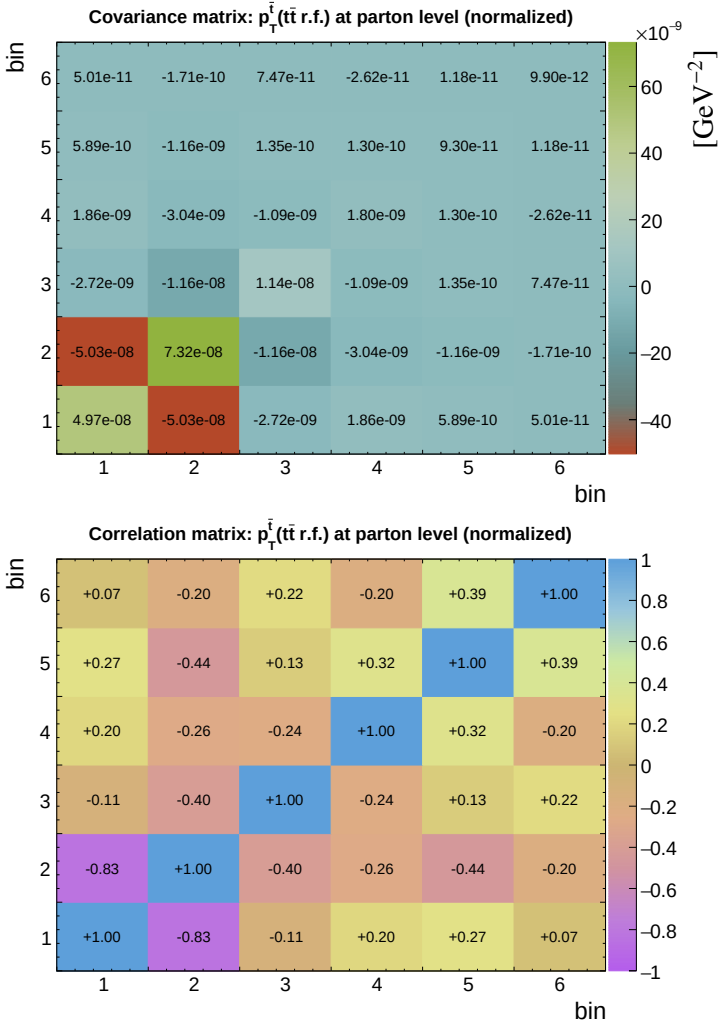

Table B.7 The result σ and its uncertainty per bin of the normalized differential $t\bar{t}$ production cross sections measured as a function of the rapidity of the top quark y_t. Measurement is performed at parton level in the full phase space. The corresponding covariance and correlation matrices are presented below the table.

bin	center	left	right	σ	Δ_σ^{stat} (%)	Δ_σ^{syst} (%)	Δ_σ^{tot} (%)
1	−2.20	−2.60	−1.80	7.37e-02	1.9	5.4	5.7
2	−1.58	−1.80	−1.35	1.62e-01	1.0	2.7	2.8
3	−1.12	−1.35	−0.90	2.31e-01	1.0	2.5	2.7
4	−0.68	−0.90	−0.45	2.79e-01	0.9	2.1	2.3
5	−0.22	−0.45	0.00	3.01e-01	0.9	2.9	3.1
6	0.22	0.00	0.45	3.04e-01	0.9	3.7	3.8
7	0.68	0.45	0.90	2.86e-01	0.9	3.3	3.4
8	1.12	0.90	1.35	2.27e-01	1.0	2.1	2.4
9	1.58	1.35	1.80	1.64e-01	1.0	3.3	3.4
10	2.20	1.80	2.60	7.74e-02	1.7	4.2	4.6

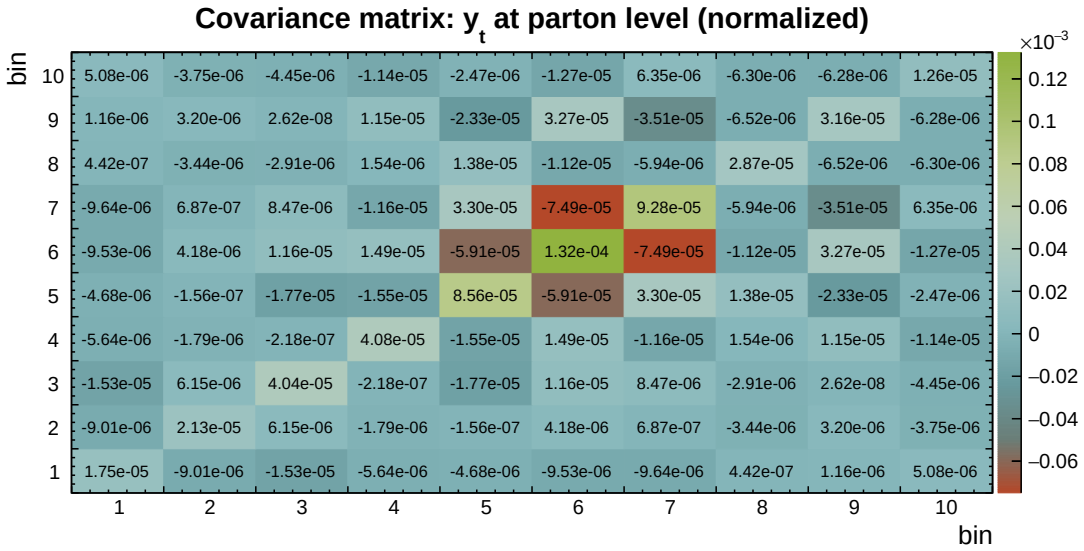

Table B.8 The result σ and its uncertainty per bin of the normalized differential $t\bar{t}$ production cross sections measured as a function of the rapidity of the top antiquark $y_{\bar{t}}$. Measurement is performed at parton level in the full phase space. The corresponding covariance and correlation matrices are presented below the table.

bin	center	left	right	σ	Δ_σ^{stat} (%)	Δ_σ^{syst} (%)	Δ_σ^{tot} (%)
1	−2.20	−2.60	−1.80	7.50e-02	1.8	4.7	5.0
2	−1.58	−1.80	−1.35	1.59e-01	1.0	2.1	2.4
3	−1.12	−1.35	−0.90	2.31e-01	1.0	2.7	2.9
4	−0.68	−0.90	−0.45	2.79e-01	0.9	2.3	2.5
5	−0.22	−0.45	0.00	3.07e-01	0.9	2.0	2.2
6	0.22	0.00	0.45	3.07e-01	0.9	2.8	2.9
7	0.68	0.45	0.90	2.77e-01	0.9	2.1	2.3
8	1.12	0.90	1.35	2.36e-01	1.0	3.9	4.0
9	1.58	1.35	1.80	1.61e-01	1.0	5.8	5.9
10	2.20	1.80	2.60	7.45e-02	1.8	5.7	6.0

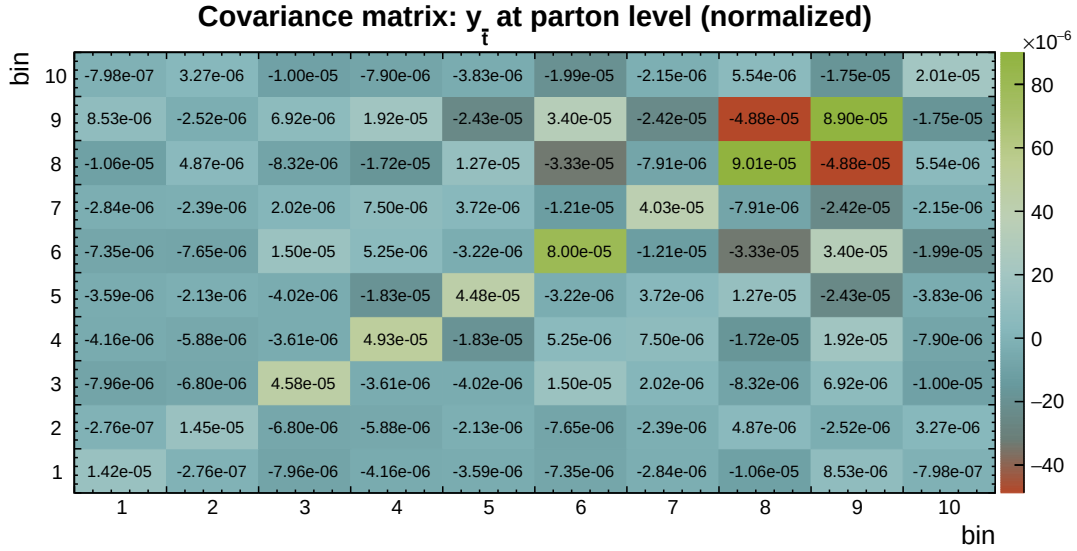

Table B.9 The result σ and its uncertainty per bin of the normalized differential $t\bar{t}$ production cross sections measured as a function of the rapidity of the leading top quark y_t *(leading)*. Measurement is performed at parton level in the full phase space. The corresponding covariance and correlation matrices are presented below the table.

bin	center	left	right	σ	Δ_σ^{stat} (%)	Δ_σ^{syst} (%)	Δ_σ^{tot} (%)
1	−2.12	−2.60	−1.65	8.21e-02	1.7	4.7	5.0
2	−1.38	−1.65	−1.10	1.91e-01	0.9	2.6	2.8
3	−0.82	−1.10	−0.55	2.70e-01	0.9	2.4	2.6
4	−0.28	−0.55	0.00	3.03e-01	0.8	2.3	2.4
5	0.28	0.00	0.55	3.04e-01	0.8	2.3	2.4
6	0.82	0.55	1.10	2.70e-01	0.9	2.1	2.3
7	1.38	1.10	1.65	1.89e-01	1.0	4.0	4.1
8	2.12	1.65	2.60	8.62e-02	1.5	5.6	5.8

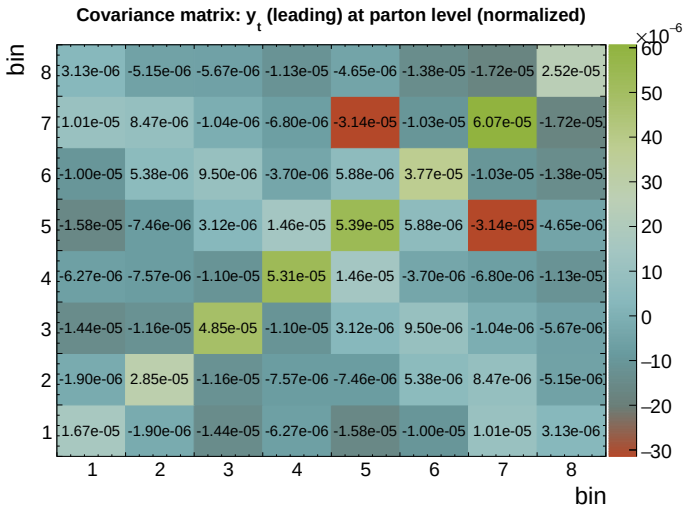

Table B.10 The result σ and its uncertainty per bin of the normalized differential $t\bar{t}$ production cross sections measured as a function of the rapidity of the trailing top quark y_t *(trailing)*. Measurement is performed at parton level in the full phase space. The corresponding covariance and correlation matrices are presented below the table.

bin	center	left	right	σ	Δ_σ^{stat} (%)	Δ_σ^{syst} (%)	Δ_σ^{tot} (%)
1	−2.12	−2.60	−1.65	8.68e-02	1.7	5.1	5.4
2	−1.38	−1.65	−1.10	1.91e-01	1.0	3.3	3.5
3	−0.82	−1.10	−0.55	2.65e-01	1.0	3.3	3.5
4	−0.28	−0.55	0.00	2.99e-01	0.9	2.3	2.5
5	0.28	0.00	0.55	2.97e-01	0.9	4.1	4.2
6	0.82	0.55	1.10	2.70e-01	1.0	3.0	3.2
7	1.38	1.10	1.65	1.97e-01	1.0	2.8	3.0
8	2.12	1.65	2.60	8.64e-02	1.7	4.5	4.8

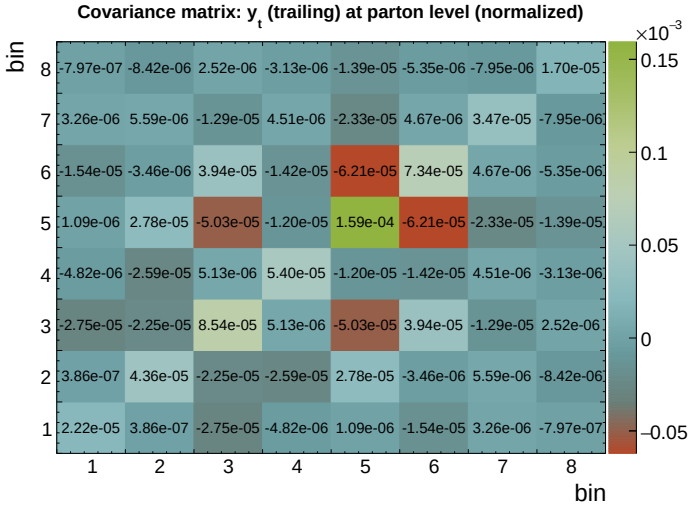

Table B.11 The result σ and its uncertainty per bin of the normalized differential $t\bar{t}$ production cross sections measured as a function of the difference in absolute rapidity between the top quark and antiquark $\Delta|y|(t,\bar{t})$. Measurement is performed at parton level in the full phase space. The corresponding covariance and correlation matrices are presented below the table.

bin	center	left	right	σ	Δ_{σ}^{stat} (%)	Δ_{σ}^{syst} (%)	Δ_{σ}^{tot} (%)
1	−2.00	−2.60	−1.40	5.24e-02	2.0	5.2	5.6
2	−1.15	−1.40	−0.90	1.93e-01	1.1	4.7	4.9
3	−0.65	−0.90	−0.40	3.21e-01	1.0	2.3	2.5
4	−0.20	−0.40	0.00	4.36e-01	1.0	3.2	3.3
5	0.20	0.00	0.40	4.43e-01	1.0	2.6	2.8
6	0.65	0.40	0.90	3.25e-01	1.1	3.9	4.1
7	1.15	0.90	1.40	1.99e-01	1.2	3.2	3.4
8	2.00	1.40	2.60	5.49e-02	1.9	7.7	7.9

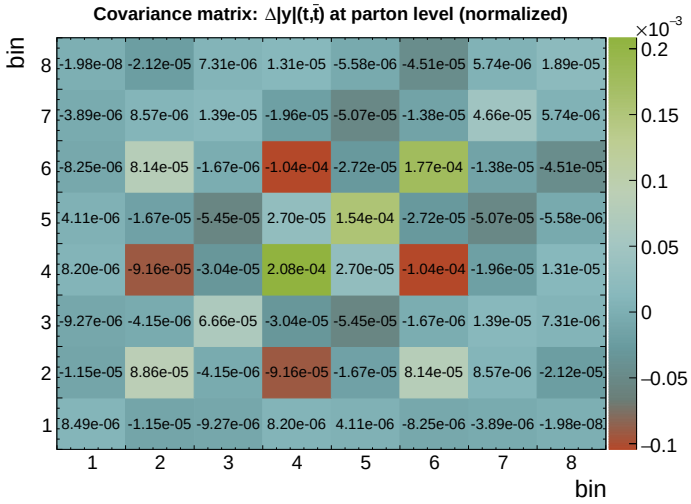

Table B.12 The result σ and its uncertainty per bin of the normalized differential $t\bar{t}$ production cross sections measured as a function of the difference in azimuthal angle between the top quark and antiquark $\Delta\phi(t,\bar{t})$. Measurement is performed at parton level in the full phase space. The corresponding covariance and correlation matrices are presented below the table.

bin	center	left	right	σ	Δ_{σ}^{stat} (%)	Δ_{σ}^{syst} (%)	Δ_{σ}^{tot} (%)
1	0.785	0.000	1.570	6.34e-02	1.1	5.3	5.4
2	2.120	1.570	2.670	2.18e-01	0.6	4.1	4.1
3	2.845	2.670	3.020	1.02e+00	0.6	2.6	2.7
4	3.081	3.020	3.142	2.50e+00	0.7	6.0	6.1

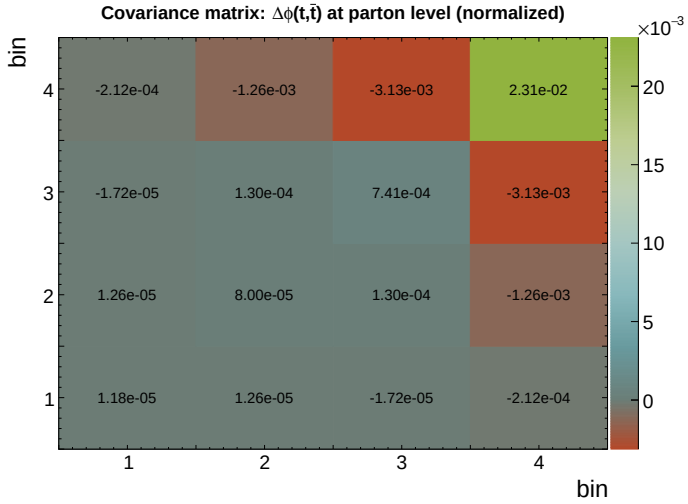

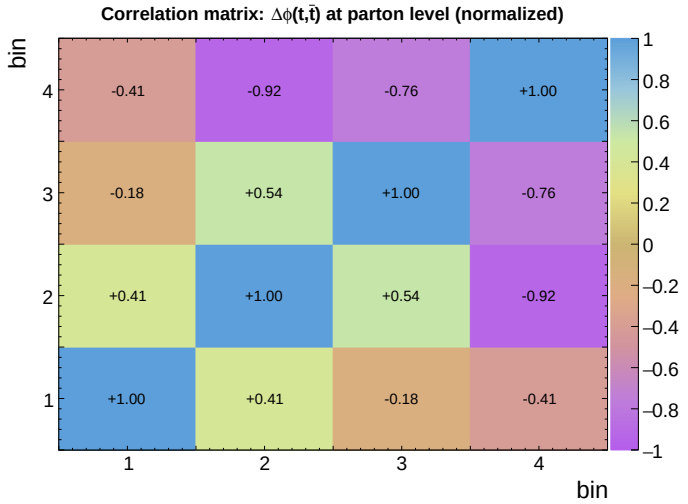

Table B.13 The result σ and its uncertainty per bin of the normalized differential $t\bar{t}$ production cross sections measured as a function of the transverse momentum of the top-quark pair $p_T^{t\bar{t}}$. Measurement is performed at parton level in the full phase space. The corresponding covariance and correlation matrices are presented below the table.

bin	center (GeV)	left (GeV)	right (GeV)	σ (GeV^{-1})	Δ_σ^{stat} (%)	Δ_σ^{syst} (%)	Δ_σ^{tot} (%)
1	20.0	0.0	40.0	1.28e-02	0.5	6.7	6.7
2	70.0	40.0	100.0	4.81e-03	1.0	12.6	12.7
3	150.0	100.0	200.0	1.51e-03	0.9	3.4	3.6
4	255.0	200.0	310.0	3.37e-04	1.5	3.7	4.0
5	365.0	310.0	420.0	8.93e-05	2.2	5.1	5.6
6	495.0	420.0	570.0	2.30e-05	3.7	6.3	7.4

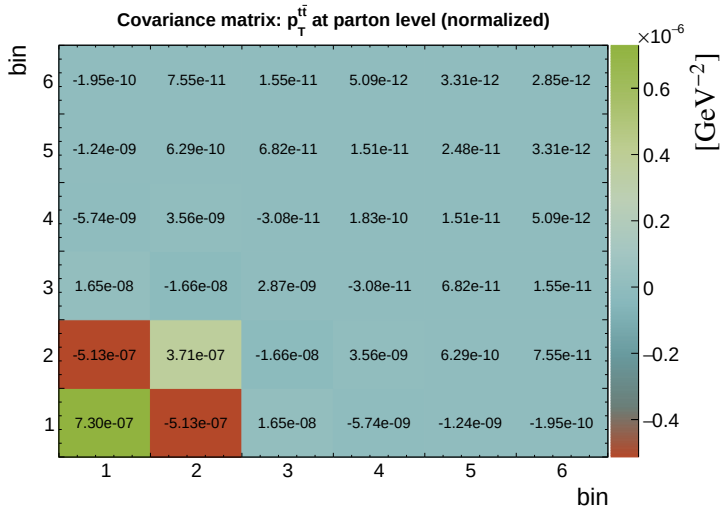

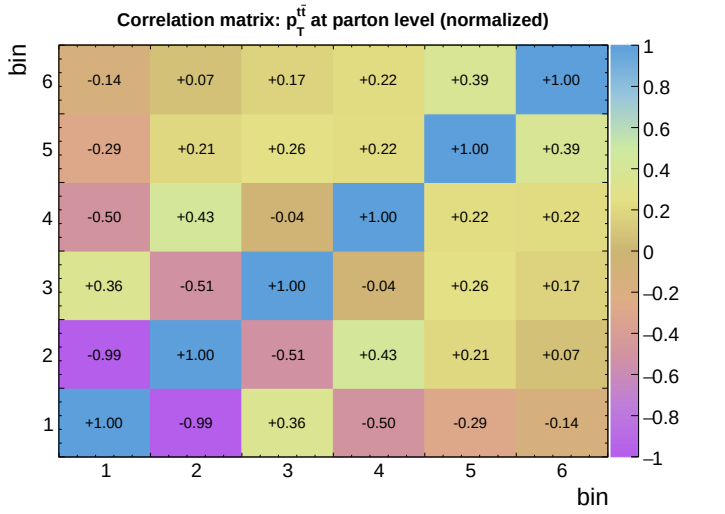

Table B.14 The result σ and its uncertainty per bin of the normalized differential $t\bar{t}$ production cross sections measured as a function of the invariant mass of the top-quark pair $m_{t\bar{t}}$. Measurement is performed at parton level in the full phase space. The corresponding covariance and correlation matrices are presented below the table.

bin	center (GeV)	left (GeV)	right (GeV)	σ (GeV^{-1})	Δ_σ^{stat} (%)	Δ_σ^{syst} (%)	Δ_σ^{tot} (%)
1	340.0	300.0	380.0	1.98e-03	1.8	9.1	9.3
2	425.0	380.0	470.0	3.99e-03	1.2	4.6	4.7
3	545.0	470.0	620.0	2.01e-03	1.1	2.8	3.1
4	720.0	620.0	820.0	6.36e-04	1.7	5.6	5.8
5	960.0	820.0	1100.0	1.44e-04	2.9	7.3	7.9
6	1300.0	1100.0	1500.0	2.72e-05	3.9	7.6	8.5
7	2000.0	1500.0	2500.0	2.45e-06	9.8	19.0	21.3

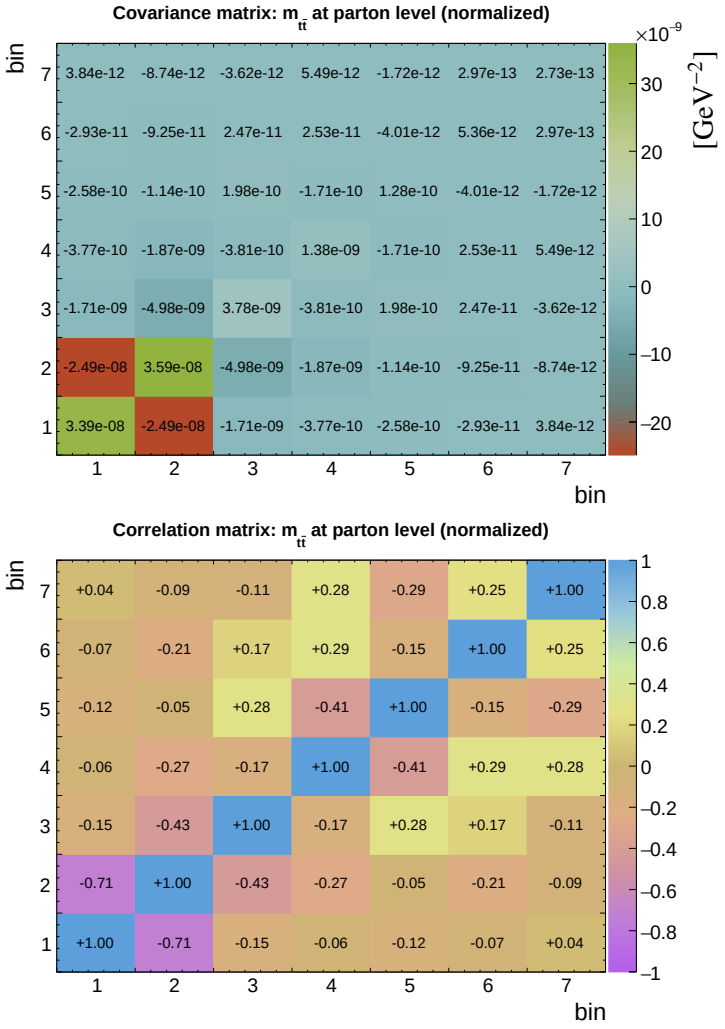

Table B.15 The result σ and its uncertainty per bin of the normalized differential $t\bar{t}$ production cross sections measured as a function of the rapidity of the top-quark pair $y_{t\bar{t}}$. Measurement is performed at parton level in the full phase space. The corresponding covariance and correlation matrices are presented below the table.

bin	center	left	right	σ	Δ_σ^{stat} (%)	Δ_σ^{syst} (%)	Δ_σ^{tot} (%)
1	−2.10	−2.60	−1.60	5.39e-02	2.4	10.9	11.1
2	−1.40	−1.60	−1.20	1.73e-01	1.1	2.3	2.5
3	−1.00	−1.20	−0.80	2.56e-01	1.0	3.6	3.8
4	−0.60	−0.80	−0.40	3.16e-01	0.9	2.4	2.6
5	−0.20	−0.40	0.00	3.69e-01	0.9	2.7	2.8
6	0.20	0.00	0.40	3.53e-01	0.9	2.4	2.5
7	0.60	0.40	0.80	3.21e-01	0.9	2.1	2.2
8	1.00	0.80	1.20	2.61e-01	1.0	2.9	3.1
9	1.40	1.20	1.60	1.69e-01	1.1	2.9	3.1
10	2.10	1.60	2.60	5.89e-02	2.1	5.7	6.1

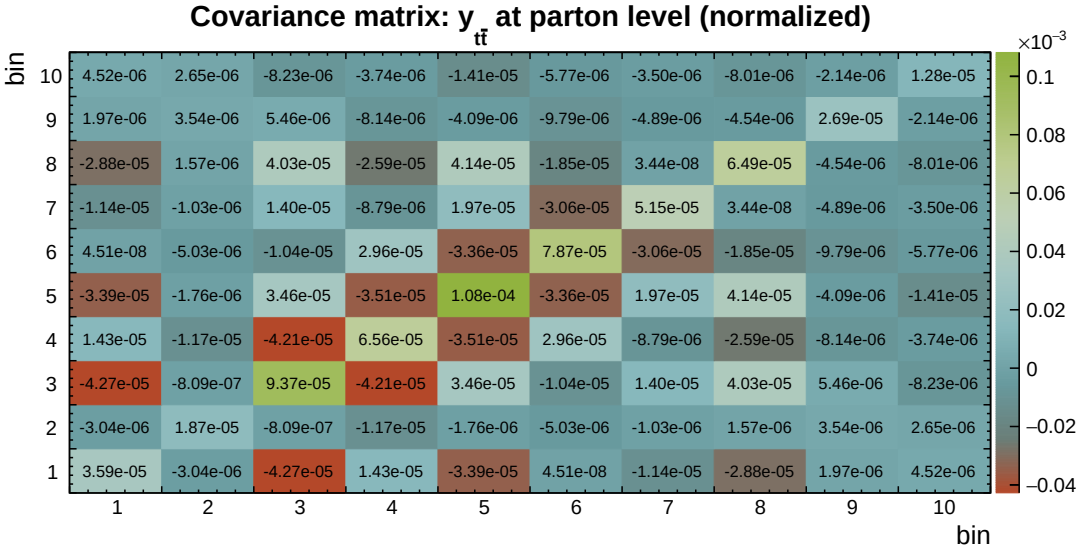

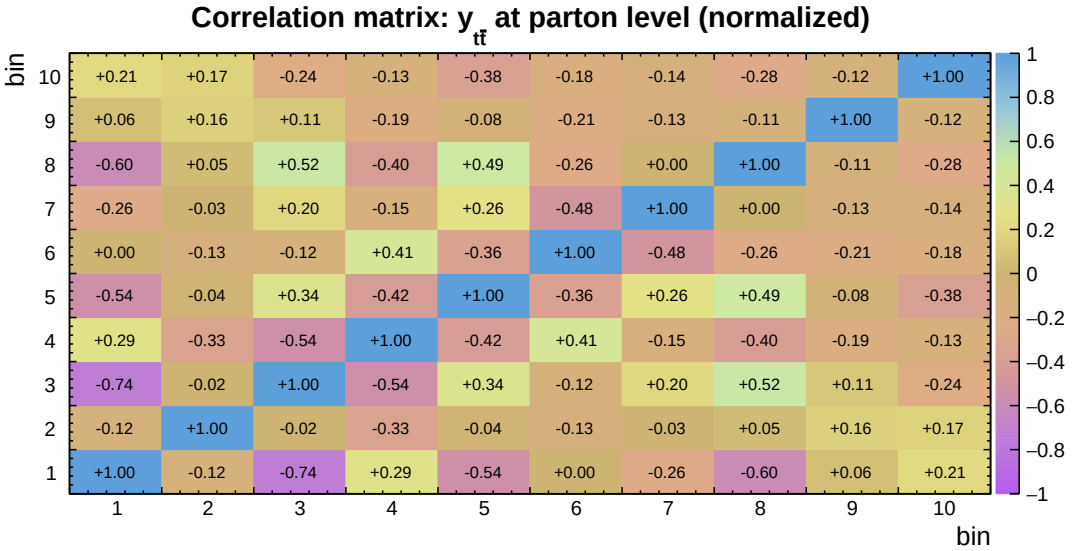

Table B.16 The result σ and its uncertainty per bin of the absolute differential $t\bar{t}$ production cross sections measured as a function of the transverse momentum of the top quark p_T^t. Measurement is performed at parton level in the full phase space. The corresponding covariance and correlation matrices are presented below the table.

bin	center (GeV)	left (GeV)	right (GeV)	σ (pb/GeV)	Δ_σ^{stat} (%)	Δ_σ^{syst} (%)	Δ_σ^{tot} (%)
1	32.5	0.0	65.0	3.49e+00	1.1	8.0	8.0
2	95.0	65.0	125.0	5.09e+00	1.0	9.2	9.2
3	162.5	125.0	200.0	2.84e+00	0.9	7.4	7.5
4	245.0	200.0	290.0	8.42e-01	1.3	6.1	6.2
5	345.0	290.0	400.0	1.87e-01	1.6	7.0	7.1
6	475.0	400.0	550.0	3.45e-02	3.8	8.8	9.6

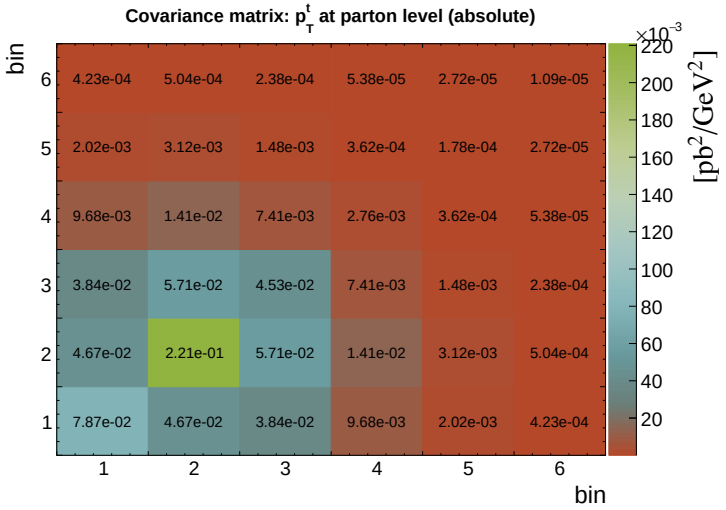

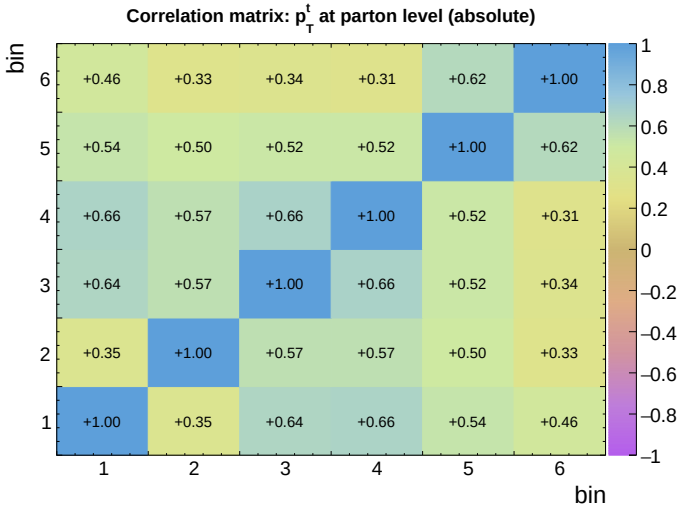

Table B.17 The result σ and its uncertainty per bin of the absolute differential $t\bar{t}$ production cross sections measured as a function of the transverse momentum of the top antiquark $p_T^{\bar{t}}$. Measurement is performed at parton level in the full phase space. The corresponding covariance and correlation matrices are presented below the table.

bin	center (GeV)	left (GeV)	right (GeV)	σ (pb/GeV)	Δ_σ^{stat} (%)	Δ_σ^{syst} (%)	Δ_σ^{tot} (%)
1	32.5	0.0	65.0	3.53e+00	1.1	8.9	8.9
2	95.0	65.0	125.0	5.10e+00	1.0	8.5	8.6
3	162.5	125.0	200.0	2.75e+00	0.9	7.7	7.7
4	245.0	200.0	290.0	8.69e-01	1.2	6.8	7.0
5	345.0	290.0	400.0	1.90e-01	1.6	6.4	6.6
6	475.0	400.0	550.0	3.34e-02	3.9	14.0	14.5

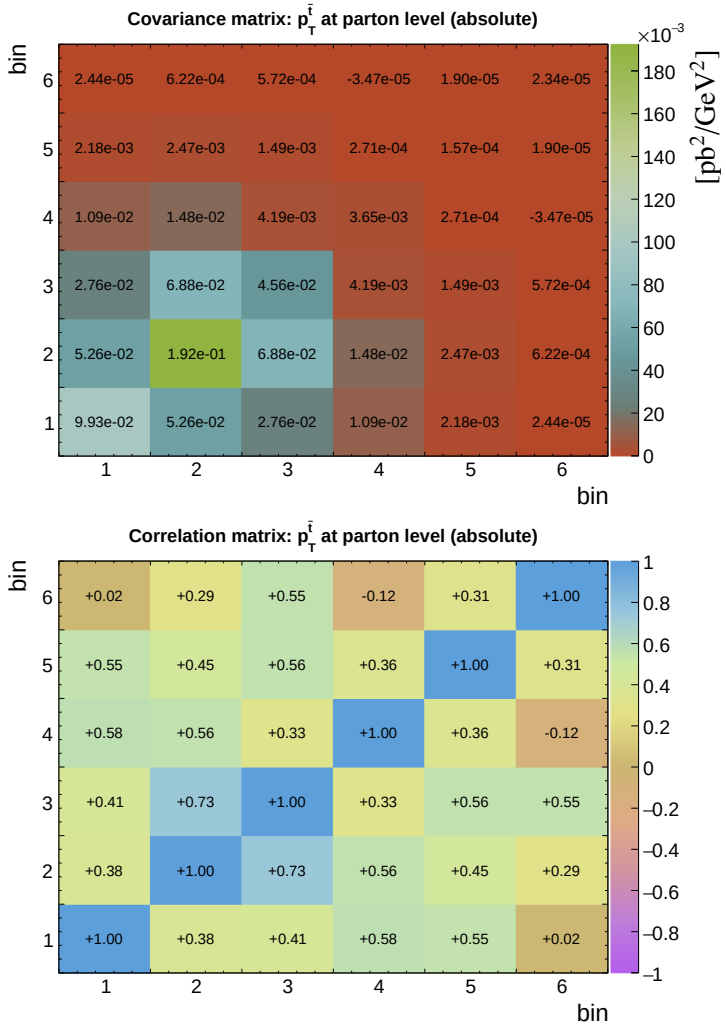

Table B.18 The result σ and its uncertainty per bin of the absolute differential $t\bar{t}$ production cross sections measured as a function of the transverse momentum of the leading top quark p_T^t *(leading)*. Measurement is performed at parton level in the full phase space. The corresponding covariance and correlation matrices are presented below the table.

bin	center (GeV)	left (GeV)	right (GeV)	σ (pb/GeV)	Δ_σ^{stat} (%)	Δ_σ^{syst} (%)	Δ_σ^{tot} (%)
1	32.5	0.0	65.0	2.22e+00	1.3	8.8	8.9
2	95.0	65.0	125.0	5.13e+00	0.7	7.9	7.9
3	162.5	125.0	200.0	3.38e+00	0.7	7.8	7.9
4	245.0	200.0	290.0	1.17e+00	0.9	6.1	6.2
5	345.0	290.0	400.0	2.74e-01	1.2	6.3	6.4
6	475.0	400.0	550.0	5.15e-02	2.8	9.0	9.5

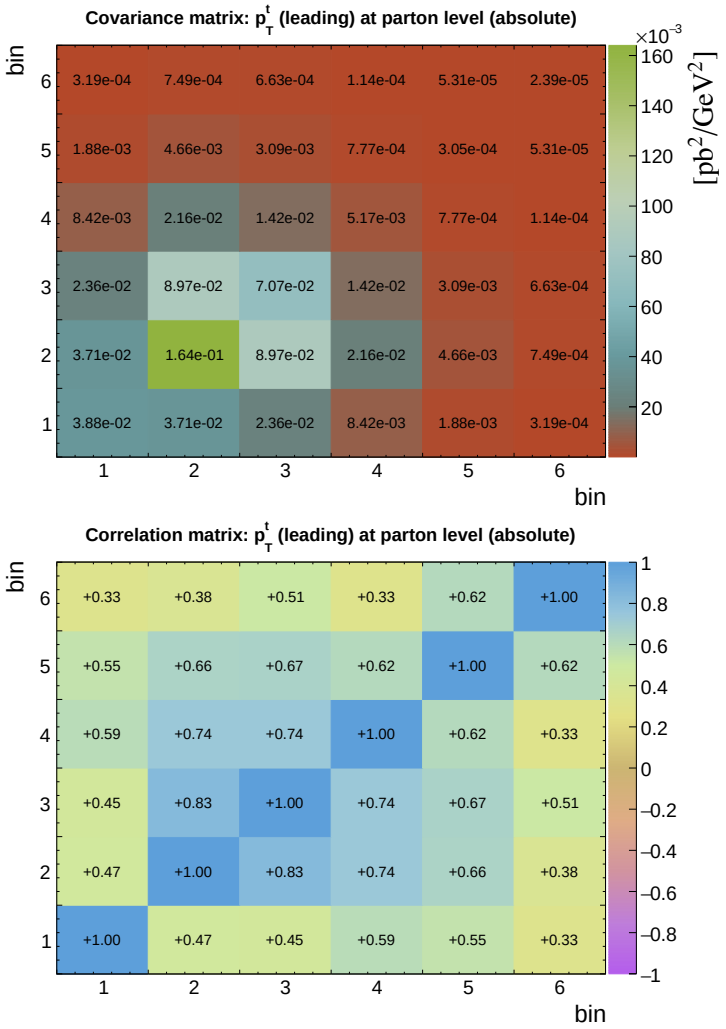

Table B.19 The result σ and its uncertainty per bin of the absolute differential $t\bar{t}$ production cross sections measured as a function of the transverse momentum of the trailing top quark p_T^t *(trailing)*. Measurement is performed at parton level in the full phase space. The corresponding covariance and correlation matrices are presented below the table.

bin	center (GeV)	left (GeV)	right (GeV)	σ (pb/GeV)	Δ_σ^{stat} (%)	Δ_σ^{syst} (%)	Δ_σ^{tot} (%)
1	32.5	0.0	65.0	4.79e+00	0.9	7.8	7.8
2	95.0	65.0	125.0	5.07e+00	1.1	9.6	9.7
3	162.5	125.0	200.0	2.23e+00	1.2	7.2	7.3
4	245.0	200.0	290.0	5.46e-01	1.9	7.9	8.1
5	345.0	290.0	400.0	1.05e-01	2.4	8.1	8.5
6	475.0	400.0	550.0	1.65e-02	6.5	16.2	17.4

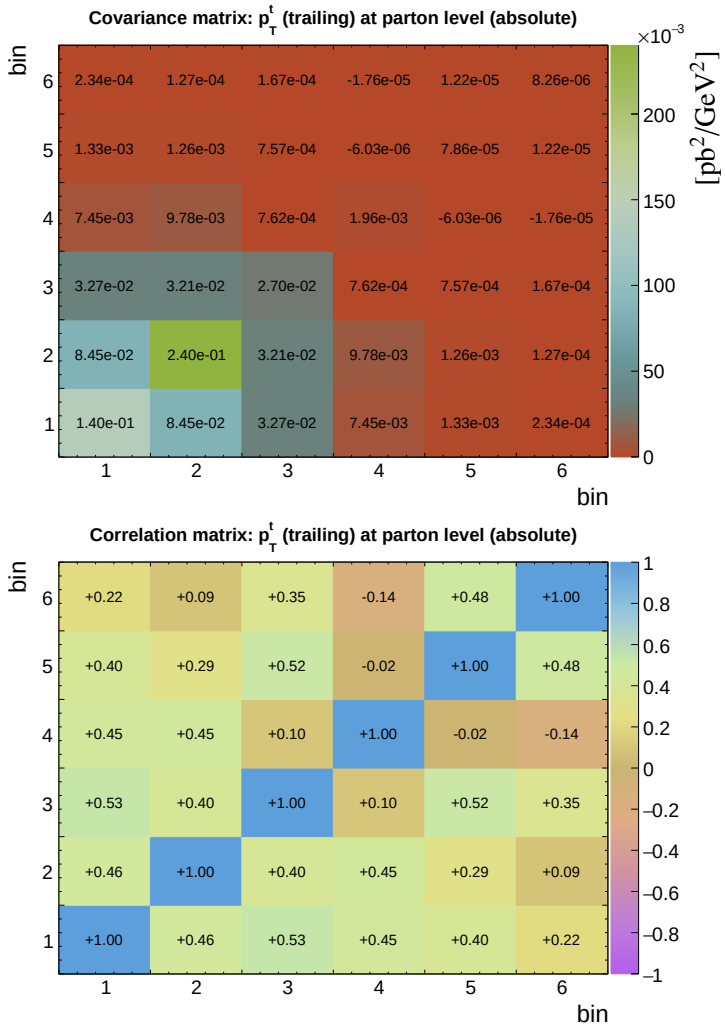

Table B.20 The result σ and its uncertainty per bin of the absolute differential $t\bar{t}$ production cross sections measured as a function of the transverse momentum of the top quark in the rest frame of the $t\bar{t}$-system p_T^t *($t\bar{t}$ rest frame)*. Measurement is performed at parton level in the full phase space. The corresponding covariance and correlation matrices are presented below the table.

bin	center (GeV)	left (GeV)	right (GeV)	σ (pb/GeV)	Δ_σ^{stat} (%)	Δ_σ^{syst} (%)	Δ_σ^{tot} (%)
1	32.5	0.0	65.0	3.81e+00	1.1	7.8	7.8
2	95.0	65.0	125.0	5.28e+00	1.1	9.3	9.3
3	162.5	125.0	200.0	2.67e+00	1.0	7.2	7.2
4	245.0	200.0	290.0	6.97e-01	1.5	6.4	6.6
5	345.0	290.0	400.0	1.42e-01	1.9	6.5	6.8
6	475.0	400.0	550.0	2.23e-02	5.1	11.9	13.0

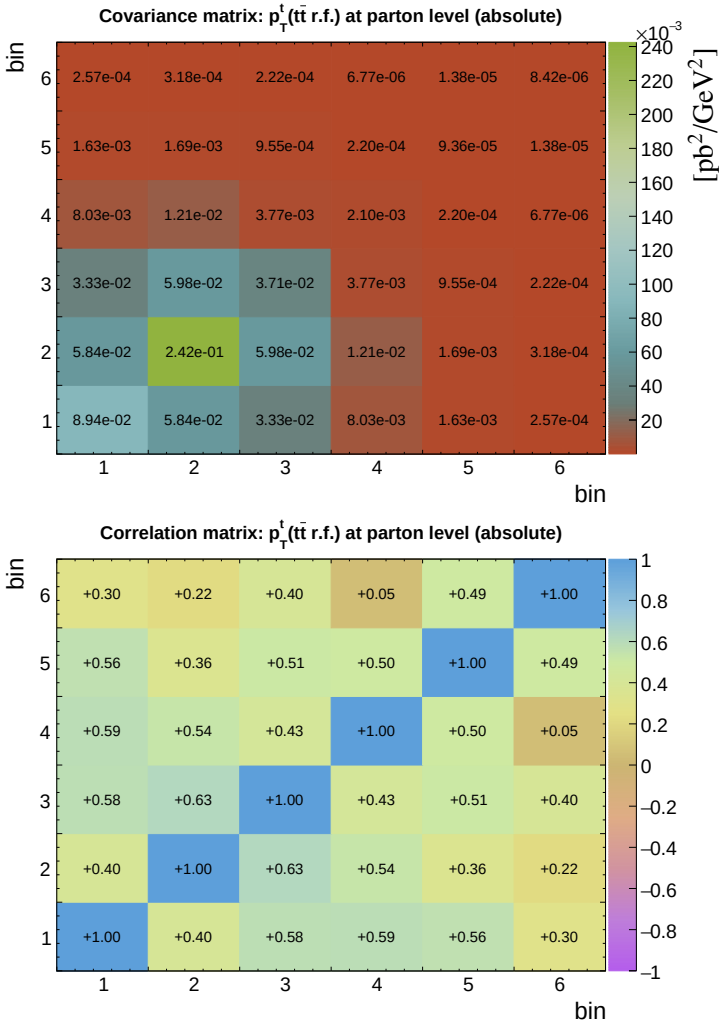

Table B.21 The result σ and its uncertainty per bin of the absolute differential $t\bar{t}$ production cross sections measured as a function of the transverse momentum of the top antiquark in the rest frame of the $t\bar{t}$-system $p_T^{\bar{t}}$ *($t\bar{t}$ rest frame)*. Measurement is performed at parton level in the full phase space. The corresponding covariance and correlation matrices are presented below the table.

bin	center (GeV)	left (GeV)	right (GeV)	σ (pb/GeV)	Δ_σ^{stat} (%)	Δ_σ^{syst} (%)	Δ_σ^{tot} (%)
1	32.5	0.0	65.0	3.81e+00	1.1	7.8	7.8
2	95.0	65.0	125.0	5.28e+00	1.1	9.3	9.3
3	162.5	125.0	200.0	2.67e+00	1.0	7.2	7.2
4	245.0	200.0	290.0	6.97e-01	1.5	6.4	6.6
5	345.0	290.0	400.0	1.42e-01	1.9	6.5	6.8
6	475.0	400.0	550.0	2.23e-02	5.1	11.9	13.0

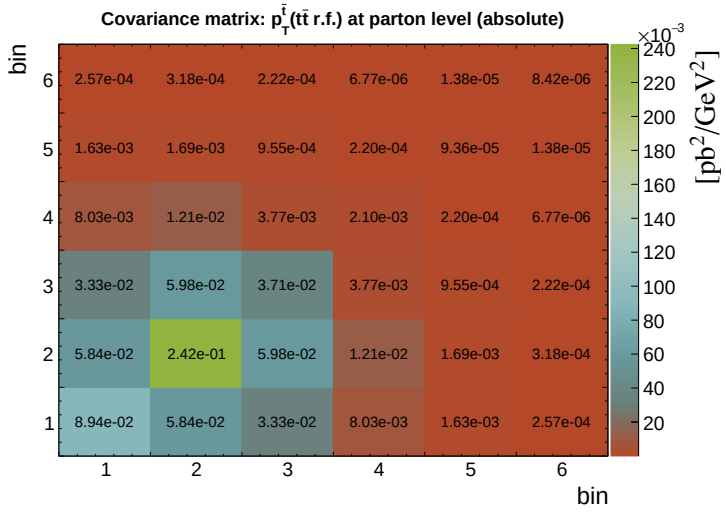

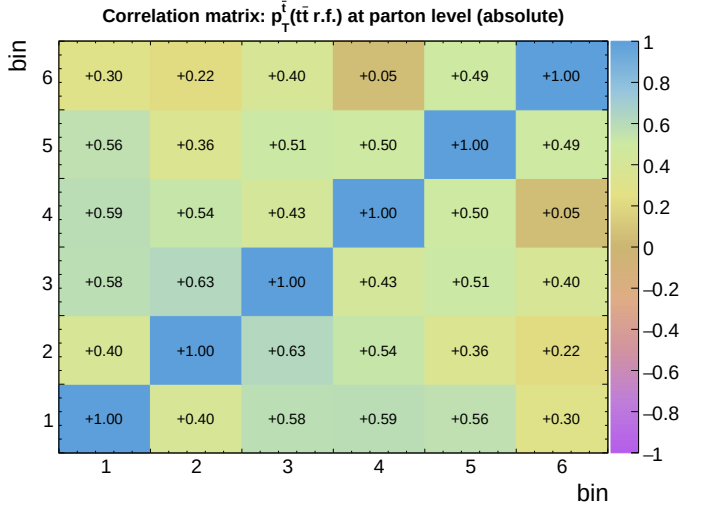

Table B.22 The result σ and its uncertainty per bin of the absolute differential $t\bar{t}$ production cross sections measured as a function of the rapidity of the top quark y_t. Measurement is performed at parton level in the full phase space. The corresponding covariance and correlation matrices are presented below the table.

bin	center	left	right	σ (pb)	Δ_σ^{stat} (%)	Δ_σ^{syst} (%)	Δ_σ^{tot} (%)
1	−2.20	−2.60	−1.80	6.00e+01	2.0	10.2	10.4
2	−1.58	−1.80	−1.35	1.32e+02	1.0	7.4	7.5
3	−1.12	−1.35	−0.90	1.88e+02	1.0	7.0	7.0
4	−0.68	−0.90	−0.45	2.27e+02	0.9	6.9	7.0
5	−0.22	−0.45	0.00	2.45e+02	0.9	7.0	7.1
6	0.22	0.00	0.45	2.47e+02	0.9	7.7	7.8
7	0.68	0.45	0.90	2.33e+02	0.9	7.0	7.1
8	1.12	0.90	1.35	1.84e+02	1.0	7.1	7.2
9	1.58	1.35	1.80	1.33e+02	1.0	7.8	7.8
10	2.20	1.80	2.60	6.30e+01	1.8	8.9	9.1

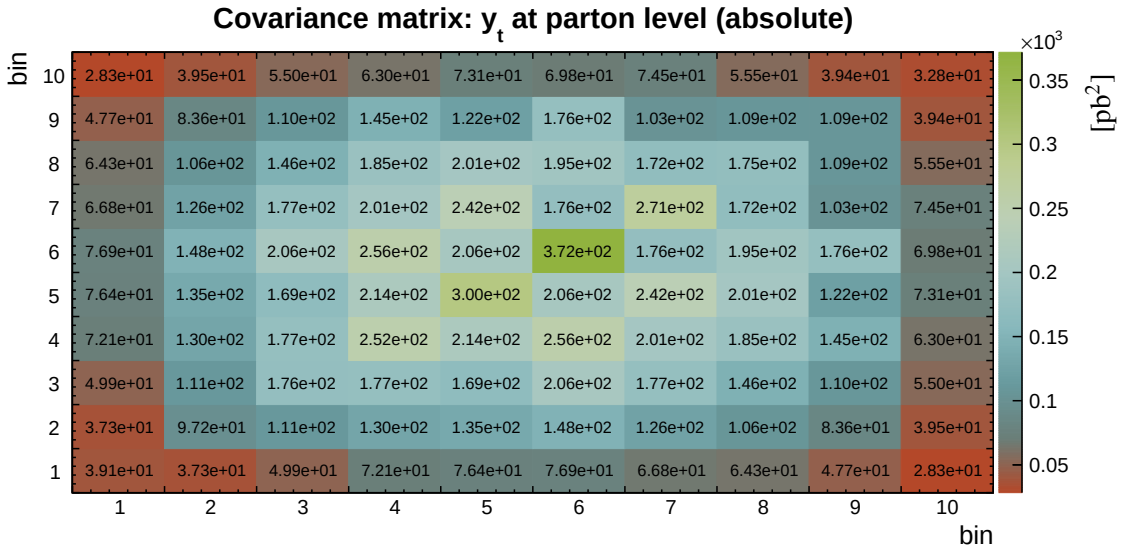

Table B.23 The result σ and its uncertainty per bin of the absolute differential $t\bar{t}$ production cross sections measured as a function of the rapidity of the top antiquark $y_{\bar{t}}$. Measurement is performed at parton level in the full phase space. The corresponding covariance and correlation matrices are presented below the table.

bin	center	left	right	σ (pb)	Δ_{σ}^{stat} (%)	Δ_{σ}^{syst} (%)	Δ_{σ}^{tot} (%)
1	−2.20	−2.60	−1.80	6.11e+01	1.9	9.6	9.8
2	−1.58	−1.80	−1.35	1.30e+02	1.1	7.6	7.7
3	−1.12	−1.35	−0.90	1.88e+02	1.0	6.9	7.0
4	−0.68	−0.90	−0.45	2.27e+02	1.0	6.9	7.0
5	−0.22	−0.45	0.00	2.50e+02	0.9	7.2	7.3
6	0.22	0.00	0.45	2.50e+02	0.9	6.9	6.9
7	0.68	0.45	0.90	2.26e+02	0.9	6.9	6.9
8	1.12	0.90	1.35	1.92e+02	0.9	7.3	7.4
9	1.58	1.35	1.80	1.31e+02	1.0	9.2	9.3
10	2.20	1.80	2.60	6.07e+01	1.9	9.9	10.1

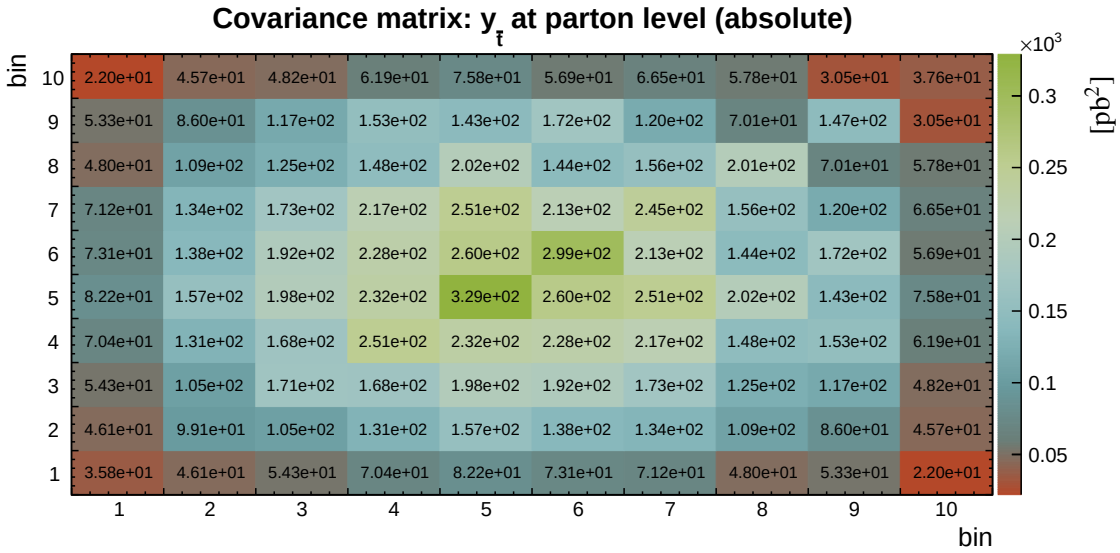

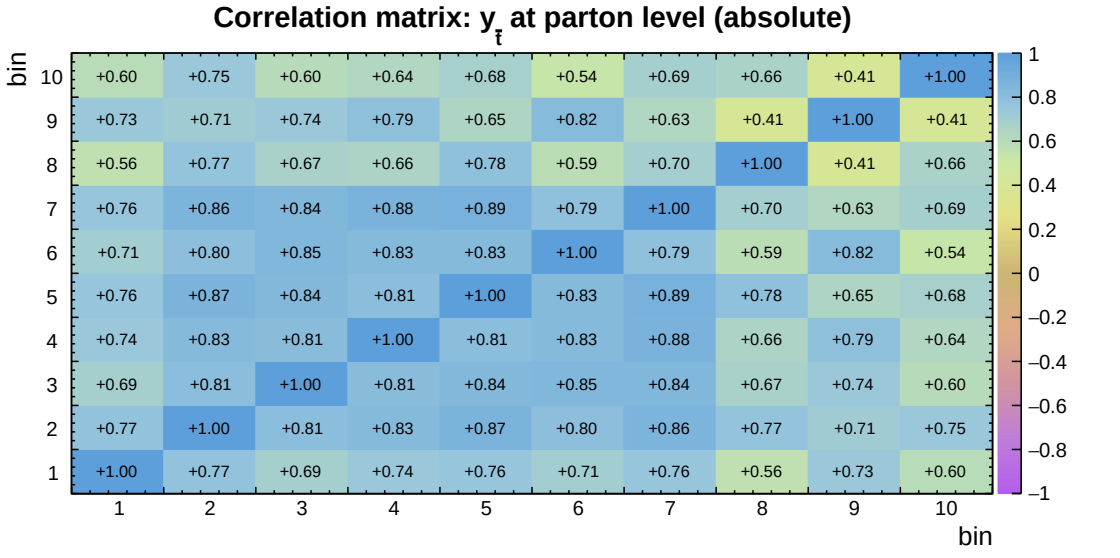

Table B.24 The result σ and its uncertainty per bin of the absolute differential $t\bar{t}$ production cross sections measured as a function of the rapidity of the leading top quark y_t *(leading)*. Measurement is performed at parton level in the full phase space. The corresponding covariance and correlation matrices are presented below the table.

bin	center	left	right	σ (pb)	Δ_σ^{stat} (%)	Δ_σ^{syst} (%)	Δ_σ^{tot} (%)
1	−2.12	−2.60	−1.65	6.71e+01	1.8	9.7	9.9
2	−1.38	−1.65	−1.10	1.56e+02	1.0	7.6	7.7
3	−0.82	−1.10	−0.55	2.21e+02	0.8	6.7	6.7
4	−0.28	−0.55	0.00	2.47e+02	0.8	6.8	6.8
5	0.28	0.00	0.55	2.48e+02	0.9	6.8	6.8
6	0.82	0.55	1.10	2.21e+02	0.9	6.7	6.7
7	1.38	1.10	1.65	1.55e+02	1.0	8.5	8.5
8	2.12	1.65	2.60	7.04e+01	1.6	9.6	9.7

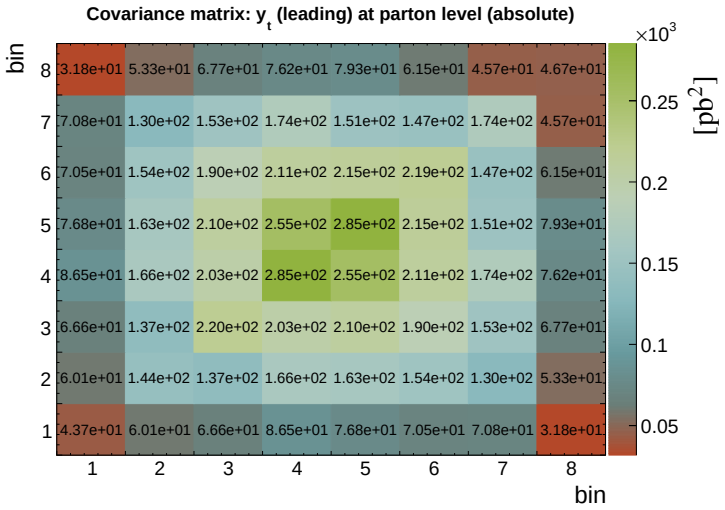

Table B.25 The result σ and its uncertainty per bin of the absolute differential $t\bar{t}$ production cross sections measured as a function of the rapidity of the trailing top quark y_t *(trailing)*. Measurement is performed at parton level in the full phase space. The corresponding covariance and correlation matrices are presented below the table.

bin	center	left	right	σ (pb)	Δ_σ^{stat} (%)	Δ_σ^{syst} (%)	Δ_σ^{tot} (%)
1	−2.12	−2.60	−1.65	7.06e+01	1.9	10.3	10.5
2	−1.38	−1.65	−1.10	1.55e+02	1.0	7.6	7.7
3	−0.82	−1.10	−0.55	2.16e+02	0.9	6.8	6.8
4	−0.28	−0.55	0.00	2.43e+02	0.9	7.2	7.2
5	0.28	0.00	0.55	2.42e+02	0.9	7.8	7.9
6	0.82	0.55	1.10	2.19e+02	0.9	6.9	6.9
7	1.38	1.10	1.65	1.60e+02	1.0	7.4	7.5
8	2.12	1.65	2.60	7.03e+01	1.8	8.8	9.0

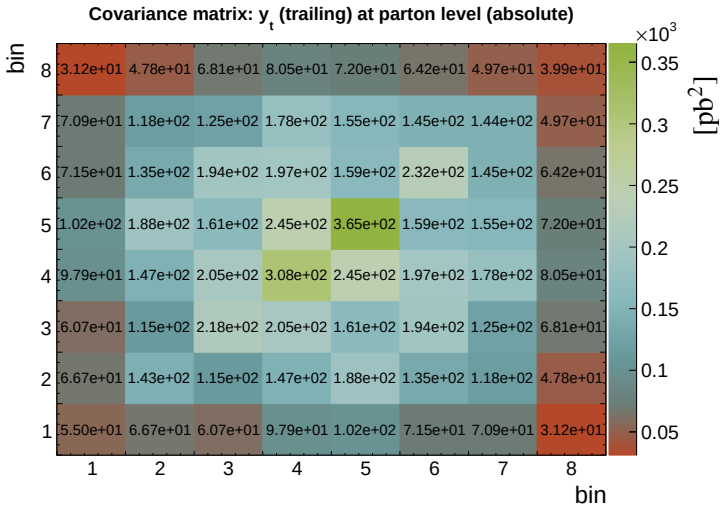

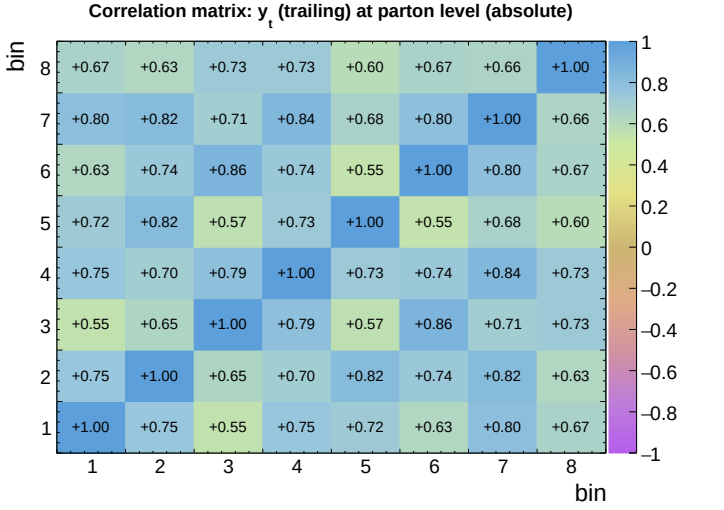

Table B.26 The result σ and its uncertainty per bin of the absolute differential $t\bar{t}$ production cross sections measured as a function of the difference in absolute rapidity between the top quark and anti-quark $\Delta|y|(t,\bar{t})$. Measurement is performed at parton level in the full phase space. The corresponding covariance and correlation matrices are presented below the table.

bin	center	left	right	σ (pb)	Δ_σ^{stat} (%)	Δ_σ^{syst} (%)	Δ_σ^{tot} (%)
1	−2.00	−2.60	−1.40	4.36e+01	2.1	9.3	9.6
2	−1.15	−1.40	−0.90	1.61e+02	1.2	8.5	8.6
3	−0.65	−0.90	−0.40	2.67e+02	1.0	7.6	7.6
4	−0.20	−0.40	0.00	3.63e+02	1.0	6.8	6.9
5	0.20	0.00	0.40	3.69e+02	1.0	6.5	6.6
6	0.65	0.40	0.90	2.71e+02	1.1	8.0	8.1
7	1.15	0.90	1.40	1.66e+02	1.2	8.1	8.2
8	2.00	1.40	2.60	4.57e+01	1.9	10.3	10.5

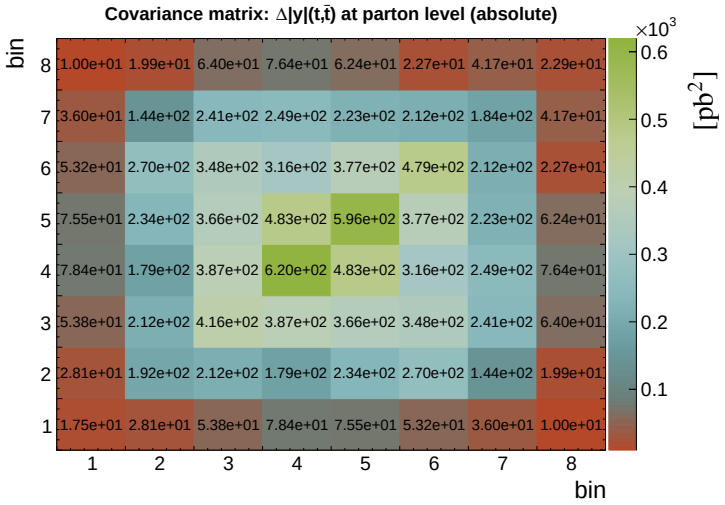

Table B.27 The result σ and its uncertainty per bin of the absolute differential $t\bar{t}$ production cross sections measured as a function of the difference in azimuthal angle between the top quark and antiquark $\Delta\phi(t,\bar{t})$. Measurement is performed at parton level in the full phase space. The corresponding covariance and correlation matrices are presented below the table.

bin	center	left	right	σ (pb)	Δ_{σ}^{stat} (%)	Δ_{σ}^{syst} (%)	Δ_{σ}^{tot} (%)
1	0.785	0.000	1.570	5.29e+01	1.1	9.2	9.3
2	2.120	1.570	2.670	1.82e+02	0.6	8.8	8.8
3	2.845	2.670	3.020	8.49e+02	0.6	7.4	7.4
4	3.081	3.020	3.142	2.09e+03	0.8	8.0	8.1

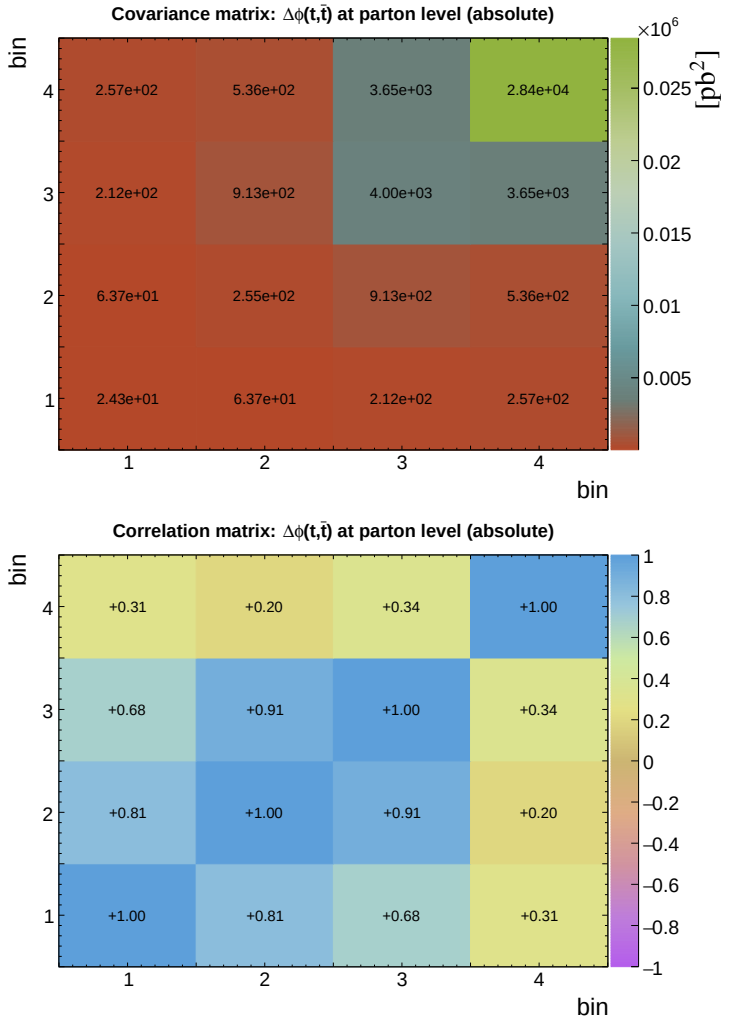

Table B.28 The result σ and its uncertainty per bin of the absolute differential $t\bar{t}$ production cross sections measured as a function of the transverse momentum of the top-quark pair $p_T^{t\bar{t}}$. Measurement is performed at parton level in the full phase space. The corresponding covariance and correlation matrices are presented below the table.

bin	center (GeV)	left (GeV)	right (GeV)	σ (pb/GeV)	Δ_σ^{stat} (%)	Δ_σ^{syst} (%)	Δ_σ^{tot} (%)
1	20.0	0.0	40.0	1.07e+01	0.6	9.4	9.5
2	70.0	40.0	100.0	4.05e+00	1.0	14.2	14.2
3	150.0	100.0	200.0	1.27e+00	0.9	8.1	8.1
4	255.0	200.0	310.0	2.84e-01	1.5	8.2	8.3
5	365.0	310.0	420.0	7.52e-02	2.2	8.8	9.1
6	495.0	420.0	570.0	1.93e-02	3.7	9.4	10.1

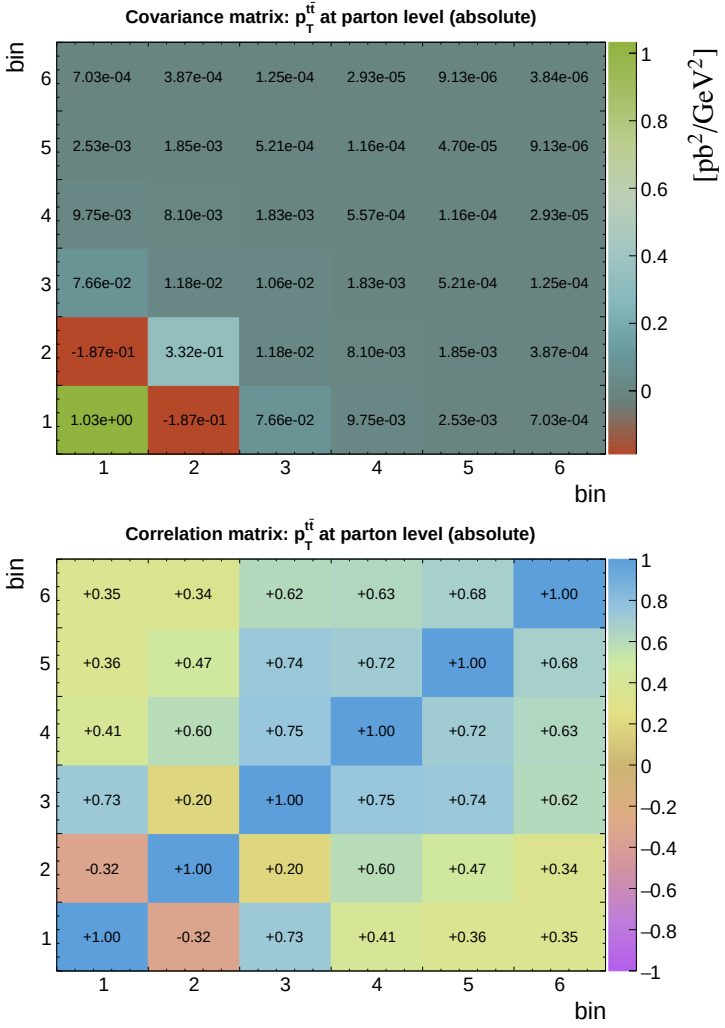

Table B.29 The result σ and its uncertainty per bin of the absolute differential $t\bar{t}$ production cross sections measured as a function of the invariant mass of the top-quark pair $m_{t\bar{t}}$. Measurement is performed at parton level in the full phase space. The corresponding covariance and correlation matrices are presented below the table.

bin	center (GeV)	left (GeV)	right (GeV)	σ (pb/GeV)	Δ_σ^{stat} (%)	Δ_σ^{syst} (%)	Δ_σ^{tot} (%)
1	340.0	300.0	380.0	1.66e+00	1.9	9.8	9.9
2	425.0	380.0	470.0	3.35e+00	1.2	9.7	9.7
3	545.0	470.0	620.0	1.69e+00	1.1	7.2	7.3
4	720.0	620.0	820.0	5.35e-01	1.7	7.1	7.3
5	960.0	820.0	1100.0	1.21e-01	2.9	9.6	10.0
6	1300.0	1100.0	1500.0	2.28e-02	3.9	9.2	10.0
7	2000.0	1500.0	2500.0	2.06e-03	9.8	18.6	21.0

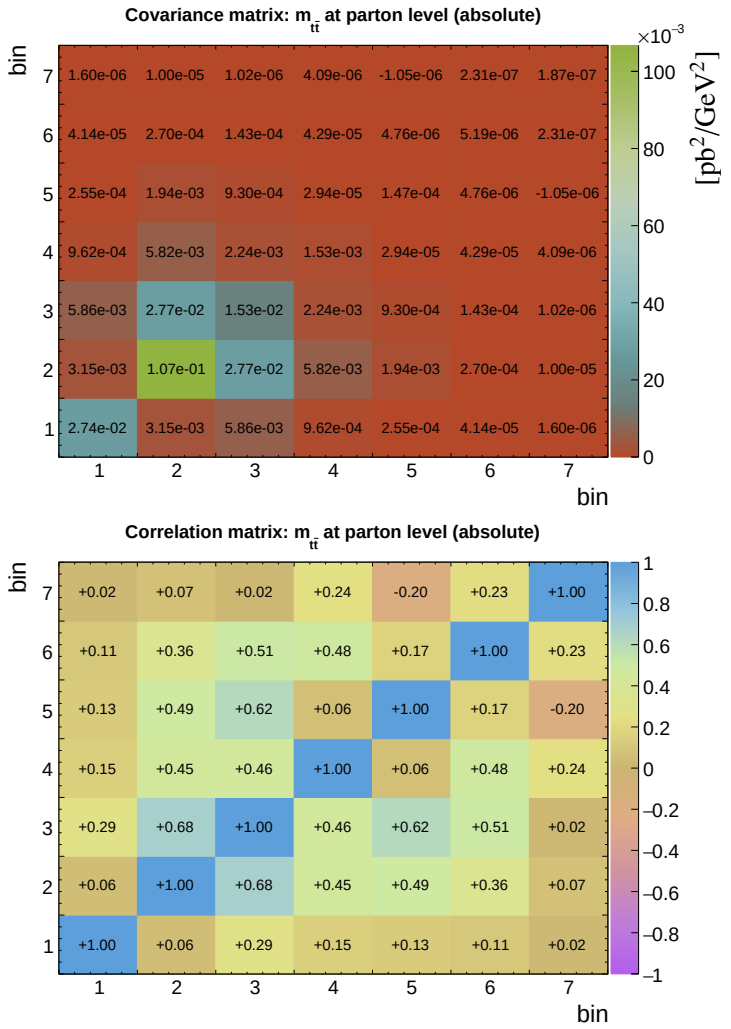

Table B.30 The result σ and its uncertainty per bin of the absolute differential $t\bar{t}$ production cross sections measured as a function of the rapidity of the top-quark pair $y_{t\bar{t}}$. Measurement is performed at parton level in the full phase space. The corresponding covariance and correlation matrices are presented below the table.

bin	center	left	right	σ (pb)	Δ_σ^{stat} (%)	Δ_σ^{syst} (%)	Δ_σ^{tot} (%)
1	−2.10	−2.60	−1.60	4.44e+01	2.5	14.6	14.8
2	−1.40	−1.60	−1.20	1.42e+02	1.1	7.3	7.3
3	−1.00	−1.20	−0.80	2.11e+02	1.0	7.4	7.5
4	−0.60	−0.80	−0.40	2.60e+02	0.9	7.3	7.3
5	−0.20	−0.40	0.00	3.04e+02	0.8	6.3	6.3
6	0.20	0.00	0.40	2.91e+02	0.9	7.2	7.2
7	0.60	0.40	0.80	2.64e+02	0.9	7.2	7.2
8	1.00	0.80	1.20	2.15e+02	0.9	6.9	6.9
9	1.40	1.20	1.60	1.40e+02	1.1	8.0	8.1
10	2.10	1.60	2.60	4.85e+01	2.2	10.6	10.8

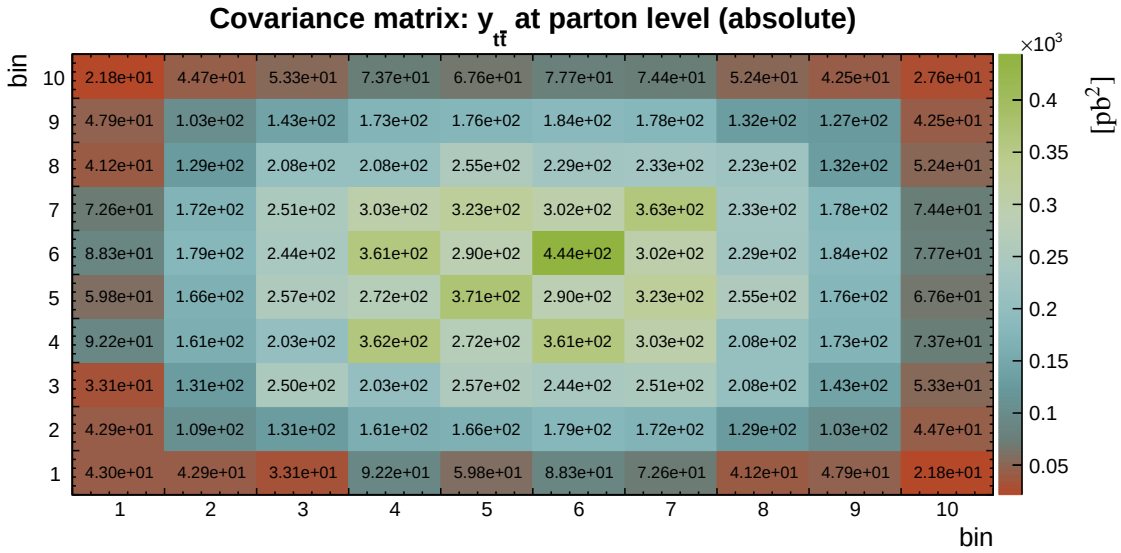

Table B.31 The result σ and its uncertainty per bin of the normalized differential $t\bar{t}$ production cross sections measured as a function of the transverse momentum of the top quark p_T^t. Measurement is performed at particle level in a fiducial phase space. The corresponding covariance and correlation matrices are presented below the table.

bin	center (GeV)	left (GeV)	right (GeV)	σ (GeV^{-1})	Δ_σ^{stat} (%)	Δ_σ^{syst} (%)	Δ_σ^{tot} (%)
1	32.5	0.0	65.0	3.99e-03	0.9	4.1	4.2
2	95.0	65.0	125.0	5.73e-03	0.9	4.4	4.5
3	162.5	125.0	200.0	3.37e-03	0.9	3.4	3.5
4	245.0	200.0	290.0	1.15e-03	1.3	3.5	3.8
5	345.0	290.0	400.0	2.91e-04	1.5	4.6	4.8
6	475.0	400.0	550.0	5.52e-05	3.7	6.5	7.5

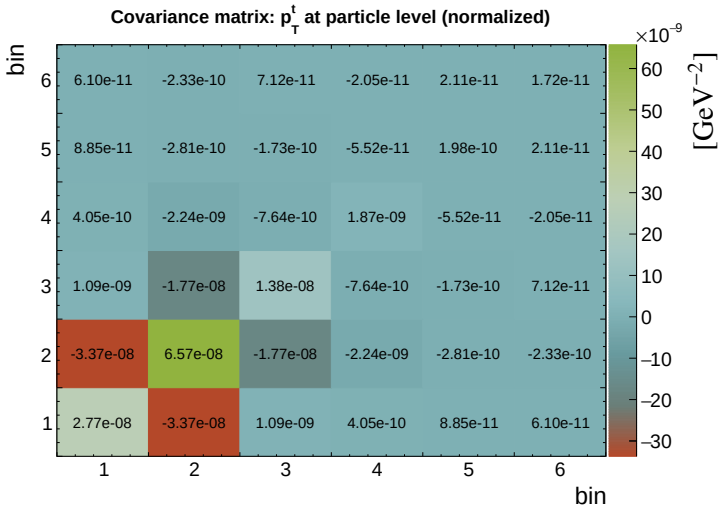

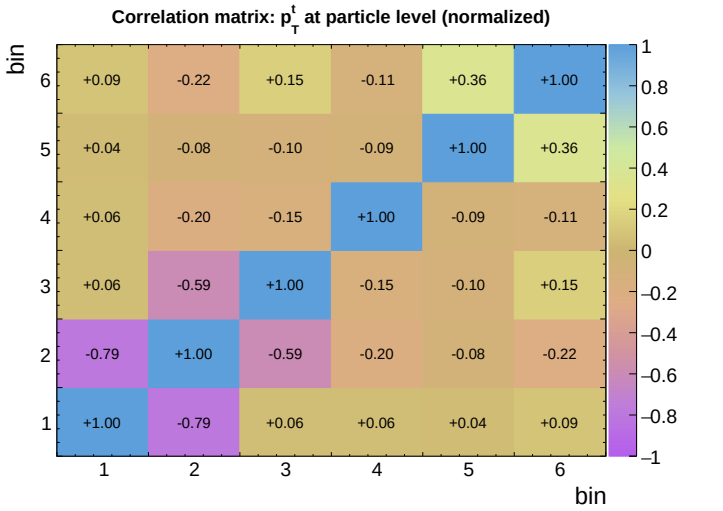

Table B.32 The result σ and its uncertainty per bin of the normalized differential $t\bar{t}$ production cross sections measured as a function of the transverse momentum of the top antiquark $p_T^{\bar{t}}$. Measurement is performed at particle level in a fiducial phase space. The corresponding covariance and correlation matrices are presented below the table.

bin	center (GeV)	left (GeV)	right (GeV)	σ (GeV^{-1})	Δ_σ^{stat} (%)	Δ_σ^{syst} (%)	Δ_σ^{tot} (%)
1	32.5	0.0	65.0	4.04e-03	0.9	5.1	5.1
2	95.0	65.0	125.0	5.75e-03	0.9	3.3	3.5
3	162.5	125.0	200.0	3.28e-03	0.9	3.3	3.4
4	245.0	200.0	290.0	1.19e-03	1.2	4.5	4.7
5	345.0	290.0	400.0	2.94e-04	1.5	4.2	4.4
6	475.0	400.0	550.0	5.37e-05	3.8	12.5	13.1

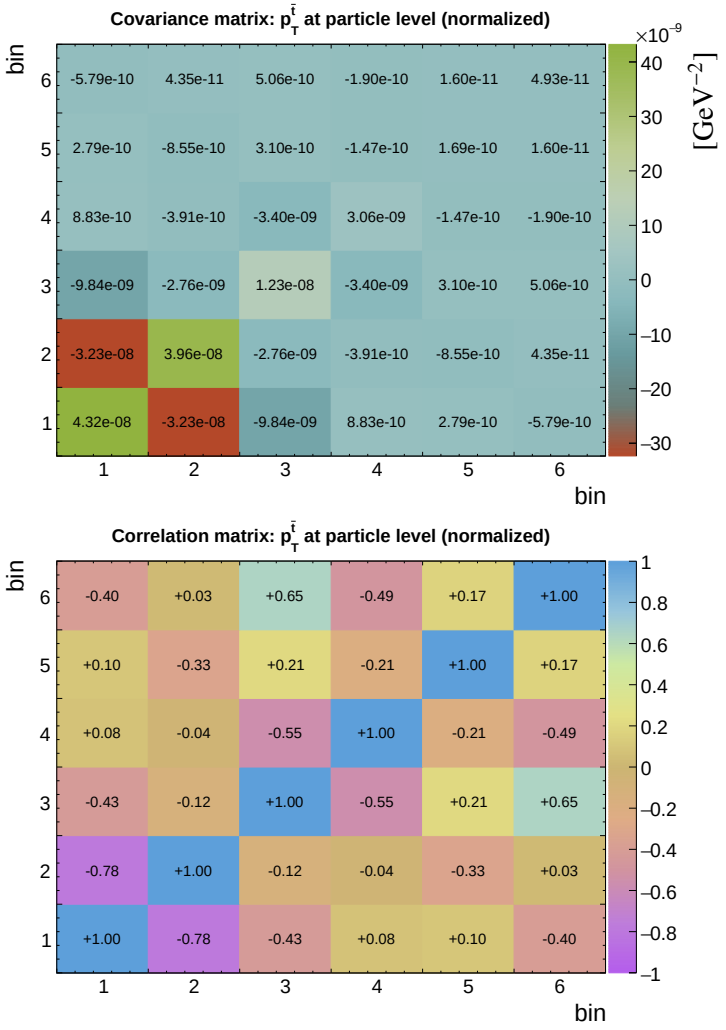

Table B.33 The result σ and its uncertainty per bin of the normalized differential $t\bar{t}$ production cross sections measured as a function of the transverse momentum of the leading top quark p_T^t *(leading)*. Measurement is performed at particle level in a fiducial phase space. The corresponding covariance and correlation matrices are presented below the table.

bin	center (GeV)	left (GeV)	right (GeV)	σ (GeV^{-1})	Δ_σ^{stat} (%)	Δ_σ^{syst} (%)	Δ_σ^{tot} (%)
1	32.5	0.0	65.0	2.47e-03	1.1	5.5	5.6
2	95.0	65.0	125.0	5.74e-03	0.7	2.5	2.6
3	162.5	125.0	200.0	3.94e-03	0.7	2.6	2.7
4	245.0	200.0	290.0	1.57e-03	0.9	2.9	3.1
5	345.0	290.0	400.0	4.20e-04	1.2	3.4	3.5
6	475.0	400.0	550.0	8.32e-05	2.8	6.4	7.0

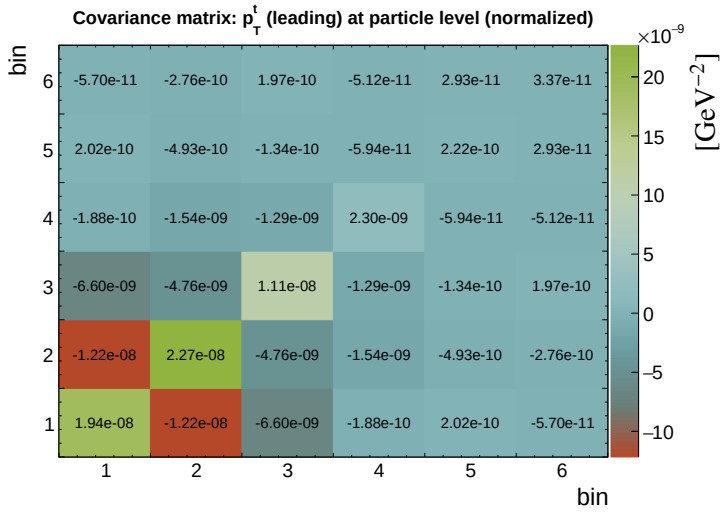

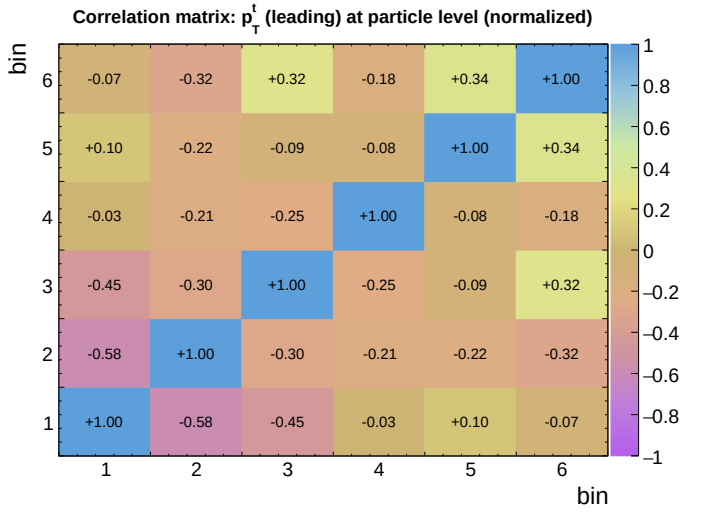

Table B.34 The result σ and its uncertainty per bin of the normalized differential $t\bar{t}$ production cross sections measured as a function of the transverse momentum of the trailing top quark p_T^t *(trailing)*. Measurement is performed at particle level in a fiducial phase space. The corresponding covariance and correlation matrices are presented below the table.

bin	center (GeV)	left (GeV)	right (GeV)	σ (GeV^{-1})	Δ_σ^{stat} (%)	Δ_σ^{syst} (%)	Δ_σ^{tot} (%)
1	32.5	0.0	65.0	5.53e-03	0.7	3.5	3.6
2	95.0	65.0	125.0	5.74e-03	1.0	4.2	4.4
3	162.5	125.0	200.0	2.73e-03	1.2	4.2	4.4
4	245.0	200.0	290.0	7.71e-04	1.8	6.6	6.9
5	345.0	290.0	400.0	1.66e-04	2.3	7.2	7.5
6	475.0	400.0	550.0	2.59e-05	6.2	16.6	17.7

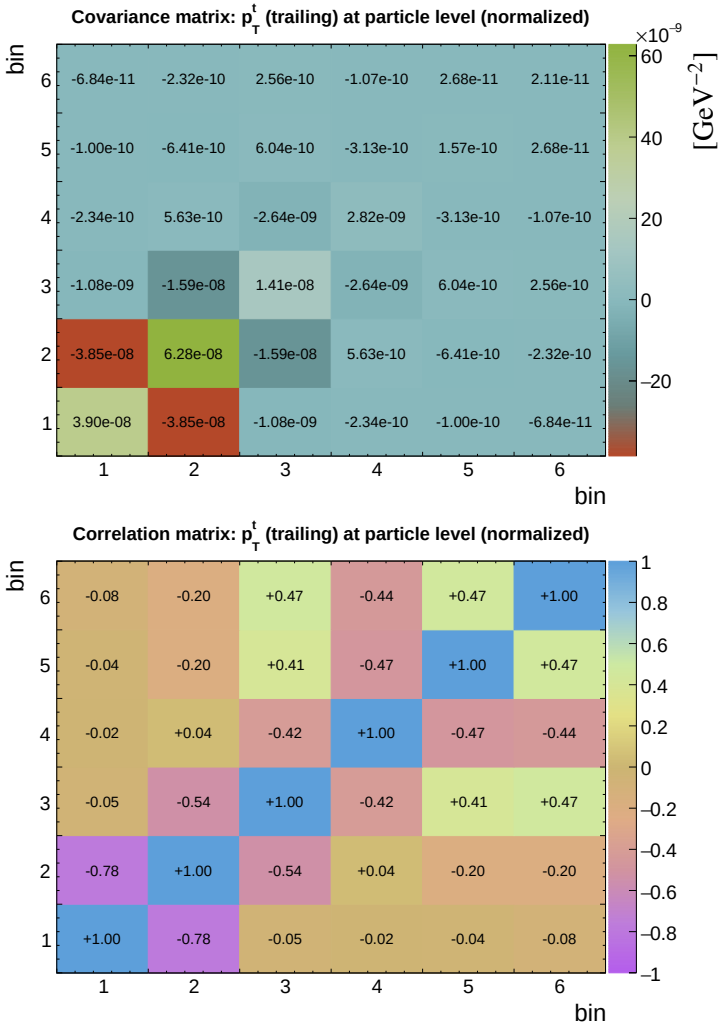

Table B.35 The result σ and its uncertainty per bin of the normalized differential $t\bar{t}$ production cross sections measured as a function of the transverse momentum of the top quark in the rest frame of the $t\bar{t}$-system p_T^t *($t\bar{t}$ rest frame)*. Measurement is performed at particle level in a fiducial phase space. The corresponding covariance and correlation matrices are presented below the table.

bin	center (GeV)	left (GeV)	right (GeV)	σ (GeV^{-1})	Δ_σ^{stat} (%)	Δ_σ^{syst} (%)	Δ_σ^{tot} (%)
1	32.5	0.0	65.0	4.38e-03	0.9	4.0	4.1
2	95.0	65.0	125.0	5.94e-03	0.9	3.6	3.8
3	162.5	125.0	200.0	3.21e-03	1.0	3.0	3.2
4	245.0	200.0	290.0	9.77e-04	1.5	4.3	4.5
5	345.0	290.0	400.0	2.27e-04	1.8	4.8	5.1
6	475.0	400.0	550.0	3.63e-05	5.0	10.6	11.7

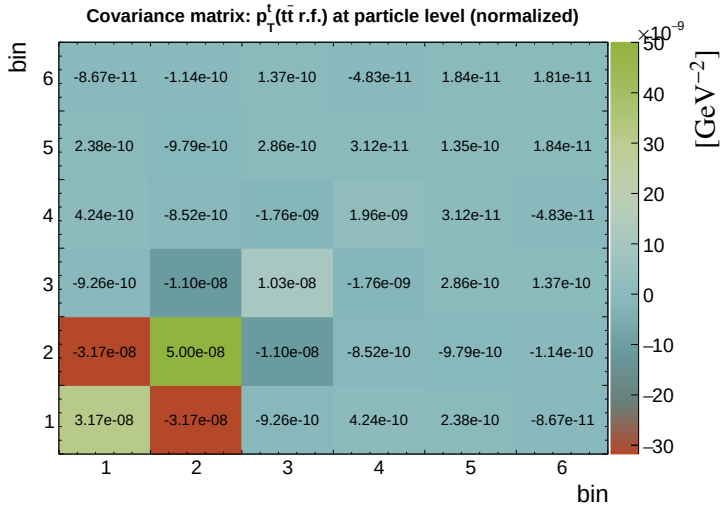

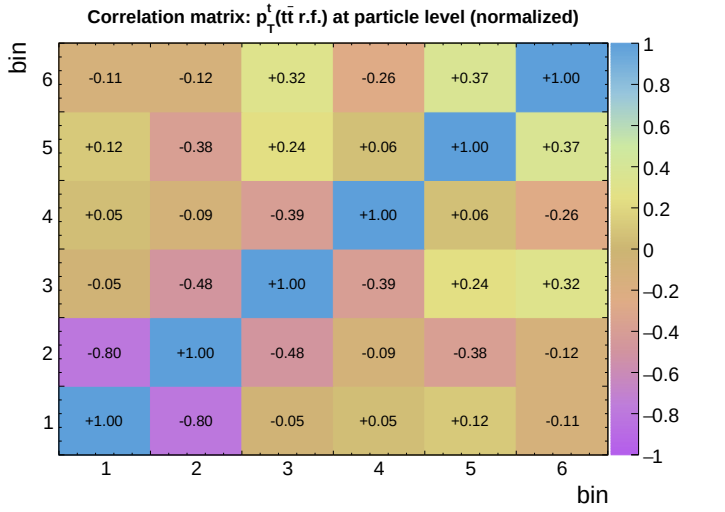

Table B.36 The result σ and its uncertainty per bin of the normalized differential $t\bar{t}$ production cross sections measured as a function of the transverse momentum of the top antiquark in the rest frame of the $t\bar{t}$-system $p_T^{\bar{t}}$ *($t\bar{t}$ rest frame)*. Measurement is performed at particle level in a fiducial phase space. The corresponding covariance and correlation matrices are presented below the table.

bin	center (GeV)	left (GeV)	right (GeV)	σ (GeV^{-1})	Δ_σ^{stat} (%)	Δ_σ^{syst} (%)	Δ_σ^{tot} (%)
1	32.5	0.0	65.0	4.38e-03	0.9	4.0	4.1
2	95.0	65.0	125.0	5.94e-03	0.9	3.6	3.8
3	162.5	125.0	200.0	3.21e-03	1.0	3.0	3.2
4	245.0	200.0	290.0	9.77e-04	1.5	4.3	4.5
5	345.0	290.0	400.0	2.27e-04	1.8	4.8	5.1
6	475.0	400.0	550.0	3.63e-05	5.0	10.6	11.7

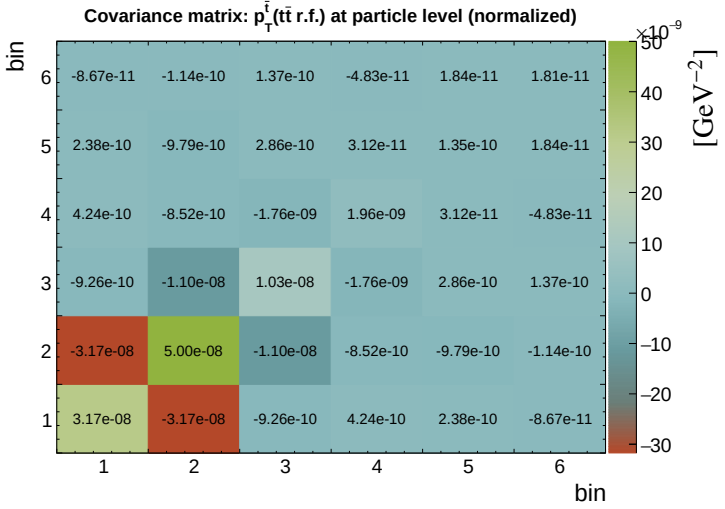

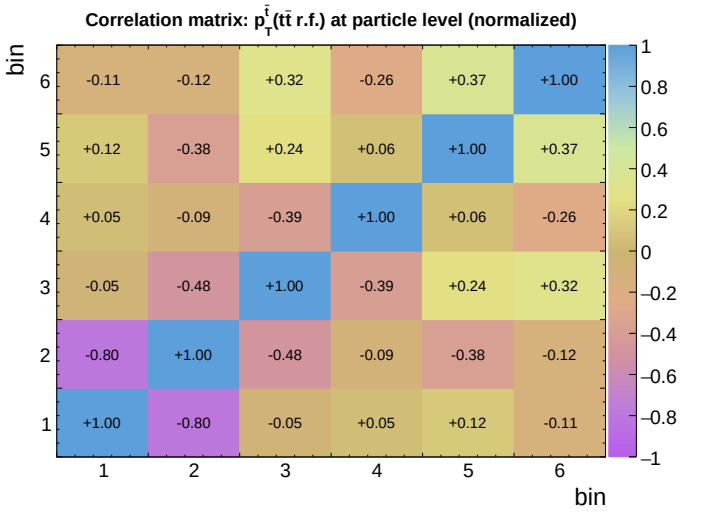

Table B.37 The result σ and its uncertainty per bin of the normalized differential $t\bar{t}$ production cross sections measured as a function of the rapidity of the top quark y_t. Measurement is performed at particle level in a fiducial phase space. The corresponding covariance and correlation matrices are presented below the table.

bin	center	left	right	σ	Δ_σ^{stat} (%)	Δ_σ^{syst} (%)	Δ_σ^{tot} (%)
1	−2.20	−2.60	−1.80	3.15e-02	1.9	5.4	5.8
2	−1.58	−1.80	−1.35	1.45e-01	1.0	2.5	2.6
3	−1.12	−1.35	−0.90	2.48e-01	0.9	2.2	2.4
4	−0.68	−0.90	−0.45	3.14e-01	0.9	1.9	2.1
5	−0.22	−0.45	0.00	3.43e-01	0.9	2.8	3.0
6	0.22	0.00	0.45	3.46e-01	0.8	3.3	3.4
7	0.68	0.45	0.90	3.20e-01	0.8	3.1	3.2
8	1.12	0.90	1.35	2.44e-01	0.9	1.9	2.1
9	1.58	1.35	1.80	1.46e-01	1.0	3.2	3.3
10	2.20	1.80	2.60	3.31e-02	1.8	4.4	4.7

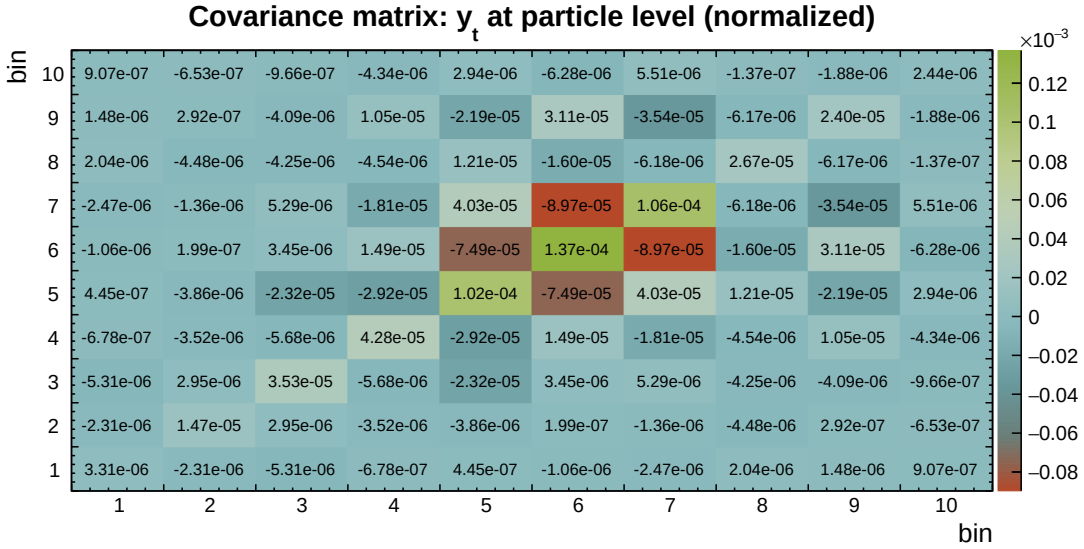

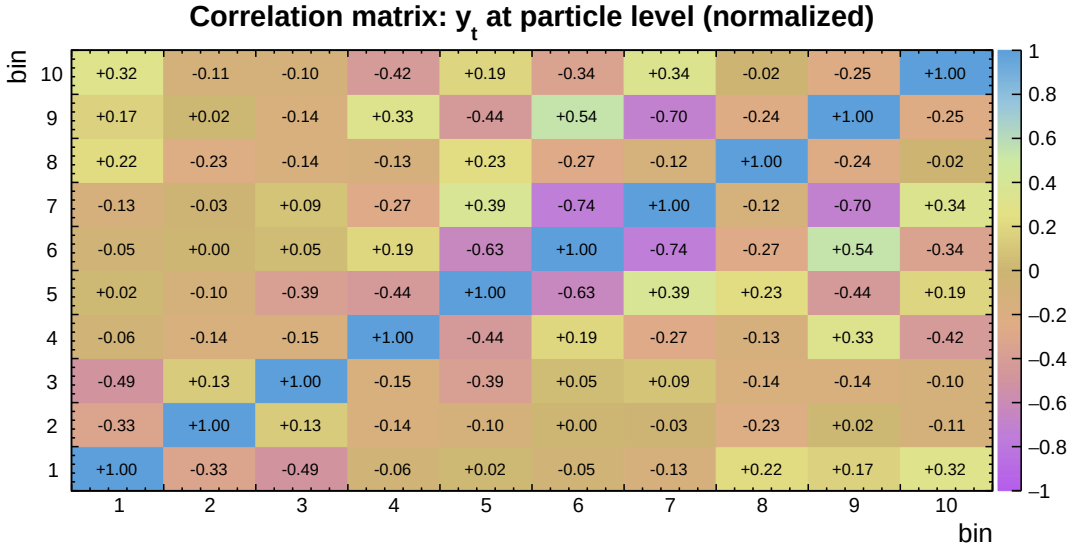

Table B.38 The result σ and its uncertainty per bin of the normalized differential $t\bar{t}$ production cross sections measured as a function of the rapidity of the top antiquark $y_{\bar{t}}$. Measurement is performed at particle level in a fiducial phase space. The corresponding covariance and correlation matrices are presented below the table.

bin	center	left	right	σ	Δ_σ^{stat} (%)	Δ_σ^{syst} (%)	Δ_σ^{tot} (%)
1	−2.20	−2.60	−1.80	3.21e-02	1.9	5.1	5.4
2	−1.58	−1.80	−1.35	1.43e-01	1.0	2.4	2.6
3	−1.12	−1.35	−0.90	2.46e-01	0.9	2.8	2.9
4	−0.68	−0.90	−0.45	3.13e-01	0.9	2.1	2.3
5	−0.22	−0.45	0.00	3.50e-01	0.9	1.9	2.1
6	0.22	0.00	0.45	3.49e-01	0.8	2.5	2.6
7	0.68	0.45	0.90	3.12e-01	0.9	2.0	2.2
8	1.12	0.90	1.35	2.52e-01	0.9	3.6	3.7
9	1.58	1.35	1.80	1.43e-01	1.0	5.5	5.6
10	2.20	1.80	2.60	3.19e-02	1.9	6.5	6.7

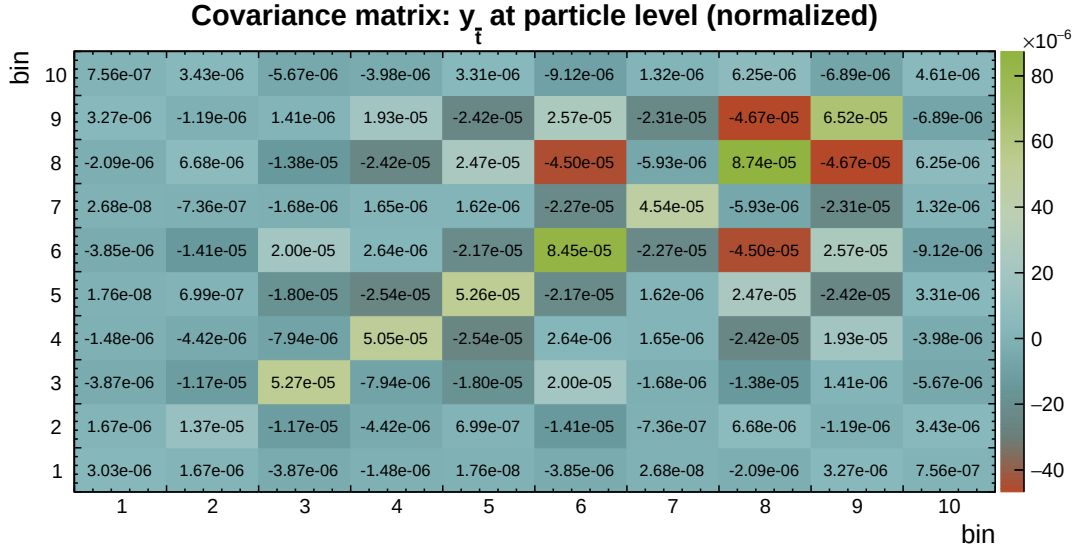

Table B.39 The result σ and its uncertainty per bin of the normalized differential $t\bar{t}$ production cross sections measured as a function of the rapidity of the leading top quark y_t *(leading)*. Measurement is performed at particle level in a fiducial phase space. The corresponding covariance and correlation matrices are presented below the table.

bin	center	left	right	σ	Δ_σ^{stat} (%)	Δ_σ^{syst} (%)	Δ_σ^{tot} (%)
1	−2.12	−2.60	−1.65	4.33e-02	1.7	5.3	5.6
2	−1.38	−1.65	−1.10	1.90e-01	0.9	2.5	2.7
3	−0.82	−1.10	−0.55	2.99e-01	0.8	2.0	2.1
4	−0.28	−0.55	0.00	3.44e-01	0.8	1.9	2.1
5	0.28	0.00	0.55	3.44e-01	0.8	2.0	2.1
6	0.82	0.55	1.10	3.00e-01	0.8	1.5	1.7
7	1.38	1.10	1.65	1.88e-01	0.9	3.7	3.8
8	2.12	1.65	2.60	4.54e-02	1.6	6.0	6.2

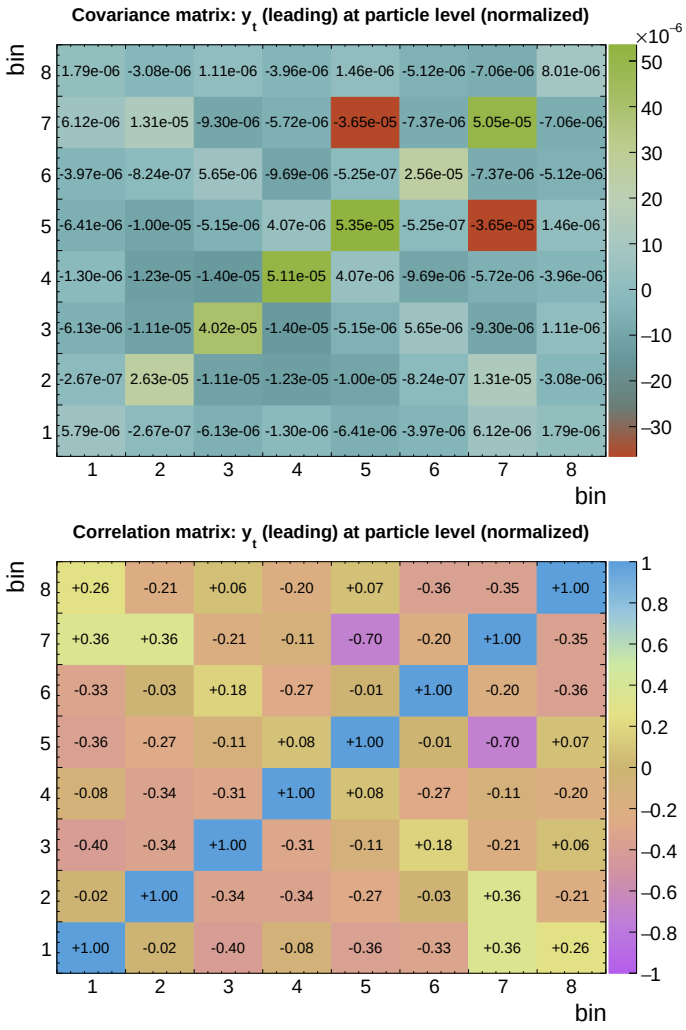

Table B.40 The result σ and its uncertainty per bin of the normalized differential $t\bar{t}$ production cross sections measured as a function of the rapidity of the trailing top quark y_t *(trailing)*. Measurement is performed at particle level in a fiducial phase space. The corresponding covariance and correlation matrices are presented below the table.

bin	center	left	right	σ	Δ_σ^{stat} (%)	Δ_σ^{syst} (%)	Δ_σ^{tot} (%)
1	−2.12	−2.60	−1.65	4.46e-02	1.8	5.2	5.5
2	−1.38	−1.65	−1.10	1.90e-01	0.9	3.0	3.2
3	−0.82	−1.10	−0.55	2.96e-01	0.8	3.0	3.1
4	−0.28	−0.55	0.00	3.42e-01	0.8	2.1	2.2
5	0.28	0.00	0.55	3.40e-01	0.9	3.7	3.8
6	0.82	0.55	1.10	3.01e-01	0.9	2.7	2.8
7	1.38	1.10	1.65	1.95e-01	0.9	2.5	2.7
8	2.12	1.65	2.60	4.42e-02	1.7	4.6	4.9

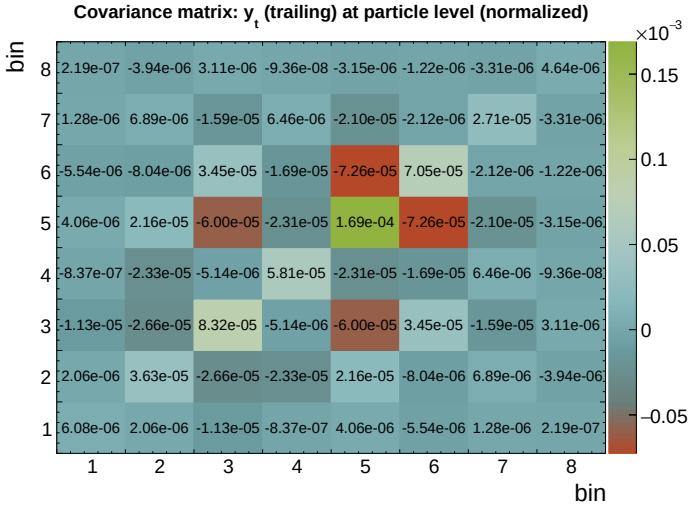

Table B.41 The result σ and its uncertainty per bin of the normalized differential $t\bar{t}$ production cross sections measured as a function of the difference in absolute rapidity between the top quark and antiquark $\Delta|y|(t,\bar{t})$. Measurement is performed at particle level in a fiducial phase space. The corresponding covariance and correlation matrices are presented below the table.

bin	center	left	right	σ	Δ_{σ}^{stat} (%)	Δ_{σ}^{syst} (%)	Δ_{σ}^{tot} (%)
1	−2.00	−2.60	−1.40	2.82e-02	1.9	5.2	5.6
2	−1.15	−1.40	−0.90	1.79e-01	1.0	4.1	4.2
3	−0.65	−0.90	−0.40	3.45e-01	0.9	2.4	2.6
4	−0.20	−0.40	0.00	5.00e-01	0.9	2.9	3.0
5	0.20	0.00	0.40	5.07e-01	0.9	2.1	2.3
6	0.65	0.40	0.90	3.49e-01	0.9	3.3	3.4
7	1.15	0.90	1.40	1.83e-01	1.1	3.0	3.2
8	2.00	1.40	2.60	2.93e-02	1.8	7.1	7.3

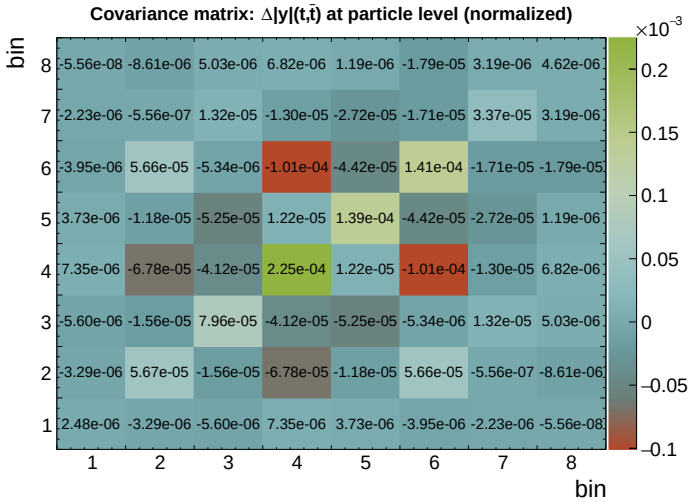

Table B.42 The result σ and its uncertainty per bin of the normalized differential $t\bar{t}$ production cross sections measured as a function of the difference in azimuthal angle between the top quark and antiquark $\Delta\phi(t,\bar{t})$. Measurement is performed at particle level in a fiducial phase space. The corresponding covariance and correlation matrices are presented below the table.

bin	center	left	right	σ	Δ_{σ}^{stat} (%)	Δ_{σ}^{syst} (%)	Δ_{σ}^{tot} (%)
1	0.785	0.000	1.570	6.28e-02	1.1	4.9	5.0
2	2.120	1.570	2.670	2.23e-01	0.5	3.5	3.6
3	2.845	2.670	3.020	1.05e+00	0.5	2.3	2.4
4	3.081	3.020	3.142	2.36e+00	0.7	5.7	5.7

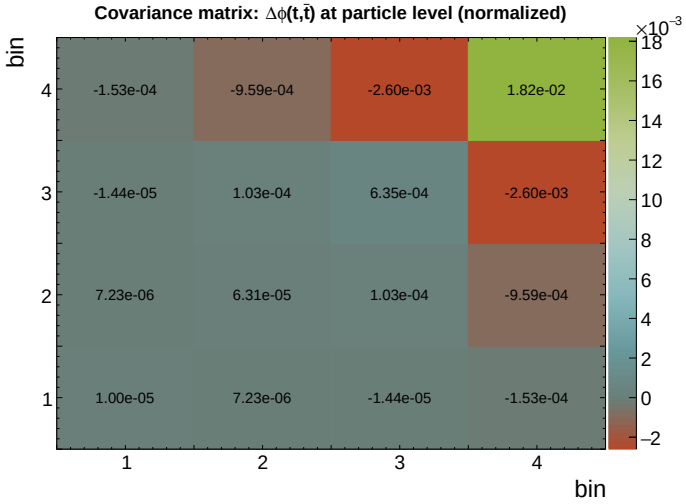

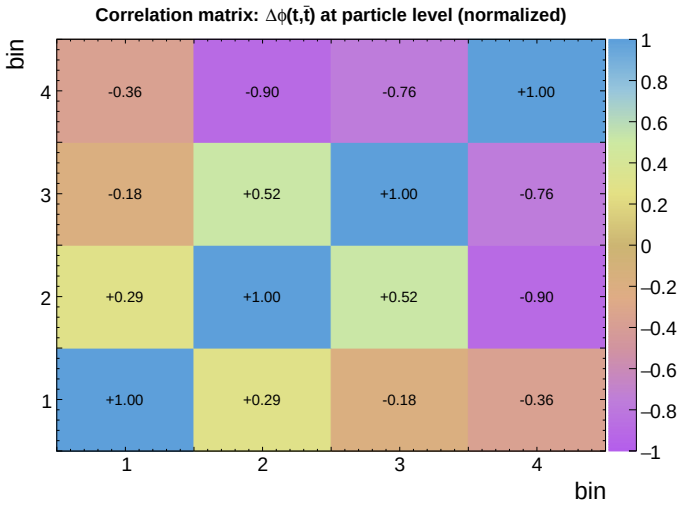

Table B.43 The result σ and its uncertainty per bin of the normalized differential $t\bar{t}$ production cross sections measured as a function of the transverse momentum of the top-quark pair $p_T^{t\bar{t}}$. Measurement is performed at particle level in a fiducial phase space. The corresponding covariance and correlation matrices are presented below the table.

bin	center (GeV)	left (GeV)	right (GeV)	σ (GeV^{-1})	Δ_σ^{stat} (%)	Δ_σ^{syst} (%)	Δ_σ^{tot} (%)
1	20.0	0.0	40.0	1.17e-02	0.5	6.6	6.7
2	70.0	40.0	100.0	5.35e-03	0.8	10.9	10.9
3	150.0	100.0	200.0	1.58e-03	0.9	3.8	3.9
4	255.0	200.0	310.0	3.51e-04	1.5	3.7	4.0
5	365.0	310.0	420.0	9.53e-05	2.3	5.9	6.3
6	495.0	420.0	570.0	2.45e-05	4.0	6.4	7.6

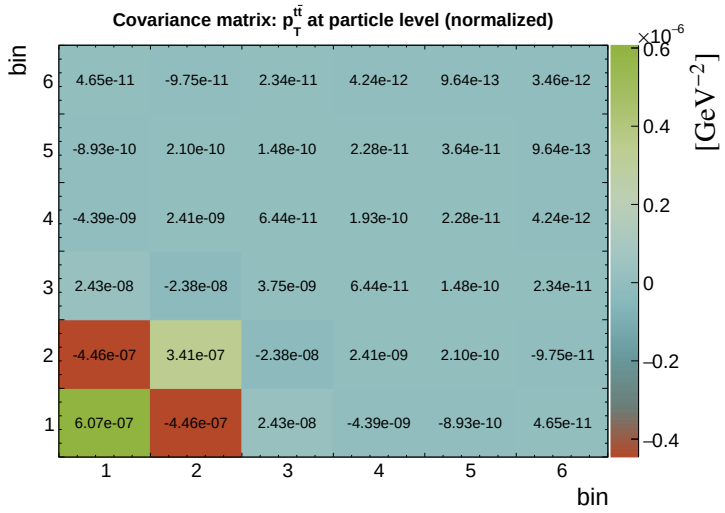

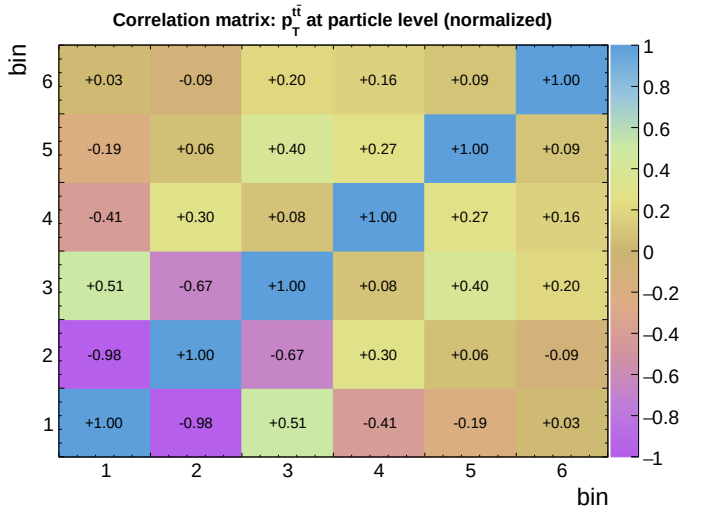

Table B.44 The result σ and its uncertainty per bin of the normalized differential $t\bar{t}$ production cross sections measured as a function of the invariant mass of the top-quark pair $m_{t\bar{t}}$. Measurement is performed at particle level in a fiducial phase space. The corresponding covariance and correlation matrices are presented below the table.

bin	center (GeV)	left (GeV)	right (GeV)	σ (GeV^{-1})	Δ_σ^{stat} (%)	Δ_σ^{syst} (%)	Δ_σ^{tot} (%)
1	340.0	300.0	380.0	2.72e-03	1.2	5.9	6.0
2	425.0	380.0	470.0	3.64e-03	1.3	5.3	5.5
3	545.0	470.0	620.0	1.92e-03	1.2	2.9	3.1
4	720.0	620.0	820.0	5.98e-04	1.7	5.0	5.3
5	960.0	820.0	1100.0	1.31e-04	2.8	7.5	8.0
6	1300.0	1100.0	1500.0	2.19e-05	3.7	8.1	8.9
7	2000.0	1500.0	2500.0	1.53e-06	9.3	21.6	23.5

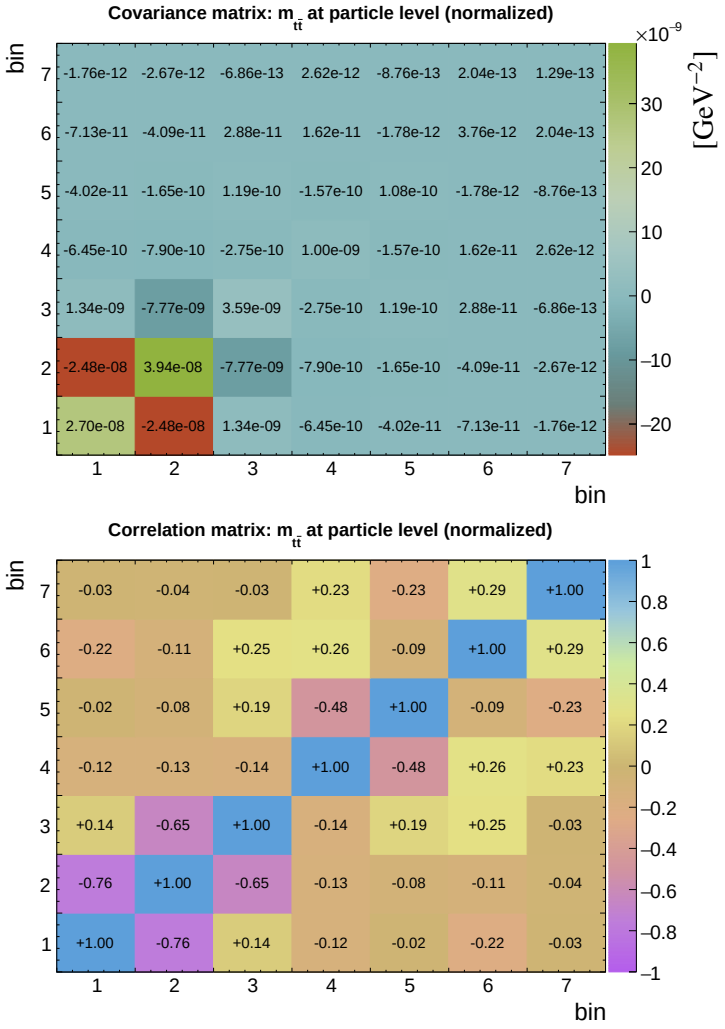

Table B.45 The result σ and its uncertainty per bin of the normalized differential $t\bar{t}$ production cross sections measured as a function of the rapidity of the top-quark pair $y_{t\bar{t}}$. Measurement is performed at particle level in a fiducial phase space. The corresponding covariance and correlation matrices are presented below the table.

bin	center	left	right	σ	Δ_{σ}^{stat} (%)	Δ_{σ}^{syst} (%)	Δ_{σ}^{tot} (%)
1	−2.10	−2.60	−1.60	1.41e-02	2.5	11.7	11.9
2	−1.40	−1.60	−1.20	1.28e-01	1.1	2.6	2.8
3	−1.00	−1.20	−0.80	2.60e-01	0.9	2.9	3.1
4	−0.60	−0.80	−0.40	3.73e-01	0.8	2.3	2.5
5	−0.20	−0.40	0.00	4.58e-01	0.8	2.1	2.2
6	0.20	0.00	0.40	4.40e-01	0.8	2.1	2.3
7	0.60	0.40	0.80	3.78e-01	0.8	1.9	2.1
8	1.00	0.80	1.20	2.65e-01	0.9	2.5	2.6
9	1.40	1.20	1.60	1.25e-01	1.1	3.2	3.3
10	2.10	1.60	2.60	1.54e-02	2.2	5.6	6.1

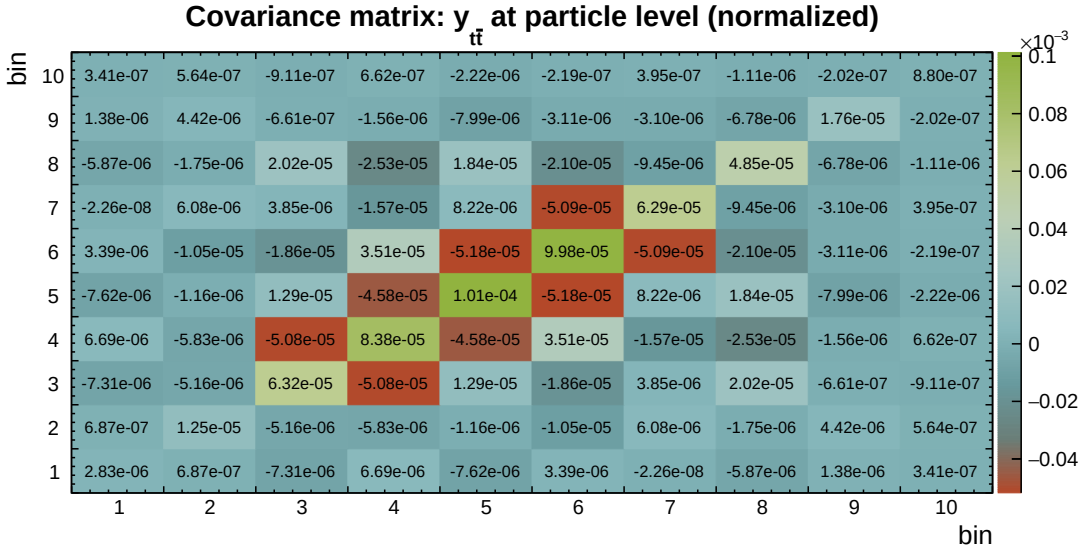

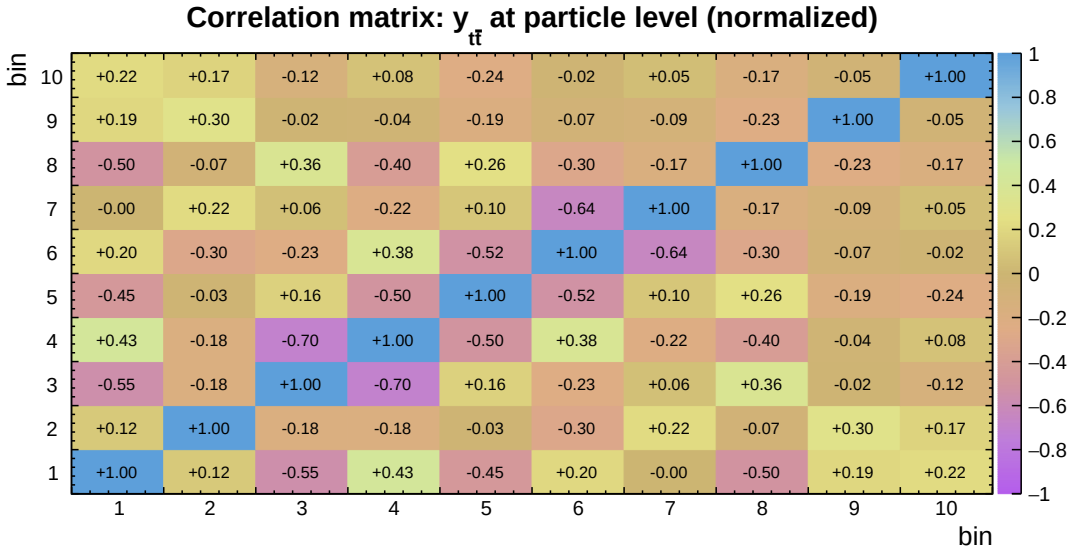

Table B.46 The result σ and its uncertainty per bin of the normalized differential $t\bar{t}$ production cross sections measured as a function of the transverse momentum of the lepton p_T^{ℓ}. Measurement is performed at particle level in a fiducial phase space. The corresponding covariance and correlation matrices are presented below the table.

bin	center (GeV)	left (GeV)	right (GeV)	σ (GeV^{-1})	Δ_σ^{stat} (%)	Δ_σ^{syst} (%)	Δ_σ^{tot} (%)
1	30.0	20.0	40.0	1.85e-02	0.3	1.1	1.1
2	55.0	40.0	70.0	1.25e-02	0.3	0.9	0.9
3	95.0	70.0	120.0	4.01e-03	0.4	1.1	1.2
4	150.0	120.0	180.0	7.25e-04	0.9	1.7	2.0
5	290.0	180.0	400.0	5.06e-05	2.0	3.5	4.1

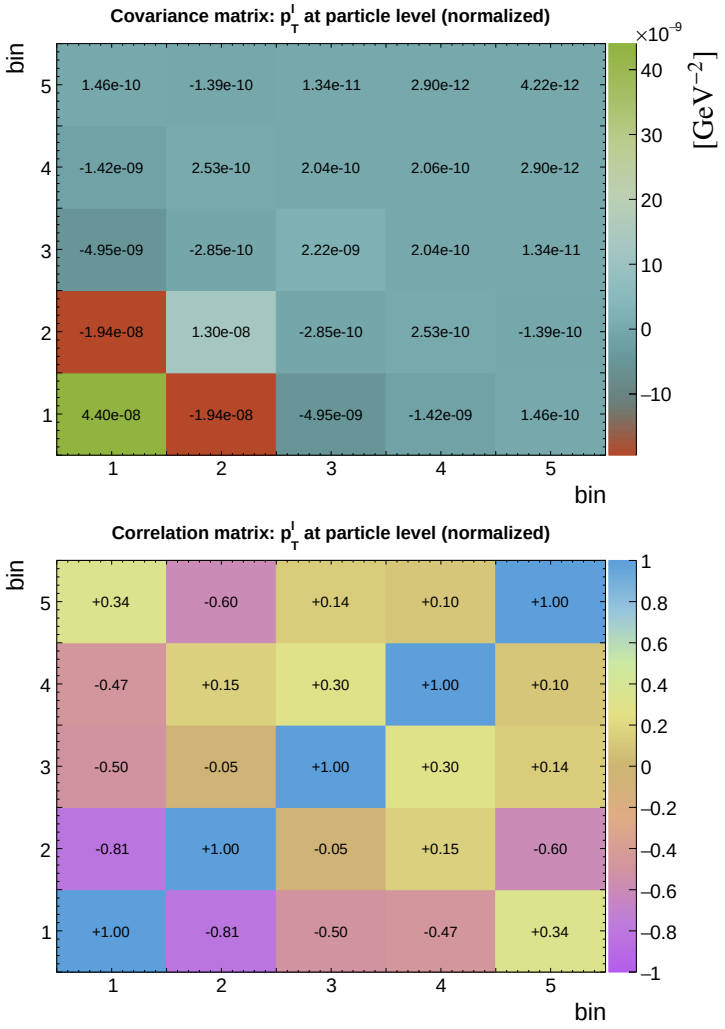

Table B.47 The result σ and its uncertainty per bin of the normalized differential $t\bar{t}$ production cross sections measured as a function of the transverse momentum of the antilepton $p_T^{\bar{\ell}}$. Measurement is performed at particle level in a fiducial phase space. The corresponding covariance and correlation matrices are presented below the table.

bin	center (GeV)	left (GeV)	right (GeV)	σ (GeV^{-1})	Δ_σ^{stat} (%)	Δ_σ^{syst} (%)	Δ_σ^{tot} (%)
1	30.0	20.0	40.0	1.84e-02	0.3	1.0	1.1
2	55.0	40.0	70.0	1.26e-02	0.3	0.5	0.6
3	95.0	70.0	120.0	4.00e-03	0.4	1.1	1.2
4	150.0	120.0	180.0	7.29e-04	0.9	1.9	2.1
5	290.0	180.0	400.0	4.90e-05	2.1	4.0	4.5

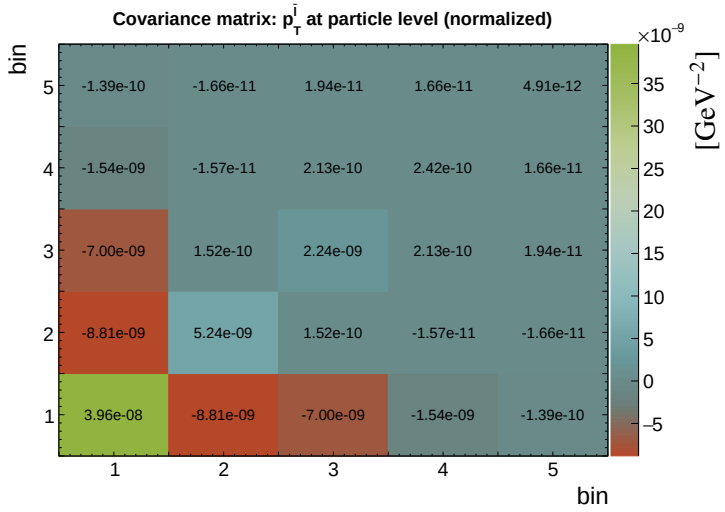

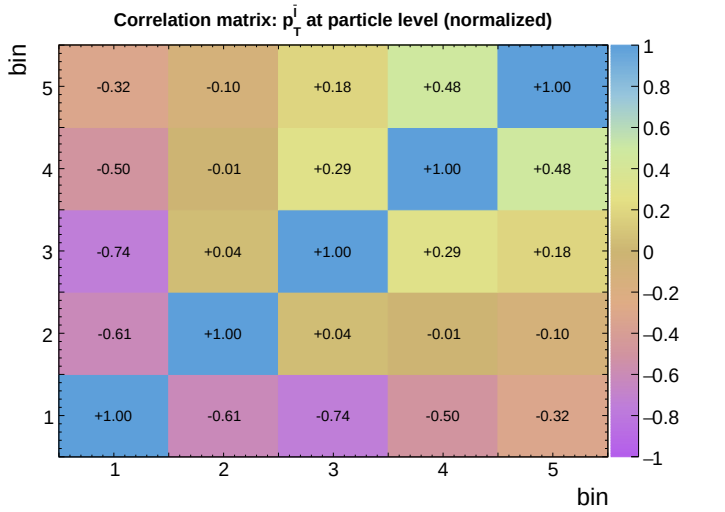

Table B.48 The result σ and its uncertainty per bin of the normalized differential $t\bar{t}$ production cross sections measured as a function of the transverse momentum of the leading lepton p_T^{ℓ} *(leading)*. Measurement is performed at particle level in a fiducial phase space. The corresponding covariance and correlation matrices are presented below the table.

bin	center (GeV)	left (GeV)	right (GeV)	σ (GeV^{-1})	Δ_σ^{stat} (%)	Δ_σ^{syst} (%)	Δ_σ^{tot} (%)
1	30.0	20.0	40.0	7.01e-03	0.6	2.5	2.6
2	55.0	40.0	70.0	1.44e-02	0.3	0.6	0.7
3	95.0	70.0	120.0	6.56e-03	0.3	0.9	1.0
4	150.0	120.0	180.0	1.31e-03	0.7	1.6	1.7
5	290.0	180.0	400.0	9.39e-05	1.5	3.4	3.7

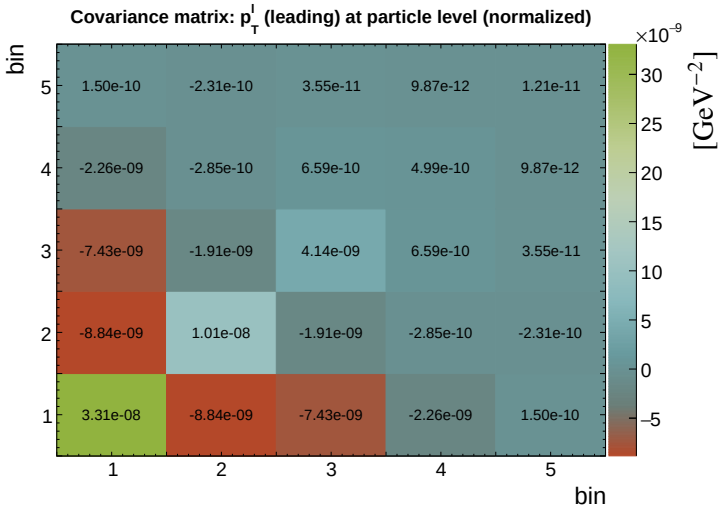

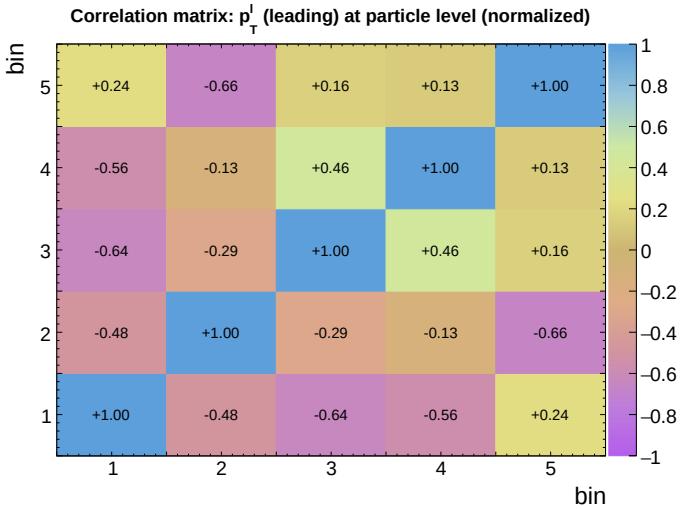

Table B.49 The result σ and its uncertainty per bin of the normalized differential $t\bar{t}$ production cross sections measured as a function of the transverse momentum of the trailing lepton p_T^{ℓ} *(trailing)*. Measurement is performed at particle level in a fiducial phase space. The corresponding covariance and correlation matrices are presented below the table.

bin	center (GeV)	left (GeV)	right (GeV)	σ (GeV^{-1})	Δ_σ^{stat} (%)	Δ_σ^{syst} (%)	Δ_σ^{tot} (%)
1	27.5	20.0	35.0	3.18e-02	0.2	1.0	1.0
2	42.5	35.0	50.0	1.92e-02	0.4	1.0	1.1
3	70.0	50.0	90.0	5.06e-03	0.4	1.1	1.2
4	115.0	90.0	140.0	5.49e-04	1.2	2.3	2.5
5	270.0	140.0	400.0	1.90e-05	3.0	3.3	4.4

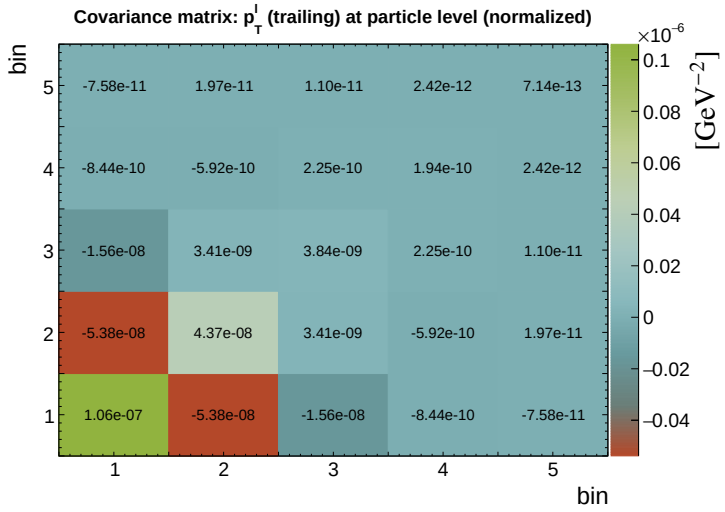

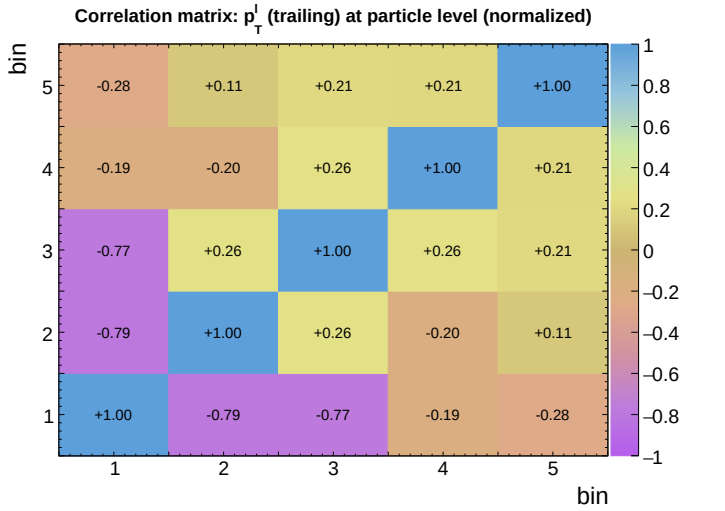

Table B.50 The result σ and its uncertainty per bin of the normalized differential $t\bar{t}$ production cross sections measured as a function of the pseudorapidity of the lepton η_ℓ. Measurement is performed at particle level in a fiducial phase space. The corresponding covariance and correlation matrices are presented below the table.

bin	center	left	right	σ	Δ_σ^{stat} (%)	Δ_σ^{syst} (%)	Δ_σ^{tot} (%)
1	−2.25	−2.40	−2.10	6.91e-02	1.5	3.9	4.2
2	−1.95	−2.10	−1.80	1.01e-01	1.2	2.6	2.9
3	−1.65	−1.80	−1.50	1.47e-01	1.0	1.7	2.0
4	−1.35	−1.50	−1.20	1.93e-01	0.9	1.6	1.8
5	−1.05	−1.20	−0.90	2.44e-01	0.8	1.4	1.6
6	−0.75	−0.90	−0.60	2.83e-01	0.7	1.4	1.5
7	−0.45	−0.60	−0.30	3.12e-01	0.7	1.3	1.4
8	−0.15	−0.30	0.00	3.18e-01	0.7	1.0	1.2
9	0.15	0.00	0.30	3.17e-01	0.7	0.8	1.0
10	0.45	0.30	0.60	3.11e-01	0.7	0.9	1.2
11	0.75	0.60	0.90	2.80e-01	0.7	0.8	1.1
12	1.05	0.90	1.20	2.46e-01	0.8	1.5	1.7
13	1.35	1.20	1.50	1.91e-01	0.9	1.5	1.8
14	1.65	1.50	1.80	1.51e-01	1.1	2.3	2.5
15	1.95	1.80	2.10	1.04e-01	1.2	2.6	2.8
16	2.25	2.10	2.40	6.53e-02	1.6	3.5	3.8

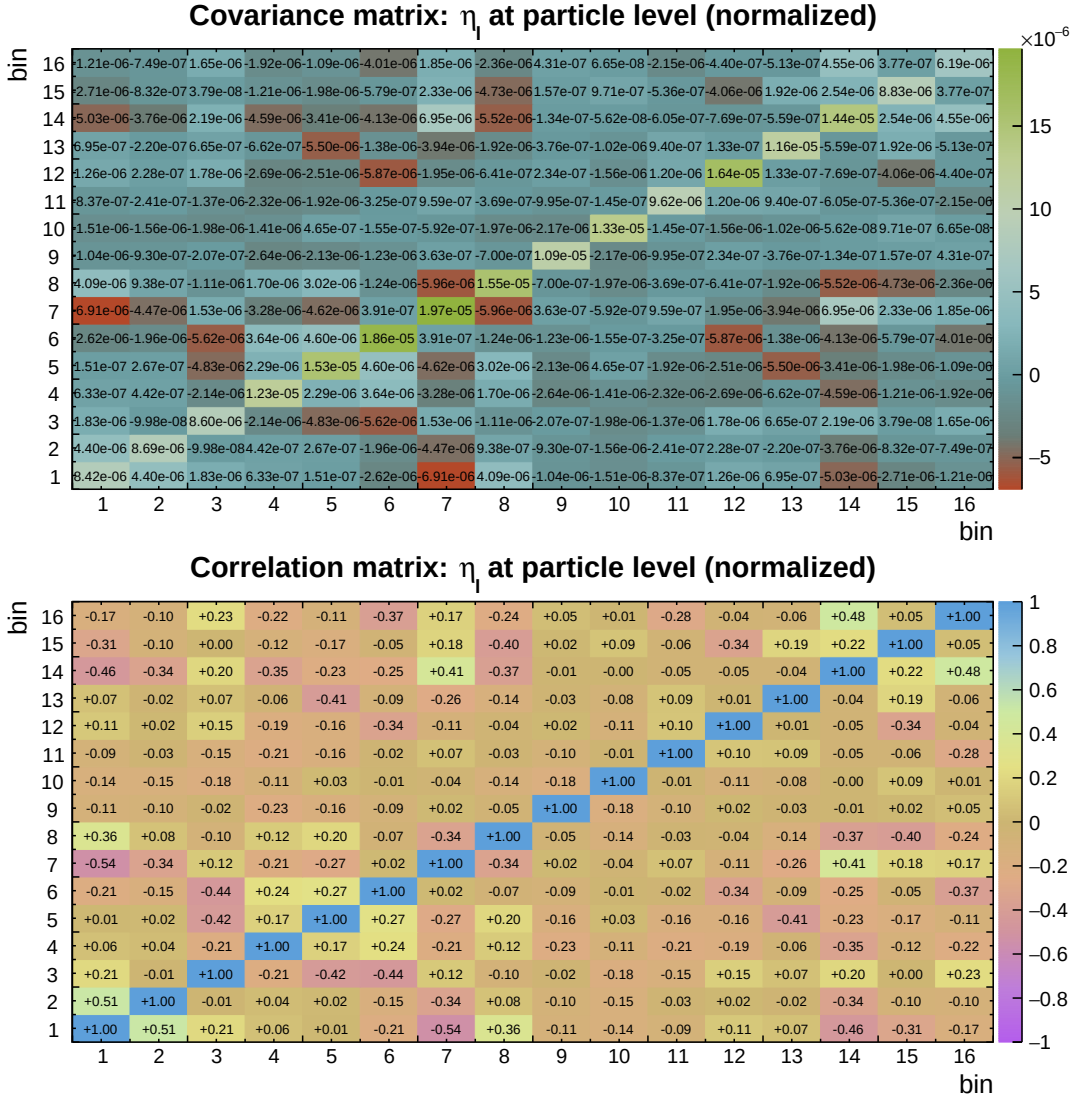

Table B.51 The result σ and its uncertainty per bin of the normalized differential $t\bar{t}$ production cross sections measured as a function of the pseudorapidity of the antilepton $\eta_{\bar{\ell}}$. Measurement is performed at particle level in a fiducial phase space. The corresponding covariance and correlation matrices are presented below the table.

bin	center	left	right	σ	Δ_{σ}^{stat} (%)	Δ_{σ}^{syst} (%)	Δ_{σ}^{tot} (%)
1	−2.25	−2.40	−2.10	6.86e-02	1.5	2.8	3.2
2	−1.95	−2.10	−1.80	1.04e-01	1.2	2.7	3.0
3	−1.65	−1.80	−1.50	1.51e-01	1.0	1.7	2.0
4	−1.35	−1.50	−1.20	1.98e-01	0.9	1.1	1.4
5	−1.05	−1.20	−0.90	2.44e-01	0.8	1.2	1.4
6	−0.75	−0.90	−0.60	2.80e-01	0.7	1.2	1.4
7	−0.45	−0.60	−0.30	3.06e-01	0.7	0.7	1.0
8	−0.15	−0.30	0.00	3.13e-01	0.7	1.4	1.5
9	0.15	0.00	0.30	3.20e-01	0.7	1.0	1.2
10	0.45	0.30	0.60	3.06e-01	0.7	1.0	1.2
11	0.75	0.60	0.90	2.87e-01	0.7	1.3	1.5
12	1.05	0.90	1.20	2.39e-01	0.8	1.3	1.5
13	1.35	1.20	1.50	1.95e-01	0.9	1.6	1.8
14	1.65	1.50	1.80	1.51e-01	1.1	1.6	1.9
15	1.95	1.80	2.10	1.07e-01	1.2	1.6	2.0
16	2.25	2.10	2.40	6.63e-02	1.6	3.1	3.4

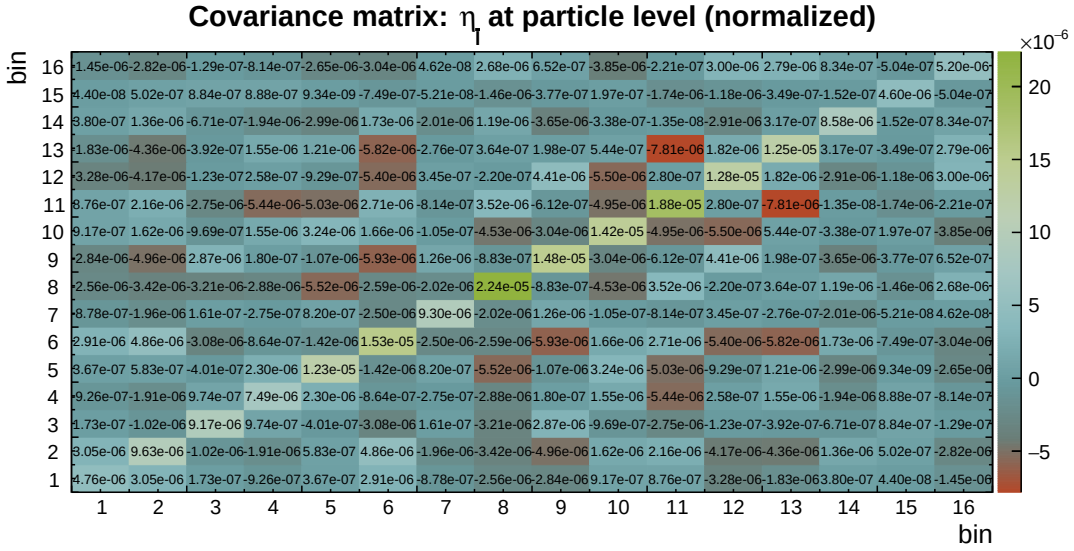

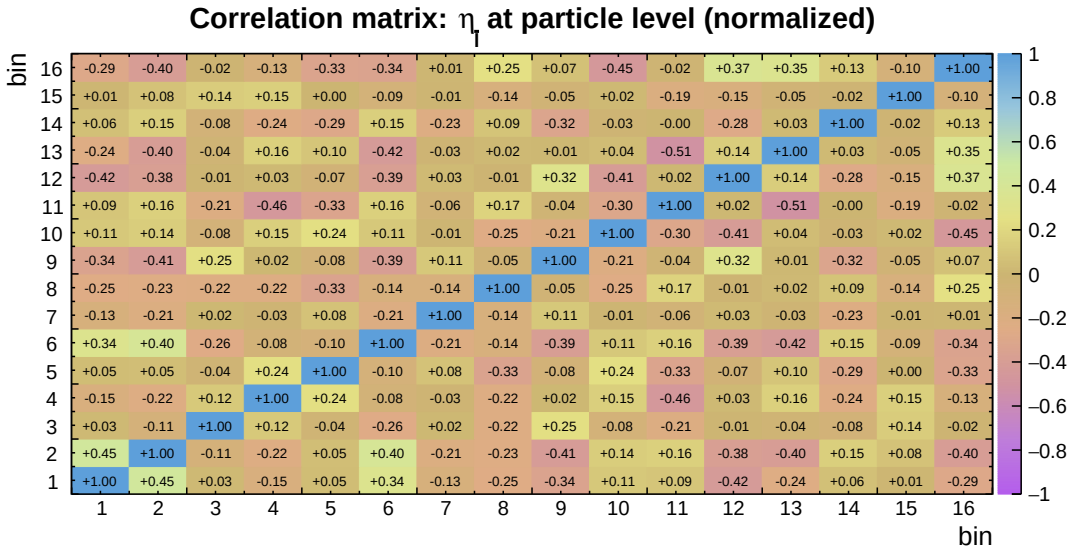

Table B.52 The result σ and its uncertainty per bin of the normalized differential $t\bar{t}$ production cross sections measured as a function of the pseudorapidity of the leading lepton η_ℓ *(leading)*. Measurement is performed at particle level in a fiducial phase space. The corresponding covariance and correlation matrices are presented below the table.

bin	center	left	right	σ	Δ_σ^{stat} (%)	Δ_σ^{syst} (%)	Δ_σ^{tot} (%)
1	−2.25	−2.40	−2.10	6.10e-02	1.7	3.5	3.8
2	−1.95	−2.10	−1.80	9.44e-02	1.3	3.2	3.5
3	−1.65	−1.80	−1.50	1.46e-01	1.1	1.7	2.0
4	−1.35	−1.50	−1.20	1.94e-01	0.9	1.6	1.9
5	−1.05	−1.20	−0.90	2.43e-01	0.8	1.2	1.4
6	−0.75	−0.90	−0.60	2.90e-01	0.7	1.2	1.4
7	−0.45	−0.60	−0.30	3.18e-01	0.7	1.2	1.4
8	−0.15	−0.30	0.00	3.21e-01	0.7	1.3	1.5
9	0.15	0.00	0.30	3.26e-01	0.7	1.2	1.4
10	0.45	0.30	0.60	3.15e-01	0.7	1.3	1.5
11	0.75	0.60	0.90	2.87e-01	0.7	1.3	1.5
12	1.05	0.90	1.20	2.45e-01	0.8	1.4	1.6
13	1.35	1.20	1.50	1.92e-01	0.9	1.5	1.7
14	1.65	1.50	1.80	1.46e-01	1.1	2.9	3.1
15	1.95	1.80	2.10	9.55e-02	1.4	2.8	3.1
16	2.25	2.10	2.40	5.91e-02	1.7	2.7	3.2

Covariance matrix: η_l (leading) at particle level (normalized)

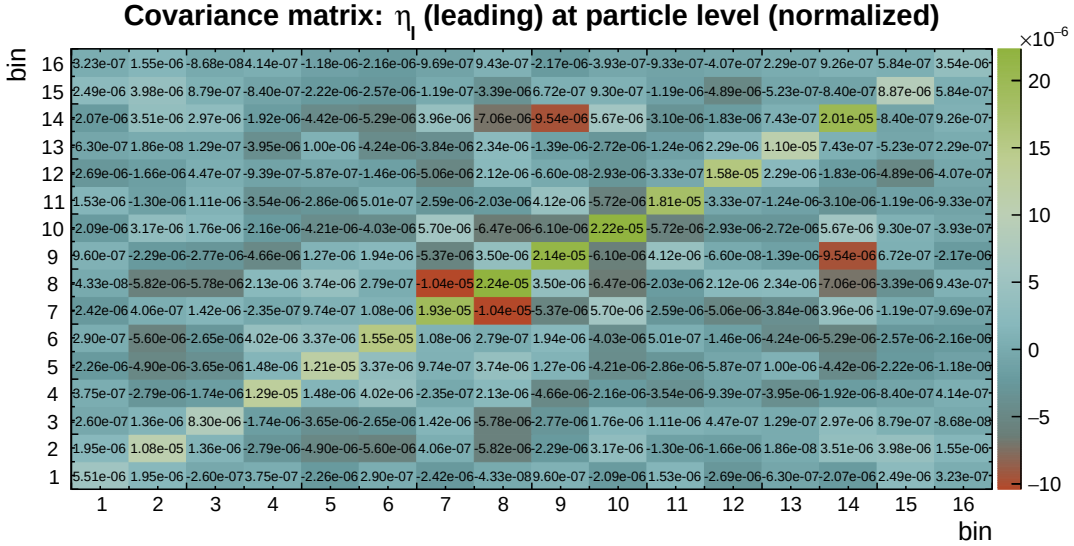

Correlation matrix: η_l (leading) at particle level (normalized)

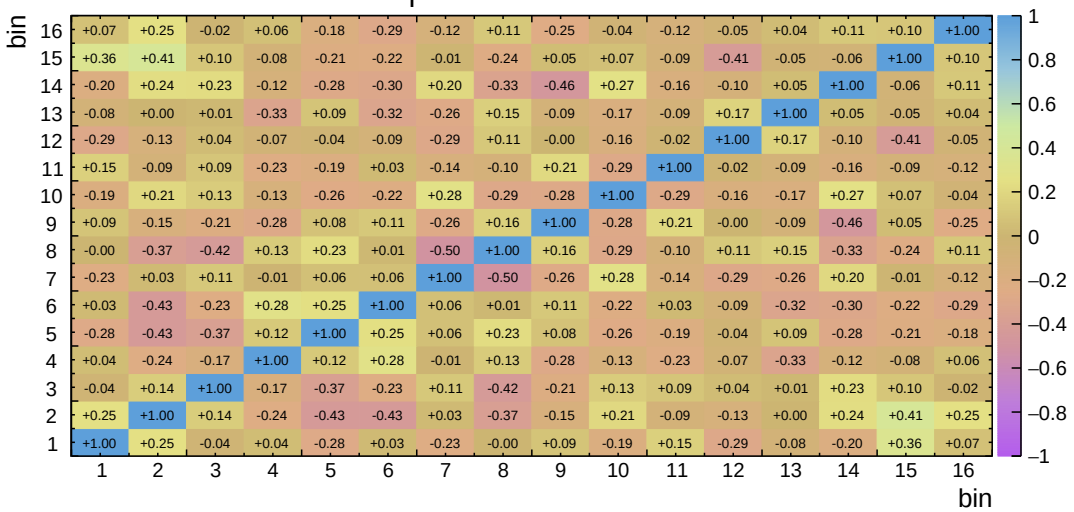

Table B.53 The result σ and its uncertainty per bin of the normalized differential $t\bar{t}$ production cross sections measured as a function of the pseudorapidity of the trailing lepton η_ℓ *(trailing)*. Measurement is performed at particle level in a fiducial phase space. The corresponding covariance and correlation matrices are presented below the table.

bin	center	left	right	σ	Δ_σ^{stat} (%)	Δ_σ^{syst} (%)	Δ_σ^{tot} (%)
1	−2.25	−2.40	−2.10	7.66e-02	1.5	2.2	2.6
2	−1.95	−2.10	−1.80	1.11e-01	1.2	2.6	2.9
3	−1.65	−1.80	−1.50	1.52e-01	1.0	2.2	2.4
4	−1.35	−1.50	−1.20	1.97e-01	0.9	1.7	1.9
5	−1.05	−1.20	−0.90	2.45e-01	0.8	1.4	1.6
6	−0.75	−0.90	−0.60	2.73e-01	0.7	1.5	1.7
7	−0.45	−0.60	−0.30	3.00e-01	0.7	0.8	1.1
8	−0.15	−0.30	0.00	3.10e-01	0.7	1.1	1.3
9	0.15	0.00	0.30	3.09e-01	0.7	0.9	1.2
10	0.45	0.30	0.60	3.03e-01	0.7	0.9	1.1
11	0.75	0.60	0.90	2.80e-01	0.7	0.9	1.2
12	1.05	0.90	1.20	2.40e-01	0.8	1.4	1.6
13	1.35	1.20	1.50	1.95e-01	0.9	1.1	1.4
14	1.65	1.50	1.80	1.56e-01	1.1	1.7	2.0
15	1.95	1.80	2.10	1.16e-01	1.2	2.2	2.5
16	2.25	2.10	2.40	7.23e-02	1.5	3.2	3.6

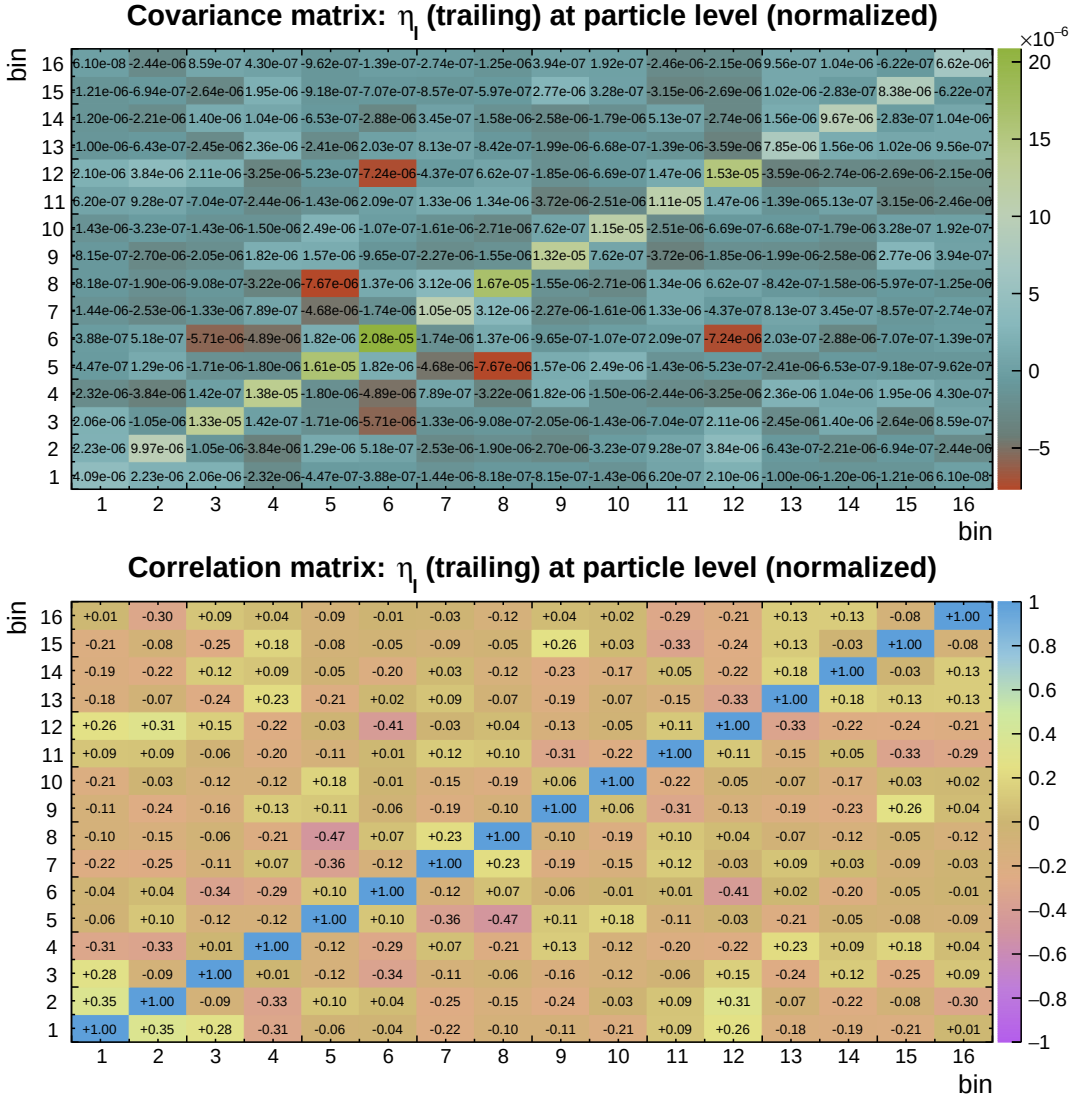

Table B.54 The result σ and its uncertainty per bin of the normalized differential $t\bar{t}$ production cross sections measured as a function of the difference in absolute pseudorapidity between the lepton and antilepton $\Delta|\eta|(\ell,\bar{\ell})$. Measurement is performed at particle level in a fiducial phase space. The corresponding covariance and correlation matrices are presented below the table.

bin	center	left	right	σ	Δ_σ^{stat} (%)	Δ_σ^{syst} (%)	Δ_σ^{tot} (%)
1	−2.05	−2.40	−1.70	3.52e-02	1.3	2.4	2.7
2	−1.45	−1.70	−1.20	1.35e-01	0.8	1.4	1.6
3	−1.00	−1.20	−0.80	2.45e-01	0.7	1.1	1.3
4	−0.60	−0.80	−0.40	3.52e-01	0.5	0.9	1.1
5	−0.20	−0.40	0.00	4.30e-01	0.5	0.9	1.0
6	0.20	0.00	0.40	4.28e-01	0.5	0.8	0.9
7	0.60	0.40	0.80	3.49e-01	0.5	1.0	1.1
8	1.00	0.80	1.20	2.40e-01	0.7	1.1	1.3
9	1.45	1.20	1.70	1.32e-01	0.8	1.3	1.5
10	2.05	1.70	2.40	3.41e-02	1.4	2.5	2.8

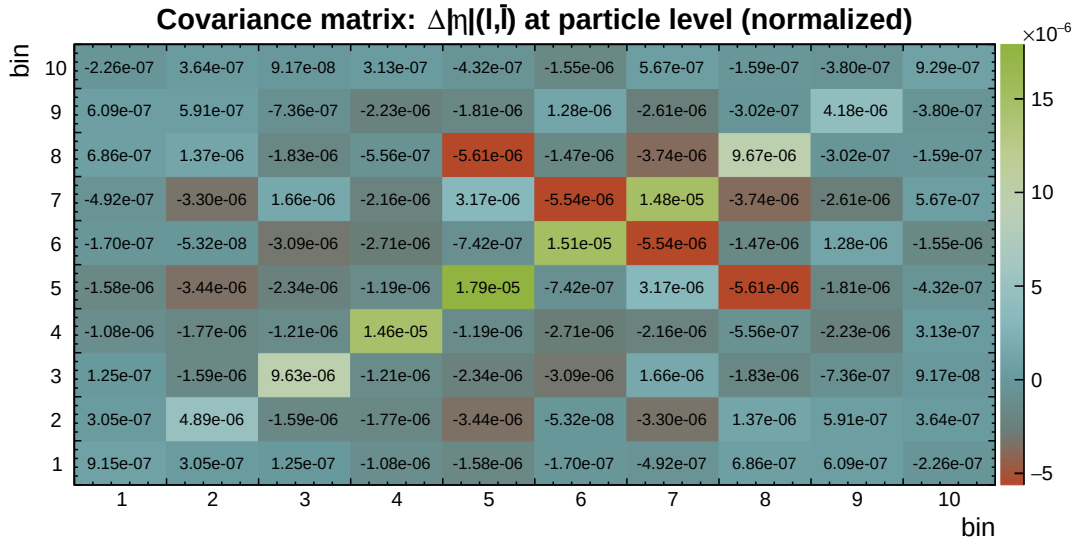

Table B.55 The result σ and its uncertainty per bin of the normalized differential $t\bar{t}$ production cross sections measured as a function of the difference in azimuthal angle between the lepton and antilepton $\Delta\phi(\ell,\bar{\ell})$. Measurement is performed at particle level in a fiducial phase space. The corresponding covariance and correlation matrices are presented below the table.

bin	center	left	right	σ	Δ_σ^{stat} (%)	Δ_σ^{syst} (%)	Δ_σ^{tot} (%)
1	0.200	0.000	0.400	1.94e-01	0.8	1.5	1.7
2	0.590	0.400	0.780	2.47e-01	0.7	1.3	1.5
3	0.960	0.780	1.140	2.78e-01	0.7	0.9	1.2
4	1.310	1.140	1.480	2.99e-01	0.7	1.0	1.2
5	1.640	1.480	1.800	3.26e-01	0.7	0.7	1.0
6	1.950	1.800	2.100	3.52e-01	0.7	0.8	1.0
7	2.240	2.100	2.380	3.74e-01	0.6	0.9	1.1
8	2.510	2.380	2.640	3.93e-01	0.6	0.8	1.0
9	2.765	2.640	2.890	4.20e-01	0.6	1.0	1.1
10	3.016	2.890	3.142	4.18e-01	0.6	0.9	1.1

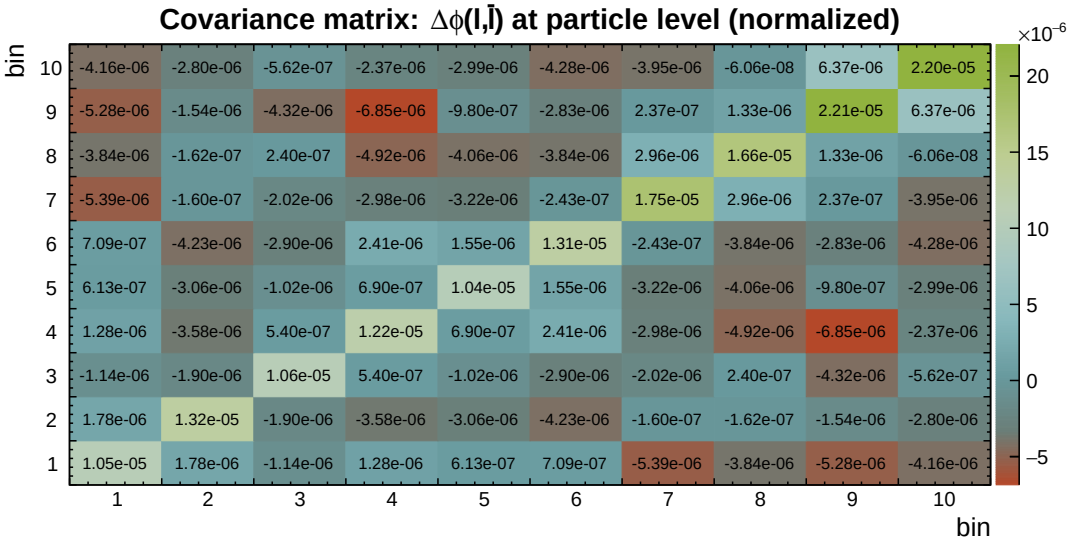

Table B.56 The result σ and its uncertainty per bin of the normalized differential $t\bar{t}$ production cross sections measured as a function of the transverse momentum of the lepton pair $p_T^{\ell\bar{\ell}}$. Measurement is performed at particle level in a fiducial phase space. The corresponding covariance and correlation matrices are presented below the table.

bin	center (GeV)	left (GeV)	right (GeV)	σ (GeV^{-1})	Δ_σ^{stat} (%)	Δ_σ^{syst} (%)	Δ_σ^{tot} (%)
1	5.0	0.0	10.0	1.69e-03	1.9	4.0	4.4
2	15.0	10.0	20.0	4.68e-03	1.1	2.3	2.6
3	30.0	20.0	40.0	7.59e-03	0.6	1.0	1.1
4	50.0	40.0	60.0	1.09e-02	0.4	0.8	0.9
5	80.0	60.0	100.0	9.55e-03	0.3	0.5	0.6
6	125.0	100.0	150.0	3.04e-03	0.5	1.0	1.2
7	275.0	150.0	400.0	1.26e-04	1.2	3.4	3.6

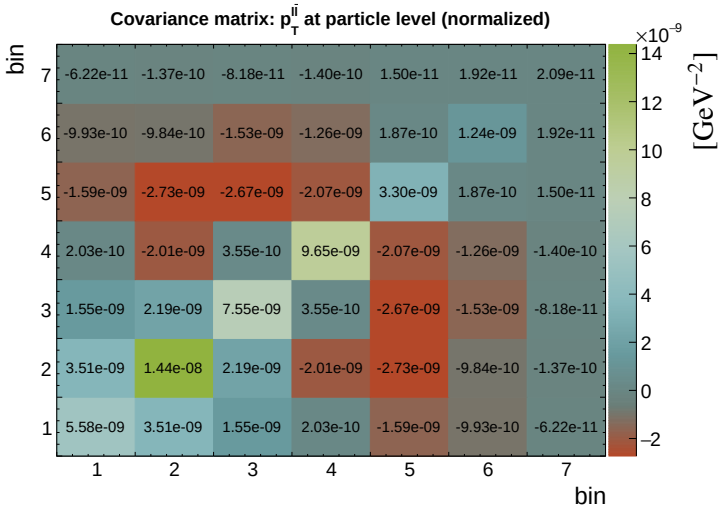

Table B.57 The result σ and its uncertainty per bin of the normalized differential $t\bar{t}$ production cross sections measured as a function of the invariant mass of the lepton pair $m_{\ell\bar{\ell}}$. Measurement is performed at particle level in a fiducial phase space. The corresponding covariance and correlation matrices are presented below the table.

bin	center (GeV)	left (GeV)	right (GeV)	σ (GeV^{-1})	Δ_{σ}^{stat} (%)	Δ_{σ}^{syst} (%)	Δ_{σ}^{tot} (%)
1	25.0	20.0	30.0	3.44e-03	1.2	4.1	4.2
2	40.0	30.0	50.0	5.34e-03	0.6	1.9	2.0
3	63.0	50.0	76.0	7.66e-03	0.4	1.9	1.9
4	91.0	76.0	106.0	7.47e-03	0.5	1.7	1.7
5	118.0	106.0	130.0	5.45e-03	0.6	0.8	1.0
6	150.0	130.0	170.0	3.48e-03	0.5	1.2	1.3
7	215.0	170.0	260.0	1.34e-03	0.6	1.5	1.6
8	455.0	260.0	650.0	1.15e-04	0.9	1.8	2.0

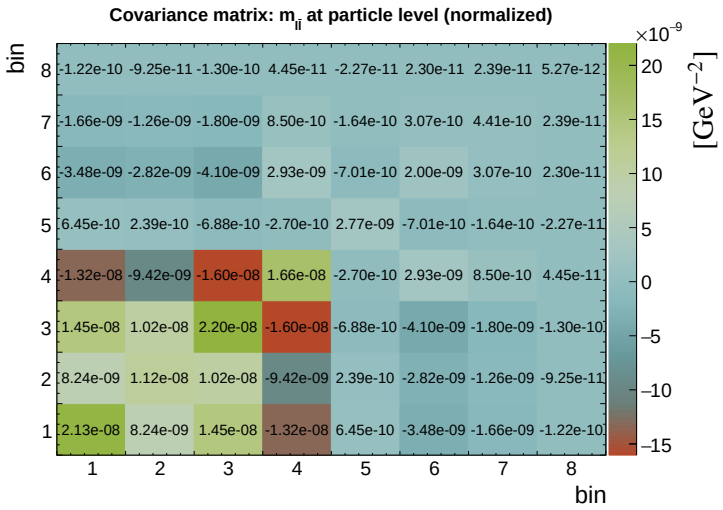

Table B.58 The result σ and its uncertainty per bin of the normalized differential $t\bar{t}$ production cross sections measured as a function of the transverse momentum of the leading b-jet p_T^b *(leading)*. Measurement is performed at particle level in a fiducial phase space. The corresponding covariance and correlation matrices are presented below the table.

bin	center (GeV)	left (GeV)	right (GeV)	σ (GeV^{-1})	Δ_σ^{stat} (%)	Δ_σ^{syst} (%)	Δ_σ^{tot} (%)
1	45.0	30.0	60.0	6.23e-03	0.7	6.0	6.0
2	77.5	60.0	95.0	1.16e-02	0.4	1.2	1.3
3	122.5	95.0	150.0	5.41e-03	0.5	2.3	2.3
4	190.0	150.0	230.0	1.13e-03	0.8	3.7	3.8
5	365.0	230.0	500.0	6.53e-05	2.0	5.2	5.5

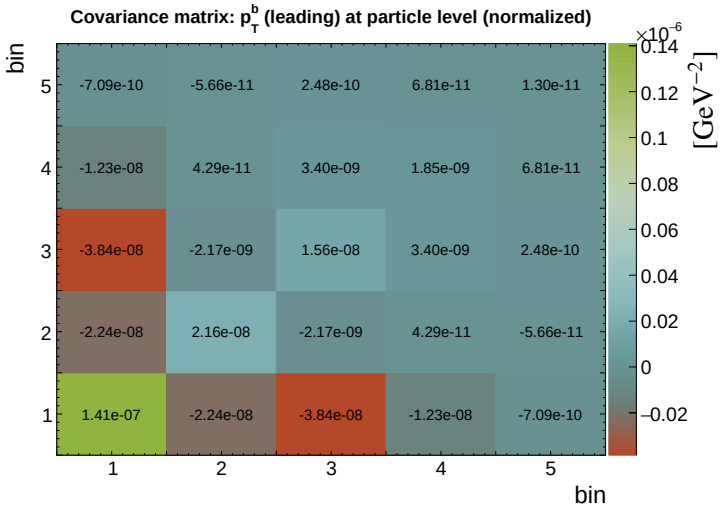

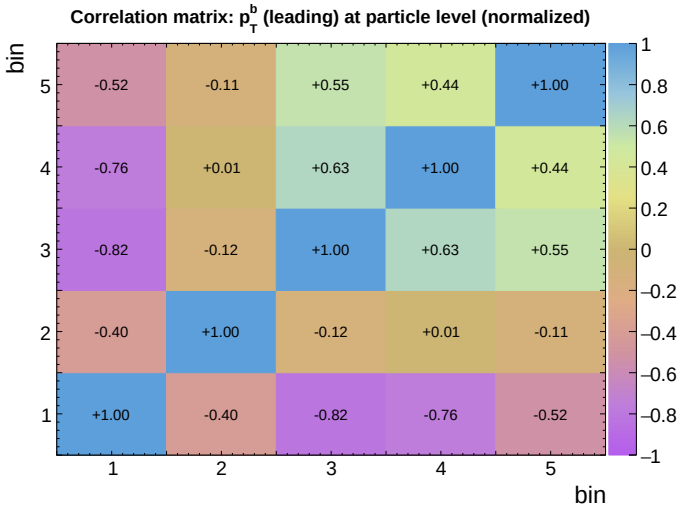

Table B.59 The result σ and its uncertainty per bin of the normalized differential $t\bar{t}$ production cross sections measured as a function of the transverse momentum of the trailing b-jet p_T^b *(trailing)*. Measurement is performed at particle level in a fiducial phase space. The corresponding covariance and correlation matrices are presented below the table.

bin	center (GeV)	left (GeV)	right (GeV)	σ (GeV^{-1})	Δ_σ^{stat} (%)	Δ_σ^{syst} (%)	Δ_σ^{tot} (%)
1	37.5	30.0	45.0	2.48e-02	0.5	3.9	3.9
2	57.5	45.0	70.0	1.54e-02	0.5	2.1	2.2
3	90.0	70.0	110.0	4.69e-03	0.7	3.2	3.2
4	140.0	110.0	170.0	8.16e-04	1.2	3.7	3.9
5	335.0	170.0	500.0	2.30e-05	3.4	8.9	9.5

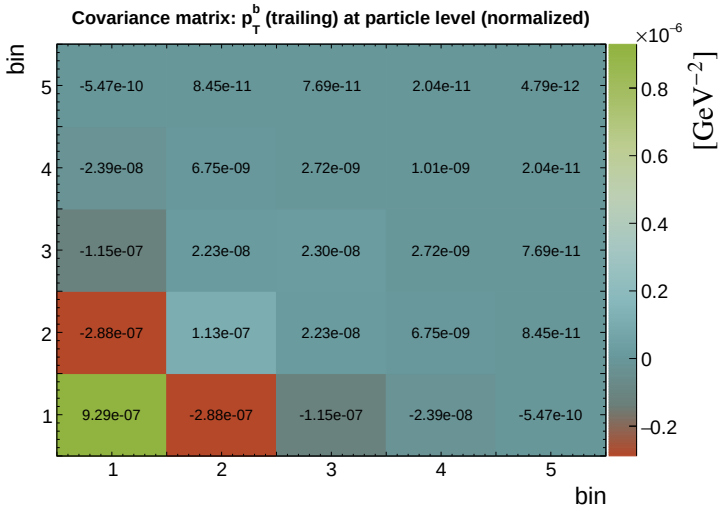

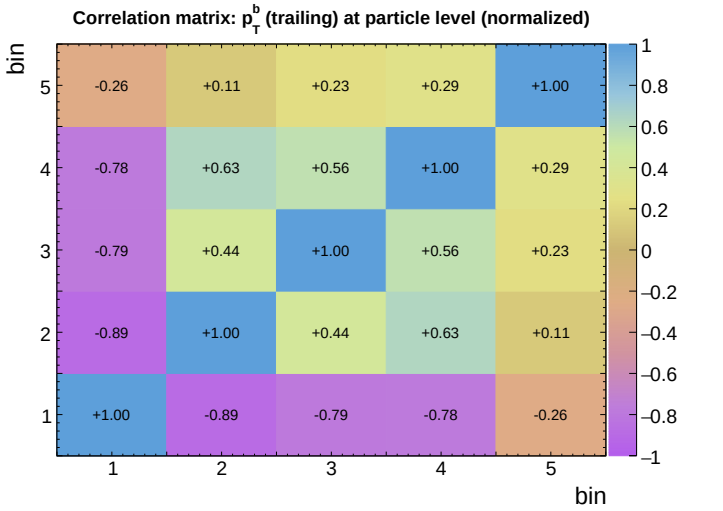

Table B.60 The result σ and its uncertainty per bin of the normalized differential $t\bar{t}$ production cross sections measured as a function of the pseudorapidity of the leading b-jet η_b *(leading)*. Measurement is performed at particle level in a fiducial phase space. The corresponding covariance and correlation matrices are presented below the table.

bin	center	left	right	σ	Δ_σ^{stat} (%)	Δ_σ^{syst} (%)	Δ_σ^{tot} (%)
1	−2.10	−2.40	−1.80	8.03e-02	1.2	5.2	5.3
2	−1.50	−1.80	−1.20	1.62e-01	0.8	2.3	2.4
3	−0.90	−1.20	−0.60	2.69e-01	0.6	1.5	1.6
4	−0.30	−0.60	0.00	3.19e-01	0.5	1.6	1.7
5	0.30	0.00	0.60	3.26e-01	0.5	1.5	1.6
6	0.90	0.60	1.20	2.61e-01	0.6	1.1	1.3
7	1.50	1.20	1.80	1.68e-01	0.8	2.0	2.2
8	2.10	1.80	2.40	8.11e-02	1.1	4.3	4.4

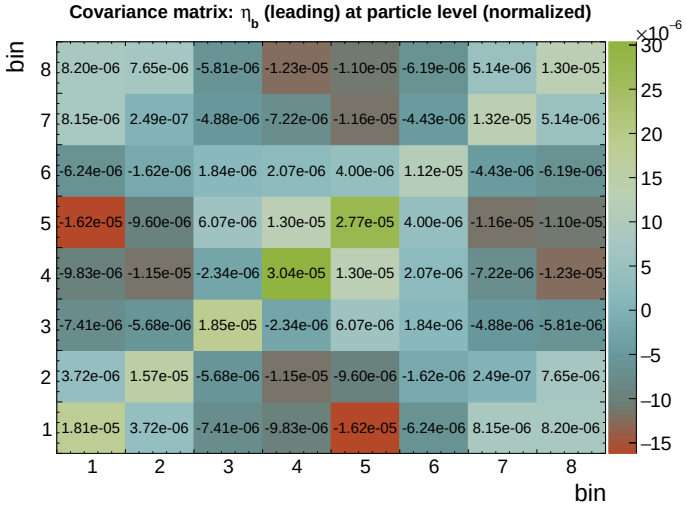

Table B.61 The result σ and its uncertainty per bin of the normalized differential $t\bar{t}$ production cross sections measured as a function of the pseudorapidity of the trailing b-jet η_b *(trailing)*. Measurement is performed at particle level in a fiducial phase space. The corresponding covariance and correlation matrices are presented below the table.

bin	center	left	right	σ	Δ_σ^{stat} (%)	Δ_σ^{syst} (%)	Δ_σ^{tot} (%)
1	−2.10	−2.40	−1.80	9.96e-02	1.1	3.4	3.6
2	−1.50	−1.80	−1.20	1.71e-01	0.8	2.3	2.4
3	−0.90	−1.20	−0.60	2.52e-01	0.6	1.3	1.5
4	−0.30	−0.60	0.00	3.01e-01	0.6	1.8	1.9
5	0.30	0.00	0.60	3.10e-01	0.6	1.5	1.6
6	0.90	0.60	1.20	2.58e-01	0.6	1.3	1.4
7	1.50	1.20	1.80	1.78e-01	0.8	1.8	1.9
8	2.10	1.80	2.40	9.68e-02	1.1	4.5	4.6

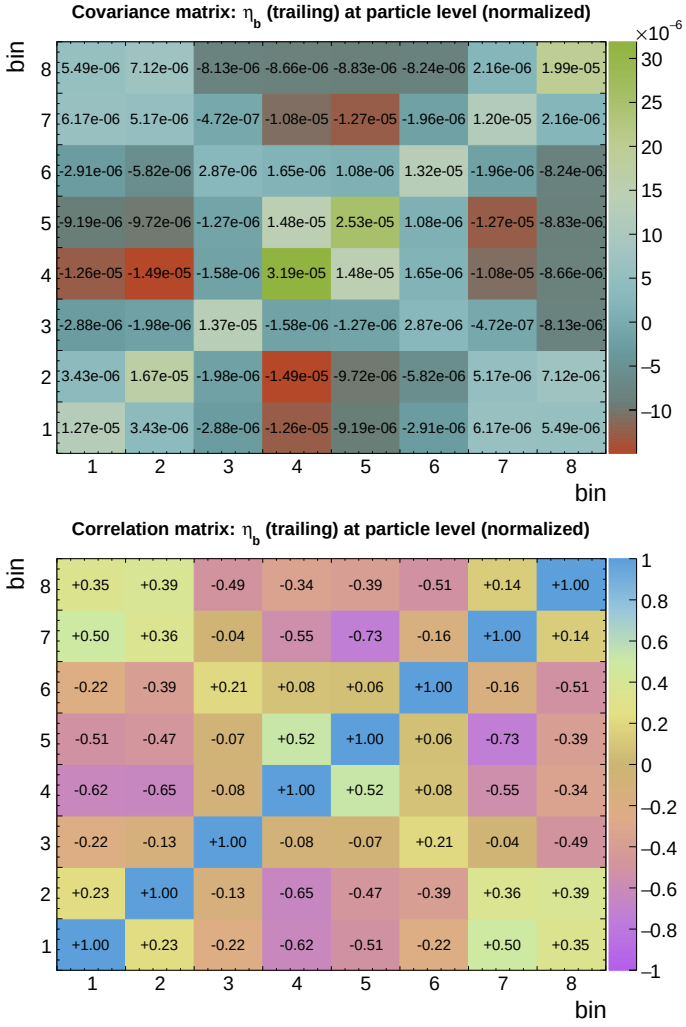

Table B.62 The result σ and its uncertainty per bin of the normalized differential $t\bar{t}$ production cross sections measured as a function of the transverse momentum of the b-jet pair $p_T^{b\bar{b}}$. Measurement is performed at particle level in a fiducial phase space. The corresponding covariance and correlation matrices are presented below the table.

bin	center (GeV)	left (GeV)	right (GeV)	σ (GeV^{-1})	Δ_σ^{stat} (%)	Δ_σ^{syst} (%)	Δ_σ^{tot} (%)
1	15.0	0.0	30.0	3.52e-03	0.8	4.1	4.2
2	45.0	30.0	60.0	7.18e-03	0.5	3.0	3.1
3	80.0	60.0	100.0	8.92e-03	0.4	1.8	1.8
4	140.0	100.0	180.0	3.67e-03	0.4	4.4	4.4
5	290.0	180.0	400.0	1.30e-04	1.5	9.0	9.1

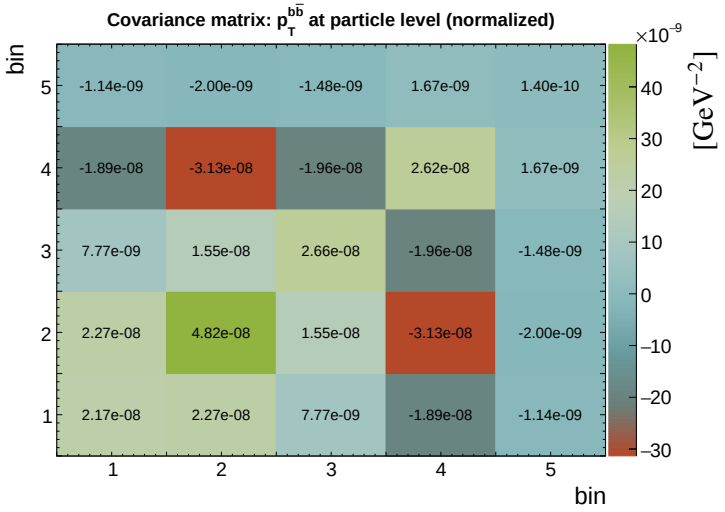

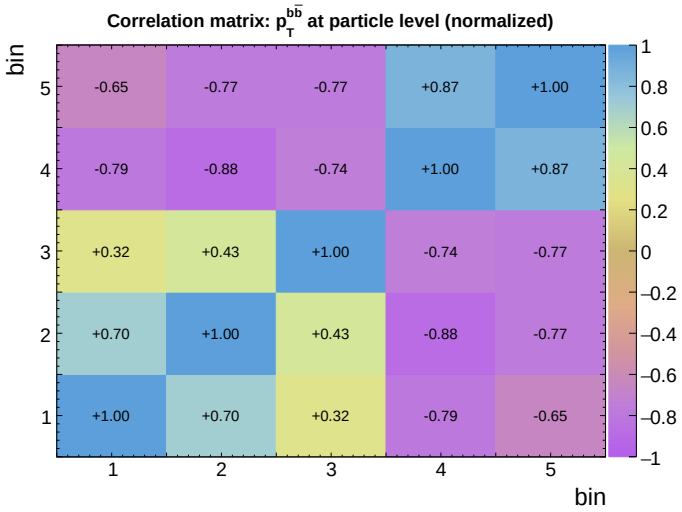

Table B.63 The result σ and its uncertainty per bin of the normalized differential $t\bar{t}$ production cross sections measured as a function of the invariant mass of the b-jet pair $m_{b\bar{b}}$. Measurement is performed at particle level in a fiducial phase space. The corresponding covariance and correlation matrices are presented below the table.

bin	center (GeV)	left (GeV)	right (GeV)	σ (GeV^{-1})	Δ_{σ}^{stat} (%)	Δ_{σ}^{syst} (%)	Δ_{σ}^{tot} (%)
1	30.0	0.0	60.0	1.22e-03	0.9	3.6	3.7
2	90.0	60.0	120.0	4.96e-03	0.4	1.8	1.9
3	180.0	120.0	240.0	3.82e-03	0.3	0.7	0.7
4	445.0	240.0	650.0	4.15e-04	0.6	3.3	3.4

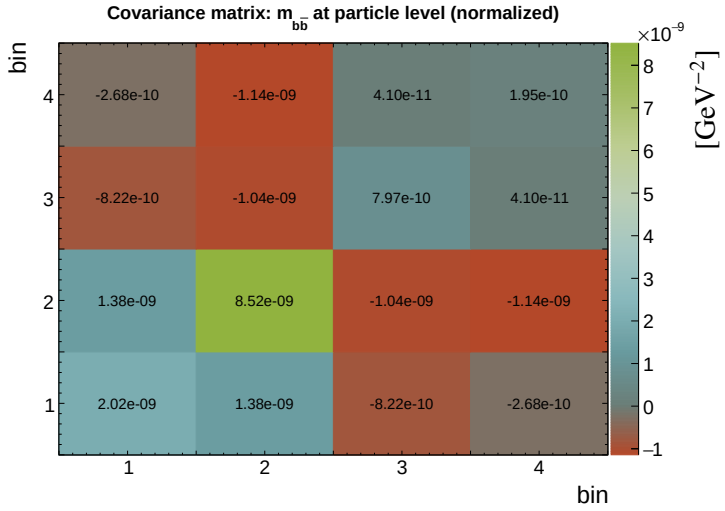

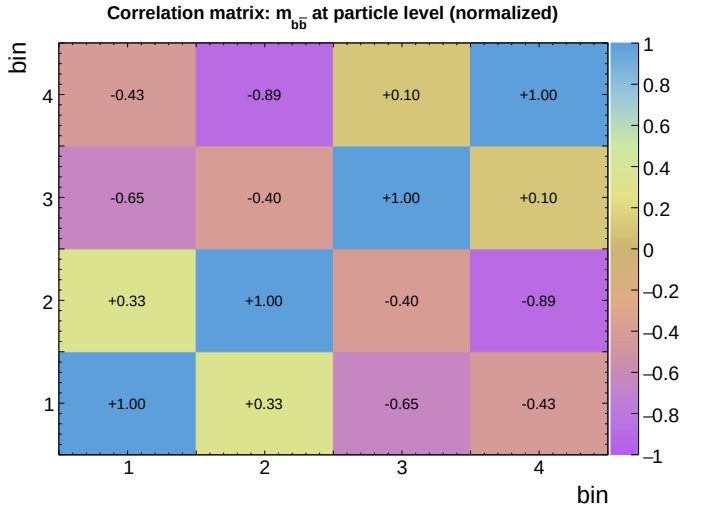

Table B.64 The result σ and its uncertainty per bin of the normalized differential $t\bar{t}$ production cross sections measured as a function of the jet multiplicity N_{jets}. Measurement is performed at particle level in a fiducial phase space. The corresponding covariance and correlation matrices are presented below the table.

bin	center	left	right	σ	Δ_{σ}^{stat} (%)	Δ_{σ}^{syst} (%)	Δ_{σ}^{tot} (%)
1	2.0	1.5	2.5	5.32e-01	0.2	3.0	3.0
2	3.0	2.5	3.5	3.03e-01	0.5	1.9	1.9
3	4.0	3.5	4.5	1.16e-01	0.9	5.6	5.7
4	5.0	4.5	5.5	3.68e-02	1.6	8.5	8.7
5	6.0	5.5	6.5	1.04e-02	2.6	10.1	10.4
6	7.0	6.5	7.5	2.51e-03	5.4	16.9	17.8

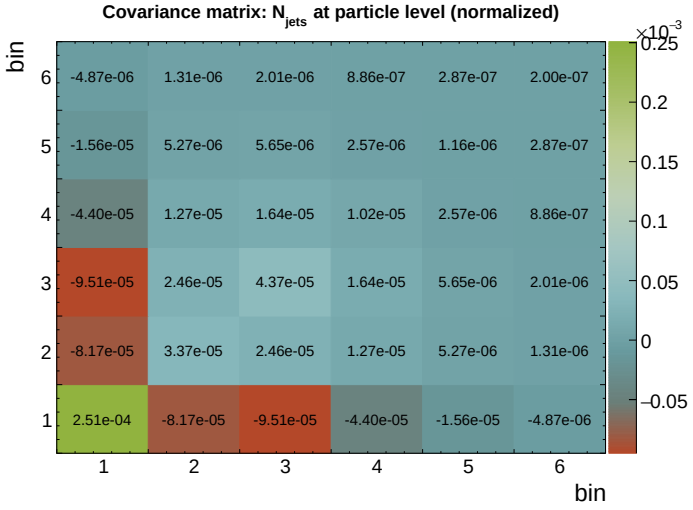

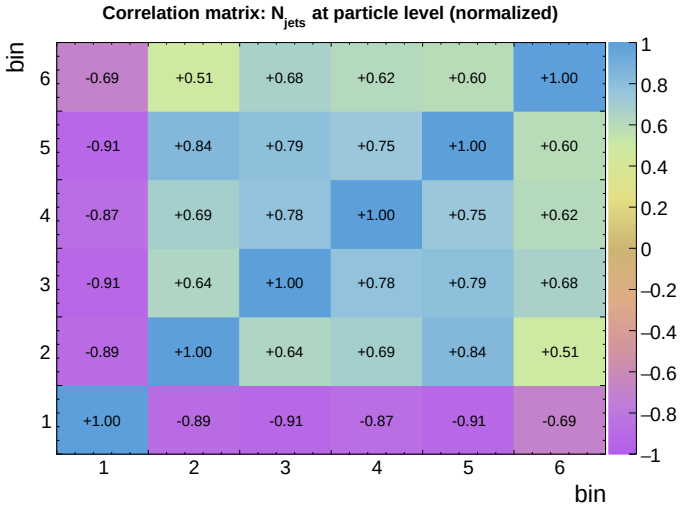

Table B.65 The result σ and its uncertainty per bin of the absolute differential $t\bar{t}$ production cross sections measured as a function of the transverse momentum of the top quark p_T^t. Measurement is performed at particle level in a fiducial phase space. The corresponding covariance and correlation matrices are presented below the table.

bin	center (GeV)	left (GeV)	right (GeV)	σ (pb/GeV)	Δ_σ^{stat} (%)	Δ_σ^{syst} (%)	Δ_σ^{tot} (%)
1	32.5	0.0	65.0	4.53e-02	1.0	7.2	7.3
2	95.0	65.0	125.0	6.51e-02	0.9	8.3	8.3
3	162.5	125.0	200.0	3.82e-02	0.9	6.7	6.7
4	245.0	200.0	290.0	1.31e-02	1.3	5.9	6.0
5	345.0	290.0	400.0	3.30e-03	1.5	7.2	7.3
6	475.0	400.0	550.0	6.26e-04	3.7	8.9	9.6

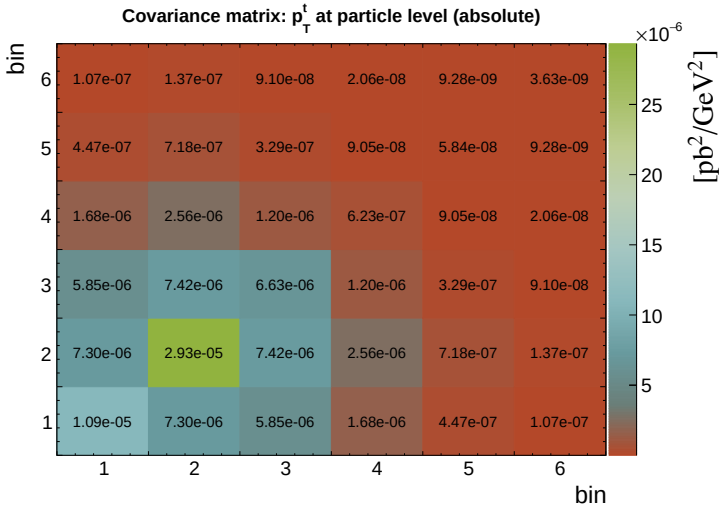

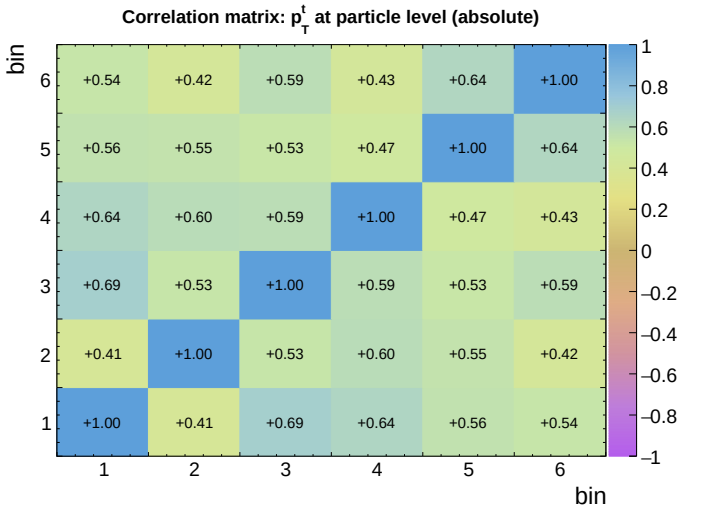

Table B.66 The result σ and its uncertainty per bin of the absolute differential $t\bar{t}$ production cross sections measured as a function of the transverse momentum of the top antiquark $p_T^{\bar{t}}$. Measurement is performed at particle level in a fiducial phase space. The corresponding covariance and correlation matrices are presented below the table.

bin	center (GeV)	left (GeV)	right (GeV)	σ (pb/GeV)	Δ_σ^{stat} (%)	Δ_σ^{syst} (%)	Δ_σ^{tot} (%)
1	32.5	0.0	65.0	4.58e-02	1.0	8.0	8.1
2	95.0	65.0	125.0	6.52e-02	0.9	7.5	7.5
3	162.5	125.0	200.0	3.72e-02	0.9	6.9	7.0
4	245.0	200.0	290.0	1.35e-02	1.2	6.5	6.6
5	345.0	290.0	400.0	3.33e-03	1.5	6.6	6.8
6	475.0	400.0	550.0	6.09e-04	3.8	14.2	14.7

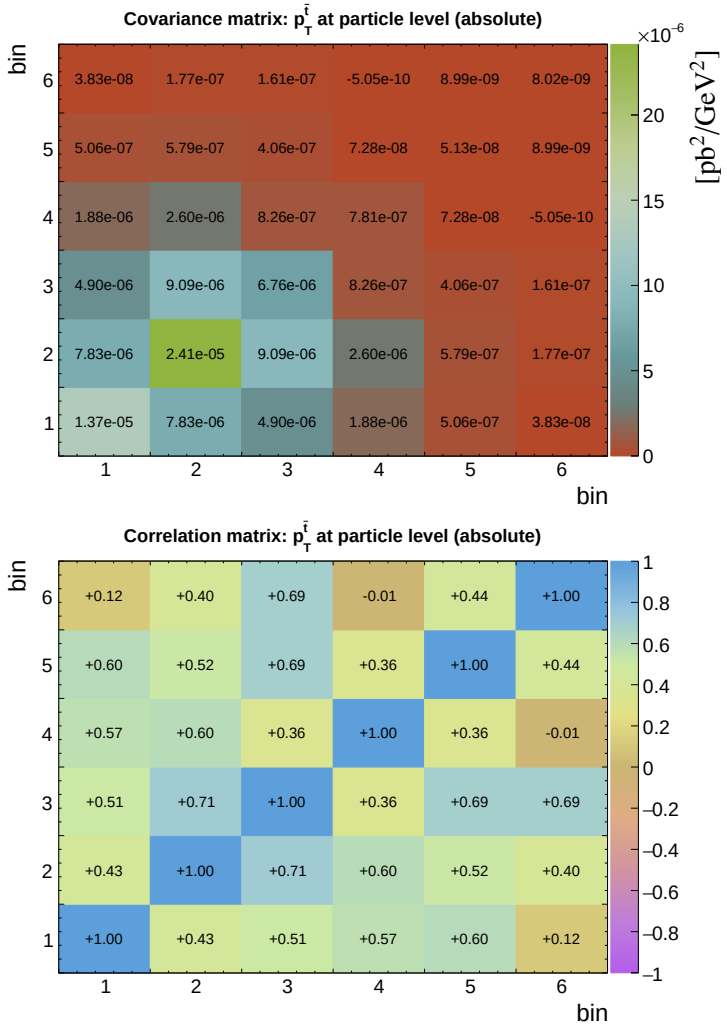

Table B.67 The result σ and its uncertainty per bin of the absolute differential $t\bar{t}$ production cross sections measured as a function of the transverse momentum of the leading top quark p_T^t *(leading)*. Measurement is performed at particle level in a fiducial phase space. The corresponding covariance and correlation matrices are presented below the table.

bin	center (GeV)	left (GeV)	right (GeV)	σ (pb/GeV)	Δ_σ^{stat} (%)	Δ_σ^{syst} (%)	Δ_σ^{tot} (%)
1	32.5	0.0	65.0	2.81e-02	1.2	8.1	8.2
2	95.0	65.0	125.0	6.50e-02	0.8	7.1	7.1
3	162.5	125.0	200.0	4.46e-02	0.7	7.0	7.1
4	245.0	200.0	290.0	1.78e-02	1.0	5.7	5.8
5	345.0	290.0	400.0	4.76e-03	1.2	6.2	6.4
6	475.0	400.0	550.0	9.43e-04	2.8	8.9	9.3

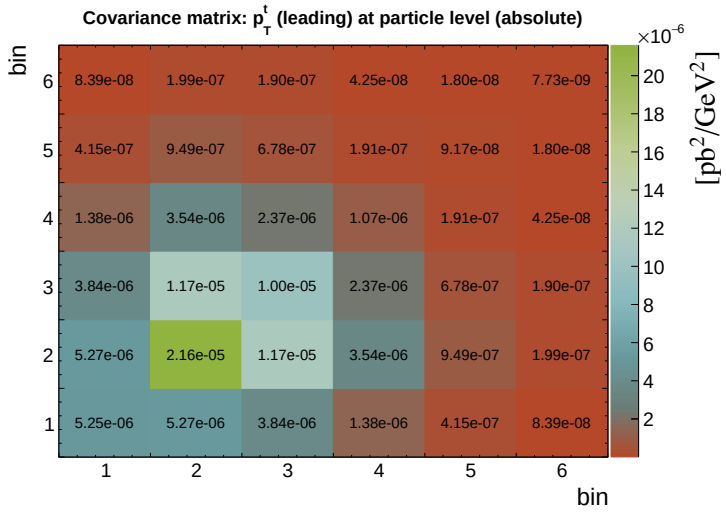

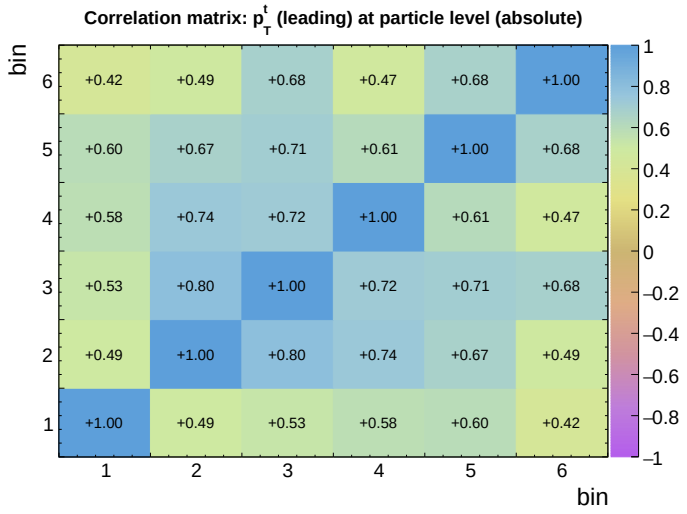

Table B.68 The result σ and its uncertainty per bin of the absolute differential $t\bar{t}$ production cross sections measured as a function of the transverse momentum of the trailing top quark p_T^t *(trailing)*. Measurement is performed at particle level in a fiducial phase space. The corresponding covariance and correlation matrices are presented below the table.

bin	center (GeV)	left (GeV)	right (GeV)	σ (pb/GeV)	Δ_σ^{stat} (%)	Δ_σ^{syst} (%)	Δ_σ^{tot} (%)
1	32.5	0.0	65.0	6.29e-02	0.8	7.1	7.1
2	95.0	65.0	125.0	6.52e-02	1.0	8.4	8.4
3	162.5	125.0	200.0	3.10e-02	1.2	6.5	6.6
4	245.0	200.0	290.0	8.76e-03	1.8	7.9	8.1
5	345.0	290.0	400.0	1.89e-03	2.3	9.2	9.5
6	475.0	400.0	550.0	2.95e-04	6.2	17.8	18.8

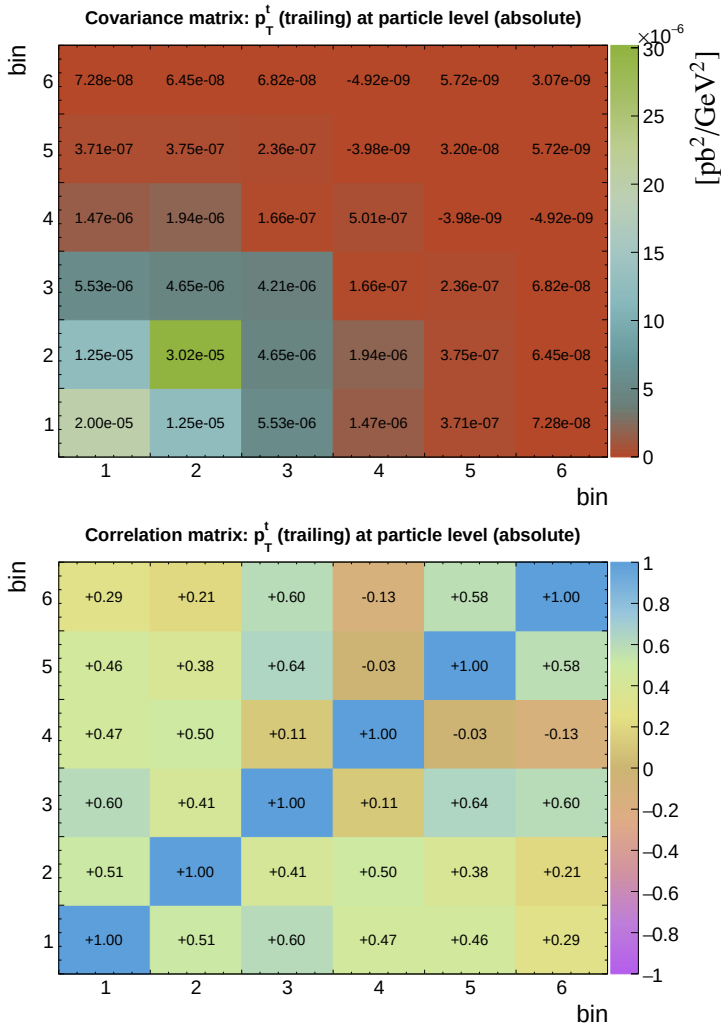

Table B.69 The result σ and its uncertainty per bin of the absolute differential $t\bar{t}$ production cross sections measured as a function of the transverse momentum of the top quark in the rest frame of the $t\bar{t}$-system p_T^t *($t\bar{t}$ rest frame)*. Measurement is performed at particle level in a fiducial phase space. The corresponding covariance and correlation matrices are presented below the table.

bin	center (GeV)	left (GeV)	right (GeV)	σ (pb/GeV)	Δ_σ^{stat} (%)	Δ_σ^{syst} (%)	Δ_σ^{tot} (%)
1	32.5	0.0	65.0	4.97e-02	0.9	7.1	7.2
2	95.0	65.0	125.0	6.74e-02	1.0	8.0	8.0
3	162.5	125.0	200.0	3.64e-02	1.0	6.5	6.6
4	245.0	200.0	290.0	1.11e-02	1.5	6.2	6.4
5	345.0	290.0	400.0	2.58e-03	1.8	6.9	7.2
6	475.0	400.0	550.0	4.12e-04	5.0	12.5	13.5

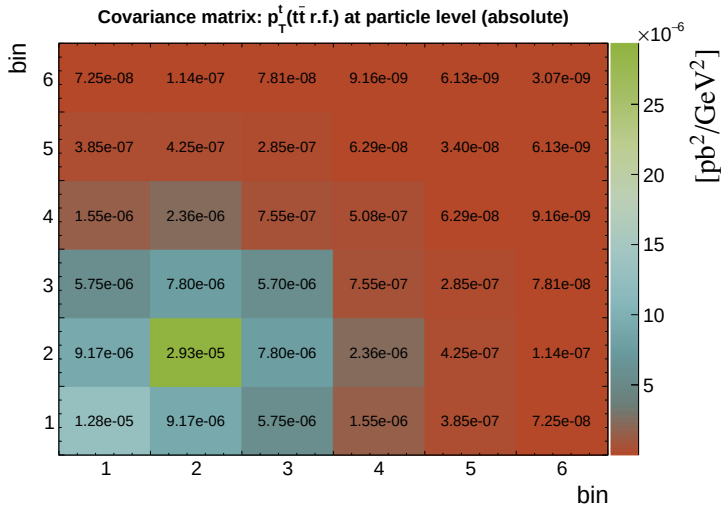

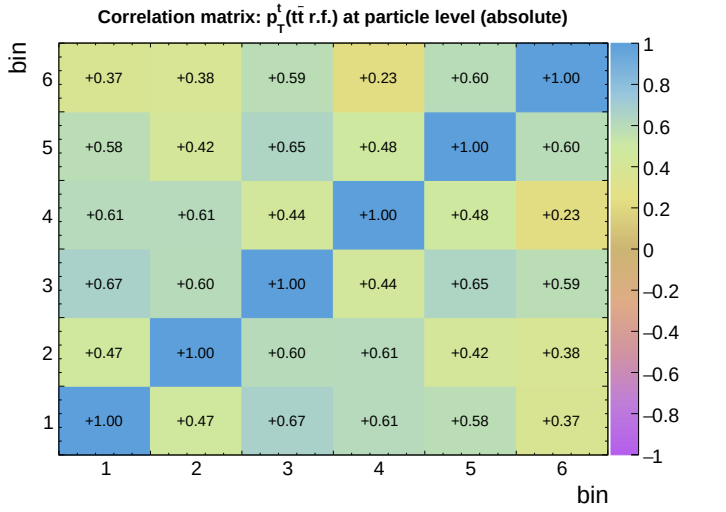

Table B.70 The result σ and its uncertainty per bin of the absolute differential $t\bar{t}$ production cross sections measured as a function of the transverse momentum of the top antiquark in the rest frame of the $t\bar{t}$-system $p_T^{\bar{t}}$ *($t\bar{t}$ rest frame)*. Measurement is performed at particle level in a fiducial phase space. The corresponding covariance and correlation matrices are presented below the table.

bin	center (GeV)	left (GeV)	right (GeV)	σ (pb/GeV)	Δ_σ^{stat} (%)	Δ_σ^{syst} (%)	Δ_σ^{tot} (%)
1	32.5	0.0	65.0	4.97e-02	0.9	7.1	7.2
2	95.0	65.0	125.0	6.74e-02	1.0	8.0	8.0
3	162.5	125.0	200.0	3.64e-02	1.0	6.5	6.6
4	245.0	200.0	290.0	1.11e-02	1.5	6.2	6.4
5	345.0	290.0	400.0	2.58e-03	1.8	6.9	7.2
6	475.0	400.0	550.0	4.12e-04	5.0	12.5	13.5

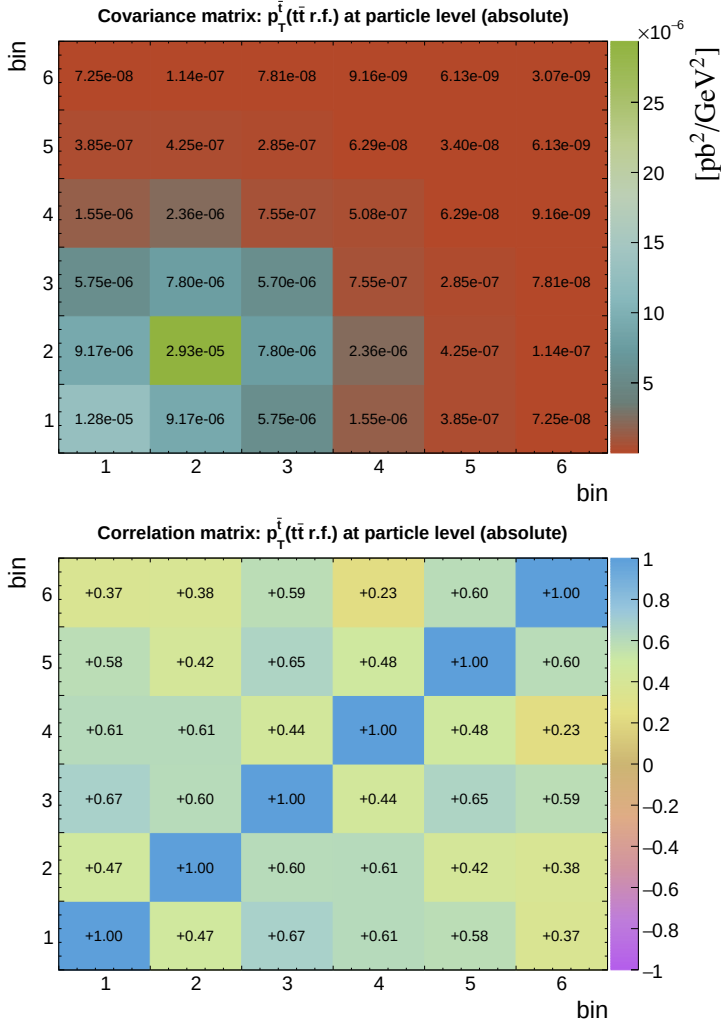

Table B.71 The result σ and its uncertainty per bin of the absolute differential $t\bar{t}$ production cross sections measured as a function of the rapidity of the top quark y_t. Measurement is performed at particle level in a fiducial phase space. The corresponding covariance and correlation matrices are presented below the table.

bin	center	left	right	σ (pb)	Δ_σ^{stat} (%)	Δ_σ^{syst} (%)	Δ_σ^{tot} (%)
1	−2.20	−2.60	−1.80	3.56e-01	1.9	9.4	9.6
2	−1.58	−1.80	−1.35	1.64e+00	1.0	6.7	6.8
3	−1.12	−1.35	−0.90	2.81e+00	1.0	6.3	6.4
4	−0.68	−0.90	−0.45	3.55e+00	0.9	6.4	6.5
5	−0.22	−0.45	0.00	3.88e+00	0.9	6.4	6.5
6	0.22	0.00	0.45	3.91e+00	0.9	7.0	7.0
7	0.68	0.45	0.90	3.62e+00	0.9	6.5	6.5
8	1.12	0.90	1.35	2.75e+00	0.9	6.5	6.5
9	1.58	1.35	1.80	1.66e+00	1.0	7.3	7.3
10	2.20	1.80	2.60	3.74e-01	1.8	8.2	8.4

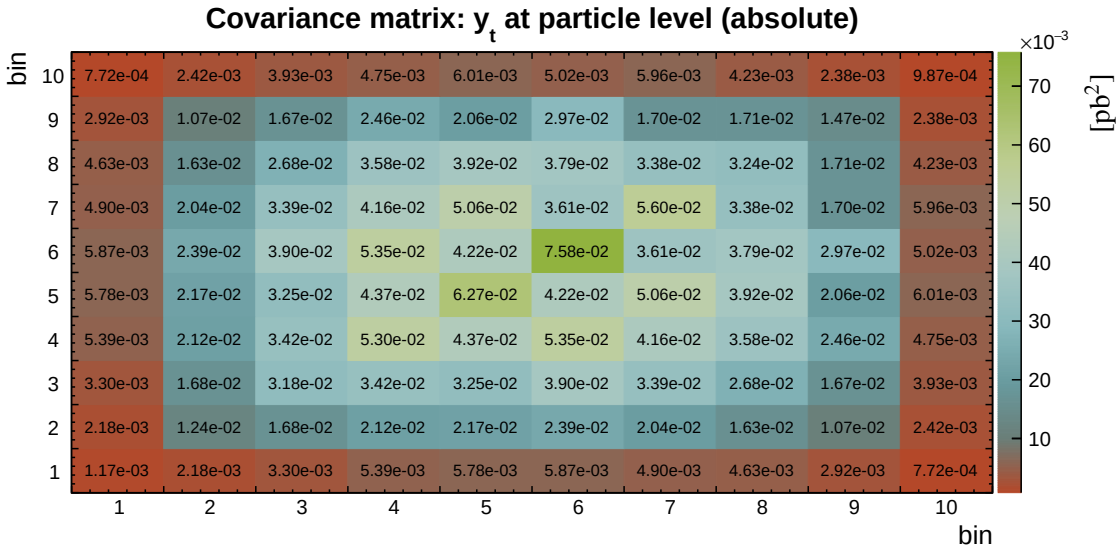

Table B.72 The result σ and its uncertainty per bin of the absolute differential $t\bar{t}$ production cross sections measured as a function of the rapidity of the top antiquark $y_{\bar{t}}$. Measurement is performed at particle level in a fiducial phase space. The corresponding covariance and correlation matrices are presented below the table.

bin	center	left	right	σ (pb)	Δ_σ^{stat} (%)	Δ_σ^{syst} (%)	Δ_σ^{tot} (%)
1	−2.20	−2.60	−1.80	3.63e-01	1.9	9.2	9.3
2	−1.58	−1.80	−1.35	1.62e+00	1.0	7.1	7.2
3	−1.12	−1.35	−0.90	2.79e+00	1.0	6.5	6.6
4	−0.68	−0.90	−0.45	3.54e+00	0.9	6.3	6.3
5	−0.22	−0.45	0.00	3.96e+00	0.9	6.5	6.6
6	0.22	0.00	0.45	3.94e+00	0.9	6.5	6.6
7	0.68	0.45	0.90	3.52e+00	0.9	6.2	6.3
8	1.12	0.90	1.35	2.85e+00	0.9	6.6	6.7
9	1.58	1.35	1.80	1.62e+00	1.0	8.5	8.6
10	2.20	1.80	2.60	3.60e-01	1.9	9.4	9.6

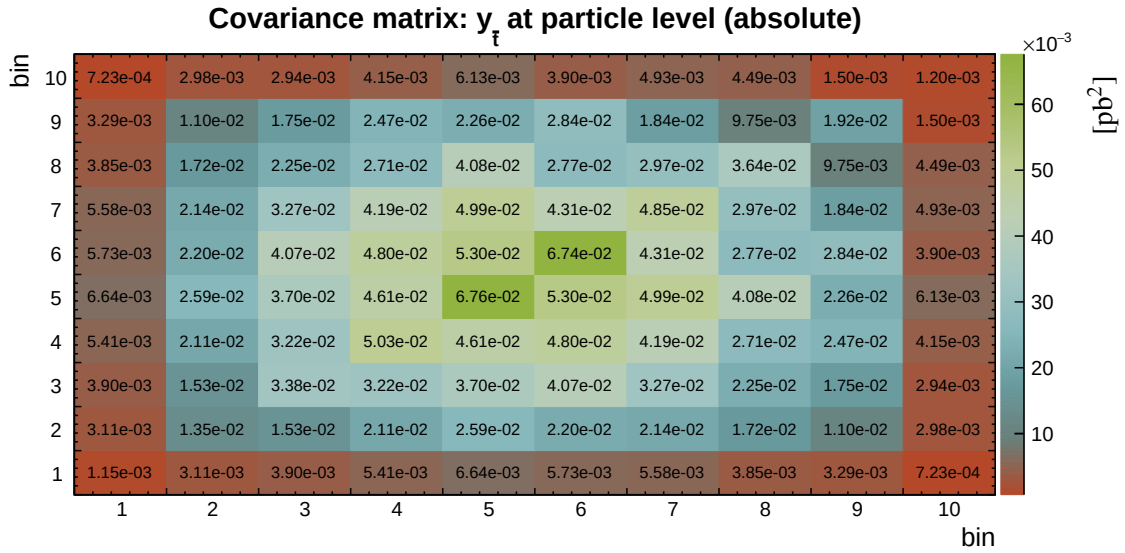

Table B.73 The result σ and its uncertainty per bin of the absolute differential $t\bar{t}$ production cross sections measured as a function of the rapidity of the leading top quark y_t *(leading)*. Measurement is performed at particle level in a fiducial phase space. The corresponding covariance and correlation matrices are presented below the table.

bin	center	left	right	σ (pb)	Δ_σ^{stat} (%)	Δ_σ^{syst} (%)	Δ_σ^{tot} (%)
1	−2.12	−2.60	−1.65	4.89e-01	1.7	9.3	9.5
2	−1.38	−1.65	−1.10	2.15e+00	0.9	7.1	7.2
3	−0.82	−1.10	−0.55	3.38e+00	0.8	6.1	6.1
4	−0.28	−0.55	0.00	3.89e+00	0.8	6.1	6.1
5	0.28	0.00	0.55	3.89e+00	0.8	6.1	6.1
6	0.82	0.55	1.10	3.39e+00	0.8	6.1	6.1
7	1.38	1.10	1.65	2.13e+00	0.9	7.9	7.9
8	2.12	1.65	2.60	5.13e-01	1.6	8.8	9.0

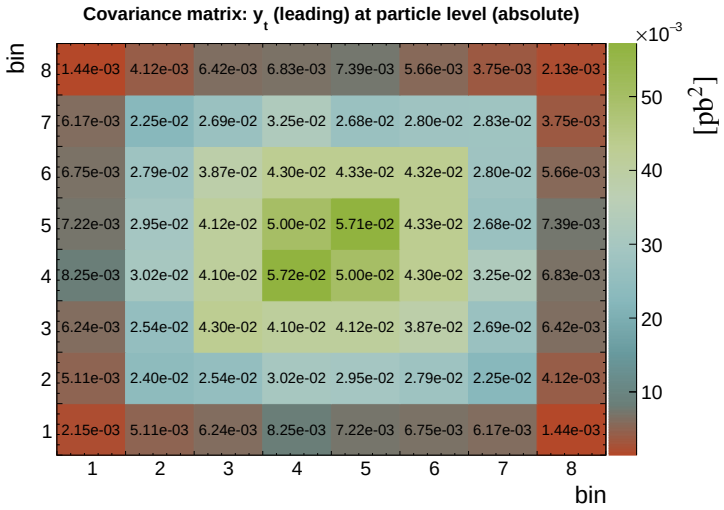

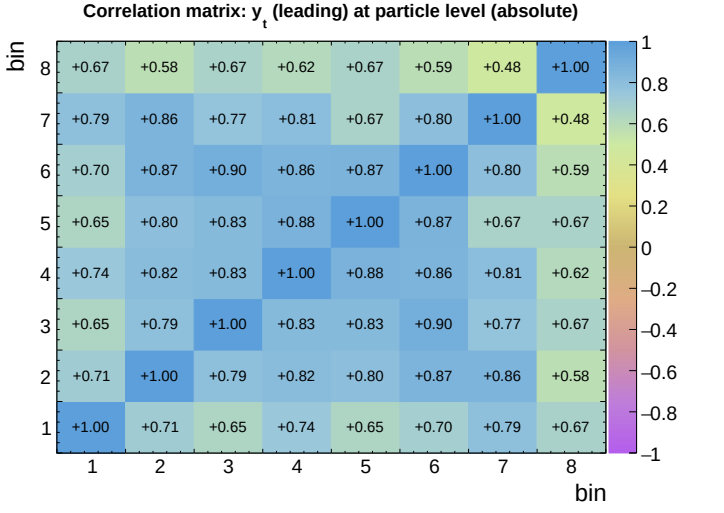

Table B.74 The result σ and its uncertainty per bin of the absolute differential $t\bar{t}$ production cross sections measured as a function of the rapidity of the trailing top quark y_t *(trailing)*. Measurement is performed at particle level in a fiducial phase space. The corresponding covariance and correlation matrices are presented below the table.

bin	center	left	right	σ (pb)	Δ_σ^{stat} (%)	Δ_σ^{syst} (%)	Δ_σ^{tot} (%)
1	−2.12	−2.60	−1.65	5.04e-01	1.8	9.4	9.6
2	−1.38	−1.65	−1.10	2.15e+00	1.0	7.0	7.0
3	−0.82	−1.10	−0.55	3.35e+00	0.9	6.2	6.3
4	−0.28	−0.55	0.00	3.86e+00	0.9	6.6	6.6
5	0.28	0.00	0.55	3.85e+00	0.9	7.2	7.3
6	0.82	0.55	1.10	3.40e+00	0.9	6.3	6.3
7	1.38	1.10	1.65	2.20e+00	0.9	6.7	6.8
8	2.12	1.65	2.60	5.00e-01	1.7	8.3	8.5

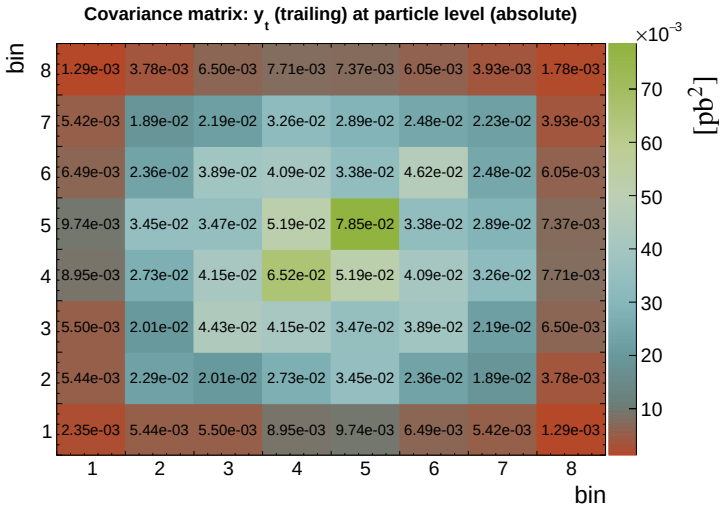

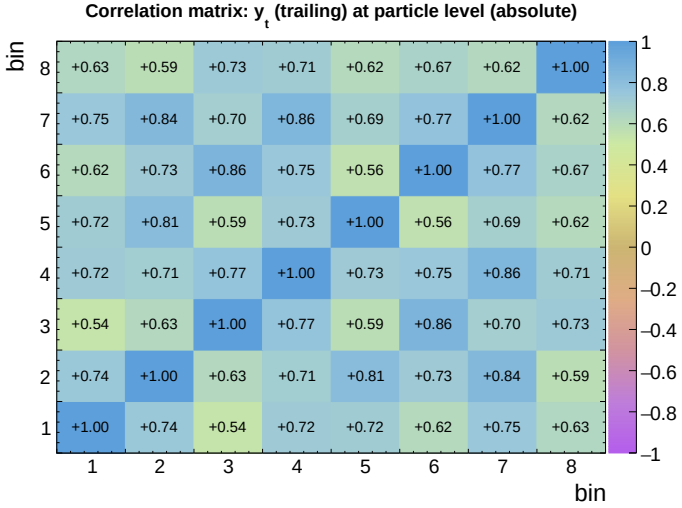

Table B.75 The result σ and its uncertainty per bin of the absolute differential $t\bar{t}$ production cross sections measured as a function of the difference in absolute rapidity between the top quark and antiquark $\Delta|y|(t,\bar{t})$. Measurement is performed at particle level in a fiducial phase space. The corresponding covariance and correlation matrices are presented below the table.

bin	center	left	right	σ (pb)	Δ_{σ}^{stat} (%)	Δ_{σ}^{syst} (%)	Δ_{σ}^{tot} (%)
1	−2.00	−2.60	−1.40	3.19e-01	1.9	8.4	8.7
2	−1.15	−1.40	−0.90	2.02e+00	1.1	7.6	7.6
3	−0.65	−0.90	−0.40	3.90e+00	0.9	6.9	7.0
4	−0.20	−0.40	0.00	5.65e+00	0.9	6.3	6.3
5	0.20	0.00	0.40	5.73e+00	0.9	6.0	6.1
6	0.65	0.40	0.90	3.95e+00	0.9	7.1	7.2
7	1.15	0.90	1.40	2.07e+00	1.1	7.2	7.2
8	2.00	1.40	2.60	3.31e-01	1.8	9.0	9.2

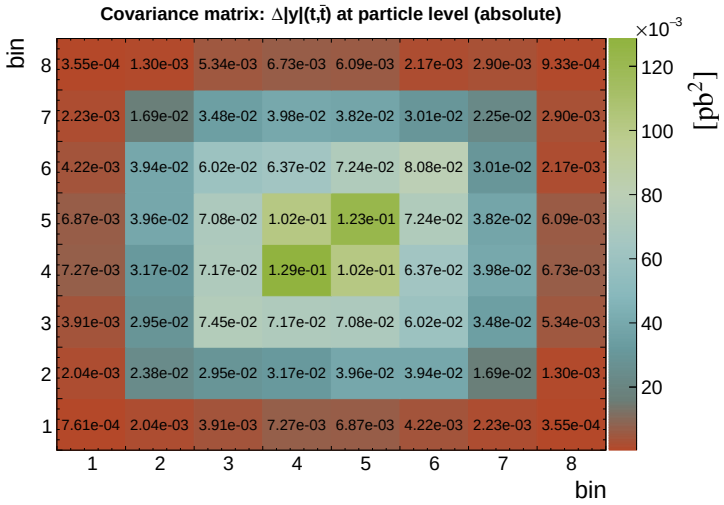

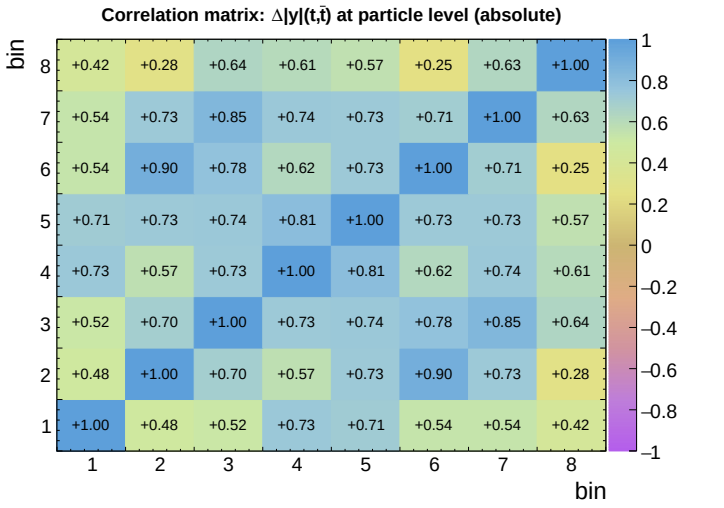

Table B.76 The result σ and its uncertainty per bin of the absolute differential $t\bar{t}$ production cross sections measured as a function of the difference in azimuthal angle between the top quark and antiquark $\Delta\phi(t,\bar{t})$. Measurement is performed at particle level in a fiducial phase space. The corresponding covariance and correlation matrices are presented below the table.

bin	center	left	right	σ (pb)	Δ_σ^{stat} (%)	Δ_σ^{syst} (%)	Δ_σ^{tot} (%)
1	0.785	0.000	1.570	7.11e-01	1.1	8.4	8.4
2	2.120	1.570	2.670	2.52e+00	0.6	7.9	7.9
3	2.845	2.670	3.020	1.19e+01	0.6	6.8	6.8
4	3.081	3.020	3.142	2.67e+01	0.7	7.3	7.3

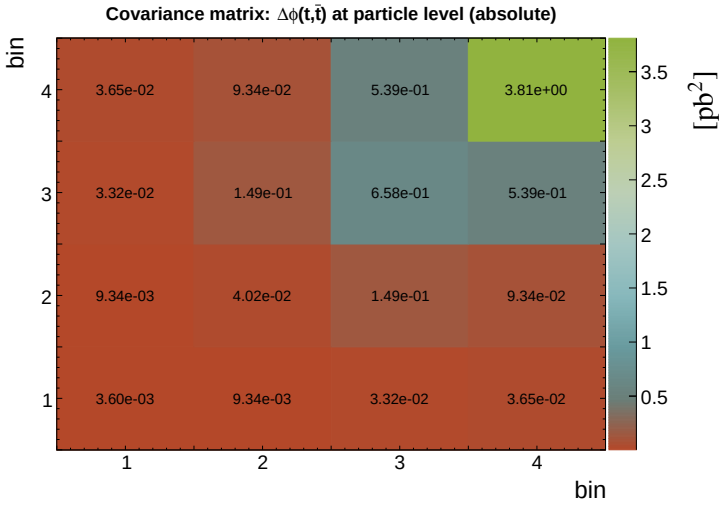

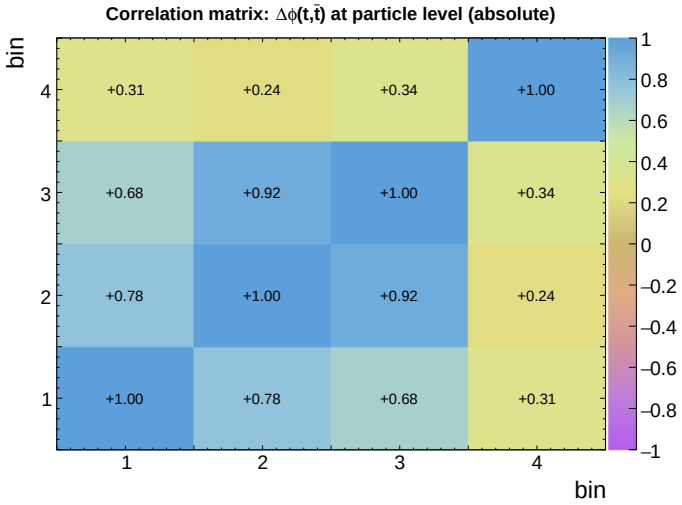

Table B.77 The result σ and its uncertainty per bin of the absolute differential $t\bar{t}$ production cross sections measured as a function of the transverse momentum of the top-quark pair $p_T^{t\bar{t}}$. Measurement is performed at particle level in a fiducial phase space. The corresponding covariance and correlation matrices are presented below the table.

bin	center (GeV)	left (GeV)	right (GeV)	σ (pb/GeV)	Δ_σ^{stat} (%)	Δ_σ^{syst} (%)	Δ_σ^{tot} (%)
1	20.0	0.0	40.0	1.32e-01	0.5	8.6	8.6
2	70.0	40.0	100.0	6.05e-02	0.9	12.9	12.9
3	150.0	100.0	200.0	1.79e-02	0.9	7.2	7.2
4	255.0	200.0	310.0	3.97e-03	1.5	7.7	7.8
5	365.0	310.0	420.0	1.08e-03	2.3	8.9	9.2
6	495.0	420.0	570.0	2.77e-04	4.0	9.6	10.4

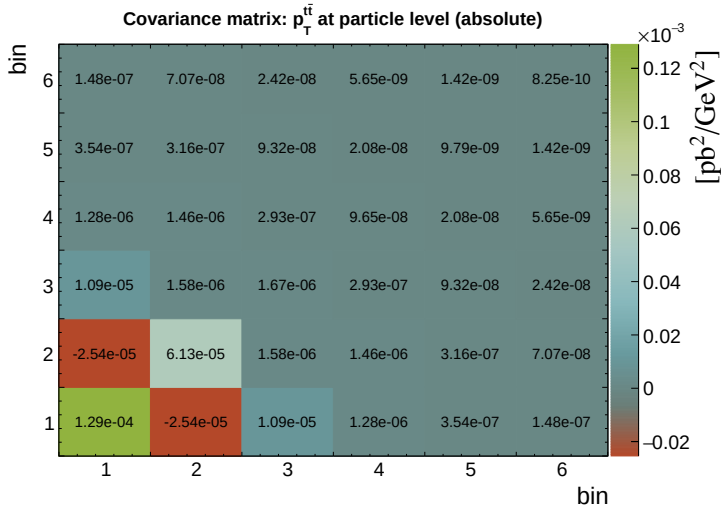

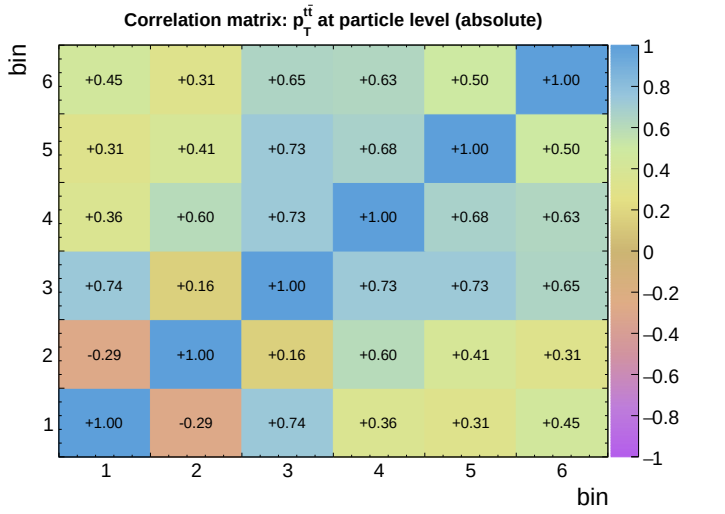

Table B.78 The result σ and its uncertainty per bin of the absolute differential $t\bar{t}$ production cross sections measured as a function of the invariant mass of the top-quark pair $m_{t\bar{t}}$. Measurement is performed at particle level in a fiducial phase space. The corresponding covariance and correlation matrices are presented below the table.

bin	center (GeV)	left (GeV)	right (GeV)	σ (pb/GeV)	Δ_{σ}^{stat} (%)	Δ_{σ}^{syst} (%)	Δ_{σ}^{tot} (%)
1	340.0	300.0	380.0	3.08e-02	1.2	7.4	7.5
2	425.0	380.0	470.0	4.12e-02	1.3	9.5	9.6
3	545.0	470.0	620.0	2.18e-02	1.2	6.3	6.4
4	720.0	620.0	820.0	6.76e-03	1.7	6.9	7.2
5	960.0	820.0	1100.0	1.48e-03	2.8	9.4	9.8
6	1300.0	1100.0	1500.0	2.48e-04	3.7	9.9	10.5
7	2000.0	1500.0	2500.0	1.73e-05	9.3	21.8	23.7

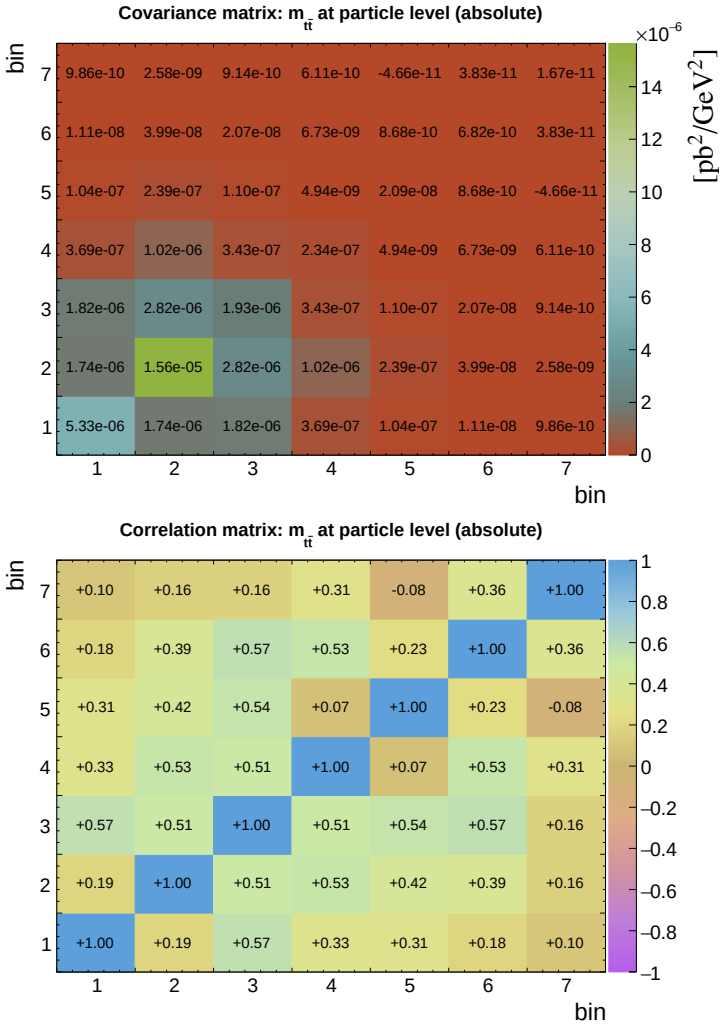

Table B.79 The result σ and its uncertainty per bin of the absolute differential $t\bar{t}$ production cross sections measured as a function of the rapidity of the top-quark pair $y_{t\bar{t}}$. Measurement is performed at particle level in a fiducial phase space. The corresponding covariance and correlation matrices are presented below the table.

bin	center	left	right	σ (pb)	Δ_{σ}^{stat} (%)	Δ_{σ}^{syst} (%)	Δ_{σ}^{tot} (%)
1	−2.10	−2.60	−1.60	1.60e-01	2.5	14.3	14.5
2	−1.40	−1.60	−1.20	1.45e+00	1.1	6.8	6.9
3	−1.00	−1.20	−0.80	2.94e+00	1.0	6.5	6.6
4	−0.60	−0.80	−0.40	4.21e+00	0.9	6.6	6.7
5	−0.20	−0.40	0.00	5.18e+00	0.8	5.8	5.8
6	0.20	0.00	0.40	4.97e+00	0.8	6.7	6.7
7	0.60	0.40	0.80	4.27e+00	0.8	6.5	6.5
8	1.00	0.80	1.20	3.00e+00	0.9	6.2	6.3
9	1.40	1.20	1.60	1.42e+00	1.1	7.4	7.5
10	2.10	1.60	2.60	1.75e-01	2.2	9.6	9.8

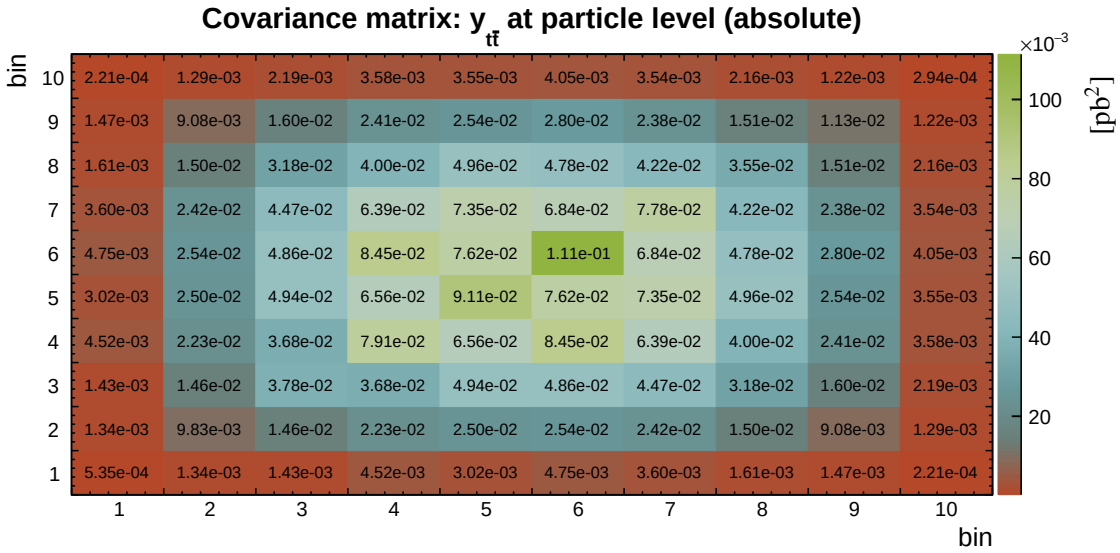

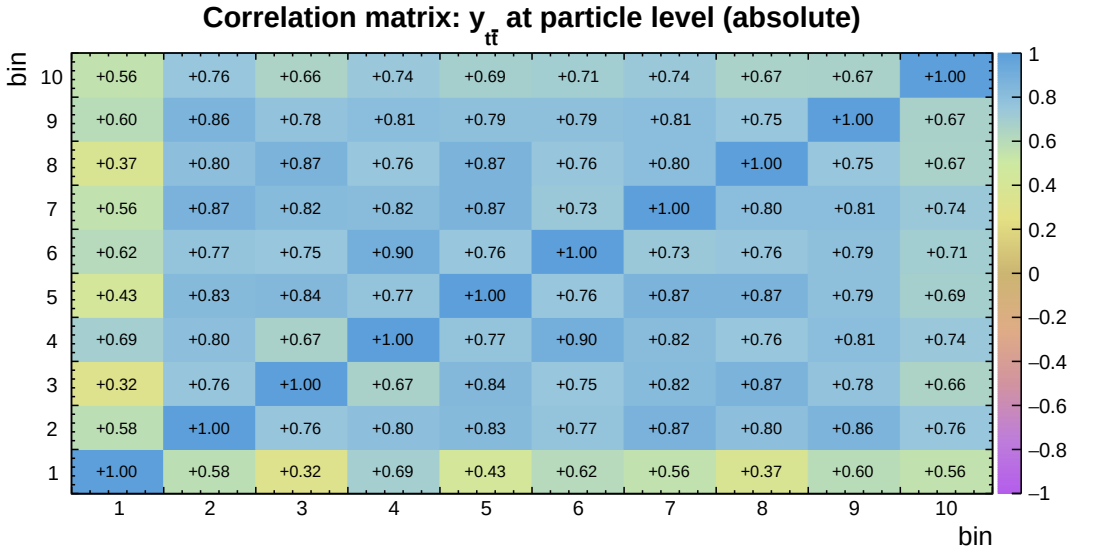

Table B.80 The result σ and its uncertainty per bin of the absolute differential $t\bar{t}$ production cross sections measured as a function of the transverse momentum of the lepton p_T^{ℓ}. Measurement is performed at particle level in a fiducial phase space. The corresponding covariance and correlation matrices are presented below the table.

bin	center (GeV)	left (GeV)	right (GeV)	σ (pb/GeV)	Δ_{σ}^{stat} (%)	Δ_{σ}^{syst} (%)	Δ_{σ}^{tot} (%)
1	30.0	20.0	40.0	2.09e-01	0.4	6.7	6.7
2	55.0	40.0	70.0	1.42e-01	0.4	5.9	5.9
3	95.0	70.0	120.0	4.55e-02	0.5	6.0	6.1
4	150.0	120.0	180.0	8.22e-03	1.0	6.4	6.5
5	290.0	180.0	400.0	5.74e-04	2.0	7.3	7.6

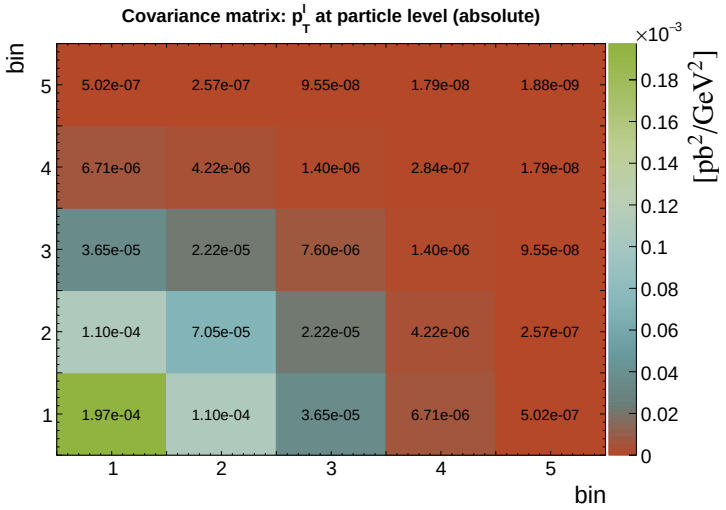

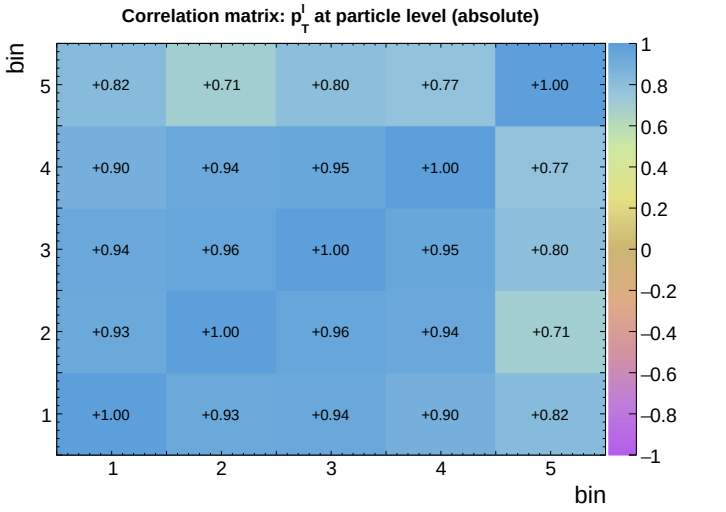

Table B.81 The result σ and its uncertainty per bin of the absolute differential $t\bar{t}$ production cross sections measured as a function of the transverse momentum of the antilepton $p_T^{\bar{\ell}}$. Measurement is performed at particle level in a fiducial phase space. The corresponding covariance and correlation matrices are presented below the table.

bin	center (GeV)	left (GeV)	right (GeV)	σ (pb/GeV)	Δ_σ^{stat} (%)	Δ_σ^{syst} (%)	Δ_σ^{tot} (%)
1	30.0	20.0	40.0	2.08e-01	0.4	6.7	6.7
2	55.0	40.0	70.0	1.43e-01	0.4	5.9	5.9
3	95.0	70.0	120.0	4.53e-02	0.5	6.0	6.0
4	150.0	120.0	180.0	8.27e-03	1.0	6.7	6.7
5	290.0	180.0	400.0	5.55e-04	2.1	8.0	8.2

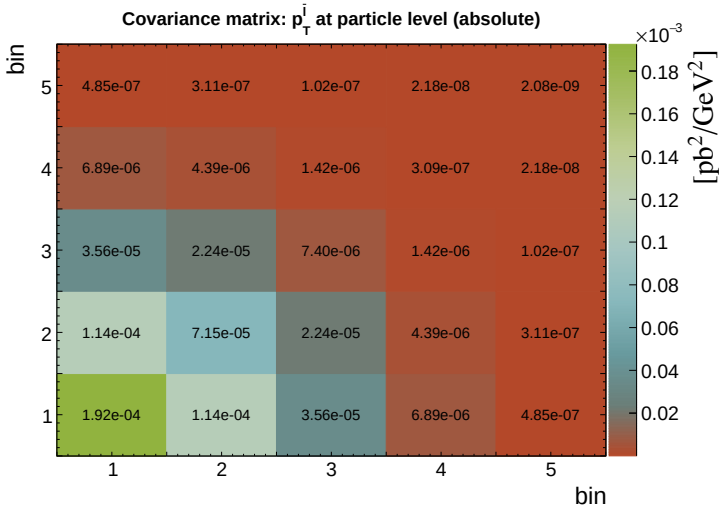

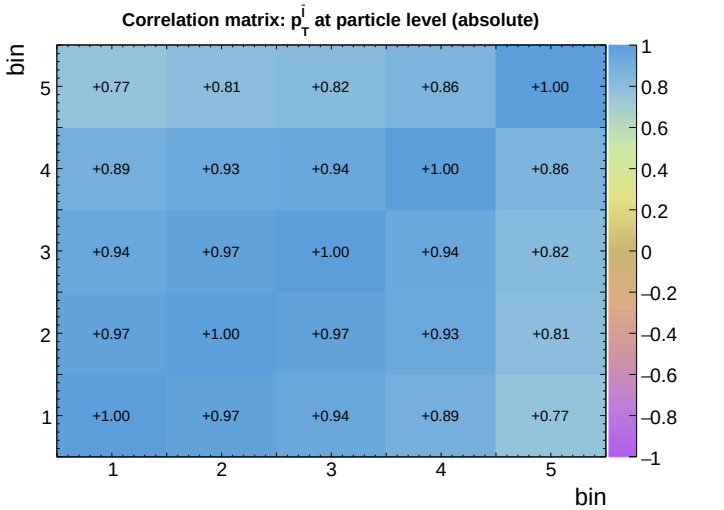

Table B.82 The result σ and its uncertainty per bin of the absolute differential $t\bar{t}$ production cross sections measured as a function of the transverse momentum of the leading lepton p_T^{ℓ} *(leading)*. Measurement is performed at particle level in a fiducial phase space. The corresponding covariance and correlation matrices are presented below the table.

bin	center (GeV)	left (GeV)	right (GeV)	σ (pb/GeV)	Δ_σ^{stat} (%)	Δ_σ^{syst} (%)	Δ_σ^{tot} (%)
1	30.0	20.0	40.0	7.96e-02	0.6	7.6	7.6
2	55.0	40.0	70.0	1.64e-01	0.4	6.1	6.1
3	95.0	70.0	120.0	7.45e-02	0.4	6.0	6.0
4	150.0	120.0	180.0	1.49e-02	0.7	6.4	6.5
5	290.0	180.0	400.0	1.07e-03	1.5	7.4	7.5

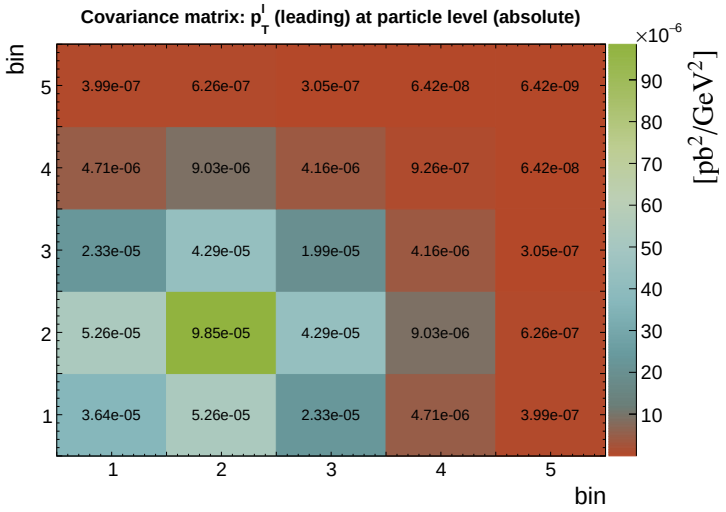

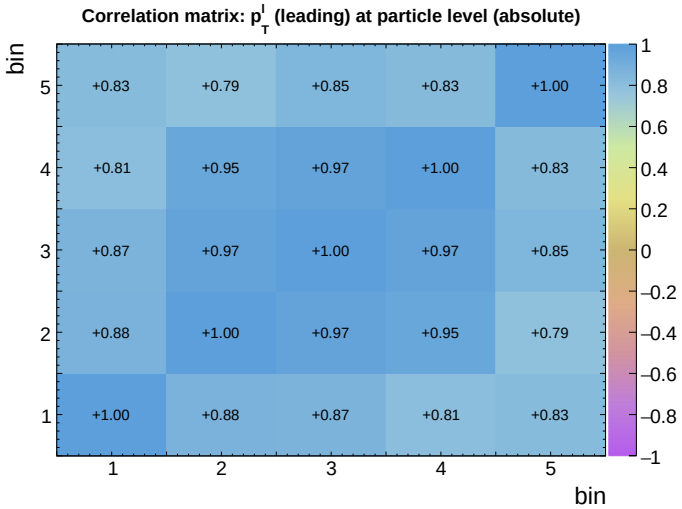

Table B.83 The result σ and its uncertainty per bin of the absolute differential $t\bar{t}$ production cross sections measured as a function of the transverse momentum of the trailing lepton p_T^{ℓ} *(trailing)*. Measurement is performed at particle level in a fiducial phase space. The corresponding covariance and correlation matrices are presented below the table.

bin	center (GeV)	left (GeV)	right (GeV)	σ (pb/GeV)	Δ_σ^{stat} (%)	Δ_σ^{syst} (%)	Δ_σ^{tot} (%)
1	27.5	20.0	35.0	3.61e-01	0.3	6.8	6.8
2	42.5	35.0	50.0	2.17e-01	0.4	5.6	5.6
3	70.0	50.0	90.0	5.74e-02	0.5	6.0	6.0
4	115.0	90.0	140.0	6.23e-03	1.2	6.6	6.7
5	270.0	140.0	400.0	2.16e-04	3.0	7.3	7.9

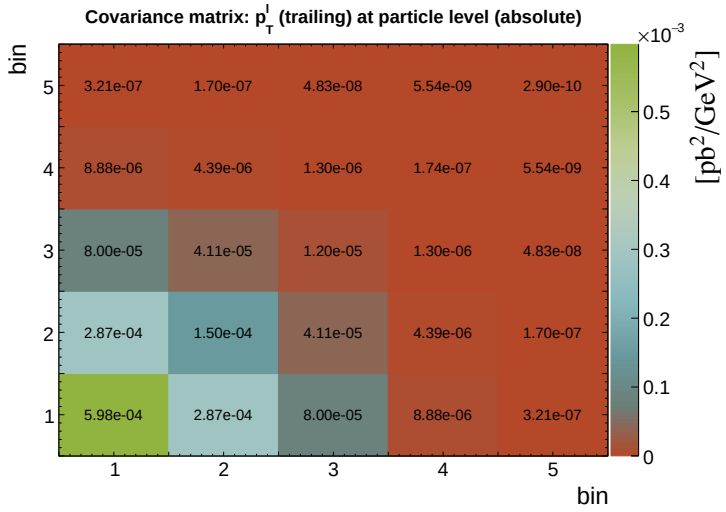

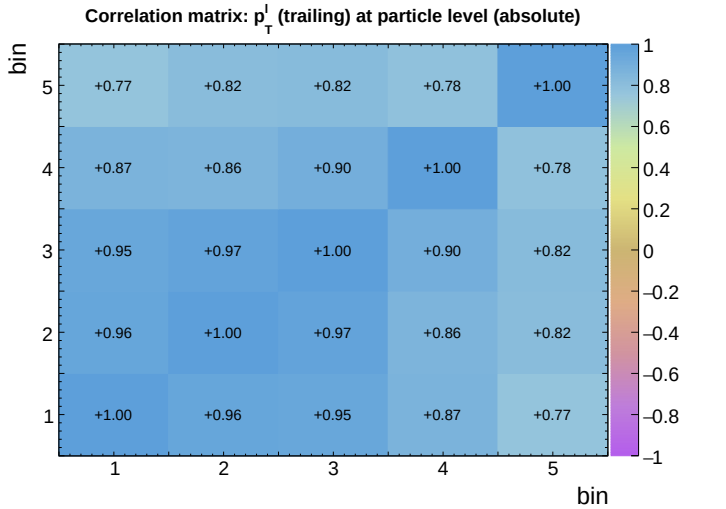

Table B.84 The result σ and its uncertainty per bin of the absolute differential $t\bar{t}$ production cross sections measured as a function of the pseudorapidity of the lepton η_ℓ. Measurement is performed at particle level in a fiducial phase space. The corresponding covariance and correlation matrices are presented below the table.

bin	center	left	right	σ (pb)	Δ_σ^{stat} (%)	Δ_σ^{syst} (%)	Δ_σ^{tot} (%)
1	−2.25	−2.40	−2.10	7.81e-01	1.5	7.8	7.9
2	−1.95	−2.10	−1.80	1.14e+00	1.2	7.5	7.6
3	−1.65	−1.80	−1.50	1.67e+00	1.0	6.2	6.3
4	−1.35	−1.50	−1.20	2.19e+00	0.9	6.4	6.5
5	−1.05	−1.20	−0.90	2.75e+00	0.8	6.2	6.3
6	−0.75	−0.90	−0.60	3.20e+00	0.7	6.0	6.1
7	−0.45	−0.60	−0.30	3.52e+00	0.7	6.1	6.1
8	−0.15	−0.30	0.00	3.60e+00	0.7	6.2	6.3
9	0.15	0.00	0.30	3.58e+00	0.7	6.3	6.3
10	0.45	0.30	0.60	3.52e+00	0.7	6.2	6.2
11	0.75	0.60	0.90	3.17e+00	0.7	6.1	6.1
12	1.05	0.90	1.20	2.78e+00	0.8	6.1	6.2
13	1.35	1.20	1.50	2.16e+00	0.9	6.6	6.6
14	1.65	1.50	1.80	1.71e+00	1.1	6.3	6.4
15	1.95	1.80	2.10	1.18e+00	1.3	7.1	7.2
16	2.25	2.10	2.40	7.38e-01	1.6	7.5	7.7

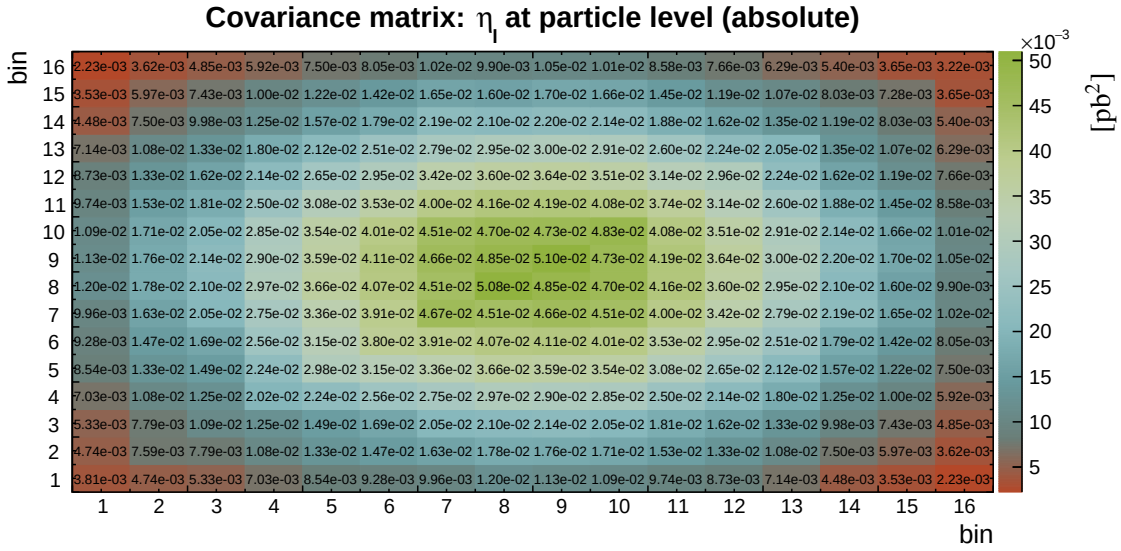

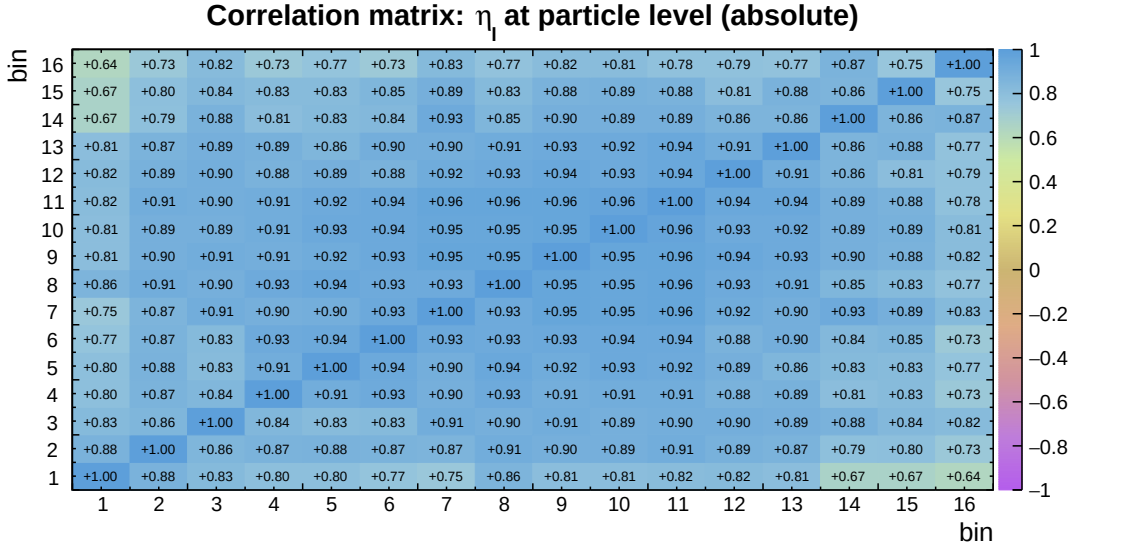

Table B.85 The result σ and its uncertainty per bin of the absolute differential $t\bar{t}$ production cross sections measured as a function of the pseudorapidity of the antilepton $\eta_{\bar{\ell}}$. Measurement is performed at particle level in a fiducial phase space. The corresponding covariance and correlation matrices are presented below the table.

bin	center	left	right	σ (pb)	Δ_{σ}^{stat} (%)	Δ_{σ}^{syst} (%)	Δ_{σ}^{tot} (%)
1	−2.25	−2.40	−2.10	7.75e-01	1.6	7.0	7.2
2	−1.95	−2.10	−1.80	1.18e+00	1.2	6.9	7.0
3	−1.65	−1.80	−1.50	1.70e+00	1.0	6.4	6.5
4	−1.35	−1.50	−1.20	2.23e+00	0.9	6.1	6.1
5	−1.05	−1.20	−0.90	2.76e+00	0.8	6.2	6.3
6	−0.75	−0.90	−0.60	3.16e+00	0.7	6.3	6.3
7	−0.45	−0.60	−0.30	3.45e+00	0.7	6.2	6.2
8	−0.15	−0.30	0.00	3.53e+00	0.7	6.4	6.4
9	0.15	0.00	0.30	3.61e+00	0.7	6.2	6.3
10	0.45	0.30	0.60	3.46e+00	0.7	6.0	6.1
11	0.75	0.60	0.90	3.24e+00	0.7	6.1	6.2
12	1.05	0.90	1.20	2.70e+00	0.8	6.5	6.6
13	1.35	1.20	1.50	2.20e+00	0.9	6.3	6.4
14	1.65	1.50	1.80	1.70e+00	1.1	6.4	6.5
15	1.95	1.80	2.10	1.21e+00	1.3	6.6	6.7
16	2.25	2.10	2.40	7.50e-01	1.6	7.4	7.6

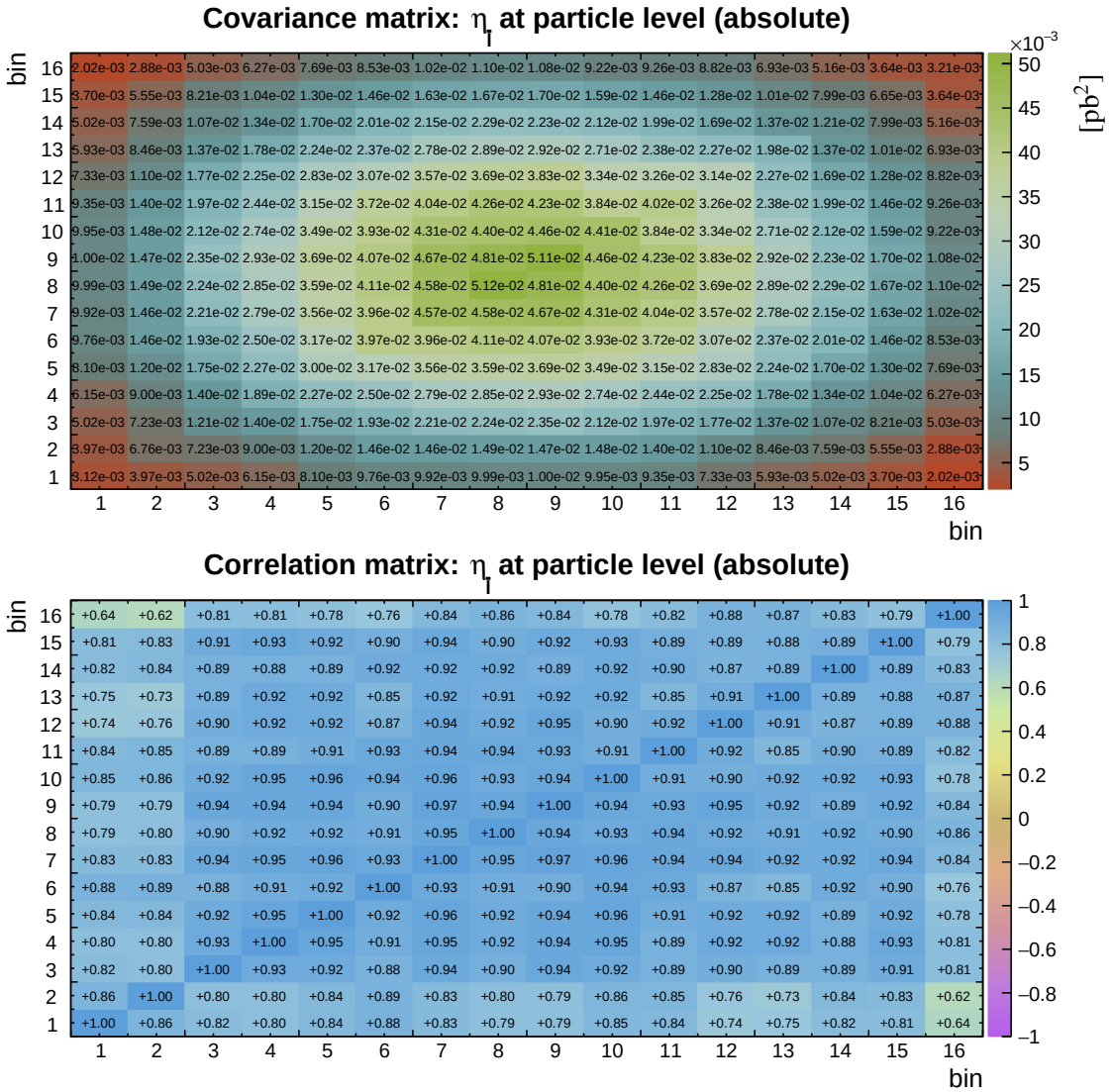

Table B.86 The result σ and its uncertainty per bin of the absolute differential $t\bar{t}$ production cross sections measured as a function of the pseudorapidity of the leading lepton η_ℓ *(leading)*. Measurement is performed at particle level in a fiducial phase space. The corresponding covariance and correlation matrices are presented below the table.

bin	center	left	right	σ (pb)	Δ_σ^{stat} (%)	Δ_σ^{syst} (%)	Δ_σ^{tot} (%)
1	−2.25	−2.40	−2.10	6.90e-01	1.7	7.5	7.7
2	−1.95	−2.10	−1.80	1.07e+00	1.3	7.8	7.9
3	−1.65	−1.80	−1.50	1.66e+00	1.1	6.2	6.2
4	−1.35	−1.50	−1.20	2.20e+00	0.9	6.3	6.4
5	−1.05	−1.20	−0.90	2.75e+00	0.8	6.2	6.2
6	−0.75	−0.90	−0.60	3.28e+00	0.7	6.1	6.2
7	−0.45	−0.60	−0.30	3.59e+00	0.7	6.1	6.1
8	−0.15	−0.30	0.00	3.62e+00	0.7	6.3	6.4
9	0.15	0.00	0.30	3.69e+00	0.7	6.2	6.3
10	0.45	0.30	0.60	3.56e+00	0.7	6.1	6.2
11	0.75	0.60	0.90	3.25e+00	0.7	6.1	6.1
12	1.05	0.90	1.20	2.77e+00	0.8	6.3	6.4
13	1.35	1.20	1.50	2.17e+00	0.9	6.4	6.5
14	1.65	1.50	1.80	1.65e+00	1.1	6.4	6.5
15	1.95	1.80	2.10	1.08e+00	1.4	7.6	7.7
16	2.25	2.10	2.40	6.69e-01	1.7	7.3	7.5

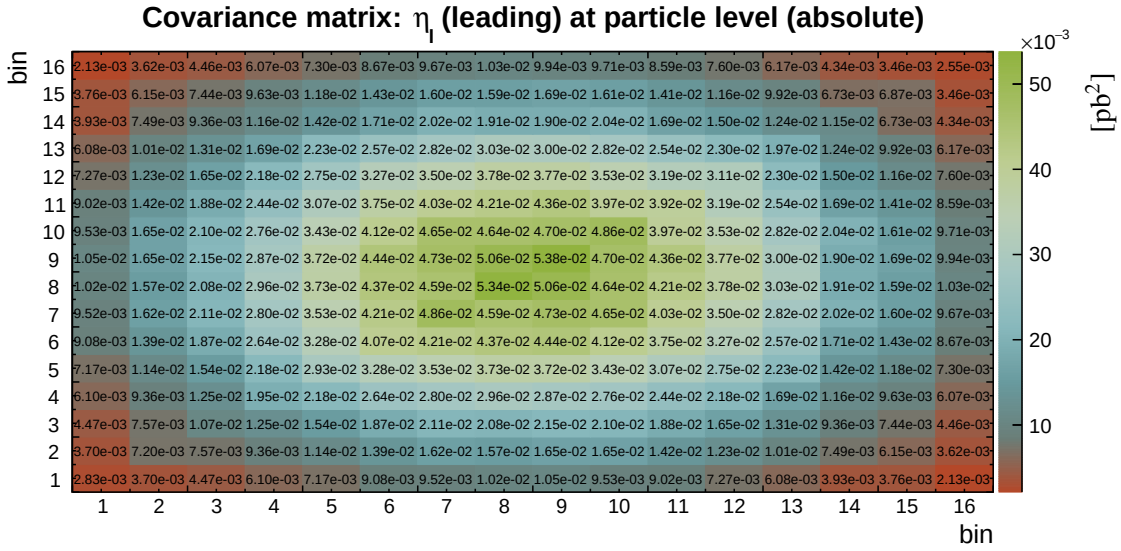

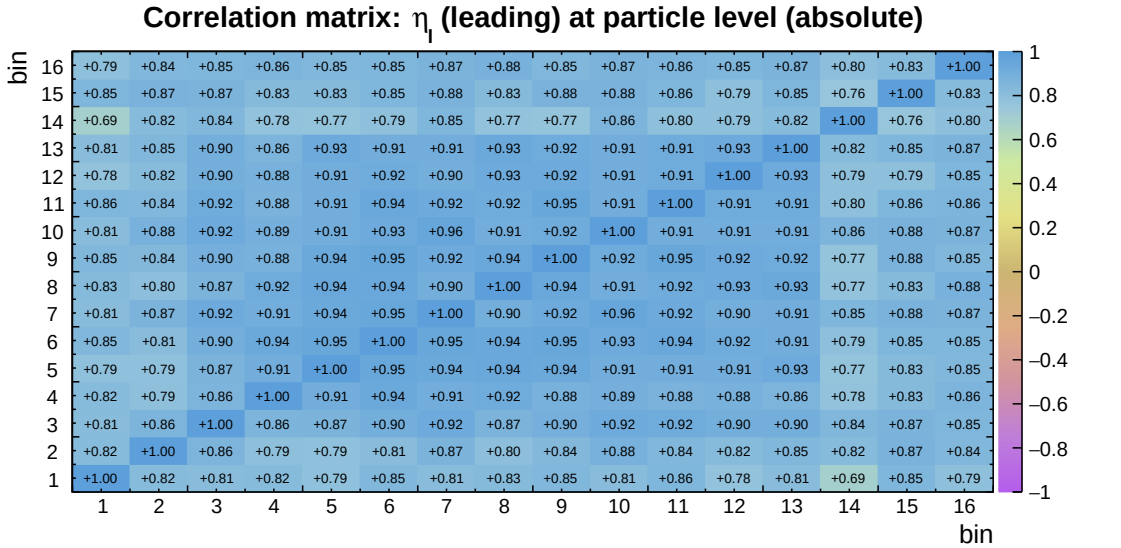

Table B.87 The result σ and its uncertainty per bin of the absolute differential $t\bar{t}$ production cross sections measured as a function of the pseudorapidity of the trailing lepton η_ℓ *(trailing)*. Measurement is performed at particle level in a fiducial phase space. The corresponding covariance and correlation matrices are presented below the table.

bin	center	left	right	σ (pb)	Δ_σ^{stat} (%)	Δ_σ^{syst} (%)	Δ_σ^{tot} (%)
1	−2.25	−2.40	−2.10	8.66e-01	1.5	6.8	7.0
2	−1.95	−2.10	−1.80	1.25e+00	1.2	6.9	7.0
3	−1.65	−1.80	−1.50	1.72e+00	1.0	6.5	6.6
4	−1.35	−1.50	−1.20	2.22e+00	0.9	6.3	6.3
5	−1.05	−1.20	−0.90	2.77e+00	0.8	6.3	6.3
6	−0.75	−0.90	−0.60	3.09e+00	0.8	6.1	6.2
7	−0.45	−0.60	−0.30	3.39e+00	0.7	6.2	6.2
8	−0.15	−0.30	0.00	3.50e+00	0.7	6.2	6.3
9	0.15	0.00	0.30	3.50e+00	0.7	6.3	6.3
10	0.45	0.30	0.60	3.42e+00	0.7	6.1	6.1
11	0.75	0.60	0.90	3.17e+00	0.7	6.1	6.2
12	1.05	0.90	1.20	2.71e+00	0.8	6.3	6.4
13	1.35	1.20	1.50	2.20e+00	0.9	6.4	6.5
14	1.65	1.50	1.80	1.76e+00	1.1	6.6	6.7
15	1.95	1.80	2.10	1.31e+00	1.2	6.6	6.7
16	2.25	2.10	2.40	8.17e-01	1.6	7.3	7.5

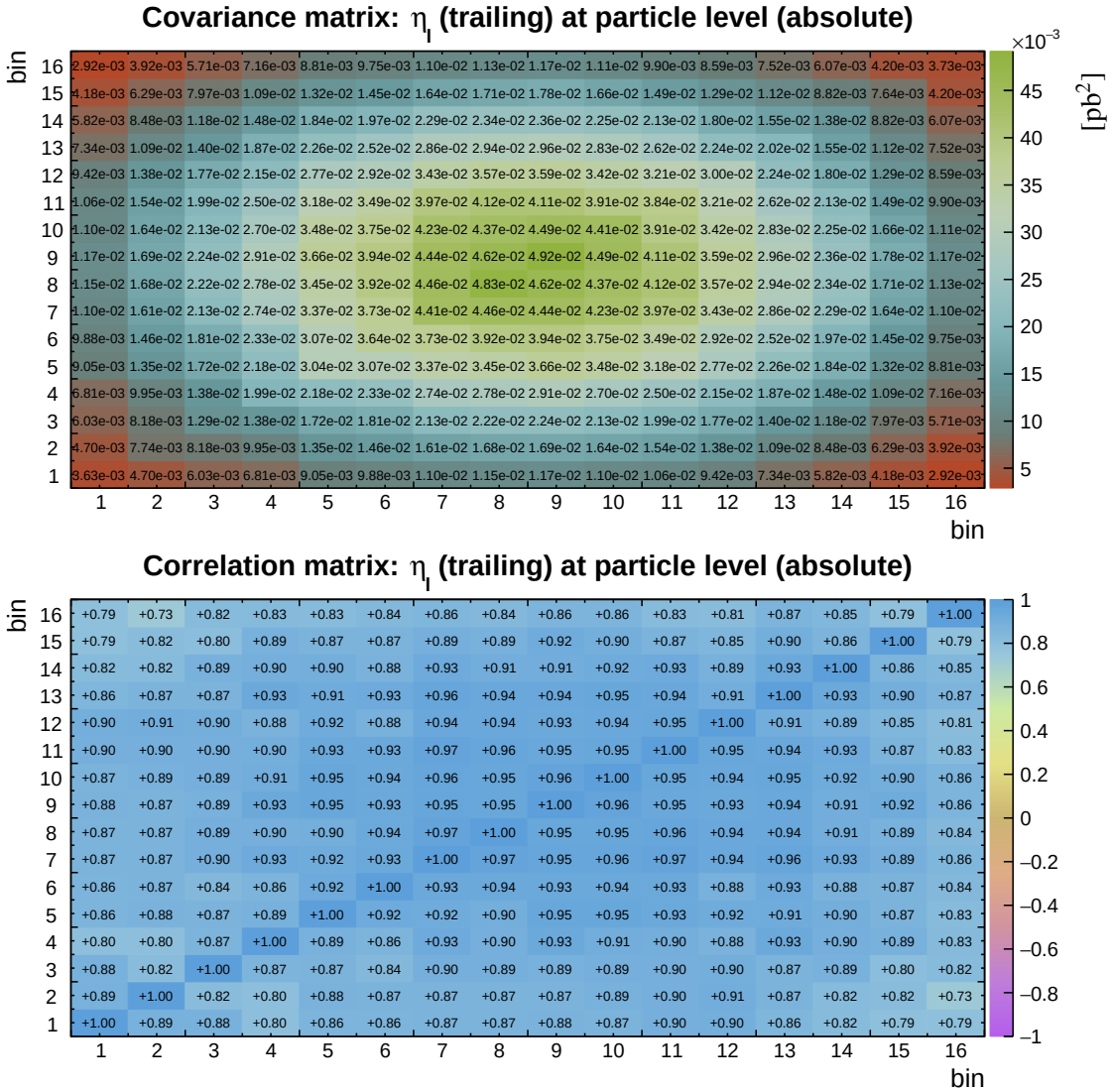

Table B.88 The result σ and its uncertainty per bin of the absolute differential $t\bar{t}$ production cross sections measured as a function of the difference in absolute pseudorapidity between the lepton and antilepton $\Delta|\eta|(\ell,\bar{\ell})$. Measurement is performed at particle level in a fiducial phase space. The corresponding covariance and correlation matrices are presented below the table.

bin	center	left	right	σ (pb)	Δ_{σ}^{stat} (%)	Δ_{σ}^{syst} (%)	Δ_{σ}^{tot} (%)
1	−2.05	−2.40	−1.70	3.98e-01	1.4	6.3	6.5
2	−1.45	−1.70	−1.20	1.53e+00	0.8	6.0	6.0
3	−1.00	−1.20	−0.80	2.77e+00	0.7	6.2	6.2
4	−0.60	−0.80	−0.40	3.98e+00	0.6	6.2	6.3
5	−0.20	−0.40	0.00	4.86e+00	0.5	6.4	6.4
6	0.20	0.00	0.40	4.84e+00	0.5	6.3	6.3
7	0.60	0.40	0.80	3.95e+00	0.6	6.2	6.3
8	1.00	0.80	1.20	2.71e+00	0.7	6.2	6.3
9	1.45	1.20	1.70	1.50e+00	0.8	6.2	6.3
10	2.05	1.70	2.40	3.86e-01	1.4	6.5	6.7

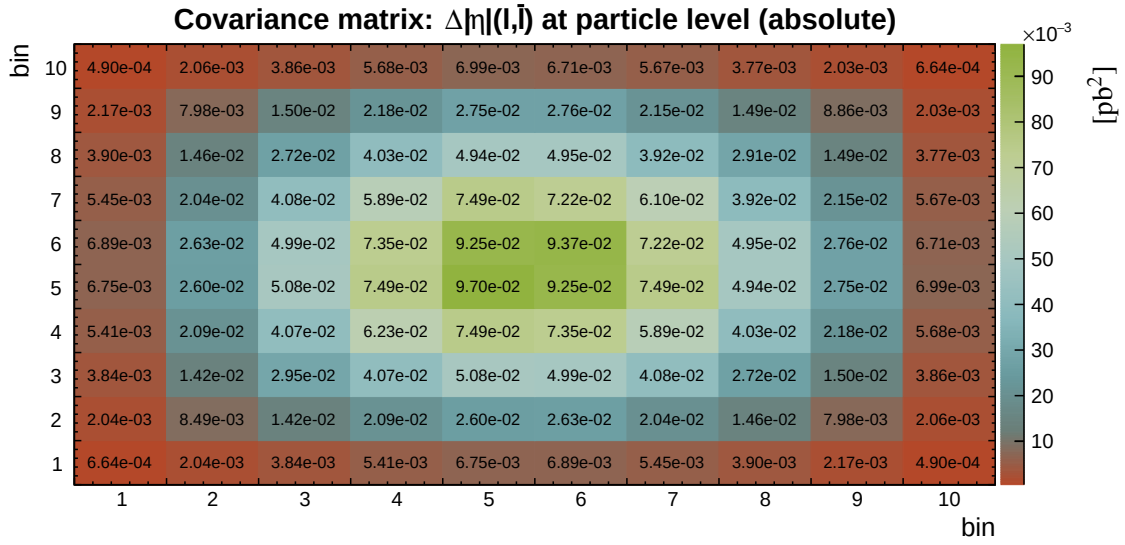

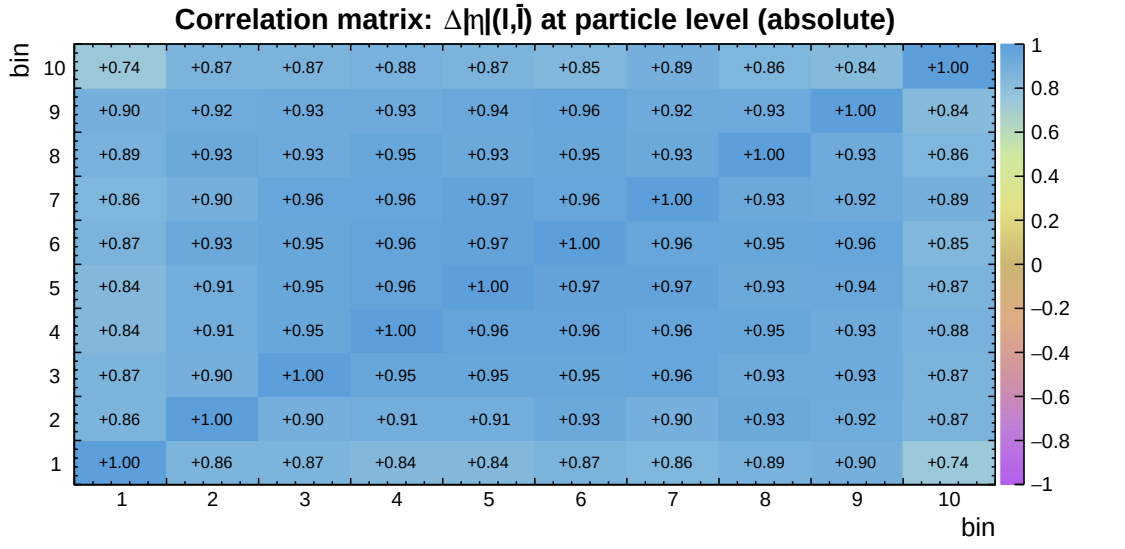

Table B.89 The result σ and its uncertainty per bin of the absolute differential $t\bar{t}$ production cross sections measured as a function of the difference in azimuthal angle between the lepton and antilepton $\Delta\phi(\ell,\bar{\ell})$. Measurement is performed at particle level in a fiducial phase space. The corresponding covariance and correlation matrices are presented below the table.

bin	center	left	right	σ (pb)	Δ_{σ}^{stat} (%)	Δ_{σ}^{syst} (%)	Δ_{σ}^{tot} (%)
1	0.200	0.000	0.400	2.19e+00	0.8	6.4	6.4
2	0.590	0.400	0.780	2.79e+00	0.7	6.4	6.4
3	0.960	0.780	1.140	3.14e+00	0.7	6.2	6.3
4	1.310	1.140	1.480	3.38e+00	0.7	6.1	6.1
5	1.640	1.480	1.800	3.69e+00	0.7	6.1	6.2
6	1.950	1.800	2.100	3.98e+00	0.7	6.2	6.2
7	2.240	2.100	2.380	4.24e+00	0.7	6.4	6.4
8	2.510	2.380	2.640	4.45e+00	0.6	6.1	6.2
9	2.765	2.640	2.890	4.75e+00	0.6	6.2	6.3
10	3.016	2.890	3.142	4.72e+00	0.6	6.4	6.4

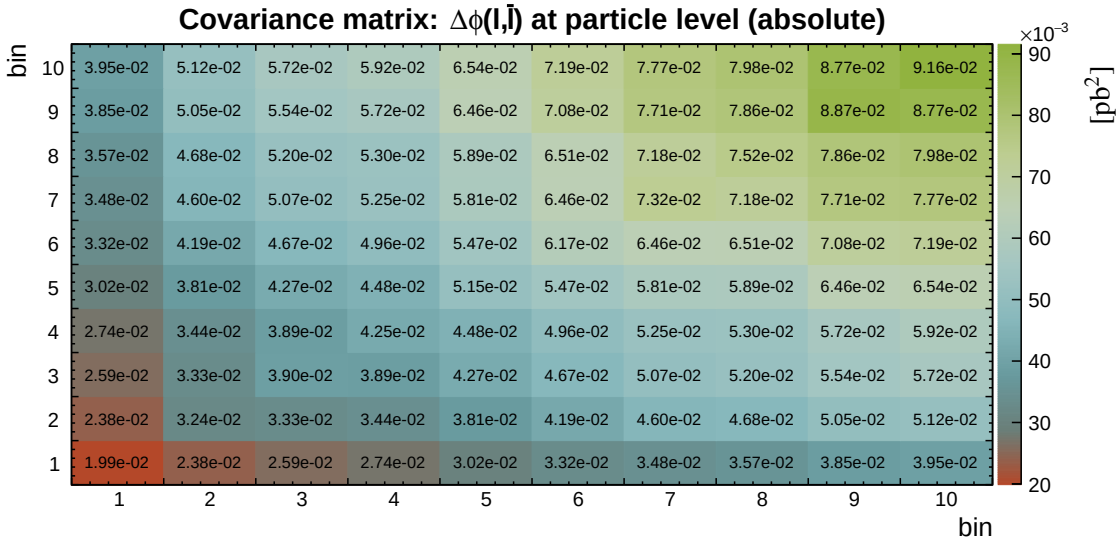

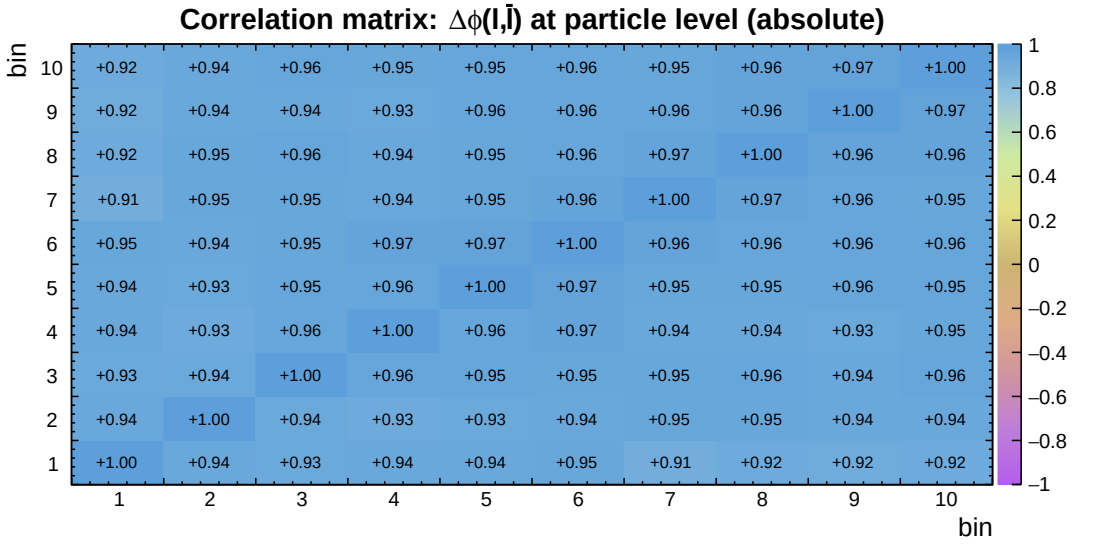

Table B.90 The result σ and its uncertainty per bin of the absolute differential $t\bar{t}$ production cross sections measured as a function of the transverse momentum of the lepton pair $p_T^{\ell\bar{\ell}}$. Measurement is performed at particle level in a fiducial phase space. The corresponding covariance and correlation matrices are presented below the table.

bin	center (GeV)	left (GeV)	right (GeV)	σ (pb/GeV)	Δ_σ^{stat} (%)	Δ_σ^{syst} (%)	Δ_σ^{tot} (%)
1	5.0	0.0	10.0	1.91e-02	1.9	8.1	8.3
2	15.0	10.0	20.0	5.30e-02	1.1	7.0	7.1
3	30.0	20.0	40.0	8.59e-02	0.6	6.5	6.6
4	50.0	40.0	60.0	1.24e-01	0.5	6.3	6.3
5	80.0	60.0	100.0	1.08e-01	0.4	5.9	5.9
6	125.0	100.0	150.0	3.44e-02	0.6	6.1	6.1
7	275.0	150.0	400.0	1.42e-03	1.2	7.6	7.7

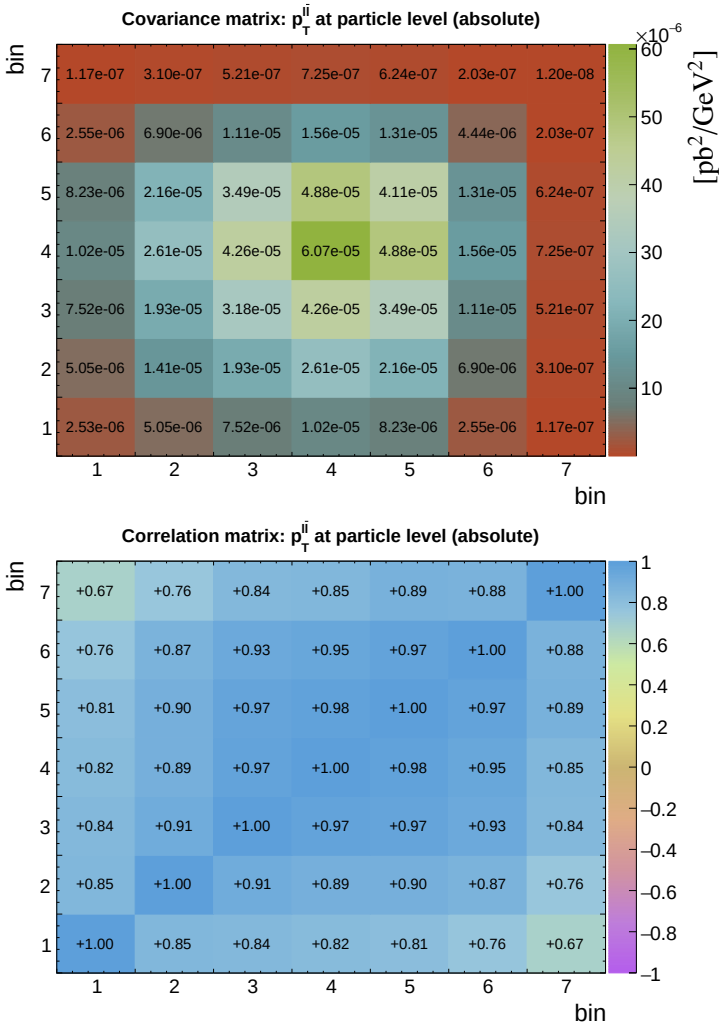

Table B.91 The result σ and its uncertainty per bin of the absolute differential $t\bar{t}$ production cross sections measured as a function of the invariant mass of the lepton pair $m_{\ell\bar{\ell}}$. Measurement is performed at particle level in a fiducial phase space. The corresponding covariance and correlation matrices are presented below the table.

bin	center (GeV)	left (GeV)	right (GeV)	σ (pb/GeV)	Δ_σ^{stat} (%)	Δ_σ^{syst} (%)	Δ_σ^{tot} (%)
1	25.0	20.0	30.0	3.90e-02	1.2	8.6	8.7
2	40.0	30.0	50.0	6.06e-02	0.7	6.9	6.9
3	63.0	50.0	76.0	8.69e-02	0.5	7.0	7.0
4	91.0	76.0	106.0	8.48e-02	0.6	5.7	5.7
5	118.0	106.0	130.0	6.18e-02	0.6	6.0	6.1
6	150.0	130.0	170.0	3.95e-02	0.6	5.9	5.9
7	215.0	170.0	260.0	1.52e-02	0.6	5.9	6.0
8	455.0	260.0	650.0	1.30e-03	0.9	6.2	6.3

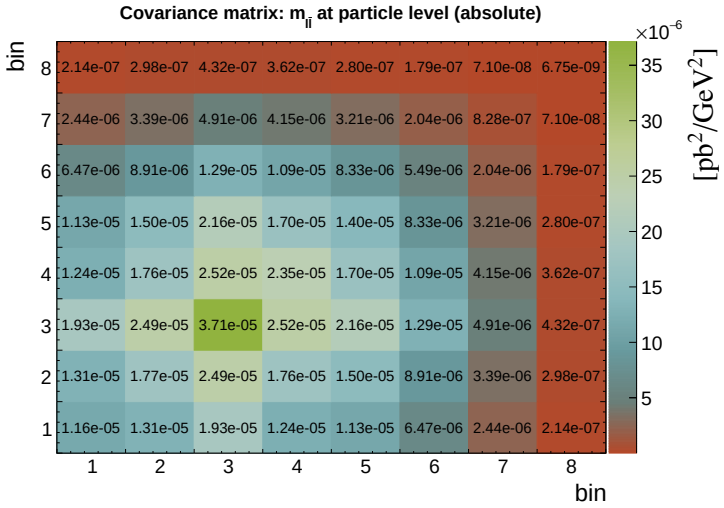

Table B.92 The result σ and its uncertainty per bin of the absolute differential $t\bar{t}$ production cross sections measured as a function of the transverse momentum of the leading b-jet p_T^b *(leading)*. Measurement is performed at particle level in a fiducial phase space. The corresponding covariance and correlation matrices are presented below the table.

bin	center (GeV)	left (GeV)	right (GeV)	σ (pb/GeV)	Δ_σ^{stat} (%)	Δ_σ^{syst} (%)	Δ_σ^{tot} (%)
1	45.0	30.0	60.0	7.04e-02	0.7	7.9	7.9
2	77.5	60.0	95.0	1.31e-01	0.5	5.9	5.9
3	122.5	95.0	150.0	6.11e-02	0.5	7.1	7.1
4	190.0	150.0	230.0	1.28e-02	0.8	8.2	8.3
5	365.0	230.0	500.0	7.37e-04	2.0	9.1	9.3

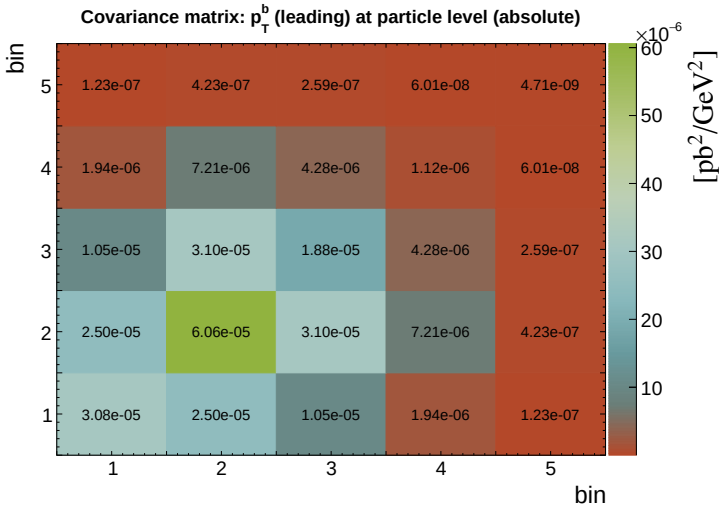

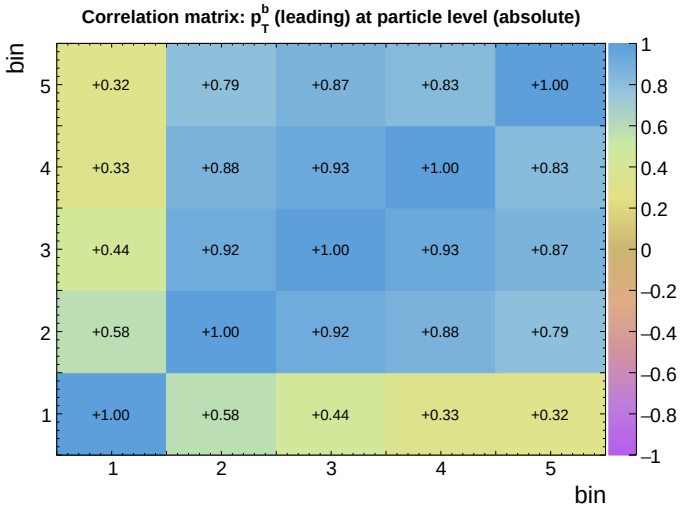

Table B.93 The result σ and its uncertainty per bin of the absolute differential $t\bar{t}$ production cross sections measured as a function of the transverse momentum of the trailing b-jet p_T^b *(trailing)*. Measurement is performed at particle level in a fiducial phase space. The corresponding covariance and correlation matrices are presented below the table.

bin	center (GeV)	left (GeV)	right (GeV)	σ (pb/GeV)	Δ_σ^{stat} (%)	Δ_σ^{syst} (%)	Δ_σ^{tot} (%)
1	37.5	30.0	45.0	2.80e-01	0.5	6.9	7.0
2	57.5	45.0	70.0	1.73e-01	0.6	6.6	6.6
3	90.0	70.0	110.0	5.29e-02	0.7	7.1	7.2
4	140.0	110.0	170.0	9.21e-03	1.3	7.6	7.7
5	335.0	170.0	500.0	2.60e-04	3.4	11.2	11.7

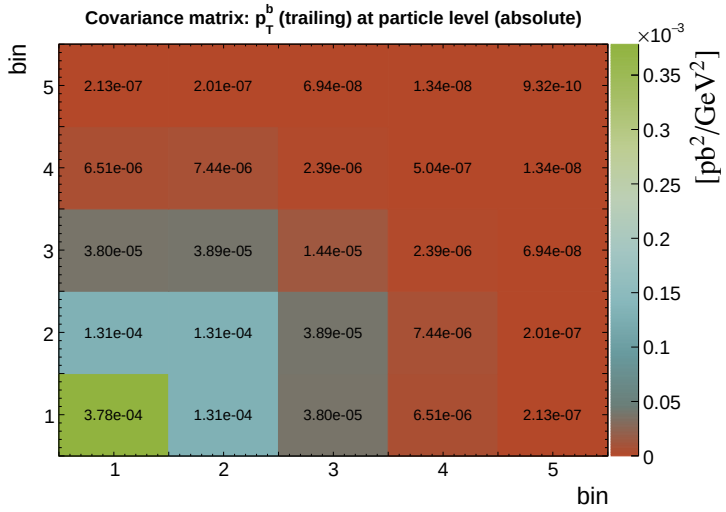

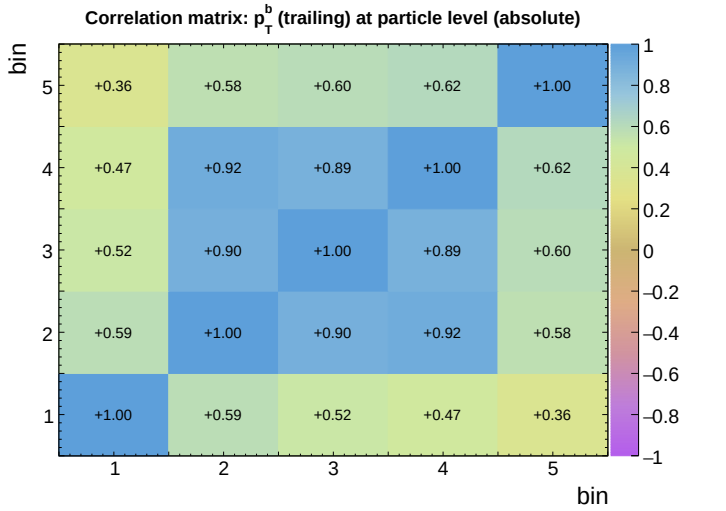

Table B.94 The result σ and its uncertainty per bin of the absolute differential $t\bar{t}$ production cross sections measured as a function of the pseudorapidity of the leading b-jet η_b *(leading)*. Measurement is performed at particle level in a fiducial phase space. The corresponding covariance and correlation matrices are presented below the table.

bin	center	left	right	σ (pb)	Δ_σ^{stat} (%)	Δ_σ^{syst} (%)	Δ_σ^{tot} (%)
1	−2.10	−2.40	−1.80	9.08e-01	1.2	9.6	9.7
2	−1.50	−1.80	−1.20	1.83e+00	0.8	7.1	7.2
3	−0.90	−1.20	−0.60	3.05e+00	0.6	5.8	5.9
4	−0.30	−0.60	0.00	3.60e+00	0.6	5.9	5.9
5	0.30	0.00	0.60	3.68e+00	0.6	5.7	5.7
6	0.90	0.60	1.20	2.95e+00	0.6	6.0	6.0
7	1.50	1.20	1.80	1.90e+00	0.8	6.9	6.9
8	2.10	1.80	2.40	9.17e-01	1.2	9.0	9.0

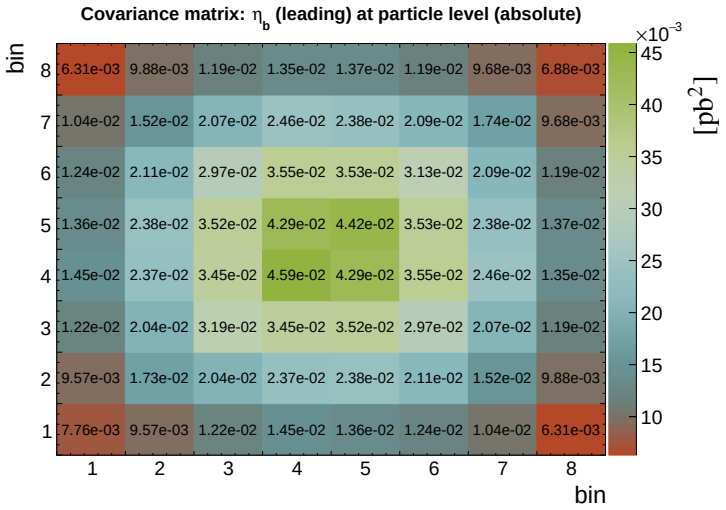

Table B.95 The result σ and its uncertainty per bin of the absolute differential $t\bar{t}$ production cross sections measured as a function of the pseudorapidity of the trailing b-jet η_b *(trailing)*. Measurement is performed at particle level in a fiducial phase space. The corresponding covariance and correlation matrices are presented below the table.

bin	center	left	right	σ (pb)	Δ_σ^{stat} (%)	Δ_σ^{syst} (%)	Δ_σ^{tot} (%)
1	−2.10	−2.40	−1.80	1.13e+00	1.1	7.8	7.8
2	−1.50	−1.80	−1.20	1.94e+00	0.8	7.0	7.1
3	−0.90	−1.20	−0.60	2.85e+00	0.7	6.1	6.1
4	−0.30	−0.60	0.00	3.41e+00	0.6	5.9	5.9
5	0.30	0.00	0.60	3.50e+00	0.6	5.8	5.8
6	0.90	0.60	1.20	2.92e+00	0.7	5.8	5.9
7	1.50	1.20	1.80	2.01e+00	0.8	6.8	6.9
8	2.10	1.80	2.40	1.09e+00	1.1	9.0	9.1

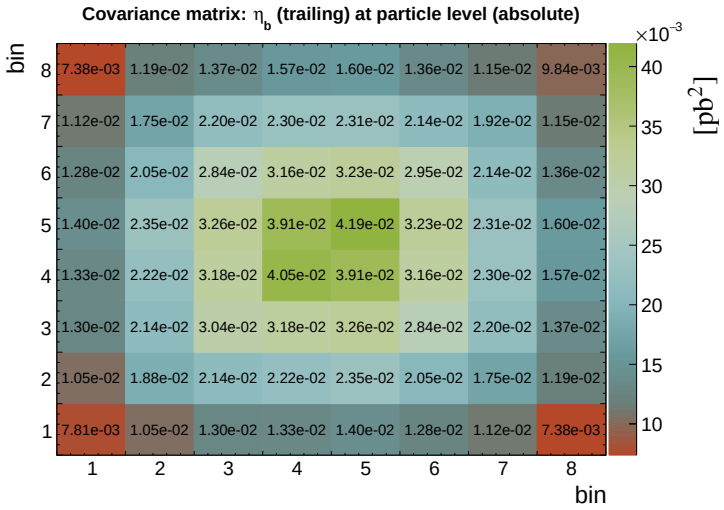

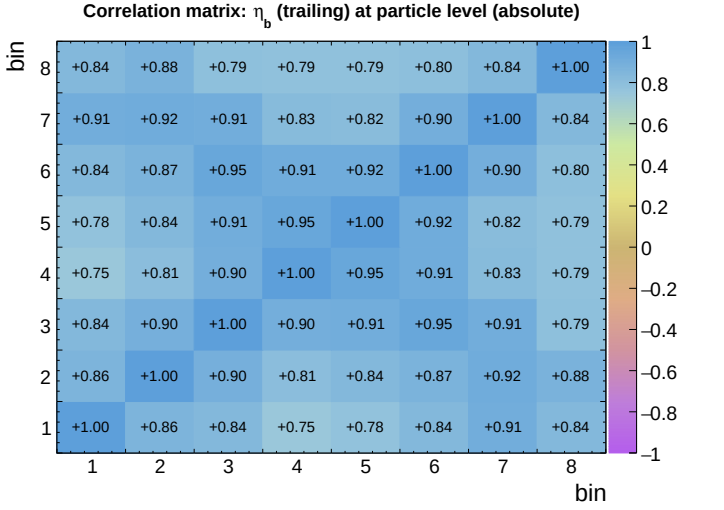

Table B.96 The result σ and its uncertainty per bin of the absolute differential $t\bar{t}$ production cross sections measured as a function of the transverse momentum of the b-jet pair $p_T^{b\bar{b}}$. Measurement is performed at particle level in a fiducial phase space. The corresponding covariance and correlation matrices are presented below the table.

bin	center (GeV)	left (GeV)	right (GeV)	σ (pb/GeV)	Δ_σ^{stat} (%)	Δ_σ^{syst} (%)	Δ_σ^{tot} (%)
1	15.0	0.0	30.0	3.98e-02	0.8	6.5	6.6
2	45.0	30.0	60.0	8.12e-02	0.6	5.8	5.8
3	80.0	60.0	100.0	1.01e-01	0.4	5.6	5.6
4	140.0	100.0	180.0	4.15e-02	0.4	8.8	8.9
5	290.0	180.0	400.0	1.47e-03	1.5	13.1	13.2

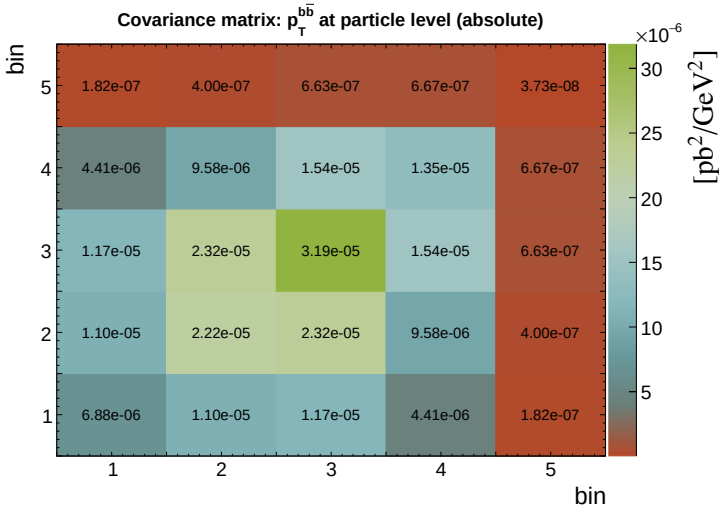

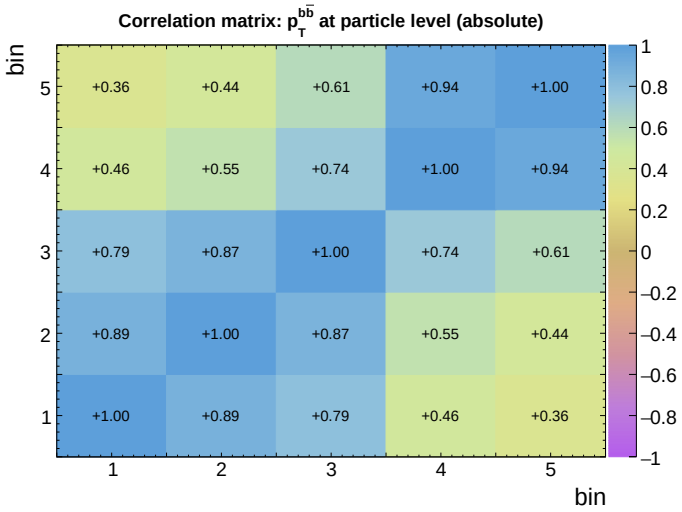

Table B.97 The result σ and its uncertainty per bin of the absolute differential $t\bar{t}$ production cross sections measured as a function of the invariant mass of the b-jet pair $m_{b\bar{b}}$. Measurement is performed at particle level in a fiducial phase space. The corresponding covariance and correlation matrices are presented below the table.

bin	center (GeV)	left (GeV)	right (GeV)	σ (pb/GeV)	Δ_{σ}^{stat} (%)	Δ_{σ}^{syst} (%)	Δ_{σ}^{tot} (%)
1	30.0	0.0	60.0	1.38e-02	0.9	7.0	7.1
2	90.0	60.0	120.0	5.59e-02	0.4	6.0	6.1
3	180.0	120.0	240.0	4.31e-02	0.4	6.1	6.1
4	445.0	240.0	650.0	4.68e-03	0.6	7.8	7.8

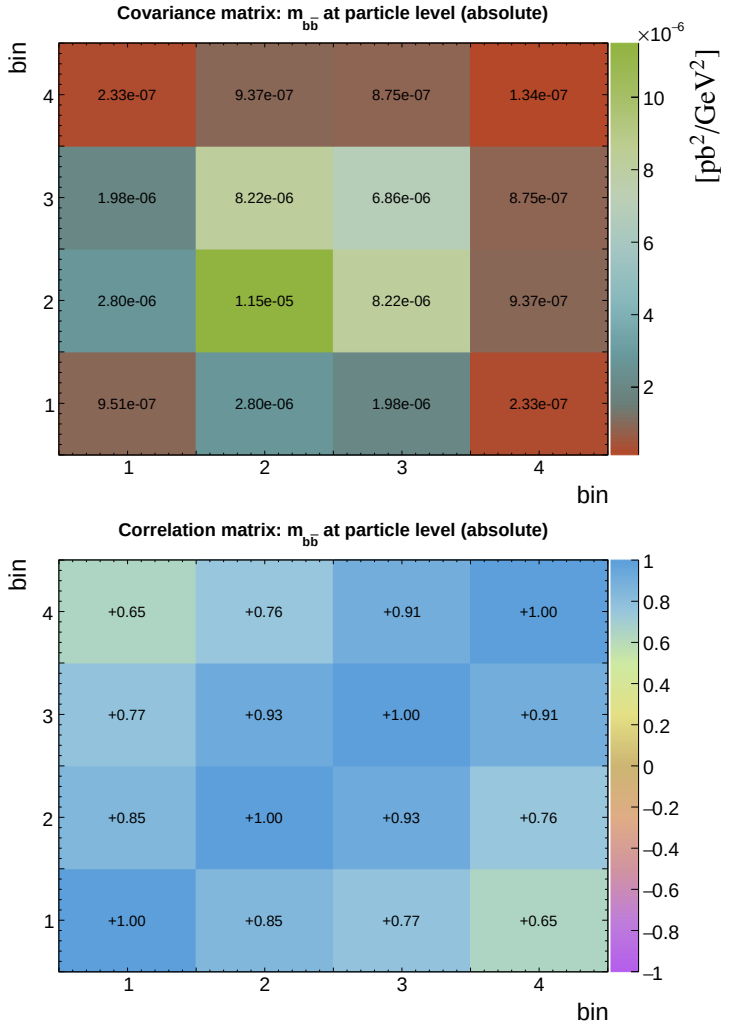

Table B.98 The result σ and its uncertainty per bin of the absolute differential $t\bar{t}$ production cross sections measured as a function of the jet multiplicity N_{jets}. Measurement is performed at particle level in a fiducial phase space. The corresponding covariance and correlation matrices are presented below the table.

bin	center	left	right	σ (pb)	Δ_{σ}^{stat} (%)	Δ_{σ}^{syst} (%)	Δ_{σ}^{tot} (%)
1	2.0	1.5	2.5	6.01e+00	0.3	5.7	5.7
2	3.0	2.5	3.5	3.42e+00	0.5	7.0	7.0
3	4.0	3.5	4.5	1.31e+00	0.9	9.8	9.8
4	5.0	4.5	5.5	4.16e-01	1.6	12.5	12.6
5	6.0	5.5	6.5	1.17e-01	2.7	13.8	14.0
6	7.0	6.5	7.5	2.84e-02	5.4	20.1	20.8

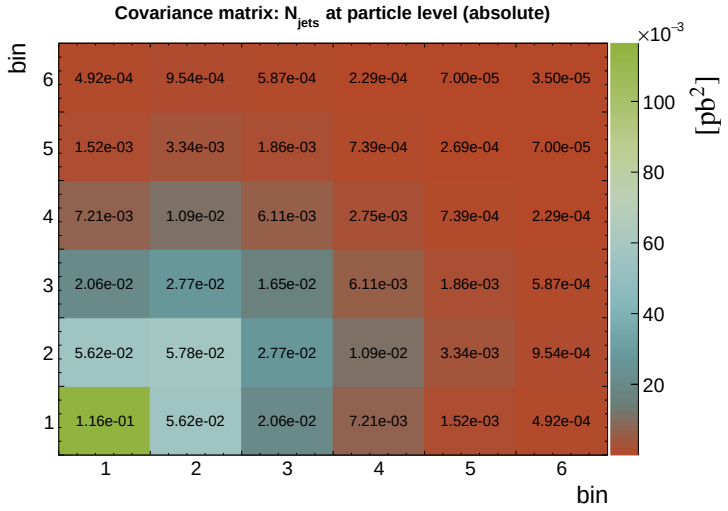

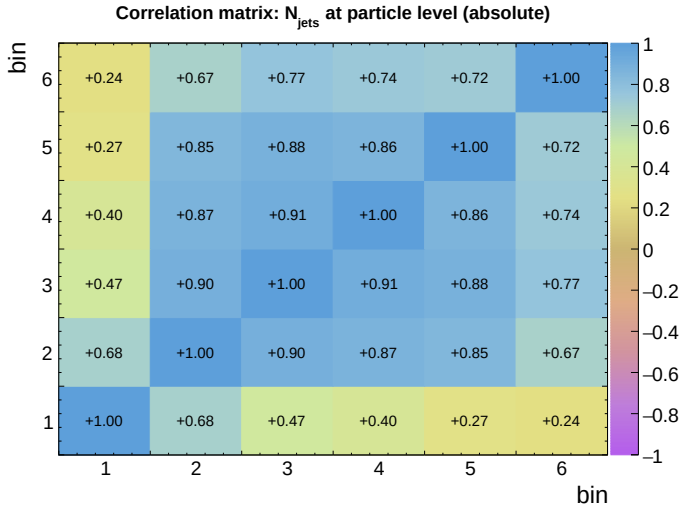

Appendix C

Uncertainties and migrations in the differential cross section measurements

Here, a summary of the uncertainties and migrations among bins for the differential $t\bar{t}$ production cross sections is presented. The measurements are performed in the dilepton decay channel using the data of $L = 35.9$ fb^{-1} recorded by the CMS detector in 2016 during pp collisions at $\sqrt{s} = 13$ TeV.

The differential $t\bar{t}$ production cross sections which are measured at both parton and particle levels:

- transverse momentum of the top quark p_T^t in Figure C.1,
- transverse momentum of the top antiquark $p_T^{\bar{t}}$ in Figure C.2,
- transverse momentum of the leading top quark p_T^t *(leading)* in Figure C.3,
- transverse momentum of the trailing top quark p_T^t *(trailing)* in Figure C.4,
- transverse momentum of the top quark in the rest frame of the $t\bar{t}$-system p_T^t *($t\bar{t}$ rest frame)* in Figure C.5,
- transverse momentum of the top antiquark in the rest frame of the $t\bar{t}$-system $p_T^{\bar{t}}$ *($t\bar{t}$ rest frame)* in Figure C.6,
- rapidity of the top quark y_t in Figure C.7,
- rapidity of the top antiquark $y_{\bar{t}}$ in Figure C.8,
- rapidity of the leading top quark y_t *(leading)* in Figure C.9,
- rapidity of the trailing top quark y_t *(trailing)* in Figure C.10,
- difference in absolute rapidity between the top quark and antiquark $\Delta|y|(t,\bar{t})$ in Figure C.11,
- difference in azimuthal angle between the top quark and antiquark $\Delta\phi(t,\bar{t})$ in Figure C.12,
- transverse momentum of the top-quark pair $p_T^{t\bar{t}}$ in Figure C.13,
- invariant mass of the top-quark pair $m_{t\bar{t}}$ in Figure C.14,

- rapidity of the top-quark pair $y_{t\bar{t}}$ in Figure C.15.

The differential $t\bar{t}$ production cross sections which are measured only at particle level:

- transverse momentum of the lepton p_T^{ℓ} in Figure C.16,
- transverse momentum of the antilepton $p_T^{\bar{\ell}}$ in Figure C.16,
- transverse momentum of the leading lepton p_T^{ℓ} *(leading)* in Figure C.17,
- transverse momentum of the trailing lepton p_T^{ℓ} *(trailing)* in Figure C.17,
- pseudorapidity of the lepton η_{ℓ} in Figure C.18,
- pseudorapidity of the antilepton $\eta_{\bar{\ell}}$ in Figure C.18,
- pseudorapidity of the leading lepton η_{ℓ} *(leading)* in Figure C.19,
- pseudorapidity of the trailing lepton η_{ℓ} *(trailing)* in Figure C.19,
- difference in absolute pseudorapidity between the lepton and antilepton $\Delta|\eta|(\ell,\bar{\ell})$ in Figure C.20,
- difference in azimuthal angle between the lepton and antilepton $\Delta\phi(\ell,\bar{\ell})$ in Figure C.20,
- transverse momentum of the lepton pair $p_T^{\ell\bar{\ell}}$ in Figure C.21,
- invariant mass of the lepton pair $m_{\ell\bar{\ell}}$ in Figure C.21,
- transverse momentum of the leading b-jet p_T^{b} *(leading)* in Figure C.22,
- transverse momentum of the trailing b-jet p_T^{b} *(trailing)* in Figure C.22,
- pseudorapidity of the leading b-jet η_b *(leading)* in Figure C.23,
- pseudorapidity of the trailing b-jet η_b *(trailing)* in Figure C.23,
- transverse momentum of the b-jet pair $p_T^{b\bar{b}}$ in Figure C.24,
- invariant mass of the b-jet pair $m_{b\bar{b}}$ in Figure C.24,
- jet multiplicity N_{jets} in Figure C.25.

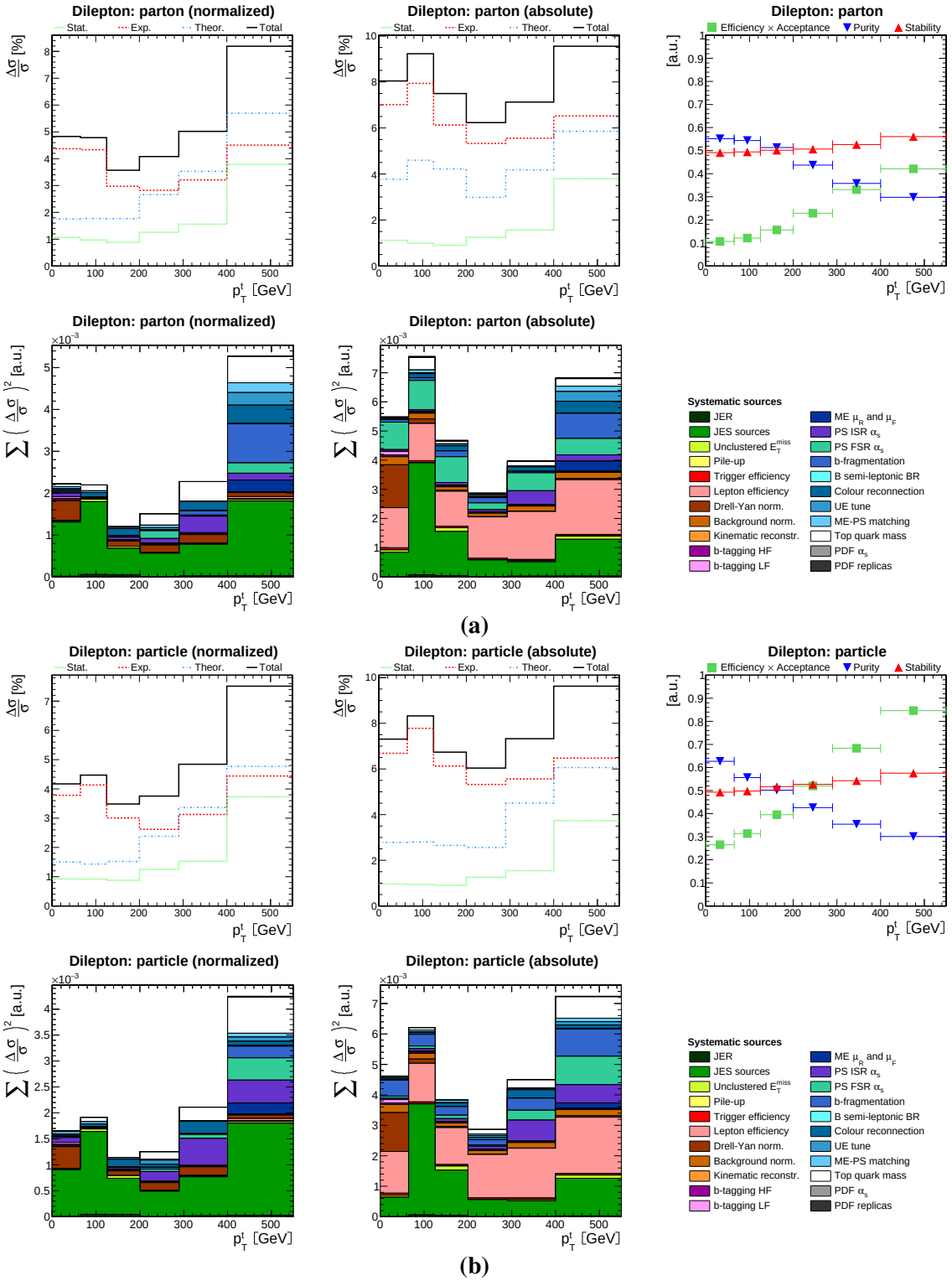

Figure C.1 A summary of the uncertainties and migrations among bins for the differential $t\bar{t}$ production cross sections as a function of the transverse momentum of the top quark p_T^t. Figure **(a)** corresponds to measurements at parton level in the full phase space. Upper row: a summary of uncertainties per bin for normalized (left) and absolute (middle) differential cross sections; efficiency × acceptance, purity and stability per bin (right). Lower row: a summary of systematic uncertainties per bin for normalized (left) and absolute (middle; here, the uncertainties on the luminosity and decay branching ratio of the signal process are not shown) differential cross sections; sources of systematic uncertainty (right). Figure **(b)** shows the same for measurements at particle level in a fiducial phase space.

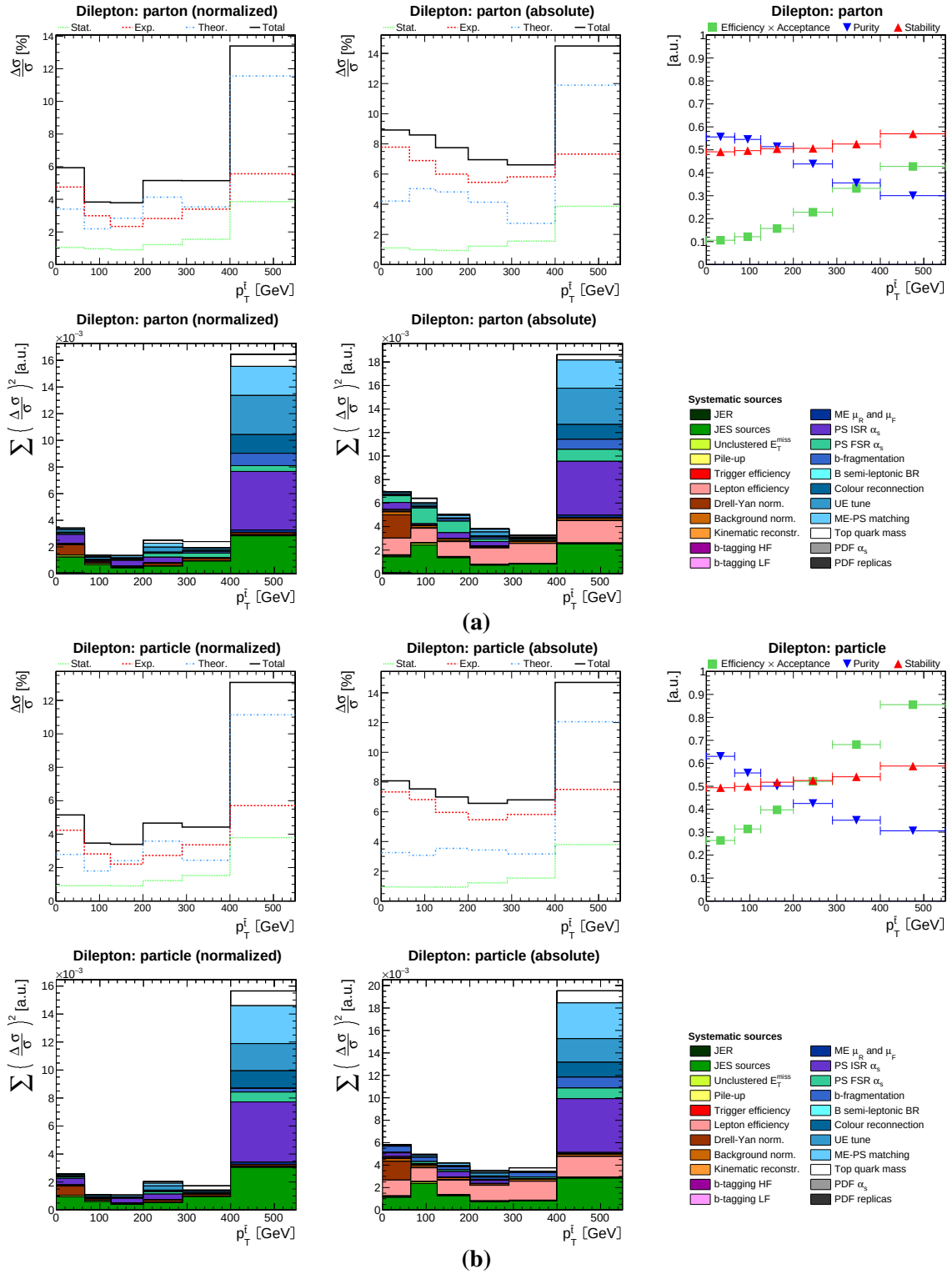

Figure C.2 A summary of the uncertainties and migrations among bins for the differential $t\bar{t}$ production cross sections as a function of the transverse momentum of the top antiquark $p_T^{\bar{t}}$. Figure **(a)** corresponds to measurements at parton level in the full phase space. Upper row: a summary of uncertainties per bin for normalized (left) and absolute (middle) differential cross sections; efficiency × acceptance, purity and stability per bin (right). Lower row: a summary of systematic uncertainties per bin for normalized (left) and absolute (middle; here, the uncertainties on the luminosity and decay branching ratio of the signal process are not shown) differential cross sections; sources of systematic uncertainty (right). Figure **(b)** shows the same for measurements at particle level in a fiducial phase space.

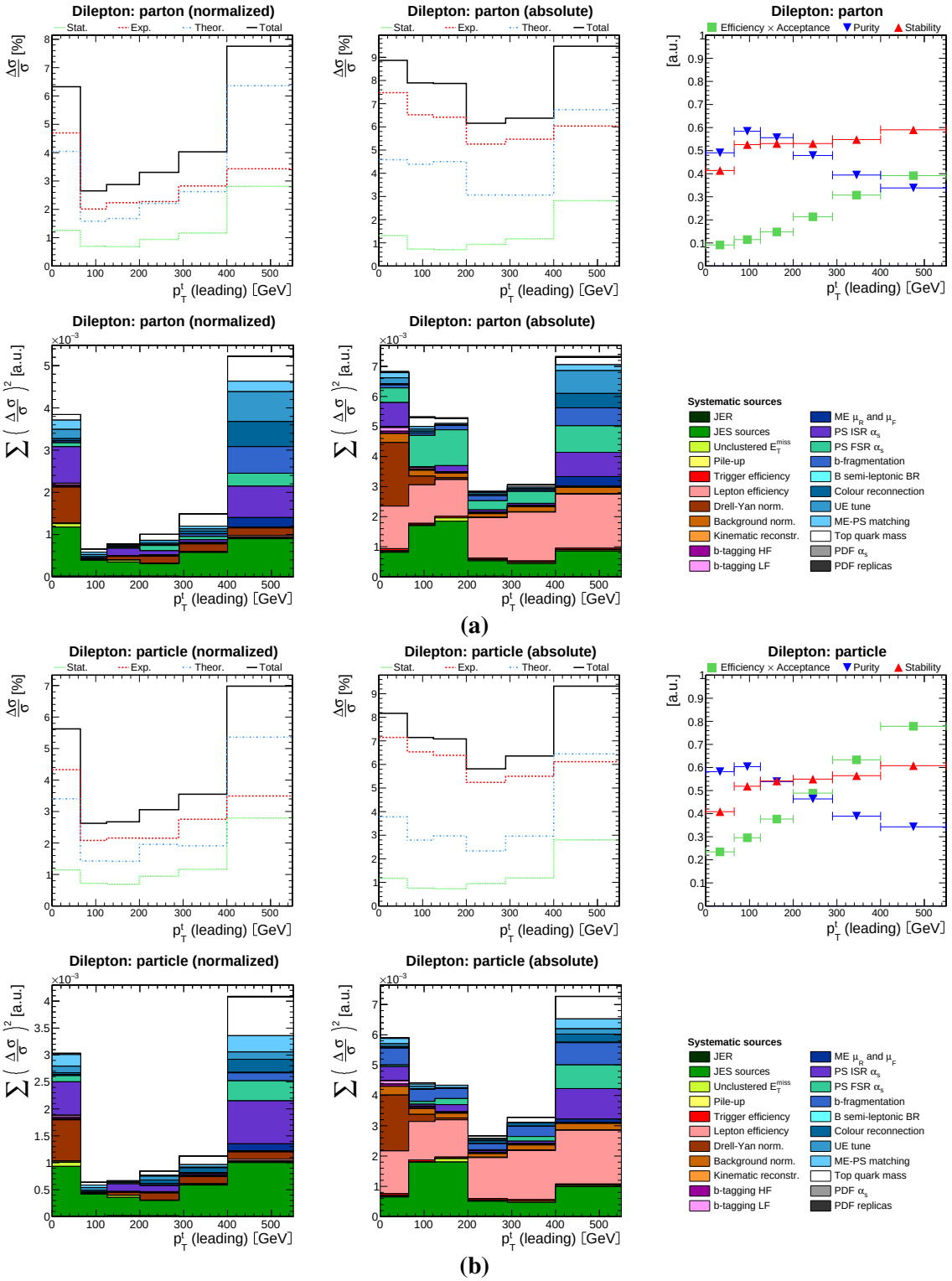

Figure C.3 A summary of the uncertainties and migrations among bins for the differential $t\bar{t}$ production cross sections as a function of the transverse momentum of the leading top quark p_T^t *(leading)*. Figure **(a)** corresponds to measurements at parton level in the full phase space. Upper row: a summary of uncertainties per bin for normalized (left) and absolute (middle) differential cross sections; efficiency × acceptance, purity and stability per bin (right). Lower row: a summary of systematic uncertainties per bin for normalized (left) and absolute (middle; here, the uncertainties on the luminosity and decay branching ratio of the signal process are not shown) differential cross sections; sources of systematic uncertainty (right). Figure **(b)** shows the same for measurements at particle level in a fiducial phase space.

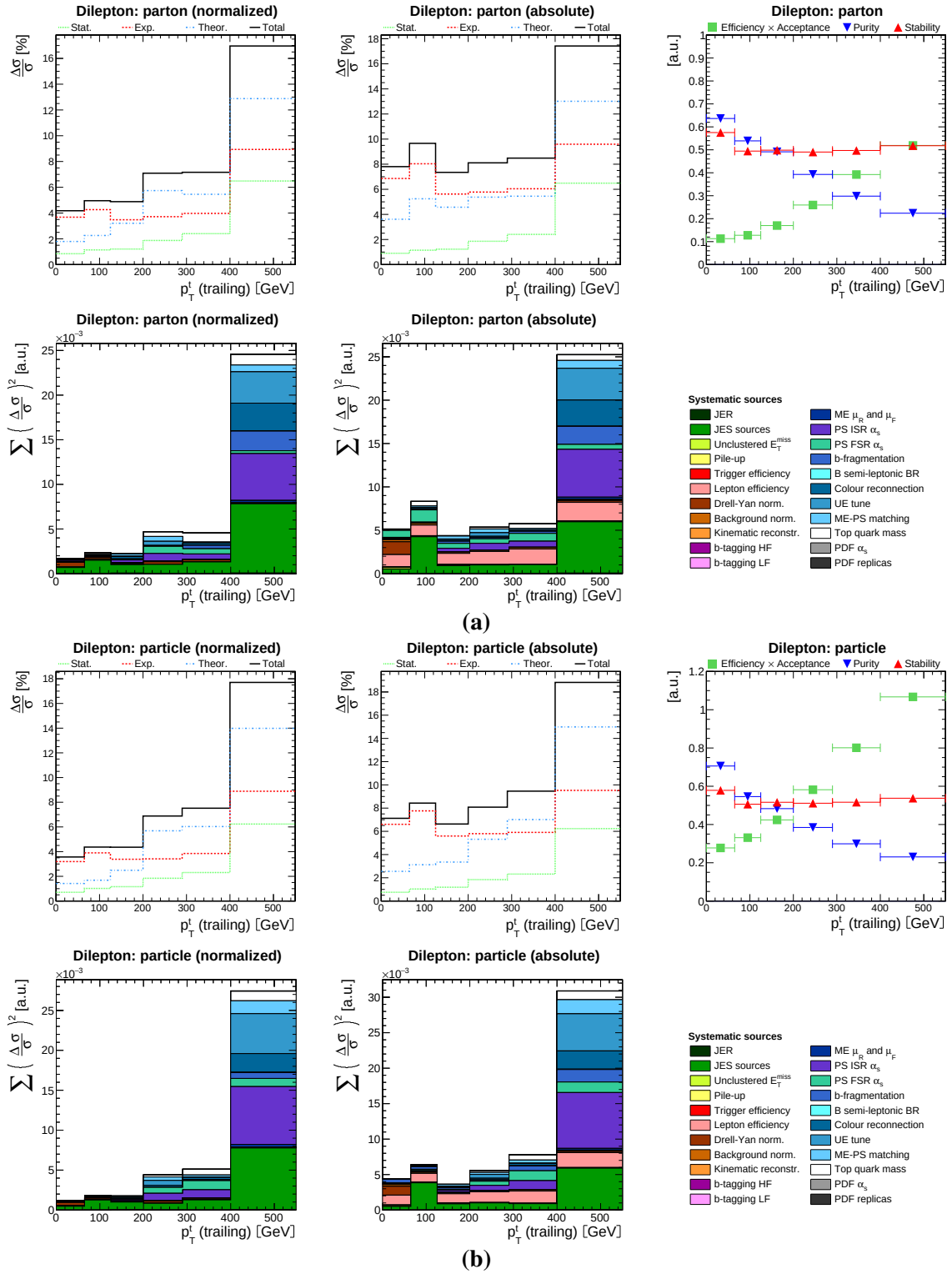

Figure C.4 A summary of the uncertainties and migrations among bins for the differential $t\bar{t}$ production cross sections as a function of the transverse momentum of the trailing top quark p_T^t *(trailing)*. Figure **(a)** corresponds to measurements at parton level in the full phase space. Upper row: a summary of uncertainties per bin for normalized (left) and absolute (middle) differential cross sections; efficiency × acceptance, purity and stability per bin (right). Lower row: a summary of systematic uncertainties per bin for normalized (left) and absolute (middle; here, the uncertainties on the luminosity and decay branching ratio of the signal process are not shown) differential cross sections; sources of systematic uncertainty (right). Figure **(b)** shows the same for measurements at particle level in a fiducial phase space.

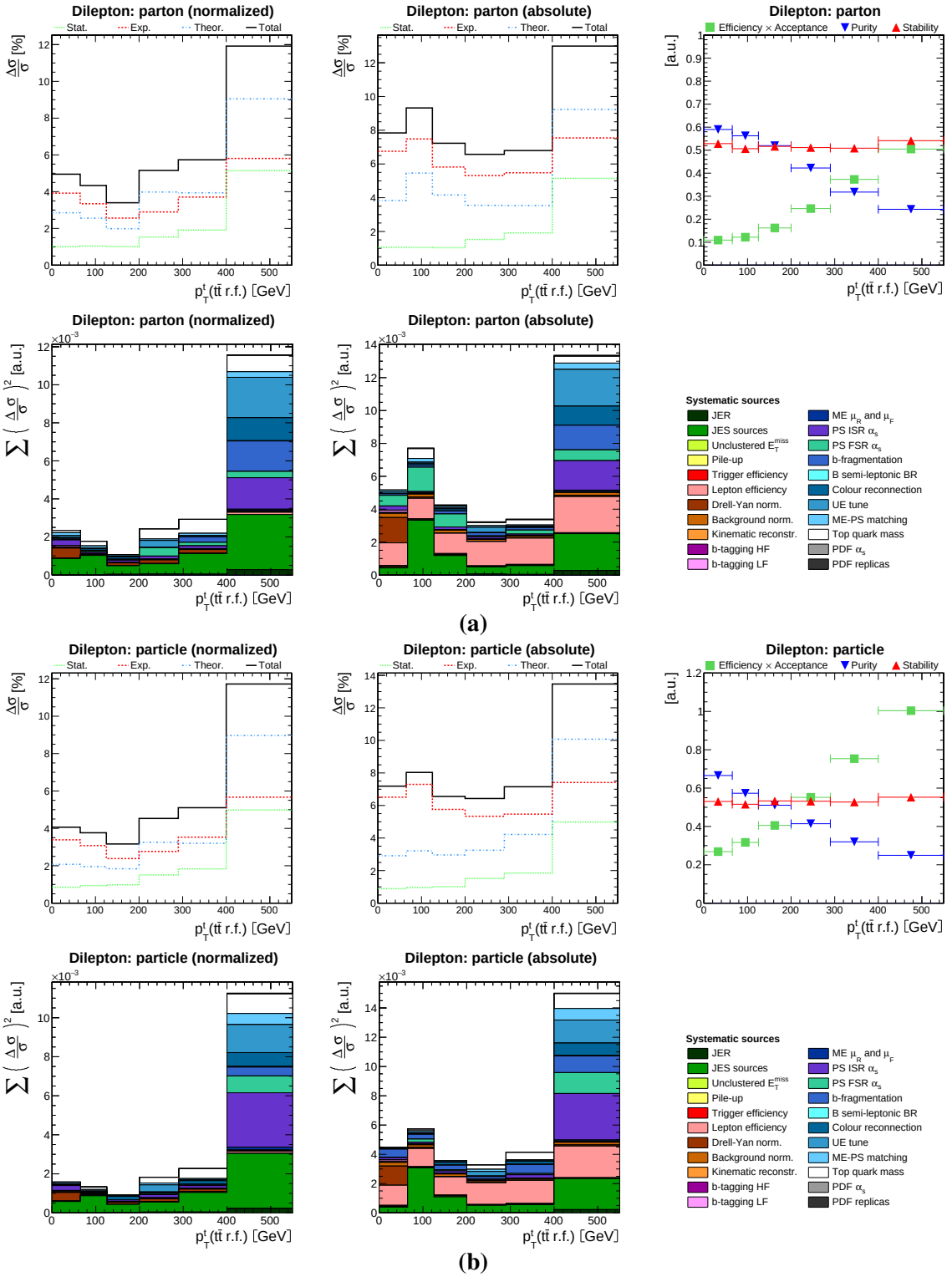

Figure C.5 A summary of the uncertainties and migrations among bins for the differential $t\bar{t}$ production cross sections as a function of the transverse momentum of the top quark in the rest frame of the $t\bar{t}$-system p_T^t *($t\bar{t}$ rest frame)*. Figure **(a)** corresponds to measurements at parton level in the full phase space. Upper row: a summary of uncertainties per bin for normalized (left) and absolute (middle) differential cross sections; efficiency × acceptance, purity and stability per bin (right). Lower row: a summary of systematic uncertainties per bin for normalized (left) and absolute (middle; here, the uncertainties on the luminosity and decay branching ratio of the signal process are not shown) differential cross sections; sources of systematic uncertainty (right). Figure **(b)** shows the same for measurements at particle level in a fiducial phase space.

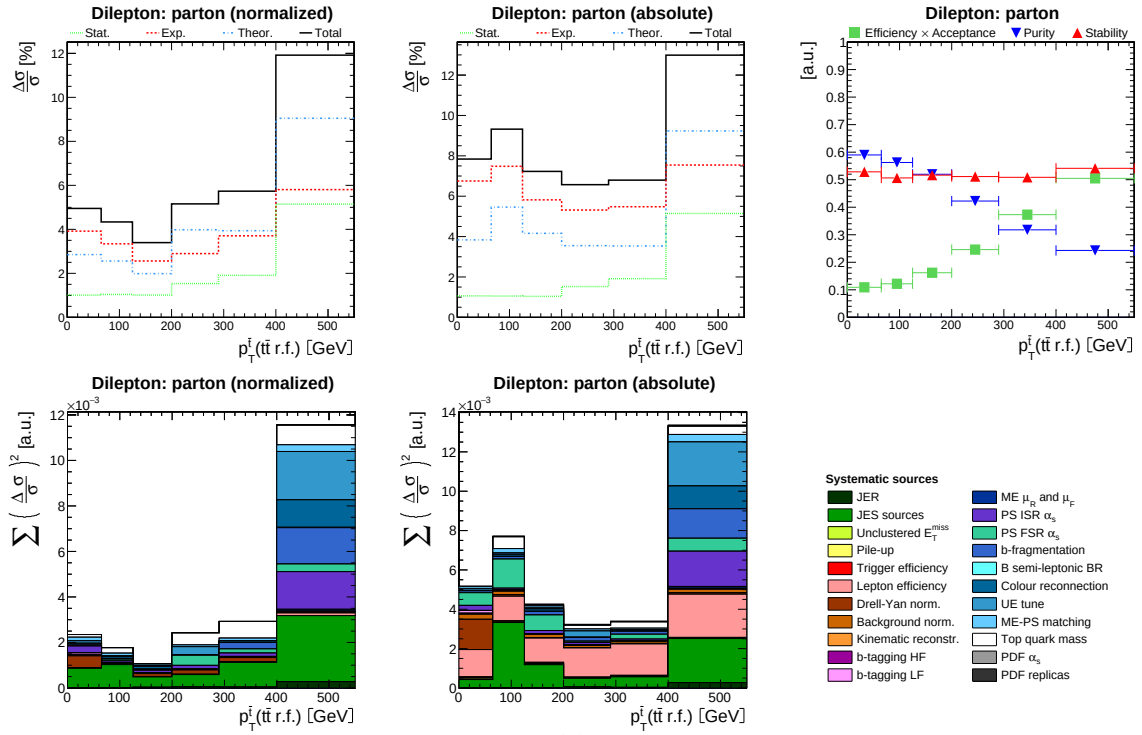

(a)

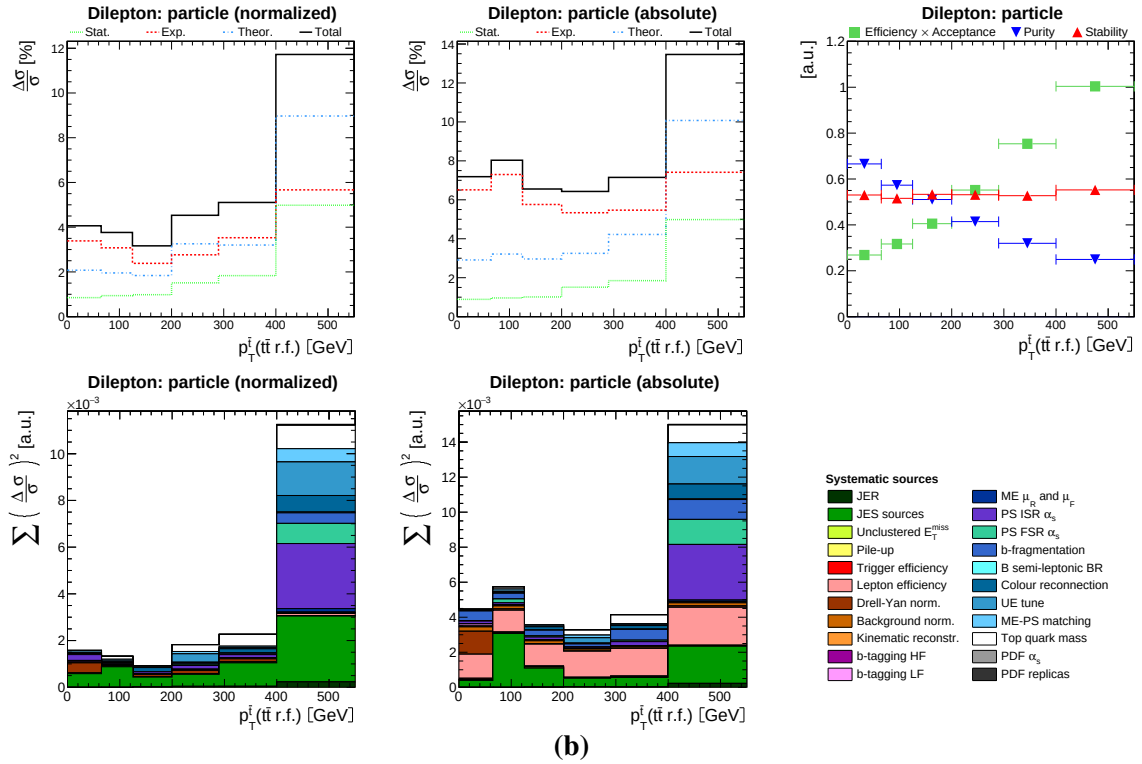

(b)

Figure C.6 A summary of the uncertainties and migrations among bins for the differential $t\bar{t}$ production cross sections as a function of the transverse momentum of the top antiquark in the rest frame of the $t\bar{t}$-system $p_T^{\bar{t}}$ *($t\bar{t}$ rest frame)*. Figure **(a)** corresponds to measurements at parton level in the full phase space. Upper row: a summary of uncertainties per bin for normalized (left) and absolute (middle) differential cross sections; efficiency × acceptance, purity and stability per bin (right). Lower row: a summary of systematic uncertainties per bin for normalized (left) and absolute (middle; here, the uncertainties on the luminosity and decay branching ratio of the signal process are not shown) differential cross sections; sources of systematic uncertainty (right). Figure **(b)** shows the same for measurements at particle level in a fiducial phase space.

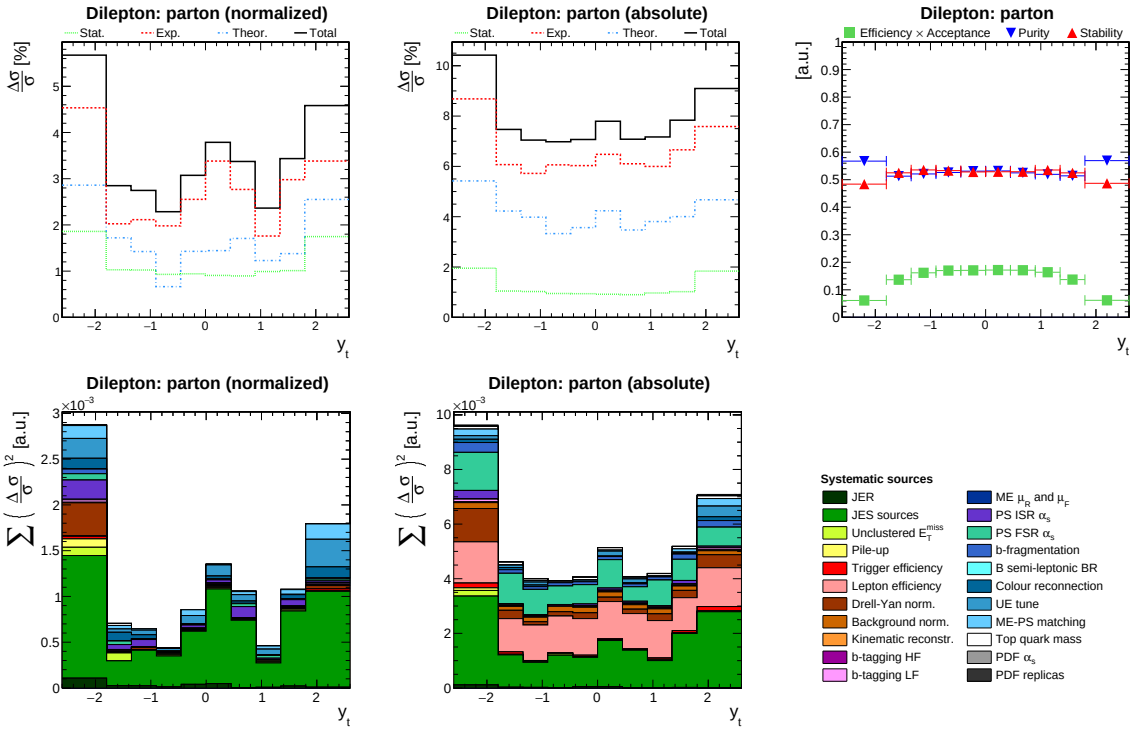

(a)

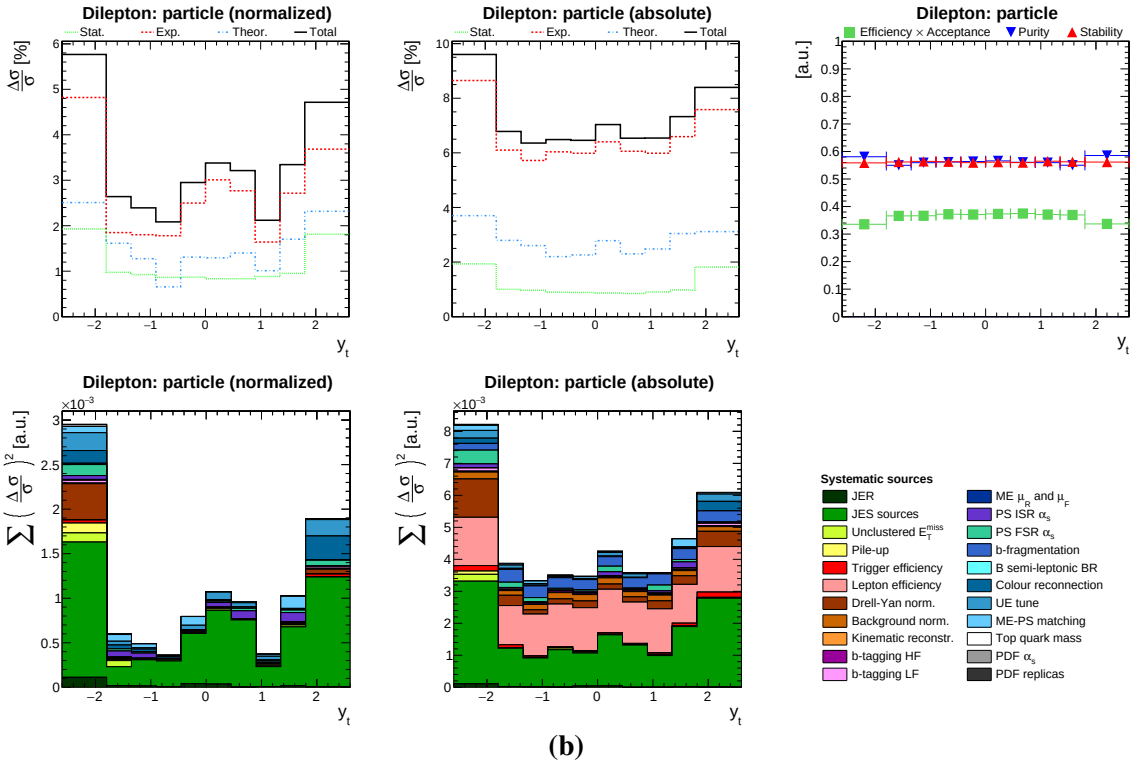

(b)

Figure C.7 A summary of the uncertainties and migrations among bins for the differential $t\bar{t}$ production cross sections as a function of the rapidity of the top quark y_t. Figure **(a)** corresponds to measurements at parton level in the full phase space. Upper row: a summary of uncertainties per bin for normalized (left) and absolute (middle) differential cross sections; efficiency × acceptance, purity and stability per bin (right). Lower row: a summary of systematic uncertainties per bin for normalized (left) and absolute (middle; here, the uncertainties on the luminosity and decay branching ratio of the signal process are not shown) differential cross sections; sources of systematic uncertainty (right). Figure **(b)** shows the same for measurements at particle level in a fiducial phase space.

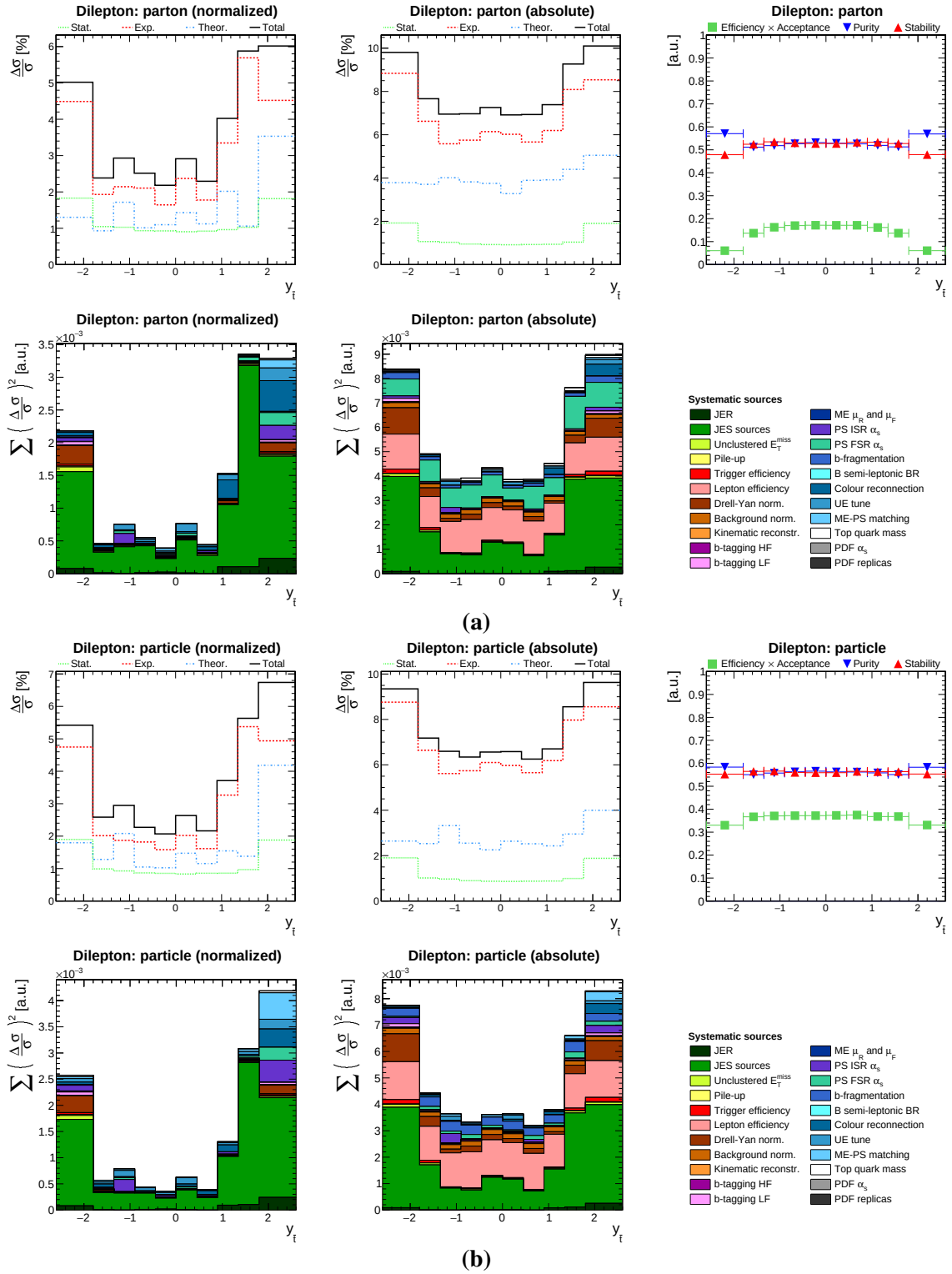

Figure C.8 A summary of the uncertainties and migrations among bins for the differential $t\bar{t}$ production cross sections as a function of the rapidity of the top antiquark $y_{\bar{t}}$. Figure **(a)** corresponds to measurements at parton level in the full phase space. Upper row: a summary of uncertainties per bin for normalized (left) and absolute (middle) differential cross sections; efficiency × acceptance, purity and stability per bin (right). Lower row: a summary of systematic uncertainties per bin for normalized (left) and absolute (middle; here, the uncertainties on the luminosity and decay branching ratio of the signal process are not shown) differential cross sections; sources of systematic uncertainty (right). Figure **(b)** shows the same for measurements at particle level in a fiducial phase space.

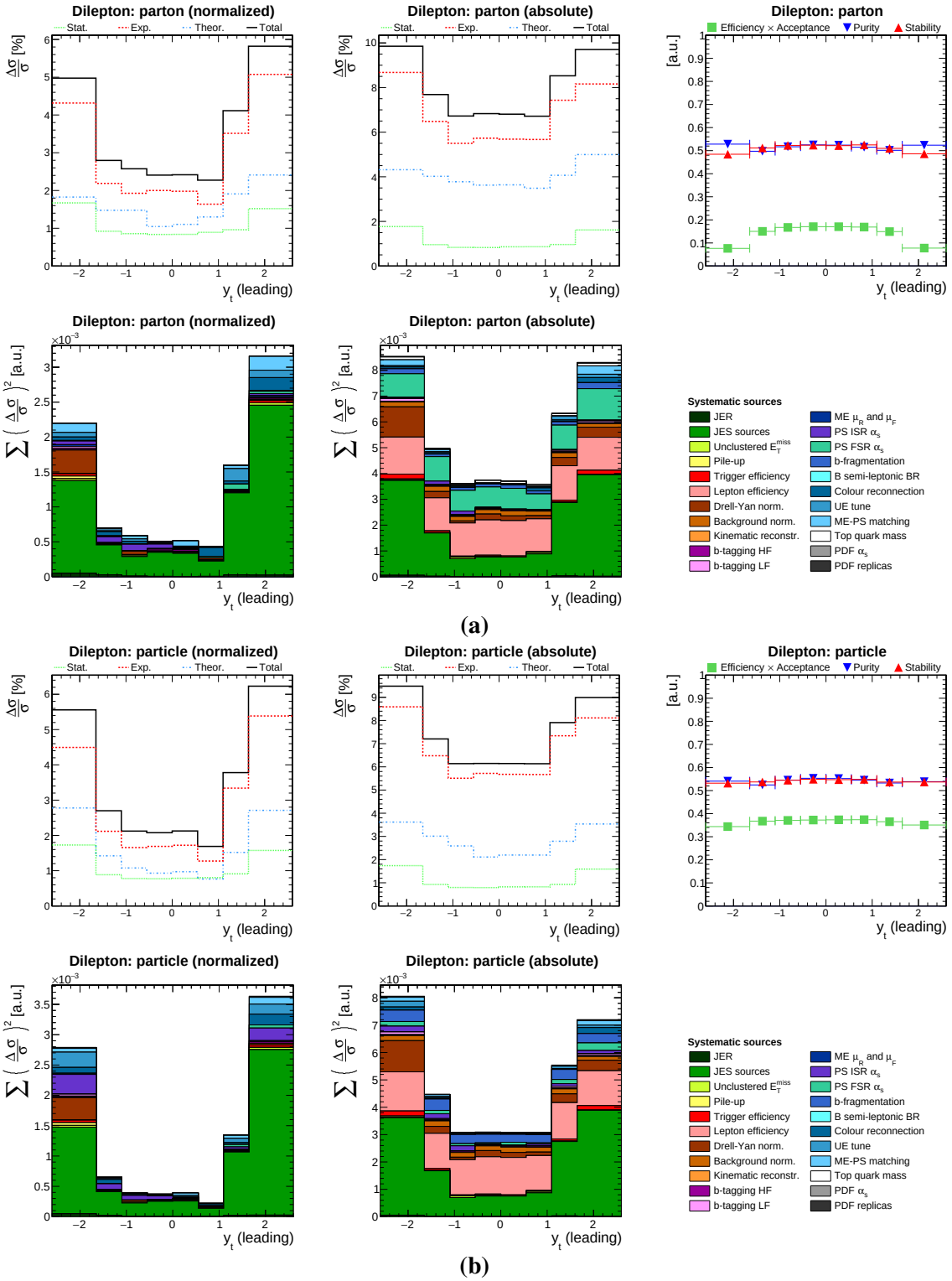

Figure C.9 A summary of the uncertainties and migrations among bins for the differential $t\bar{t}$ production cross sections as a function of the rapidity of the leading top quark y_t *(leading)*. Figure **(a)** corresponds to measurements at parton level in the full phase space. Upper row: a summary of uncertainties per bin for normalized (left) and absolute (middle) differential cross sections; efficiency × acceptance, purity and stability per bin (right). Lower row: a summary of systematic uncertainties per bin for normalized (left) and absolute (middle; here, the uncertainties on the luminosity and decay branching ratio of the signal process are not shown) differential cross sections; sources of systematic uncertainty (right). Figure **(b)** shows the same for measurements at particle level in a fiducial phase space.

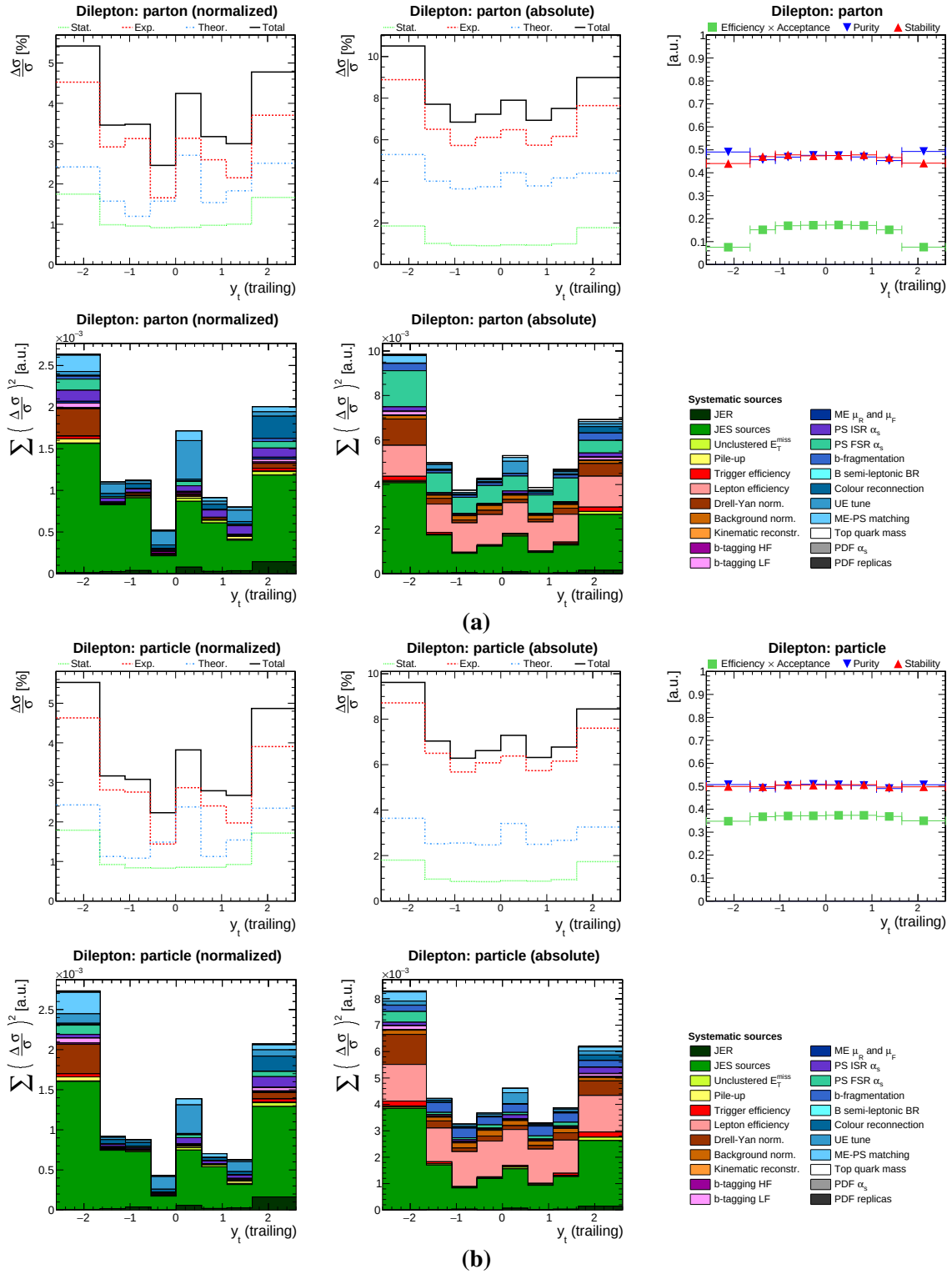

Figure C.10 A summary of the uncertainties and migrations among bins for the differential $t\bar{t}$ production cross sections as a function of the rapidity of the trailing top quark y_t *(trailing)*. Figure **(a)** corresponds to measurements at parton level in the full phase space. Upper row: a summary of uncertainties per bin for normalized (left) and absolute (middle) differential cross sections; efficiency × acceptance, purity and stability per bin (right). Lower row: a summary of systematic uncertainties per bin for normalized (left) and absolute (middle; here, the uncertainties on the luminosity and decay branching ratio of the signal process are not shown) differential cross sections; sources of systematic uncertainty (right). Figure **(b)** shows the same for measurements at particle level in a fiducial phase space.

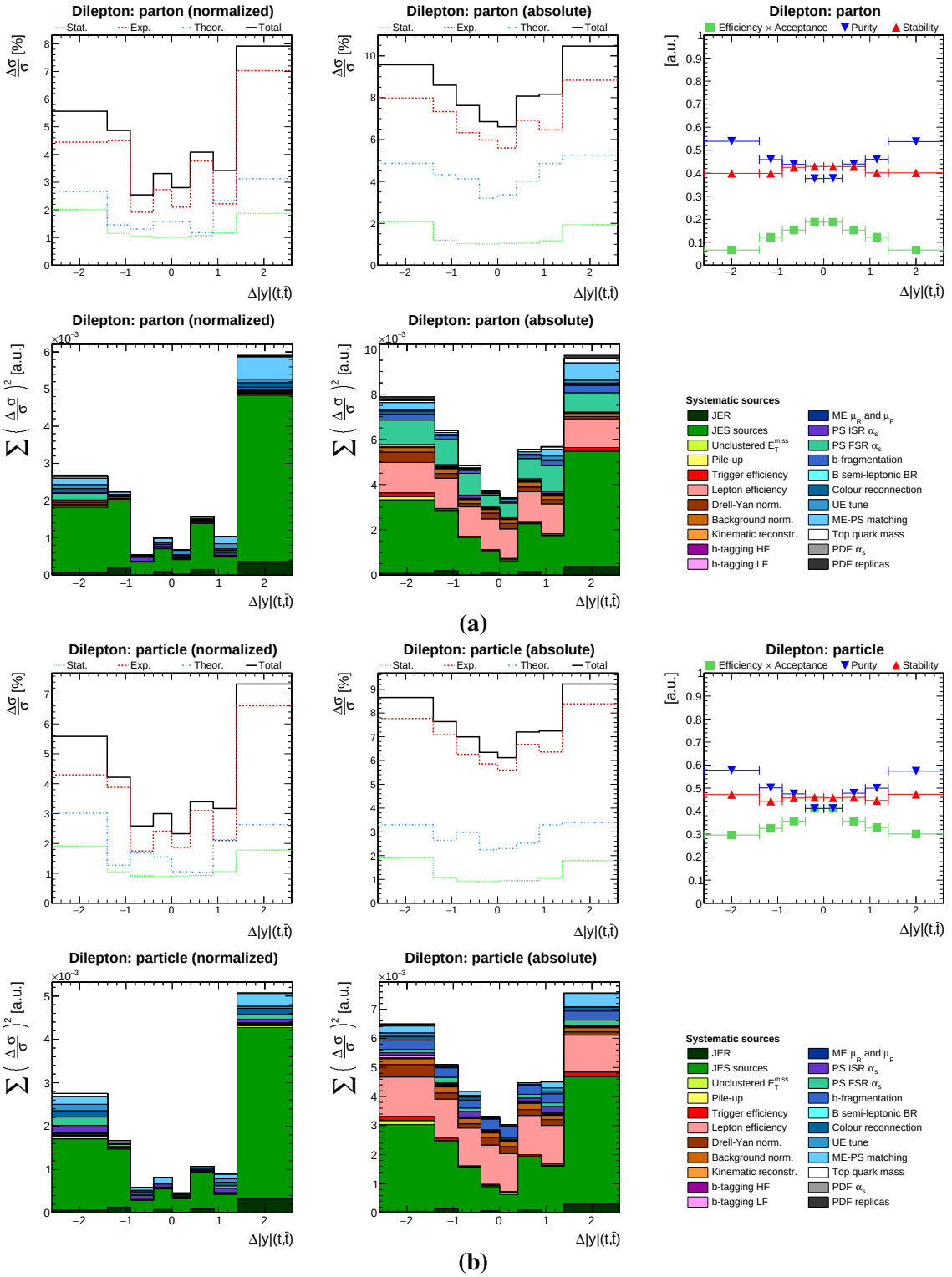

Figure C.11 A summary of the uncertainties and migrations among bins for the differential $t\bar{t}$ production cross sections as a function of the difference in absolute rapidity between the top quark and antiquark $\Delta|y|(t,\bar{t})$. Figure **(a)** corresponds to measurements at parton level in the full phase space. Upper row: a summary of uncertainties per bin for normalized (left) and absolute (middle) differential cross sections; efficiency × acceptance, purity and stability per bin (right). Lower row: a summary of systematic uncertainties per bin for normalized (left) and absolute (middle; here, the uncertainties on the luminosity and decay branching ratio of the signal process are not shown) differential cross sections; sources of systematic uncertainty (right). Figure **(b)** shows the same for measurements at particle level in a fiducial phase space.

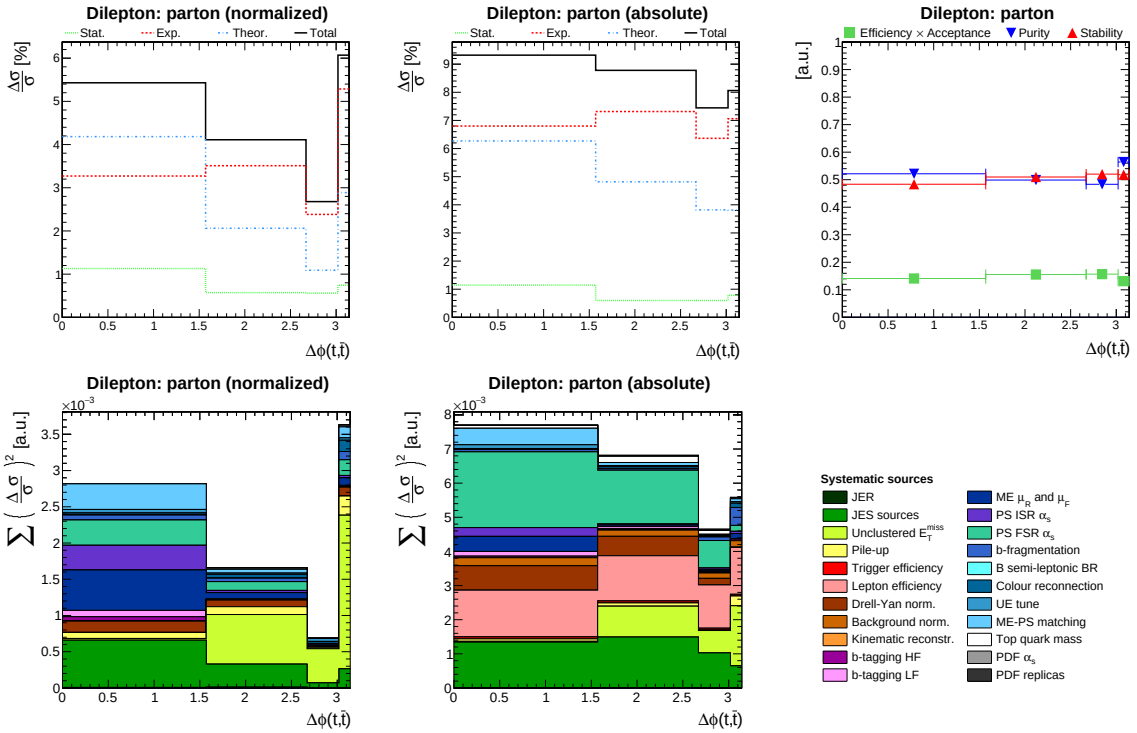

(a)

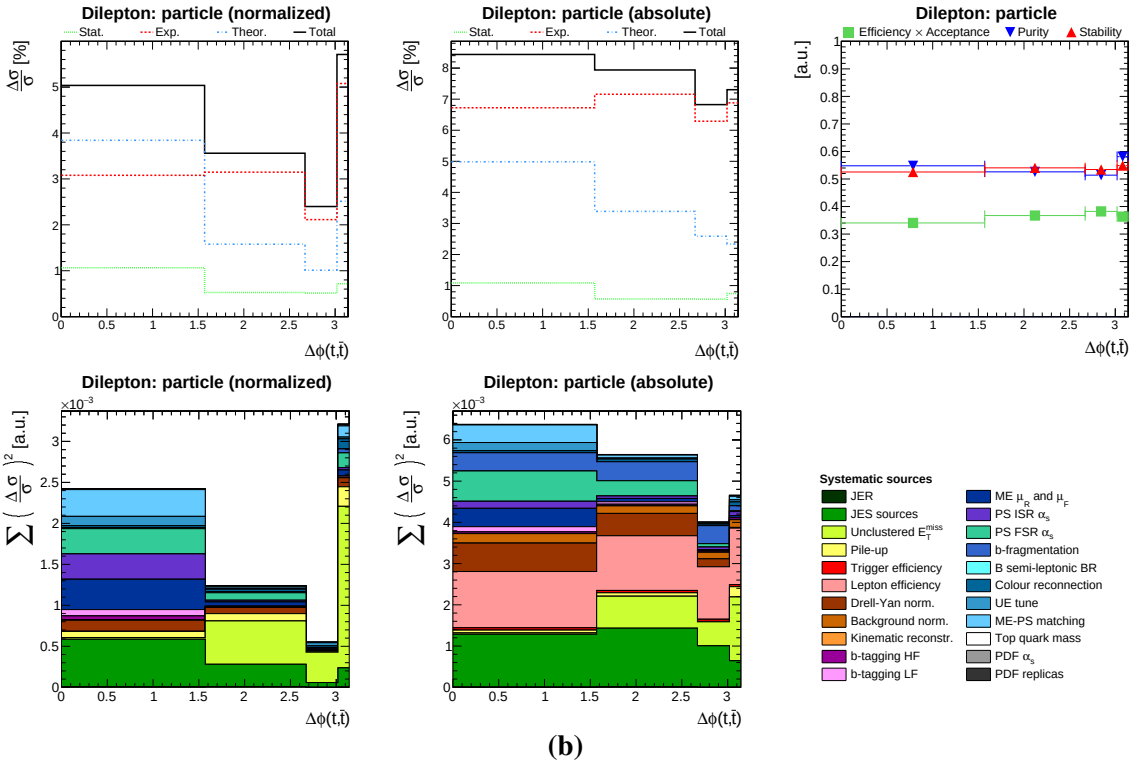

(b)

Figure C.12 A summary of the uncertainties and migrations among bins for the differential $t\bar{t}$ production cross sections as a function of the difference in azimuthal angle between the top quark and antiquark $\Delta\phi(t,\bar{t})$. Figure **(a)** corresponds to measurements at parton level in the full phase space. Upper row: a summary of uncertainties per bin for normalized (left) and absolute (middle) differential cross sections; efficiency × acceptance, purity and stability per bin (right). Lower row: a summary of systematic uncertainties per bin for normalized (left) and absolute (middle; here, the uncertainties on the luminosity and decay branching ratio of the signal process are not shown) differential cross sections; sources of systematic uncertainty (right). Figure **(b)** shows the same for measurements at particle level in a fiducial phase space.

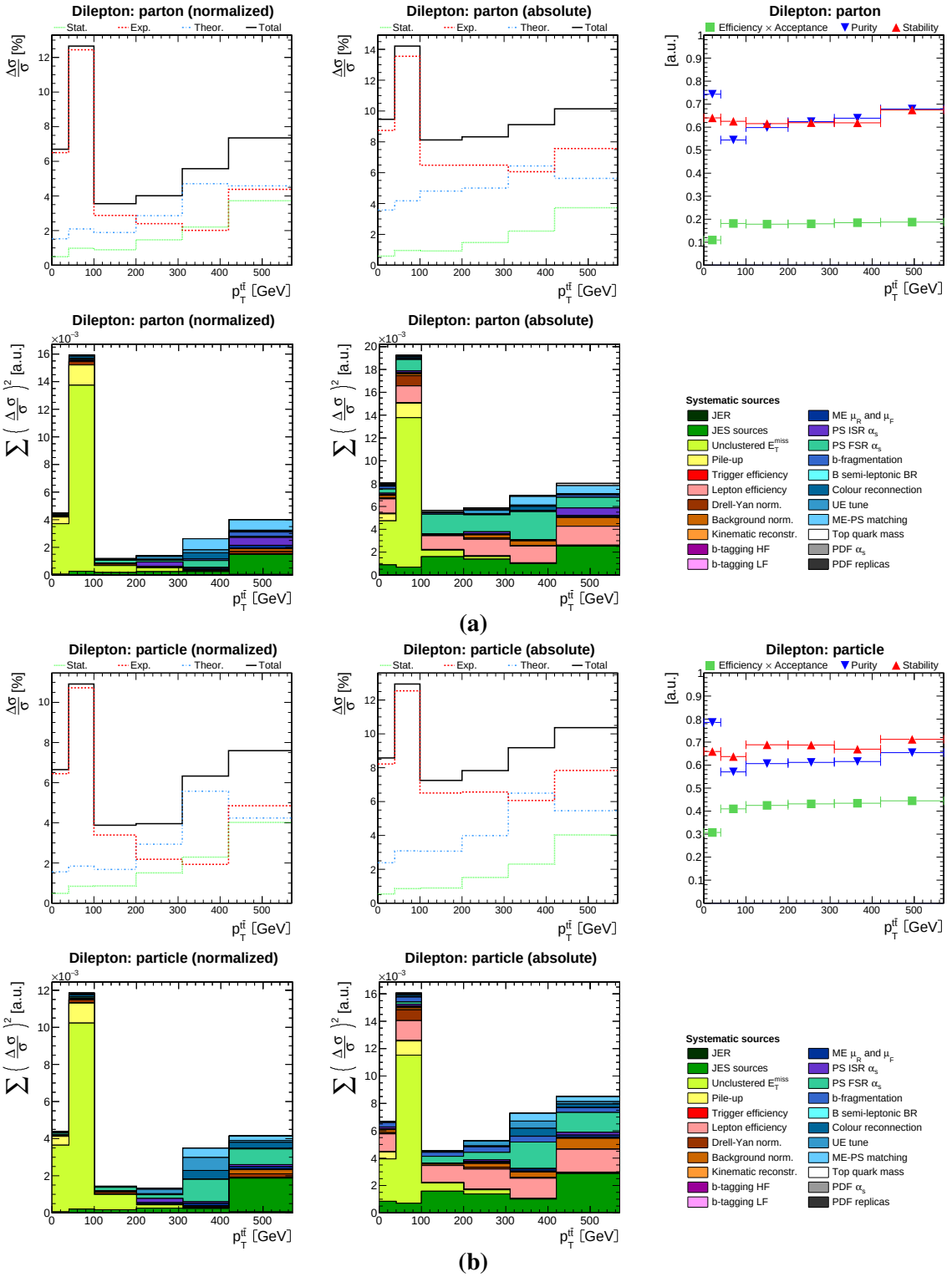

Figure C.13 A summary of the uncertainties and migrations among bins for the differential $t\bar{t}$ production cross sections as a function of the transverse momentum of the top-quark pair $p_T^{t\bar{t}}$. Figure **(a)** corresponds to measurements at parton level in the full phase space. Upper row: a summary of uncertainties per bin for normalized (left) and absolute (middle) differential cross sections; efficiency × acceptance, purity and stability per bin (right). Lower row: a summary of systematic uncertainties per bin for normalized (left) and absolute (middle; here, the uncertainties on the luminosity and decay branching ratio of the signal process are not shown) differential cross sections; sources of systematic uncertainty (right). Figure **(b)** shows the same for measurements at particle level in a fiducial phase space.

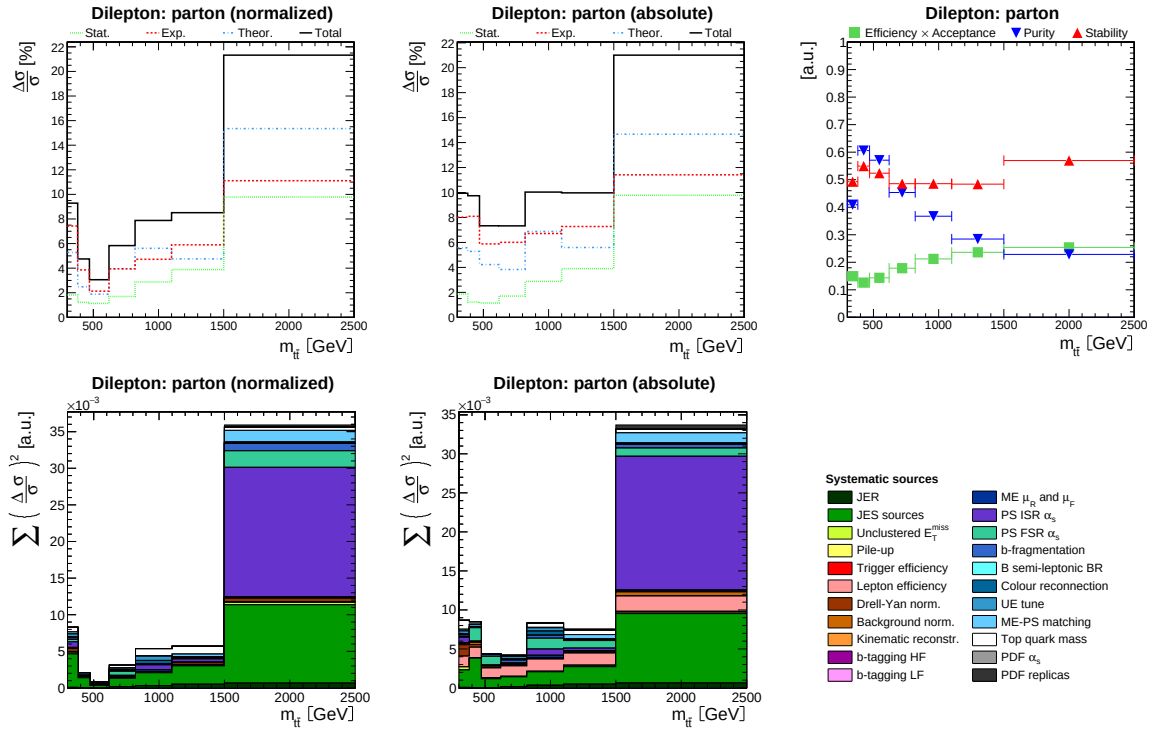

(a)

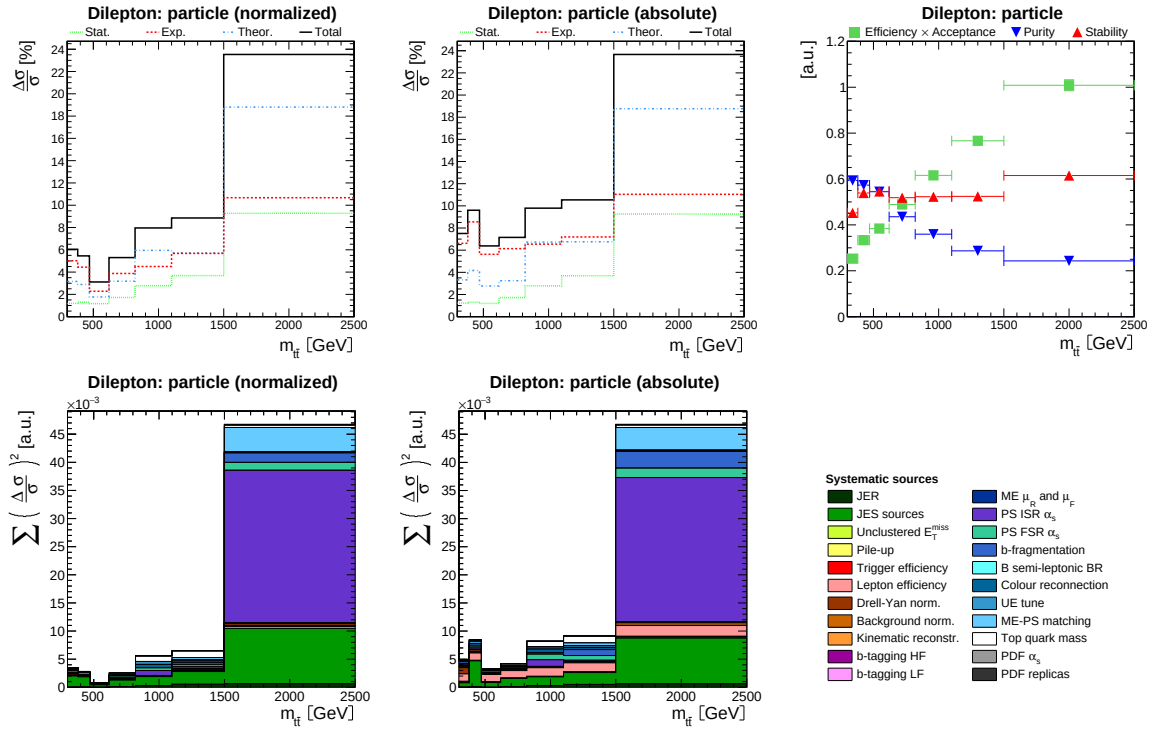

(b)

Figure C.14 A summary of the uncertainties and migrations among bins for the differential $t\bar{t}$ production cross sections as a function of the invariant mass of the top-quark pair $m_{t\bar{t}}$. Figure **(a)** corresponds to measurements at parton level in the full phase space. Upper row: a summary of uncertainties per bin for normalized (left) and absolute (middle) differential cross sections; efficiency × acceptance, purity and stability per bin (right). Lower row: a summary of systematic uncertainties per bin for normalized (left) and absolute (middle; here, the uncertainties on the luminosity and decay branching ratio of the signal process are not shown) differential cross sections; sources of systematic uncertainty (right). Figure **(b)** shows the same for measurements at particle level in a fiducial phase space.

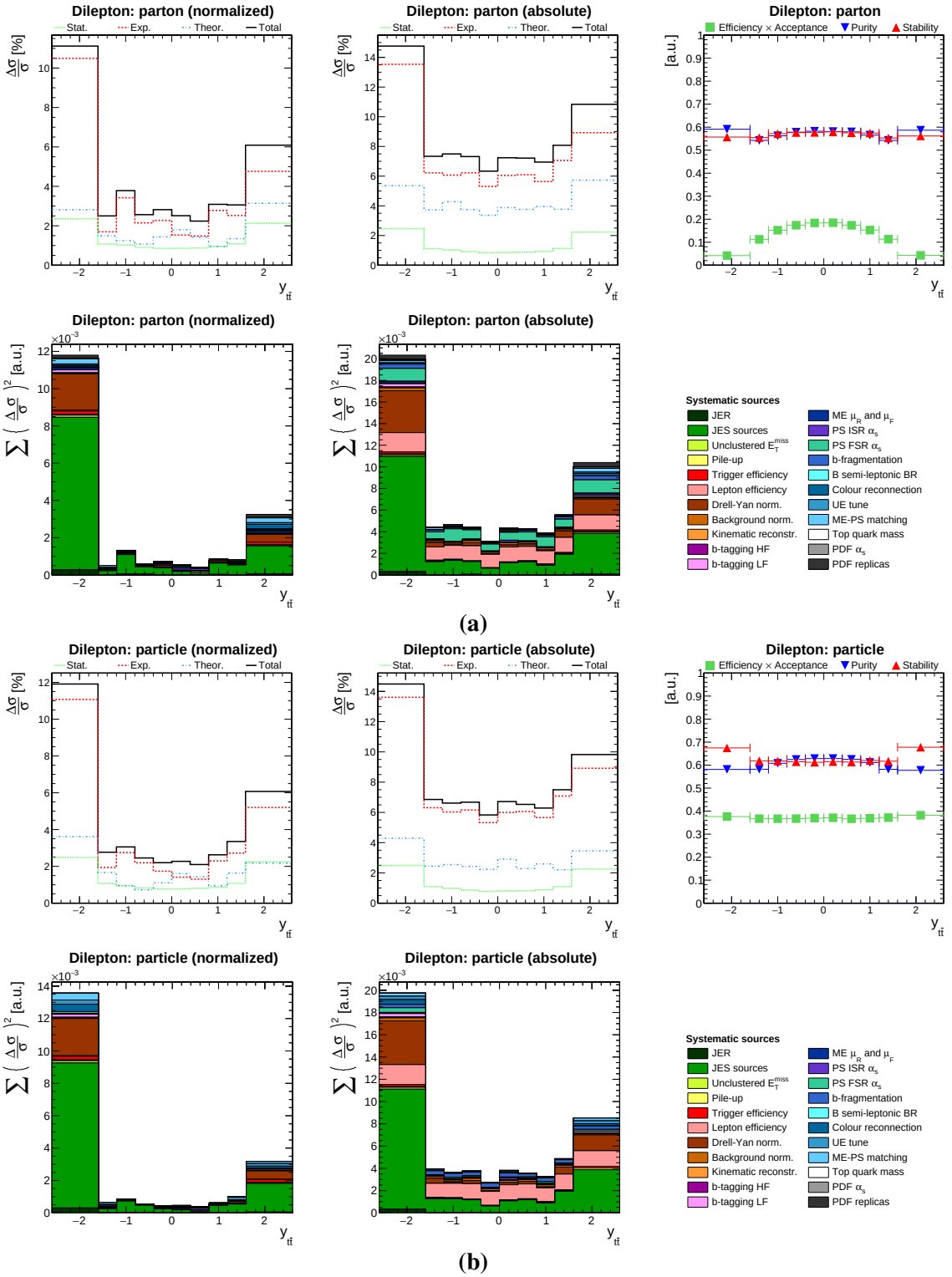

Figure C.15 A summary of the uncertainties and migrations among bins for the differential $t\bar{t}$ production cross sections as a function of the rapidity of the top-quark pair $y_{t\bar{t}}$. Figure **(a)** corresponds to measurements at parton level in the full phase space. Upper row: a summary of uncertainties per bin for normalized (left) and absolute (middle) differential cross sections; efficiency × acceptance, purity and stability per bin (right). Lower row: a summary of systematic uncertainties per bin for normalized (left) and absolute (middle; here, the uncertainties on the luminosity and decay branching ratio of the signal process are not shown) differential cross sections; sources of systematic uncertainty (right). Figure **(b)** shows the same for measurements at particle level in a fiducial phase space.

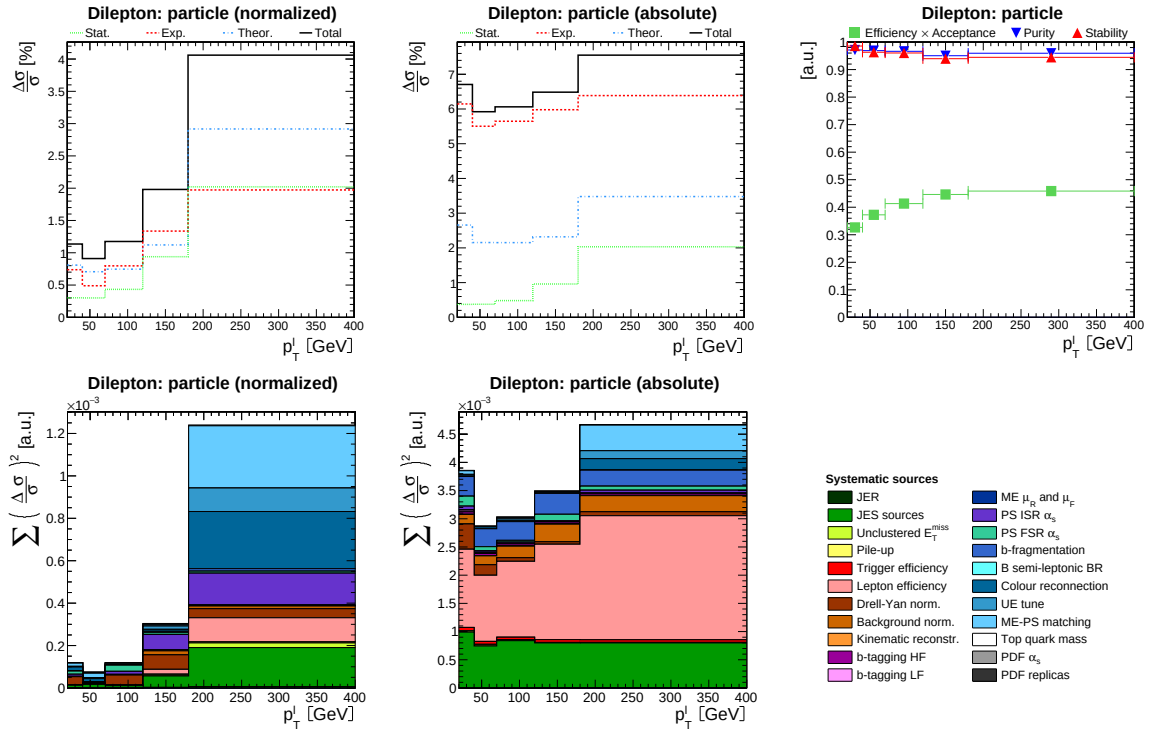

(a)

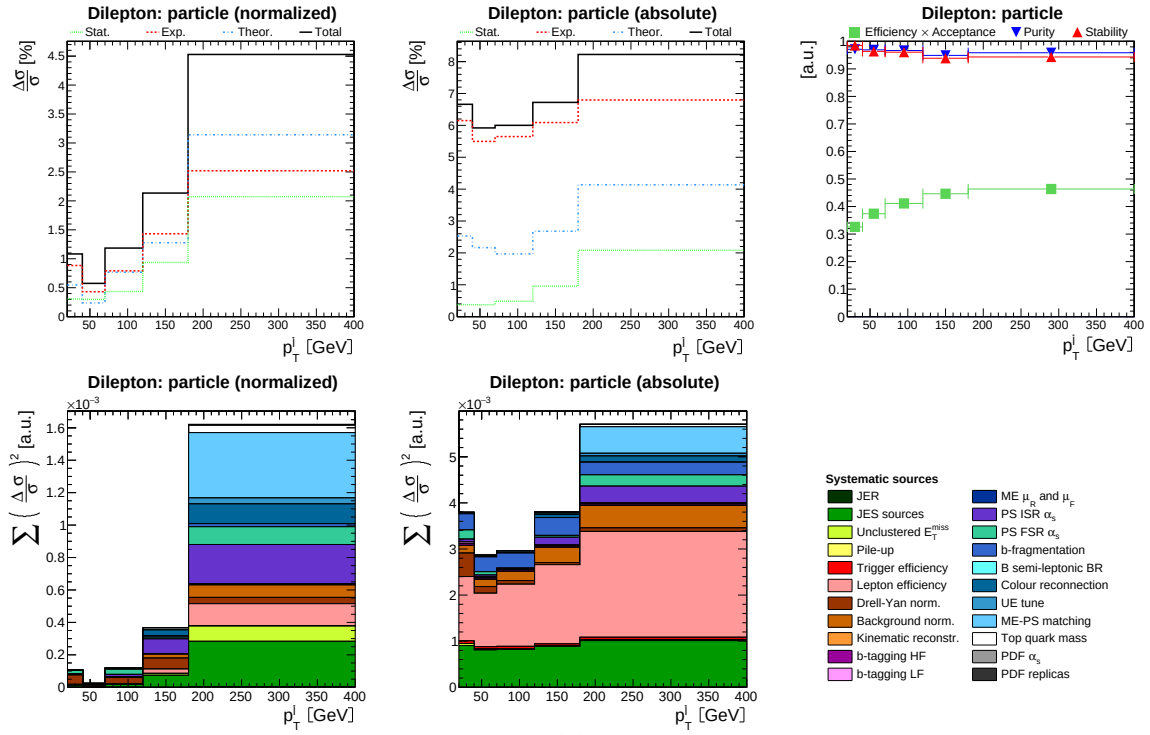

(b)

Figure C.16 In Figure **(a)**, a summary of the uncertainties and migrations among bins for the differential $t\bar{t}$ production cross sections as a function of the transverse momentum of the lepton p_T^{ℓ}. Measurements are performed at particle level in a fiducial phase space. Upper row: a summary of uncertainties per bin for normalized (left) and absolute (middle) differential cross sections; efficiency × acceptance, purity and stability per bin (right). Lower row: a summary of systematic uncertainties per bin for normalized (left) and absolute (middle; here, the uncertainties on the luminosity and decay branching ratio of the signal process are not shown) differential cross sections; sources of systematic uncertainty (right). Figure **(b)** shows the same for measurements as a function of the transverse momentum of the antilepton $p_T^{\bar{\ell}}$.

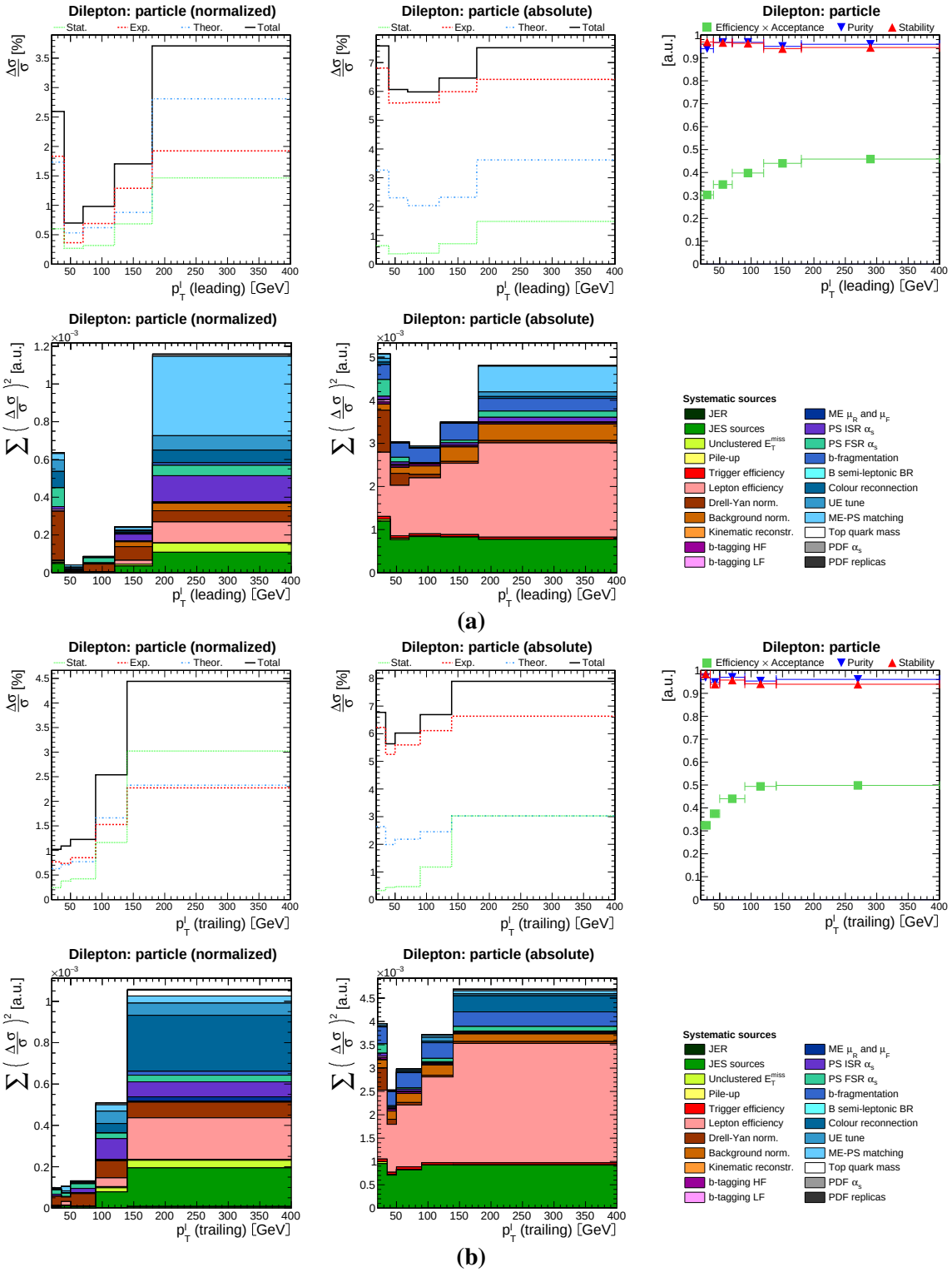

Figure C.17 In Figure **(a)**, a summary of the uncertainties and migrations among bins for the differential $t\bar{t}$ production cross sections as a function of the transverse momentum of the leading lepton p_T^{ℓ} *(leading)*. Measurements are performed at particle level in a fiducial phase space. Upper row: a summary of uncertainties per bin for normalized (left) and absolute (middle) differential cross sections; efficiency × acceptance, purity and stability per bin (right). Lower row: a summary of systematic uncertainties per bin for normalized (left) and absolute (middle; here, the uncertainties on the luminosity and decay branching ratio of the signal process are not shown) differential cross sections; sources of systematic uncertainty (right). Figure **(b)** shows the same for measurements as a function of the transverse momentum of the trailing lepton p_T^{ℓ} *(trailing)*.

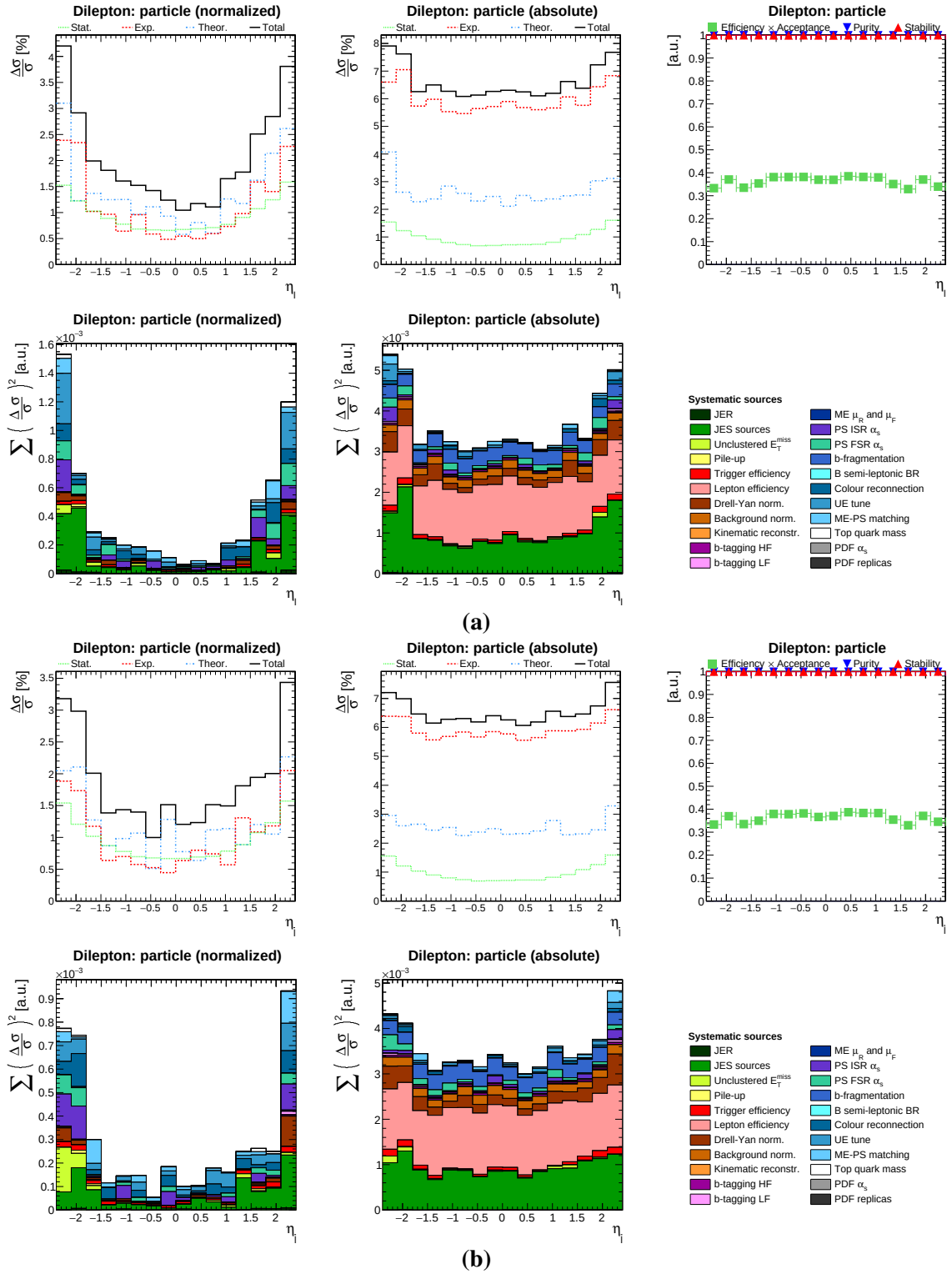

Figure C.18 In Figure **(a)**, a summary of the uncertainties and migrations among bins for the differential $t\bar{t}$ production cross sections as a function of the pseudorapidity of the lepton η_ℓ. Measurements are performed at particle level in a fiducial phase space. Upper row: a summary of uncertainties per bin for normalized (left) and absolute (middle) differential cross sections; efficiency × acceptance, purity and stability per bin (right). Lower row: a summary of systematic uncertainties per bin for normalized (left) and absolute (middle; here, the uncertainties on the luminosity and decay branching ratio of the signal process are not shown) differential cross sections; sources of systematic uncertainty (right). Figure **(b)** shows the same for measurements as a function of the pseudorapidity of the antilepton $\eta_{\bar{\ell}}$.

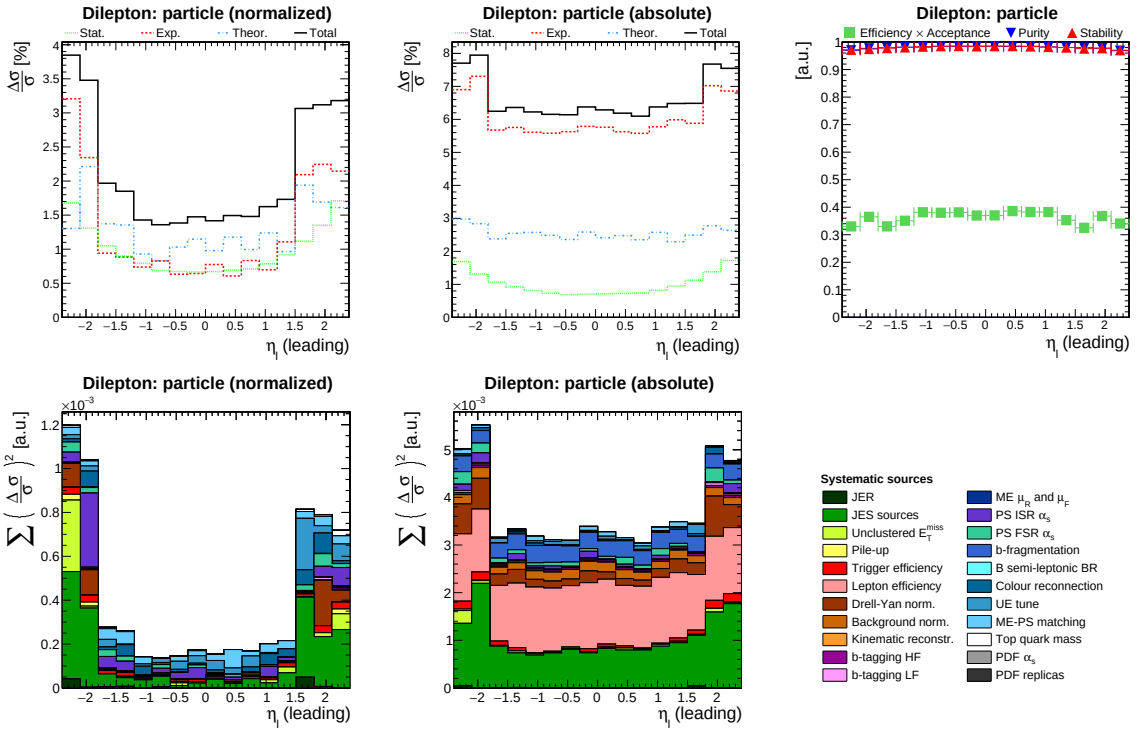

(a)

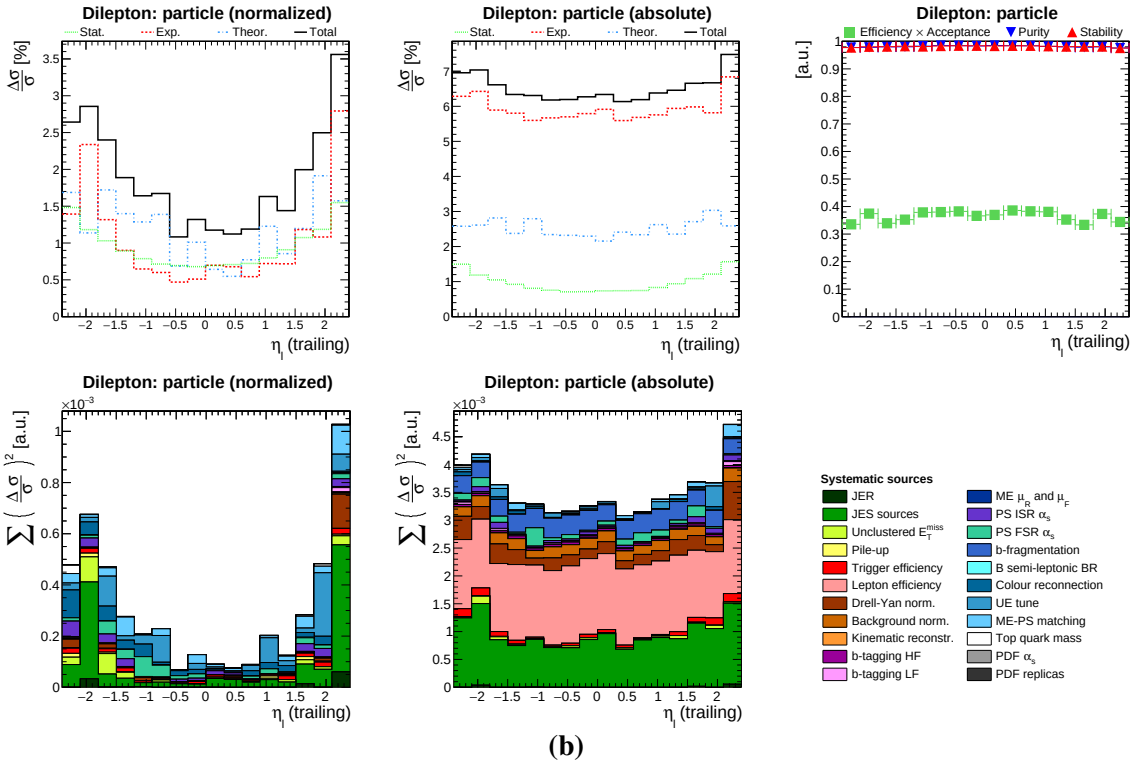

(b)

Figure C.19 In Figure **(a)**, a summary of the uncertainties and migrations among bins for the differential $t\bar{t}$ production cross sections as a function of the pseudorapidity of the leading lepton η_ℓ *(leading)*. Measurements are performed at particle level in a fiducial phase space. Upper row: a summary of uncertainties per bin for normalized (left) and absolute (middle) differential cross sections; efficiency × acceptance, purity and stability per bin (right). Lower row: a summary of systematic uncertainties per bin for normalized (left) and absolute (middle; here, the uncertainties on the luminosity and decay branching ratio of the signal process are not shown) differential cross sections; sources of systematic uncertainty (right). Figure **(b)** shows the same for measurements as a function of the pseudorapidity of the trailing lepton η_ℓ *(trailing)*.

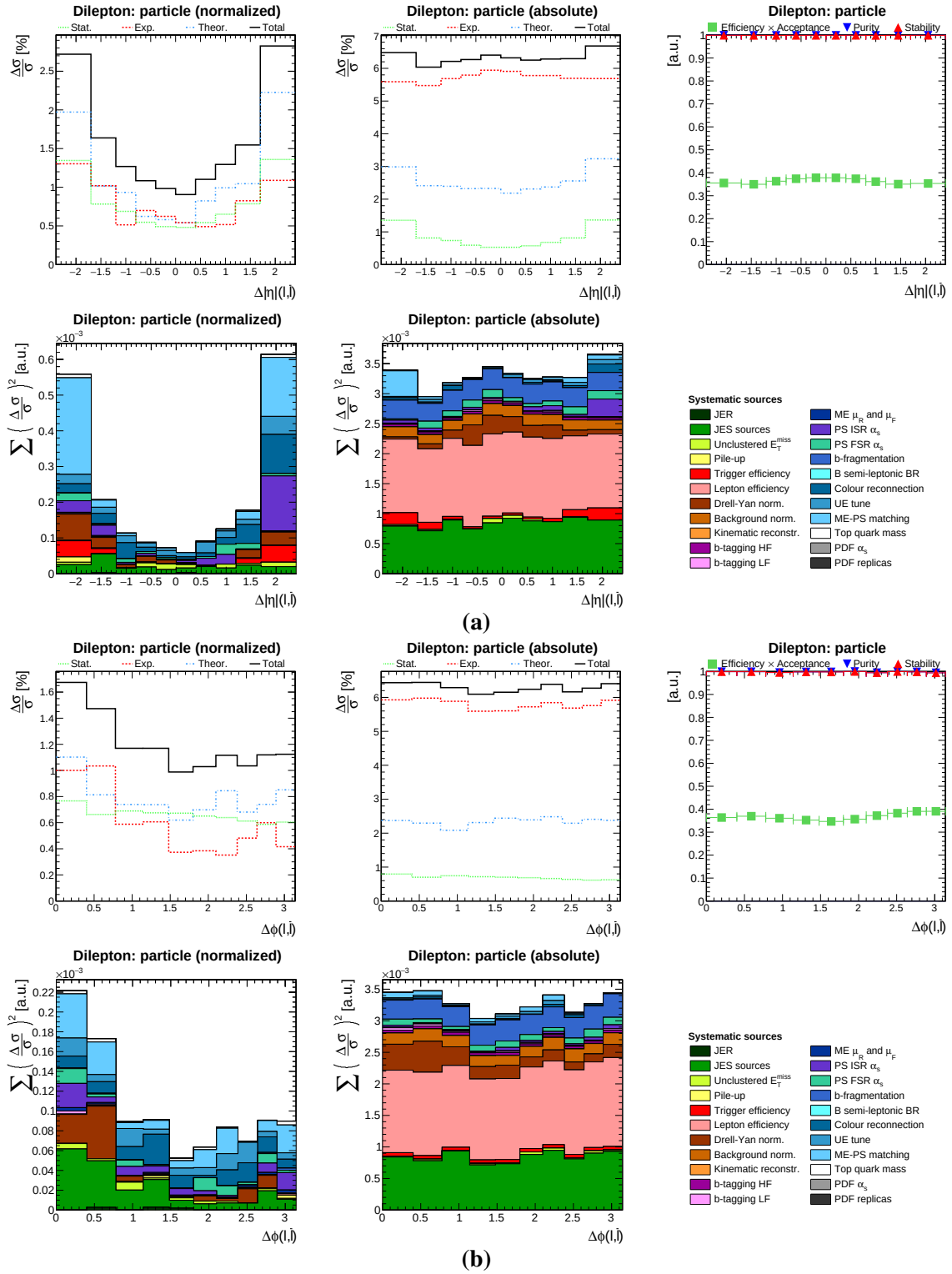

Figure C.20 In Figure **(a)**, a summary of the uncertainties and migrations among bins for the differential $t\bar{t}$ production cross sections as a function of the difference in absolute pseudorapidity between the lepton and antilepton $\Delta|\eta|(\ell,\bar{\ell})$. Measurements are performed at particle level in a fiducial phase space. Upper row: a summary of uncertainties per bin for normalized (left) and absolute (middle) differential cross sections; efficiency × acceptance, purity and stability per bin (right). Lower row: a summary of systematic uncertainties per bin for normalized (left) and absolute (middle; here, the uncertainties on the luminosity and decay branching ratio of the signal process are not shown) differential cross sections; sources of systematic uncertainty (right). Figure **(b)** shows the same for measurements as a function of the difference in azimuthal angle between the lepton and antilepton $\Delta\phi(\ell,\bar{\ell})$.

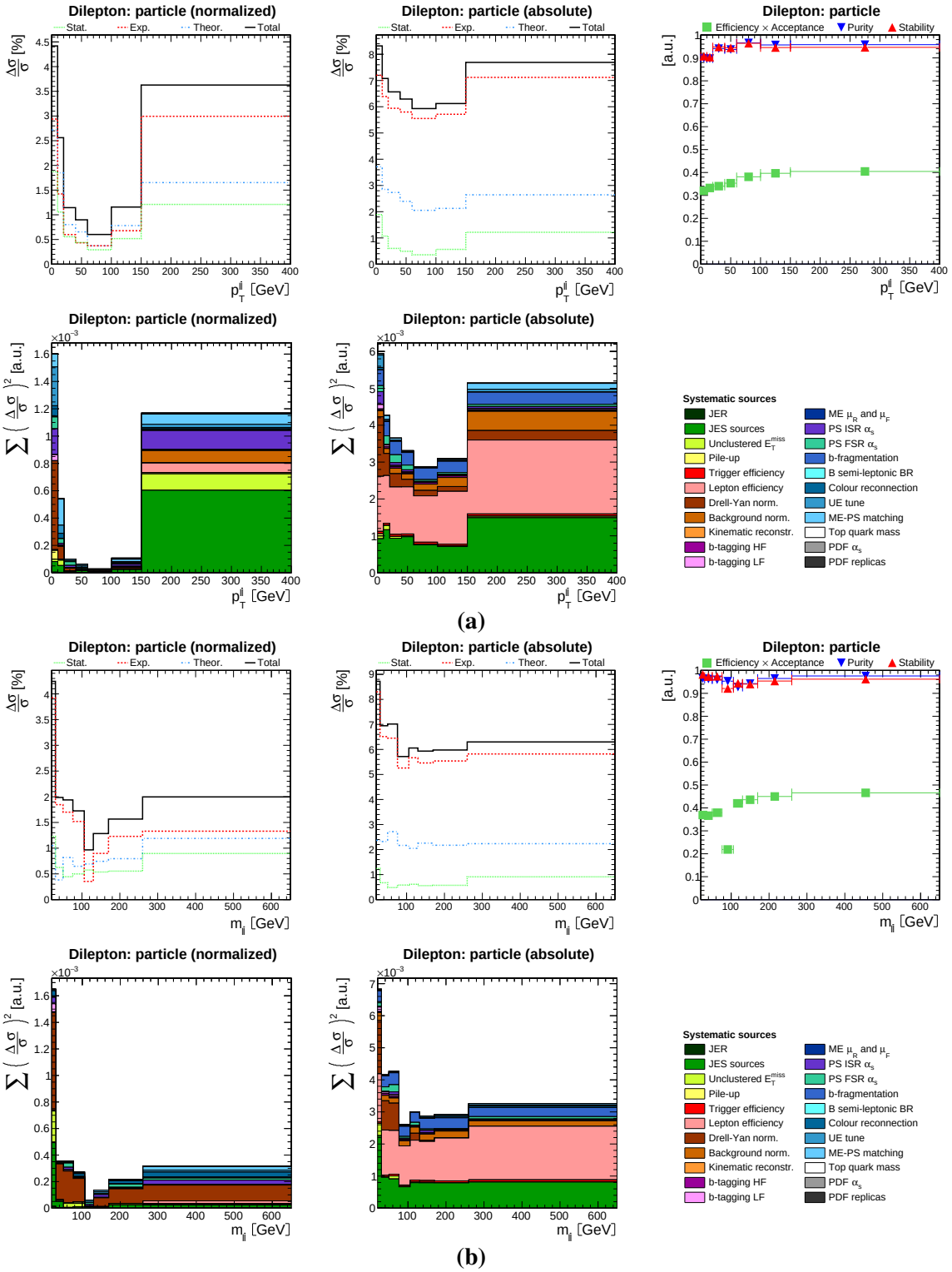

Figure C.21 In Figure **(a)**, a summary of the uncertainties and migrations among bins for the differential $t\bar{t}$ production cross sections as a function of the transverse momentum of the lepton pair $p_T^{\ell\bar{\ell}}$. Measurements are performed at particle level in a fiducial phase space. Upper row: a summary of uncertainties per bin for normalized (left) and absolute (middle) differential cross sections; efficiency × acceptance, purity and stability per bin (right). Lower row: a summary of systematic uncertainties per bin for normalized (left) and absolute (middle; here, the uncertainties on the luminosity and decay branching ratio of the signal process are not shown) differential cross sections; sources of systematic uncertainty (right). Figure **(b)** shows the same for measurements as a function of the invariant mass of the lepton pair $m_{\ell\bar{\ell}}$.

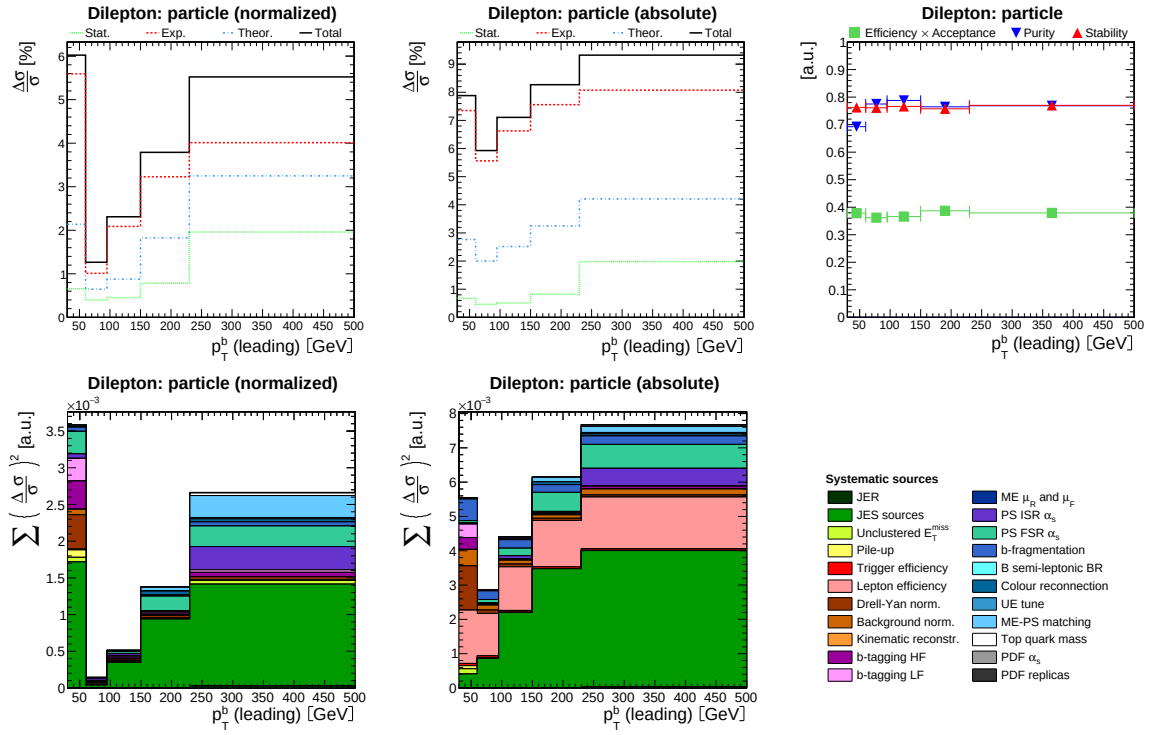

(a)

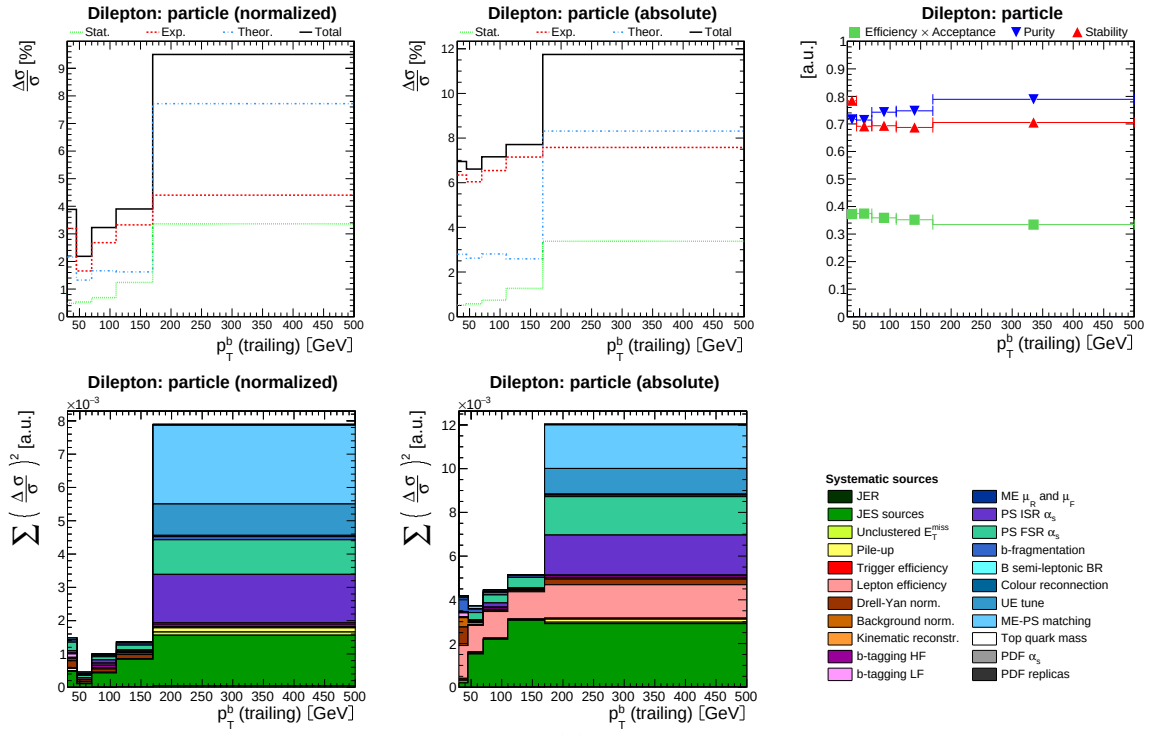

(b)

Figure C.22 In Figure **(a)**, a summary of the uncertainties and migrations among bins for the differential $t\bar{t}$ production cross sections as a function of the transverse momentum of the leading b-jet p_T^b *(leading)*. Measurements are performed at particle level in a fiducial phase space. Upper row: a summary of uncertainties per bin for normalized (left) and absolute (middle) differential cross sections; efficiency × acceptance, purity and stability per bin (right). Lower row: a summary of systematic uncertainties per bin for normalized (left) and absolute (middle; here, the uncertainties on the luminosity and decay branching ratio of the signal process are not shown) differential cross sections; sources of systematic uncertainty (right). Figure **(b)** shows the same for measurements as a function of the transverse momentum of the trailing b-jet p_T^b *(trailing)*.

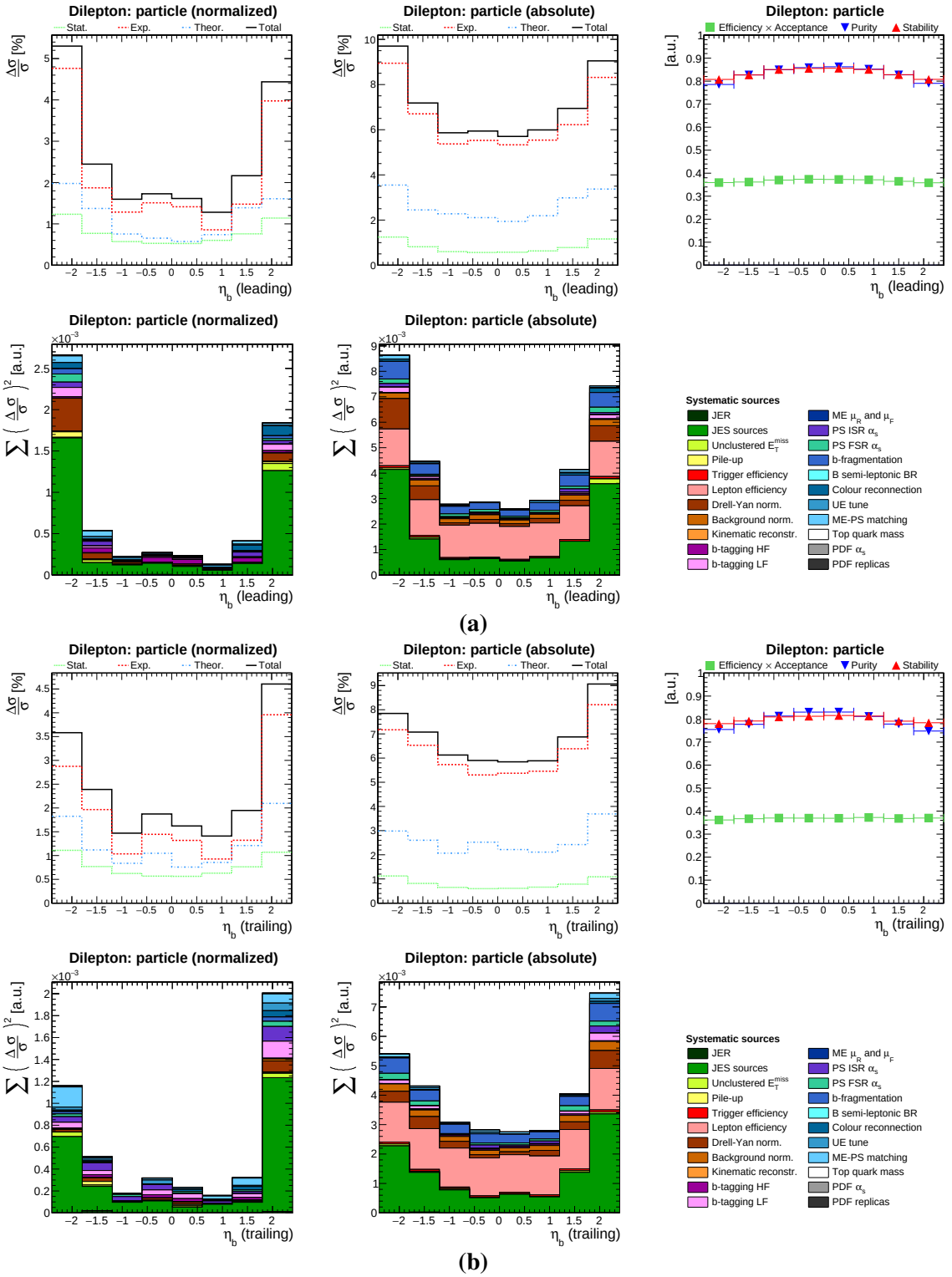

Figure C.23 In Figure **(a)**, a summary of the uncertainties and migrations among bins for the differential $t\bar{t}$ production cross sections as a function of the pseudorapidity of the leading b-jet η_b *(leading)*. Measurements are performed at particle level in a fiducial phase space. Upper row: a summary of uncertainties per bin for normalized (left) and absolute (middle) differential cross sections; efficiency × acceptance, purity and stability per bin (right). Lower row: a summary of systematic uncertainties per bin for normalized (left) and absolute (middle; here, the uncertainties on the luminosity and decay branching ratio of the signal process are not shown) differential cross sections; sources of systematic uncertainty (right). Figure **(b)** shows the same for measurements as a function of the pseudorapidity of the trailing b-jet η_b *(trailing)*.

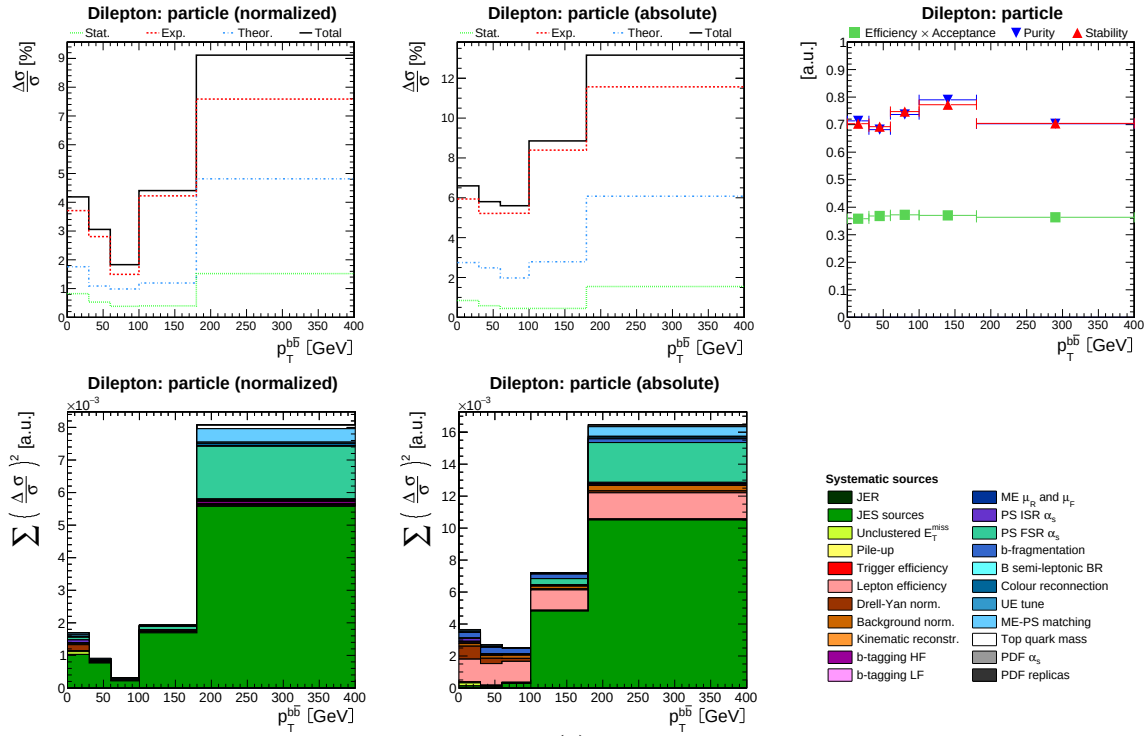

(a)

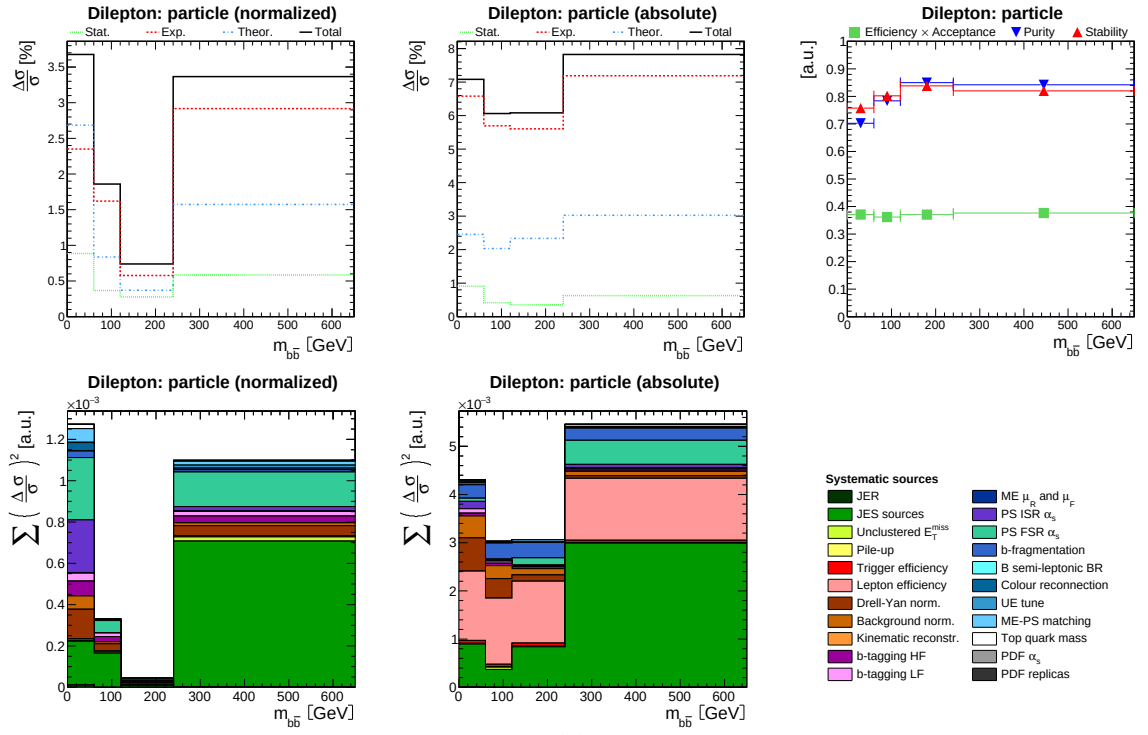

(b)

Figure C.24 In Figure **(a)**, a summary of the uncertainties and migrations among bins for the differential $t\bar{t}$ production cross sections as a function of the transverse momentum of the b-jet pair $p_T^{b\bar{b}}$. Measurements are performed at particle level in a fiducial phase space. Upper row: a summary of uncertainties per bin for normalized (left) and absolute (middle) differential cross sections; efficiency × acceptance, purity and stability per bin (right). Lower row: a summary of systematic uncertainties per bin for normalized (left) and absolute (middle; here, the uncertainties on the luminosity and decay branching ratio of the signal process are not shown) differential cross sections; sources of systematic uncertainty (right). Figure **(b)** shows the same for measurements as a function of the invariant mass of the b-jet pair $m_{b\bar{b}}$.

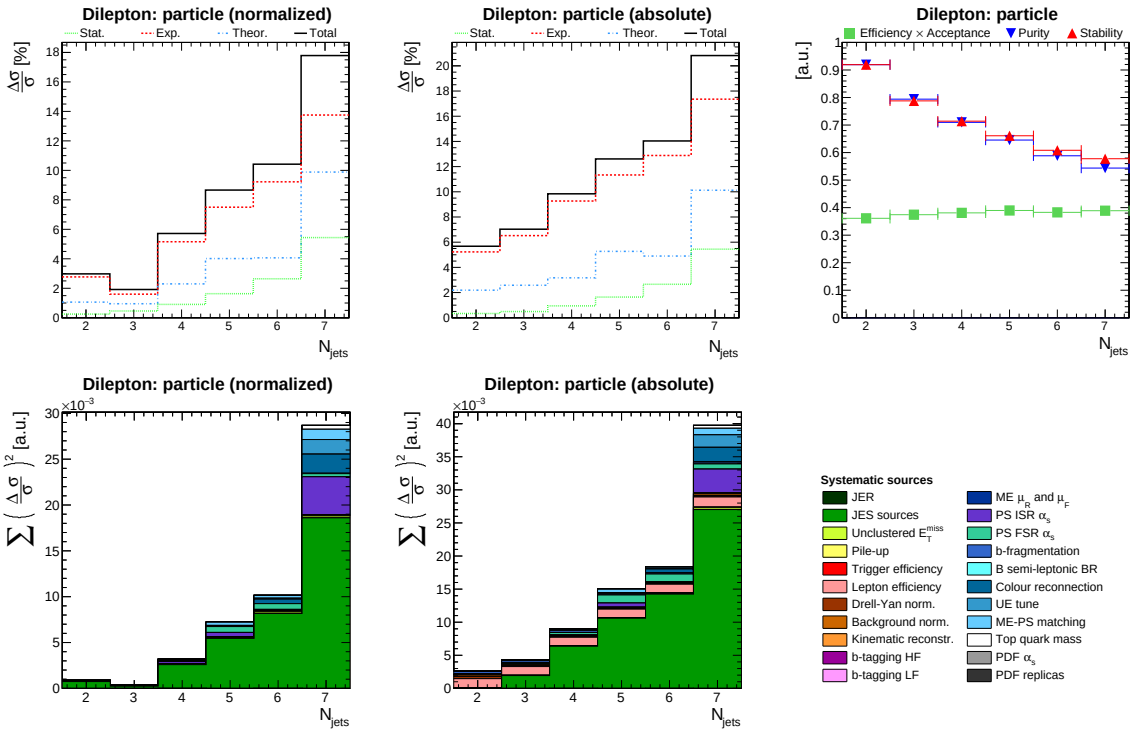

Figure C.25 A summary of the uncertainties and migrations among bins for the differential $t\bar{t}$ production cross sections as a function of the jet multiplicity N_{jets}. Measurements are performed at particle level in a fiducial phase space. Upper row: a summary of uncertainties per bin for normalized (left) and absolute (middle) differential cross sections; efficiency × acceptance, purity and stability per bin (right). Lower row: a summary of systematic uncertainties per bin for normalized (left) and absolute (middle; here, the uncertainties on the luminosity and decay branching ratio of the signal process are not shown) differential cross sections; sources of systematic uncertainty (right).

Appendix D

Additional quality tests of the unfolding method

D.1 Closure test verifying the statistical properties of the unfolding method

Here, the dedicated closure test for the normalized differential $t\bar{t}$ production cross section measurement presented in Section 7.1.1 is described. This measurement is performed in the dilepton decay channel using the first data sample recorded in 2015 by the CMS detector during pp collisions at $\sqrt{s} = 13$ TeV, corresponding to an integrated luminosity $L = 42$ pb^{-1}. As mentioned in Section 7.1.1, one of the biggest challenges of the aforementioned measurement is the small number of events per differential bins. In total, only 306 data events in the combined channel are observed. Thus, large statistical fluctuations per bin can potentially influence the unfolded result. Therefore, the unfolding method is tested to see whether it is sensitive to the true shape of signal spectra and can provide a reasonable estimate of the statistical uncertainty due to the limited number of data events. This was successfully demonstrated using a dedicated closure test verifying the statistical properties of the unfolding method, which is briefly discussed in the following.

To conduct the closure test, the pseudo-data distribution, constructed as described in Section 5.3.1 (see subsection "Consistency check"), is smeared within Poisson statistics according to $L = 42$ pb^{-1}. This corresponds to one pseudo-experiment. Additional pseudo-data distributions are constructed using the weighting procedure, based on the top quark transverse momenta, described in Section 5.3.1 (see subsection "Check for a bias towards the simulation") and different values of the parameter s governing the reweighting strength (referred to as "slope" in the following; see the description of the weighting procedure). A

total of 10000 pseudo-experiments are built for each individual channel (e^+e^-, $e^\pm\mu^\mp$, $\mu^+\mu^-$) and for the different slopes of the reweighted distributions. For each pseudo-experiment, the normalized differential cross section is calculated using the reference POWHEG v2+PYTHIA8 $t\bar{t}$ sample (relevant for this analysis) to unfold the pseudo-data.

The measured differential cross sections for each pseudo-experiment in each top quark p_T bin are expected to be distributed according to a gaussian distribution around the corresponding theory prediction (used for the construction of the relevant pseudo-data) in each particular bin. Moreover, the RMS value[†] of such distributions and its comparison with the average statistical uncertainty of the measured differential cross sections per bin σ_{SVD}[‡] as provided by the unfolding method and calculated over all 10000 pseudo-experiments, can be used to test the performance of the unfolding procedure in cases with low statistics in data:

- if RMS/σ_{SVD} >> 1 one can expect that spread of the unfolded results is too large and the unfolding method does not have enough sensitivity to the true level information;
- values of RMS/σ_{SVD} << 1 can indicate that the statistical uncertainty provided by the unfolding method is overestimated or the unfolding procedure introduces a bias towards a particular input value;
- values of RMS/$\sigma_{SVD} \approx 1$ indicate that result of the unfolding is not biased and the statistical uncertainty is neither overestimated nor underestimated.

In these cases, the RMS value can be replaced by the sigma parameter derived from the gaussian fit, σ_G, to the distributions described above, which also provides information about the position of the peak.

In the following, the results of the aforementioned study are presented only for the $e^\pm\mu^\mp$ channel as example.

The results of this study are shown in Figures D.2 and D.3 for the different bins of the top quark p_T distribution. The black histogram corresponds to the nominal (non-reweighted) input distribution. The different colours represent the different slopes used to reweight the input distribution. A gaussian fit is also performed to the nominal distribution and indicated in the plots. From these plots it can be seen that peak position of the gaussian is close to the corresponding theory prediction (see Figure D.1). In addition, given the separation of different coloured histograms for the different slopes, it seems that the true level information can be easily distinguished by the unfolding method, even in case of large

[†]RMS stands for "root mean square"; refers to the Gaussian RMS width, i.e. the standard deviation

[‡]SVD stands for "singular value decomposition" as given by the name of the unfolding method used in this work

statisical fluctuations in data. Moreover, σ_G/σ_{SVD} values are indeed ≈ 1 for all bins. The same is observed for the e^+e^- and $\mu^+\mu^-$ channels.

From this closure test it can be concluded that the unfolding method used in this work performs well also when using data samples with relatively low statistics.

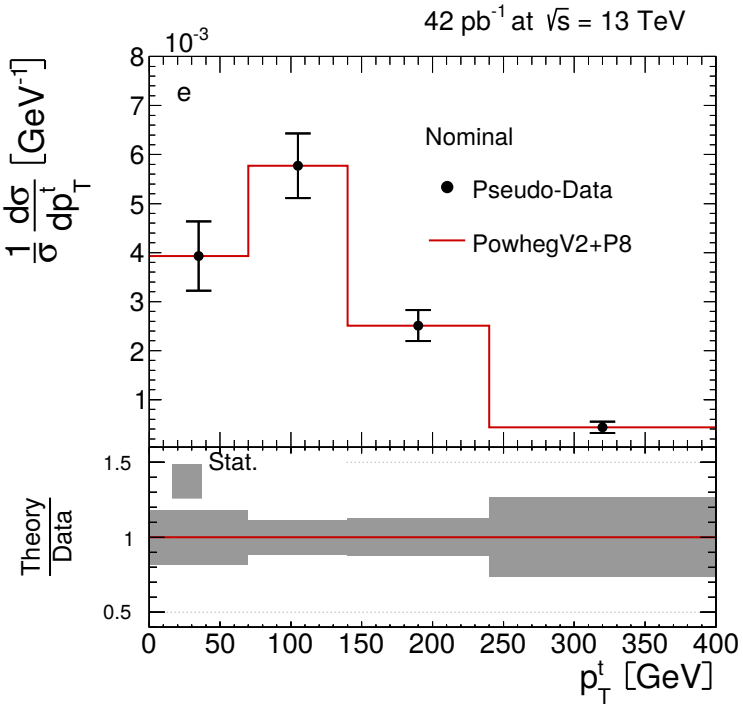

Figure D.1 Normalized differential $t\bar{t}$ production cross sections as a function of the top quark p_T using a basic (non-reweighted and non-smeared) pseudo-data sample based on POWHEG v2+PYTHIA8 and unfolded using the reference POWHEG v2+PYTHIA8 simulation relevant for this analysis. The results are presented for the $e^{\pm}\mu^{\mp}$ channel.

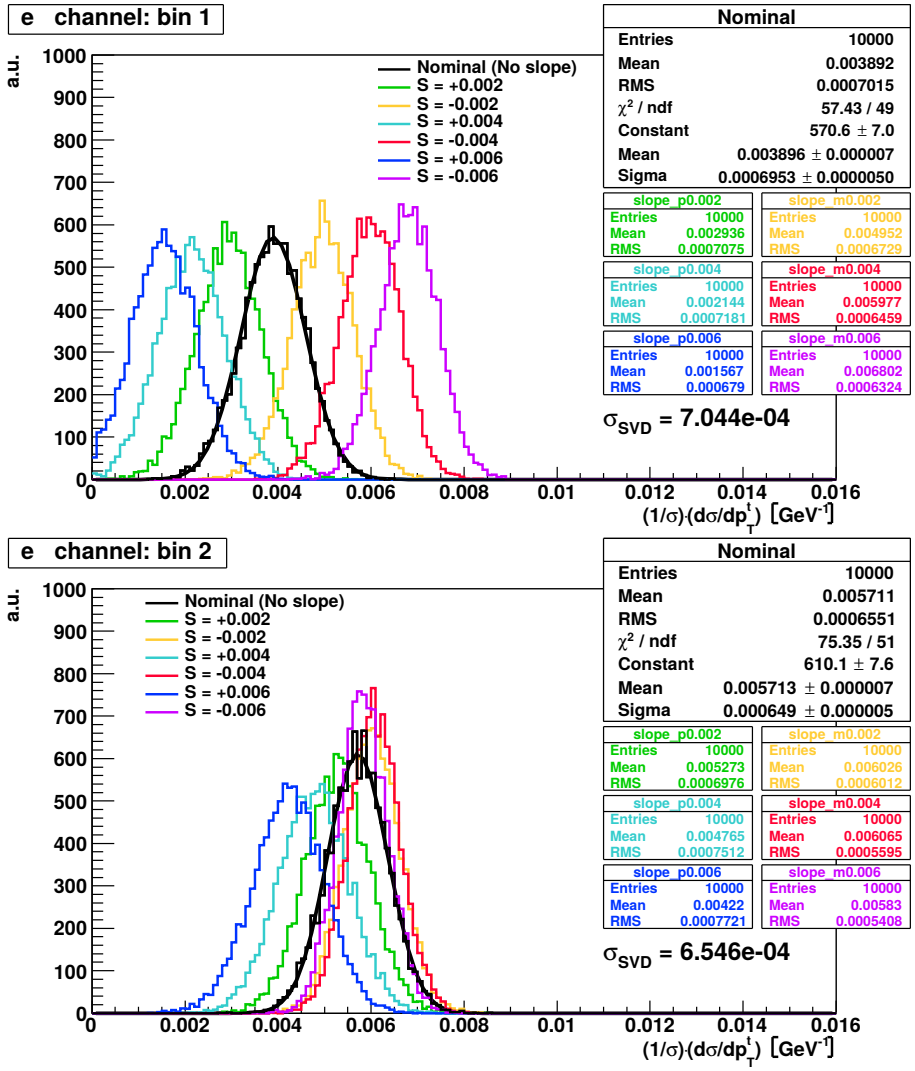

Figure D.2 Normalized differential $t\bar{t}$ production cross section as a function of the top quark p_T from 10000 pseudo-experiments in bin [0.0, 70.0) GeV (upper plot) and in bin [70.0, 140.0) GeV (lower plot). The results are presented for the $e^{\pm}\mu^{\mp}$ channel, for variations of the shape of the signal with different slopes: no slope (nominal), ±0.002, ±0.004, and ±0.006.

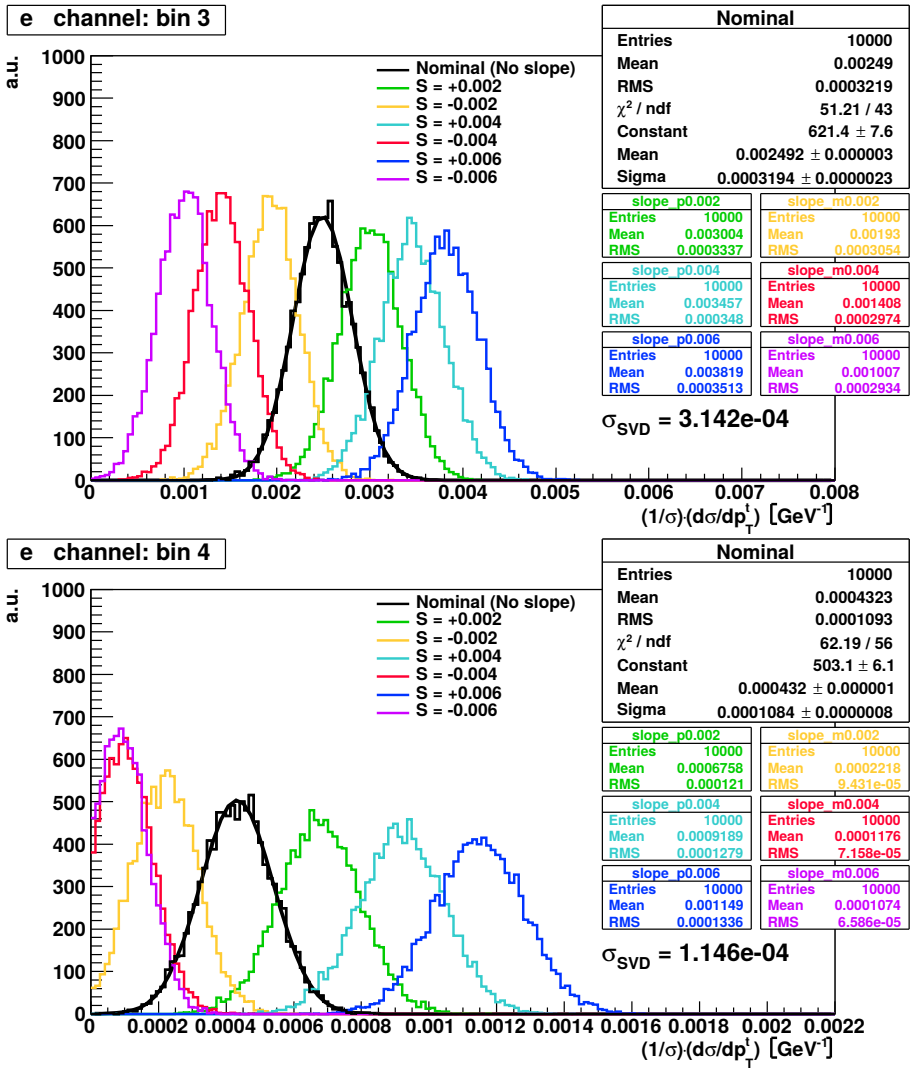

Figure D.3 Normalized differential $t\bar{t}$ production cross section as a function of the top quark p_T from 10000 pseudo-experiments in bin [140.0, 240.0) GeV (upper plot) and in bin [240.0, 400.0) GeV (lower plot). The results are presented for the the $e^{\pm}\mu^{\mp}$ channel, for variations of the shape of the signal with different slopes: no slope (nominal), ±0.002, ±0.004, and ±0.006.

D.2 Closure test verifying the influence of the top quark p_T mismodelling on the unfolded results

Here, a simple closure test targeted to verify the effect of the top quark p_T mismodelling on the unfolded results is presented. This closure test was conducted in the context of the normalized differential $t\bar{t}$ production cross section measurement presented in Section 7.1.2. This measurement is performed in the dilepton decay channel using the complete data sample recorded in 2015 by the CMS detector during pp collisions at $\sqrt{s} = 13$ TeV, corresponding to an integrated luminosity $L = 2.2$ fb^{-1}.

As can be seen in Figure 7.2, the distribution of the top quark transverse momentum is mismodelled by the Powheg v2+Pythia8. The data unfolding performed in this measurement uses the Powheg v2+Pythia8 simulation as basis model. Obviously, the top quark p_T mismodelling propagates to all information provided by the simulation for the unfolding, in particular to the normalization and shape of $t\bar{t}$ signal and $t\bar{t}$ background processes, and, thus, to the response matrices. To verify an effect of this mismodelling on the unfolded result, a simple study can be performed via the top quark p_T reweighting of the reference $t\bar{t}$ simulation to the data and using it to determine the unfolded result as would be done in the standard analysis. As given by Equations 5.3 and 5.5 (see Section 5.2), the unfolded data is obtained after the background subtraction. The potential changes in the normalization of unfolded data due to the top quark p_T reweighting of the reference $t\bar{t}$ simulation are automatically cancelled due to the signal fraction coefficient f_{sig}. Moreover, considering that the response matrix is governed by the detector resolution to the studied observable and this resolution is expected to be independent from the shape of the measured spectrum, the response matrix is expected to be mostly unaffected by the aforementioned reweighting. However, the improvement in the modelling of the top quark p_T affects the shape of the $t\bar{t}$ background subtracted from the data. Thus, the unfolded results are required to be checked for the sensitivity to this effect.

To perform the aforementioned study, the normalized differential $t\bar{t}$ production cross section are measured as a function of the top quark p_T. Two measurements are conducted in completely the same way, but in the first case the standard $t\bar{t}$ simulation is used and in the second case this $t\bar{t}$ simulation is reweighted to match the data. As mentioned above, the reweighting changes the $t\bar{t}$ signal and the $t\bar{t}$ background, as well as the relevant response matrix. The reconstructed top quark p_T distribution before and after the reweighting is shown in Figure D.4 (the details of the reweighting procedure are omitted). To clarify, when performing the measurement in the second case, the reconstructed data have been subtracted by the reweighted $t\bar{t}$ background and unfolded using the reweighted response matrix. The results of both measurements are shown in Figure D.5. As can be seen from the figure,

the effect of the reweighting on the unfolded results is negligible. Thus, this closure test demonstrates that the unfolded results are not affected by the top quark p_T mismodelling present in the basis model used for the unfolding.

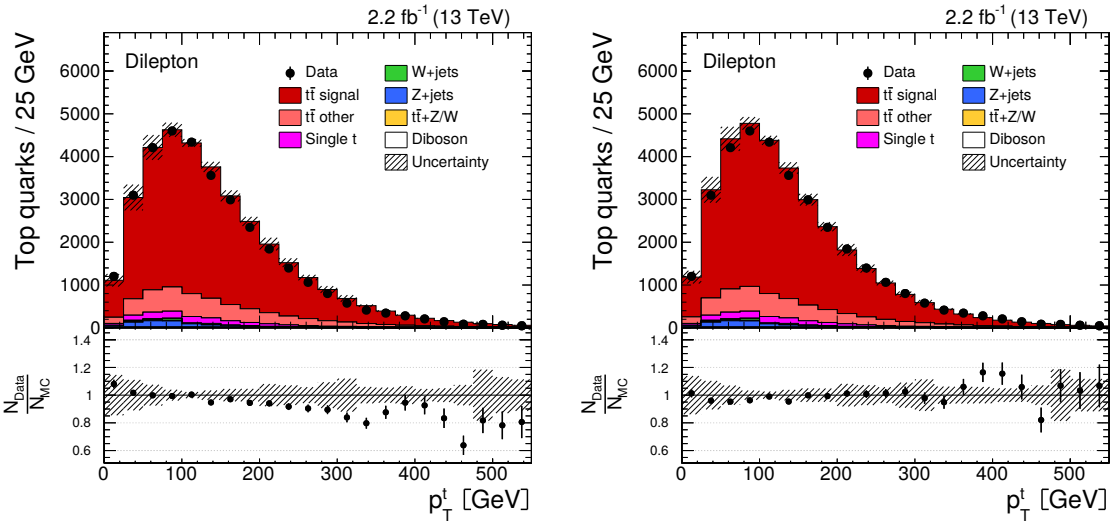

Figure D.4 The reconstructed top quark p_T distribution before (left) and after (right) the reweighting of the reference $t\bar{t}$ simulation POWHEG v2+PYTHIA8.

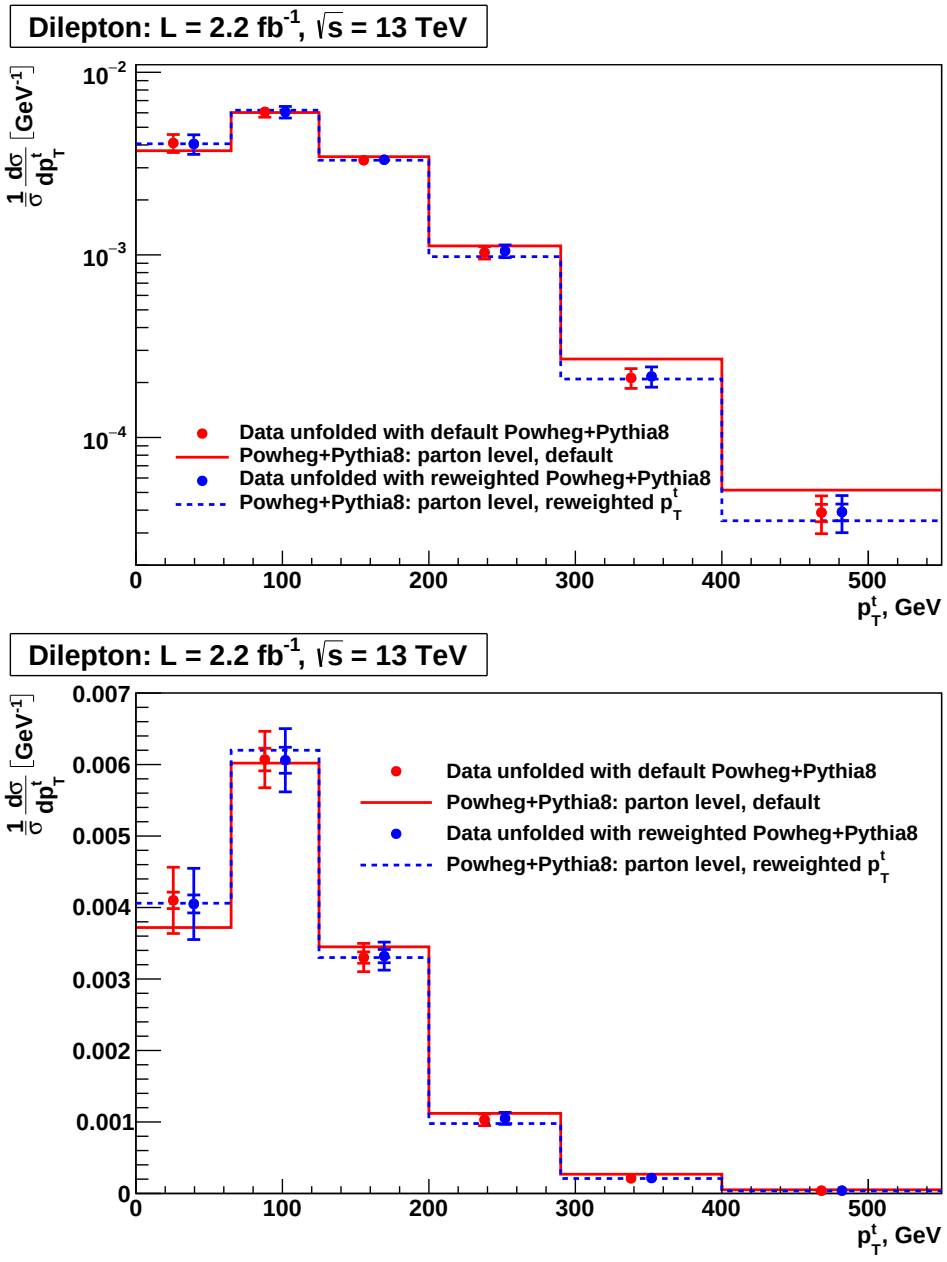

Figure D.5 Normalized differential $t\bar{t}$ production cross sections measured as a function of the top quark p_T before and after the top quark p_T reweighting in the basis simulation (POWHEG v2+PYTHIA8) used for the unfolding. The effect of the reweighting on the unfolded results is negligible. The upper plot is given with the logarithmic scale for the vertical axis.

Bibliography

[1] Particle Data Group (C. Patrignani et al.), *The Review of Particle Physics*, Chin. Phys. C **40:100001** (2016), and 2017 update.

[2] Particle Data Group, *Quarks (summary tables)*, http://pdg.lbl.gov/2017/tables/rpp2017-sum-quarks.pdf.

[3] ATLAS Collaboration, *Measurement of top quark pair differential cross sections in the dilepton channel in pp collisions at* $\sqrt{s}$ *= 7 and 8 TeV with ATLAS*, Phys. Rev. D **94:092003** (2016), https://doi.org/10.1103/PhysRevD.94.092003.

[4] ATLAS Collaboration, *Measurements of top-quark pair differential cross-sections in the lepton+jets channel in pp collisions at* $\sqrt{s}$ *= 8 TeV using the ATLAS detector*, Eur. Phys. J. C **76:538** (2016), https://doi.org/10.1140/epjc/s10052-016-4366-4.

[5] ATLAS Collaboration, *Measurements of top-quark pair differential cross-sections in the lepton+jets channel in pp collisions at* $\sqrt{s}$ *= 13 TeV using the ATLAS detector*, J. High Energ. Phys. **2017:191** (2017), https://doi.org/10.1007/JHEP11(2017)191.

[6] ATLAS Collaboration, *Measurements of top-quark pair differential cross-sections in the* $e\mu$ *channel in pp collisions at* $\sqrt{s}$ *= 13 TeV using the ATLAS detector*, Eur. Phys. J. C **77:292** (2017), https://doi.org/10.1140/epjc/s10052-017-4821-x.

[7] CMS Collaboration, *Measurement of differential top-quark-pair production cross sections in pp collisions at* $\sqrt{s}$ *= 7 TeV*, Eur. Phys. J. C **73:2339** (2013), https://doi.org/10.1140/epjc/s10052-013-2339-4.

[8] CMS Collaboration, *Measurement of the differential cross section for top quark pair production in pp collisions at* $\sqrt{s}$ *= 8 TeV*, Eur. Phys. J. C **75:542** (2015), https://doi.org/10.1140/epjc/s10052-015-3709-x.

[9] CMS Collaboration, *Measurement of normalized differential* $t\bar{t}$ *cross sections in the dilepton channel from pp collisions at* $\sqrt{s}$ *= 13 TeV*, J. High Energ. Phys. **submitted** (2017), arXiv:1708.07638 [hep-ex].

[10] CMS Collaboration, *Measurement of differential cross sections for top quark pair production using the lepton+jets final state in proton-proton collisions at 13 TeV*, Phys. Rev. D **95:092001** (2017), https://doi.org/10.1103/PhysRevD.95.092001.

[11] CMS Collaboration, *Measurement of differential cross sections for the production of top quark pairs and of additional jets in lepton+jets events from pp collisions at* $\sqrt{s}$ *= 13 TeV*, Phys. Rev. D. **submitted** (2018), arXiv:1803.08856 [hep-ex].

[12] CMS Collaboration, *First measurement of the differential cross section for $t\bar{t}$ production in the dilepton final state at $\sqrt{s}$ = 13 TeV*, CMS-PAS-TOP-15-010 (2015), https://cds.cern.ch/record/2047866/.

[13] CMS Collaboration, *Measurement of the differential cross section for $t\bar{t}$ production in the dilepton final state at $\sqrt{s}$ = 13 TeV*, CMS-PAS-TOP-16-011 (2016), https://cds.cern.ch/record/2140061/.

[14] J. H. Kühn et al., *Charge Asymmetry in Hadroproduction of Heavy Quarks*, Phys. Rev. Lett. **81:49** (1998), https://doi.org/10.1103/PhysRevLett.81.49.

[15] C. Gross et al., *Light axigluon explanation of the Tevatron $t\bar{t}$ asymmetry and multijet signals at the LHC*, Phys. Rev. D **87:014004** (2013), https://doi.org/10.1103/PhysRevD.87.014004.

[16] P. Langacker, *The physics of heavy Z′ gauge bosons*, Rev. Mod. Phys. **81:1199** (2009), https://doi.org/10.1103/RevModPhys.81.1199.

[17] R. Gaitan et al., *Top quark chromoelectric and chromomagnetic dipole moments in a two Higgs doublet model with CP violation*, Phys. Rev. D **92:094025** (2015), https://doi.org/10.1103/PhysRevD.92.094025.

[18] Y. Chong-Xing et al., *Top Quark Chromomagnetic Dipole Moment in the Littlest Higgs Model with T-Parity*, Commun. Theor. Phys. **50:441** (2008), https://doi.org/10.1088/0253-6102/50/2/32.

[19] R. Martinez et al., *Anomalous chromomagnetic dipole moment of the top quark in the standard model and beyond*, Phys. Rev. D **65:057301** (2002), https://doi.org/10.1103/PhysRevD.65.057301.

[20] M. Fabbrichesi et al., *Stringent limits on top-quark compositeness from $t\bar{t}$ production at the Tevatron and the LHC*, Phys. Rev. D **89:074028** (2014), https://doi.org/10.1103/PhysRevD.89.074028.

[21] G. Altarelli, *The Standard Model of Particle Physics*, CERN-PH-TH/2005-206 (2005), arXiv:hep-ph/0510281.

[22] M. E. Peskin and D. V. Schroeder, *An Introduction to Quantum Field Theory*, Addison-Wesley, 1995.

[23] Carsten Burgard, *Example: Standard model of physics (subject to copyright protection: licensed under "Attribution 2.5 Generic (CC BY 2.5)")*, http://www.texample.net/tikz/examples/model-physics/.

[24] L3 Collaboration, *Measurement of the Running of the Fine-Structure Constant*, Phys. Lett. B **476:40-48** (2000), https://doi.org/10.1016/S0370-2693(00)00122-2.

[25] Particle Data Group, *Gauge and Higgs Bosons (summary tables)*, http://pdg.lbl.gov/2017/tables/rpp2017-sum-gauge-higgs-bosons.pdf.

[26] A. Höcker et al., *CP Violation and the CKM Matrix*, Ann. Rev. Nucl. Part. Sci. **56:501-567** (2006), https://doi.org/10.1146/annurev.nucl.56.080805.140456.

[27] CMS Collaboration, *Measurement of the inclusive 3-jet production differential cross section in proton–proton collisions at 7 TeV and determination of the strong coupling constant in the TeV range*, Eur. Phys. J. C **75:186** (2015), https://doi.org/10.1140/epjc/s10052-015-3376-y.

[28] S. L. Glashow, *Partial-symmetries of weak interactions*, Nuclear Physics **22:579-588** (1961), https://doi.org/10.1016/0029-5582(61)90469-2.

[29] G. Altarelli, *The Standard Electroweak Theory and Beyond*, CERN-TH/2000-291 (2000), arXiv:hep-ph/0011078v1.

[30] ALEPH Collaboration, CDF Collaboration, D0 Collaboration, DELPHI Collaboration, L3 Collaboration, OPAL Collaboration, SLD Collaboration, LEP Electroweak Working Group, Tevatron Electroweak Working Group, SLD electroweak heavy flavour groups, *Precision Electroweak Measurements and Constraints on the Standard Model*, CERN-PH-EP/2010-095 (2010), arXiv:1012.2367v2 [hep-ex].

[31] P. W. Higgs, *Broken Symmetries and the Masses of Gauge Bosons*, Phys. Rev. Lett. **13:508** (1964), https://doi.org/10.1103/PhysRevLett.13.508.

[32] ATLAS Collaboration, *Observation of a new particle in the search for the Standard Model Higgs boson with the ATLAS detector at the LHC*, Phys. Lett. B **716:1-29** (2012), https://doi.org/10.1016/j.physletb.2012.08.020.

[33] CMS Collaboration, *Observation of a new boson at a mass of 125 GeV with the CMS experiment at the LHC*, Phys. Lett. B **716:30-61** (2012), https://doi.org/10.1016/j.physletb.2012.08.021.

[34] S. T. Petcov, *The Nature of Massive Neutrinos*, Adv. High Energy Phys. **2013:852987** (2013), https://doi.org/10.1155/2013/852987.

[35] S. V. Troitsky, *Unsolved problems in particle physics*, Phys.-Usp. **55:72** (2012), https://doi.org/10.3367/UFNe.0182.201201d.0077.

[36] S. P. Martin, *A Supersymmetry Primer*, Advanced Series on Directions in High Energy Physics (Perspectives on Supersymmetry) **18:1-98** (1998), https://doi.org/10.1142/9789812839657_0001.

[37] L. Randall et al., *Large Mass Hierarchy from a Small Extra Dimension*, Phys. Rev. Lett. **83:3370** (1999), https://doi.org/10.1103/PhysRevLett.83.3370.

[38] M. Schmaltz and D. Tucker-Smith, *Little Higgs Review*, Ann. Rev. Nucl. Part. Sci. **55:229-270** (2005), https://doi.org/10.1146/annurev.nucl.55.090704.151502.

[39] M. Kobayashi et al., *CP-Violation in the Renormalizable Theory of Weak Interaction*, Progress of Theoretical Physics **49:652–657** (1973), https://doi.org/10.1143/PTP.49.652.

[40] U. Husemann, *Top-Quark Physics: Status and Prospects*, Progress in Particle and Nuclear Physics **95:48-97** (2017), https://doi.org/10.1016/j.ppnp.2017.03.002.

[41] J. C. Collins et al., *Factorization of Hard Processes in QCD*, Adv. Ser. Direct. High Energy Phys. **5:1-91** (1988), arXiv:hep-ph/0409313 [hep-ph].

[42] B. Delamotte, *A hint of renormalization*, Am. J. Phys **72:170** (2004), https://doi.org/10.1119/1.1624112.

[43] NNPDF Collaboration, *Parton distributions from high-precision collider data*, Eur. Phys. J. C **submitted** (2017), arXiv:1706.00428v2 [hep-ph].

[44] M. Beneke et al., *Hadronic top-quark pair production with NNLL threshold resummation*, Nuclear Physics B **855:695** (2012), https://doi.org/10.1016/j.nuclphysb.2011.10.021.

[45] M. Cacciari et al., *Top-pair production at hadron colliders with next-to-next-to-leading logarithmic soft-gluon resummation*, Physics Letters B **710:612** (2012), https://doi.org/10.1016/j.physletb.2012.03.013.

[46] P. Bärnreuther et al., *Percent-Level-Precision Physics at the Tevatron: Next-to-Next-to-Leading Order QCD Corrections to* $q\bar{q} \to t\bar{t} + X$, Phys. Rev. Lett. **109:132001** (2012), https://doi.org/10.1103/PhysRevLett.109.132001.

[47] M. Czakon and A. Mitov, *NNLO corrections to top-pair production at hadron colliders: the all-fermionic scattering channels*, J. High Energ. Phys. **2012:54** (2012), https://doi.org/10.1007/JHEP12(2012)054.

[48] M. Czakon and A. Mitov, *NNLO corrections to top pair production at hadron colliders: the quark-gluon reaction*, J. High Energ. Phys. **2013:80** (2013), https://doi.org/10.1007/JHEP01(2013)080.

[49] M. Czakon et al., *Total Top-Quark Pair-Production Cross Section at Hadron Colliders Through* $O(\alpha_S^4)$, Phys. Rev. Lett. **110:252004** (2013), https://doi.org/10.1103/PhysRevLett.110.252004.

[50] M. Czakon and A. Mitov, *Top++: A program for the calculation of the top-pair cross-section at hadron colliders*, Comput. Phys. Commun. **185:2930** (2014), https://doi.org/10.1016/j.cpc.2014.06.021.

[51] M. Czakon et al., *High-Precision Differential Predictions for Top-Quark Pairs at the LHC*, Phys. Rev. Lett. **116:082003** (2016), https://doi.org/10.1103/PhysRevLett.116.082003.

[52] M. Czakon et al., *Top-pair production at the LHC through NNLO QCD and NLO EW*, J. High Energ. Phys. **2017:186** (2017), https://doi.org/10.1007/JHEP10(2017)186.

[53] N. Kidonakis, *NNNLO soft-gluon corrections for the top-quark* p_T *and rapidity distributions*, Phys. Rev. D **91:031501(R)** (2015), https://doi.org/10.1103/PhysRevD.91.031501.

[54] D0 Collaboration, *Useful Diagrams of Top Signals and Backgrounds*, https://www-d0.fnal.gov/Run2Physics/top/top_public_web_pages/top_feynman_diagrams.html.

[55] LHCTopWG, *NLO single-top channel cross sections: ATLAS-CMS recommended predictions for single-top cross sections using the Hathor v2.1 program (topic revision: r34)*, https://twiki.cern.ch/twiki/bin/view/LHCPhysics/SingleTopRefXsec.

[56] M. Aliev et al., *HATHOR – HAdronic Top and Heavy quarks crOss section calculatoR*, Comput. Phys. Commun. **182:1034-1046** (2011), https://doi.org/10.1016/j.cpc.2010.12.040.

[57] P. Kant et al., *HATHOR for single top-quark production: Updated predictions and uncertainty estimates for single top-quark production in hadronic collisions*, Comput. Phys. Commun. **191:74-89** (2015), https://doi.org/10.1016/j.cpc.2015.02.001.

[58] A. Giammanco, *Single top quark production at the LHC*, Reviews in Physics **1:1-12** (2016), https://doi.org/10.1016/j.revip.2015.12.001.

[59] CMS Collaboration, *Measurement of spin correlations in $t\bar{t}$ production using the matrix element method in the muon+jets final state in pp collisions at $\sqrt{s} = 8$ TeV*, Phys. Lett. B **758:321-346** (2016), https://doi.org/10.1016/j.physletb.2016.05.005.

[60] U. Haisch et al., *Simplified dark matter top-quark interactions at the LHC*, J. High Energ. Phys. **2015:78** (2015), https://doi.org/10.1007/JHEP06(2015)078.

[61] L. Evans (ed.) and P. Bryant (ed.), *LHC Machine*, JINST **3:S08001** (2008), https://doi.org/10.1088/1748-0221/3/08/S08001.

[62] TE-EPC-LPC in LHC, *Accelerator complex at CERN*, https://te-epc-lpc.web.cern.ch/te-epc-lpc/machines/pagesources/Cern-Accelerator-Complex.jpg.

[63] ALICE Collaboration, *The ALICE experiment at the CERN LHC*, JINST **3:S08002** (2008), https://doi.org/10.1088/1748-0221/3/08/S08002.

[64] ATLAS Collaboration, *The ATLAS Experiment at the CERN Large Hadron Collider*, JINST **3:S08003** (2008), https://doi.org/10.1088/1748-0221/3/08/S08003.

[65] CMS Collaboration, *The CMS experiment at the CERN LHC*, JINST **3:S08004** (2008), https://doi.org/10.1088/1748-0221/3/08/S08004.

[66] LHCb Collaboration, *The LHCb Detector at the LHC*, JINST **3:S08005** (2008), https://doi.org/10.1088/1748-0221/3/08/S08005.

[67] CMS Collaboration, *CMS Physics: Technical Design Report Volume 1: Detector Performance and Software*, Geneva : CERN (2006), CMS-TDR-8-1.

[68] CMS Collaboration, *CMS Luminosity Measurements for the 2016 Data Taking Period*, CMS-PAS-LUM-17-001, 2017.

[69] LHC-Commissioning, *Performance 2016*, https://lhc-commissioning.web.cern.ch/lhc-commissioning/performance/2016-performance.htm.

[70] CMS Collaboration, *CMS Physics : Technical Design Report Volume 2: Physics Performance*, Geneva : CERN (2007), CMS-TDR-8-2.

[71] CMS Collaboration, *Figures from the CMS Physics Technical Design Report Volume 1: Detector Performance and Software*, CMS-PHO-GEN-2006-001, 2006.

[72] L. Borrello et al., *Sensor Design for the CMS Silicon Strip Tracker*, CMS-NOTE-2003-020, 2003.

[73] CMS Collaboration, *Energy calibration and resolution of the CMS electromagnetic calorimeter in pp collisions at* $\sqrt{s}$ *= 7 TeV*, JINST **8:P09009** (2013), arXiv:1306.2016v2 [hep-ex].

[74] CMS HCAL Collaboration, *Design, performance, and calibration of CMS hadron-barrel calorimeter wedges*, Eur. Phys. J. C **55:159** (2008), https://doi.org/10.1140/epjc/s10052-008-0573-y.

[75] CMS HCAL Collaboration, *Design, Performance, and Calibration of CMS Hadron Endcap Calorimeters*, CMS-NOTE-2008-010, 2008.

[76] CMS HCAL Collaboration, *Design, performance, and calibration of CMS forward calorimeter wedges*, Eur. Phys. J. C **53:139** (2008), https://doi.org/10.1140/epjc/s10052-007-0459-4.

[77] CMS Collaboration, *The CMS muon project: Technical Design Report*, Geneva : CERN (1997), CMS-TDR-3.

[78] CMS Collaboration, *The performance of the CMS muon detector in proton-proton collisions at* $\sqrt{s}$ *= 7 TeV at the LHC*, JINST **8:P11002** (2013), arXiv:1306.6905v2 [physics.ins-det].

[79] CMS Collaboration, *Technical proposal for the upgrade of the CMS detector through 2020*, Geneva : CERN (2011), CMS-UG-TP-1.

[80] CMS Collaboration (J. Butler et al.), *Technical Proposal for the Phase-II Upgrade of the CMS Detector*, Geneva : CERN (2015), CMS-TDR-15-02.

[81] N. Metropolis et al., *The Monte Carlo Method*, J. Am. Stat. Assoc. **44:247** (1949), https://doi.org/10.1080/01621459.1949.10483310.

[82] N. Bartosik, *website (2016)*, http://bartosik.pp.ua.

[83] P. Nason, *A new method for combining NLO QCD with shower Monte Carlo algorithms*, J. High Energ. Phys. **11:040** (2004), https://doi.org/10.1088/1126-6708/2004/11/040.

[84] S. Frixione et al., *Matching NLO QCD computations with parton shower simulations: the POWHEG method*, J. High Energ. Phys. **11:070** (2007), https://doi.org/10.1088/1126-6708/2007/11/070.

[85] S. Alioli et al., *A general framework for implementing NLO calculations in shower Monte Carlo programs: the POWHEG BOX*, J. High Energ. Phys. **2010:43** (2010), https://doi.org/10.1007/JHEP06(2010)043.

[86] S. Frixione et al., *A positive-weight next-to-leading-order Monte Carlo for heavy flavour hadroproduction*, J. High Energ. Phys. **09:126** (2007), https://doi.org/10.1088/1126-6708/2007/09/126.

[87] J. Alwall et al., *The automated computation of tree-level and next-to-leading order differential cross sections, and their matching to parton shower simulations*, J. High Energ. Phys. **2014:79** (2014), https://doi.org/10.1007/JHEP07(2014)079.

[88] P. Artoisenet et al., *Automatic spin-entangled decays of heavy resonances in Monte Carlo simulations*, J. High Energ. Phys. **2013:15** (2013), https://doi.org/10.1007/JHEP03(2013)015.

[89] T. Sjöstrand et al., *An introduction to PYTHIA 8.2*, Comput. Phys. Commun. **191:159** (2015), https://doi.org/10.1016/j.cpc.2015.01.024.

[90] M. Bähr et al., *Herwig++ physics and manual*, Eur. Phys. J. C **58:639** (2008), https://doi.org/10.1140/epjc/s10052-008-0798-9.

[91] A. Buckley et al., *General-purpose event generators for LHC physics*, Physics Reports **504:145-233** (2011), https://doi.org/10.1016/j.physrep.2011.03.005.

[92] T. Sjöstrand et al., *Transverse-Momentum-Ordered Showers and Interleaved Multiple Interactions*, Eur. Phys. J. C **39:129** (2005), https://doi.org/10.1140/epjc/s2004-02084-y.

[93] B. Andersson et al., *Parton fragmentation and string dynamics*, Phys. Rep. **97:31-145** (1983), https://doi.org/10.1016/0370-1573(83)90080-7.

[94] T. Sjöstrand et al., *PYTHIA 6.4 physics and manual*, J. High Energ. Phys. **05:026** (2006), https://doi.org/10.1088/1126-6708/2006/05/026.

[95] D. Amati et al., *Preconfinement as a property of perturbative QCD*, Phys. Lett. B **83:87-92** (1979), https://doi.org/10.1016/0370-2693(79)90896-7.

[96] R. Field, *Min-Bias and the Underlying Event at the LHC*, Lecture presented at XXXI Physics in Collision **PIC2011** (2012), arXiv:1202.0901 [hep-ph].

[97] S. Argyropoulos et al., *Effects of color reconnection on $t\bar{t}$ final states at the LHC*, J. High Energ. Phys. **2014:43** (2014), https://doi.org/10.1007/JHEP11(2014)043.

[98] S. Argyropoulos et al., *Color reconnection in $t\bar{t}$ final states*, https://indico.cern.ch/event/340357/contributions/1733545/attachments/667577/917604/ColorReconnection.pdf.

[99] J. R. Christiansen et al., *String formation beyond leading colour*, J. High Energ. Phys. **2015:3** (2015), https://doi.org/10.1007/JHEP08(2015)003.

[100] PYTHIA event generator, *Colour Reconnection*, http://home.thep.lu.se/Pythia/pythia82html/ColourReconnection.html.

[101] S. Gieseke et al., *Colour reconnections in Herwig++*, Eur. Phys. J. C **72:2225** (2012), https://doi.org/10.1140/epjc/s10052-012-2225-5.

[102] S. Agostinelli et al., *Geant4 – a simulation toolkit*, Nucl. Instr. Meth. Phys. Res. A **506:250** (2003), https://doi.org/10.1016/S0168-9002(03)01368-8.

[103] M. Rovere, *The Data Quality Monitoring Software for the CMS experiment at the LHCC*, J. Phys.: Conf. Ser. **664:072039** (2015), https://doi.org/10.1088/1742-6596/664/7/072039.

[104] CMS Collaboration, *Event generator tunes obtained from underlying event and multiparton scattering measurements*, Eur. Phys. J. C **76:155** (2016), https://doi.org/10.1140/epjc/s10052-016-3988-x.

[105] CMS Collaboration, *Investigations of the impact of the parton shower tuning in Pythia 8 in the modelling of $t\bar{t}$ at $\sqrt{s}$ = 8 and 13 TeV*, CMS-PAS-TOP-16-021, 2016.

[106] R. Frederix and S. Frixione, *Merging meets matching in MC@NLO*, J. High Energ. Phys. **2012:61** (2012), https://doi.org/10.1007/JHEP12(2012)061.

[107] M. H. Seymour et al., *Constraining MPI models using σ_{eff} and recent Tevatron and LHC Underlying Event data*, J. High Energ. Phys. **2013:113** (2013), https://doi.org/10.1007/JHEP10(2013)113.

[108] NNPDF Collaboration, *Parton distributions for the LHC Run II*, J. High Energ. Phys. **2015:40** (2015), https://doi.org/10.1007/JHEP04(2015)040.

[109] E. Re, *Single-top Wt-channel production matched with parton showers using the POWHEG method*, Eur. Phys. J. C **71:1547** (2007), https://doi.org/10.1140/epjc/s10052-011-1547-z.

[110] N. Kidonakis, *Top Quark Production*, KSU-HEP-110113 (2013), arXiv:1311.0283 [hep-ph].

[111] N. Kidonakis, *Two-loop soft anomalous dimensions for single top quark associated production with a W^- or H^-*, Phys. Rev. D **82:054018** (2010), https://doi.org/10.1103/PhysRevD.82.054018.

[112] J. M. Campbell et al., *Vector boson pair production at the LHC*, J. High Energ. Phys. **2011:18** (2011), https://doi.org/10.1007/JHEP07(2011)018.

[113] T. Gehrmann et al., *W^+W^- Production at Hadron Colliders in Next to Next to Leading Order QCD*, Phys. Rev. Lett. **113:212001** (2014), https://doi.org/10.1103/PhysRevLett.113.212001.

[114] J. M. Campbell and R. K. Ellis, *MCFM for the Tevatron and the LHC*, Nucl. Phys. B - Proceedings Supplements **205–206:10-15** (2010), https://doi.org/10.1016/j.nuclphysbps.2010.08.011.

[115] R. Gavin et al., *FEWZ 2.0: A code for hadronic Z production at next-to-next-to-leading order*, Comput. Phys. Commun. **182:2388-2403** (2011), https://doi.org/10.1016/j.cpc.2011.06.008.

[116] R. Gavin et al., *W physics at the LHC with FEWZ 2.1*, NUHEP-TH/12-01 (2012), arXiv:1201.5896 [hep-ph].

[117] Y. Li and F. Petriello, *Combining QCD and electroweak corrections to dilepton production in the framework of the FEWZ simulation code*, Phys. Rev. D **86:094034** (2012), https://doi.org/10.1103/PhysRevD.86.094034.

[118] S. Hoeche et al., *Matching Parton Showers and Matrix Elements*, Proceedings of the "HERA and the LHC" workshop, CERN/DESY 2004/2005 (2006), arXiv:hep-ph/0602031.

[119] P. Skands et al., *Tuning PYTHIA 8.1: the Monash 2013 tune*, Eur. Phys. J. C **74:3024** (2014), https://doi.org/10.1140/epjc/s10052-014-3024-y.

[120] CMS Collaboration, *Particle-flow reconstruction and global event description with the CMS detector*, JINST **12:P10003** (2017), https://doi.org/10.1088/1748-0221/12/10/P10003.

[121] CMS Collaboration, *Description and performance of track and primary-vertex reconstruction with the CMS tracker*, JINST **9:P10009** (2014), https://doi.org/10.1088/1748-0221/9/10/P10009.

[122] CMS Collaboration, *Measurement of the Top Quark Pair Production Cross Section in Proton-Proton Collisions at* $\sqrt{s}$ *= 13 TeV*, Phys. Rev. Lett. **116:052002** (2016), https://doi.org/10.1103/PhysRevLett.116.052002.

[123] CMS Collaboration, *Measurement of the* $t\bar{t}$ *production cross section using events in the* $e\mu$ *final state in pp collisions at* $\sqrt{s}$ *= 13 TeV*, Eur. Phys. J. C **77:172** (2017), https://doi.org/10.1140/epjc/s10052-017-4718-8.

[124] CMS Collaboration, *Muon Identification and Isolation efficiency on full 2016 dataset*, CMS-DP-2017-007, 2017.

[125] CMS Collaboration, *Measurement of the inclusive W and Z production cross sections in pp collisions at* $\sqrt{s}$ *= 7 TeV with the CMS experiment*, J. High Energ. Phys. **2011:132** (2011), https://doi.org/10.1007/JHEP10(2011)132.

[126] CMS Collaboration, *Electron and photon performance in CMS with the full 2016 data sample*, CMS-DP-2017-004, 2017.

[127] M. Cacciari et al., *The anti-*k_t *jet clustering algorithm*, J. High Energ. Phys. **0804:063** (2008), https://doi.org/10.1088/1126-6708/2008/04/063.

[128] M. Cacciari et al., *FastJet user manual*, Eur. Phys. J. C **72:1896** (2012), https://doi.org/10.1140/epjc/s10052-012-1896-2.

[129] CMS Collaboration, *Jet algorithms performance in 13 TeV data*, CMS-PAS-JME-16-003, 2017.

[130] CMS Collaboration, *Jet energy scale and resolution in the CMS experiment in pp collisions at 8 TeV*, JINST **12:P02014** (2017), arXiv:1607.03663v2 [hep-ex].

[131] CMS Collaboration, *Jet energy scale and resolution performances with 13TeV data*, CMS-DP-2016-020, 2016.

[132] T. Sakuma for the CMS Collaboration, *CMS-doc-12312-v1: Missing ET Schematic Diagram*, https://cms-docdb.cern.ch/cgi-bin/PublicDocDB/ShowDocument?docid=12312.

[133] CMS Collaboration, *Performance of the CMS missing transverse energy reconstruction in pp data at* $\sqrt{s} = 8$ *TeV*, JINST **10:P02006** (2015), https://doi.org/10.1088/1748-0221/10/02/P02006.

[134] CMS Collaboration, *Performance of missing energy reconstruction in 13 TeV pp collision data using the CMS detector*, CMS-PAS-JME-16-004, 2016.

[135] CMS Collaboration, *Identification of heavy-flavour jets with the CMS detector in pp collisions at 13 TeV*, JINST **submitted** (2017), arXiv:1712.07158v1 [physics.ins-det].

[136] CMS Collaboration, *Measurement of the* $t\bar{t}$ *production cross section and the top quark mass in the dilepton channel in pp collisions at* $\sqrt{s} = 7$ *TeV*, J. High Energ. Phys. **2011:49** (2011), https://doi.org/10.1007/JHEP07(2011)049.

[137] L. Sonnenschein, *Algebraic approach to solve* $t\bar{t}$ *dilepton equations*, Phys. Rev. D **72:095020** (2005), https://doi.org/10.1103/PhysRevD.72.095020.

[138] L. Sonnenschein, *Analytical solution of* $t\bar{t}$ *dilepton equations*, Phys. Rev. D **73:054015** (2006), https://doi.org/10.1103/PhysRevD.73.054015.

[139] CMS Collaboration, *Measurement of double-differential cross sections for top quark pair production in pp collisions at* $\sqrt{s} = 8$ *TeV and impact on parton distribution functions*, Eur. Phys. J. C **77:459** (2017), https://doi.org/10.1140/epjc/s10052-017-4984-5.

[140] I. Korol, *Measurement of Double Differential* $t\bar{t}$ *Production Cross Sections with the CMS Detector*, Universität Hamburg, Dr. Diss., DESY-THESIS-2016-011 (2016), https://doi.org/10.3204/DESY-THESIS-2016-011.

[141] A. Hoecker and V. Kartvelishvili, *SVD Approach to Data Unfolding*, Nucl. Instrum. Meth. A **372:469-481** (1996), arXiv:hep-ph/9509307v2.

[142] S. Schmitt, *Data Unfolding Methods in High Energy Physics*, EPJ Web Conf. **137:11008** (2017), https://doi.org/10.1051/epjconf/201713711008.

[143] A. N. Tikhonov, *Solution of incorrectly formulated problems and the regularization method*, Sov. Math. Dokl. **4:1035** (1963).

[144] ROOT Framework, *TSVDUnfold Class Reference*, https://root.cern.ch/doc/master/classTSVDUnfold.html.

[145] CMS Collaboration, *Object definitions for top quark analyses at the particle level*, CMS-NOTE-2017-004, 2017.

[146] PYTHIA event generator, *Particle Properties*, http://home.thep.lu.se/~torbjorn/pythia81html/ParticleProperties.html.

[147] LHCTopWG, *LHCTopWG - LHC Top Physics Working Group*, https://twiki.cern.ch/twiki/bin/view/LHCPhysics/LHCTopWG.

[148] M. Cacciari and G. P. Salam, *Pileup subtraction using jet areas*, Phys. Lett. B **659:119-126** (2008), https://doi.org/10.1016/j.physletb.2007.09.077.

[149] O. Behnke et al. (ed.), *Data Analysis in High Energy Physics: A Practical Guide to Statistical Methods*, WILEY-VCH, 2013.

[150] CMS Collaboration, *Top Quark Physics Analysis Group*, https://twiki.cern.ch/twiki/bin/view/CMSPublic/PhysicsResultsTOP.

[151] ATLAS Collaboration, *Measurement of the Inelastic Proton-Proton Cross Section at $\sqrt{s}$ = 13 TeV with the ATLAS Detector at the LHC*, Phys. Rev. Lett. **117:182002** (2016), https://doi.org/10.1103/PhysRevLett.117.182002.

[152] J. Alwall et al., *A standard format for Les Houches Event Files*, Comput. Phys. Commun. **176:300-304** (2007), arXiv:hep-ph/0609017v1.

[153] CMS Collaboration, *Measurement of the top quark mass using proton-proton data at $\sqrt{(s)}$ = 7 and 8 TeV* , Phys. Rev. D **93:072004** (2016), https://doi.org/10.1103/PhysRevD.93.072004.

[154] CMS Collaboration, *Measurement of the top quark mass with lepton+jets final states in pp collisions at $\sqrt{s}$ = 13 TeV*, CMS-PAS-TOP-17-007, 2017.

[155] PYTHIA event generator, *Fragmentation*, http://home.thep.lu.se/Pythia/pythia82html/Fragmentation.html.

[156] M. G. Bowler, *e^+e^- production of heavy quarks in the string model*, Z. Phys. C - Particles and Fields **11:169** (1981), https://doi.org/10.1007/BF01574001.

[157] CMS Collaboration, *Measurement of differential cross sections for top quark pair production and associated jets using the lepton+jets final state in proton-proton collisions at 13 TeV*, CMS-PAS-TOP-17-002, 2017.

[158] C. Peterson et al., *Scaling violations in inclusive e^+e^- annihilation spectra*, Phys. Rev. D **27:105** (1983), https://doi.org/10.1103/PhysRevD.27.105.

[159] Particle Data Group, *$B^{\pm}$ (review)*, http://pdg.lbl.gov/2017/listings/rpp2017-list-B-plus-minus.pdf.

[160] M. Guzzi et al., *Top-quark pair production at hadron colliders: differential cross section and phenomenological applications with DiffTop*, J. High Energ. Phys. **2015:82** (2015), https://doi.org/10.1007/JHEP01(2015)082.

[161] S. Dulat et al., *New parton distribution functions from a global analysis of quantum chromodynamics*, Phys. Rev. D **93:033006** (2016), https://doi.org/10.1103/PhysRevD.93.033006.

[162] A. D. Martin et al., *Parton distributions for the LHC*, Eur. Phys. J. C **63:189** (2009), https://doi.org/10.1140/epjc/s10052-009-1072-5.

[163] M. Czakon et al., *Dynamical scales for multi-TeV top-pair production at the LHC*, J. High Energ. Phys. **2017:71** (2017), https://doi.org/10.1007/JHEP04(2017)071.

[164] B. D. Pecjak et al., *Resummed Differential Cross Sections for Top-Quark Pairs at the LHC*, Phys. Rev. Lett. **116:202001** (2016), https://doi.org/10.1103/PhysRevLett.116.202001.

[165] D0 Collaboration and M. Czakon et al., *Measurement of the pole mass of the top quark using differential $t\bar{t}$ cross sections in $p\bar{p}$ collisions at $\sqrt{s}$ = 1.96 TeV*, D0 Note 6473-CONF, 2016.

[166] J. Tellinghuisen, *Statistical Error Propagation*, J. Phys. Chem. A **105:15** (2001), https://doi.org/10.1021/jp003484u.

[167] W. Bernreuther et al., *A set of top quark spin correlation and polarization observables for the LHC: Standard Model predictions and new physics contributions*, J. High Energ. Phys. **2015:1** (2015), https://doi.org/10.1007/JHEP12(2015)026.

[168] R. Frederix et al., *Top pair invariant mass distribution: a window on new physics*, J. High Energ. Phys. **01:047** (2009), https://doi.org/10.1088/1126-6708/2009/01/047.

[169] R. M. Harris et al., *Cross sections for leptophobic topcolor Z′ decaying to top–antitop*, Eur. Phys. J. C **72:2072** (2012), https://doi.org/10.1140/epjc/s10052-012-2072-4.

[170] X.-Q. Li et al., *Light top squark in precision top quark sample*, Phys. Rev. D **89:077703** (2014), https://doi.org/10.1103/PhysRevD.89.077703.

[171] C. P. Burgess, *Introduction to Effective Field Theory*, Ann. Rev. Nucl. Part. Sci. **57:329-362** (2007), https://doi.org/10.1146/annurev.nucl.56.080805.140508.

[172] D. B. Franzosi et al., *Probing the top-quark chromomagnetic dipole moment at next-to-leading order in QCD*, Phys. Rev. D **91:114010** (2015), https://doi.org/10.1103/PhysRevD.91.114010.

[173] B. M. Waugh et al., *HZTool and Rivet: Toolkit and Framework for the Comparison of Simulated Final States and Data at Colliders*, Contribution to CHEP06 conference (2006), arXiv:hep-ph/0605034.

[174] CMS Collaboration, *Measurements of $t\bar{t}$ spin correlations and top quark polarization using dilepton final states in pp collisions at $\sqrt{s}$ = 8 TeV*, Phys. Rev. D **93:052007** (2016), https://doi.org/10.1103/PhysRevD.93.052007.

[175] W. Bernreuther and Z.-G. Si, *Top quark spin correlations and polarization at the LHC: Standard model predictions and effects of anomalous top chromo moments*, Phys. Lett. B **725:115-122** (2013), https://doi.org/10.1016/j.physletb.2013.06.051.

[176] CMS Collaboration, *Measurements of differential cross sections for $t\bar{t}$ production in proton-proton collisions at $\sqrt{s}$ = 13 TeV using events containing two leptons*, CMS-TOP-17-014, in preparation.

[177] HEPData, *High Energy Physics Data Repository*, https://hepdata.net/.

[178] Q.-H. Cao et al., *Probing Higgs width and top quark Yukawa coupling from $t\bar{t}H$ and $t\bar{t}t\bar{t}$ productions*, Phys. Rev. D **95:053004** (2017), https://doi.org/10.1103/PhysRevD.95.053004.

[179] F. Bezrukov and M. Shaposhnikov, *Why should we care about the top quark Yukawa coupling?*, J. Exp. Theor. Phys. **120:335** (2015), https://doi.org/10.1134/S1063776115030152.

[180] G. Apollinari et al. (ed.), *High-Luminosity Large Hadron Collider (HL-LHC) : Preliminary Design Report*, Geneva : CERN (CERN Yellow Reports: Monographs, CERN-2015-005) (2015), https://doi.org/10.5170/CERN-2015-005.

[181] CLIC and CLICdp Collaborations, *Updated baseline for a staged Compact Linear Collider*, Geneva : CERN (CERN Yellow Reports: Monographs, CERN-2016-004) (2016), https://doi.org/10.5170/CERN-2016-004.

[182] M. Mangano (ed.), *Physics at the FCC-hh, a 100 TeV pp collider*, Geneva : CERN (CERN Yellow Reports: Monographs, 3/2017; CERN-2017-003-M) (2017), https://doi.org/10.23731/CYRM-2017-003.

[183] H. Baer et al., *The International Linear Collider Technical Design Report - Volume 2: Physics*, ILC-REPORT-2013-040 (2013), arXiv:1306.6352v1 [hep-ph].

Acknowledgments

First of all, I would like to thank Dr. Maria Aldaya Martin and Prof. Dr. Elisabetta Gallo for provided supervision and supporting me towards the successful completion of this work. Besides this, I would like to express my gratitude to other members of my thesis committee: Prof. Dr. Dieter Horns, Prof. Dr. Gudrid Moortgat-Pick, and Dr. Christian Sander.

I am thankful to Maria Aldaya Martin and Elisabetta Gallo for thoroughly proofreading my thesis. In this regard, my special thanks also go to Carmen Diez Pardos for commenting on my first draft which helped me to significantly improve it. In addition, I would like to thank Till Arndt, Paolo Gunnellini, James Keaveney, Gerrit Van Onsem, and Oleksandr Zenaiev for their valuable feedback on selected chapters of my thesis.

My special thanks go to DESY and the CMS experiment for providing me an opportunity to work in the perfect collaborative environment and to perform the measurement at the unprecedented collision energy.

I am very grateful to you Maria Aldaya Martin for inviting me to your group and introducing me to the top physics community, for granting me enough freedom to work in a way I like and on physics topics I preferred, as well as for continuously believing in me and my skills. I deeply appreciate your professional advices and expertise that you shared with me, while always being attentive and understanding in cases of need. Thank you very much.

I am very lucky that I could work with you James Keaveney, Carmen Diez Pardos, and Johannes Hauk. You were always open for discussions that helped me to deepen my understanding of particle physics and shape my measurements. In particular, thank you James Keaveney for broadening my perspective in top physics and beyond, thank you Carmen Diez Pardos for explaining me various experimental techniques, and thank you Johannes Hauk for teaching me good programming practices. All of you, thank you for having interest in working with me and for inspiring me to be a better scientist.

I am proud that I could work at DESY, where I have met many of excellent colleagues and friends. Working with all of you was a great pleasure. Besides people mentioned previously, I want to specifically thank Till Arndt, Oleksandr Zenaiev, Ievgen Korol, Alexander Grohsjean, Andreas Meyer, Ivan Asin Cruz, Ali Harb and Oleksii Turkot for numerous discussions on different topics related to my work.

I would like to thank my officemates: Till Arndt, Engin Eren, Svenja Pflitsch, Ievgen Korol, and Ivan Asin Cruz. Guys, we always had the coolest office at all iterations. My PhD years wouldn't be the same without you. Thank you, my friends.

Finally, I would like to heartfully thank my family. Thank you my dear parents for supporting me over the years and agreeing to all my decisions. I am thankful to my brother and his wife for constantly being proud of me. At last, I am eternally grateful to my beloved Viktoriia for her kindness, understanding, patience and calming words. All of you are the most precious contributors to my success.

Eidesstattliche Versicherung

Hiermit versichere ich an Eides statt, die vorliegende Dissertationsschrift selbst verfasst und keine anderen als die angegebenen Hilfsmittel und Quellen benutzt zu haben.

Die eingereichte schriftliche Fassung entspricht der auf dem elektronischen Speichermedium.

Die Dissertation wurde in der vorgelegten oder einer ähnlichen Form nicht schon einmal in einem früheren Promotionsverfahren angenommen oder als ungenügend beurteilt.

Hamburg, den 25.04.2018 Mykola Savitskyi

Declaration on oath

I hereby declare, on oath, that I have written the present dissertation by my own and have not used other than the acknowledged resources and aids.

Hamburg, 25.04.2018 Mykola Savitskyi

Some of the results presented in this thesis are shown or used in the following publications:

[176] CMS Collaboration, *Measurements of differential cross sections for $t\bar{t}$ production in proton-proton collisions at $\sqrt{s}$ = 13 TeV using events containing two leptons*, CMS-TOP-17-014, in preparation.

[9] CMS Collaboration, *Measurement of normalized differential $t\bar{t}$ cross sections in the dilepton channel from pp collisions at $\sqrt{s}$ = 13 TeV*, J. High Energ. Phys. **submitted** (2017), arXiv:1708.07638 [hep-ex].

[13] CMS Collaboration, *Measurement of the differential cross section for $t\bar{t}$ production in the dilepton final state at $\sqrt{s}$ = 13 TeV*, CMS-PAS-TOP-16-011 (2016), https://cds.cern.ch/record/2140061/.

[12] CMS Collaboration, *First measurement of the differential cross section for $t\bar{t}$ production in the dilepton final state at $\sqrt{s}$ = 13 TeV*, CMS-PAS-TOP-15-010 (2015), https://cds.cern.ch/record/2047866/.